STRUCTURAL STABILITY RESEARCH COUNCIL

ANNUAL STABILITY CONFERENCE

PROCEEDINGS

2006

STRUCTURAL STABILITY RESEARCH COUNCIL

PROCEEDINGS

2006 Annual Stability Conference

February 8-11, 2006
San Antonio, Texas

Reports on Current Research Activities

Published by the
Structural Stability Research Council
University of Missouri-Rolla

DISCLAIMER

The opinions, findings, conclusions, and recommendations expressed herein are those of the authors only and do not necessarily reflect the views of the Structural Stability Research Council, the editors, or the conference sponsors.

ISBN 1-879749-73-4

Proceedings Compiled by
Christina Stratman
SSRC Administrator

STRUCTURAL STABILITY RESEARCH COUNCIL
University of Missouri-Rolla
301 Butler-Carlton Hall
Rolla, MO 65409-0030
Phone: 573-341-6610
Fax: 573-341-4476
Email: ssrc@umr.edu
Web: www.stabilitycouncil.org

Printed in the United States of America

FOREWORD

I am now completing the 2006 Annual Meeting my 4th and final year of service as your SSRC Chair. With this pending change in SSRC leadership, I can fondly reflect on the continuing progress and achievements made by the Council during this term. We all share the laudable common objective of advancing structural stability knowledge through our professional and volunteer efforts. SSRC unites us in these endeavors and central purpose, with opportunities and unique channels to discuss, review, and disseminate new information. Of course, the solid organizational and numerous technical underpinnings already created by the entire SSRC and my predecessors were invaluable in forming an ever growing continuum of which we can all be proud., and to which I know each member has contributed in some manner .

It has been easy and wonderful to work in this capacity over these years with the entire Executive Committee, Task Group and committee Chairs, Headquarters staff , and membership. Everyone has been most cooperative to not only fulfill their regular operational responsibilities, but also creatively searching for new ways to effectively function in the still rapidly evolving environment of computational and communication technology, as well as professional, industrial and association realities.

Several key issues have dominated SSRC administrative efforts durign the start of this 21st century. The streamlining and relocation of our Headquarters to the University of Missouri-Rolla, under the very capable direction of Roger LaBoube and his administrative assistant, Christina Stratman, has been successful in efficiently maintaining the necessary SSRC support services with minimum expenses. The Council's overall budgeting process has become necessarily conservative due to the limited recurring income from dues, with greater dependence placed on self-generated revenue from continuing education short courses. In this manner, the Council's finances have become much more controllable and predictable. In general, I am greatly pleased that the SSRC

finances remain in a healthy state, thanks to the ongoing vigilance of the Finance Committee and its long-standing Chair, Don Sherman

Another important element of our restructuring has been the scheduling of SSRC Annual Stability Conferences (ASC) in conjunction with the AISC North American Steel Construction Conference, rather than as the stand-alone, independent events prior to 2001. This very positive collaboration has yearly positioned SSRC into a much broader forum with greatly reduced event planning/coordinating duties and related costs, while enabling the development of high-quality Council program tracks and meetings.

The fifth presentation of the prestigious Lynn S. Beedle Award will be made during this Feb. 8-11, 2006 Conference in San Antonio, TX , as well as the SSRC Vinnakota Award that continues to be instrumental in generating wide interest from graduate students and younger faculty researchers. Well deserved congratulations are extended to these Award recipients! The Council's Program Committee has again developed excellent sessions for all. In addition to the SSRC program track during the main sessions, a full day of Council Task Group meetings and supplementary technical presentations is set for Feb. 11th. These Proceedings document all these current developments and findings for the benefit of our Membership and the profession. The excellent work of the SSRC authors/presenters is appreciated, and it should be of great interest to both engineering researchers and practitioners.

SSRC has made good strides to stay abreast of the modern "electronic" world by upgrading the Council's Website, together with conducting more informational transmittals through email and the Website. I'm sure even more in this regard will be done in the coming years, possibly eventually reaching the availability in electronic form of ASC Proceedings, the Guide, and other popular documents.

The Council's many Task Groups, the heart of our organization, are actively pursuing stability-related challenges. A recent example of its practical implications is a number of our members being very instrumental, as part of a special joint AISC and SSRC Ad Hoc Committee, in drafting a newly expanded set of direct frame stability design provisions for the 2005 AISC Specification that has recently been released. These criteria enable, for the first time in the US use of notional loads, reduced member properties, other coefficients and limits with either first or second-order

analysis but without the traditional effective length K-factor in column design (K=1) for many cases. This represents another milestone development in steel column and frame design in the US to which SSRC has made significant input.

Initial work is proceeding for the next update of the Council's "flagship" *Guide to Stability Design Criteria for Metal Structures*, which is now in its 5th Edition. Task Groups will again be given specific assignments and issues to address for the Guide's many Chapters in order to maintain this well-recognized book as the state-of-the-art reference.

We have been fortunate to have attracted a number of enthusiastic younger members who have become active in the Council's ranks, and seek even more. It is only through our Membership's collective energy and knowledge that SSRC can progress towards further accomplishments in the future.

In closing, our thanks to AISC for again hosting the 2006 ASC in conjunction with the NASCC, Sam Easterling, Vice-Chairman of SSRC, Don Sherman, Chair of the SSRC Finance Committee and Reidar Bjorhovde, Past Chairman of SSRC for their assistance in selecting and organizing this 2006 SSRC ASC program and Proceedings, and to Christina Stratman for compiling the proceedings.

I am indeed honored to have been a part of SSRC's rich and illustrious history of now more than 60 years, and trust that you consider my recent service to the Council as its Chair to have been productive. With naturally close ties to our past but cognizant of future needs and constraints, SSRC remains as relevant as ever. With best wishes to all for continued successes.

Sincerely,

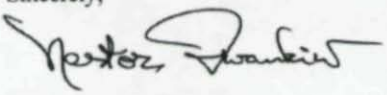

Nestor Iwankiw
SSRC Chairman

TABLE OF CONTENTS

TABLE OF CONTENTS

TABLE OF CONTENTS

TABLE OF CONTENTS

TABLE OF CONTENTS

TESTING OF WRAP-AROUND GUSSET PLATES IN TENSION

Bo Dowswell[1] *and Fouad H. Fouad*[2]

INTRODUCTION

Gusset plates are used in steel buildings to connect bracing members to other structural members in the lateral force resisting system. Horizontal bracing is commonly used to resist lateral loads in industrial structures and in commercial buildings where floor and roof diaphragms cannot carry the loads. Figure 1 shows a typical horizontal bracing connection at a beam-to-beam intersection. Where a horizontal brace is located at a beam-to-column intersection, the gusset plate must be cut out around the column as shown in Figure 2. These are known as wrap-around gusset plates.

[1] Principal, Structural Design Solutions, LLC, 2806 Ruffner Road, Suite 106, Birmingham, AL. 35210

[2] Professor and Chair, Department of Civil and Environmental Engineering, The University of Alabama at Birmingham, 1075 13th Street South, Birmingham, AL 35294

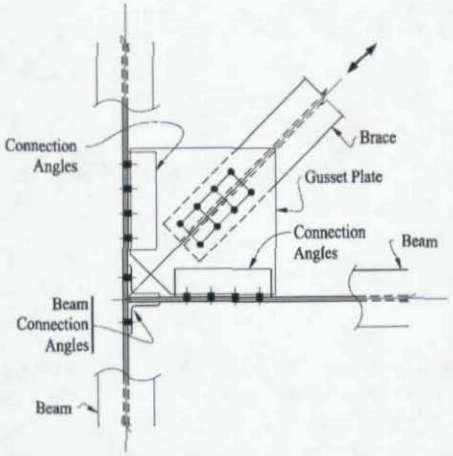

Figure 1. Horizontal brace connection at beam-to-beam intersection.

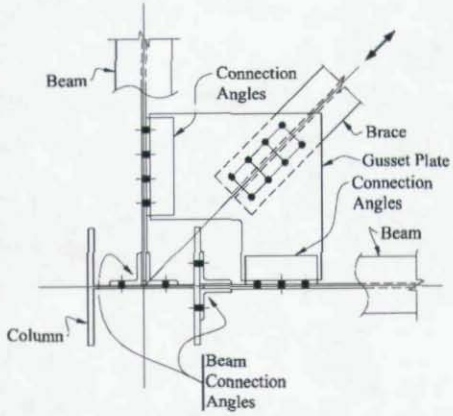

Figure 2. Horizontal brace connection at beam-to-column intersection.

Problem Statement

Due to the increasing complexity of building designs, horizontal bracing members are being used to resist very large forces. A large number of research projects have been dedicated to the analysis and design of standard gusset plates; however, there are no published methods for designing wrap-around gusset plates. Dowswell and Fouad (2006a) presented a review of the factors affecting the design of wrap-around gusset plates including modes of failure that are unique to such gusset plates. These issues need to be addressed so engineers can provide safe and economical designs.

Objectives

The purpose of this research was to gain a better understanding of the behavior of wrap-around gusset plates in tension.

EXISTING LITERATURE

A large number of research projects have been dedicated to the analysis and design of standard gusset plates. Failure modes for standard gusset plates have been identified and design procedures are well documented in the literature. However, failure modes unique to wrap-around gusset plates have not been studied nor are guidelines for their design available in the literature. Dowswell and Fouad (2006a) summarized the existing research on the stress distribution in standard gusset plates. Dowswell and Barber (2004) summarized previous experiments and finite element studies on gusset plates in compression. Dowswell and Fouad (2006b) reviewed the existing experimental research on statically loaded gusset plates.

EXPERIMENTAL PROGRAM

Five wrap-around gusset plates were tested monotonically in tension. The specimens were loaded until the load versus deflection curve started to level off due to the decreasing stiffness of the specimen. The load versus deflection data was recorded and plotted. The specimens had strain gages installed in the areas of the highest stresses. The strain

gage data was recorded and plotted versus the load. The specimens were loaded slowly, so the behavior could be observed during the tests.

Specimens

The specimens were fabricated by a shop experienced in steel structures and certified by AISC for complex steel buildings. The specimens were flame-cut to shape and had a re-entrant corner radius of 1 in. Five different gusset plates were fabricated. The dimensions are shown in Figure 3. By fabricating the specimens with short slots in each leg, and using finger-tight bolts, the in-plane moment restraint was released.

The plate material was A36. To determine the actual mechanical properties of the material, tension coupons were taken from the same parent plate as the specimens. The coupons were tested in accordance with ASTM A370 (2003). The 1/4 in. plates had a yield strength of 56.7 ksi, an ultimate strength of 71.2 ksi, and a modulus of elasticity of 30,000 ksi. The 3/8 in. plates had a yield strength of 48.8 ksi, an ultimate strength of 70.6 ksi, and a modulus of elasticity of 29,000 ksi. The thickness of each specimen was measured using a SONAGAGE II ultrasonic thickness meter by SONATEST. The results are shown in Table 1.

In order to measure the geometric imperfections in the plates, photographs were taken of each specimen showing the two longest edges. The out-of-flatness was measured graphically in the computer program *photo editor* relative to the plate thickness. The actual out-of-flatness was then determined by scaling the dimensions based on the actual plate thickness. The typical out-of-flatness resembled a half sine wave. The maximum out-of-flatness for all specimens was 0.028 in.

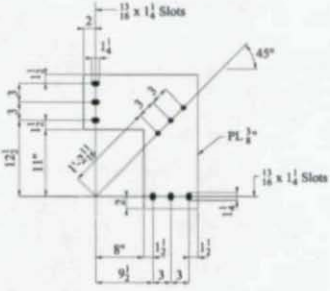

Specimen 2T

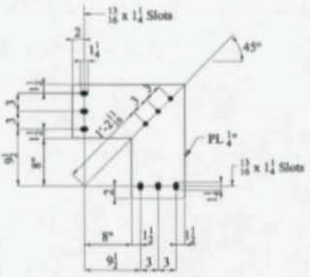

Specimen 6T

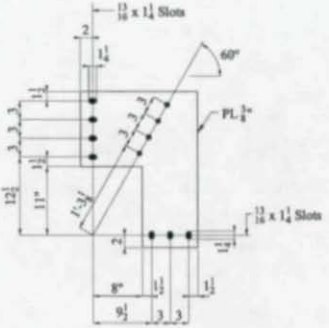

Specimen 8T

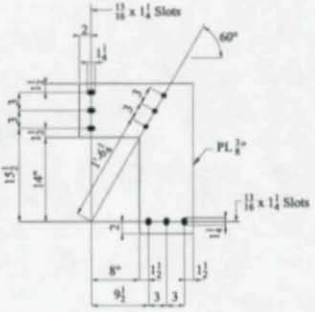

Specimen 9T

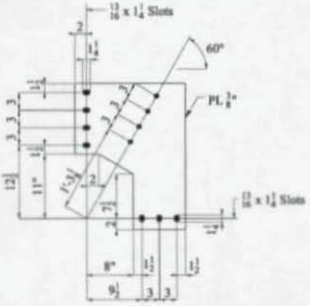

Specimen 10T

Figure 3. Fabrication drawings.

Table 1. Measured plate thickness.

Specimen	Nominal Thickness (in.)	Measured Thickness (in.)
2T	3/8	0.391
6T	1/4	0.235
8T	3/8	0.384
9T	3/8	0.380
10T	3/8	0.387

Instrumentation, Testing Machine, and Test Frame

Electrical strain gages were bonded to each specimen in the areas of the highest stresses. Elastic finite element models were used to locate the most highly stressed regions on the plate. The models showed that the highest stresses were longitudinal flexural stresses at the critical section of each leg. The critical section is at the re-entrant corner, perpendicular to the length of each leg. The gages were mounted according to Figure 4. The strain gage data was recorded using a MEGADAK data acquisition system.

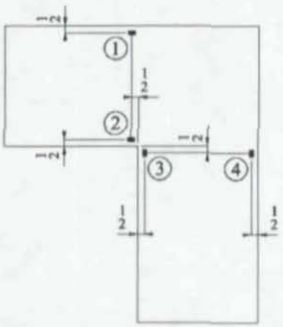

Specimens 2T, 6T, 8T, and 9T

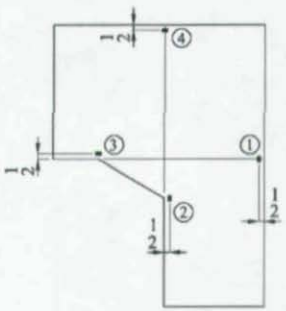

Specimen 10T

Figure 4. Strain gage locations.

A test frame fabricated specifically for testing the gusset plates is shown in Figure 5. Generally, the frame consisted of two parts: a brace member, and a frame simulating the beams shown in Figure 2. The channels marked M2, shown in Figure 6, acted as the brace member. To provide a knife-edge connection between the brace and the specimen, the channels had ¼ in. square bars tilted at 45° welded between the bolt holes. M3 acted as the beams, and was fabricated from 4x4x1/2 angles welded together at a right angle as shown in Figure 7. To provide a pinned boundary condition, the frame was required to pivot about the work point in the plane of the specimen. To accomplish this, a single 1½ in. diameter A490 bolt was used at the corner where the angles were welded together. The bolt was tightened to a finger-tight condition. This also allowed the same frame to be used with all of the specimens without adjusting the angle of the test frame. To provide a knife-edge connection, ¼ in. square bars were welded to the angles as with member M2. M1 and M4 were plates that attached the test frame members to the grips of the testing machine.

The loads were applied to the specimens using a 600 kip Tinius Olsen Super-L Universal Testing Machine with a Model CMH 289 Controler and a Model 290 Display. The test configuration with a specimen and the test frame mounted in the testing machine is shown in Figure 8.

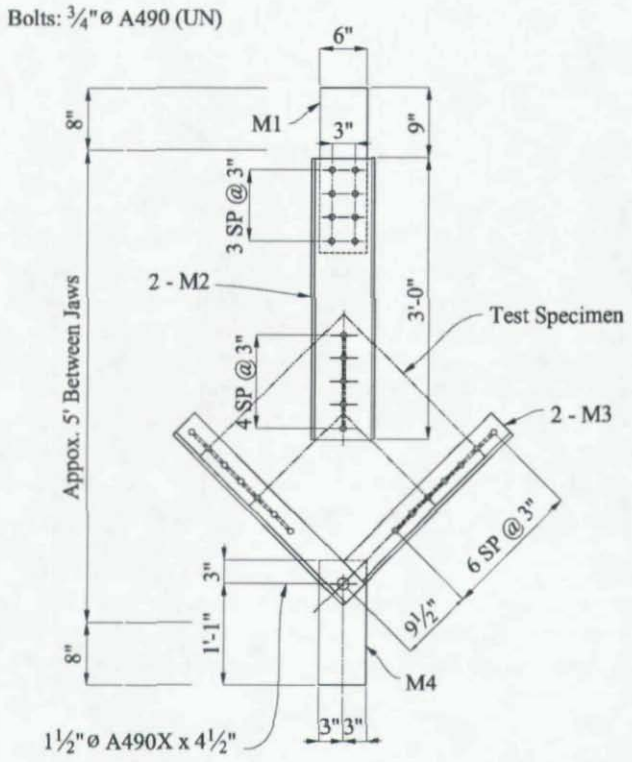

Figure 5. Assembled test frame.

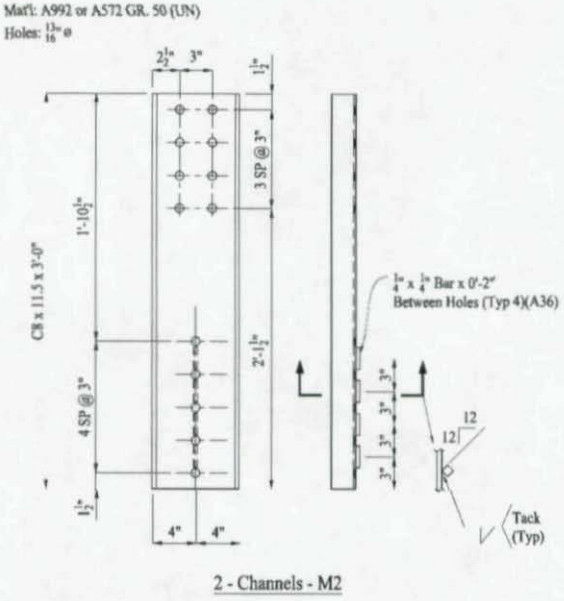

Figure 6. Fabrication drawing for M2.

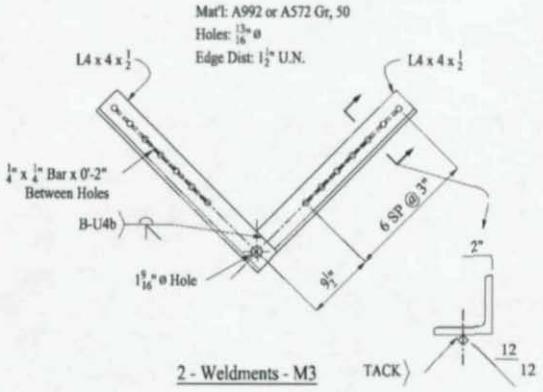

Figure 7. Fabrication drawing for M3.

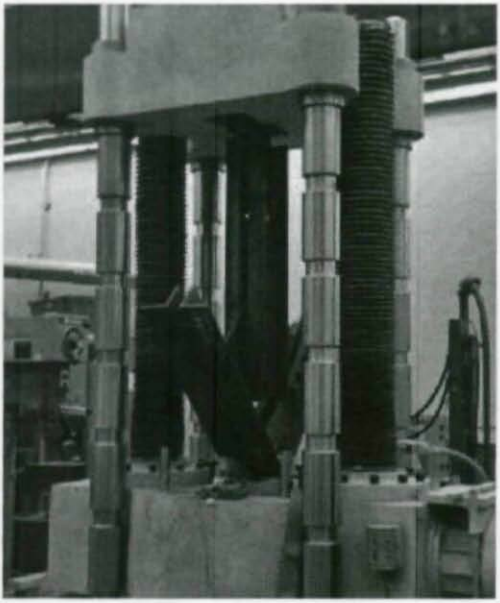

Figure 8. Testing machine and test frame.

RESULTS

Load vs. Deflection

All of the specimens behaved in a ductile manner, and none of the specimens fractured. Load vs. deflection plots for Specimens 2T and 9T are shown in Figure 9. The plots for the remaining specimens were similar in shape. The tests were generally characterized by a load-deflection curve divided into three parts. The first stage was dominated by bolt slippage and slippage of the loading grips. The second stage was the linear range, and the third stage was the nonlinear range. The tests were stopped when significant nonlinear deformations were observed.

Out-of-Plane Deformations

All of the specimens had a permanent out-of-plane deformation, which was at its maximum at the re-entrant corner, where the two legs met. This deformation for Specimen 2T can be seen in Figure 10. The lateral deformation was accompanied by twisting, indicating a lateral-torsional buckling type of failure. The maximum out-of-plane deformation for Specimen 10T occurred at approximately the mid-length of the diagonal cut at the re-entrant corner. The maximum permanent deformation was measured, with the following results: 1.2 in. for Specimen 2T, 1.2 in. for Specimen 6T, 0.6 in. for Specimen 8T, 0.7 in. for Specimen 9T, and 0.4 in. for Specimen 10T.

Stress Measurements

The strain gage data was plotted in terms of stress instead of strain so the yield point could be easily identified. Hooke's law was used to convert the strain gage readings to stresses. The disadvantage of this method is that the stresses displayed beyond the yield point of the material are not accurate and only give a qualitative measure of the strain. The term "apparent stress" is used in this paper to signify that the displayed stresses are not accurate over the full range of data.

The strain gage data for Specimens 9T and 10T are shown in Figure 11. The strain versus load behavior was similar for all of the specimens. From the strain gage data, it was determined that there were generally three stages of behavior. In the first stage, the material behaved elastically. In the second stage, the material still appeared to be approximately linear; however, it is clear from the data that much of the material is above the yield point. This behavior is due to a combination of residual stresses, strain hardening, biaxial stresses at the re-entrant corner, and stress redistribution due to yielding. When a substantial portion of the specimen had yielded, stiffness was lost, and the specimen buckled. The third stage is post-buckling. All of the specimens carried more load after buckling occurred.

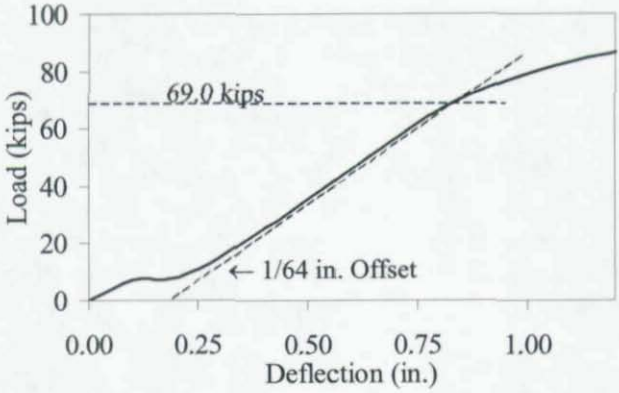

a. Specimen 2T

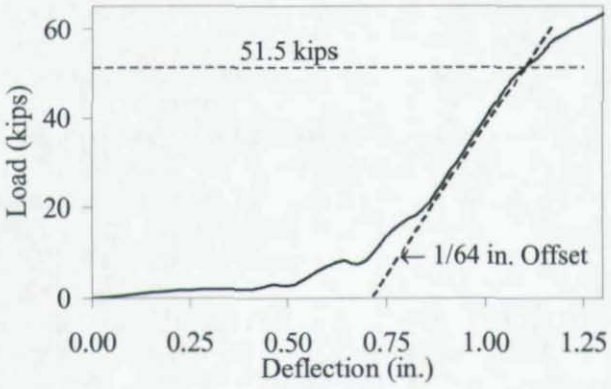

b. Specimen 9T

Figure 9. Load vs. deflection plots.

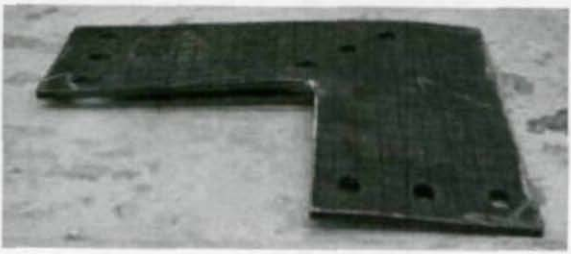

b. top view.

b. side view of longer edge.

Figure 10. Specimen 2T after test.

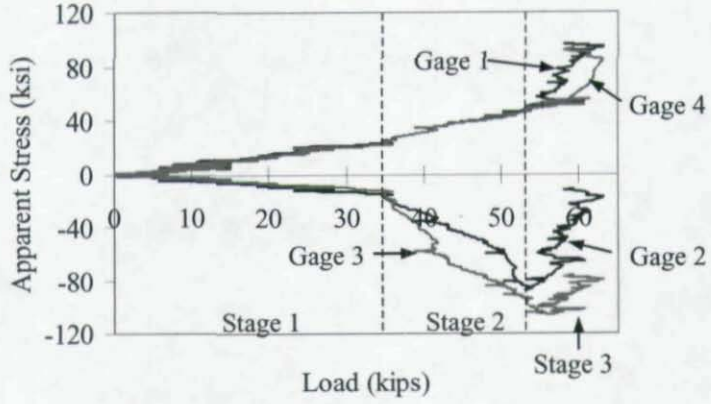

a. Specimen 9T

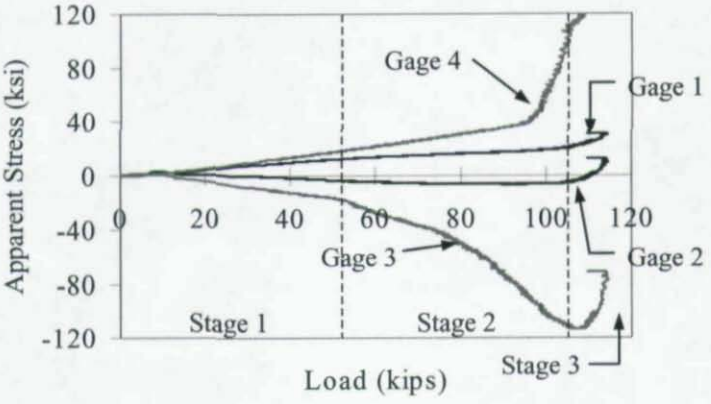

b. Specimen 10T

Figure 11. Apparent stress versus load plot for specimens 9T and 10T.

In the early stages of loading the strain gage readings for all of the specimens were linear. The readings for gages located at each edge of a particular gusset plate leg were approximately equal in magnitude, but were of opposite sense, indicating that the legs were in almost pure flexure.

Experimental Loads

Because the load vs. deflection curves did not have a well-defined yield point, the experimental yield loads, P_{ey} were determined using a 1/64 in. offset relative to the linear portion of the load vs. deflection plots as shown in Figure 9. The yield load is where the load vs. deflection curve crosses the 1/64 in. offset line. The results are shown in Table 2

Table 2. Test loads.

Spec. No.	Test Loads (k)	
	P_{ey}	P_{eu}
2T	69.0	89.9
6T	42.3	53.6
8T	85.30	91.20
9T	51.5	63.6
10T	96.2	109.8

P_{ey} test yield load determined using a 1/64 in. offset.

P_{eu} maximum test load

CONCLUSIONS

Five wrap-around gusset plates were tested in tension. The results of the tests will help to provide a better understanding of the behavior of these gusset plates. The experiments indicated that wrap-around gusset plates are subject to limit states common to flexural members. In the early stages of loading the strain gage readings were linear. The readings for gages located at each edge of a particular gusset plate leg

were approximately equal in magnitude, but were of opposite sense, indicating that the legs were in almost pure flexure. All of the plates had a permanent out-of-plane deformation due to inelastic buckling in the vicinity of the re-entrant corner. The out-of-plane deformation was accompanied by twist of the gusset plate legs, indicating a lateral-torsional buckling failure.

ACKNOWLEDGEMENTS

The test frame and specimens were fabricated and donated to the project by Gipson Steel, Inc. Bell Steel Company supplied the bolts. The testing was performed in the structures laboratory at the Department of Civil and Environmental Engineering at The University of Alabama at Birmingham. The assistance of lab supervisor, Richard Hawkins was invaluable and is appreciated.

REFERENCES

ASTM A370-03a (2003), "Standard Test Method and Definitions for Mechanical Testing of Steel Products," ASTM International, West Conshohocken, PA.

Dowswell, B., and Barber, S. (2004), "Buckling of Gusset Plates: A Comparison of Design Equations to Test Data," *Proceedings, 2004 Annual Stability Conference,* Structural Stability Research Council, pp. 199-221.

Dowswell, B. and Fouad, F. H. (2006a), "Factors Affecting the Capacity of Wrap-Around Gusset Plates," Submitted to AISC Engineering Journal.

Dowswell, B. and Fouad, F. H. (2006b), "Wrap-Around Gusset Plates in Compression," Submitted to AISC Engineering Journal.

On the use of fiber reinforced composites to improve structural ductility in steel flexural members

N. B. Accord[1], C. J. Earls[2], K. A. Harries[3]

ABSTRACT

An innovative use of fiber reinforced polymer (FRP) composite materials, to control the manifestation of local buckling in a steel section during plastic hinging is discussed in the present paper. Specifically, details related to how the high stiffness and linear behavior of FRP materials may be utilized to provide "bracing" against flange local buckling (FLB), in a way that strategically leverages the unique mechanical properties of each material, FRP and steel, in an efficient application domain, are discussed. This research is analytical in nature; employing the commercially available finite element software system ADINA.

INTRODUCTION

The past several years have seen increased use of fiber reinforced polymers (FRP) to help strengthen and repair concrete structures through retrofit programs involving the application of FRP strips and thin plates (Bakis et al. 2002). In comparison to

[1] Research Associate, Department of Civil & Environmental Engineering, University of Pittsburgh, Pittsburgh, Pennsylvania, 15261.
[2] Chairman and Associate Professor, W. K. Whiteford Faculty Fellow, Department of Civil & Environmental Engineering, University of Pittsburgh, Pittsburgh, Pennsylvania, 15261.
[3] Assistant Professor, Department of Civil & Environmental Engineering, University of Pittsburgh, Pittsburgh, Pennsylvania, 15261.

the use of FRP-concrete composite systems, relatively little work has been done on applications involving FRP-steel composites. One promising application area for the latter case involves enhancing the ductility in steel connection regions through the use of FRP reinforcing strategies. In such a case, the FRP-steel composite system employed at the member level can utilize the unique properties of the FRP material, in conjunction with the properties of the underlying steel element, to efficiently stabilize the member cross-section (i.e. enforcing a nodal line within a critical plate component). It appears that this approach is unusual; few related studies are found in the literature.

Ekiz et al. (2004) demonstrate the use of carbon FRP (CFRP) wraps to enhance the plastic hinge behavior of double-channel members modeled on chord members of a special truss moment frame. Two cases are considered, one where the entire gross cross section is wrapped, the second where only the extending flanges are wrapped; both methods exhibited improved behavior of the hinge as compared to unwrapped specimens. The presence of the CFRP wrap increased the size of the yielded plastic hinge region, inhibited the occurrence of local buckling and delayed the onset of lateral torsional buckling. These effects resulted in reduced strain demands, increased rotational capacity, and improved energy dissipation capacity in the plastic hinge region.

Sayed-Ahmed (2004) performed a finite element based study of the use of CFRP strips on the compression region of the web sections of I-beams. This research is most germane to the current discussion since it had as its aim the improvement of plate response to compressive loading (although this was not clearly demonstrated – as discussed below). Four different I-sections with varying web-depth to thickness (h_w/t_w) slenderness ratios were investigated. The finite element analyses showed that through the use of the CFRP strips, the local buckling of the

beam webs was delayed, resulting in increases in critical load and ultimate strength. The critical local buckling load was shown to increase 20-60%, and subsequently the ultimate strength was increased by 2-9% (for the varying depth to thickness ratios). It is noted that Sayed-Ahmed placed the FRP strip at the mid-depth of the web; and thus was not actually focusing on the case of compression buckling since the FRP strip was located at the cross-sectional neutral axis (i.e. precisely the location of zero stress).

GLASS FIBER REINFORCED POLYMER (GFRP)

GFRP composite materials are created by a process wherein glass fiber strands and woven fabrics are wetted-out and cured within a polymeric matrix. The fibers used in the FRP are higher in strength and in stiffness as compared with the mechanical properties of the polymeric matrix material. Generally, the fibers in GFRP are aligned in a fashion that permits them to contribute strength and stiffness within the principle stress direction associated with the dominant structural response of the element under consideration.

The polymeric matrix serves to confine, protect, and transfer force into, and between, the glass fibers. Epoxy, polyester and vinylester resins are commonly used for GFRP applications. While GFRP materials possess reasonably large material stiffness in directions coinciding with the principal fiber orientation, the modulus of elasticity is still approximately one order of magnitude less than that of steel. As a result of this modular mismatch, GFRP-steel retrofit strategies that rely on strength enhancement through reinforcement of the steel section by direct shear transfer into the GFRP will invariably be inefficient. What is sought in the present research program is a reinforcing methodology that leverages the important strength and stiffness characteristics of each material as a means for

realizing significant performance enhancement of entire cross-sections; rather than modest incremental strength gains in constituent cross-sectional components.

The present research employs a program of investigation based on the application of nonlinear finite element modeling strategies implemented within the ADINA software system. Specifically, GFRP strips are applied longitudinally to the compression flange of cantilever steel I-shaped beams. As noted above, GFRP has a modulus of elasticity that is approximately one order of magnitude less than steel. The present paper demonstrates that this under-match in stiffness is an asset within the proposed reinforcing context since it allows the stress levels in the GFRP to remain low; even when the underlying steel is flowing plastically. Notionally this is a benefit since the flexural resistance within bonded GFRP strips is then still available to provide bracing against plate buckling manifestations in the underlying steel.

BEAM GEOMETRY

The beams modeled in this study employed bonded 25.4 mm (1") x 6.35 mm (0.25") GFRP strips on the compression flange of cantilevered steel I-section beams. A flexible transition zone was employed at the interface between the steel and the GFRP in order to model an adhesive bond layer that might be used in the practical application of the proposed approach. The GFRP strips were oriented so that their principal fiber orientation corresponded with the beam longitudinal axis. The GFRP strips were subsequently shifted to several different cross-sectional locations along both the top and the bottom of the compression flange of the I-section as a parameter of investigation. In addition, the longitudinal length of the GFRP strips (measured from the fixed end of the cantilever) was also varied as a

parameter for study in the beams; information in this regard can be found in Figure 1.

The steel I-sections considered herein has a depth of 381mm (15"), flange width of 152.4 mm (6"), and web thickness of 6.35 mm (0.25"). Other beam geometrical properties, varied as part of the current work, are detailed in Figure 1; along with the general beam geometry. All of the beams included in the study were 3.81m (150") in length. The interfacial zone between the GFRP material and the underlying steel was modeled in a simplified way to be consistent with an adhesive layer. This layer was idealized as a 1.27 mm (0.05") thick linear elastic, isotropic zone of material placed between the steel I-section flange and the FRP strips.

In addition to the GFRP reinforced beams, two bare steel beams were modeled as baseline cases representing the unreinforced condition; from which any improvements in performance could be gauged. These models had no GFRP strips, and their geometric proportions and material properties were identical to the steel components used in the GFRP reinforced beams. These beams dimensions are shown in Figure 1; along with the model naming convention adopted herein.

FINITE ELEMENT ANALYSIS

The finite element method forms the basis for the research program reported on herein. Specifically, the commercially available software package, ADINA (ADINA 2003), is used in the current work. All models used in the current work consider both geometric (large rotation/small strain) and material (multi-linear plasticity for steel) nonlinear effects. The nonlinear solution strategy used in all of the modeling is based on a combined method of load and displacement control wherein the spherical constant arc-length method (Crisfield 1981) is used in

regions along the equilibrium path far from critical points, and a scheme based on constant increments of external work is employed within regions along the equilibrium path that are close to critical points (Bathe and Dvorkin 1983).

Figures 2 and 3 depict the finite element analogs of the cantilever beam geometry treated. The boundary and loading conditions used were chosen so as to create an accurate model of a cantilever beam subjected to a concentrated load. The fixed end of the beam was fully fixed along all lines and surfaces including those of the attached FRP; thus affecting the case of "perfect bond" at the beam's fixed end. The free end of the cantilever was free; except for lateral bracing of the web to prevent out of plane movement. A concentrated force was applied to the free end of the cantilever at the lower flange-web junction (see Figure 2).

The mesh of the steel I-section was constructed using 4-node ADINA MITC4 shell finite elements. This shell employs an assumed strain approach to improve its ability to properly model transverse shearing effects within the element; especially as the shell element becomes thin. Two-node rigid beam elements were placed along plate centerlines of the cross-section at the free end of the cantilever to ensure proper load transfer from the load point to the entire beam cross-section (i.e. to reduce any shear-lag effects along the member length by fully activating the cross-section at the loaded free end). Fully integrated 8-Node continuum finite elements were used to model the volumes of the GFRP and the interface material.

Finite element models of the steel portion of the beam were created from meshes of nonlinear shell finite elements whose mechanical properties were made to be consistent with A36 steel (250 MPa minimum specified yield strength). To obtain these

material properties the stress-strain relationship of A36 steel was directly inputted into the ADINA program. Precise material properties of the GFRP are less clear due to the variety of manufacture specific considerations. For the purpose of the present study, the GFRP mechanical properties were modeled to match the material properties found through tests performed by Yulismana (2005) at the University of Pittsburgh. These results indicated that the GFRP material had a compression modulus of approximately 27.6 GPa (4000 ksi). The interface (adhesive) material was modeled as an isotropic elastic material with a modulus ¼ that of the GFRP material. This interfacial stiffness was approximated as an upper bound from the average modulus values for adhesives as found in manufacturer brochures.

To ensure that physically meaningful equilibrium paths are followed in the post buckling range of loading a displacement imperfection was superimposed on the nonlinear models used in the present work. To create the proper initial imperfections a linearized eigenvalue buckling analysis (Bathe and Dvorkin 1983) was performed on the beams to identify reasonable approximations to the dominant buckling modes of the structural elements. The displacement field corresponding to the lowest energy eigenmode (mode 1) was adopted in this study. The imperfection from this mode was then scaled by a factor of L/1000 (L= length of beam) and applied to the nonlinear model, creating an appropriate initial imperfection. The L/1000 factor was selected based on permissible out-of straightness specified in the Code of Standard Practice for Steel Buildings and Bridges (AISC 2000). Results from a verification study validating the current modeling approach are presented elsewhere (Accord 2005, Accord and Earls 2005).

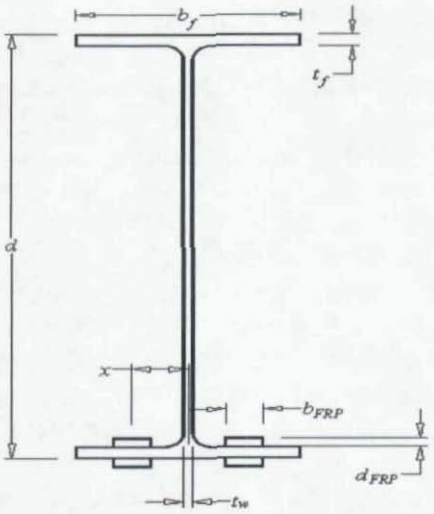

Figure 1 Schematic of geometric properties of modeled beams

	D (mm)	b_f (mm)	t_f (mm)	t_w (mm)	L (m)	L_{FRP} (m)	b_{FRP} (mm)	d_{FRP} (mm)	x (mm)
Steel1	381	152.4	10.16	6.35	3.8	-	-	-	-
Steel2	381	152.4	5.08	6.35	3.8	-	-	-	-
B9	381	152.4	10.16	6.35	3.8	3.8	25.4	6.35	38.1
B10	381	152.4	10.16	6.35	3.8	3.8	25.4	6.35	38.1
B11	381	152.4	10.16	6.35	3.8	3.8	25.4	6.35	50.8
B12	381	152.4	10.16	6.35	3.8	3.8	25.4	6.35	63.5
B13	381	152.4	10.16	6.35	3.8	3.8	25.4	6.35	25.4
B14	381	152.4	10.16	6.35	3.8	3.8	25.4	6.35	12.7
B15	381	152.4	10.16	6.35	3.8	1.9	25.4	6.35	38.1
B16	381	152.4	10.16	6.35	3.8	.76	25.4	6.35	38.1
B17	381	152.4	5.08	6.35	3.8	3.8	25.4	6.35	50.8
B18	381	152.4	5.08	6.35	3.8	3.8	25.4	6.35	63.5
B19	381	152.4	5.08	6.35	3.8	3.8	25.4	6.35	25.4
B20	381	152.4	5.08	6.35	3.8	3.8	25.4	6.35	12.7
B21	381	152.4	5.08	6.35	3.8	1.9	25.4	6.35	38.1
B22	381	152.4	5.08	6.35	3.8	.76	25.4	6.35	38.1

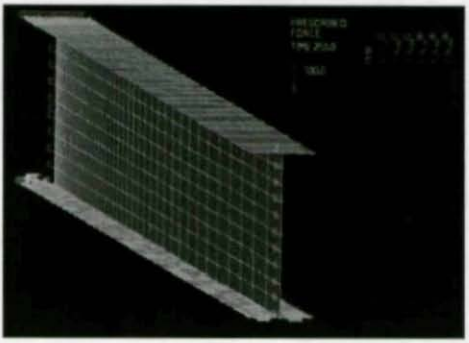

Figure 2 Depiction of finite element model showing loading and boundary conditions

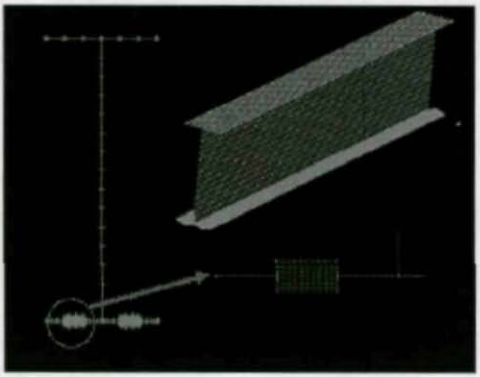

Figure 3 Depiction of finite element idealization of FRP-steel composite beam

RESULTS

The results of the present study are presented in the form of load-deflection plots coinciding with different parametric combinations of GFRP strip location and bonded length. The load-deflection plots depict beam response under the action of

the concentrated load applied gradually to the free end of the cantilevered beams as measured from the unloaded, undeformed state. The deflection values in the plots represent the deflection of the free end of the beams.

Figure 4 shows the load-deflection plot for the beams which have a flange thickness of 10.2 mm (0.4") (i.e. Beams 9-16). The bare steel model response is plotted along with the various steel-GFRP model results so as to highlight the effects of varying the cross-sectional locations of the GFRP strips. Figure 5 shows the load-deflection plots of the bare steel model, and the models where GFRP strips were positioned at the centerline of the flange outstands (x = 38.1 mm), while the length of the strips along the longitudinal axis (measured from the fixed end) is varied. In considering the effects of increased compression flange thickness, additional beam models were considered. Figures 6 and 7 show the load-deflection plots for Beams 10, 17, 18, 19, 20, 21, 22 and bare steel; these beams have similar geometrical properties and GFRP strip layouts to the beams described above except their flange thickness is reduced to 5.1 mm (0.2").

Moment-rotation plots (Accord 2005) were generated for all of the cases mentioned above so that cross-sectional rotation capacity (R) could be ascertained for the purposes of gauging structural ductility. The rotation capacity values for the beams tested are provided in Table 1.

Table 1 Rotation capacities for modeled beams

	R
Steel 1 / 2	1.2 / 0.1
B9	5.7
B10	3.6

Table 1 cont'd

B11	7
B12	7
B13	4.1
B14	4.5
B15	6.5
B16	3.7
B17	4.7
B18	5.5
B19	2.7
B20	2.5
B21	3.3
B22	1.8

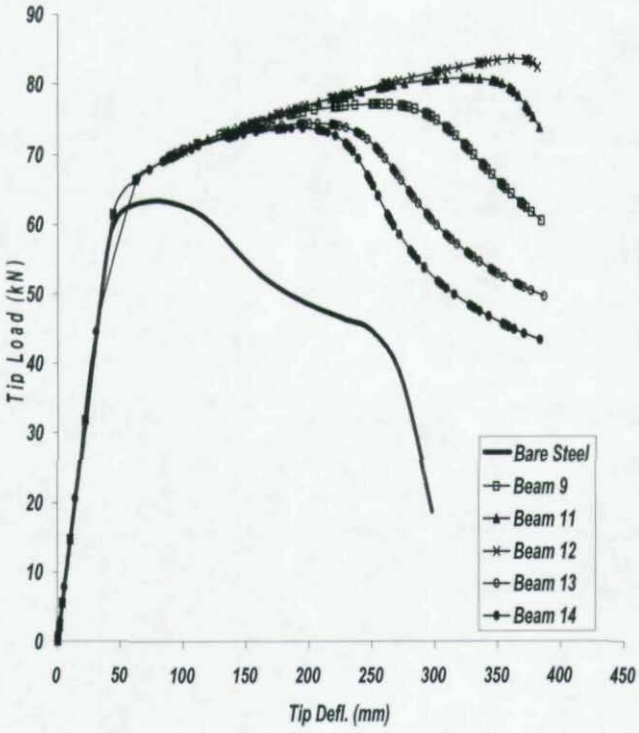

Figure 4 Load-deflection plot showing results as FRP strips are positioned across the width of the compression flange, t_f= 10.2 mm (0.4")

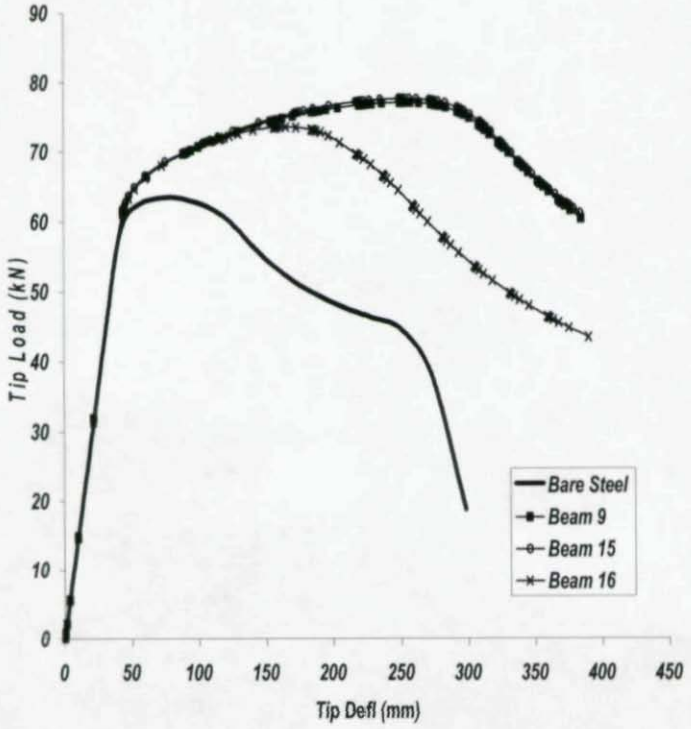

Figure 5 Load-deflection plot showing results as FRP strip longitudinal lengths are varied along the compression flange, t_f = 10.2 mm (0.4")

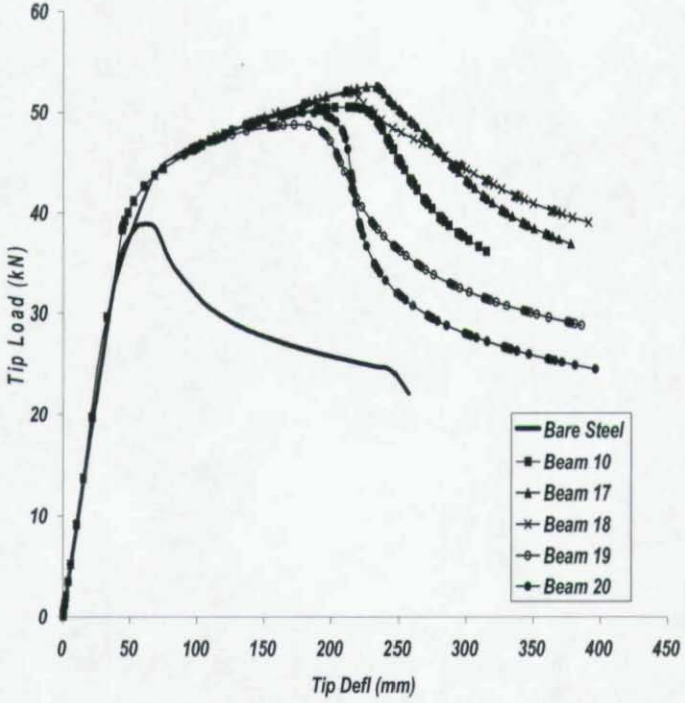

Figure 6 Load-deflection plot showing results as FRP strips are positioned across the width of the compression flange, t_f = 5.1 mm (0.2")

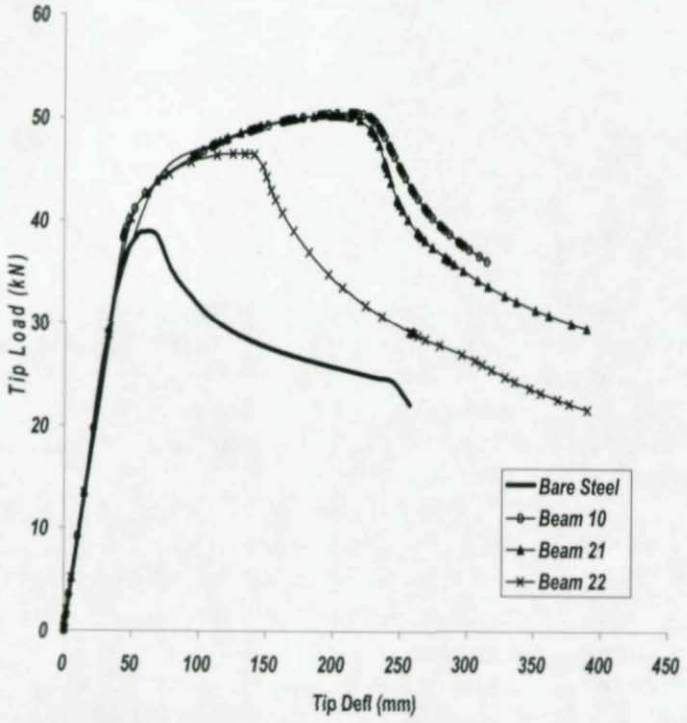

Figure 7 Load-deflection plot showing results as FRP strip longitudinal lengths are varied along the compression flange, t_f = 5.1 mm (0.2")

DISCUSSION

The bare steel beams modeled in the current research display a much different physical behavior than that of the GFRP reinforced steel beam models. The bare steel models for both the 10.2 mm and 5.1 mm flange thicknesses experienced severe compression flange local buckling in the plastic hinge region of the beam, as the ultimate load was achieved. The onset of the

local buckling in the compression flange prompted local buckling in the adjacent web-portion; also in compression. However, the bare steel beams did not experience significant lateral deflections in the compression flange. This was precisely the opposite behavior from what was displayed in the GFRP reinforced cases. The GFRP reinforced members with 10.2 mm flange widths and full length GFRP strips (Beam 9, Beam 11, Beam 12, Beam 13, and Beam 14) exhibited a much different physical behavior during loading. These beams did not experience local buckling. At loads approaching ultimate, the beams began to deflect laterally and twist, indicating that the GFRP reinforcement was stabilizing the beam against local buckling and forcing it into a higher order mode: in this case, lateral-torsional buckling. Similar trends were obtained from the FRP reinforced flanges with 5.1 mm thickness. It is pointed out that even at the very large rotation capacities observed in the GFRP reinforced steel members, the GFRP strains were relatively low and at no time did the GFRP stresses and adhesive stresses exceed approximately one half of their assumed ultimate capacities (thus supporting the use of linear-elastic material models for the GFRP and adhesive layer).

The load-deflection plots gleaned from the current finite element modeling effort show that a higher ultimate load is achieved with the addition of GFRP strips to the bare steel. In addition the plots indicate that the effectiveness of the GFRP reinforcing can be optimized by strategic placement (widthwise) and sizing (lengthwise) of the GFRP strips.

CONCLUSIONS

Based on the results of this research, it appears that the addition of longitudinally oriented GFRP strips to the compression flange of cantilevered steel beams with an I-shaped cross-section may serve to effectively brace constituent cross-sectional plate

components against the occurrence of local buckling during plastic hinging; thereby increasing the structural ductility of the member.

Results from the present work also indicate that varying the placement of the GFRP strips along the compression flange width, and adjusting the GFRP strip bonded length along the beam longitudinal axis, can significantly improve the effectiveness and efficiency of the GFRP-steel system. Consistent with this notion, it appears that placing the GFRP strips closer to the compression flange tips in I-shaped beams maximizes the effectiveness of the system; presumably since the flange tips experience the greatest deflection during local buckling and thus derive the greatest benefit from increased resistance to this action.

While it is that the underlying assumptions employed in the current research are significant, particularly that of strain compatibility across the FRP-steel interface (e.g. perfect bond between steel and GFRP) the results from this work point out the merits of the concept and highlight the value in performing further investigation to determine the practicality of this reinforcing approach. Clearly a detailed experimental program would be requisite for any specific design recommendations to be made.

REFERENCES

Accord, N. (2005) On the use of fiber reinforced composite elements to enhance structural steel member ductility, *M.S. Thesis*, Department of Civil & Environmental Engineering, University of Pittsburgh, Pittsburgh, Pennsylvania.

Accord, N. B., Earls, C.J. (2005, in Review) On the Use of Fiber Reinforced Polymer Composite Elements to Enhance Structural

Steel Member Ductility, *Journal of Composites for Construction*, American Society of Civil Engineers, Reston, Virginia.

ADINA (2003) Theory and Modeling Guide, Volume I: ADINA, *Report ARD 03-7*, ADINA Research and Development, Inc., Watertown, MA.

AISC (2000) Code of Standard Practice for Steel Buildings and Bridges, American Institute of Steel Construction Inc., Chicago, Illinois.

Bakis, C.E., Bank, L.C., Brown, V.L., Cosenza, E., Davalos, J.F., Lesko, J.J., Machida, A., Rizkalla, S.H. and Triantafillou, T.C. (2002) Fiber-Reinforced Polymer Composites for Construction – State-of-the-Art Review, *ASCE Journal of Composites for Construction*, Vol. 6, No. 2, pp 73-87.

Bathe, K.J. and Dvorkin, E. (1983) On the Automated Solution of Nonlinear Finite Element Equations, *Computers and Structures*, Vol. 17, No. 5-6, pp. 871-879.

Crisfield, M.A., (1981) A Fast Incremental/Iterative Solution Procedure that Handles 'Snap-Through,' *Computers & Structures,* Vol. 13, Pergamon Press Ltd., Great Britain, pp. 55-62.

Ekiz, E., El-Tawil, S. Parra-Montesinos, G. and Goel, S. 2004. Enhancing Plastic Hinge Behavior in Steel Flexural Members Using CFRP Wraps *Proceedings of the 13th World Conference on Earthquake Engineering*, Vancouver, August 2004.

Sayed-Ahmed, E.Y. (2004) Strengthening of Thin-walled Steel I-Section Beams Using CFRP Strips. *Proceedings of the 4th*

Advanced Composites for Bridges and Structures Conference, Calgary, Canada.

Yulismana, J. (2005) Experimental study of the behavior of fiber reinforced polymer deck systems, *Ph.D. Dissertation*, Department of Civil & Environmental Engineering, University of Pittsburgh, Pittsburgh, Pennsylvania.

THE INFLUENCE OF WEB-PLUMBNESS IN HORIZONTALLY CURVED STEEL I-GIRDER BRIDGES

Brandon W. Chavel[1], Thomas D. Howell[2], Christopher J. Earls[3]

INTRODUCTION

Horizontally curved steel I-girder bridge systems fit well into the space constrained context of the urban infrastructural environment as a result of the ability of these systems to facilitate difficult roadway alignments while at the same time maintaining a compact geometric footprint. Such flexibility in terms of space requirement in this bridge type may be leveraged to avoid particularly difficult right-of-way acquisition scenarios while at the same time eliminating potential interferences with existing, adjacent infrastructure assets. However, this versatility does come at a cost: curved steel I-girder bridge systems require more

[1] Doctoral Candidate, Dept. of Civil and Environmental Engineering, Univ. of Pittsburgh, PA 15261, USA. Structural Designer, HDR Engineering, Inc., 3 Gateway Center, Pittsburgh, PA 15222, USA, Brandon.Chavel@hdrinc.com.
[2] Research Assistant, Dept. of Civil and Environmental Engineering, Univ. of Pittsburgh, Pittsburgh, PA 15261, USA, tdh3+@pitt.edu.
[3] Chairman and Associate Professor, William Kepler Whiteford Faculty Fellow, Dept. of Civil and Environmental Engineering, 949 Benedum Hall, Univ. of Pittsburgh, Pittsburgh, PA 15261, USA, earls@engr.pitt.edu.

engineering than their straight girder counterparts. In addition, issues related to efficient construction staging and sequencing become exceedingly important within the context of horizontally curved steel I-girder bridges.

One issue that has proved particularly vexing for these systems relates to the understanding of the effects that web-plumbness may play in terms of its impact on curved steel I-girder bridge performance. Specifically when should the engineer/designer worry about a web-out-of-plumb condition eroding the performance of a curved steel I-girder bridge system? The present research findings from a series of detailed nonlinear finite element analyses are aimed at providing insight into the web-plumbness issue. Figure 1 illustrates the difference between what is considered web-plumb and web out-of-plumb in design practice.

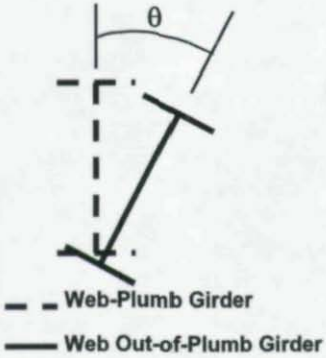

Figure 1 – Web-Plumb and Web Out-of-Plumb Classification

The current research uses the designs from a series of typical curved steel I-girder bridges (based on actual structural drawings) in order to identify a representative bridge system of suitable overall dimensions and cross-sectional proportions to serve as a subject structure for the research described herein. The aim of this work is to investigate what effect, if any girder web out-of-plumbness has on the response of sub assemblages, and entire bridge systems, that are based on dimensions of the subject structure. Specifically, the effects of out-of-plumb webs

on the construction induced response of the system are investigated: changes in cross-frame demands and in girder flange stresses as a result of out-of-plumbness are considered.

The current paper presents an accounting of the changes in girder flange stresses and cross-frame demands for a representative three-span continuous, six-girder full bridge system, as various degrees of web out-of-plumbness are introduced.

RESEARCH MOTIVATION

There are two generally accepted final positions of horizontally curved steel I-girder bridge cross-section at the time of initial placement into service: girder webs vertically out-of-plumb or girder webs vertically plumb; the latter historically being more popular with Owners. For the purposes of the current discussion, final position of the bridge cross-section is defined herein as the bridge configuration assumed after all dead loads have been imposed on the structure. The girder webs will be vertically out-of-plumb at the final position when the girders and cross-frames are both detailed for the web-plumb position at the no-load condition (approximately achieved in a practical sense through the use of intermittent falsework support). Cross-frame member lengths are determined assuming that the girders are to remain plumb in the no-load position (i.e. not displaying any displacements or rotations due to self-weight or additional dead loads). Currently, there are no specification provisions (AASHTO 1993, 2003, and 2005) that would limit the amount of dead load out-of-plane cross-sectional rotation. As a result, it is simply not clear what is acceptable in practice; a condition that may sometimes lead to misunderstandings and subsequent litigation.

One interesting byproduct of this condition is that Owners may place a premium on ensuring that girder webs are plumb under the action of full dead loading. One currently employed strategy for attempting to achieve this desired condition is described as follows. The girders and cross-frames are both detailed to a condition in which the girders are

out-of-plumb in the supported, or no-load condition; and then subsequently rotate to a plumb position upon the application of dead loads. Cross-frame member lengths are calculated based on the displacements of the structure due to applied dead loads, including steel self-weight. Because curved I-girders rotate out-of-plane due to their curvature when unsupported, this rotation must be countered by fabricating a twist into the girder web about the longitudinal axis of the girder. Due to the complexity and costs associated with the fabrication of this twist, it is rarely done in practice, and as an alternate approach, only the cross-frames ultimately are detailed to fit the girders in the condition in which girder webs are vertically plumb at the final position. Such an approach obviously necessitates the imposition of additional forces during construction to bring the misaligned members into position. This method of forcing disparately detailed members together is referred to herein as "inconsistent detailing."

Inconsistent detailing results in cross-frame member lengths that are incompatible with girders in the theoretical no-load position at the time of erection. Therefore, the cross-frame members will have to be forced into place, twisting the girder webs out-of-plumb during erection. The direction of the out-of-plumb twist will be in the opposite sense of the natural out-of-plane rotation that will occur in the girders upon the application of dead load. Since the cross-frames are being forced into position, locked-in girder and cross-frame member stresses will develop; these are typically unaccounted for by the designer. This condition can result in significant construction difficulties because the girders must be twisted and pulled with cranes in the field to fit with the cross-frames; this required twisting can be difficult to achieve when the flanges of the cross-section are stocky; or result in buckling of slender flanges (Chavel and Earls 2001).

These heroic lengths in stemming girder web out-of-plumbness lead to a great deal of complication, added expense, and unnecessary litigation; all due to a lack of understanding regarding the importance of the issue. The lack of guidance in this regard coming from the current ASSHTO LRFD obviously does nothing to allay this situation (AASHTO 1993, 2003, 2005). Although it is pointed out that the current AASHTO

LRFD Specification, with 2005 interims (AASHTO 2005), does somewhat address the issues in regard to detailing and erection of horizontally curved steel I-girder bridges. The current specification defines two intended positions of horizontally curved I-girder bridges as either: girder webs theoretically plumb; or girder webs out-of-plumb. Discussion is provided, in the commentary, as to how to achieve these final girder positions, such as detailing both girders and cross-frames for web-plumbness at no-load, or steel dead load, and detailing the girders and cross-frames inconsistently to achieve web-plumbness at the no-load condition. However, no definitive guidance is given as to which detailing methods should be used, or as to when girder web-plumbness needs to be achieved.

PRIOR RESEARCH

An evaluation of the structural capacity of: individual straight and individual curved, simple-span steel I-girders rotated out-of-plane has been previously reported on by the authors (Chavel and Earls 2005). Differences in response in the rotated beams were compared with equivalent, un-rotated beam. The straight I-girders considered in this earlier study has a span length of 12ft (3.7m) and a web depth of 17in (432mm), while the curved I-girders has a span length of 16.4ft (5.0m), a radius of curvature of 65.6ft (20m), and a web depth of 12in (307mm).

Results of the referenced study show that the ultimate load capacity of the beam is reduced as the out-of-plane rotation angle increases. However, this reduction is quite small, such that for the straight girder case, when the subject girders are rotated out-of-plane 2 degrees, the ultimate load capacity only reduces by 0.8%; similarly a 1.1% capacity reduction was observed in the curved I-girder. For comparison purposes, it is noted that in practice, curved steel I-girder bridges may experience an out-of-plane rotation of approximately 1 to 2 degrees (Chavel and Earls 2001, 2004). For reference, the load-vertical deflection response at mid-span, for each degree of web out-of-plane rotation, is reproduced herein as figure 2.

While the ultimate capacity is only modestly affected by web plumbness, it is observed that the flange tip stresses do increase much more significantly as the subject girders are rotated out-of-plane. For a web out-of-plane rotation of 2 degrees, the straight I-girder top flange tip stress increases by 8.0%, and the curved I-girder top flange tip stress increases by 3.0%. Therefore, in certain design contexts, it may be appropriate to consider the increased stress caused by the girder being in an out-of-plumb position. More generally speaking, it may not be necessary to consider the reduced structural capacity caused by the girder being in an out-of-plumb position since it does not strongly influence the member capacity at the occurrence of the controlling limit state.

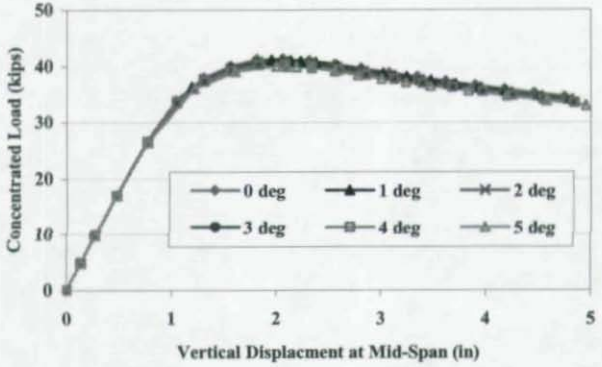

Figure 2 – Curved Girder Load-Vertical Deflection Response for Varied Angle of Web Out-of-Plane Rotation

Since this earlier research was limited to consideration of girders that were not of proportions that would make them typical as bridge members, the current research work aims to carry out similar web-plumbness studies on bridge size girders and also now bridge size systems; including cross-framing. To this end, the current study

investigates the changes in girder flange stresses and cross-frame demands for the three-span continuous, six-girder full bridge system; considering various degrees of web out-of-plumbness.

FINITE ELEMENT MODEL DESCRIPTION

A nonlinear finite element model of the subject bridge system is constructed using the commercial finite element program ADINA (ADINA 2003) to study the behavior of a typical curved girder bridge under induced out-of-plumb conditions resulting from various imperfection displacement fields. In order to provide some level of confidence in the modeling assumptions being employed, the FE models are based on an existing representative bridge; thus the resulting dead load displacements are subsequently verified using the available girder camber diagrams.

The finite element modeling techniques employed above serve as a basis for constructing the models employed in the research reported on herein. The mesh density utilized is such that the models considered have more that 3 million degrees of freedom each. This level of detail is far in excessive of what is needed for the present study; however, the model designs are governed by the requirements for future work involving inelastic plate buckling effects at ultimate; hence the apparently extreme mesh density.

The proportions of the bridge system considered in the present research emanated from a review of the actual designs of a series of typical curved steel I-girder bridges; suitable overall dimensions and cross-sectional proportions are thusly obtained. Specifically, the focus of the current work is a steel I-girder bridge that is a 443ft three-span continuous curved structure having a constant radius of 509ft. The spans contain 30 total girder sections connected with K-type cross-frames, and set upon radial piers so as to result in spans of approximately 130ft, 174ft, and 139ft. Each of the six 72" deep girder lines, spaced at 10'-2 1/2" on center, is stiffened with 47 transverse web stiffeners of varying thickness and 31 cross frame connection

plates proportioned to accept the cross frame forces. A plan view sketch of the subject structure is shown in figure 3.

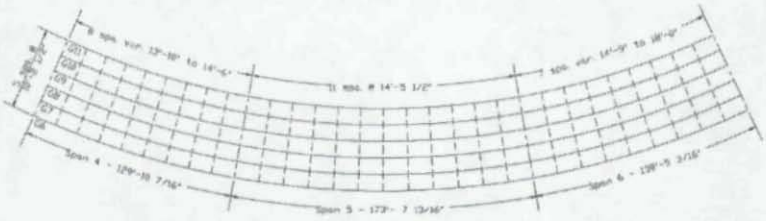

Figure 3 – Plan View of Curved I-Girder Bridge

In order to reduce to complexity of the model, certain dimensional generalizations are carried out for this representative study (i.e. it not so much the performance of any particular bridge that is at issue; rather it is the performance of a class of bridges, possessing certain signature geometric features that are at issue). Dimensional generalization is achieved within each girder line through the application of weighted averages, for plate thicknesses and widths; applied to the entire length to ensure satisfactory mesh conformity at flange and web transitions. The flange plate sizes used in the model are shown in table 1. Additionally, cross frames were proportioned such that brace strength are never be an impediment to the study of the girder response (i.e. robust circular cross-sections are assigned to cross-frame elements to ensure that they do not fail prior to the girders.

Table 1 – Flange plate sizes used in model

Girder	Bottom Flange		Top Flange	
	t_f (in)	b_f (in)	t_f (in)	b_f (in)
G11	1.568	19.833	1.264	17.357
G10	1.571	19.855	1.267	17.381
G9	1.573	19.877	1.269	17.407
G8	1.578	19.906	1.273	17.443
G7	1.581	19.931	1.276	17.473
G6	1.584	19.958	1.279	17.504

Each of the 30 total girder sections is partitioned into meshes of shell elements set along the mid-plane of each plate component and subsequently assigned a thickness. The modeling techniques employed in this study are similar to verified modeling techniques employed in previous studies (Chavel and Earls 2001 and 2004). ADINA 4-node shell elements (MITC4) are used throughout the current study to comprise the web, flanges, transverse stiffeners, and cross-frame connection plates of each girder line.

Mesh conformity is preserved throughout the model and the flange element aspect ratios never exceed 1.1 to 1 (length assumed to be tangential length measured on outside radius.) The length of each flange element is calibrated to exactly match the length of the corresponding web element at the web-flange intersection to once again ensure mesh conformity. Girder webs are modeled using a height to length aspect ratios of 2 to 1; this aspect ratio is selected so that the already large models do not become intractably large. It is once again noted that this level of modeling refinement is only employed to permit the use of these same models in future research undertakings

The cross frames are modeled using ADINA 2-noded beam elements. Five elements are used in the cross-frame assemblies to accommodate the geometry of bracing members intersection. The cross frames are connected to the cross frame brace plates at the 31 representative locations within the spans. For simplicity, gusset plate connections are not modeled directly. Rather, constraint equations are employed to provide and idealized bracing configuration

Field splices are not explicitly modeled in this study. Field splice locations are assumed to transfer full shear and moment and are represented with an uninterrupted mesh. To connect each plate section, ADINA constraint equations were used to enforce master node translational and rotational degrees of freedom on corresponding slave nodes.

For support locations, the subject bridge employs longitudinally and transversely guided rollers in addition to conventional non-directional

bearing pads. In order to model the rollers at different pier locations, skewed coordinate systems are assigned to constrained nodes at the pier locations.

The loads applied in this study include dead load due to the steel superstructure. To apply this load, a mass proportional body force is applied to the structure using a standard steel density of 490 lb/ft^3. The thickness of cross frame members is increased to account for the omission of gusset plate connections.

A plan view and an isometric view of the finite element model are shown in figures 4 and 5, respectively.

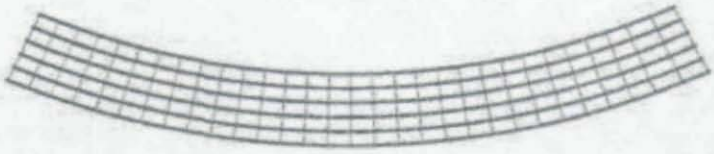

Figure 4 – Plan View of Finite Element Model

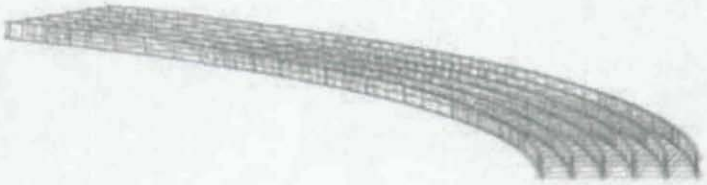

Figure 5 – Isometric View of Finite Element Model

Cross-sectional rotations are introduced in a periodic fashion through the use of half-sine wave displacement fields possessing a half wavelength corresponding to each of the three spans. The imperfection field is created such that the center of rotation is taken as the lower flange-web-junction; the this point does not move out of plane as a result of the imposed initial imperfection field; while the

opposite is true for the top flange-web-junction location; this point translates the furthest out of plane as a result of the imperfection field.

The modeling considers geometric nonlinearity, but not material nonlinearity.

ANALYSIS RESULTS

The finite element models of the subject bridge are used to investigate what effect, if any, girder web out-of-plumbness has on the response of bridge systems. The out-of-plumb behavior is investigated for 1 degree increments of out-of-plumb rotation at the three mid-span points; a periodic half-sine function scales the rotational displacement field throughout the remainder of the span. Girder top and bottom flange stresses and cross-frame demands are monitored for each degree of out-of-plumb rotation, up to 5 degrees. The only load considered in this current study is the girder steel self-weight.

Girder Flange Stresses

The girder flange stresses are monitored at three specific locations, so as to investigate the conditions of maximum positive and negative vertical bending moment. As shown in figure 6, girder flange stresses are monitored at 0.5L of span 2, 0.4L of span 3, and at Pier 3, where L refers to the individual span length. At each location, flange stresses (von Mises) are reported at one-quarter points of each of the unbraced lengths between cross-frames, in proximity to the sample locations, so as to monitor the lateral flange bending behavior. Furthermore, stresses are reported at the flange tips as shown in figure 7, so as to record to the maximum von Mises stress in the flange section.

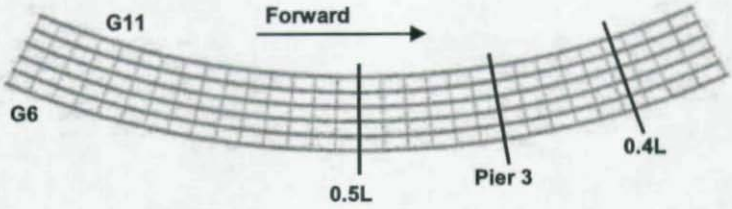

Figure 6 – Monitored Girder Flange Stress Locations

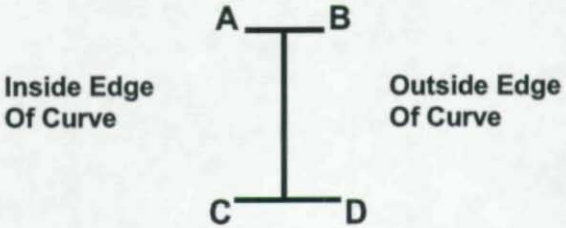

Figure 7 – Identification of Flange Tips (Looking Forward)

Shown in figure 8 are the girder G6 bottom flange von Mises stresses at the 0.5L, span 2 location; which is the location of maximum positive vertical bending moment in this span. The von Mises stresses are reported at the outside tip of the bottom flange, location D in figure 7. The increased stress at the cross-frame locations ("X-frame" in figure 8) is due to the lateral flange bending that is present in curved steel I-girder bridges. The stresses that result from lateral flange bending are a result of the flange acting as a continuous beam over several supports in the lateral direction; where the cross-frames are the points of support. This behavior is observed no matter what degree of web out-of-plumbness is imposed on the model.

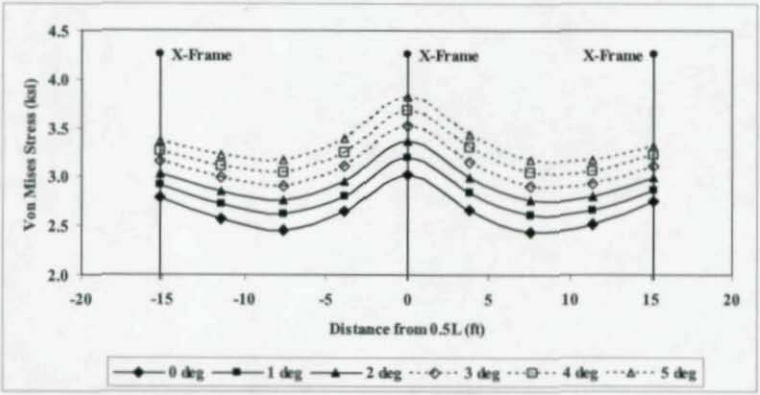

Figure 8 – Girder G6 Bottom Flange von Mises Stress at 0.5L Span 2, Girder Flange Location D

However, of more importance in regard to the current study, is the increase in bottom flange von Mises stress, as the cross-section rotation increases from the 0 degree to the 5 degree web-out-of-plumbness cases. As the girder is rotated from the 0 degree position to the 5 degree position, the maximum von Mises stress at the 0.5L, Span 2 location increases by 0.8 ksi, or a 26% increase at the flange tip location. The same behavior holds true in the middle of the cross-frame bay shown in figure 7; here the von Mises stress increases by 0.7 ksi, or a 30% change in flange tip stress between the 0 degree and 5 degree web-plumbness cases.

A similar behavior is also noted for the innermost girder, girder G11, as shown in figure 9. However, the out-of-plumbness results in a larger increase in stresses at the 0.5L span 2 location. As the girder is rotated from the 0 degree position to the 5 degree position, the maximum von Mises stress at the 0.5L Span 2 location increases by approximately 1.0 ksi, or a 59% increase in flange tip stress.

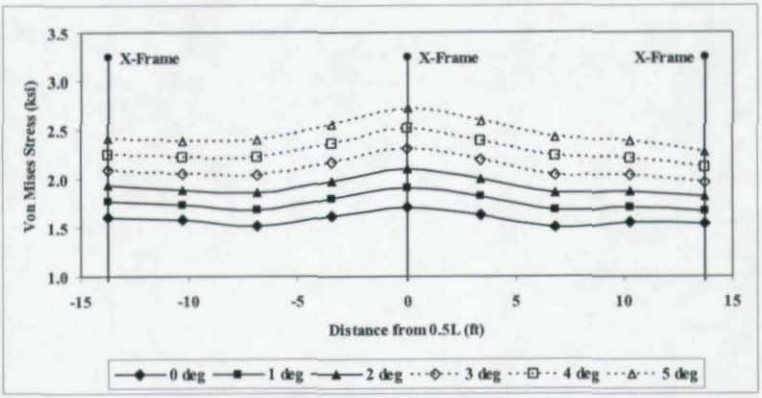

Figure 9 – Girder G11 Bottom Flange von Mises Stress at 0.5L Span 2, Girder Flange Location D

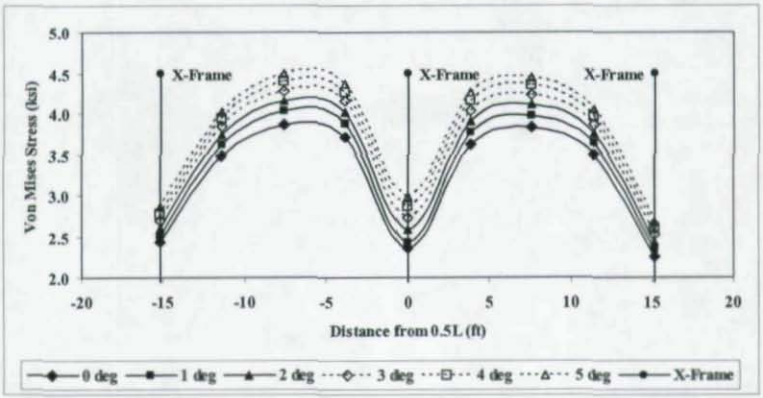

Figure 10 – *Girder G6 Top Flange von Mises Stress at 0.5L Span 2, Girder Flange Location A*

At 0.5L of Span 2, the top flange is observed to have a similar behavior as the bottom flange; however the top flange tip stresses decrease at

location B, but increase at location A, as the girder is rotated out-of-plumb. This behavior is shown in figures 10 and 11. This behavior is a direct result of the fact that flange tip A moves further away from the neutral axis of the girder as the cross-section is rotated out-of-plumb, while flange tip B moves closer to the neutral axis. Therefore the von Mises stresses increase at location A, while they decrease at location B, as the girder out-of-plumbness increases, as shown in figures 11 and 12.

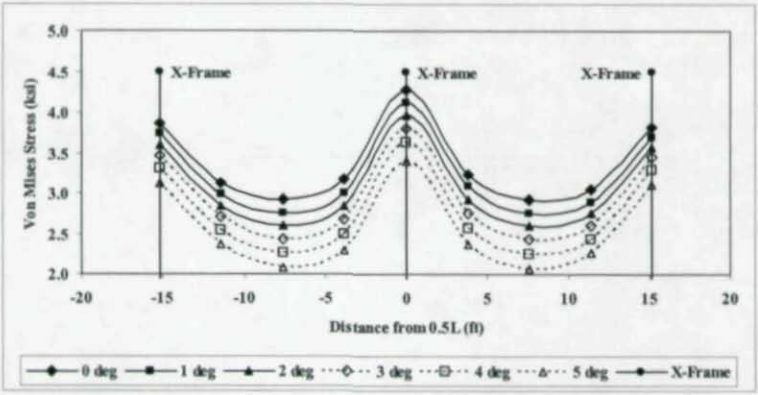

Figure 11 – Girder G6 Top Flange von Mises Stress at 0.5L Span 2, Girder Flange Location B

Furthermore, it is interesting to point out the effect that lateral flange bending of the top flange has on the flange tip stresses at 0.5L of span 2. The top flange at 0.5L of span 2 is in compression due to the vertical bending moment. However, the lateral flange bending causes tension in flange tip A (inside edge); and compression in flange tip B (outside edge). Therefore, the total stress at flange tip A is reduced by the lateral flange bending stress, as shown in figure 10, while the total stress at flange tip B is increased by the lateral flange bending stress, a shown in figure 11.

It is observed that the top flange tip stress at Pier 3, at girder flange location B, increases as the girder web out-of-plumb rotation increases. This top flange tip stresses at location B of girder G6 are shown in figure 12. As the girder is rotated from the 0 degree position to the 5 degree position, the maximum von Mises stress at the Pier 3 location increases by approximately 1.2 ksi, or an 18% increase in flange tip stress at Flange tip B. In comparing the top flange tip stresses at girder flange tip location B, for the 0.5L span 2 (figure 11) and Pier 3 (figure 12) locations, it is evident that the web out-of-plumbness has an opposite effect. At the 0.5L span 2 location the 0 degree web-plumbness case produces the maximum tip stress, however at the Pier 3 location the 5 degree web-plumbness case governs.

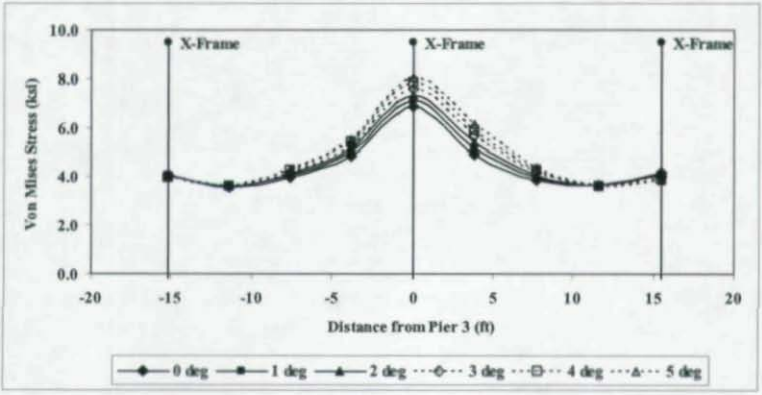

Figure 12 – Girder G6 Top Flange von Mises Stress at Pier 3, Girder Flange Location B

Also monitored are the girder flange stresses at the maximum positive vertical bending moment location in span 3, and 0.4L of the span. As shown in figure 13, as the cross-section is rotated from the 0 degree position to the 5 degree position, the girder G6 maximum von Mises stress near the 0.4L Span 3 location increases by 0.9 ksi, or a 37% increase in the bottom flange tip stress (location D). This behavior is

similar to that of the 0.5L span 2 location, also a location of maximum positive vertical bending moment.

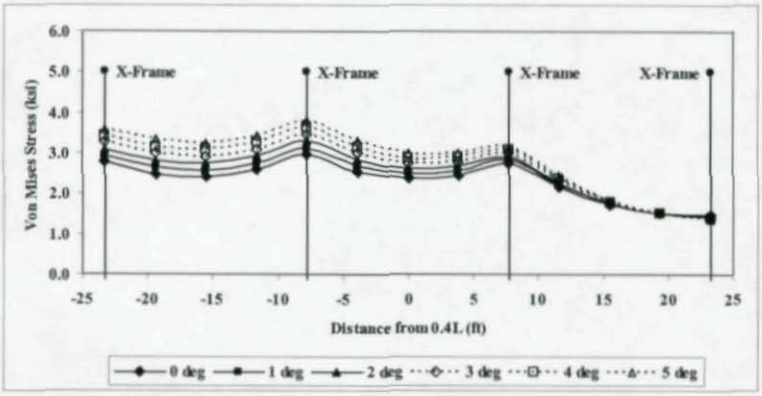

Figure 13 – Girder G6 Bottom Flange von Mises Stress at 0.4L Span 1, Girder Flange Location D

Cross-Frame Member Axial Forces

The cross-frame member axial forces are somewhat affected by the out-of-plumbness of the cross-section. The cross-frames in the subject bridge are "K" type cross-frames, utilizing a top and bottom chord and two diagonals, as shown in figure 14.

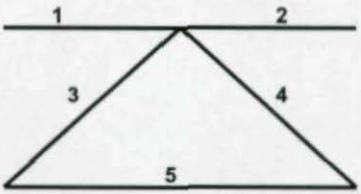

Figure 14 – "K" Type Cross-Frame Member Identification (Looking Forward)

In general, at regions of positive vertical bending moment, the cross-frame member axial forces do not significantly change due to the increase in girder web out-of-plumbness. For example, the diagonal members of the cross-frames at 0.5L span 2 and 0.4L span 3, only experience a maximum change in axial force of approximately 0.15 kips, translating to only a 7% change in axial load.

Conversely, at the Pier 3 location, there is a more significant change in the cross-frame member axial forces for all members. The diagonal members are subjected to a maximum change in axial force of 1.0 kips, with a 37% change in axial load. It should be noted however, that the axial forces in all cross-frame members are relatively small due to steel dead load only, with a maximum axial force of 4.5 kips at Pier 3.

CONCLUSIONS

The current study employs the use of a nonlinear finite element model of a typical horizontally curved steel I-girder bridge to investigate the effects of girder web-plumbness. It is evident that as the cross-section is subjected to increasing out-of-plumb position (as a result of an initial displacement filed), there is in increase in the maximum flange tip stress at mid-span and support locations. The flange tip stresses on the outside edge of the bottom flange and the inside edge of the top flange will increase as the out-of-of-plumb rotation angle increases. However, the flange tip stresses on the inside edge of the bottom flange and the outside edge of the top flange decrease as the initial imperfection out-of-plumb rotation angle increases. This behavior is a direct result of the fact that one flange tip moves further away from the neutral axis of the girder as the cross-section is rotated out-of-plumb, while the flange tip moves closer to the neutral axis.

It is also observed that the cross-frame member axial forces are affected by the web-out-of-plumb condition. Typically, it is observed that diagonal member force will increase in magnitude at locations of maximum positive moment as the initial out-of-plumb rotation angle increases. However, the behavior of the top and bottom chords is not as

general, where in some locations the magnitude of force increases while at other locations the magnitude of force will decrease.

The results of the current study demonstrate that there is an increase of girder flange tip stresses, and a change in cross-frame member demands, as the initial out-of-plumb rotation angle of the cross-section increases. Therefore, it may be necessary for the engineer to consider these effects, due to web-plumbness under various dead-load conditions, when structures are constructed, especially in regard to design checks associated with constructability. However, the increase in flange tip stresses does not necessarily suggest that the ultimate load capacity of the section is reduced, due to the fact that only a single flange tip is subjected to a stress increase and not the entire flange. The ultimate load capacity of this particular structure, as well as sub-assemblages will be presented in a future paper.

REFERENCES

ADINA, (2003), Theory and Modeling Guide, Volume I: ADINA, *Report ARD 03-7*, ADINA Research and Development, Inc., Watertown, MA.

American Association of State Highway and Transportation Officials (AASHTO), (1993 and 2003), *Guide Specifications for Horizontally Curved Steel Girder Highway Bridges*, Washington, D.C.

American Association of State Highway and Transportation Officials (AASHTO), (2005), *AASHTO LRFD Bridge Design Specifications, 3rd Edition with 2005 Interim*, Washington, D.C.

Chavel B.W., Earls, C.J., (2001), "Evaluation of Erection Procedures of the Curved Span of the Ford City Steel I-Girder Bridge," Report No. CE/ST 18, Department of Civil Engineering, University of Pittsburgh, Pittsburgh, Pennsylvania.

Chavel B.W., Earls, C.J., (2004), "Deflection of Horizontally Curved I-Girder Bridge Members Under Construction," Report No. CE/ST 28, Department of Civil Engineering, University of Pittsburgh, Pittsburgh, Pennsylvania.

Chavel, B.W. and Earls, C.J., (2005), "Structural Capacity of Curved Steel I-Girders in a Web-Out-of-Plumb Position," Structural Stability Research Council Conference, Montreal, Quebec, Canada.

ON THE STRENGTH AND STABILITY OF SLAB ON STEEL I-GIRDER BRIDGE SYSTEMS DAMAGED BY TRUCK STRIKES

C. J. Stull[1], C. J. Earls[2], B. Akinci[3]

ABSTRACT

Slab on steel stringer bridge systems are a staple in our Nation's surface transportation system. Unfortunately, it is somewhat common to have a scenario wherein an over-height truck encounters a particularly low bridge; subsequently leading to a truck strike to the overhead steel superstructure.

Given the mass of typical trucks, coupled with the high velocity associated with interstate travel, relatively large amounts of kinetic energy can be transmitted to the overhead bridge during such a truck strike event. Typically, the slab on steel stringer bridge will dissipate this energy through the development of plastic deformations in the steel stringers (leading to twisted and / or dented flanges as well as out-of-plumb girder webs), plastic buckling of cross-frame and diaphragm members, unwanted relative motions at the bearings leading to

[1] Doctoral Candidate, Dept. of Civil and Environmental Engineering, Univ. of Pittsburgh, PA 15261, USA.
[2] Chairman and Associate Professor, William Kepler Whiteford Faculty Fellow, Dept. of Civil & Environmental Engineering, Univ. of Pittsburgh, Pittsburgh, PA, 15261., USA. earls@engr.pitt.edu
[3] Assistant Professor, Dept. of Civil & Environmental Engineering, Carnegie Mellon University, Pittsburgh, PA, 15213, USA.

misalignments between the superstructure and the underlying substructure; and in the case of composite slab to steel stringer systems, damage to the composite action occurring at the steel-to-concrete interface. Correctly assessing this damage and arriving at a rational means for determining reserve capacity in the damaged system presents a formidable challenge to the bridge engineer. Stability is a very important theme within the context of strength evaluation due to the fact that large initial imperfections may now be present throughout the damaged bridge system, and also since previously effective bracing members, may now be compromised as a direct result of the damage that they sustained during the event.

The current paper describes, and reports on preliminary results from, an on-going research program involving multiple laser scanning technologies that are coupled with the latest image processing techniques to provide reliable, high resolution point cloud data sets suitable for constructing detailed solid models of the structural system. The solid models are themselves suitable for meshing and analysis with state-of-the-art commercial multi-purpose nonlinear finite element software systems such as ADINA. In this approach, fidelity to the complex in-situ geometry is maintained so that virtual "load testing" may be carried out.

INTRODUCTION

The problem of assessing steel I-girder bridge systems damaged by over-height truck strikes is one for which conventional analysis approaches do not readily present a practical and efficient solution. Complicating issues inherent in this problem can include diversity in potential structural layouts that must be treatable (straight, skewed, or curved systems), the presence of various types of intermediate lateral bracing, the many different bridge bearing designs, etc.; all of which dramatically effect behavior of the overall system. Similar problems are encountered when attempting to standardize an assessment protocol; as it is that any current assessment relies heavily upon

"engineering judgment", which, in its purest form, is simply an opinion. This, of course, leads to the real possibility that one could receive two divergent assessments of the same damaged bridge. Anecdotal evidence seems to indicate that this happens with some regularity.

The present paper reports on preliminary results from an on-going research program aimed at devising, developing, and deploying a novel approach to the treatment of the problem outlined in the foregoing. Specifically, a non-destructive condition assessment technique is described wherein three primary technologies are employed: laser scanning systems (both time-of-flight and phase-based ranging systems) used to acquire point cloud data sets corresponding to discrete locations on damaged bridge structures; modeling software such as Geomagic or Solidworks to register and process the afore-mentioned point cloud data sets; and ADINA, a commercially available nonlinear finite element analysis software system: for use in the performance of virtual load tests.

LASER SCANNING TECHNOLOGIES

Two types of laser scanning technologies will be utilized throughout this research program; each based on a slightly different principal of operation: time-of-flight and phase-based systems. The CYRAX time-of-flight ranging system, manufactured by Leica Geosystems HDS LLC, was already owned and operated by the PennDOT District 12-0 Survey Team, thereby presenting a convenient solution to examine the capabilities of this type of non-contact digitizer. In the case of the phase-based ranging system, the Department of Civil and Environmental Engineering at Carnegie Mellon University has acquired a Z+F (Zoller + Frohlich) laser scanning system for use in one of the current authors' research programs.

While it is that both instruments emit laser radiation so that it is reflected back by a target of interest to an on-board receiver, there are several practical differences. The CYRAX scanner is based on time-of-flight principles while the Z+F scanner uses phase-based technology to acquire data. Since phase-based technology utilizes a continuous laser beam (whereas the time-of-flight technology uses a pulsing laser beam), the data acquisition process is much faster in the former case and thus total data acquisition times may be reduced. This aspect of performance may be important under certain conditions when fast data collection and assessment are critical. In addition, the CYRAX system employs a 1mW (green) laser while the Z+F system employs a 23mW (red) laser. These differences in laser radiation wavelength and power may be important in relation to the performance of the scanners in less than optimal scanning environments (i.e. when scanning through smoke and dust); this is currently being investigated.

These two scanning technologies are also different in terms of their ambiguity intervals, vertical and horizontal fields of view, accuracies and resolutions. These differences are important to experiment with due to the need for high-speed data collection over long ranges as well as the need for high accuracy of the data collected to enable detailed computational analysis. An evaluation of the technological feasibility and process applicability of both scanners, for the unique characteristics of the data collection and analysis issues associated with the proposed work, is currently underway.

DATA REDUCTION AND PARASOLID MODEL GENERATION

Registration of point cloud data into a form that is suitable for the creation of a parasolid model for subsequent importation into ADINA is primarily handled through the use of two software packages: Geomagic v8 and Solidworks 2005. The primary purpose of each software package is as follows: Geomagic focuses on the reduction and registration of the raw laser scanner data into a 3-D solid model

whereas the focus of Solidworks is the further reduction of said model into a mid-plane parasolid model; thus allowing the use of the more refined shell elements in the analysis; versus the continuum elements implied in the 3-D solid model arrived at directly through application of Geomagic. As a result of the extra step from Geomagic to Solidworks, fewer overall global degrees of freedom are required to arrive at a sufficiently accurate computational analog for the damaged bridge. This is an extremely important point to consider when performing nonlinear finite element analyses in pursuit of a virtual load test scenario. In such cases as this, both geometric and material nonlinearity must be treated, and hence incremental solution procedures are employed. Any reduction in the required degrees of freedom necessary for an accurate solution translates into significant economy with relation to required computational resources and required time in the finite element solver.

While the registration of data is relatively simple for a single scan, a major challenge can be found in the management of multiple scans; the physical limitations of the laser scanner line of site in a given instrument set-up position results in the need for multiple scans in order to obtain a complete point cloud of the entire structure (i.e. a data set that is complete and free of occluded geometric features). The alignment and registration of the eight to twelve individual point clouds is usually sufficient for most of the bridge structures considered thus far in the present work. The registration of the data may be accomplished either through the use of predefined targets within the data (in the case of the CYRAX scanner), or (in the case of the Z+F scanner) the utilization of predefined algorithms in the Geomagic software to find common points and / or surfaces, and aligning the data accordingly.

In addition to registration of the scanned data from the damaged bridge structures, in certain cases it could be advantageous to also explore registration of the pre-damage, as-built geometry so as to identify deviations between the pre-impact and post-impact bridge. These

deviations can be used as an assessment tool in support of routine bridge inspection activities.

The task of performing validation studies using laser scanners and image processing techniques is iterative in nature in that the point cloud data from each of the scanner systems will need to be collected and then reduced and processed in order to determine the usefulness of the data set for building the finite element models required for performance of a virtual load test. The current research is working to identify a "best practices" guide for executing laser scanning for the purposes of obtaining data sets useful for the creation of a parasolid model within which auto-meshing algorithms may be deployed so that a well-formed and useful finite element mesh can be applied to the geometry.

SUBJECT BRIDGE STRUCTURE

The subject structure chosen for this research program actually consists of two adjacent bridges; however, due to similarities between the two, only one will be described here. The pertinent features of the bridge are that it consists of a three-span continuous (8230 mm (27 ft), 15240 mm (50 ft), and 8230 mm (27 ft) respectively) slab on beam superstructure with a thirty degree skew angle applied from northwest to southeast. The superstructure consists of a 191 mm (7.5 in) concrete deck over six W24x76 steel girders with top flanges imbedded in the deck to develop full composite action.

Further expanding on the superstructure, intermediate diaphragm members consist of two sections: W16x36 and C15x33.9. The varying locations of these members are depicted graphically in Figure 3. Also noteworthy in terms of important structural features is the presence of top and bottom cover plates located on each steel I-girder through the middle 7925 mm (26 ft) of the center span, as well as two 6096 mm (20 ft) sections, where the center of each is offset 1524 mm (5 ft) outward from their respective pier locations. Finally, each of the six girders also

has two splice plates, one located at a 2286 mm (7.5 ft) offset inward from the westernmost pier, with the other offset inward from the easternmost pier.

Bearing conditions consist of genuine pinned connections at the west end of the bridge and rocker-type bearings at each of the two piers and the east end abutment. Typical concrete abutment details, as well as hammerhead-style concrete piers, round out the superstructure. However, it is the steel superstructure that forms the primary focus of this on-going research program discussed herein.

FINITE ELEMENT MODELING APPROACH

In an effort to maintain both the feasibility as well as the fidelity of a finite element model, as compared with the real-world artifact that is the subject of modeling, it becomes necessary to employ certain idealizations with regard to problematic physical geometry. While complex geometrical features present within a structure would require a significant effort to precisely reproduce within the context of a computational model, their salient features may be incorporated in an idealized fashion into the models such that the response measures being considered are reliably provided. Examples of geometric features that are considered in an idealized way, and not through overt modeling, are: field splices, cover plates, diaphragm connections, etc. In each of the cases, the model is adjusted (increased shell thicknesses for cover plates; constraint equations for bolted end connections, etc.) to provide a behavioral analogue that is useful for the ultimate purposes of the modeling effort.

The finite element models employed in the current work consider both geometric and material nonlinearities. Consistent with this are the use of nonlinear element formulation types: four-node ADINA MITC4 shell finite elements, eight-node continuum elements, and two-node quadratic beam elements. The six steel I-girders, as well as the

diaphragm connector plates found throughout the structure, are modeled using shell elements located at the mid-surface of the constituent plate components; beam elements are used in the modeling of the diaphragm members. Material properties represent those specified in the original subject bridge specifications: ASTM A7 steel - input as a plastic multi-linear material model, the properties of which are obtained from ASCE-WRC (1971). Also, due to a program limitation based on the cross-sections utilized, diaphragm members consist of a linear-elastic isotropic material model: E = 203.3 GPa (29500 ksi), $\nu = 0.3$.

Two different approaches are taken with regard to including a concrete deck that is to act compositely with the underlying steel superstructure: a deck attached directly to the top flange of the steel I-girder wherein the deck is comprised of eight-node continuum finite elements throughout (See Figure 3); and a deck attached to the top flange of the steel I-girder through the use of rigid links employed to maintain the proper positioning of MITC4 shell finite elements at the centroid of the concrete deck (See Figure 4). In both approaches a linear-elastic isotropic material representation of the concrete in the deck is employed; the mechanical response characteristics of which are made to be representative of PennDOT "Class A" concrete ($f_c^{'}$ = 20.7 GPa (3000 psi)). While each approach has its advantage (mainly in regard to the computational expense associated with floating point operations), preliminary results obtained from a linear-elastic analysis of each model show nearly identical behaviors, as would be expected. It is pointed out that idealization of the concrete as a linearly elastic material is a gross approximation; one that is only undertaken during these early stages of the research when other aspects of the modeling approach are being studied and verified.

DISCUSSION OF ONGOING RESEARCH

As an early phase of the present work, a smaller mock-up test program is undertaken so as to identify and better understand issues that could

come up during the large scale operations associated with the complete scanning and modeling of entire bridge structures. This preliminary investigation involved a test model that was scanned with a Digibot III laser scanning system to attain a point cloud data set for a W8x10 steel section possessing an overall length of approximately 610 mm (24 in) (See Figure 5). In order to produce similar conditions as would be seen in the subject bridge, prior to the laser scan, a localized plastic deformation of the bottom flange of the beam is produced through the use of Balwin-Lima-Hamilton Universal Testing Machine. Using processes very much consistent with those described in the preceding sections, the point cloud data set is reduced to a simple mid-plane model of the test beam.

However, given the rather abbreviated length of the test beam, artificial surfaces (of a continuous nature) are added to both ends of the beam; thereby creating a more representative model with regard to Bernoulli beam behavior. The final beam is 6096 mm (10 ft) long, resulting in a length-to-depth ratio of 30 (as compared with the initial ratio of 3).

While the addition of these geometric extensions may not immediately be seen as directly applicable to the current research work; the opposite is true. One must consider the need to expedite the process of creating viable geometric entities in the undamaged bridge section; for ultimate use in the creation of the parasolid model needed in conjunction with the auto-meshing facilities used in the current work. Indeed much time can be saved in scanning and model creation if attention is focused on ascertaining detailed topological information regarding only the damaged sections of the bridge girder. Idealizations related to the superstructure geometry surrounding the damaged region can go a long way in expediting the data acquisition, model creation, and subsequent analysis time. However, membership in the point cloud data sets must still include far-field features (as compared with the region of damage alone) so that global bearing shifting, or significant misalignments resulting from the damage-inducing impact may be considered.

A discussion of the issues encountered during the construction of this test model follows; with particular emphasis on generalizing this to the subject bridge point cloud data sets.

As previously stated, the registration of multiple point cloud data sets has proven to be a significant challenge. While the native algorithms in Geomagic are able to recognize, with relative accuracy, the location and orientation of common points and / or surfaces, care must be taken with regard to the relative "noise" of each point cloud data set. Figure 6 shows an edge-on view of the point cloud data for a 610 mm (24 in) length of a steel I-girder from the subject bridge; the Z+F ranging system was employed in this particular instance. While the presence of a highly dense region of data indicates the location of the surface that is reflecting the laser radiation, the deviation between a best-fit plane and the extreme points results in a highly irregular tessellated surface (See Figure 7). These irregularities can be resolved through the use of noise reducing algorithms within Geomagic; however, care must be taken to ensure that these noise reducing algorithms do not in fact reduce the point cloud data to an extent where damaged regions are no longer correctly reproduced.

A reduced noise point cloud data set may then be tessellated through the application of a Delaunay tessellation algorithm wherein a faceted surface made from triangular patches forms a hull. This hull may then be fitted with a smoothed surface employing so-called NURBs: Non-rational Uniform B-Splines. The NURB surface may then be exported to ADINA through the parasolid file format. Once a sufficiently accurate parasolid model has been generated and subsequently imported into ADINA, auto-meshing algorithms are then applied to the geometry resulting in a shell finite element model (dominantly quadrilateral in nature) suitable for the conduct of virtual load testing. A major issue encountered during this auto-meshing process, however, is that of nodal coincidence being consistent at intersecting mesh edges (flange to flange and flange to web). This very issue can be seen in

Figure 8 at the flange-web junction where nodal coordinates, while only 2 mm (0.125 in) apart at the greatest, result in free element edges in excess of 13 mm (0.5 in). Given the relative consistency of these nodal discontinuities, it becomes obvious that the intended stress distributions through this junction will not be achieved since portions of the mesh will only be partially attached to other such regions.

One possible solution to this problem is the simple application of constraint equations in order to tie free nodes together, resulting in a semi-continuous mesh; however, the time requirement involved in such a task is quite significant when considering an entire bridge structure, and hence is not a viable option. In the case of the mesh generation from Figure 8, decreasing the mesh density from a 6 mm (0.25 in) to 25 mm (1 in) element length resolves this issue with no additional time requirements (See Figure 9); as opposed to the previously mentioned solution. It must be noted that a practical approach to the model in question would also dictate that such a high mesh density is absurd in practice, but for the purposes of the present discussion, the above models were generated.

FUTURE RESEARCH

Carrying forward the problem resolutions and knowledge gleaned from the test modeling efforts, furthering the progress with regard to the subject bridge is primarily a matter of point cloud data registration. While the primary focus of the research is on the assessment of the residual load carrying capacity of the damaged subject bridge, certain geometric issues must me addressed in order that efficient use of the auto-meshing algorithms within ADINA may occur. Therefore, it appears that the primary time-intensive process comes about as a result of the complications discussed above in relation to the relative noise of the point cloud data sets as well as the registration of multiple point cloud data sets for representation of the entire structure. As the research continues, however, it is expected that these difficulties will be addressed directly.

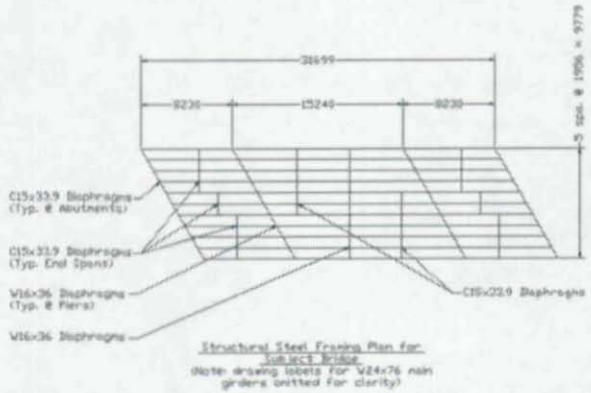

Figure 1 Structural steel framing plan

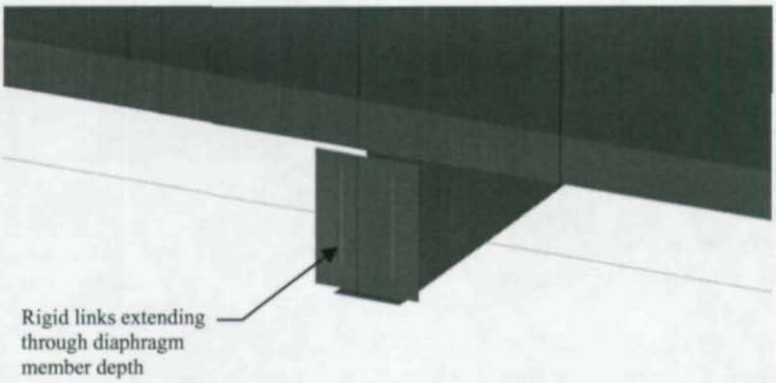

Figure 2 Representative examples of diaphragm rigid beam elements tying into shell element connector plates

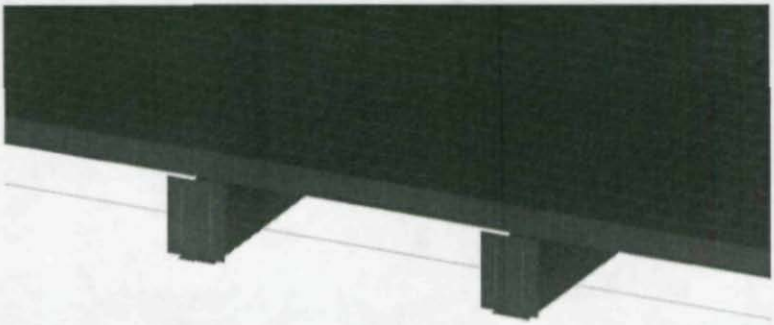

Figure 3 Representative example of a typical cross-section through the "continuum finite element deck" model

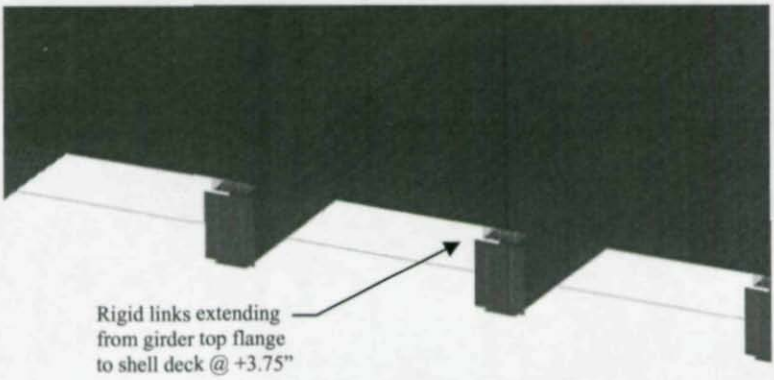

Figure 4 Representative example of a typical cross-section through the "shell finite element deck" model

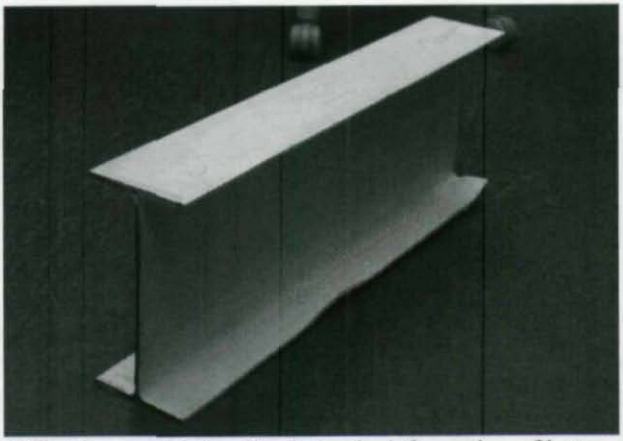

Figure 5 Test beam with localized plastic deformation of bottom flange

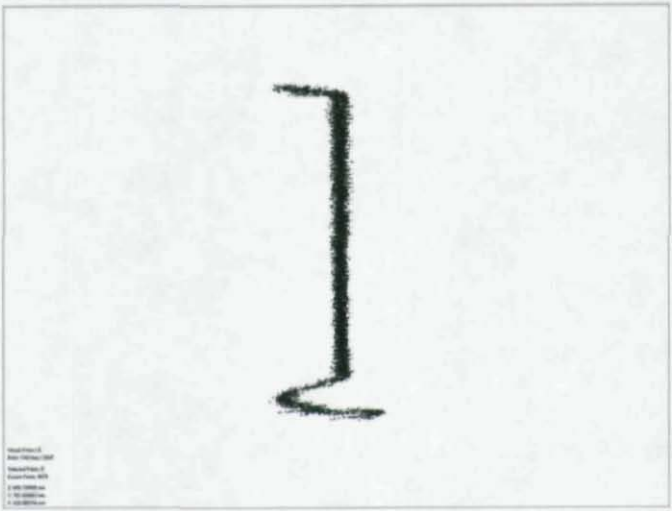

Figure 6 Edge-on view of steel I-girder point cloud data set produced with Z+F phase-based ranging system

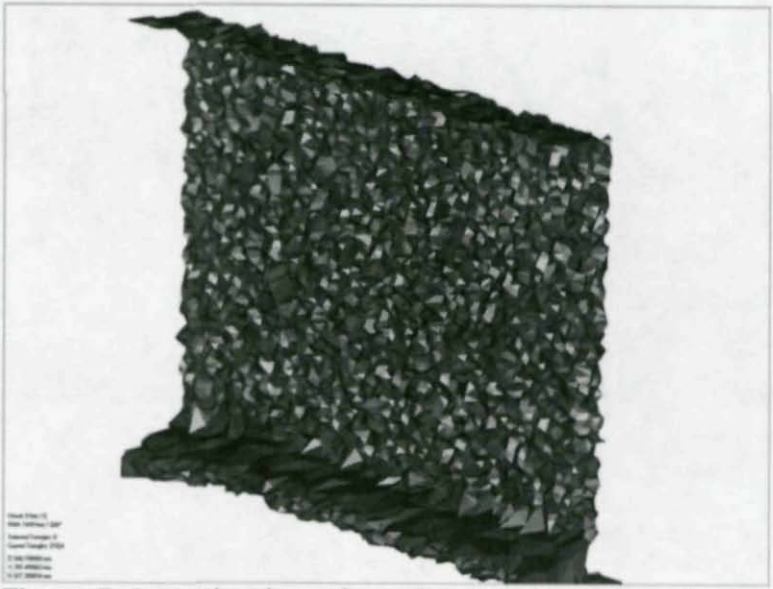

Figure 7 Isometric view of tessellated surface produced when considering the section from Figure 6

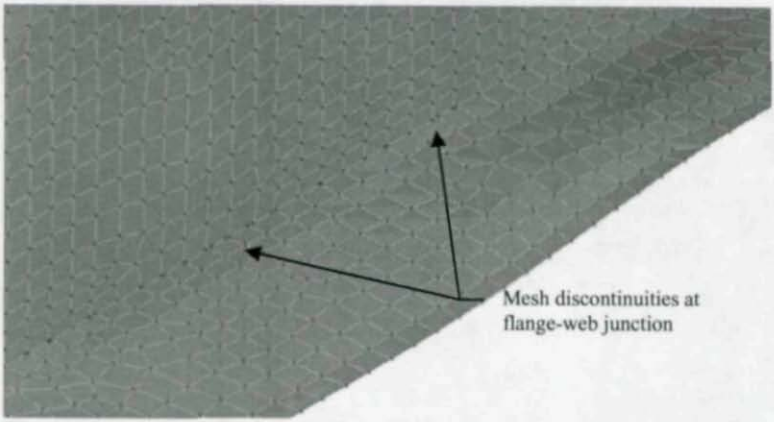

Figure 8 6 mm (0.25 in) shell finite element mesh of the test model flange-web junction displaying nodal discontinuities within the mesh

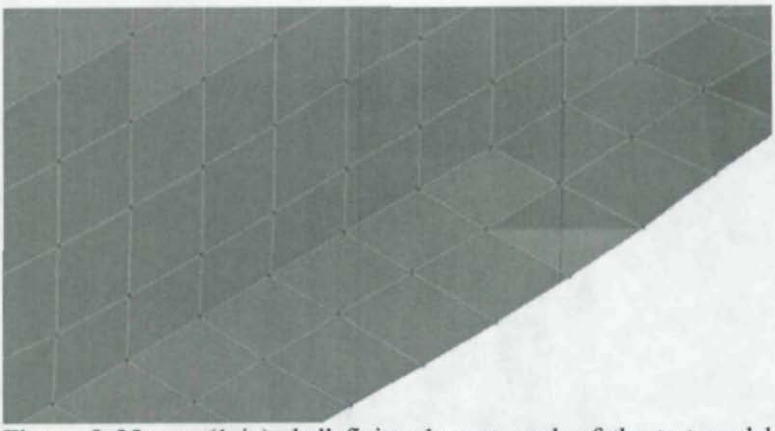

Figure 9 25 mm (1 in) shell finite element mesh of the test model flange-web junction displaying full nodal continuity along the entirety

REFERENCES

ADINA (2003) Theory and Modeling Guide, Volume I: ADINA, *Report ARD 03-7*, ADINA Research and Development, Inc., Watertown, MA.

Plastic Design in Steel: A Guide and Commentary (1971), Joint Committee of the Welding Research Council and the American Society of Civil Engineers, New York, New York, pp. 42.

DESIGN GUIDE AND AID FOR MOMENT OF BUILT-UP CRANE RUNWAY GIRDERS

Dung M. Lue[1] *Duane S. Ellifritt*[2] *Wei T. Hsu*[3]

ABSTRACT

It is a common practice in crane runway girders to place a channel, open-side down, over the top flange of a W- or S-section. The built-up WC (W-section with Channel) or SC (S-section with Channel) section has been proven to be efficient and economical. However, the theoretical moment calculation for WC/SC section is not an easy task and the difficulty comes from the evaluation of the torsional properties including warping constant (C_w), monosymmetric parameter (β_x), and torsional constant (J). The current LRFD provides no theoretical formulas for moments of WC/SC sections, but does give the approximate formulas (without the use of C_w and β_x) which were derived from singly symmetric I-shaped sections. Results from this study show that the LRFD formulas underestimate the elastic moment strength of WC/SC girders. This paper first summarizes the formulas of the torsional properties (C_w, β_x, J) for WC/SC sections using the complex mathematical integrations. Those sophisticated mathematical functions were solved numerically by a developed computer program. The moment parameters and torsional properties of WC/SC sections calculated based on the theory and LRFD are furnished in tabular form to assist engineers to design the built-up girders. Finally, a rational yet

[1] Associate Professor / SSRC Member-at-Large, Dept. of Civil Engineering, National Chung-Hsing Univ., Taichung, Taiwan 402

[2] Crom Professor / SSRC Life Member, Dept. of Civil & Costal Engineering, Univ. of Florida, Gainesville, Florida 32611

[3] Graduate Student, Dept. of Civil Engineering, National Chung-Hsing Univ., Taichung, Taiwan 402

simplified design approach is proposed and applied to the WC/SC girder sections included in the current ASD and LRFD design manuals.

INTRODUCTION

Doubly and singly symmetric I-sections (Figures 1 and 2) have been widely used for crane runway girders. Substantial research in the past has been devoted to the girders with these sections (Clark and Hill, 1960; Galambos, 1968; Heins, 1975; Moore, 1985; Kubo and Fukumoto, 1988; Hulshizer, 1991). The built-up WC/SC girders shown in Figures 3 and 4 being commonly used in the United States is rather limited (Lue and Ellifritt, 1993, 1998, 2003). The exact design formula for such sections is not seen in any of the AISC Specifications (1986, 1989, 1993, 1999). The so-called singly symmetric formulas given in the LRFD (1986, 1993, 1999) were actually derived based on the girder with singly symmetric I-section as briefly described in this paper. This study shows that the LRFD underestimates the elastic critical moments of WC/SC girders 12~28% depending upon the unbraced length L_b. This paper first summarizes the theoretical formulas for the design of WC/SC girders, which involve mathematical integrations. These complex functions can be rewritten in terms of numerical expressions by realizing that the section is made up of thin-walled plate elements. The required moment parameters (M_p, M_r, L_p, L_r, B_1, and B_2) and torsional properties (β_x, C_w, and J) for theoretical analysis are computed and tabulated for practical purposes. The LRFD moment parameters (M_p, M_r, L_p, L_r , I_y, I_{yc}, h, J, B_1, and B_2) for the design of WC/SC girders are also given and tabulated. This new set of design parameters and properties will enable practicing engineers to perform more in-depth design on WC/SC girders. As part of this study, a rational and simplified approach is presented for the design use of WC/SC girders listed in the current ASD and LRFD design manuals.

ELASTIC MOMENTS FOR WC/SC GIRDERS BASED ON THEORY AND LRFD

1. Elastic Moment Based on Theory

According to Clark and Hill (1960) and Galambos (1968), the theoretical elastic moment M_{cr} of a girder may be expressed as follows:

$$M_{cr} = \frac{C_b \pi}{KL} \sqrt{EI_y GJ} \left(B_1 + \sqrt{1 + B_2 + B_1^2} \right) \tag{1}$$

where

$$B_1 = \frac{\pi \beta_x}{(2KL)} \sqrt{\frac{EI_y}{GJ}} \qquad B_2 = \frac{\pi^2 EC_w}{(KL)^2 GJ} \qquad J = \int_A r^2 dA \tag{1.a}$$

In Eqs. 1 and 1.a, r is the distance from any point on the section to shear center. E, G, J, C_b, C_w, and KL are elastic modulus, shear modulus, torsional constant, bending coefficient, warping constant, and effective length, respectively. The monosymmetric parameter β_x results from the difference between the area of compression and the area of tension. Eq. 1 is applicable to any doubly and singly symmetric sections. For a girder with doubly symmetric section, Eq. 1 can be simplified as shown below since $\beta_x = 0$.

$$M_{cr} = \frac{C_b \pi}{KL} \sqrt{EI_y GJ} \sqrt{1 + B_2} \tag{2}$$

2. Elastic Moment Based on LRFD

In 1980, Kitipornchai and Trahair proposed a mathematical model β_x for the crane girder used in Australia (Figure 5). The model is given as

$$\beta_x = 0.9h \left(\frac{2I_{yc}}{I_y} - 1 \right) \left\{ 1 - \left(\frac{I_y}{I_x} \right)^2 \right\} \left(1 + \frac{D_L}{2D} \right) \tag{3}$$

where h, D, *and* D_L are as shown in Figure 5, and I_{yc} and I_y are the moment of inertia of the compression area and the moment of inertia of the whole area with respect to y-axis, respectively. If the model β_x is applied to singly symmetric I-section (Figure 2), the value of $(D_L/2D)$ becomes small and negligible, and the above equation can be reduced to

$$\beta_x = 0.9h \left(\frac{2I_{yc}}{I_y} - 1 \right) \left\{ 1 - \left(\frac{I_y}{I_x} \right)^2 \right\} \tag{4}$$

According to Salmon and Johnson (1996), the sectional properties C_w, I_y, and I_{yc} for singly symmetric I-sections (Fig. 2) may be expressed as

$$C_w = \frac{h^2 b_1^3 t_1 \alpha}{12} \qquad \alpha = \frac{1}{1+(b_1/b_2)^3(t_1/t_2)} \tag{5}$$

$$I_y = \frac{t_1 b_1^3}{12} + \frac{t_2 b_2^3}{12} \qquad I_{yc} = \frac{t_1 b_1^3}{12} \tag{6}$$

where b_1, b_2, t_1, t_2, *and* h are top flange width, bottom flange width, top flange thickness, bottom flange thickness, and center distance between top and bottom flanges, respectively. With E = 29,000 ksi, G = 11,200 ksi, $KL = L_b$, and β_x given in Eq. 4, B_1 from Eq. 1.a becomes

$$B_1 = 2.25\left(\frac{2I_{yc}}{I_y} - 1\right)\left(\frac{h}{L_b}\right)\sqrt{\frac{I_y}{J}} \tag{7}$$

With E = 29,000 ksi, G = 11,200 ksi, $KL = L_b$, I_y, I_{yc} given in Eq. 6, and C_w given in Eq. 5, B_2 from Eq. 1.a yields

$$B_2 = 25\left(1 - \frac{I_{yc}}{I_y}\right)\left(\frac{I_{yc}}{J}\right)\left(\frac{h}{L_b}\right)^2 \tag{8}$$

With E = 29,000 ksi, G = 11,200 ksi, and $KL = L_b$, the multiplier term in the right hand side of Eq. 1 can be further simplified as

$$\frac{\pi C_b}{(KL)}\sqrt{EI_y GJ} = \frac{56618C_b}{L_b}\sqrt{I_y J} \approx \frac{57000C_b}{L_b}\sqrt{I_y J} \approx \frac{2EC_b}{L_b}\sqrt{I_y J} \tag{9}$$

Therefore, Eq. 1 is approximated to

$$M_{cr} = \frac{\pi C_b}{KL}\sqrt{EI_y GJ}\left(B_1 + \sqrt{1 + B_2 + B_1^2}\right)$$

$$\approx \frac{2EC_b}{L_b}\sqrt{I_y J}\left(B_1 + \sqrt{1 + B_2 + B_1^2}\right) \tag{10}$$

where

$$B_1 = 2.25\left(\frac{2I_{yc}}{I_y} - 1\right)\left(\frac{h}{L_b}\right)\sqrt{\frac{I_y}{J}} \quad B_2 = 25\left(1 - \frac{I_{yc}}{I_y}\right)\left(\frac{I_{yc}}{J}\right)\left(\frac{h}{L_b}\right)^2 \tag{10.a}$$

Eqs. 10 and 10.a represent the elastic moment formulas for the girders with singly symmetric I-section. These formulas appear in footnote [e] of Table A-F1.1 in the LRFD Specification (1999). The above brief

derivation shows that the LRFD elastic design moment of singly symmetric girder sections was actually derived based on a singly symmetric I-section. Applying the LRFD design formulas directly to a WC/SC girder (also singly symmetric) is incorrect as it would underestimate the design strength of a WC/SC girder.

TORSIONAL PROPERTIES FOR WC/SC GIRDERS

As described above, three torsional properties (β_x, C_w, and J) are required to evaluate the theoretical elastic moment of a WC/SC girder. Because the WC/SC section consists of open thin-walled plate elements (Figure 6), the computation of the torsional properties can be greatly simplified by reexpressing the theoretical integration formulas in numerical expressions. Detailed numerical treatment for the torsional property formulas is described as follows:

1. Warping Constant C_w in Terms of Integration and Numerical Forms
According to Galambos (1968) and Heins (1975), the warping constant in terms of integral forms can be given as (See Figure 6)

$$C_w = \int_0^E W_n^2 \; t \; ds \tag{11}$$

where

$$W_n = \frac{1}{A}\int_0^E w_s t ds - w_s \qquad w_s = \int_0^S \rho_s \; ds_s \tag{11.a}$$

In Eq. 11a, w_s is the unit warping with respect to the shear center of section (torsion center), W_n is normalized unit warping, ρ_s is the distance between elemental tangent and the shear center, t is plate element thickness, and s is length along the plate element middle line. Since calculation of the warping constant is relative to the shear center, the section's shear center must first be located in order to perform the evaluation of C_w. According to Galambos (1968) and Heins (1975), the numerical formula for the warping constant may be expressed as

$$C_w = \frac{1}{3}\sum_1^n (W_{ni}^2 + W_{ni} W_{nj} + W_{nj}^2) \; t_{ij} \; L_{ij} \tag{12}$$

where

$$W_{ni} = \frac{1}{2A}\sum_{1}^{n}(w_{si} + w_{sj})\ t_{ij}\ L_{ij} - w_{si} \tag{12.a}$$

$$W_{nj} = \frac{1}{2A}\sum_{1}^{n}(w_{si} + w_{sj})\ t_{ij}\ L_{ij} - w_{sj} \tag{12.b}$$

In Eqs. 12.a and 12.b, n is the total number of sectional plate elements. In the above equation set,

$$w_s = \sum \rho_s L \tag{12.c}$$

where ρ_s is the distance between the element tangent and the shear center defined as positive if shear center is to the left of an observer standing at P and looking toward the positive direction of the tangent, L is the length of plate element, w_s = the unit warping with respect to the shear center of section, and t = the plate element thickness. Subscripts i and j specify the nodal points of plate element.

2. Monosymetric Parameter β_x in Integration and Numerical Forms

According to Galambos (1968), the theoretical formula for β_x can be expressed as

$$\beta_x = \frac{1}{I_x}\int_A y(x^2 + y^2)\,dA - 2Y_o \tag{13}$$

where x and y coordinates are with respect to the centroid of section, I_x the moment of inertia of section area with respect to x-axis, A the area of section, and Y_o is the vertical distance between the shear center and the centroid. Based on the derivations by the authors, the integral form of β_x can be rewritten into numerical formulas as follows.

$$\beta_x = \frac{1}{I_x}\left\{\sum_{1}^{n}\left[\frac{1}{6}(x_j{}^3 - x_i{}^3)(y_j{}^2 - y_i{}^2) + \frac{1}{4}(x_j - x_i)(y_j{}^4 - y_i{}^4)\right]\right\} - 2Y_o \tag{14}$$

where (x_i,y_i) and (x_j,y_j) are the coordinates for the nodal points of the plate elements as shown in Figure 7.

3. Torsional Constant J in Terms of Integration and Numerical Forms

Since the WC/SC section is an open thin-walled section, the theoretical formula for J based on the basic mechanics may be expressed as

$$J = \int_0^E r^2 \, dA \tag{15}$$

where r is the distance from any point on the cross section to the shear center. The numerical expression for J can be further simplified as

$$J = \sum_1^n \frac{1}{3} b_i \, t_i^3 \tag{16}$$

where n and i represent the total number and the identification number of plate elements, respectively (See Figure 7).

MOMENT CURVES FOR WC/SC GIRDERS

Fundamental theory and LRFD moment curves are summarized in this section. Note that the moment curves are expressed in terms of unbraced lengths (L_b).

1. The Value of L_p

L_p is the largest unbraced length (L_b) that the section can generate plastic moment. In this study, the value of L_p is calculated based on the LRFD Eq. F1-4 which is given by

$$L_p = 1.76 \, r_{yc} \sqrt{\frac{E}{F_{yf}}} \tag{17}$$

2. The Value of L_r

L_r is the unbraced length (L_b) that the largest allowable elastic moment occurs. It can be obtained by letting $M_{cr} = M_r$ with $C_b = 1.0$. M_{cr} is the elastic moment obtained from Eq. 1 or Eq. 10, and M_r is the limiting buckling moment as defined in the LRFD namely

$$M_r = F_L \, S_{xc} \le F_y \, S_{xt} \tag{18}$$

where $F_L = (F_{yf} - F_r)$ or F_{yw}, whichever is smaller (19)

In Eqs. 18 and 19, F_{yf} is the flange yield stress, F_r the residual stress, F_{yw} the web yield stress, S_{xc} the section modulus for compression area, and S_{xt} is the section modulus for tension area.

L_r Based on Theory (L_{r1})

Theoretical L_r can be derived by setting M_{cr} (Eq. 1) equal to M_r (Eq. 18) and assuming $C_b = 1.0$. Thus derived L_r is referred as L_{r1} in this paper.

L_r Based on LRFD (L_{r2})

LRFD L_r can be derived by setting M_{cr} (Eq. 10) equal to M_r (Eq. 18) and assuming $C_b = 1.0$. Thus derived L_r is referred as L_{r2} in this paper.

3. Moment Curves for WC/SC Girders

Moment Curves Based on Theory

When $L_b \le L_p$,

$$M_n = M_p = F_y Z \le 1.5M_y = 1.5F_y S_x \tag{20}$$

where M_p is the plastic moment of section.

When $L_p \le L_b \le L_r$ ($L_r = L_{r1}$),

$$M_n = C_b \left\{ M_P - (M_P - M_r)\left(\frac{L - L_p}{L_r - L_p} \right) \right\} \tag{21}$$

When $L_b \ge L_r$, the elastic moment curve is obtained by using Eq. 1.

Moment Curve Based on LRFD

When $L_b \le L_p$,

$$M_n = M_p = F_y Z \le 1.5M_y = 1.5F_y S_x \tag{22}$$

When $L_p \le L_b \le L_r$ ($L_r = L_{r2}$),

$$M_n = C_b \left\{ M_P - (M_P - M_r)\left(\frac{L - L_p}{L_r - L_p} \right) \right\} \tag{23}$$

When $L_b \ge L_r$, the elastic moment curve is obtained by using Eq. 10. Typical WC/SC moment curves based on the theory and LRFD are plotted in Figure 8 for comparison purpose.

MOMENT PARAMETERS FOR WC/SC GIRDERS

For a complete analysis of a WC/SC girder, a number of moment parameters are required. Some required parameters such as β_x, C_w, J, *and* L_r are obtained through a rather tedious procedure, which is definitely not an easy task for practicing engineers.

1. Moment Parameters for the Theoretical Curve

The required design parameters for a theoretical analysis of WC/SC girder include M_p, M_r, L_p, L_r, C_w, β_x, J, B_1, and B_2. It was found that the values of $B_1 L_b$ and $B_2 L_b^2$ (where $L_b = KL$) are constants which can be shown in Eqs. 24 and 25 below.

$$B_1 = \frac{\pi \beta_x}{(2KL)}\sqrt{\frac{EI_y}{GJ}} \Rightarrow B_1 = \frac{\pi \beta_x}{(2L_b)}\sqrt{\frac{EI_y}{GJ}} \Rightarrow B_1 L_b = \frac{\pi \beta_x}{2}\sqrt{\frac{EI_y}{GJ}} \quad (24)$$

$$B_2 = \frac{\pi^2 EC_w}{(KL)^2 GJ} \Rightarrow B_2 = \frac{\pi^2 EC_w}{(L_b)^2 GJ} \Rightarrow B_2 L_b^{\,2} = \frac{\pi^2 EC_w}{GJ} \quad (25)$$

For evaluation and comparison purposes, all required parameters were calculated for all WC/SC girders listed in the ASD and LRFD design manuals. Owing to the limited space allowed in this paper, only a portion of the computed parameters (i.e., the WC-sections included in LRFD design manual) are being provided, as listed in Tables 1 and 2. Such tables will help practitioners to better design the WC/SC girders.

2. Moment Parameters for the LRFD Curve

The required design parameters for the LRFD moment analysis of WC/SC girder include M_p, M_r, L_p, L_r, I_y, I_{yc}, h, J, B_1, and B_2. As above, the values of B_1L_b and $B_2L_b^2$ are constants as shown in Eqs. 26 and 27 below.

$$B_1 \cong 2.25\left(\frac{2I_{yc}}{I_y} - 1\right)\left(\frac{h}{L_b}\right)\sqrt{\frac{I_y}{J}} \Rightarrow B_1 L_b \cong 2.25h\left(\frac{2I_{yc}}{I_y} - 1\right)\sqrt{\frac{I_y}{J}} \quad (26)$$

$$B_2 \cong 25\left(1 - \frac{I_{yc}}{I_y}\right)\left(\frac{I_{yc}}{J}\right)\left(\frac{h}{L_b}\right)^2 \Rightarrow B_2 L_b^{\,2} \cong 25h^2\left(1 - \frac{I_{yc}}{I_y}\right)\left(\frac{I_{yc}}{J}\right) \quad (27)$$

All moment parameters required for WC/SC girders to proceed the LRFD design are calculated. Some (only the WC-sections listed in the LRFD design manual) of these parameters are given in Tables 1 and 3. These tables will satisfy those who wish to exactly follow the LRFD design on the WC/SC girders.

ILLUSTRATED EXAMPLE

A built-up section consisting of *W12×26* and *C10×15.3* with $C_b = 1.0$ and $F_y = 50$ *ksi*. Plot the complete nominal moment curves (M_n *vs.* L_b) based on the theory and the third edition of LRFD. For illustration purposes, $KL = L_b = 55$ *ft* is assumed to calculate the elastic moment using the theory, the LRFD, and the proposed methods.

Solution:

Built-up WC section properties and constants from the LRFD design manual: $A=12.10\ in.^2$, $r_y = 2.64\ in.$, $S_2 = 70.5\ in.^3$, $S_1 = 36.3\ in.^3$, $E=29{,}000\ ksi$, $G=11{,}200\ ksi$, and $Z_x = 47.0\ in^3$.

1. Plot the Complete Moment Curve Using the Theory

M_p and L_p Values

$M_p = F_y Z \le 1.5M_y = 1.5F_y S_x$ Thus, we obtain $M_p = 2350$ k-in.

$$r_{yc} = \sqrt{\frac{I_{yc}}{A_c + b_f \times t_f}} = \sqrt{\frac{75.95}{4.48 + 6.49 \times 0.38}} = 3.307\ in.$$

$I_{yc} = I_{yw}/2 + I_{xc} = 17.3/2 + 67.3 = 75.95\ in.^4$ and $F_{yf} = 50\ ksi$

$$L_p = r_{yc}\lambda_p = 1.76 r_{yc}\sqrt{\frac{E}{F_{yf}}} = 1.76 \times 3.307 \times \sqrt{\frac{29000}{50}} = 140.16\ in.$$

Therefore, M_p =2350 k-in. and L_p =140.16 in.

M_r and L_r Values

$M_r = F_L S_{xc} \le F_{yf} S_{xt}$ F_L = smaller of $(F_{yf} - F_r)$ or F_{yw}

Thus, we obtain $M_r = 1815$ k-in.

L_r is the L_b when $M_{cr} = M_r$ with $C_b = 1.0$ (as shown below) and it can be obtained with the aid of Microsoft Excel. For $W12\times26$ and $C10\times15.3$, based on the developed program LTBMN the following values can be obtained: $\beta_x = 9.916$ in. , C_w=1301.6 in.^{6} , $J = 0.876$ in.^{4}, and $I_y = I_{yw} + I_{xc} = 17.3 + 67.3 = 84.6$ in.^{4}.

$$B_1 = \frac{\pi\beta_x}{2KL}\sqrt{\frac{EI_y}{GJ}} = \frac{\pi \times 9.916}{2L_b}\sqrt{\frac{29000 \times 84.6}{11200 \times 0.876}} = \frac{246.31}{L_b}$$

$$B_2 = \frac{\pi^2 EC_w}{(KL)^2 GJ} = \frac{\pi^2 \times 29000 \times 1301.6}{L_b^{\,2} \times 11200 \times 0.876} = \frac{37972.35}{L_b^{\,2}}$$

$$M_{cr} = \frac{C_b\pi}{L_b}\sqrt{EI_y GJ}\left\{ B_1 + \sqrt{1 + B_2 + B_1^{\,2}} \right\} = M_r = 1815\ k\text{-}in.$$

which gives $L_b = L_r$ = 465.86 in.

The Demonstration of Elastic Moment Evaluation

Calculate the M_{cr} with $L_b = 55\ ft$

Since L_b = 55 ft = 660 in. > L_r = 465.86 in., the nominal moment is equal to M_{cr}. Substituting $L_b = 55\ ft = 660\ in.$ into B_1 and B_2, we get

$$B_1 = \frac{\pi\beta_x}{2KL}\sqrt{\frac{EI_y}{GJ}} = 0.37320 \qquad B_2 = \frac{\pi^2 EC_w}{(KL)^2 GJ} = 0.08717$$

We obtain $M_{cr} = \frac{C_b\pi}{KL}\sqrt{EI_y GJ}\left\{B_1 + \sqrt{1 + B_2 + B_1^2}\right\} = 1093.45\,k\text{-}in.$

2. Plot the Complete Moment Curve Using the LRFD

From above, $M_p = 2350$ k-in., $L_p = 140.16$ in., and $M_r = 1815$ k-in.

$$h = \frac{b_{fw}\cdot t_{fw}\left(d_w - \frac{t_{fw}}{2}\right) + A_c\cdot\left(d_w + t_{wc} - \bar{x}\right)}{b_{fw}\cdot t_{fw} + A_c} - \frac{t_{fw}}{2} = 11.688\ in.$$

$J = J_w + J_c = 0.3 + 0.209 = 0.509\ in.^3$

$$B_1 = 2.25\left(\frac{2I_{yc}}{I_y} - 1\right)\left(\frac{h}{L_b}\right)\sqrt{\frac{I_y}{J}} = \frac{269.718}{L_b}$$

$$B_2 = 25\left(1 - \frac{I_{yc}}{I_y}\right)\left(\frac{I_{yc}}{J}\right)\left(\frac{h}{L_b}\right)^2 = \frac{52108.4}{L_b^2}$$

L_r equals to L_b when $M_{cr} = M_r$ with $C_b = 1.0$ (as shown below) and it can be obtained through the use of Microsoft Excel.

$$M_{cr} = \frac{2EC_b}{L_b}\sqrt{I_y J}\left\{B_1 + \sqrt{1 + B_2 + B_1^2}\right\} = M_r = 1815\,k\text{-}in.$$

which gives $L_b = L_r = 412.95$ in.

The Demonstration of Elastic Moment Evaluation

Calculate M_{cr} with $L_b = 55\,ft = 660\,in.$

$M_n = M_{cr}$, which is based on Table A-F1.1 of LRFD.

$$B_1 = 2.25\left(\frac{2I_{yc}}{I_y} - 1\right)\left(\frac{h}{L_b}\right)\sqrt{\frac{I_y}{J}} = 0.4086 \quad B_2 = 25\left(1 - \frac{I_{yc}}{I_y}\right)\left(\frac{I_{yc}}{J}\right)\left(\frac{h}{L_b}\right)^2 = 0.1196$$

$$M_{cr} = \frac{2EC_b}{L_b}\sqrt{I_y J}\left\{B_1 + \sqrt{1 + B_2 + B_1^2}\right\} = 889.8\,k\text{-}in.$$

3. The Proposed Design Method (Table Method)

The procedure for the proposed method is presented as follows:

Utilizing Tables 1~3 and assuming $L_b = 55$ ft, the following design data pertaining to *W12×26 and C10×15.3* are found.

W-section	C-section	Section Properties				Theory			LRFD
		I_y (in.^{4})	I_{yc} (in.^{4})	r_{yc} (in.)	h (in.)	β_x (in.)	C_w (in.^{6})	J (in.^{4})	J (in.^{4})
W12×26	C10×15.3	84.6	76	3.31	11.7	9.92	1301.6	0.876	0.509

Method	M_p(k-ft)	M_r(k-ft)	L_p (in.)	L_r (in.)	λ_p	λ_r	B_1L_b	$B_2L_b^2$
Theory	195.8	151.3	140.2	465.9	42.4	140.9	246	37972
LRFD	195.8	151.3	140.2	413.0	42.4	124.9	270	52108

Theoretical Design

Note that the unbraced length $L_b = 55\ ft = 660\ in. > L_r = 465.86\ in.$

Utilizing Table,

$$B_1 = \frac{246}{L_b} = \frac{246}{660} = 0.37273 \qquad B_2 = \frac{37972}{L_b^2} = \frac{37972}{660^2} = 0.08717$$

$$M_{cr} = \frac{C_b\pi}{L_b}\sqrt{EI_yGJ}\left\{B_1 + \sqrt{1 + B_2 + B_1^2}\right\} = 1093\ k\text{-}in.$$

LRFD Design

Here, the unbraced length $L_b = 55\ ft = 660\ in. > L_r = 412.95\ in.$

Utilizing Table,

$$B_1 = \frac{270}{L_b} = \frac{270}{660} = 0.409 \qquad B_2 = \frac{52108}{L_b^2} = \frac{52108}{660^2} = 0.1196$$

$$M_{cr} = \frac{2EC_b}{L_b}\sqrt{I_yJ}\left\{B_1 + \sqrt{1 + B_2 + B_1^2}\right\} = 890k\text{-}in \le M_p = 2350\ k\text{-}in.$$

Comments

M_{cr} = 1093 k-in. based on the theory and M_{cr} = 890 k-in. based on the LRFD. In this particular example, the LRFD underestimates the capacity of the WC girder by 18.6%. With the useful design tables as provided, the proposed method is much easier to implement. Nominal moment curves can be plotted based on the theory and LRFD as described in this example, and the curves should be very similar to those shown in Figure 8.

CONCLUSIONS

Based on this study, the followings conclusions may be drawn.

1. Direct use of LRFD singly symmetric section formulas for built-up WC/SC girders is fundamentally incorrect. They generally underestimate the elastic critical moment by 12~ 28 percent depending on L_b value. Theoretical formulas for the flexural design of WC/SC girders are summarized in the paper. Calculations of the required moment parameters (M_p , M_r , L_p , L_r , B_1, and B_2) and torsional properties (β_x, C_w, and J) for WC/SC girders are a formidable task. These parameters and properties are being made available in tables for engineers wishing to have a more in-depth analysis on WC/SC girders.
2. In the LRFD design, calculations of the required moment parameters (M_p , M_r , L_p , L_r , I_{yc}, J, h, B_1, *and* B_2) for WC/SC girders are quite cumbersome for most engineers. These required moment parameters (M_p, M_r, L_p, L_r , I_y, I_{yc}, h, J, B_1, and B_2) for the LRFD design of WC/SC girders are hence precalculated and tabulated for those who look for a quick moment design of WC/SC girders.
3. Design guide for evaluating WC/SC girders is presented with an illustrative design example. A rational but simple approach for WC/SC girder designs is proposed. Typical WC/SC moment curves based on theory and LRFD are also plotted for comparison purposes. This additional design information should help those who wish to have a better evaluation on the lateral-torsional buckling strength of the WC/SC girders listed in the current AISC design manuals.

ACKNOWLEDGEMENTS

This research was sponsored by the National Science Council of Taiwan through grant No. NSC-84-2211-E005-030 for which the authors are most grateful. The authors also wish express their gratitude to Professor Y. Frank Chen for his valuable input in this article.

REFERENCES

AISC (1986,1993,1999), Manual of Steel Construction, Load and

Resistance Factor Design, 1st, 2nd, 3rd Editions, American Institute of Steel Construction, Chicago, Illinois.

AISC (1989), *Manual of Steel Construction*, Allowable Stress Design, 9th edition, American Institute of Steel Construction, Chicago, Illinois.

Clark, J. W. and Hill, H. N. (1960), "Lateral Buckling of Beams," Journal of Structural Engineering, ASCE, Vol. 86, No. ST7, pp.175-196.

Ellifritt, D. S. and Lue, D. M. (1998), "The Warping Constant for the W-Section with a Channel Cap," Engineering Journal, AISC, 2nd Quarter.

Galambos, T. V. (1968), Structural Members and Frames, Prentice-Hall, New Jersey, pp. 80-158.

Heins, C. P. (1975), Bending and Torsional Design in Structural Members, Lexington Books, Lexington, Massachusetts, pp. 35-80.

Hulshizer, A. J. (1991), "1989 AISC Specification (Ninth Edition) Allowable Bending Stress Design Aid," Engineering Journal, AISC, 2nd Quarter.

Kitipornchai, S. and Trahair, N. S. (1980), "Buckling Properties of Monosymmetric I-Beams," Journal of Structural Engineering, ASCE, Vol. 106, No. ST5, pp.41-957.

Kubo, M. and Fukumoto, Y. (1988), "Lateral Torsional Buckling of Thin-Walled I-Beams,"Journal of the Structural Division, ASCE, Vol. *114*, No. *ST4*, pp.*841-855*.

Lue, Tony and Ellifritt, D. S. (1993), "The Warping Constant for the W-Section with a Channel Cap," Engineering Journal, AISC, 3rd Quarter.

Lue, D. M. and Ellifritt, D. S. (2003), "Numerical Evaluation for Warping Constant of Built-up Crane Runway Beam," SSRC Annual Meeting Proceedings, April 2 ~ 5, Baltimore, Maryland, U.S.A, pp. 213-232.

Moore, W. E., II (1985), "A General Solution for the Governing Bending Equation," Engineering Journal, AISC, 1st Quarter.

Salmon, C. G. and Johnson, J. E. (1996), Steel Structures – Design and Behavior, Harper and Row, Publishers, 4th edition, NY, pp. 1009.

Table 1. Section properties (Sections from 3rd LRFD Manual), F_y = 50 ksi

W-section	*C*-section	Section properties				Theory			LRFD
		I_y (in.^{4})	I_{yc} (in.^{4})	r_{yc} (in.)	h (in.)	β_x (in.)	C_w (in.^{6})	J (in.^{4})	J (in.^{4})
W12×26	C10×15.3	84.6	76.0	3.31	11.7	9.92	1301.6	0.876	0.509
W12×26	C12×20.7	146.3	137.7	4.01	11.7	10.89	1471.3	1.129	0.669
W14×30	C10×15.3	86.9	77.1	3.3	13.3	10.82	1816.5	0.978	0.589
W14×30	C12×20.7	148.6	138.8	4.00	13.3	12.06	2030.7	1.236	0.749
W16×36	C12×20.7	153.5	141.3	3.94	15.3	13.39	3182.5	1.518	0.914
W16×36	C15×33.9	339.5	327.3	5.03	15.3	14.46	3676.2	2.553	1.555
W18×50	C12×20.7	169.1	149.1	3.79	17.4	13.67	6081.6	2.636	1.609
W18×50	C15×33.9	355.1	335.1	4.85	17.4	15.69	6950.6	3.687	2.250
W21×62	C12×20.7	186.5	157.8	3.76	20.3	14.31	11062.4	3.481	2.199
W21×62	C15×33.9	372.5	343.8	4.78	20.3	17.4	12646.8	4.675	2.840
W21×68	C12×20.7	193.7	161.4	3.71	20.4	13.81	12265.3	4.364	2.819
W21×68	C15×33.9	379.7	347.4	4.72	20.4	17.14	14102.2	5.697	3.460
W24×68	C12×20.7	199.4	164.2	3.81	23.1	14.99	16712.6	3.522	2.239
W24×68	C15×33.9	385.4	350.2	4.8	23.1	18.9	19145.5	4.725	2.880
W24×84	C12×20.7	223.4	176.2	3.68	23.3	13.53	21630.5	6.129	4.069
W24×84	C15×33.9	409.4	362.2	4.63	23.3	18.07	25162.3	7.738	4.710
W27×84	C15×33.9	421	368.0	4.75	26.0	19.41	34196.4	6.25	3.820
W27×94	C15×33.9	439	377.0	4.66	26.2	18.71	39548.1	8.227	5.040
W30×99	C15×33.9	443	379.0	4.72	29.0	20.27	49335.8	7.569	4.780
W30×99	MC18×42.7	682	618.0	5.61	29.0	23.23	54418.7	8.546	5.000
W30×116	C15×33.9	479	397.0	4.59	29.2	18.95	61785.6	11.681	7.440
W30×116	MC18×42.7	718	636.0	5.44	29.2	22.34	67642.3	12.528	7.660
W33×118	C15×33.9	502	408.5	4.7	32.2	19.72	83645.2	9.969	6.310
W33×118	MC18×42.7	741	647.5	5.54	32.1	23.64	91655.4	10.734	6.530
W33×141	C15×33.9	561	438.0	4.57	32.4	17.89	104816.	16.494	10.71
W33×141	MC18×42.7	800	677.0	5.35	32.4	22.22	115859.	17.582	10.93
W36×150	C15×33.9	585	450.0	4.6	35.0	18.30	133166.	16.934	11.11
W36×150	MC18×42.7	824	689.0	5.37	35.0	23.07	147349.	18.033	11.33

Conversion of units: 1 in. = 2.54 cm; 50 ksi = 345 MPa

Table 2. Theoretical moment parameters (Sections from 3rd LRFD), F_y = 50 ksi

W-section	*C*-section	M_p (k-ft)	M_r (k-ft)	L_p (in.)	L_r (in.)	λ_p	λ_r	B_1L_b	$B_2L_b^2$
W12×26	C10×15.3	195.8	151.3	140.2	465.9	42.4	140.9	246	37972
W12×26	C12×20.7	200.8	153.3	170.1	645.7	42.4	160.9	313	33291
W14×30	C10×15.3	251.3	191.7	140.0	426.5	42.4	129.2	258	47483
W14×30	C12×20.7	258.3	194.6	169.6	584.0	42.4	146	334	41973
W16×36	C12×20.7	346.7	261.7	167.1	527.0	42.4	133.7	341	53594
W16×36	C15×33.9	361.7	268.8	213.0	846.4	42.4	168.4	421	36800
W18×50	C12×20.7	529.2	405.4	160.8	461.6	42.4	121.7	277	58956
W18×50	C15×33.9	554.2	416.7	205.6	709.2	42.4	146.1	389	48180
W21×62	C12×20.7	762.5	575.0	159.5	418.0	42.4	111.1	265	81216
W21×62	C15×33.9	787.5	591.7	202.8	625.8	42.4	130.8	393	69125
W21×68	C12×20.7	833.3	633.3	157.1	409.6	42.4	110.5	233	71828
W21×68	C15×33.9	862.5	650.0	199.9	610.0	42.4	129.3	354	63263
W24×68	C12×20.7	933.3	700.0	161.4	397.8	42.4	104.5	285	12126
W24×68	C15×33.9	966.7	720.8	203.5	585.3	42.4	121.9	431	10353
W24×84	C12×20.7	1194.7	843.1	155.9	391.9	42.4	106.6	206	90183
W24×84	C15×33.9	1188.0	904.2	196.3	552.2	42.4	119.3	332	83095
W27×84	C15×33.9	1316.7	987.5	201.3	535.4	42.4	112.8	403	13982
W27×94	C15×33.9	1487.5	987.5	197.3	559.6	42.4	120.2	345	12285
W30×99	C15×33.9	1700.0	1250.0	200.2	501.3	42.4	106.1	392	16918
W30×99	MC18×42.7	1716.7	1266.7	237.8	641.2	42.4	114.3	525	16273
W30×116	C15×33.9	2000.0	1500.0	194.4	481.6	42.4	105	307	13517
W30×116	MC18×42.7	2050.0	1520.8	230.4	608.6	42.4	112	427	13797
W33×118	C15×33.9	2204.2	1645.8	199.4	473.2	42.4	100.6	354	21443
W33×118	MC18×42.7	2266.7	1666.7	234.8	594.8	42.4	107.4	496	21820
W33×141	C15×33.9	2645.8	1923.5	193.6	470.1	42.4	102.9	264	16240
W33×141	MC18×42.7	27.6.67	2041.7	226.8	567.5	42.4	106	379	16840
W36×150	C15×33.9	2983.3	2132.8	195.2	462.4	42.4	100.4	272	20096
W36×150	MC18×42.7	3075.0	2304.2	227.7	549.7	42.4	102.3	394	20881

Conversion of units:
1 in. = 2.54 cm; 1 ft = 0.3048 m; 1 k-ft = 0.6162 kN-m; 50 ksi = 345 MPa

Table 3. LRFD moment parameters (Sections from 3rd LRFD Manual), F_y = 50 ksi

W-section	*C*-section	M_p (k-ft)	M_r (k-ft)	L_p (in.)	L_r (in.)	λ_p	λ_r	B_1L_b	$B_2L_b^2$
W12×26	C10×15.3	195.8	151.3	140.2	413.0	42.4	124.9	270	52108
W12×26	C12×20.7	200.8	153.3	170.1	568.4	42.4	141.6	342	41343
W14×30	C10×15.3	251.3	191.7	140.0	385.1	42.4	116.6	281	65157
W14×30	C12×20.7	258.3	194.6	169.6	522.8	42.4	130.7	365	53707
W16×36	C12×20.7	346.7	261.7	167.1	477.0	42.4	121.0	376	72511
W16×36	C15×33.9	361.7	268.8	213.0	758.3	42.4	150.9	473	44655
W18×50	C12×20.7	529.2	405.4	160.8	420.5	42.4	110.8	305	82688
W18×50	C15×33.9	554.2	416.7	205.6	640.0	42.4	131.9	435	63333
W21×62	C12×20.7	762.5	575.0	159.5	387.5	42.4	103.0	291	114107
W21×62	C15×33.9	787.5	591.7	202.8	571.6	42.4	119.5	443	96448
W21×68	C12×20.7	833.3	633.3	157.1	379.5	42.4	102.4	253	99229
W21×68	C15×33.9	862.5	650.0	199.9	555.4	42.4	117.8	399	88865
W24×68	C12×20.7	933.3	700.0	161.4	374.0	42.4	98.2	317	171937
W24×68	C15×33.9	966.7	720.8	203.5	542.3	42.4	113.0	490	147547
W24×84	C12×20.7	1194.7	843.1	155.9	367.4	42.4	99.9	224	124339
W24×84	C15×33.9	1188.0	904.2	196.3	507.6	42.4	109.6	377	120622
W27×84	C15×33.9	1316.7	987.5	201.3	500.6	42.4	105.4	460	205251
W27×94	C15×33.9	1487.5	987.5	197.3	519.5	42.4	111.6	394	180548
W30×99	C15×33.9	1700.0	1250.0	200.2	473.9	42.4	100.3	445	239498
W30×99	MC18×42.7	1716.7	1266.7	237.8	599.1	42.4	106.8	618	242536
W30×116	C15×33.9	2000.0	1500.0	194.4	453.1	42.4	98.8	346	194310
W30×116	MC18×42.7	2050.0	1520.8	230.4	566.9	42.4	104.3	490	201419
W33×118	C15×33.9	2204.2	1645.8	199.4	450.6	42.4	95.8	405	311588
W33×118	MC18×42.7	2266.7	1666.7	234.8	561.0	42.4	101.3	576	322829
W33×141	C15×33.9	2645.8	1923.5	193.6	445.3	42.4	97.5	296	235081
W33×141	MC18×42.7	27.6.67	2041.7	226.8	532.2	42.4	99.4	431	249438
W36×150	C15×33.9	2983.3	2132.8	195.2	441.4	42.4	95.9	308	286229
W36×150	MC18×42.7	3075.0	2304.2	227.7	519.9	42.4	96.8	451	304819

Conversion of units:
1 in. = 2.54 cm; 1 ft = 0.3048 m; 1 k-ft = 0.6162 kN-m; 50 ksi = 345 MPa

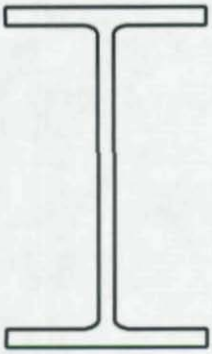

Fig. 1 Doubly symmetric I-section

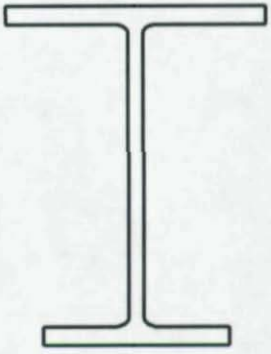

Fig. 2 Singly symmetric I-section

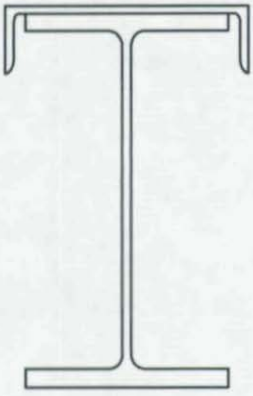

Fig. 3 Built-up WC section

Fig. 4 Built-up SC section

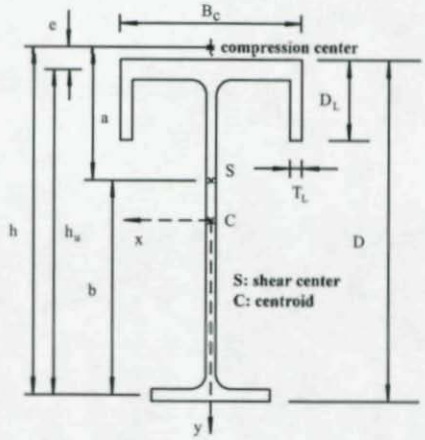

Fig. 5 Australian built-up section for crane runway girder

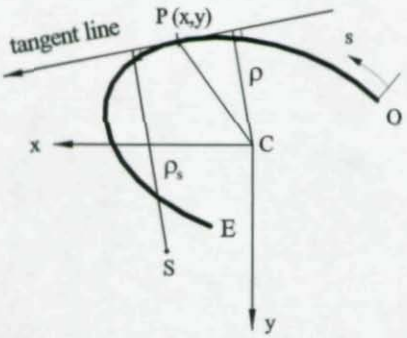

S : shear center C: centroid

ρ : distance between tangent line and centroid

$ρ_s$: distance between tangent line and shear center

Fig. 6 Coordinates and tangential distances in an open cross section

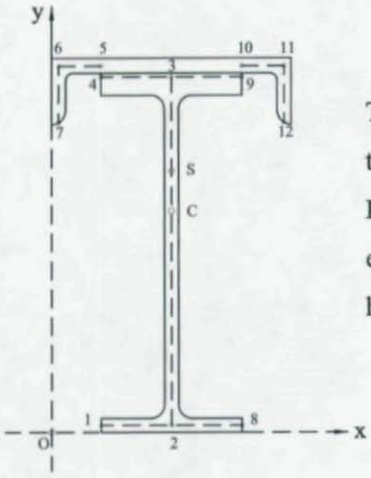

There are 11 plate elements in the built-up WC/SC section. Element 4 (point 4 to point5) and element 9 (point 10 to point 9) have thickness = 0

Fig. 7 Distribution of 11 plate elements

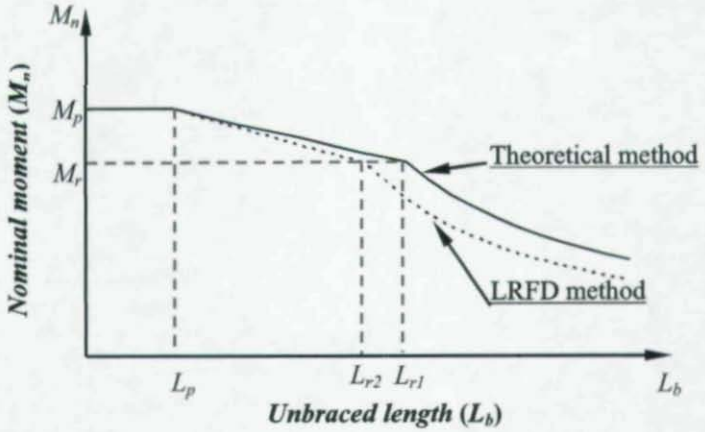

Fig. 8 Nominal moment curves for typical built-up WC/SC girder

Construction Simulation of Curved I-Girder Bridge Systems

C.-J. Chang[1] and D.W. White[1]

ABSTRACT

This paper discusses prototype capabilities for simulating the construction of curved steel I-girder bridges. The methods presented allow Engineers to script out different construction scenarios, starting with the no-load geometry of the steel components. Given a selected scenario, one can check deflections, reactions and/or stresses at different stages of the steel erection or concrete casting, determine required crane capacities, tie-down, jacking or come-along forces, incremental displacements due to removal of temporary supports, etc. Also, the capabilities can be used to determine the influence of different steel detailing methods on the bridge geometry, such as the web-plumbness under the steel or total dead load, as well as the implications of geometric tolerances on the structural performance. Many of the above considerations are impacted by geometric nonlinearity (stability effects). The proper calculation requires that equilibrium must be considered on the deformed geometry. The paper focuses on the fundamental requirements necessary to ensure correctness of the analysis results. Example simulations are presented for a representative curved I-girder bridge.

INTRODUCTION

Due to the horizontal curvature, the construction of curved steel I-girder bridges is not as straightforward as that of straight I-girder bridges. The displacement of, internal stresses in and stability of curved I-girder bridges during construction are important considerations.

---

[1] Georgia Institute of Technology, Atlanta, GA 30332-0355

Bridges are usually erected piecewise. A wide variety of steel fabrication and erection schemes may be employed depending on the bridge size and specific geometry. Because of the differential deflections of curved girders during erection, one consideration in curved steel bridge construction is the fit-up of the steel pieces in the deformed geometry of the partially erected structure. In general, girders or girder subassemblies are connected together with cross-frames after they are seated on temporary and/or permanent supports or are connected at splice locations. However, the differential deflections and rotations may make the connections difficult in certain situations.

Another important consideration is the prediction and control of the structure's geometry. Different steel detailing practices and slab casting sequences, and some erection procedures, can have a significant influence on the final constructed position. Bearings must accommodate the rotations due to dead and live loads or must be installed in a manner to ensure that their rotation limits are not exceeded, girder vertical elevations should be within tolerances accommodated by haunch depths, and tolerances on the horizontal roadway alignment should be met. Also, AASHTO (2004) indicates that in addition to considering the effects of deviations from the ideal final bridge geometry, the Engineer may need to consider the influence of locked-in construction stresses on the structural performance in some bridges.

In many cases, all of the above considerations may be only of minor significance. However, in curved bridges with longer spans, tight radii, sharp skews, and/or highly stiff or flexible flanges in the lateral direction, specific and reliable simulation of the construction processes and responses can be of significant benefit. This paper discusses prototype capabilities for calculation of the construction requirements, the structural responses during construction, and the final dead load state (stresses, deflections, forces and reactions) in general curved steel I-girder bridges. The primary design-analysis capabilities, which have been implemented in GT-Sabre (Chang 2006), are based on beam theory idealizations. The paper emphasizes the fundamental requirements for correctness of the calculations. It closes with results from example simulations for a representative curved I-girder bridge.

STEEL DETAILING PRACTICES

Understanding of steel detailing practices is key to addressing construction simulation for steel I-girder bridges. Generally speaking, steel I-girders are always fabricated with a vertical camber to compensate for their vertical dead load deflections. Furthermore, in straight skewed bridges and horizontally curved bridges with or without skewed supports, the torsional rotations of the I-girders may or may not be compensated for in the fabrication of the structural steel. The simplest practice is to fabricate the I-girders such that their webs are vertical or plumb when they are fully-supported (i.e., blocked) in their no-load geometry. Also, the simplest practice is to fabricate the cross-frames such that they fit-up with the cambered no-load geometry of the I-girders without inducing any deformations and internal stresses due to lack-of-fit. This type of detailing is referred to in this work as *No-Load Fit* or *NLF*. In this case, the final constructed state under the steel dead loads can be analyzed simply by building a model in the idealized no-load geometry and then "turning on" the steel dead loads.

Bridges that are detailed for no-load fit necessarily have out-of-plumb webs in their steel or total dead load conditions. Also, the final in-plan dead-load position of the slab is deflected from the ideal no-load geometry, and dead load rotations occur that must be accommodated at the bridge bearings. As long as these deflections do not influence the performance in any significant way, NLF detailing is generally the preferred approach. However, in structures where these deviations from the ideal geometry are larger than acceptable tolerances, other options must be considered. Given the AASHTO (2004) sanctioned elastic analysis and design procedures, the only *strength* performance consideration in setting the above tolerances, for bridges detailed for *NLF*, is whether a second-order elastic analysis should be conducted to determine the dead load stresses. All of the relevant strength issues are addressed within the AASHTO (2004) resistance equations as long as the computed second-order elastic stresses are sufficiently accurate. In many cases, the second-order elastic amplification of the bridge dead load responses is small. In these situations, a first-order analysis for the steel dead load, using a model of the complete structure, and simply

"turning on" the load, followed by a first-order analysis of the structure accounting for any effects of staged slab construction and satisfying the AASHTO (2004) requirements, results in an accurate design. Unfortunately, rigorous guidelines for when first-order analysis is not sufficient do not exist.

Incidentally, the detailing of I-girder bridges for NLF requires that all the girder connection plates must be detailed differently or all the cross-frames must be detailed differently (see Figs. 1a and 1b). This is caused by the difference in the elevation of the girders due to the different vertical cambers at the various cross-frame locations. The bolt holes in the connection plates must be at different distances from the flanges and/or the cross-frames must be detailed to account for the different cambers. These differences also occur due to superelevation, and therefore their handling does not present any special problem.

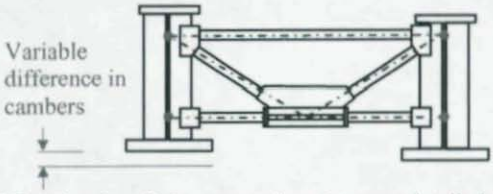

Fig. 1a. NLF option 1 – all the connection plates are detailed differently.

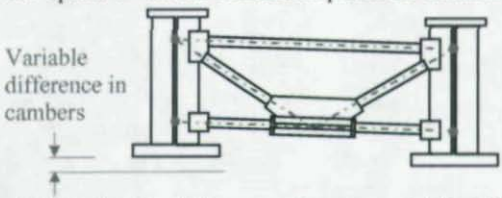

Fig. 1b. NLF option 2 – all the cross-frames are detailed differently.

In cases where displacements other than the vertical deflections must be compensated for, a common practice is to detail the cross-frames to fit-up with the I-girders in their idealized web-plumb but vertically deflected positions under either the steel dead load only or under the total dead load. These detailing practices are referred to in this paper as *Steel Dead Load Fit (SDLF)* and *Total Dead Load Fit (TDLF)*. SDLF allows the erector to target a web plumb condition at the end of the

steel erection. However, achieving a perfectly plumb web condition is obviously an unnecessary requirement. Also, since TDLF targets a web plumb condition in the final state of the structure, implying a shared responsibility among the steel erector and the concrete contractor, its practical implementation can be problematic.

Under SDLF or TDLF detailing, the cross-frames do not fit-up with the I-girders in the ideal zero-stress condition of the structure (see Fig. 2a). As shown in Fig. 2b, the girders must be twisted (i.e., their flanges must be pushed and/or pulled radially, thus changing their radius of curvature) to connect the cross-frames in the idealized no-load position. This lack-of-fit in the no-load geometry, and the resistance of the flanges to changes in their radii, induces additional "locked-in" stresses throughout the structure and influences the vertical, horizontal and twist deflections of the system. AASHTO (2004) states that the Engineer may need to consider these lack-of-fit stresses in the girder flanges or the cross-frames or diaphragms, but that the decision as to when these stresses should be evaluated is currently a matter of engineering judgment. As noted previously, the AASHTO (2004) resistance equations generally provide a sufficient strength assessment as long as the second-order elastic stresses are accurately calculated. With SDLF and TDLF detailing, these stresses should include the influence of the lack of fit when the lack-of-fit stresses are a significant fraction of the total stresses. However, any potential definition of what fraction is significant (or non-incidental) should consider the beneficial inelastic redistribution that occurs under incidental overloads, deviation from support elevation tolerances, etc. in all steel bridge structures. These attributes are factors in the development of the AASHTO provisions for elastic analysis and design, even though the above types of incidental stresses are not included in the elastic analysis and design calculations.

AASHTO (2004) describes one other method of steel detailing, but points out that it has limited use since it is generally more costly. In this method, referred to here as *Twist Camber Fit* or *TCF*, the girder top and bottom flanges are fabricated with a different radius of curvature to

compensate for the twist rotations under the steel or the total dead load, in addition to cambering to offset the vertical deflections. Correspondingly, the cross-frames are detailed to fit to the ideal twist cambered geometry without inducing any lack-of-fit stresses in the structure.

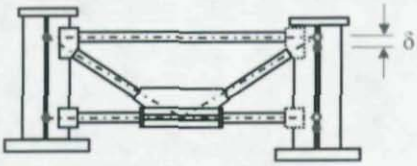

Fig. 2a. SDLF or TDLF concept 1 – lack of fit between girders and cross-frames in no-load geometry.

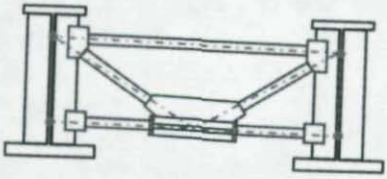

Fig. 2b. SDLF or TDLF concept 2 –forcing/twisting of the girders into position to connect the cross-frames.

Detailing for NLF, SDLF, TDLF or TCF generally should be specified by the designer. This is because this decision can have an important influence on construction requirements, the definition of and achievement of a targeted geometry for the completed structure, as well as the performance of the bridge. The differential deflections between the girders in the partially completed structure, and the corresponding forces required for assembly of the components, generally tend to be somewhat larger for SDLF and TDLF. Also, SDLF or TDLF detailing generally influences the girder vertical deflections. Although the differences between the vertical deflections for TDLF, SDLF or NLF may often be accommodated within the depth of the girder haunches, the Engineer may prefer to avoid using up the vertical tolerances provided by the haunch depths to accommodate these differences.

CONDITIONS FOR UNIQUENESS OF THE ANALYSIS RESULTS

Another key to addressing construction simulation for curved steel I-girder bridges is an understanding of when the analysis solutions are unique, or in other words, when the analysis results are independent of the order of the component assembly or load application. Basically, the conditions for uniqueness of the analysis can be stated as follows. The solution for the displacements, internal stresses, and reactions is unique for any sequence of assembly and/or loading when:

1) The no-load geometry of the structural components is the same, regardless of the sequence,
2) The connections are made ideally with zero tolerance,
3) The structure is maintained in an elastic condition, and
4) The final displacement boundary conditions at the supports are independent of the sequence.

The first three conditions are essential for simplifying the consideration of connection assembly procedures. Otherwise, the details of how even a minor joint is bolted up must be accounted for in determining the state of the structure. All four conditions are also essential for allowing the Engineer to use a model of the complete structure to analyze for the final responses in certain cases without the need to consider the erection sequence (e.g., under steel dead load only, or under total dead load when the slab is cast in one continuous stage).

Under the above four conditions, the bridge is a conservative elastic system. The second-order elastic deflections, stresses and reactions are independent of the sequence of the assembly and/or loading. Obviously, if the slab is cast in successive stages, the hypothetical no-load geometry of the various portions of the slab depends on the slab casting sequence. Each stage of the slab is typically assumed to harden into its no-load geometry in the current deformed configuration at the time of the casting. Each stage of the slab is instantiated on the current deformed geometry of the structure.

It appears to the authors that in the use of a number of prominent commercial programs in current practice, Engineers also typically instantiate new steel elements on the deformed geometry of the

structure. This leads to a false dependency of the solution on the steel erection sequence. All of the steel components must be defined in their original no-load geometry to obtain a correct analysis result. This geometry must then be subjected to its own self weight (where the self-weight deflections and stresses are significant) and assembled into the current deformed geometry of the loaded partially completed structure to determine correct construction requirements (e.g., crane forces, temporary tower reactions, come-along forces, etc.). One should note that if SDLF or TDLF detailing is employed, the analysis solution is still unique once the specifics of the detailing and the resulting lack-of-fit in the idealized no-load geometry are defined.

The second of the above conditions relates to an important general consideration in controlling the erected geometry of curved bridges. Oversize or slotted holes should be used rarely (if ever) to facilitate the erection of the structure. Use of this practice introduces a variable that may be difficult to control in achieving the desired final geometry.

The fourth condition relates to factors such as simple support conditions that are subsequently made continuous (e.g., integral abutments), or cases where a constraint is introduced along a certain degree of freedom at a support such that the final support displacement boundary conditions are a function of the construction sequence.

SPECIFIC CAPABILITIES TARGETED IN THIS RESEARCH

Given a fundamental understanding of the above detailing practices and the conditions for uniqueness of the structural analysis, it is possible to focus on a meaningful discussion of specific prototype capabilities for simulating curved I-girder bridge construction. Important construction simulation attributes implemented in this work include the following:

1) ***Modeling of the open-walled section members using beam theory, versus the use of combined beam and shell finite elements, as well as tracking and display of the 3D deformed geometry.*** The primary focus of this research is on the use of open-walled section beam theory for modeling of the I-girders. The cross-frames or diaphragms are modeled with truss and/or beam elements. Rigid offset

connections are implemented between the ends of the cross-frame elements and the corresponding girder nodal positions, and between the girder nodal positions and bearing elevations. The solutions from the resulting beam grillage models are compared to those of more rigorous models using shell finite elements for the slab and the girder webs. The visualization of the 3D deformed geometry is essential regardless of the underlying analysis approach. GT-Sabre draws the deformed geometry of the I-girder components, including the warping of the flanges, using a surface rendering of the flange and web plates.

2) ***Precise definition and modeling of the no-load geometry***. To obtain accurate predictions for all the response quantities, it is necessary in general to precisely define the physical no-load geometry, e.g., girder cambers, support elevations, positions of the cross-frames through the depth, etc. The cambered girder geometries are defined by curve fitting between specified camber locations using a combined Bezier and B-spline approach. Furthermore, the authors assume that the finite connection tolerances between the cross-frames and the girders, between girders at splice locations, and between the girders and their supports have a negligible influence on the bridge responses.

3) ***Handling of potentially significant geometric nonlinearities***. In horizontally curved I-girder bridges, the geometric nonlinearity is potentially important during construction because of the flexibility of the I-girders in torsion and lateral bending. All the analyses presented in this research are geometrically nonlinear. It should be noted that the uniqueness discussed above is not influenced by the geometric nonlinearity. One should also note that in modeling the steel erection operations, compatibility must be achieved between connecting points on the deformed structure. This necessitates the consideration of equilibrium on the deformed geometry.

4) ***Solution for deflected geometry of unconstrained components and subassemblies***. The steel erection process can be subdivided into two parts: (1) positioning, i.e., lifting a steel group and placing it in a desired position, and (2) assembly, i.e., connecting the lifted groups with supports and other portions of the structure that are already in place. A "group" is defined as any portion of the bridge that is

fabricated and/or assembled before being lifted. The group positioning involves two actions: (1) lifting the group and (2) rigid-body motion of the group to the desired position. If the Engineer is not interested in the responses due to the positioning and assembly of a given group, he or she can skip this step, instantiate the group model directly at the desired location, and "turn on" the group's gravity load. The solutions during the lifting and rigid-body motion are discussed in more detail below:

4a) Lifting. If a single girder is placed on its supports, typically it must be held by the crane(s) until another girder is connected to it with cross-frames. The single girder may or may not be tied down on its supports. The best scheme for lifting a single curved girder (resulting in the smallest induced stresses) is to lift by cables at two locations separated by a spreader beam, and to attach the cables at the intersection of a line through the member center of gravity (Davidson 1996). Several girders may be connected together with cross-frames and then lifted into position as a unit to reduce the deflections and induced stresses during the lifting operations. In this research, the crane system is modeled with cable and truss elements (spreader beams are modeled by a truss element). Generally, when a group is lifted, its center of gravity changes due to the group deformations. Therefore, the group experiences some rigid-body motion such that the resultant of the lifting forces passes through the center of gravity of its deformed geometry. To analyze the group and crane system under its self-weight, fictitious springs are placed on the model such that it is structurally stable. The forces in these springs are driven to zero during the nonlinear solution. This produces the rigid-body displacements required for alignment of the self-weight and the cable force resultants.

4b) Rigid body displacement. The deformed steel group is moved to a desired position where it is brought into contact with the erected structure and/or the supports at specific locations. A *connection* is then established between the appropriate dofs at these contact points, i.e., the nodal dofs on the lifted group and the nodal dofs at the corresponding point on the model of the erected structure are made the same.

5) ***Assembly Process***. The assembly process can be accomplished in the physical structure by seating the lifted girders or group on the bearings, and by bolting or welding to the erected structure. Field welding is acceptable for girder splicing, but it is seldom used due to the economic advantages of bolting (AISC 1994). A typical assembly process is described by AISC (1994) as follows. The girders and groups are set by a "raising gang" with a sufficient number of pieces to maintain stability after the lifting devices are disconnected. Drift pins are driven into the bolt holes to align the connection points and some bolts are installed. At least two bolts or pins are required at each connection during this stage. This is followed by the installation of the remaining cross-frames, diaphragms or bracing and the completion of all the connections by a "bolt gang."

These processes are modeled in GT-Sabre by solving for the forces required at selected nodal locations, representing cranes, jacks, come-alongs or other construction equipment, to achieve compatibility at the same or other nodal positions that are to be connected at a given erection stage. Given n degrees of freedom at which compatibility is to be established at one or more nodes, n degrees of freedom can be selected at which the software can solve for the applied forces required to achieve the desired compatibility. Given the vector of the selected displacement incompatibilities, **D**, i.e., the difference in the positions and/or the differences in the angles of orientation for the selected dofs, and given the selected unknown vector of forces that are to be applied, **P**, GT-Sabre determines a corresponding n x n tangent flexibility matrix, **F**. This flexibility matrix represents the consistently linearized solution for the displacements at each of the dofs of **D** due to unit forces at each of the dofs of **P** for the structure in its current state. Next, GT-Sabre solves the matrix equation $\mathbf{D} = \mathbf{F}\,\mathbf{P}$ to determine an estimate of the forces **P** necessary to achieve the compatibility. Due to any geometric nonlinearity, this **P** does not bring the separate parts of the structure completely into contact at the dofs of **D**. Therefore, GT-Sabre successively determines the remaining incompatibility and solves the above equations repeatedly until the connection is achieved within a specified solution tolerance. In some cases, the forces are determined to

displace the group on the erected structure to a certain position, e.g., to achieve a certain elevation at a point along a girder or to "close" a certain fraction of the displacement incompatibility.

In the physical erection of a bridge, generally crane, jacking, and come-along forces are introduced along with temporary supports to bring the desired connection points into close proximity. This is followed by localized forcing of the pieces together using drift pins and partial bolting combined with other local or global "jimmying" of the force and displacement boundary conditions to accomplish the connections. These operations are modeled in GT-Sabre by modifying the force vector **P** at selected stages of the process. It is generally difficult to achieve complete compatibility at a selected connection based solely on the application of crane forces. Typically, local forces, e.g., representing local jacking, come-along or pinning/bolting forces, are applied to completely close the incompatibility.

There are three principal assembly operations once a group has been brought into contact with the erected structure and/or the supports: (1) seating of the girders or groups on their supports, (2) girder splicing, and (3) cross-frame, diaphragm and/or bracing installation. The following subsections discuss these operations in detail.

5a) Seating of the girders or groups on their supports. Once a girder or group is brought into contact with its supports at specific locations, typically it is lowered further until a desired rotational orientation is achieved at the bearings, the girder or group is brought into contact with additional supports, and/or the girder or group is positioned at an elevation that facilitates further assembly. The above general flexibility solution procedure is used to vary the crane forces, etc. such that the desired displacements are achieved. When a physical girder or group is being seated on its supports, the erector may tie-down the group at a specific support at a certain stage of the seating process, to prevent further translation or rotation along certain directions at this point. Such tie-downs are modeled in GT-Sabre with displacement constraints at the corresponding support dofs. These tie-downs must be released at some point in subsequent stages of the assembly to avoid introducing unwanted restraints or locked-in stresses in the system.

5b) Girder splicing. Girders are spliced typically by pinning and bolting in three steps: (1) one flange is pinned; (2) the web splice is pinned progressively from the pinned flange to the other flange; (3) the other flange is pinned and the entire splice is aligned (AISC 1994). In the current study, the girder splicing is achieved in two steps as shown in Fig.3: (1) nodal translational continuity is enforced at the reference axis of the I-girder elements and (2) nodal rotational and warping continuity is established.

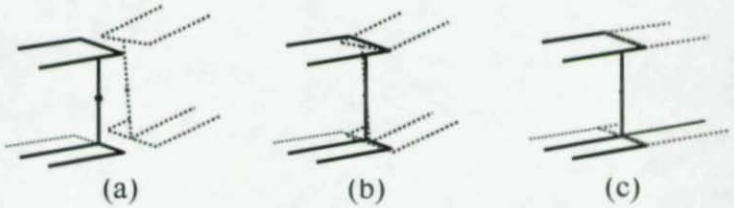

Fig. 3. Girder splicing (a) initial position; (b) translational continuity; (c) rotational and warping continuities

One should note that the above solution takes advantage of an understanding of the previously discussed concepts of uniqueness of the analysis solution. The above approach does not allow for the calculation of the detailed local forces required during the actual assembly of the splice in the field. In fact, the Engineer generally cannot possibly know this amount of detail about how the structure is erected, and certainly cannot prescribe this level of detail on the erector. However, this approach does allow for general calculation of the global crane forces, etc. required for the erection operations. The approach relies on the fact that the final solution for the state of the structure, once the splice connection is completed, is unique.

5c) Cross-frame, diaphragm and/or bracing installation. Figure 4 illustrates one possible cross-frame installation sequence. The cross-frame is first connected to the girder on the left. Then the point P_1 is connected to P_1' on the right-hand girder. Finally, P_2 is connected to P_2'. The chords of the cross-frame are modeled using beam elements and initially, full continuity of rotations and displacements is assumed between the girder on the left and the cross-frame chords, with the

cross-frame installed in the correct no-load orientation relative to the left-hand girder. This is to prevent rigid-body rotation of the cross-frame about the web of the left-hand girder prior to completing its installation. As noted previously, a rigid offset is defined between the connection points and the corresponding girder nodes once the connections are achieved. However, a rotational release is defined at the P_1 end of the top chord, when P_1 is connected to P_1', to allow free rotation in this connection during the last step of assembling P_2 to P_2'.

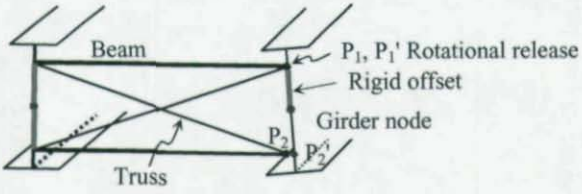

Fig. 4. Cross-frame installation.

In the above, only displacement continuity is enforced between P_1 and P_1' and P_2 and P_2' (i.e., a rotational release is also inserted at P_2 when its connection is accomplished). After the displacement continuity between the above points is achieved, the rotational continuity is also released between the chords and the left-hand girder. This gives a model in which all the members may be represented subsequently by truss elements. In the case of K-shaped cross-frames, beam elements are still needed for the chord in which the diagonal members are connected at the mid-length.

As a simplification, the self-weight of the cross-frame is typically neglected until it is fully installed. The cross-frame self weight is then "turned on." Locations are specified for crane forces, jacks and/or come-alongs to bring the points P_1-P_1' and P_2-P_2' together. The previously discussed flexibility algorithm is used to solve for the forces necessary to establish the continuity at these points. The final state of the structure associated with the cross-frame installation is independent of the assembly sequence. If desired, the six forces required to achieve

compatibility in the six displacement dofs at P_1-P_1' and P_2-P_2' can be determined in one step.

6) ***Instantiation of slab elements on the deformed geometry***. The concrete slab elements are instantiated on the deformed girder geometry as illustrated in Fig. 5. First for a girder node N_i, a new node N_{i1} is created at the top web-flange juncture along the Y direction of the nodal triad. Another new node N_{i2} is then created directly above N_{i1} (in the global Y direction) at a height above N_{i1} equal to the haunch depth plus one-half of the slab thickness. As noted previously, the slab elements are instantiated at the dead-load deformed geometry for each stage of the slab construction. The loads from the wet concrete are applied to the I-girders based on interior tributary widths and based on the lever rule (AASHTO 2004) for slab overhangs. In this work, 6-dof per node beam elements are used to represent the slab. A rotational release at node N_{i1}. The slab is represented generally by a grillage of beam elements.

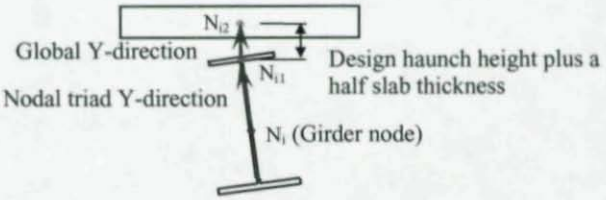

Fig. 5. New node creation for slab elements.

After completion of the slab construction, the entire bridge acts compositely. Forms, overhang brackets and temporary bracing members are removed. The weight of parapets, sidewalks, barriers and/or other components that contribute dead weight, but are placed after casting of the slab, are then applied at their actual location on the composite structure. The elevation of the bridge deck is then checked with target values. If desired, the initial camber of the girders is modified and the entire construction simulation is repeated.

DEMONSTRATION

The following examples focus on the effects of NLF or TDLF detailing on a full-scale composite I-girder bridge tested by FHWA (Chang 2006; Jung 2006). The discussion focuses on the influence of these detailing methods on the bridge response under total dead load. The analysis results using the above beam-grillage approach are compared to an ABAQUS FEA model (HKS 2005) in which shell elements are used for the girder webs. The slab is cast in a continuous stage for the test bridge; hence, the influence of slab casting sequence is not considered. Next, the ABAQUS FEA model is used to study the influence of the above two detailing methods on the ultimate strength of the test bridge. The reader is referred to the above base reports for detailed discussion of the various methods and comparison to the experimental test results. The physical test bridge was constructed with NLF detailing.

Description of the Composite Test Bridge

Figure 6 shows the girder cross-section, bridge cross-section and plan views of the composite test bridge. The bridge consists of three prismatic I-girders spaced radially at 8.75 ft. The measured flange and web dimensions are detailed in Figs.6a-c. The radius of curvature is 208.75 ft for the outside girder G3, 200 ft for the middle girder G2 and 191.25 ft for the inside girder G1. The span of G2 is 90 ft along its arc length. A709 Grade 50 steel is used for all the steel plates with the exception of the bottom flange of G3, which is HPS 70W. The steel elastic modulus E is taken as 29,600 ksi from (Jung 2006).

The bridge slab is a conventional 8 in thick cast-in-place concrete slab with 3 in haunches and 3 ft overhangs. The average concrete cylinder strength (f_c') is 4.87 ksi at 28 days and 4.91 ksi at 298 days (just prior to the start of strength testing). The concrete elastic modulus is taken as 4,030 ksi using the first of these values and the AASHTO (2004) equation for normal density concrete.

The test bridge has five equally-spaced K-shaped cross-frame locations. Except as noted below, the cross-frame members are 5 in diameter circular tubes with ¼ in wall thickness and F_y = 73 ksi. These members have the same axial stiffness as typical cross-frame members. Tubes are

used within the test bridge to facilitate measurement of internal forces. The cross-frame members are sized to remain below their proportional limit throughout the development of the ultimate strength of the composite bridge. For ultimate strength testing, the diagonals between G2 and G3, at the mid- and ¼-span locations were reinforced by splitting and welding 6 in x ¼ in tubes around the outside of the 5 in diameter tubes. Also, the bottom chord of these cross-frames was reinforced in the same fashion between G3 and the K joint.

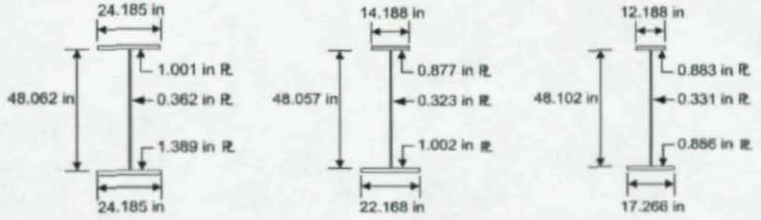

(a) G3 cross-section (b) G2 cross-section (c) G1 cross-section

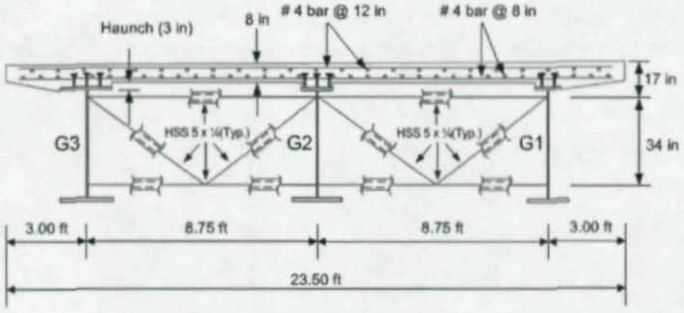

(d) Bridge cross-section

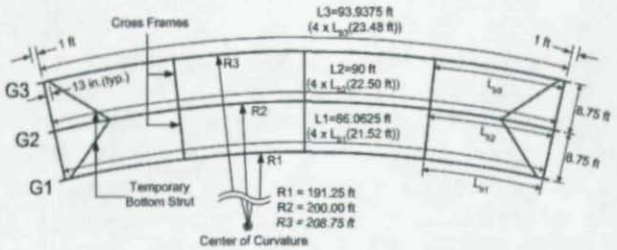

(e) Bridge plan

Fig. 6. Composite test bridge geometry.

The test bridge construction sequence is as follows: (1) G1, G2, and G3 were blocked to their camber profiles. Holes were drilled and the cross-frames were assembled in the no-load position. Bottom flange diagonals were attached between G1 and G2 to prevent raking between these girders during lifting. (2) The cross-frames were disassembled between G2 and G3 and the G1-G2 pair was set on the abutments. (3) G3 was set on the abutments and held with the crane. The cross-frames were then assembled in the order indicated in Fig. 7 and bottom flange diagonals were installed between G2 and G3. (4) Finally, forms were placed, the bridge slab was cast in one continuous stage, and the forms and temporary bracing were removed after hardening of the slab.

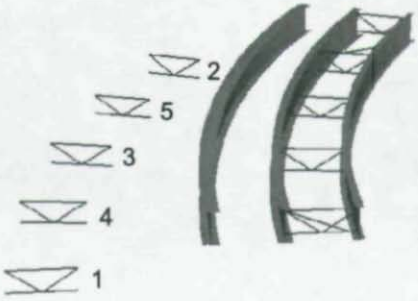

Fig. 7. Test bridge during an intermediate stage of the erection sequence.

Influence of NLF versus TDLF detailing on the dead-load bridge response. Table 1 summarizes the total dead load results for the test bridge based on the actual NLF detailing and using a hypothetical TDLF detailing. The girder cambers based on the TDLF detailing, obtained using the beam grillage model, are used in both solutions. Similar results are obtained with the above mentioned ABAQUS FEA model. One can observe that the method of detailing has a significant influence on the final girder elevations, twists and radial displacements.

***Influence of different detailing methods on bridge ultimate strength*:** Figure 9 illustrates the full nonlinear FEA load-deflection response of the NLF and TDLF ABAQUS models subjected to the ultimate strength test load pattern (Jung 2006), which represents two lane loads plus side-by-side trucks placed at the middle of the bridge to produce the maximum flexure on G3. One can observe that the ultimate strength behavior is practically identical for these two cases until loads significantly larger than the indicated elastic design limits.

Table 1. Bridge responses for NLF and TDLF detailing.

Girder	Load Condition & Cross-Frame detailing	Elevation (in)	Twist Angle (degree)	Radial Deflection top/bottom flgs.**
G1	No-load cambered position	0.927*	0.000	0.000
	Total dead load (NLF)	-0.528	-0.768 °	-1.124 / -0.456
	Total dead load (TDLF)	*-0.027*	*0.011°*	*-0.320 / -0.329*
G2	No-load cambered position	1.908*	0.000	0.000
	Total dead load (NLF)	-0.904	-0.834 °	-1.155 / -0.428
	Total dead load (TDLF)	*0.048*	*-0.039°*	*-0.340 / -0.306*
G3	No-load cambered position	3.672*	0.000	0.000
	Total dead load (NLF)	-0.670	-1.008 °	-1.271 / -0.393
	Total dead load (TDLF)	*-0.015*	*-0.210°*	*-0.418 / -0.235*

* Initial cambers based on TDLF ** Positive toward center of curvature

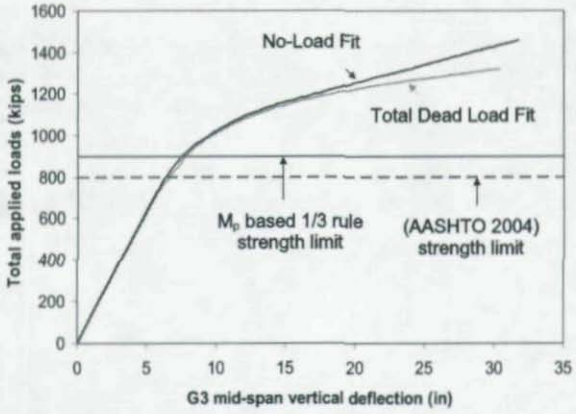

Fig. 9. Bridge ultimate strength based on NLF and TDLF detailing.

CONCLUDING REMARKS

This paper presents prototype capabilities for simulating the construction of curved steel I-girder bridges. The finite element methodology for handling the construction simulation has been implemented in the GT-Sabre software system. Based on the provided demonstration, the following concluding remarks are drawn:

1. The Total Dead Load Fit (TDLF) detailing method effectively reduces the girder web out-of-plumbness and vertical deflections under the total dead load. The No Load Fit (NLF) method simply lets the girders "roll" into their deflected non-plumb positions under the steel and total dead loads.

2. The system response of the Test Bridge is not affected by either NLF or TDLF detailing until well past the M_p-based 1/3 rule resistance. This implies that for some bridges, the cross-frame detailing method does not need to be considered in the strength design of the bridge. However, lack of consideration of the method of detailing does have some impact on the prediction of the required cambers.

ACKNOWLEDGEMENTS

The sponsorship of this research by Professional Services Industries, Inc. (PSI) and the Federal Highway Administration (FHWA), as well as the extensive collaboration with the FHWA and PSI staff, are gratefully acknowledged. Mr. Se-Kwon Jung is acknowledged for his assistance with the ABAQUS FEA solutions. Mr. Fred Beckmann is thanked for his extensive feedback on fabrication and erection. The findings expressed in this paper are the authors' and do not necessarily reflect the views of the above organizations or individuals.

REFERENCES

AASHTO (2004). *AASHTO LRFD Bridge Design Specifications, 3rd Edition* with 2005 Interims, American Assoc. State and Highway Transp. Officials, Washington DC.

AISC (1994). *Steel Erection for Highway, Railroad and Other Bridge Structures, Highway Structure Design Handbook*, Vol. I, Chapter 14, American Institute of Steel Construction, Chicago, IL

Chang, C.-J. (2006). "Construction Simulation for Curved Steel I-Girder Bridges," Ph.D. dissertation, Georgia Inst. Technology, Atlanta, GA

Davidson, J. S. (1996). "Nominal Bending and Shear Strength of Horizontally Curved Steel I-Girder Bridges." Ph.D. Dissertation, Auburn University, Auburn, Alabama.

HKS (2005). *ABAQUS Standard Version 6.5-1*, Hibbitt, Karlsson and Sorenson, Inc., RI.

Jung, S.K. (2006). "Inelastic Behavior of Horizontally Curved Composite I-Girder Bridge Structural Systems," Ph.D. dissertation, Georgia Inst. Technology, Atlanta, GA

LATERAL STABILITY OF PONY TRUSS WALK BRIDGES

LeRoy A. Lutz, Ph.D., P.E.[1]

ABSTRACT

The lateral stability of the compression chord of the two side trusses is the principal stability concern that is normally considered for the design of pony truss bridges. However, pony truss walk bridges are typically narrow as compared to the typical pony truss bridge used for automobile traffic. If the span of the walk bridge is sufficiently long, there is the possibility that lateral-torsional instability of the bridge can occur. The pony truss is modeled as a beam channel for evaluating the lateral-torsional stability and this capacity is compared with that of the compression chord based on elastic restraint. General recommendations are given so as to minimize the concern regarding torsional stability of pony truss walk bridges.

INTRODUCTION

Pony truss walk bridges in which the span is sufficiently long has the potential of having a lateral-torsional instability when subjected to vertical load or to combined vertical and horizontal load. Typically, the lateral stability of the individual elastically restrained compression chords of the pony truss is the primary stability concern. However, since the pony truss tends to be narrow in width relative to its height, the lateral-torsional failure mode may govern the pony truss stability. In fact there will undoubtedly be some interaction between the compression chord stability and the lateral-torsional stability.

---

[1] LeRoy A. Lutz, Ph.D., P.E., Vice President-Emeritus, Computerized Structural Design, S.C., Milwaukee, WI 53217

The pony truss will be considered as a beam element for the purpose of evaluating the lateral-torsional stability. Structurally then, the pony truss will be considered like a channel with the web horizontal and the tips of the flanges pointing upward.

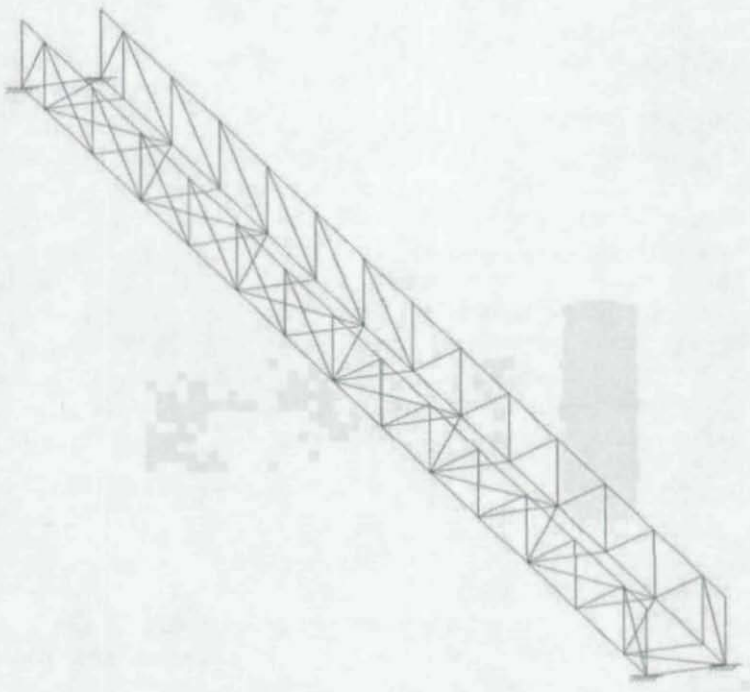

Figure 1. Pony Truss Walk Bridge

PONY TRUSS BEAM MODEL

An isometric view of a pony truss bridge is illustrated in Fig. 1. The pony truss will be considered as a channel-shaped structural section composed of two compression chord areas, A_c, and two tension chord

members, A_t. These chords are interconnected by truss web members as illustrated in Figure 2.

As a beam member $$I_{xb} = 2\frac{A_t A_c}{A_t + A_c}h^2 \quad (1)$$

with neutral axis at $$h_t = \frac{A_c}{A_t + A_c}h \quad (2)$$

and $$I_{yb} = \frac{(A_c + A_t)}{2}b^2 \quad (3)$$

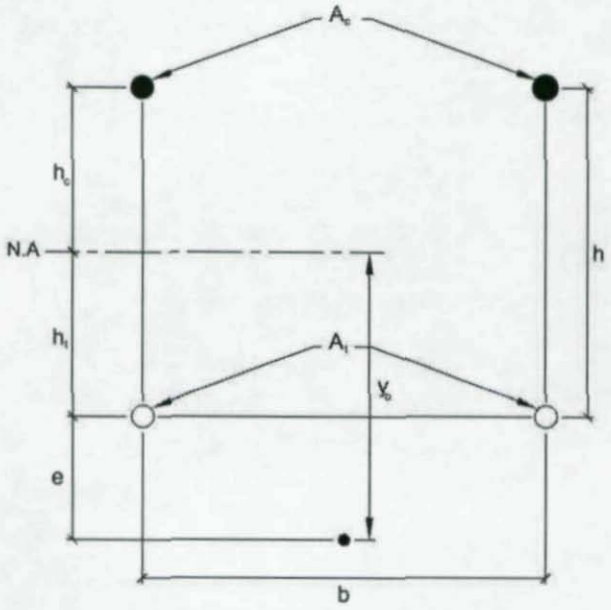

Figure 2. Pony Truss Beam Schematic

Since there is appreciable shear deformation in the truss elements, it is recommended to an equivalent I_x obtained from the actual truss deflection and the beam deflection equation. For the types of trusses examined the shear deflection was found to be about 10% of the total deflection. Therefore it is suggested that the x-axis moment of inertia be $I_x = 0.9I_{xb}$.

The actual I_y is a function of the shear deformation of the trusses and the relative size of the chord areas A_c and A_t. I_y was found to be between 60 and 70 % of I_{yb}. It is suggested that I_y be calculated from the deflection of the pony truss using a uniform horizontal load applied at the bottom of pony truss with the vertical displacement of bottom chords restrained. Using the beam deflection expression one will obtain the I_y, which occurs when there is no twist in the cross section.

The St. Venant's torsional constant J will be quite small. Use J equal to the sum of the J values of the four chord members.

The shear center location e can be shown to be $e = \dfrac{A_c h b^2}{4 I_y}$ (4)

for the pony truss cross-section (Oden (1967)) as illustrated in Figure 2.

Thus the shear center location from the centroid $y_o = e + h_t$ (5)

The critical moment for lateral-torsional stability is

$$M_{cr} = \frac{\pi^2 E I_y}{L^2}\left[\frac{\beta_x}{2} + \sqrt{\left(\frac{\beta_x}{2}\right)^2 + \left(\frac{GJL^2}{\pi^2 E I_y} + \frac{C_w}{I_y}\right)}\right] \tag{6}$$

where $\beta_x = \dfrac{1}{I_x}\int_A y(x^2 + y^2)dA - 2y_o$ (7)

For the pony truss cross-section in Figure 2 the expression for β_x becomes

$$\beta_x = \frac{2}{I_x}\left[A_t h_t^3 - A_c h_c^3\right] - 2y_o \tag{8}$$

For the pony truss, y_o is a positive value that leads to a negative value of β_x, which is appropriate when the top chords are in compression. To consider the influence of the level of stress in the compression chord as it relates to the yield strength, the provisions of Section E7 of the 2005 AISC Specification (AISC (2005)) are recommended. The elastic buckling stress F_e would be

$$F_e = M_{cr}/(2A_c h) \tag{9}$$

Q would be the factor for slender elements such as in the leg of an angle if the compression chord were an angle.

The yield moment $M_y = F_y(2A_c h)$ (10)

COMPRESSION CHORD STABILITY

The top chords (A_c in Figure 2) are elastically restrained by the U-shaped rigid frame created by the verticals in the side trusses and the cross member in the horizontal truss that connects to the two verticals (Figure 3). The stiffness or spring constant of this frame is

$$C = \frac{E}{h^2\left[h/(3I_c) + b/2I_b\right]} \tag{11}$$

which is Eq. 15.6a in the Guide to Stability Design Criteria for Metal Structures (Galambos (1998)). The required stiffness for stability bracing

$$C_{req} = C = \frac{1}{\phi}\left[5 + 3(\ell/L_e)^4\right] P_u \ell / L_e^2 \tag{12}$$

using the Lutz-Fisher procedure (Lutz & Fisher (1985)) with $\phi = 0.75$ per Appendix 6 of AISC 2005 Specification (AISC (2005)). The expression for C is based on out-of-straightness that pushes the chords either outward or inward at the same panel location.

L_e is the effective length required for the compression chord in the horizontal direction and ℓ is the panel length of the truss. If the chord is required to buckle over the length ℓ, the $C_{req} = \frac{8}{\phi} P_u / \ell$. Most often the effective length L_e exceeds ℓ which reduces the stiffness necessary to take the required value of P_u.

Both top chords could tend to move in the same direction while buckling. In this case the stiffness of the U-frame is somewhat larger than that given in Equation 11. However, the out-of-straightness leading to this type of behavior would produce a net lateral force at the top chords which would tend to twist the pony truss. This could lead to an interaction between the chord stability mode and the lateral-torsional buckling mode of the pony truss.

If the top chord were a rectangular HSS, the larger dimension or depth would be horizontal. In this case it would be likely that the top chord stability could be governed by buckling about the weak axis of the HSS which is the horizontal axis. About this axis elastic restraint of the panel points is assured since buckling is in the plane of the side trusses.

If the top chord of the pony truss were a single angle, then the minor axis of the chord would be at an angle to the horizontal axis. Thus, in this case, one would have to check minor axis buckling with only a component of the required horizontal U-frame stiffness being needed to achieve this mode of buckling. For the case of an equal-leg angle the required stiffness in Equation 12 would be multiplied by sine of 45 degrees. Both horizontal axis buckling and minor axis buckling would be checked. For all cases examined, it was found that the minor axis buckling of the angle controlled the capacity based on elastic restraint.

WALK BRIDGE EXAMPLES

Several walk bridges were examined for their capacity. Both top chord buckling and lateral-torsional buckling of the walk bridge were considered.

Example 1

This example is a 86'-3" long span providing for an approximate 4 foot wide walk area. The interior panel points are 6'-8" on center. All members are single angles except for the U-frame which is made from channels. See Figure 3. The bottom tensile chords are L6x3½x5/16 and the compression chords are L5x5x5/16. All angles are of A36 material.

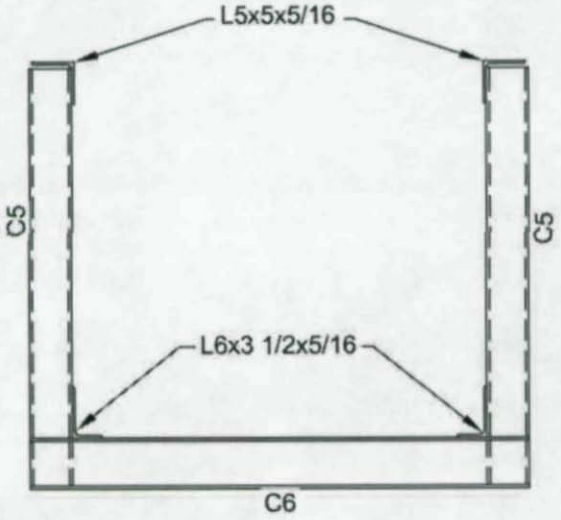

Figure 3. Bridge Cross Section

Using Eq. 6, an M_{cr} = 11,512 in-kips was obtained. Using Eqs. 9 and 10 and the provisions of Section E7 of the AISC 2005 Specification, a ϕM_n = *5416 in-kips was obtained which leads to a* ϕw_n = *0.485klf.*

Based on the elastic restraint which consists of a C6x10.5 horizontal and C5x9 verticals for the U-frame a ϕw_n = 0.428 klf was obtained. This value was based on finding a 59 kip chord design strength considering minor axis buckling. The effective length was 1.16 times 80 inches or 92.8 inches. If the panel point provided full restraint such that the effective length was 80 inches, the chord design strength could have achieved 65.6 kips.

If the bridge walkway width were reduced to 3 feet, the ϕw_n for the bridge would be reduced from 0.485 klf to 0.385 klf based on lateral-torsional stability. The design load ϕw_n based on elastic restraint of the top chord would be a bit higher than the 0.428 klf obtained for the four foot wide bridge due to a slightly stiffer U-frame. Thus lateral-torsional stability will control the design with three foot wide bridge.

Example 2

The four foot wide bridge examined in Example 1 is lengthened to 93′-4″. Initially the same L5x5x5/16 top chords were used. The design strength based on lateral torsional stability becomes 0.395 klf as compared to 0.485 klf for the 86′-3″ span. The elastic restraint criteria, with the same chord force as noted in Example 1, provides a design strength of 0.366 klf.

The top chord was then increased to an L5x5x1/2. This increased the design strength to 0.564 klf based on lateral-torsional stability and 0.521 klf based on elastic restraint. Thus the increase in the top chord size led to comparable increases in capacity based on both sources of instability.

Example 3

This example is an 82′-2″ long walk bridge with a 3 foot walkway. This bridge used C4x7.25 channels for both the vertical and horizontal U-frame members. Top chords were L6x4x3/8 or L6x4x1/2 with the long legs horizontal. The bottom chords were L6x4x3/8 with the long leg vertical in both cases examined. A36 material is used.

In these cases, minor axis flexure governed the top chord design with the effective lengths being 96.4 inches for the L6x4x3/8 chord and 103 inches for the L6x4x1/2 chord. The sine term used to modify the C_{req} (Eq. 12) was approximately 0.40.

In both cases considered, the top chord design strength based on elastic restraint governed the capacity rather than the lateral-torsional stability, ϕw_n = 0.578 klf as compared to 0.487 klf for the L6x4x3/8 top chord. For the L6x4x1/2 top chord ϕw_n = 0.797klf from lateral-torsional stability as compared to 0.596klf from elastic restraint.

The reason that this walk bridge, which was just three foot wide, was not controlled by lateral-torsional stability was due to the increased vertical stiffness from the somewhat shorter span combined with larger top and bottom chords. This leads to a noticeable reduction in the vertical deflection from a comparable vertical load.

NONSYMMETRICAL LOADING

Nonsymmetrical loading of a pony truss walk bridge can be a concern. For the bridges addressed in the examples the shear center is 15 to 20 inches below the center of the bottom chord. Thus under wind load there is a significant twist of the bridge.

An unbalanced vertical load also produces a significant twist of the bridge. The larger stretch in the tension chord on one side leads to a horizontal deflection of the horizontal truss which tends to accentuate the twist.

As an example consider the 86′-3″ long pony truss walk bridge with a four foot width that was addressed in Example 1. With the $\phi w_n = 428$ plf and a 90 plf bridge weight, the safe live load is 200 plf or 50 psf. If this load is applied symmetrically the vertical deflection at the center of the bridge is 2.90 inches. If the 200 plf is applied at one foot from the centerline of the bridge the deflection at the centerline varies from 3.89 inches to 1.91 inches across the bridge width. The top chord moves 2.36 inches laterally which is L/438. At factored load levels the lateral deflection would be L/297, considerably more than the L/500 out-of-straightness used in the direct analysis method of Appendix 7 of AISC (2005).

The load from a 90 mph design wind produces a lateral force that has its location almost 3 feet above the shear center. Using ASCE 7-02 (ASCE 7 (2002)) provisions the total lateral load is about 75 plf. This loading introduces a 1.43 inch lateral deflection of floor of the bridge and 3.15 inch lateral deflection of the top chord at service load levels. The factored compression chord force from dead plus wind load is 26.46 kips, considerably less than the 58.93 kip chord force generated at the 428 plf. With the ASCE 7 (2002) load case 1.2D + 1.6W + L the maximum compression chord force would be 53.92 kips. However, the top chord lateral deflection would be 5.04 inches at factored wind load.

The above information points to the fact that the service load deflection from wind and unbalanced live load is too high in Example 1 and that there is a need to increase the chord sizes, especially the top chord which will reduce the vertical deflection as well as the twist stiffness of the bridge. A total vertical load deflection limit of L/360 is too much for long pony truss walk bridges. The deflection limit should either be a constant value or a value which increases with the bridge width such as b/24 inches where b is the bridge width in inches.

CONCLUSIONS

A procedure is developed to evaluate the vertical load capacity of relatively narrow pony truss bridges for lateral-torsional stability using the beam stability equations. It was determined that lateral-torsional

stability is a concern for long narrow bridges. These bridges were also found to twist significantly under wind load and nonsymmetric live load.

The key to providing a good design for long pony truss walk bridges is to first control the deflection of the vertical trusses by increasing the chord areas so as to limit the twist of the bridge under the appropriate nonsymmetric service loads. Second, evaluate the load capacity based on elastic restraint of the top chord and also based on lateral-torsional stability of the truss. Increase of the top chord area appears to be more cost effective than increasing the bottom chord area.

REFERENCES

AISC (2005), *Specification for Structural Steel Buildings,"* ANSI/AISC 360-05, American Institute of Steel Construction, Chicago, IL

ASCE 7 (2002), *Minimum Design Loads for Buildings and Other Structures*, SEI/ASCE 7-02, American Society of Civil Engineers, Reston, VA

Galambos, T.V. (1998), *Guide to Stability Design Criteria for Metal Structures,"* 5th Edition, John Wiley & Sons, New York, NY

Lutz, LeRoy A. and Fisher, James M. (1985), "A Unified Approach for Stability Bracing Requirements," AISC Engineering Journal, Vol. 22, No. 4, pp.163-167

Oden, J.T. (1967) *"Mechanics of Elastic Structures,"* McGraw-Hill Book Company, New York, pp 200-201

Effects of plasticity on steel beam stability considering partial warping restraint

Ian MacPhedran[1] and Gilbert Y. Grondin[2]

ABSTRACT

While out-of-plane stability of members in a steel moment frame is improved by restraining the torsional warping displacements at the frame joints, this benefits primarily shorter members. Design of shorter flexural elements is generally governed by factors such as general cross-section yielding, local buckling, or failure in shear. This study considers only I-shaped sections and investigates the effect of yielding on the beneficial effect of warping restraint. This is of special interest since both warping and yielding are of primary importance to the flange tips of I-shaped sections. Warping displacements are greatest there, and yielding first occurs in those locations.

This paper presents a numerical investigation of the effects of yielding on the buckling strength of short steel beams with varying levels of warping end restraints. Non-linear buckling analyses are conducted on finite element models of simple frames. The benefits of warping restraint are still present, albeit reduced, for shorter flexural members. There are some inconsistencies in the numerical analyses that are

1) Corresponding Author. PhD Student, and 2) Professor, Department of Civil and Environmental Engineering, University of Alberta, Edmonton, Alberta, Canada T6G 2W2

present for shorter members. This requires more investigation.

INTRODUCTION

Inelastic buckling is a common limit state for steel members and structures. This applies to all modes of buckling, including out-of-plane instability of beams. This study will investigate the effect of end conditions with varying amounts of warping restraint on the inelastic lateral torsional buckling of beams. Varying end restraint conditions are found in frames and several common frame joint geometries as shown in Table 1 were modelled in the context of a simple portal frame (Figure 1). Various beam lengths were used in the frame, incorporating the effect of elastic and inelastic lateral torsional buckling as well as complete section plastification as the failure mode.

Table 1 Joint geometries investigated

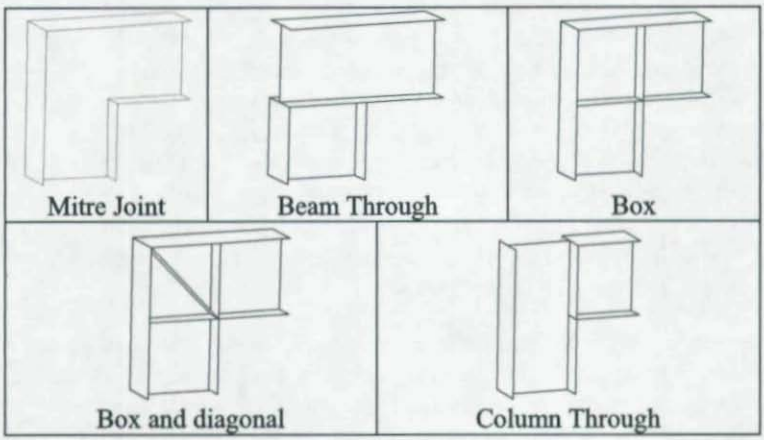

The work presented in this paper is part of a research program that has for objective the incorporation of warping compatibility at frame joints in the analysis of frame stability. As part of this work, analysis tools are being explored and case studies of various frame configurations are being generated for the validation of a more effective method of

incorporating full joint compatibility in the stiffness formulation of metal structures. In a previous paper (MacPhedran and Grondin, 2005) a comparison of solutions obtained from shell element and various beam element was conducted in the elastic range. This paper looks into the applicability of shell element models with the inelastic out-of-plane instability of frames, subject primarily to bending of the horizontal member. A secondary objective of this study is to validate finite element models and analysis methods used for the broader investigation, and ensure that the models predict the real behavior accurately.

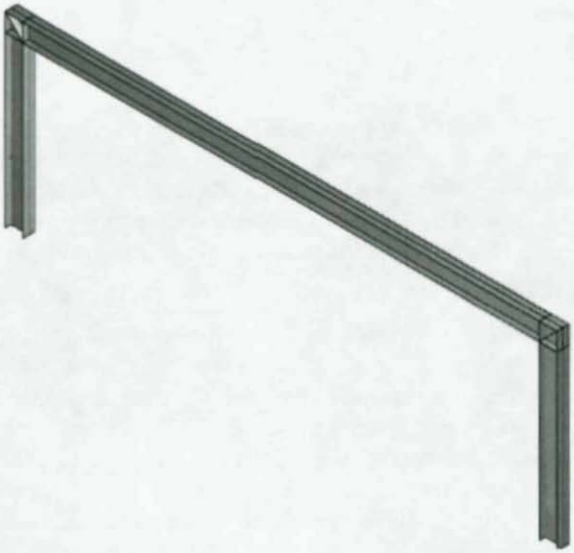

Figure 1 Typical Portal Frame, Illustrating Stiffened Box Joints

PREVIOUS STUDIES

Inelastic lateral torsional instability has been investigated for over 60 years (Galambos, 1998). The results of investigations on several geometric configurations have been presented in numerous sources such as Chen and Lui (1991) and Trahair (1993).

An earlier investigation by MacPhedran and Grondin (2005) focused on the elastic behavior and eigenvalue (bifurcation) buckling analyses. This form of analysis does not consider second order loading effects. It also does not allow the incorporation of material nonlinearities, such as material yielding.

It must be noted that elastic behavior and buckling present a much simpler problem in that the effects for flexural buckling can be somewhat, although not completely, isolated from the torsional behavior. The elastic buckling equation, can be presented as

$$M_{crw} = \sqrt{\frac{\pi^2 EI_y GJ}{k_y^2 L^2}} \cdot \sqrt{1 + \frac{\pi^2 a^2}{k_w^2 L^2}} \tag{1}$$

where E and G are the elastic and shear moduli for the material under consideration and L is the unbraced beam length, I_y is the moment of inertia about the minor principal bending axis, and J is the St. Venant torsional constant. The value a, the torsional bending constant, relates both material and cross-section properties, including C_w, the warping constant, and is expressed as $a = \sqrt{(\mathrm{E\,Cw})/(\mathrm{G\,J})}$. The effective length factors, k_y and k_w, associated with the lateral buckling and warping lengths, are both 1.0 for a simply supported beam. The flexural component can be removed from the flexural torsional buckling capacity for a restrained beam by dividing by the capacity for a similar simply supported beam, leaving only the effective length factors related to the end restraint conditions, and a value relating L to the torsional constant (L/a). This ratio is expressed in MacPhedran and Grondin (2005) as

$$R_w = \frac{M_{crw}}{M_{cr}} = \frac{1}{k_y} \cdot \sqrt{1 + \frac{\pi^2 a^2}{k_w^2 L^2}} \Big/ \sqrt{1 + \frac{\pi^2 a^2}{L^2}} \tag{2}$$

However, when yielding is considered, the effects of axial, flexural and warping strains and stresses are even more tightly coupled, in that the stresses from all loading conditions can interact to cause yielding, and the effects of warping and flexure can not be so simply reduced. This

leads to yield surfaces in several dimensions as illustrated by Daddazio *et al.* (1983) for Z sections. The work of Yang *et al.* (1989), although less broad in its scope than that of Daddazio *et al.* shows the complex interaction of yielding in various modes for I shaped sections. In short, the interactions between stresses due to different modes are too complex to uncouple easily. For this reason, the results of the elastic eigenvalue analyses of the frames are not compared to the inelastic instability analyses other than in a general sense.

Current papers on the topic of inelastic buckling, such as that of Trahair and Hancock (2004) use reduced stiffness to predict buckling, but also use elastic end restraints. Considering the inelastic behavior of the joints, is it still appropriate to view the restraints as providing the same support conditions as for elastic conditions? This question needs to be addressed.

MODELLING

The finite element analysis reported herein was conducted using the finite element program ABAQUS, version 6.4, running on Sun W1100z computers. The frame models were discretised using the shell element type S4R. Shell element S4R is a four node quadrilateral shell element. This element uses one integration point in the plane of membrane action as opposed to the four integration points that are used in a fully integrated equivalent shell element, for example S4. The reduced integration allows the shell element to avoid shear locking to which the fully integrated element may be prone. The reduced integration element provides a more flexible formulation. There can be some zero-mode instability problems with the reduced integration element (also known as hourglassing), however, the ABAQUS program features controls on this behavior that have been shown to avoid it. The element has a large displacement formulation, with finite strains. The S4R element has been used successfully to model the complex behavior of structural members with geometric and material non-linear behavior in Sheikh *et al.* (2003) and Schumacher *et al.* (1999).

The beam and columns of the portal frame model were meshed using 4 shell elements across the flange width and 6 elements through the web.

Element dimensions along the length of the beam were determined to produce a flange element aspect ratio of 1.00. The aspect ratio for the web elements was 1.05. The mesh for the box joint with diagonal stiffener is presented in Figure 2.

Five joint conditions, illustrated in Table 1, were explored in the study. While the mitred end condition is not usual for typical construction, it has been extensively studied in previous works, for example Krenk and Damkilde (1991).

Figure 1 shows a typical portal frame used for this investigation. The columns were 2000 mm long and the beam length varied from 2000 mm to 8000 mm. This range was used to test a wide range of beam behavior, from full plastic moment to elastic lateral torsional buckling.

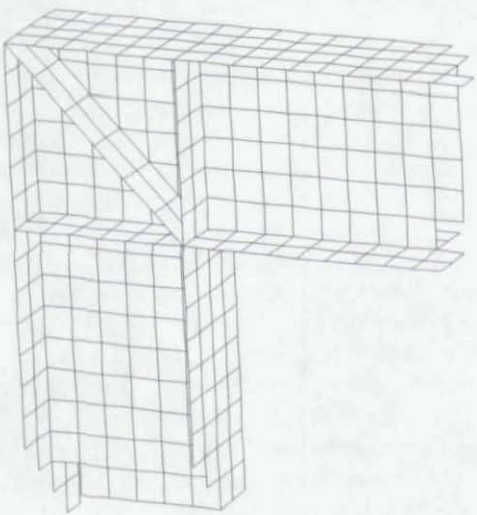

Figure 2 Detail of stiffened box joint from finite element model

The beam and columns cross-section chosen for this study was a

W200x27 wide flange section. This section was chosen for its large torsional bending constant. This is noted in this paper as the variable "a" with a value of 1088 mm for this section. This is a class 2 (compact) section in flexure for yield strengths up to 460 MPa. The critical unbraced length (L_u) at a yield strength of 300 MPa is 2.04 m. These calculations are based on the Canadian design standard CAN/CSA–S16–01 (CSA, 2001). This cross-section was also used extensively in the previous work and provided a common link between these two projects. The frames were loaded with a uniformly distributed load acting vertically down through the shear center of the beam.

Each frame was analysed using the elastic eigenvalue solver of ABAQUS, which provided an indication of the elastic buckling load, and a set of eigenvectors used for creating initial imperfections in the model. For the models represented here, only the first beam buckling mode is incorporated. These initial imperfections were scaled to limit the maximum initial imperfection to 1/200 of the member length (0.005L). Higher modes were included in other models, but did not appreciably affect the buckling loads, or the deflected shape. Higher mode imperfections were scaled to half of the first mode value. A nonlinear analysis was then performed, using these initial imperfections, an elastic-plastic material, and updated Lagrangian formulation using the modified Riks procedure available in ABAQUS.

Two sets of end restraints were modelled on the beams. In one set, the out-of-plane displacement of the bottom flange was restrained at the beam-to-column connection. This boundary condition was implemented to prevent out-of-plane buckling of the columns while allowing twisting of the beam at the supports. For the second set, all nodes of the cross-section at the beam-to-column joints were constrained to move only within the plane of loading, thus preventing twisting of the cross-section without preventing warping.

COMPARISON OF ANALYSIS RESULTS WITH DESIGN METHODS

A comparison of analysis results with current design methodologies is presented to provide a baseline against which to compare this series of analyses. The unfactored design resistances were used for this comparison. These design capacities are plotted along with the results of the analyses in figures 3 to 6.

The two standards used for this comparison are CSA S16-01 (CSA 2001), and the AISC Specification (AISC 2005). The provisions of S16-01 are such that the equivalent moment factor, ω_2, is taken as 1.0 for the given loading. The AISC specification permits the use of an equivalent moment factor, C_b, slightly modified from the one presented in Kirby and Nethercot (1979):

$$C_b = \frac{12.5M_{max}}{2.5M_{max} + 3M_A + 4M_B + 3M_C} \leq 3.0$$

where M_{max} is the maximum moment within the laterally unsupported length and M_A, M_B and M_C are the moments at the quarter points.

The results of the analyses are summarised in the figures 3 through 6. In these figures, the moment, plotted on the vertical axis, was calculated using the applied uniformly distributed load times $L^2/12$ where L is the span length, measured from the columns centreline. The horizontal axis presents the span length divided by the torsional bending constant, a. Two sets of conditions were investigated, namely, beams with yield strengths of 300 MPa and 400 MPa, and full cross-section restraint and bottom flange only restrained. As a comparison, the design curves for CSA–S16–01 and AISC 2005 are superimposed.

It can be seen that the weaker joint conditions modelled (e.g. beam through, mitre and column through) do not provide sufficient torsional end restraint to develop the capacity predicted by the design equations. These analyses indicate that while these joint configurations may provide some basis for a comparison regarding relative warping stiffness, they do not provide sufficient restraint for practical situations.

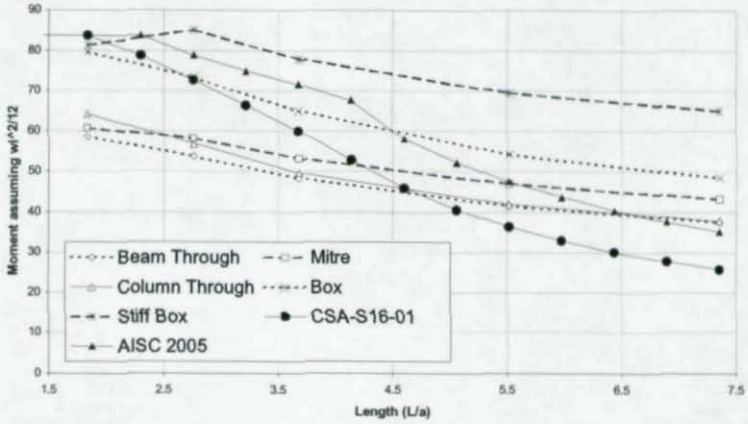

Figure 3 Moment resistance vs length, full cross-section restrained, (F_Y = 300 MPa)

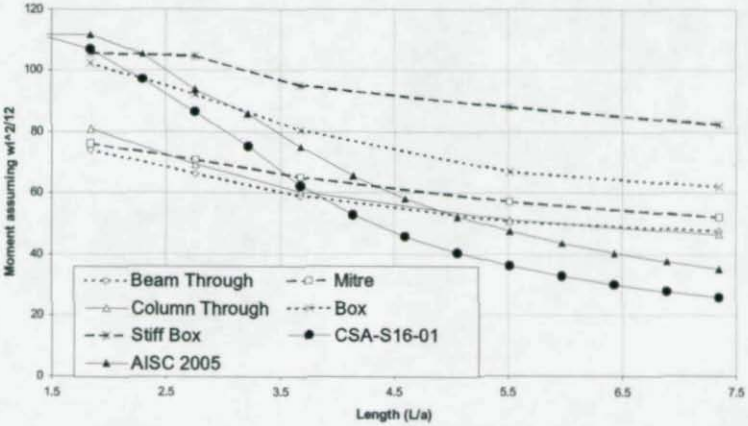

Figure 4 Moment resistance vs length, full cross-section restrained, (F_Y = 400 MPa)

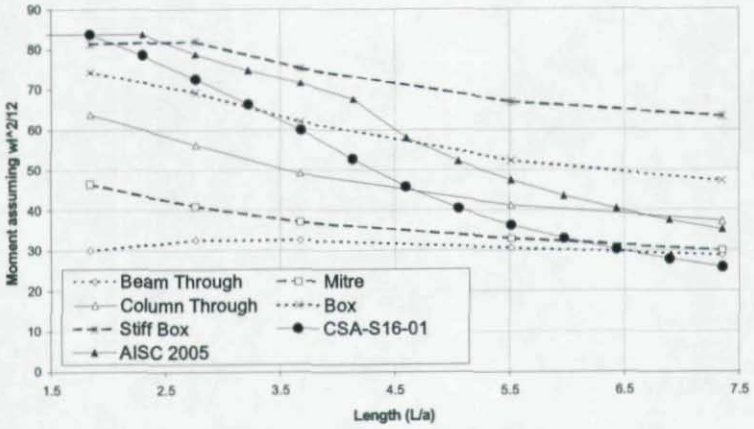

Figure 5 Moment resistance vs length, flange restrained, (F_Y = 300 MPa)

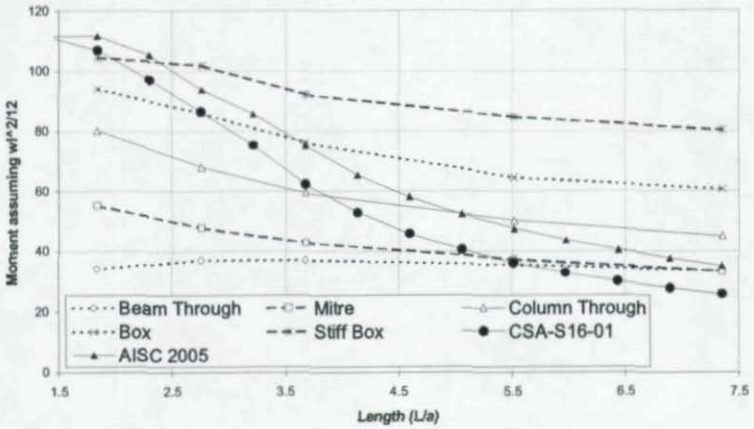

Figure 6 Moment resistance vs length, flange restrained, (F_Y = 400 MPa)

Figure 7 illustrates the lateral deflection of the shear center at midspan for a longer beam (8000 mm) using second order analysis and elastic material properties. The vertical axis presents the ratio of the beam uniform load to $12\,M_{cr}/L^2$ where M_{cr} is the elastic lateral torsional buckling moment for a beam of the same length, using an equivalent moment coefficient of 1.0.

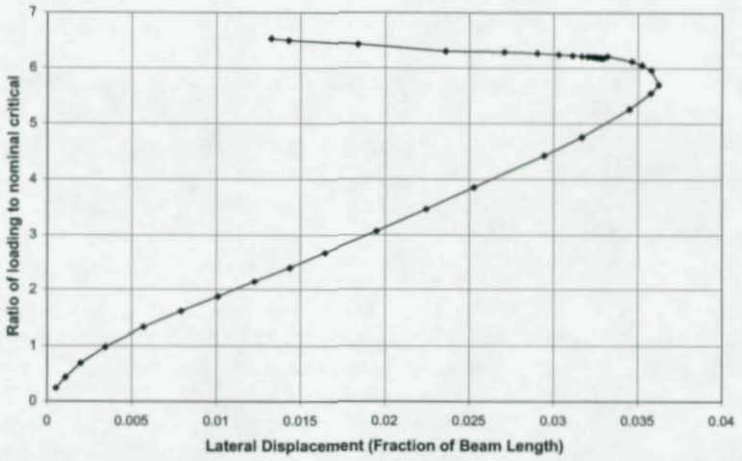

Figure 7 Load versus lateral displacement, 8 m beam with box joints, bottom flange restraint and elastic material

For longer beams, beam buckling was meant to be the governing limit state, not global frame instability. Perhaps due to this, the load - deformation curve for the elastic second order analysis did not show a localized peak load over the loading range of interest, as shown in Figure 7. As the beam moves out of plane, the frame is sufficiently stiff to provide post-buckling capacity. There is a change in the stiffness of the structure which corresponds to the strength of the frame after the beam buckles, as the beam moves back towards the plane of the frame. For those frames that showed this behavior, the maximum capacity was taken as the point where the beam starts to move back towards the plane of the frame.

This influence of frame-dominated action becomes significant for longer beams with stronger end restraints. While lateral torsional buckling of the beam appears to govern with eigenvalue analyses, the second order analysis indicates that the integrity of the frame provides higher strength than predicted by the simpler buckling analysis. Trahair (1996) observed this as well. Since the design equations do not account for this post-buckling strength, they can be considerably conservative.

The yield strength of the material does influence the buckling strength of the beam. Given two yield strengths of 300 MPa and 400 MPa, the ratio of the critical loads for similar conditions were in proportion the square root of the ratio of the yield strengths, as predicted by Kirby and Nethercot (1979). Table 2 presents the critical moments for 5 beam lengths and 5 joint types and illustrates that the ratio of the critical strengths for the 300 MPa steel versus the 400 MPa steel had a mean value of 0.832 with a standard deviation of 0.036. The approach from Kirby and Nethercot indicates a value of 0.866 ($\sqrt{0.75}$). For shorter (and stiffer) beams, inelastic buckling is replaced with full section yield, and the strength ratios become closer to that of the yield strength ratio of 0.75.

The analyses showed that there was in-plane distortion of the cross-section in all beams regardless of the end restraints. The beams with end conditions that did not provide extra support against cross-section distortion experienced distortion at the ends. While those beams with end conditions that provide extra stiffness to the cross-section, for example the "column through" condition, did not experience distortion at the ends, they did exhibit cross-sectional distortion at midspan of the beam.

An extensive numerical investigation of elastic lateral torsional buckling was presented by Nethercot and Rockey (1972). One of the results from that investigation was an equivalent moment factor (C_b) for uniformly distributed loads and various end support conditions. Figure 8 presents a comparison of their proposed C_b with the results from the elastic eigenvalue analysis conducted in this study. The three weaker end conditions are found to be considerably weaker than the laterally fixed condition presented by Nethercot and Rockey. The

stiffened connections appear to be at least as strong as the laterally fixed condition, but no end condition appears to provide full warping restraint. However, all those conditions follow the same trends as the curves presented by Nethercot and Rockey for a laterally fixed condition. The stronger end joint conditions from this study show a combination of the effects of the laterally fixed and warping fixed conditions.

Table 2 Moment capacities (kN · m) and ratios, bottom flange restrained condition

Joint Type	Yield Stress (MPa)	Beam Length (mm) 2000	3000	4000	6000	8000
Beam	300	30.0	32.5	32.5	30.6	28.7
Through	400	34.3	37.1	37.1	35.5	33.5
	Ratio	0.875	0.877	0.877	0.862	0.855
Mitre	300	46.5	41.0	37.1	33.0	30.0
	400	55.2	47.8	42.8	37.3	33.4
	Ratio	0.842	0.858	0.867	0.885	0.898
Column	300	63.8	56.2	49.2	41.3	37.2
Through	400	80.1	67.9	59.4	50.1	45.1
	Ratio	0.797	0.827	0.829	0.823	0.826
Box	300	74.4	69.3	62.1	52.3	47.2
	400	93.9	85.9	76.1	64.5	60.6
	Ratio	0.793	0.807	0.816	0.812	0.779
Stiffened	300	81.4	81.8	75.4	67.0	63.4
Box	400	104.6	101.9	92.0	84.6	80.2
	Ratio	0.779	0.803	0.819	0.792	0.791

CONCLUSIONS

The results from a study on inelastic stability of a beam supported by columns with various connection configurations are in agreement, at least in part, with previous work such as that by Kirby and Nethercot (1979). For inelastic buckling, the ratio of strengths from the analysis for different yield strengths does correspond closely with ratio of the

square roots of the yield strengths. This ratio does not hold for stiffer beams, where full plastic moments can develop, or for elastic buckling, where the strength is not affected by the yield strength.

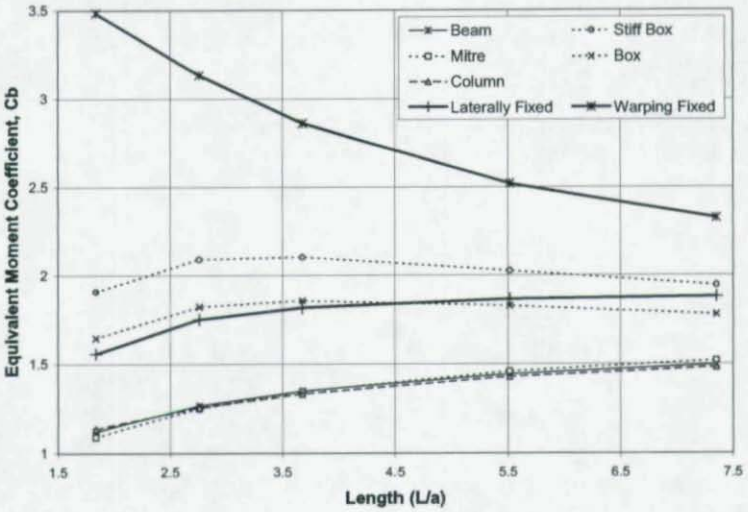

Figure 8 Comparison of equivalent moment coefficient for varying end conditions.

Also, the elastic eigenvalue analyses compare well to the work of Nethercot and Rockey (1972).

This work considers the effect of warping restraint on the lateral torsional buckling of frame members. However, it appears that distortion of the cross-section is an important factor in some of the cases. This will have to be taken into consideration in furthering the main course of study.

The weaker end conditions, such as the "column through", "beam through" and mitre joints do not provide sufficient restraint to develop the strength predicted by current design equations. Further studies will

focus more on adapting the more rigid end conditions. The weaker end conditions will continue to be used as base line conditions for comparison with the stronger end conditions as they do illustrate warping support for unstiffened joints.

While it was expected that the short beams would experience more benefit from the connections that have higher warping rigidity, the results appear to show that the longer members also experience proportionally greater benefits from the stiffer connections. This is due to the greater stiffness in connecting the beam to the columns, and the resulting increase in mobilising the post buckling strength of the full structure for the beam.

Plasticity does negate the effects of warping restraint to some extent in the buckling strength. However, there are still benefits for the frame's stability to have greater warping restraint, even over the range of intermediate beam lengths.

ACKNOWLEDGEMENTS

The authors thank Alberta Ingenuity for financial sponsorship of this research.

REFERENCES

AISC (2005) "ANSI/AISC 360-05: Specification for Structural Steel Buildings", American Institute of Steel Construction, Inc., March 9, 2005.

Chen, W.F. and Lui, E.M. (1991) *Stability Design of Steel Frames*, CRC Press, Boca Raton.

CSA (2001) "CAN/CSA-S16-01: Limit States Design of Steel Structures", Canadian Standards Association, Toronto, Ontario.

Daddazio, R.P., Bieniek, M.P. And DiMaggio, F.L. (1983) "Yield Surface for Thin Bars with Warping Restraint" ASCE Journal of Engineering Mechanics, Vol 109, No2, April 1983 pp 450-465.

Galambos, T.V. (1998) *Guide to stability design criteria for metal structures*, 5 th edition, John Wiley, (ISBN: 0-471-12742-6)

Kirby P.A. and Nethercot, D.A. (1979) *Design for Structural Stability*, Granada Publishing, London.

Krenk, S. and Damkilde, L. (1991) "Warping of joints in I-beam assemblages", ASCE, Journal of Engineering Mechanics, Vol. 117, No. 11, pp 2457-2474.

MacPhedran, I., Grondin, G.Y. (2005), "Warping restraint and steel frame instability", Proceedings of the SSRC 2005 Annual Stability Conference, Montréal, QC.

Nethercot, D.A. and Rockey, K.C. (1972) "A unified approach to the elastic buckling of beams", AISC Engineering Journal, Vol 9, No 3, pp 96-107.

Schumacher, A.S., G.Y. Grondin, G.Y., and Kulak, G.L. (1999) "Connection of Infill Panels in Steel Plate Shear Walls," Canadian Journal of Civil Engineering, Vol. 26, No. 5, pp 549-563.

Sheikh, I., Grondin, G.Y. and Elwi, A.E. (2003) "Stiffened Steel Plates Under Combined Compression and Bending," Journal of Constructional Steel Research, Vol. 59, No. 7, pp. 911-930.

Trahair, N.S. (1993) *Flexural-Torsional Buckling of Structures*, CRC Press, Boca Raton.

Trahair, N.S. (1996) "Laterally unsupported beams", Engineering Structures, Vol. 18 (10), pp 759-768.

Trahair, N.S. and Hancock, G.J. (2004). "Steel Member Strength by Inelastic Lateral Buckling", ASCE J. Struct. Engrg., Volume 130, Issue 1, pp. 64-69.

Yang Y-B, Chern, S-M, and Fan, H-T (1989). "Yield Surfaces for I-Sections with Bimoments" ASCE Journal of Structural Engineering, Vol 115, No 12, pp 3044-3058.

Strength Behavior of Horizontally Curved Composite I-Girder Bridge Structural Systems

S.-K. Jung[1] and D.W. White[1]

INTRODUCTION

Although substantial prior research has been conducted, no physical tests have been performed to investigate the maximum strength behavior of horizontally-curved composite I-girder bridge systems. Hall et al. (1999) observe that most of the prior research concerning curved composite I-girder bridges is focused on the strength and behavior of individual girders. Several investigators have focused on the system behavior of curved composite bridges (Brennan and Mandel (1979), Galambos et al. (2000) and McElwain et al. (2000)), but these studies are concerned mainly with the elastic bridge responses. Despite considerable contributions of prior research to the understanding of curved bridge behavior, these earlier efforts are somewhat limited in identifying the complete ultimate strength response of curved I-girder bridges. In order to better understand the service and ultimate load resistance of these types of structures, the Curved Steel Bridge Research Program (CSBRP) was initiated by the Federal Highway Administration (FHWA) in 1992. This project has culminated in 2005 with the experimental testing of a representative full-scale horizontally curved composite bridge. The major research objective of this test is to examine the system and component responses of a representative structure under all loading stages: non-composite dead load, composite service live load and ultimate loading. Figure 1 shows the girder cross-section, bridge cross-section and plan views of the composite test bridge. An overview of various physical attributes of the test bridge is presented in Jung et al. (2005). This reference also provides a detailed discussion of key aspects of the elastic strength design of the composite test bridge system.

[1] Georgia Institute of Technology, Atlanta, GA 30332-0355

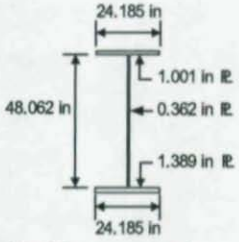

(a) G3 cross-section

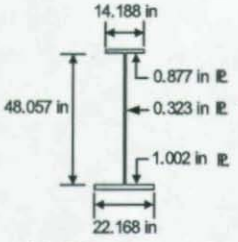

(b) G2 cross-section

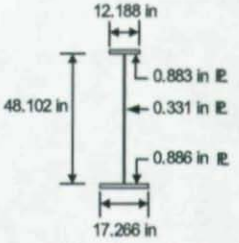

(c) G1 cross-section

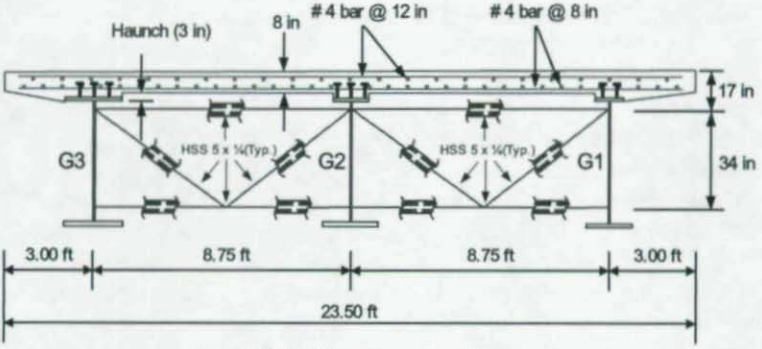

(d) Bridge cross-section

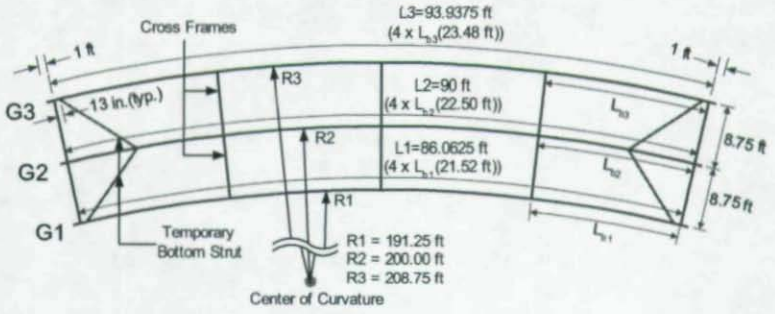

(e) Bridge plan

Fig. 1. Composite test bridge geometry.

The composite test bridge is designed using the newly adopted AASHTO (2004) design provisions for straight and curved I-girder bridges. In general, the strength resistance equations in these provisions may be written in terms of stresses as

$$f_{bu} + \frac{1}{3} f_\ell \le \phi_f F_n \tag{1}$$

where f_{bu} and f_ℓ are the elastically-computed flange major-axis and lateral bending stresses respectively, and $\phi_f F_n$ is the factored flexural resistance in terms of the flange major-axis bending stress for $f_\ell = 0$. Also, they may be written in the form

$$M_u + \frac{1}{3} S_x f_\ell \le \phi_f M_n \tag{2}$$

in terms of the major-axis bending moments, where S_x is the elastic section modulus to the flange under consideration. White and Grubb (2004) summarize the background and usage of these equations, termed the "one-third rule," and provide references to more detailed research reports and papers on their development. The term $\phi_f F_n$ in Eq. (1) is generally less than or equal to $\phi_f F_{yf}$ whereas $\phi_f M_n$ in Eq. (2) is equal to the factored plastic moment in many cases. However, for curved bridges, the AASHTO (2004) provisions restrict the design of *all* I-section members to Eq. (1). This restriction is due to limited understanding of the influence of the member yielding necessary to develop larger I-girder strengths on the system response of curved I-girder bridges (specifically, the validity of elastic analysis). The test bridge, and other bridge configurations studied parametrically as part of the CSBRP effort, are targeted at providing the necessary understanding to potentially allow use of Eq. (2) with $\phi_f M_n$ up to $\phi_f M_p$ where applicable in both curved and straight I-girder bridges.

Jung et al. (2005) observe that the test bridge system and component responses are essentially linear up to the load level when the outermost girder develops the M_p-based 1/3 rule strength, $M_u = M_p - S_x f_f(1/3)$. The present paper investigates the force transfer mechanisms in the test

bridge and the extent of nonlinearity of the bridge responses at the M_p-based 1/3 rule load level in more detail.

The overall organization of the paper is as follows. First, the overall test bridge experimental results and their comparisons to full nonlinear FEA predictions are described. This is followed by investigation of detailed bridge system and component responses, by making various cuts and considering the resulting free body diagrams from the full nonlinear FEA solution. These solutions are compared to corresponding experimental measurements in a number of cases.

CORRELATION OF FULL NONLINEAR FEA AND EXPERIMENTAL TEST RESULTS

Figure 2 shows the experimental setup for the ultimate load test of the composite test bridge. Figure 3 shows the specific laboratory loadings applied in this load case. The loading scheme shown in Fig. 3 approximates the effects of the AASHTO live load model causing the maximum flexural effects on G3 in the design analysis of the test bridge.

Fig. 2. Composite test bridge with loading fixtures, ultimate load test. (Courtesy of Federal Highway Administration)

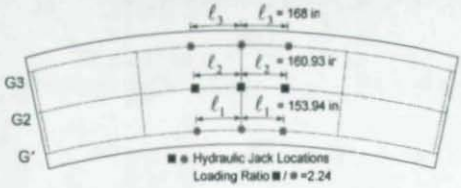

Fig. 3. Equivalent live load model used for the bridge test.

Figure 4 gives a perspective view of the deformed composite test bridge just prior to concrete slab crushing at the outside edge of the slab at mid-span. The outside tip of the girder G3 bottom flange at the mid-span reached a deflection of 24 in due to a total applied load of 1300 kips at this stage.

Fig. 4. View of deformed composite test bridge slab along G3 just prior to the concrete slab crushing (Courtesy of Federal Highway Administration)

Figure 5 compares the mid-span vertical deflections at the bottom flange outside tip of G3 computed from the full nonlinear FEA to corresponding experimental values obtained from the ultimate load test. Initial dead-load displacements are not included in this plot. It can be seen that the FEA predictions for the girder vertical deflections are in a good agreement with the experimental values.

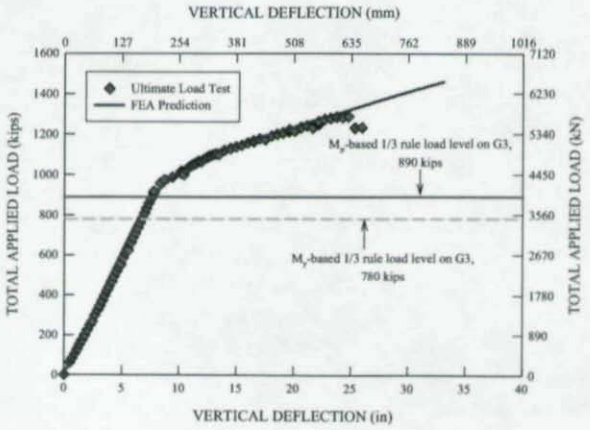

Fig. 5. Total applied load versus vertical deflection of girder G3 bottom flange outside tip at mid-span.

Figure 6 shows that the ratios of individual girder reactions to the total applied load essentially remain constant throughout the elastic and inelastic ranges. The ratios of the girder reactions to the total applied load are on average 0.09, 0.27, and 0.64 for G1, G2, and G3 respectively. Similar to the deflection responses, there is a good correlation between the FEA predictions and the experimental values for the reactions throughout the loading history.

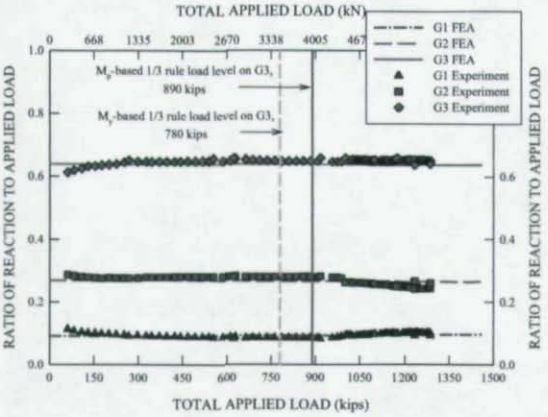

Fig. 6. Ratio of individual girder reactions to the total applied load, FEA and experimental values.

Figure 7 gives a plot of the G3 FEA internal moment at mid-span versus the corresponding vertical deflection of the G3 bottom flange outside tip. An initial dead load moment of 2364 k-ft is included in this plot. The significant strength levels marked on the plot are the M_y- and M_p-based 1/3 rule strengths of M_y-$S_x f_f(1/3)$ = 9589 k-ft and M_p-$S_x f_f(1/3)$ = 10728 k-ft, respectively. These load levels are obtained by using Eq. (2) with the results of a linear elastic FEA of the test bridge for the calculation of f_f. It is quite interesting that the internal moment on G3 increases in a predominantly linear fashion up to the M_p-based 1/3 rule strength level and then approaches asymptotically a moment slightly less than the composite section plastic moment in the absence of flange lateral bending. Similar plots for G1 and G2 show that the internal moments for both of these girders increase linearly up to the load level when G3 reaches its M_p-based 1/3 rule strength level (Jung 2006).

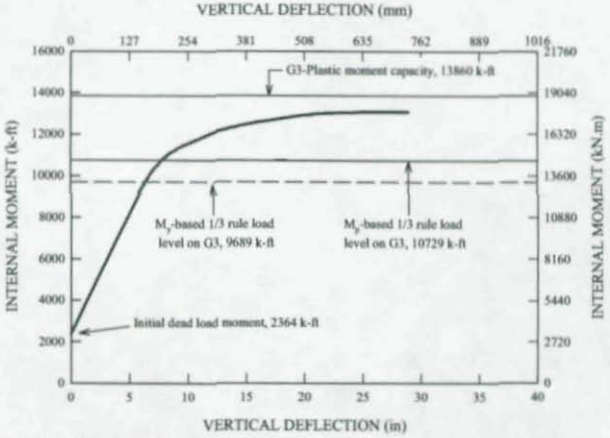

Fig. 7. G3 – FEA internal moment at mid-span versus corresponding vertical deflection of bottom flange outside tip.

Although the above responses from the experimental and FEA results indicate that the bridge components and the overall bridge system behave linearly up to the M_p-based 1/3 rule load level on G3, these responses do not necessarily imply that there are no effects of inelastic redistribution of forces between the bridge girders at this load level. Therefore, it is useful to consider a number of other detailed responses.

VERTICAL FORCES ACTING ON G3

Figure 8 shows the various vertical forces acting on G3 versus the total applied load. The separate vertical forces acting on G3 include: (1) the directly applied loads, (2) the vertical force components in the diagonal members of the quarter- and mid-span cross-frames, (3) the slab shear force transferred to G3, and (4) the vertical end reactions. The slab shear forces are obtained indirectly by subtracting the sum of the directly applied loads and the cross-frame shear forces from the total reactions. The reaction force varies linearly through the loading history as mentioned previously. However, Fig. 8 shows that the internal force components vary in a slightly nonlinear fashion. Nonetheless, the extent of nonlinearity is generally minor up to the M_p-based 1/3 rule load level of 890 kips. The prediction of the mid- and quarter-span cross-frame forces by the nonlinear FEA solution is quite accurate.

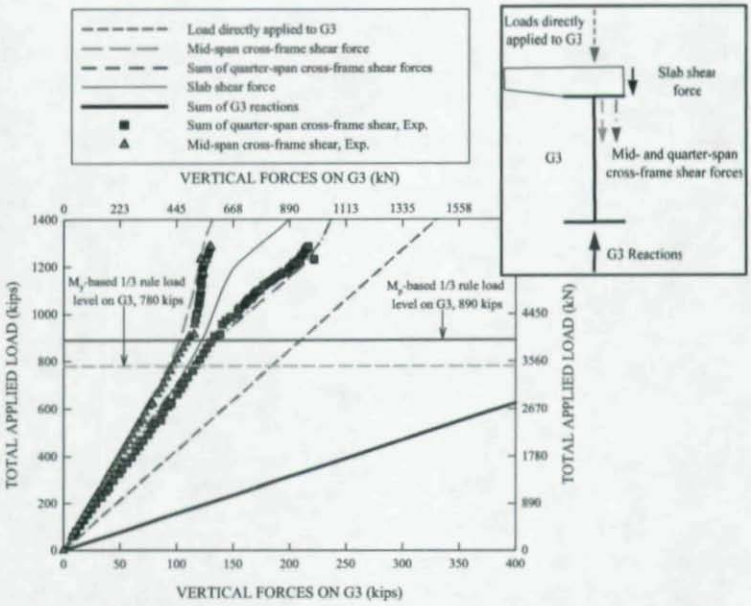

Fig. 8. Total applied load versus the vertical forces acting on G3.

Furthermore, the error of linear elastic FEA predictions (not shown in Fig. 8) for the mid- and quarter-span cross-frame shear forces is only 3 and 6 percent unconservative relative to the corresponding experimental values. In addition, it is noteworthy that the test bridge slab carries considerable shear forces to G3 throughout the loading history. In other words, together with the cross-frames, the test bridge slab plays an important role in transferring loads to G3. Similar to the cross-frame shear forces, the slab shear force curve indicates some minor nonlinear behavior after a total applied load of 890 kips.

SHEAR FORCES ON G3

Figure 9 shows the ratio of FEA internal shear forces resisted by the G3 web, flanges and slab to the total section shear for cross-sections located just to the inside of the quarter-span and the girder supports. As expected, the girder web plays a major role in resisting the girder total shear force at both locations.

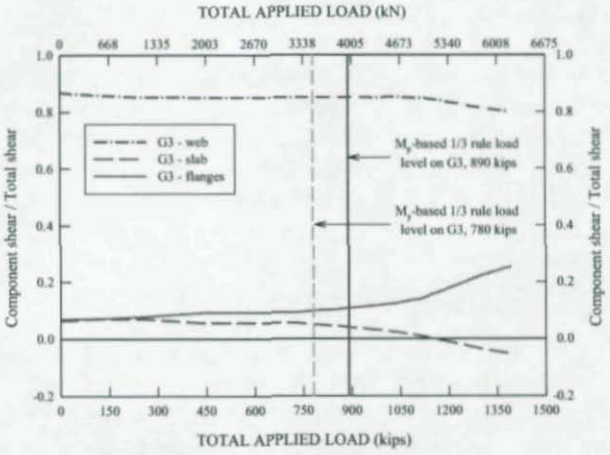

(a) just to the inside of quarter-span

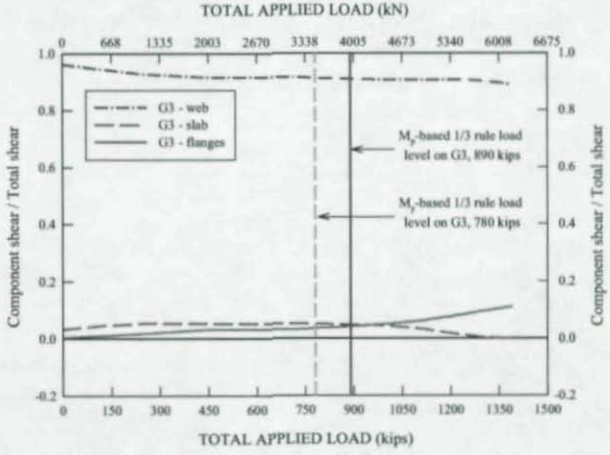

(b) just to the inside of girder supports

Fig. 9. Ratios of FEA internal shear forces resisted by the G3 web, flanges and slab to the total section shear: (a) just to the inside of quarter-span and (b) just to the inside of girder supports.

Also, it can be observed in both plots that the ratio of the slab shear force to the total shear gradually decreases with increasing applied load while the web shear contribution remains fairly constant throughout the loading history. Conversely, there is a significant increase in the shear force contribution from the girder flanges at higher load levels. These results are believed to be due to the softening of the concrete slab at higher load levels. Nonetheless, it should be noted that the changes in the shear force contributions are relatively small up to the M_p-based 1/3 rule load level.

CONCRETE SLAB STRAIN DISTRIBUTION

Figure 10 compares the longitudinal strains on the slab top surface obtained from the full nonlinear FEA to corresponding experimental values measured at the mid-span of the test bridge at the M_p-based 1/3 rule load level on G3. It should be noted that, except for some local deviations, there is a good correlation between the FEA predictions and experimental values. Also, one can see that the longitudinal strains at the mid-span vary approximately in a linear fashion across the slab width, with the largest stain occurring at the outer edge of the slab. The maximum strain at this load level is still significantly less than the nominal concrete crushing strain.

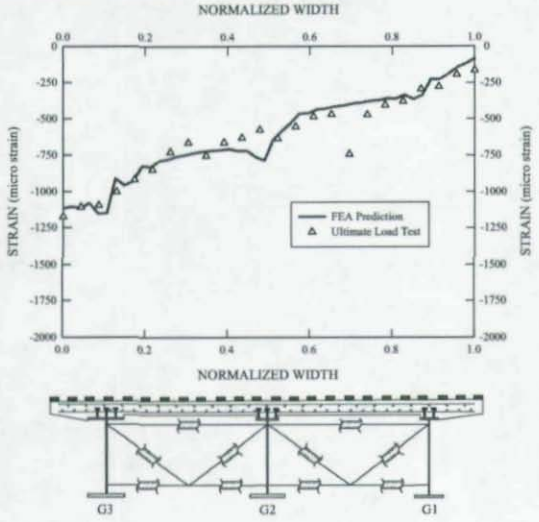

Fig. 10. Mid-span longitudinal deck strains across bridge deck width at M_p-based 1/3 rule load level, 890 kips, strains associated with concrete creep and shrinkage are not included in the plot.

CROSS-FRAME MEMBER FORCES

Figure 11 shows the axial force in the bottom chord of the mid-span cross-frame connected to G3 throughout the loading history. The member force due to dead loads is included in this plot. The FEA predictions are slightly smaller than the experimental values. The computed maximum axial force at a total applied load level of 1300 kips is 340 kips in compression. The corresponding experimental value is 361 kips. Interestingly, Fig. 11 shows that the member force reaches a plateau at high load levels. It should be noted that this plateau has nothing to do with yielding or plastification of the cross-frame members. In fact, the cross-frame members are sized to remain elastic throughout the entire loading history.

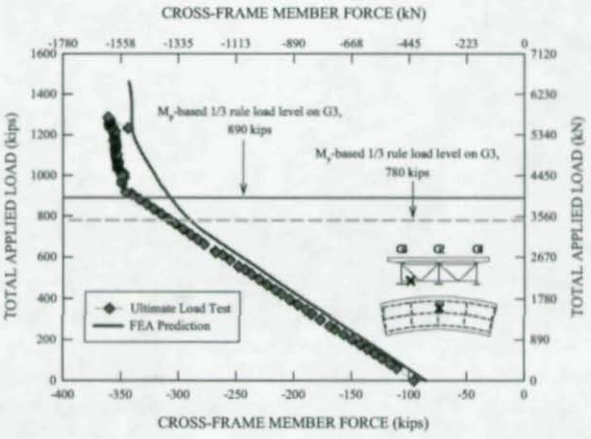

Fig. 11. Total applied load versus axial force in the bottom chord of the mid-span cross-frame connected to G3.

To understand why the plateau appears in Fig. 11, one can consider the force diagram shown in Fig. 12. In the limit when the G3 web and bottom flange are fully plastified, they tend to straighten into chords between the cross-frame locations. Fig. 12 shows a free body diagram at the mid-span of G3 for a portion of the straightened web and bottom flange segments constructed by making cuts halfway between the cross-frame locations. In this extreme configuration, the sum of the

axial forces in the web and the bottom flange can be expressed as $P = A_f F_{yf} + A_w F_{yw}$, where A_f and A_w are the areas of the bottom flange and the web, and F_{yf} and F_{yw} are the corresponding yield strengths. The maximum cross-frame bottom chord force can be estimated conservatively as 394 kips, based on the sum of the radial components of the forces P on each side of the mid-span cross-frame location. The plateau in Fig. 11 is due to the fact that the web and the bottom flange of G3 have become significantly yielded as illustrated previously by Fig. 7 as well as Fig. 13 in the following section. This in turn limits the radial reaction on the bottom chord of the cross-frame connected to G3.

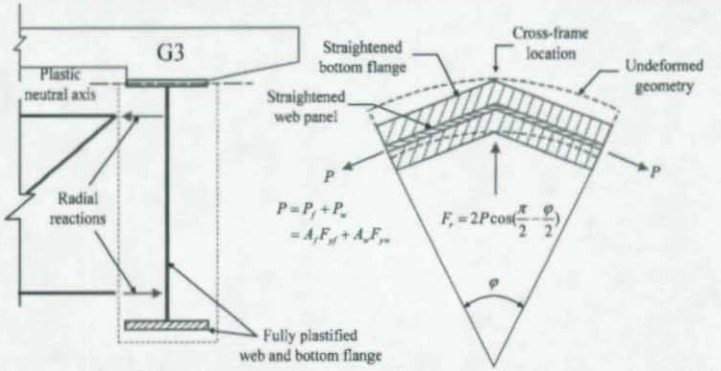

Fig. 12. Cross-frame reaction forces resisting radial components of the axial forces in fully plastified web and bottom flange.

Moreover, it should be noted that the maximum member force developed in the bottom chord of the mid-span cross-frame is slightly larger than the capacity of the cross-frame bottom chord designed elastically for the M_p-based 1/3 rule load level. Also, it is shown in Jung (2006) that the cross-frame member forces are generally insensitive to changes in the cross-frame member areas for the test bridge.

SPREAD OF YIELDING

Figure 13 shows the normalized equivalent plastic strain ratio, $\varepsilon_{eq}^{p} / \varepsilon_y$, along the normalized full length of the girder G3 for five top surface locations on its bottom flange at the G3 M_p-based 1/3 rule load level.

The top surface strains are presented since the largest plastic strain occurs at the top surface outside tip of the bottom flange. It is of interest to note that, due to the effects of flange lateral bending associated with the horizontal curvature, the yielding takes place at the outside tip of the flange at mid-span and at the inside tip of the flange at a location between the mid- and quarter-span cross-frames. Most importantly, the yielding at the mid-span exhibits a high strain gradient across the flange width. It is also of interest to note that the inside flange tip is still elastic at this location at the M_p-based 1/3 rule load level. This is due to the fact that the flange lateral bending reduces the tensile stresses on the inside of the bottom flange at the cross-frame locations.

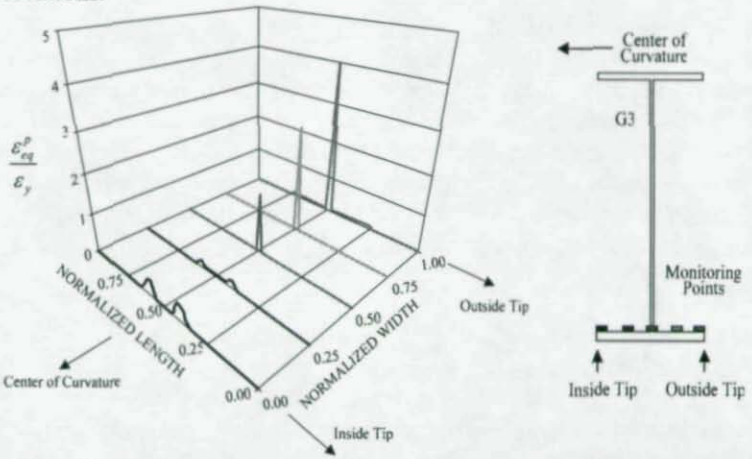

Fig. 13. Equivalent plastic strain ratio ($\varepsilon_{eq}^{p} / \varepsilon_y$) along the normalized full length of the G3 bottom flange for five top surface locations at the M_p-based 1/3 rule load level of 890 kips on G3, full nonlinear FEA.

INTERNAL MOMENT AND SHEAR FORCES

Figure 14 gives the FEA internal *dead load* moment and shear force diagrams along the normalized length for the entire bridge cross-section and for the individual bridge girders. It can be seen from the figure that a significant portion of the total bridge internal moment is carried by G3. Of the total internal dead load moment, G3 supports approximately

70 percent (2365 k-ft) while G2 and G1 support only 20 percent (683 k-ft) and 10 percent (295 k-ft) respectively. This highlights the critical role of the outside girder, G3, during construction in resisting the dead loads due to steel and concrete self weight as well as the construction loads on the noncomposite structure. Also, Fig. 14 shows that all the shear force diagrams vary almost linearly (i.e., the discrete jumps at the cross-frame locations are relatively small). The shear force diagram for G3 shows that it is subjected to concentrated forces from the cross-frames, particularly, at the quarter-span locations, while the shear force diagrams for G1 and G2 show that these girders are unloaded by upward concentrated cross-frame forces.

Figure 15 gives the total FEA internal moment and shear force variations along the normalized length for the entire bridge cross-section and for the individual bridge girders at a total applied load level of 890 kips corresponding to the M_p-based 1/3 rule load level on G3. It should be noted that both of these plots include initial moments and shears due to dead loads. Of the total internal moment on the bridge cross-section at mid-span, G3 carries 55 percent (10729 k-ft) while G1 and G2 take 12 percent (2470 k-ft) and 33 percent (6568 k-ft) respectively.

The shear force diagram in Fig. 15 shows that there are several significant jumps due to the externally applied loads and internal cross-frame forces. The first jump, located at mid-span, is caused by the externally applied loads and the cross-frame forces combined together. The second jump, located at the adjacent loading points, is caused by the directly applied loads only. The third jump, located at the quarter-span cross-frame locations, is caused by the cross-frame forces only. It should be noted that all the cross-frame forces act on G3 such that its positive internal moments are increased. In other words, all the vertical internal forces applied to G3 are acting in the downward direction. Similar to the shear force diagram for G3, the shear force diagram for G2 has three jumps at the same locations as those of G3.

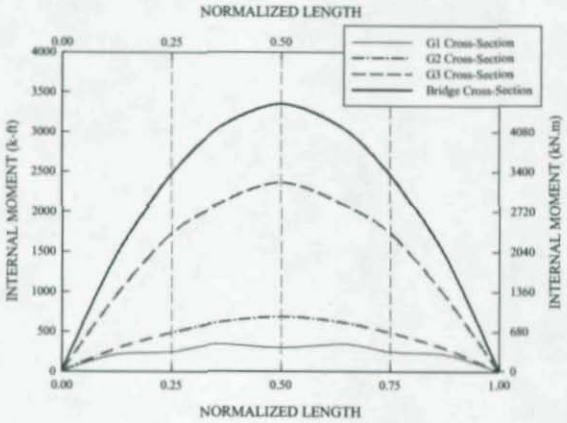

(a) Internal moments

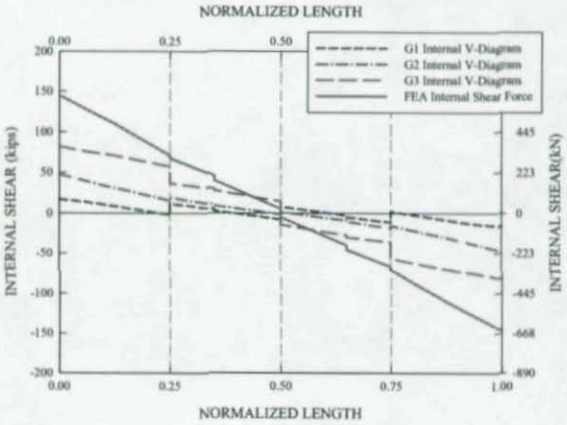

(b) Internal shear forces

Fig. 14. Dead Load - FEA internal force variations of total bridge cross-section and individual girder cross-sections along the normalized length: (a) internal moments and (b) internal shear forces.

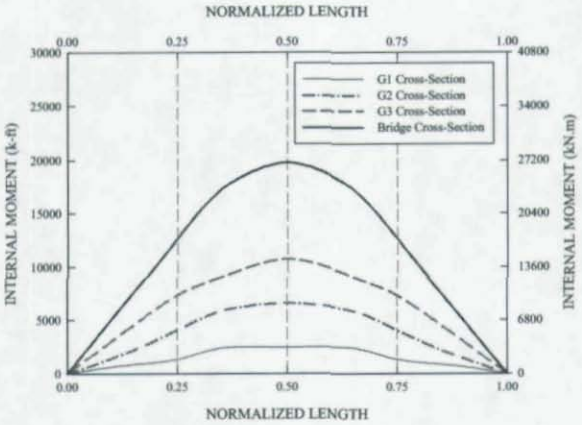

(a) Internal moments

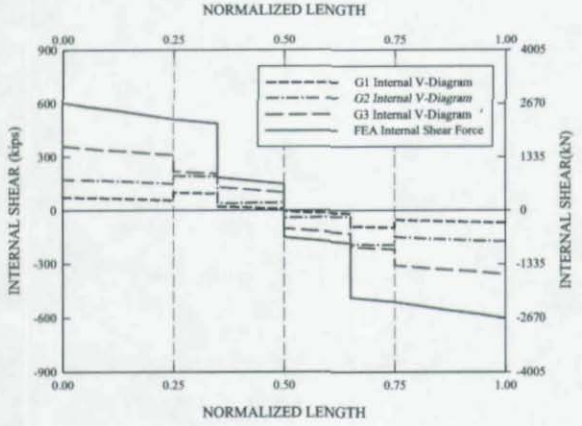

(b) Internal shear forces

Fig. 15. Live Load plus Dead Load- FEA internal moment and shear variations of total bridge cross-section and individual girder cross-sections along the normalized length at the M_p-based 1/3 rule load level on G3: (a) internal moments and (b) internal shear forces.

However, the cross-frame forces acting on G2 are in the upward direction. Contrary to the shear force diagrams for G2 and G3, the shear force diagram for G1 has only two jumps that appear at the outer loading points (see Fig. 3) and the quarter-span cross-frame locations. That is, there is no significant jump associated with the directly applied loads at mid-span. This is because the cross-frame force at this location is in the upward direction such that it almost cancels the directly applied loads. Conversely, the cross-frame forces acting on G2 at the mid-span of G2 do not completely cancel out the directly applied loads acting on G2.

Figure 16 shows the FEA live load internal shear force diagrams for the isolated G3 composite girder at a total applied load level of 890 kips. This figure shows the total live load internal shear force diagram on G3, as well as the shear force diagrams due to the directly applied loads on G3, the vertical forces transferred from the cross-frames attached to G3, and the combination of the two. It is apparent that the sum of the girder internal shear forces due to the directly applied loads and the cross-frame vertical forces do not add up to the total live load internal shear force obtained from the full nonlinear FEA results. The additional portion of the total live load shear force has to come from the slab. A careful look at the difference between the total live load shear diagram and the combined shear diagram due to the directly applied load and the cross-frame vertical forces, indicated by the hatched pattern in Fig. 16, reveals that the vertical forces transferred through the slab to G3 from the adjacent girders are nearly constant along G3 except in the vicinity of G3's ends. The vertical forces transferred through the slab are slightly larger in magnitude at G3's ends (the slope of the shear diagram increases). Figure 17 presents a conceptual representation of these vertical load distributions on G3.

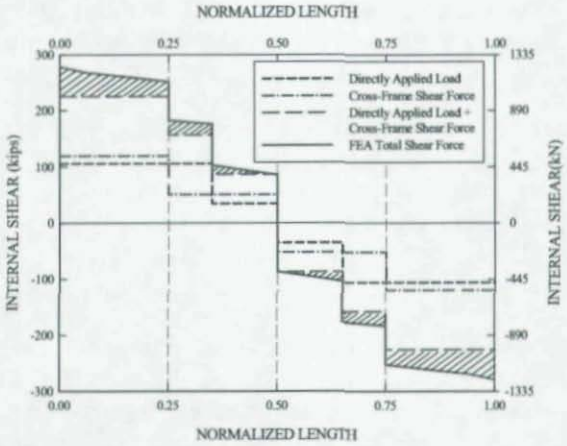

Fig. 16. Calculated live load internal FEA shear force diagrams for the isolated G3 composite section along the normalized length, and shear force diagrams due to directly applied loads, cross-frame shear forces, and a combination of the two on G3 at a total applied load level of 890 kips.

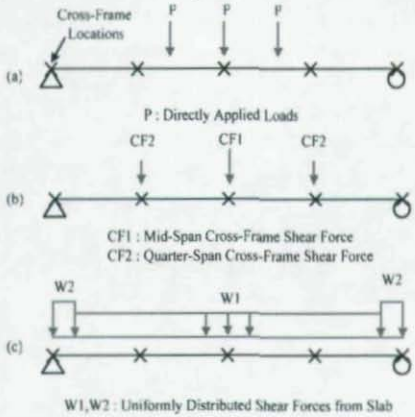

Fig. 17. A conceptual representation of internal and external vertical force components acting on G3: (a) directly applied loads, (b) cross-frame shear forces, and (c) uniformly distributed shear forces from the test bridge slab.

SUMMARY AND CONCLUSIONS

This study provides a synthesis of the experimental and full nonlinear FEA results of a full-scale horizontally curved composite bridge tested by the FHWA CSBRP. The findings of this study indicate that the component and system responses of the test bridge are predominantly linear up to the M_p-based 1/3 rule load level on the outside girder, G3. Also, the FEA internal moment and shear force diagrams of the test bridge girders emphasize the importance of the outermost girder. It is shown that the test bridge slab plays an important role in transferring the directly applied loads on the adjacent girders, G2 and G1, to the outermost girder, G3. Interestingly, the slab vertical forces transferred to G3 are nearly uniformly distributed along the girder length, except for the regions in close proximity to the girder ends. These regions are subjected to higher vertical forces than other portions of the girder. Most importantly, there is no significant change in the internal force distributions up to the M_p-based 1/3 rule load level on G3. Based on these results and the additional FEA parametric studies presented in Jung (2006), it is concluded that simply supported horizontally curved composite bridges may be designed using the strength resistance equations for straight bridges, reduced by the flange lateral bending effects due to torsion, as the base flexural resistance for the strength limit states. That is, girder bending moments in positive bending are equal to $M_u=\phi_f M_n-S_x f_f(1/3)$ with $\phi_f M_n$ as high as up to $\phi_f M_p$.

ACKNOWLEDGEMENTS

This research is funded by Professional Services Industries, Inc. (PSI) and the Federal Highway Administration (FHWA). The authors gratefully acknowledge the financial support from the sponsors. The many contributions to this work from numerous individuals who have been associated with the different phases of the FHWA CSBRP, including the PSI and FHWA staff at the Turner-Fairbank Highway Research Center, are also gratefully acknowledged. Special thanks are extended to Dr. F. Beshah for his extensive work with reduction of the experimental data. The opinions, findings and conclusions expressed in this paper are the authors' and do not necessarily reflect the views of the above individuals, groups and organizations.

REFERENCES

AASHTO (2004). *AASHTO LRFD Bridge Design Specifications, 3rd Edition* with 2005 Interims, American Association of State and Highway Transportation Officials, Washington D.C.

AASHTO (2003). *Guide Specifications for Horizontally Curved Steel Girder Highway Bridges*, American Association of State and Highway Transportation Officials, Washington D.C.

Brennan, P.J. and Mandel, J.A. (1979). "Curved Girder Bridge Model Analysis and Testing," *Proceedings*, IABSE, P-19/78, 1-20.

Galambos, T.V., Hajjar, J.F., Huang, W.-H., Pulver, B.E., Leon, R.T., and Rudie, B.J. (2000). "Comparison of Measured and Computed Stresses in A Steel Curved Girder Bridge," *Journal of Bridge Engineering*, ASCE, 5(3),191-199.

Hall, D.H. and Yoo, C.H. (1999). "Improved Design Specifications for Horizontally Curved Steel Girder Bridges," *NCHRP Report 424*, NCHRP, Washington, D.C.

HKS (2004), *ABAQUS/Standard Version 6.4-1*, Hibbitt, Karlsson & Sorensen, Inc., Pawtucket, RI.

Jung, S.-K. (2006). "Inelastic Behavior of Horizontally Curved Composite I-Girder Bridge Structural Systems," Ph.D. dissertation, Georgia Institute of Technology, Atlanta, GA.

Jung, S.-K., White, D.W., Beshah, F. and Wright, W. (2005). "Ultimate Strength of Horizontally Curved Composite I-Girder Bridge Structural Systems," Proc. of Annual Technical Session, SSRC, April 2005.

McElwain, B.A. and Laman, J.A. (2000). "Experimental Verification of HorizontallyCurved I-Girder Bridge Behavior," *Journal of Bridge Engineering*, ASCE, 5(4),284-292.

White, D.W. and Grubb, M.A. (2004). "Comprehensive Update to AASHTO LRFD Provisions for Flexural Design of Bridge I-Girders," *Proceedings*, Structures Congress, ASCE, 8pp.

IN-PLANE STABILITY OF SEMICIRCULAR STEEL ARCHES LOADED IN BENDING AND COMPRESSION

Dagowin B. la Poutré [1] *and H.H. Snijder*[1]

ABSTRACT

In this paper, the in-plane stability of semicircular steel arches loaded in bending and compression is investigated. The arches have wide flange ribs, are in-plane hinged at the supports, and are loaded by a single point load at the crown. It is the objective to derive buckling curves for these types of arches. The plastic strengths of the arches are determined analytically and are compared to numerically obtained plastic strengths. Then the eigenvalue is determined numerically and compared to analytical solutions from the literature. Finally, a full non-linear Finite Element Analysis is performed to determine the actual elastic-plastic buckling loads. The FEA includes the effects of the bending process of the arches, for which the proper stress-strain relations and residual stress patterns are used. Furthermore, geometric imperfections are included. Based on the FEA results, buckling curves are suggested for the load case investigated in this paper.

1 INTRODUCTION

1.1 State of the art

The in-plane stability of arches has been studied by a number of researchers. Early studies were limited to analytical solutions of the

[1] Department of Structural Design, Faculty of Architecture, Building and Planning
Eindhoven University of Technology,
P.O. Box 513, 5600 MB Eindhoven, The Netherlands

elastic stability. DaDeppo & Schmidt, 1969, proposed analytical solutions for the load case investigated in this paper. Bradford, et al., 2002, also investigated the elastic stability of this load case for shallow and deep circular arches. For deep arches they proposed an equation that is nearly identical to the Dadeppo & Schmidt equation. For the plastic strength of the arches, most researchers took the section strength. Pi & Trahair, 1999, proposed to reduce the section strength based on the slenderness of the arch. The plastic collapse strength of the whole arch was investigated experimentally by Jukes, et al., 1983.
A design equation for non-uniform combined compression and bending was proposed by Pi & Trahair, 1999, and an iterative design equation for the load case under investigation was proposed Verstappen, et al., 1998.

1.2 Present research

This paper investigates if arches can be designed against in-plane stability using the existing design procedures from Eurocode 3 (ENV 1993). For this procedure, one needs to know the plastic strength and eigenvalue which determine the non-dimensional slenderness of the arch. Based on the non-dimensional slenderness, a reduction factor can be obtained from the appropriate buckling curve. The reduction factor χ times the plastic strength gives the maximal load that an arch can carry before instability occurs. In the next sections it is investigated whether this procedure can be applied to the investigated load case.

1.3 Load case

Semicircular arches, hinged in-plane and loaded by a concentrated load at the crown are investigated. Figure 1 shows the moment and normal force distribution and Equation 1 gives the moment distribution and Equation 2 the normal force distribution. Note that for semi-circular arches $\gamma = \pi/2$. The maximum bending moments occurs at the crown and is given by Equation 3. The second largest bending moment occurs at an angle $\phi_{2nd} = \arctan(\pi/2) = 57.6^{\circ}$ and is equal to $M_{2nd} = -0.0927 \cdot F \cdot R_n$, with F = applied load and R_n = nominal radius. The second largest bending moment coincides with the largest normal force, which occurs at the location where the tangent to the arch is parallel to the funicular line, see Figure 1b.

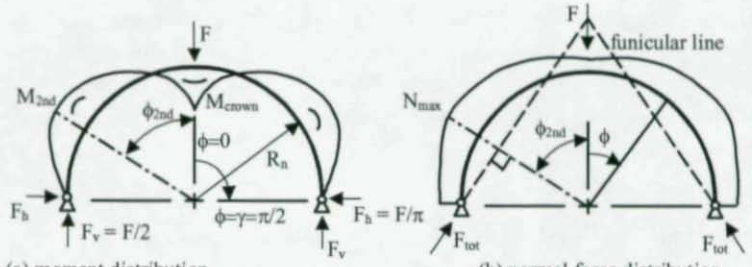

Figure 1. Investigated load case.

$$0< \phi < \gamma:\ M(\phi) = F \cdot R_n \left[\frac{1}{2} - \frac{\sin\phi}{2} - \frac{\cos\phi}{\pi} \right] \tag{1}$$

$$0< \phi < \gamma:\ N(\phi) = F \cdot R_n \left[\frac{1}{2} - \frac{1}{\pi} \right] \tag{2}$$

$$M_{crown} = F \cdot R_n \left[\frac{1}{2} - \frac{1}{\pi} \right] \tag{3}$$

2 BENDING PROCESS

Arches can be produced in several ways: they can be welded together from curved plates, they can be roller bent at ambient temperature, or the can be formed by induction bending at elevated temperatures. The type of bending process determines what happens to the residual stresses and material properties. For wide flange beams, roller bending is most commonly used and this paper will be confined to arches produced with this process.

In the roller-bending process, a straight member is passed through three rollers in pyramid configuration, see Figure 2. After each pass, the middle roller is moved inwards until the desired curvature is obtained. At the inside of the tension flange, a flange support-roller prevents the web from crippling. The outer flange is plastically stretched and the inner one plastically compressed at ambient temperatures, thus cold

working the material and changing the stress-strain characteristics. Due to the geometry of the bending machine, the ends of the member cannot pass completely through the machine, leaving them more or less straight, and they are cut off, see Figure 2.

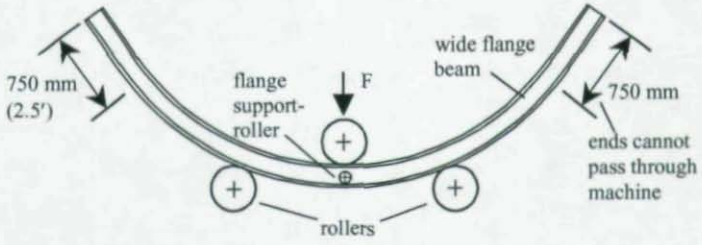

Figure 2. Pyramid type three roller process.

During bending, the flanges are strained through the elastic region of the material (1) into the yielding (2) region, and, depending on the ultimate curvature, into the hardening (3) of the steel, see Figure 3a. While the member leaves the bending machine, it unloads elastically (4) and a permanent strain remains at the flanges, see Figure 3b.

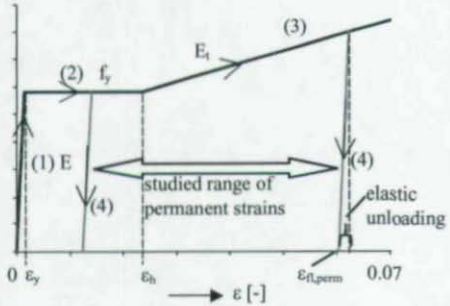

(a) stress-strain relation during bending

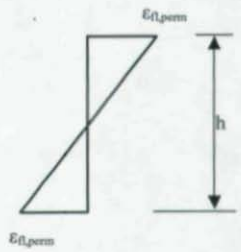

(b) permanent strain over the depth of the section after bending

Figure 3. Stress-strain relation.

Equation 4 gives the permanent strain at the flanges after bending and Equation 5 gives the dimensionless bent ratio. In this paper, arches bent to eight different bent ratios, ranging from 8.3 to 39.8, were studied, see Table 1 (Appendix). The larger the bent ratio is the more slender the arch is.

Five different wide flanges beams from the standard rolled European series were selected ranging from compact (HEA 100) to deep (HEB 1000). Figure 4 shows these sections next to each other, where they are scaled to one depth for better comparison. These five sections were used in the analyses presented in this paper.

$$\varepsilon_{fl,perm} = \frac{h}{2 \cdot R_n} \tag{4}$$

$$\text{bent ratio} = \frac{l}{2 \cdot \varepsilon_{fl,perm}} = \frac{R_n}{h} \tag{5}$$

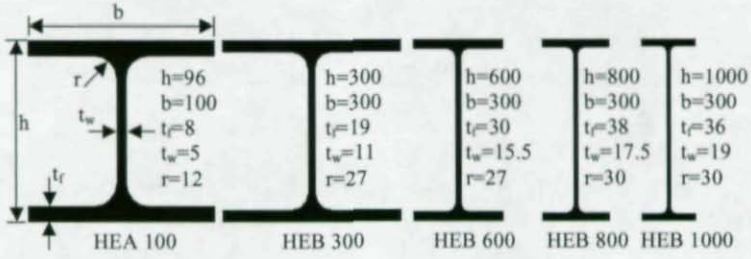

Figure 4. Studied wide flange beams.

3 PLASTIC STRENGTH

3.1 Analytical

An in-plane hinged arch is hyper static to the first degree. If this arch is loaded beyond the elastic bending capacity, a hinge occurs at the location where the combination of axial force and bending moment gives yielding of the full section. At the crown, full section yielding is reached first, but with one plastic hinge the arch remains stable. Upon

further load increase, a second plastic hinge will occur at either both or one of the points of the second largest bending moments. In the hand analysis, it is assumed that only one additional plastic hinge occurs which causes the arch to fail in a sway mode, see Figure 5.

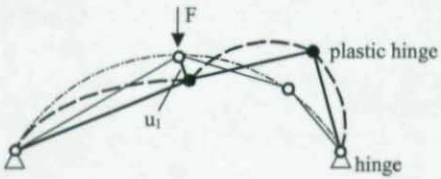

(a) sway collapse mechanism

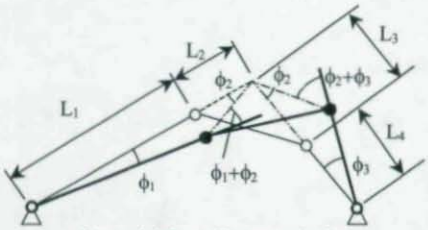

(b) model for collapse analysis

Figure 5. Plastic collapse analysis.

The hand analysis is based upon equilibrium between the internal and external work. For the geometry of a semicircular arch the internal work of the plastic hinges can be expressed by Equation 6 and the external work by Equation 7. In Equation 6, M_p is the full plastic moment of the section defined by $M_p = W_p \cdot f_y$ in which W_p is plastic section modulus and f_y the yield strength. For the plastic section modulus the listed values (Arbed, 1995) were used, and for the yield strength the actual value of the material, see Section 3.2.

$$W_{int} = M_p(\phi_1 + 2\cdot\phi_2 + \phi_3) = M_p\left(1 + 2\frac{L_1}{L_2} + \frac{L_1 \cdot L_3}{L_2 \cdot L_4}\right)\phi_1 = 8.077 M_p \phi_1 \quad (6)$$

$$W_{ext} = F \cdot u_1 \cdot \cos(\pi/4) = F \cdot \phi_1 \cdot L_1 \cos(\pi/4) = F \cdot \phi_1 \cdot R_n \quad (7)$$

$$L_1 = \sqrt{2} \cdot R_n$$

$$L_2 = \sqrt{2} \cdot R_n \left[\frac{\sqrt{2} \cdot \sin(\pi/4 + \phi_{2nd}/2)}{\sin(\pi/2 + \phi_{2nd}/2)} - 1 \right]$$

With:

$$L_3 = 2 \cdot R_n \left[\frac{1}{\sin(\pi/2 + \phi_{2nd}/2)} - \sin(\pi/4 + \phi_{2nd}/2) \right]$$

$$L_4 = 2 \cdot \sin(\pi/4 - \phi_{2nd}/2) \cdot R_n$$

From these two equations, the plastic collapse load can be equated and is given by Equation 8. The results are listed in Table 2.

$$F_{pl,ana} = \frac{8.077 \cdot M_p}{R_n} \tag{8}$$

3.2 Numerical

With a material nonlinear analysis (MNA), the plastic collapse of the arches was simulated. The material was modeled bi-linear with an elastic branch up to yielding and a plastic branch after yielding. The yield strength was taken as f_y = 291 [N/mm^2] which was the actual yield strength of the steel used in the experiments by La Poutré, 2005. The geometry of the finite element model is discussed in Section 5.
The FE-results agreed generally very well with the analytical results. Only for the very stocky arches (HEA 100 and HEB 300 at a bent ratio of 8.3), the FE-results were considerably lower (>21%) than the analytical calculations, which might be due to the influence of the normal force.

4 EIGENVALUE

DaDeppo & Schmidt, 1969, derived an analytical equation for the eigenvalue of deep slender arches loaded by a single load at the crown and permitted to sway in-plane. Their investigation resulted in Equation 9, in which E = modulus of elasticity and I_y = major moment of inertia.

$$F_{eig,ana} = \frac{5.86 \cdot EI_y}{R_n^2} \tag{9}$$

The equation of Dadeppo & Schmidt was compared to results from the finite element method, obtained through an eigenvalue analysis, see Table 3 and Figure 7. It was found that the results matched rather well for slender arches, but for arches with a smaller bent ratio than 22.4, local flange buckling could occur at the crown before overall in-plane sway buckling occurred. The cells shaded gray in Table 3 indicate flange buckling occurring prior to overall buckling. The difference between local and overall buckling is illustrated by Figure 6. Based on this analysis, the value of 22.4 seems an appropriate limit for an arch to be called slender.

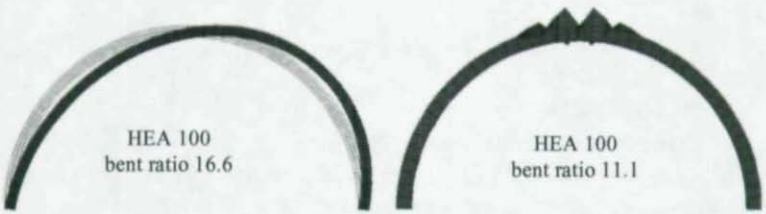

Figure 6. Arch buckled in sway mode and in local flange buckling.

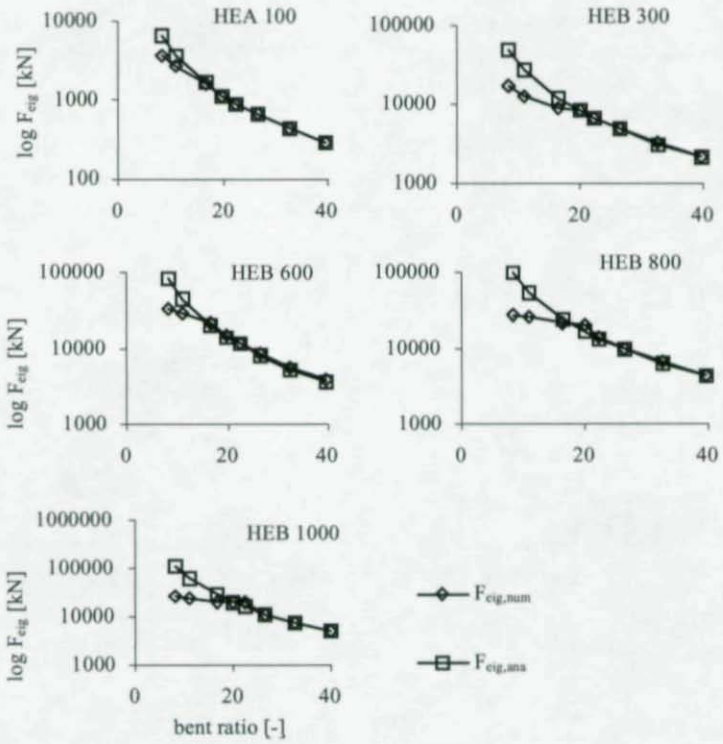

Figure 7. Analytical and numerical eigenvalues

5 NONLINEAR FINITE ELEMENT ANALYSIS

5.1 Modeling of geometry and material

The arch was modeled in the finite element program Ansys. The cross section comprises six 4-node shell elements for the flanges and the web. The fillets of the actual section contribute to the bending stiffness but cannot be modeled with shell elements. Nevertheless they are important for the stiffness of the section (La Poutré, et al., 2004). Instead of fillets, beam elements were used to compensate for the

fillets, see Figure 8a. In the length of the arch, a minimum of k = 44 elements were used, Figure 8b. From the HEB 600 to the HEB 1000 sections, this number was increased for the more slender arches to comply with the maximum aspect ratio of $1/20^{th}$ for the elements. For these arches, the number of elements in the span was determined with Equation 10, in which b = flange width, h = section depth and k = positive even integer larger or equal to 44.

$$\frac{6\pi \cdot (R_n + h/2)}{k \cdot b} \leq 20 \qquad (10)$$

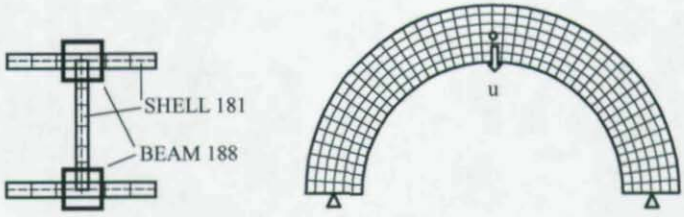

Figure 8. Modeling of cross section for FEA.

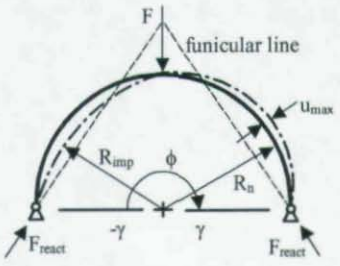

Figure 9. Radial imperfection for nonlinear analyses.

Real arches are never perfectly circular. Due to various reasons, imperfections are present in the real arch and they need to be modeled in the FE-simulations. Imperfections generally reduce the load an arch can carry and in order to not overestimate the ultimate load, an

imperfection shape that works negatively on the load carrying capacity needs to be selected. Therefore, a form similar to the elastic buckling mode (see Fig. 6) has been modeled by Equation 11, in which R_n = nominal radius and $u_{max} = R_n/100$ the maximum imperfection. Figure 9 illustrates the imperfection, which reduces the distance from the arch rib to the funicular line on one side, while it increases it on the other side, giving the arch a preference to fail in a sway mode.

$$-\gamma < \phi < \gamma: \quad R(\phi) = R_n + \sin(\phi) \cdot u_{max} \tag{11}$$

Currently, no in-plane imperfection limits are given in constructional steel standards, therefore, a limit needed to be selected. A very small imperfection would give high ultimate loads, which might be unrealistic in practice. A very large imperfection would mean a visually distorted arch that would not be acceptable to be built. The selected imperfection u_{max} is within these two extremes. Figure 10 illustrated the influence of the imperfection on the ultimate load for one arch.

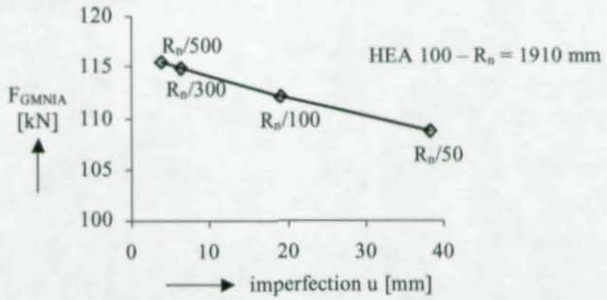

Figure 10. Influence of imperfection on ultimate load.

Due to the bending process, the material has been cold worked and the effect of cold-working becomes stronger with smaller bent ratios. In La Poutré, 2005, these effects have been determined with tensile tests. In Figure 11a stress-strain curves for several bent ratios and for a straight beam are given. It can be observed that the yield plateau has disappeared, the ultimate tensile strength has increased and the ductility reduced. For steels without a yield plateau, the 0.2% offset proof stress

($f_{0.2}$) is usually used to indicated the yield point. From Figure 11b, it can be observed that f0.2 has considerably increased due to the cold working. Generally, it can be stated that the increase is largest with smaller bent ratios (La Poutré, 2005).
The stress-strain curves were approximated with a multi-linear material model with seven sections, see Figure 11b, which was used in the analyses. To obtain the static stress-strain values, a procedure described in Technical Memorandum B.7 in Galambos, 1998, was adopted. In this procedure, the tensile test was regularly stopped and the approximate curve was fitted through those static points (Fig. 10b).

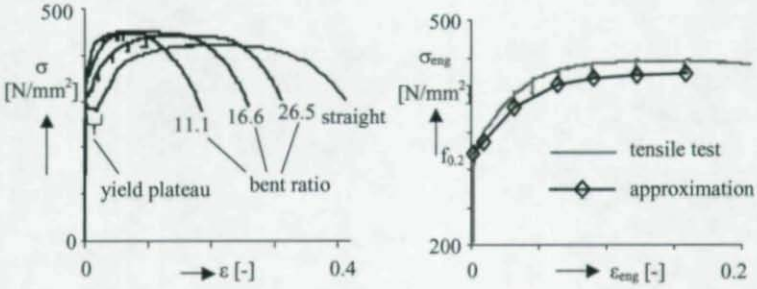

(a) influence of the bending process on steel

(b) multi-linear approximation of stress-strain relation

Figure 11. Material behavior.

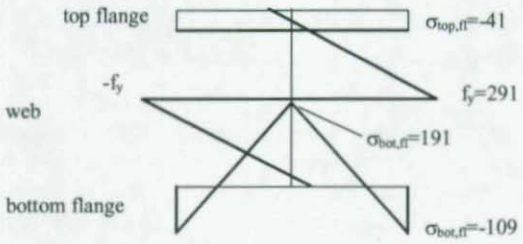

Figure 12. Residual stress pattern for FEA.

The bending process also changed the residual stress pattern. For the different bent ratios, the residual stress was measured experimentally by La Poutré, 2005. From the results, a residual stress pattern was adopted that is in equilibrium over the cross section and fits the experimental results, see Figure 12.

5.2 Analyses

The analyses included geometric and material nonlinearities, geometric imperfections and residual stresses and is referred to as GMNIA (Geometric and Material Non-linear Imperfect Analysis). In Table 4, the ultimate loads of these analyses are listed. Figure 13 shows the mode in which the arches failed, as well as the undeformed outline of the arch. For stocky arches, the sway failure mode is less pronounced than for the more slender arches. The failure mode observed in the GMNIA-analyses resembles the assumed mechanism mode in the plastic hand analysis, see Figure 5.

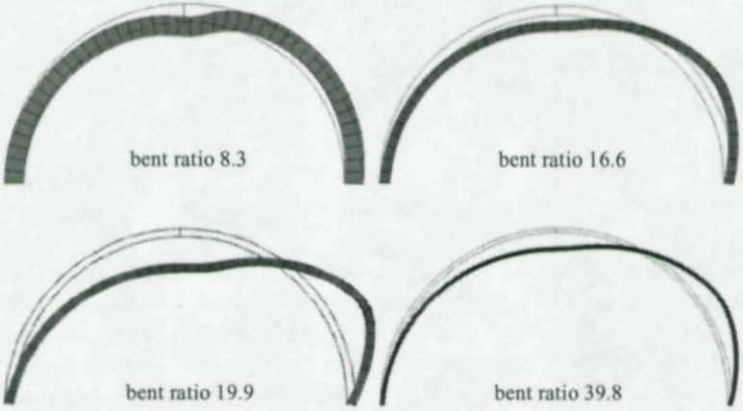

Figure 13. Failure modes according to GMNIA analyses for arches of different slenderness.

6 DESIGN

For the stability of columns and beams, buckling curves are available in many structural steel design standards. For structures other than columns and beams, no buckling curves are specified in the literature. However, recently two methods, the General and the Overall Method, have been specified in Eurocode 3 to design structures under general loading for stability. Backgrounds on the General Method can be found in Müller, 2003, and on the Overall Method in Greiner, 2003. These two methods are only slightly different and in this section, the Overall Method will be applied to the stability of arches.

With the eigenvalue, determined in Section 4, and the plastic strength, determined in Section 3, a non-dimensional slenderness $\overline{\lambda}_{ov}$ (Eq. 12) can be determined. The slenderness can be determined with either the analytically or the numerically obtained values. With the FE-simulated ultimate loads, a reduction factor χ can be determined with Equation 13, for which either the analytical or the numerical plastic strength can be entered. In Table 4 all non-dimensional slendernesses and reduction factors are given.

$$\overline{\lambda}_{ov,num} = \sqrt{\frac{F_{pl,num}}{F_{eig,num}}} \quad \wedge \quad \overline{\lambda}_{ov,ana} = \sqrt{\frac{F_{pl,ana}}{F_{eig,ana}}} \tag{12}$$

$$\chi_{num} = \frac{F_{GMNIA}}{F_{pl,MNA}} \quad \wedge \quad \chi_{ana} = \frac{F_{GMNIA}}{F_{pl,ana}} \tag{13}$$

Figure 14 shows the reduction factors plotted against the non-dimensional slenderness. At the top, this is done for the numerical values and at the bottom for the analytical values. It appears that the reduction factors for most arches are larger than buckling curve 'a' of Eurocode 3. Normally, a structure cannot be stronger than the plastic collapse load (χ = 1). Due to the bending process, the strength of the steel has increased which produced these higher ultimate loads. For the more slender arches with bent ratio 26.5 – 32.6, the reduction factors are smaller than buckling curve 'a' but larger than buckling curve 'd', which seems to be the appropriate curve for those bent ratios. The

reduction factors for the most slender arches with bent ratio 39.8 fall below buckling curve 'd' and for those the Overall Method needs a buckling curve even below curve d.

When the reduction factors are based on analytical values, also the reduction factors for the most stocky arches (HEA 100 and HEB 300 at bent ratio 8.3) fall below the buckling curves. This is due to the overestimation of the analytical plastic collapse load, which could be improved by including the reducing effect of the normal force on the bending moment capacity.

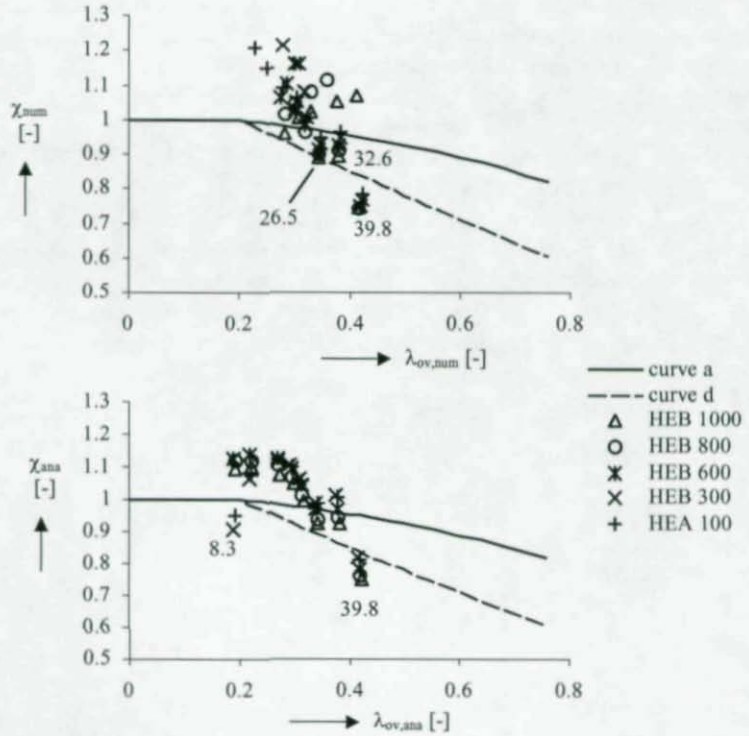

Figure 14. Analytical and numerical reduction factors for in-plane stability of arches.

7 CONCLUSIONS

This paper studied the in-plane stability of circular steel wide-flange arches, loaded by a concentrated load at the crown. Five different European wide flange beams were studied at seven different bent ratios. Firstly, the plastic collapse load was determined with an analytical analysis and compared to finite element simulations. The results corresponded generally very well. Only for very stocky arches with bent ratios of 8.3 and 11.1, the analytical analysis overestimated the FE-collapse load. Secondly, finite element simulations of the eigenvalue were compared to an analytical equation for the elastic stability by DaDeppo & Schmidt, 1969. This comparison showed that the eigenvalue of arches with bent ratios larger than 22.4 could be accurately determined with the analytical equation. Thirdly, the arches were designed using the Overall Method from Eurocode 3. In the design, the effects of the bending process on the steel stress-strain curve and the residual stresses have been incorporated. The design showed that buckling curve 'a' can be used for arches with bent ratios up to 22.4 and buckling curve 'd' for arches with bent ratios between 26.5 – 32.6. For more slender arches, care must be taken in the design because no buckling curve is available. Also, the analytical analysis for the plastic collapse load must be modified to include the influence of normal force on the plastic moment capacity for the most stocky arches.

REFERENCES

ENV 1993 (1992). *Eurocode 3: Design of steel structures.* Brussels: European Committee for Standardisation (CEN).

Sales programme, structural shapes (1995). Luxembourg: Profil Arbed. 64 p.

Galambos, T. V. (Ed.) (1998). *Guide to Stability Design Criteria for Metal Structures*. 5th edition. New York: John Wiley & Sons. 911 p.

Bradford, M. A., Uy, B., & Pi, Y.-L. (2002). In-plane elastic stability of arches under a central concentrated load. *J Eng Mech-ASCE,* 128(7), 710-719

DaDeppo, D. A. & Schmidt, R. (1969). Nonlinear analysis of buckling and postbuckling behavior of circular arches. *Z Angew Math Phys,* 20 847-857

Greiner, R. (2003). Concept of the numerically-based buckling check of steel structures. *Steel struct and bridges conf* Prague, 17 Sept. 2003. Prague: Czech Technical University. pp. 511-516

Jukes, S. G., Hassani, F. P., & Whittaker, B. N. (1983). Characteristics of steel arch support systems for the mine roadway. Part I, Modelling theory, instrumentation and preliminary results. *Mining Sci Technol,* 1 43-58

La Poutré, D. B., Bakker, M. C. M., Snijder, H. H., and Hoenderkamp, J. C. D. (2004). Modeling steel wide-flange beams with FEM. In J. Walraven, J. Blaauwendraad, T. Scarpas, & H. H. Snijder (Eds.), *5th Int PhD Symposium in Civil Eng (PhDCE 5).* Delft, 16 June 2004. Leiden, the Netherlands: A.A. Balkema. pp. 657-665

La Poutré, D. (2005). *Inelastic spatial stability of circular steel wide flange arches*. PhD-thesis. Eindhoven: Technische Universiteit Eindhoven. 190 p.

Müller, C. (2003). *Zum Nachweis ebener Tragwerke aus Stahl gegen seitliches Ausweichen*. PhD-thesis. RWTH Aachen. 104 p.

Pi, Y.-L. & Trahair, N. S. (1999). In-plane buckling and design of steel arches. *J Struc Eng-ASCE,* 125(11), 1291-1298

Verstappen, I., Snijder, H. H., Bijlaard, F. S. K., & Steenbergen, H. M. G. M. (1998). Design rules for steel arches - In plane stability. *J Constr Steel Res,* 46(1-3), 125-126

APPENDIX

Table 1. Bent ratios and sections studied.

bent ratio	$\varepsilon_{fl,perm}$ [%]	R_n [mm]				
		HEA 100	HEB 300	HEB 600	HEB 800	HEB 1000
8.3	6.03	796	2490	4980	6640	8300
11.1	4.54	1061	3330	6660	8880	11100
16.6	3.02	1592	4980	9960	13280	16600
19.9	2.51	1910	5970	11940	15920	19900
22.4	2.23	2149	6720	13440	17920	22400
26.5	1.89	2546	7950	15900	21200	26500
32.6	1.54	3125	9780	19560	26080	32600
39.8	1.26	3820	11940	23880	31840	39800

Table 2. Plastic collapse loads.

bent ratio	HEA 100			HEB 300			HEB 600		
	$F_{pl,hand}$ [kN]	$F_{pl,MNA}$ [kN]	Diff. [%]	$F_{pl,ana}$ [kN]	$F_{pl,MNA}$ [kN]	Diff. [%]	$F_{pl,ana}$ [kN]	$F_{pl,MNA}$ [kN]	Diff. [%]
8.3	244.3	192.5	21.2	1758.2	1313.2	25.3	3022.0	2926.3	3.2
11.1	183.3	171.7	6.3	1314.7	1202.2	8.6	2259.7	2324.7	-2.9
16.6	122.1	125.4	-2.7	879.1	911.6	-3.7	1511.0	1601.8	-6.0
19.9	101.8	105.7	-3.8	733.3	770.3	-5.0	1260.4	1344.3	-6.7
22.4	90.5	95.4	-5.4	651.5	687.4	-5.5	1119.8	1194.8	-6.7
26.5	76.4	79.5	-4.1	550.7	587.6	-6.7	946.5	1003.4	-6.0
32.6	62.2	65.2	-4.8	447.6	479.6	-7.1	769.4	810.2	-5.3
39.8	50.9	53.0	-4.1	366.7	390.3	-6.4	630.2	657.3	-4.3

Note: Difference calculated with $F_{pl,hand}$ as norm.

Table 2. Continued.

bent ratio	HEB 800			HEB 1000		
	$F_{pl,ana}$ [kN]	$F_{pl,MNA}$ [kN]	Diff. [%]	$F_{pl,ana}$ [kN]	$F_{pl,MNA}$ [kN]	Diff. [%]
8.3	3608.7	3618.7	-0.3	4193.6	4290.0	-2.3
11.1	2698.4	2810.0	-4.1	3135.8	3292.0	-5.0
16.6	1804.4	1903.5	-5.5	2096.8	2207.0	-5.3
19.9	1505.2	1587.0	-5.4	1749.1	1826.0	-4.4
22.4	1337.2	1409.0	-5.4	1553.9	1615.0	-3.9
26.5	1130.3	1183.0	-4.7	1313.5	1364.0	-3.8
32.6	918.8	953.4	-3.8	1067.7	1099.0	-2.9
39.8	752.6	773.7	-2.8	874.5	880.8	-0.7

Table 3. Analytical and numerical eigenvalues.

bent ratio	HEA 100			HEB 300			HEB 600		
	$F_{eig,num}$ [kN]	$F_{eig,ana}$ [kN]	Diff. [%]	$F_{eig,num}$ [kN]	$F_{eig,ana}$ [kN]	Diff. [%]	$F_{eig,num}$ [kN]	$F_{eig,ana}$ [kN]	Diff. [%]
8.3	3704.6	6622.5	44.1	17077	48768	65.0	32196	82830	61.1
11.1	2791.1	3727.5	25.1	12785	27268	53.1	28617	46313	38.2
16.6	1610.2	1655.6	2.7	9046.2	12192	25.8	21140	20708	-2.1
19.9	1143.9	1150.2	0.6	8335.4	8484	1.7	14834	14409	-2.9
22.4	913.5	908.6	-0.5	6667	6696	0.4	11756	11372	-3.4
26.5	658.7	647.3	-1.8	4833.3	4784	-1.0	8412	8126	-3.5
32.6	441.7	429.7	-2.8	3234.3	3161	-2.3	5570.9	5369	-3.8
39.8	297.6	287.6	-3.5	2187.9	2121	-3.2	3746.7	3602	-4.0

Note: Difference calculated with $F_{pl,hand}$ as norm.

Table 3. Continued.

bent ratio	HEB 800			HEB 1000		
	$F_{eig,num}$ [kN]	$F_{eig,ana}$ [kN]	Diff. [%]	$F_{eig,num}$ [kN]	$F_{eig,ana}$ [kN]	Diff. [%]
8.3	28031	97843	71.4	25209	112422	77.6
11.1	26133	54707	52.2	23376	62858	62.8
16.6	21218	24461	13.3	20401	28106	27.4
19.9	19776	17021	-16.2	19295	19557	1.3
22.4	13889	13434	-3.4	20333	15435	-31.7
26.5	9953.6	9598	-3.7	11450	11029	-3.8
32.6	6594.1	6342	-4.0	7575.9	7287	-4.0
39.8	4428.3	4255	-4.1	5089.3	4889	-4.1

Table 4. Ultimate GMNIA-loads, non-dimensional slenderness and reduction factor.

	HEA 100					HEB 300				
bent ratio	F_{GMNIA} [kN]	$\lambda_{ov,ana}$ [-]	$\lambda_{ov,num}$ [-]	χ_{ana} [-]	χ_{num} [-]	F_{GMNIA} [kN]	$\lambda_{ov,ana}$ [-]	$\lambda_{ov,num}$ [-]	χ_{ana} [-]	χ_{num} [-]
8.3	231.9	0.19	0.23	0.95	1.20	1592	0.19	0.28	0.91	1.21
11.1	197.4	0.22	0.25	1.08	1.15	1393	0.22	0.31	1.06	1.16
16.6	137.2	0.27	0.28	1.12	1.09	984	0.27	0.32	1.12	1.08
19.9	112.0	0.30	0.30	1.10	1.06	810	0.29	0.30	1.10	1.05
22.4	95.6	0.32	0.32	1.06	1.00	690	0.31	0.32	1.06	1.00
26.5	75.4	0.34	0.35	0.99	0.95	545	0.34	0.35	0.99	0.93
32.6	62.7	0.38	0.38	1.01	0.96	453	0.38	0.39	1.01	0.94
39.8	41.4	0.42	0.42	0.81	0.78	300	0.42	0.42	0.82	0.77

Table 4. Continued.

	HEB 600					HEB 800				
bent ratio	F_{GMNIA} [kN]	$\lambda_{ov,ana}$ [-]	$\lambda_{ov,num}$ [-]	χ_{ana} [-]	χ_{num} [-]	F_{GMNIA} [kN]	$\lambda_{ov,ana}$ [-]	$\lambda_{ov,num}$ [-]	χ_{ana} [-]	χ_{num} [-]
8.3	3394	0.19	0.30	1.12	1.16	4030	0.19	0.36	1.12	1.11
11.1	2569	0.22	0.29	1.14	1.11	3027	0.22	0.33	1.12	1.08
16.6	1700	0.27	0.28	1.12	1.06	1993	0.27	0.30	1.10	1.05
19.9	1380	0.30	0.30	1.09	1.03	1612	0.30	0.28	1.07	1.02
22.4	1169	0.31	0.32	1.04	0.98	1355	0.32	0.32	1.01	0.96
26.5	914	0.34	0.35	0.97	0.91	1062	0.34	0.34	0.94	0.90
32.6	747	0.38	0.38	0.97	0.92	867	0.38	0.38	0.94	0.91
39.8	494	0.42	0.42	0.78	0.75	576	0.42	0.42	0.77	0.74

Table 4. Continued.

	HEB 1000				
bent ratio	F_{GMNIA} [kN]	$\lambda_{ov,ana}$ [-]	$\lambda_{ov,num}$ [-]	χ_{ana} [-]	χ_{num} [-]
8.3	4593	0.19	0.41	1.10	1.07
11.1	3459	0.22	0.38	1.10	1.05
16.6	2257	0.27	0.33	1.08	1.02
19.9	1835	0.30	0.31	1.05	1.01
22.4	1543	0.32	0.28	0.99	0.96
26.5	1211	0.35	0.35	0.92	0.89
32.6	984	0.38	0.38	0.92	0.90
39.8	655	0.42	0.42	0.75	0.74

CODE IMPLICATIONS ON THE DESIGN AND USE OF SEMI-RIGID CONNECTIONS IN HIGH SEISMIC REGIONS

John W. Barry[1]

INTRODUCTION

General:

Since the Northridge earthquake of January 17, 1994 there has been a drive in the United States to modify the building codes and specifications to force better seismic behavior and performance of structures. Documents resulting from the SAC studies post the Northridge earthquake resulted in publications such as FEMA 355 and ultimately the AISC seismic design provisions. Part of the SAC studies looked at alternatives to the use of fully welded connections in high seismic areas, namely the use of partially restrained or semi-rigid connections in steel lateral resistant frames. The studies and seismic provisions that followed as a result, stopped short of fully realizing the possible benefits of using a semi-rigid connection.

The idea behind the use of semi-rigid connections is at the surface simple, connections fall in the realm of fixity somewhere between fully fixed and pinned. For most structures, code and common practice choose to idealize connections as either fixed, a fully welded connection capable of transferring the full plastic capacity of the beam across a connections with no rotational deformations, or pinned, no resistance to rotational deformations and as a result a connection which transfers no moment across the joint. In reality no connection is truly

[1]Graduate Research Assistant, University of Illinois at Urbana-Champaign (UIUC), Urbana, IL, USA. Email: jwbarry2@uiuc.edu

pinned nor fixed. Semi-rigid connections exploit this fact allowing for first a connection that does not have the full plastic capacity of the section and second accounting for true rotational capacity and ductility of a connection. In turn a designer now has a connection available to resist lateral loads while not being required to use a fully welded, or heavily bolted connection.

There exist many benefits in choosing a semi-rigid connection as opposed to a fully welded connection. Semi-rigid connections reduce the amount of moment that can be transferred into a column, resulting in a lighter column when using the codified strong column weak beam theory of design. Also, the reduced stiffness of the connection results in a period elongation of the frame which in turn reduces the seismic lateral loading that a frame will see, resulting in a lighter frame. In addition the erection time is improved; connections are bolted not welded in the field. As a result, less skilled labor is required and there is better quality control of construction. In summary lighter frames, quicker erection, and less skilled labor all result in a more economical and efficient framing system.

Objectives:

The code of practice for using semi-rigid connections in the United States lags several decades behind the findings of academics and researchers. This statement becomes even stronger when viewed in the context of using semi-rigid connections in high seismic areas. Modern codes frown upon the formation of plastic hinges in connections and in turn try to force the plastic hinge to develop in the beam a distance away from the connection. In addition no design guides currently exist in evaluation of the rotational capacity of semi-rigid connections; in turn it becomes impossible for a designer to follow code requirements to model the deformation of connections in a lateral analysis. Finally the code penalizes the reduction in connection strength by still maintaining heavy columns in response to beam size, which may increase in a semi-rigid frame.

This works tries to collect previous work on semi-rigid connections performance, behavior and design methodology into one source, while

filling in the gaps that still exist to practically design and use semi-rigid connections in a high seismic area; something that has not previously been accomplished in the United States. The work further tries to show that the period elongation of a building and the controlled plastic hinge location provided by the connection result in a preferential behavior of the frame despite the lack of code and specification compliance.

Through the use of dynamic non-linear analysis nine different frames with varying connection stiffness and strength and varying code compliance are modeled under eight different earthquake records both near and far source which are scaled to several different design parameters. A comparison of applied forces, internal and overall story drifts is made between the different frames as a result of the applied dynamic loading. Finally a look at the stability and failure mechanism is observed for each of the frames under the application of different strong motion records.

The work culminates with recommendations for changes in codes and creations of design guides to help promote the use of semi-rigid connections by designers, especially in high seismic areas, where their benefits might be most effective. A topical investigation of the economics of semi-rigid connections is also included. A break down of the cost as a result of materials, labor and erection time is made for each of the nine frames. Attention is also given to the difficulty of repair and loss of use of a building post a major earthquake in addition to a brief look at limit states for semi-rigid frames as the main source of lateral resistance.

Previous Work:

This work picks up on the heals of previous research that has sought to qualify connections as having a stable hysteretic behavior and sufficient ductility to be used in areas of high seismicity. Work by Elnashai and Elghazouli propose with careful design and consideration of dynamic loads that semi-rigid connections can safely and effectively be used in high seismic regions (Elnashai 1994). This statement follows several years of tests conducted at Imperial College and the University of Tokyo on top and seat angle with shear tab connections. The research

concludes that there is a reduction in frame stiffness due to the implementation of semi-rigid joints and sufficient evidence that overstrength factors for columns should be placed on connection capacity as opposed to beam capacity.

In addition to physical work on connections practitioners such as Springfield have offered suggestions that a range of buildings exist in which semi-rigid connections could prove beneficial due to both their economics and their ability to control the performance of a building, by controlling the distribution of moments throughout a frame (Springfield 1987). The author suggests that a serious economic study needs to ensue with a unifying recourse of design methodology and practice to truly take into account what he believes to be the synergistic effects by accounting for the connection behavior in frame design. This author agrees with the suggestions and finding of Springfield but feels that the synergistic effects can only improve in high seismic areas and that there also must be work done in code modification to truly reap the benefits of semi-rigid connections.

Still large gaps remain to be filled for designers to successfully begin using semi-rigid connections on a production level. In addition poor design approaches such as flexible-moment connections must be replaced by modern methodologies of design that account for changes in knowledge and computation power. The use of flexible moment connections are discredited in this paper despite resent publications that suggest such connections are still a viable method of design (Carter 2005). The design methodology is at best antiquated, and has far exceeded its beneficial era.

DESIGN PHILOSOPHY

Overview:

To make the conclusions of this research the most general and applicable, all buildings where designed to the most common building codes and design provisions, with the help of common design guides. In this case IBC2000 was used for all loading combinations, with

ASCE 7-02 and the AISC seismic design provision (2002). All steel members were designed in accordance with LRFD third edition. Though IBC2000 is not the applicable building code of California, the location of the building was chosen to be in Los Angeles where a peak ground acceleration of .4g was imposed by code. It should be noted that there are very strong correlations between the California Building Code and Unified Building Code which have been merged into the creation of the International Building Code. Further, some local jurisdictions of California have even attempted to adopt the International Building Code, though prohibited by the California Building Standards Commission.

To draw conclusion of the code adequacy and conservatism, three sets of frames where designed that enforce varying levels of code rigidity. The details of the frames are discussed further in subsequent sections. For this section the major provisions that where modified in the design of the frames are discussed below so that the reader can follow the logic of the frame design, analysis and comparisons.

LRFD Requirments:

The Load & Resistance Factor Design Manual along with AISC Design Guides provide a designer with no guidance to design semi-rigid connections. Section A.2 of the specification define connections of type "PR" or partially restrained. By definition this classification would encompass all connection not capable of carrying more than 90% of a beams fully plastic capacity or connections that rotate more than 10% of a beams simple span rotation (Salmon 1980). Therefore semi-rigid connections, the connections of interest, would fall under the heading of PR connections.

The former Allowable Stress Design Manual took PR connections one step further by subdividing them into "Type 2" also known as a pinned connections, defined as a connection which does not resist more than 20% of the beams plastic capacity and rotates at least 80% of that of a simple span beam, and "Type 3" connections, connections which fall between the realm of a fixed and pinned connection. Type 3 connections are referred to throughout this paper as semi-rigid

connections. It should be interesting to note how the new steel manual will meld these differences when the combined manual is published.

The manual offers three regulations to follow when using a type PR connection when connection restraint is ignored: members must be sized to resist gravity loads as a pinned/pinned condition, connections must be adequate to resist factored loads, and connections must poses sufficient rotational ductility to resist failure of welds and fasteners. Neither the manual nor AISC design guides suggest any method to account for a connections rotational restraint. They do however offer a design methodology known as Flexible Moment Connections (FMCs).

FMCs use a simplified design approach that follows the three restrictions mentioned above. They begin by designing members to resist gravity loads in a pinned/pinned condition without accounting for the partial fixity at the ends of the member. They then perform a frame analysis with connections modeled as fixed connections to resist the lateral loading. The actual connection used in an FMC approach provides much more than a pinned connection and is in fact approaching that of a fixed connection. Because of this, the second and third rules proposed in section A.2 are satisfied, knowing that the connection will never be overstressed.

There are several shortcomings of the design approach. First FMC does not look at second order effects and can not truly determine the stability of the frame. Second the design approach can lead to very large beams, when using a strong column weak beam theory this leads to even larger columns. Finally the true behavior of a system is never known and compensated for by conservatism, which does not always correlate to preferred behavior in a dynamic system.

For this research FMC methodology will be employed to size beams for gravity loads, and therefore dictate the size of the columns on some of the frames analyzed. A more robust approach will be taken for other frames that account for the moment-rotation relationship and size the beams for gravity loads accordingly.

Seismic Design Provisions:
The seismic design provisions used for this paper, published in May of 2002 follow closely to FEMA 355 a document formed as a result of the Northridge Earthquake in 1994. This document includes much of the research that followed the Earthquake as part of the SAC projects. The parts of interest to the design or frames used in analysis are those of Part I Section 9. This section refers to Special Moment Frames (SMF), which is the frame used for analysis in accordance with IBC2000.

The Seismic Design Provision consists of several key clauses that dramatically affect the design of a building and its connections. At its most basic level is the codified strong column weak beam theory, a theory which is rooted well in research and design ideology. The goal of the theory is to force ideal behavior of a structure during a seismic event, mainly the forced creation of plastic hinges in the beams prior to the columns, thereby increasing ductility and preventing collapse. This has been coded into the provision in section 9.6 using formula 9-3. The essence of the section is the plastic capacity of the column must exceed that of the beam by a factor of 1.21 and also account for the moment induced into the connection by the shear in the beam. In total columns can be required to have a plastic capacity exceeding the beam capacity by as much as 25%. For the design of frames for this paper, this rule was strictly enforced in two of the frame sets and relaxed for the final set of frames.

In addition to the SCWB theory section 9.2a-2 places a strict limit on the minimum strength of a connection based on the nominal plastic moment capacity of a beam. Often in the design of beams in high seismic areas designers may choose to implement a forced location for a plastic hinge by reducing a beam cross section, one technique commonly used is know as a dog bone. By removing portions of the flanges of a beam, a weaker section is formed and therefore controls the location of the plastic hinge while also limiting the moment that can be transferred into the column. This clause puts a minimum level on the reduction in moment when designing a column by only allowing an 80% decrease in the force regardless of the reduction capacity in the

beam. The clause significantly effects semi-rigid connections which often use connections that transfer much less than 80% of a beams plastic capacity. The results are frames with large columns despite reduced forces. For this paper frames will be designed both enforcing this clause and relaxing its minimum reduction level.

A final portion of section 9 to be identified is 9.2b, the section requiring prequalification of all connections. The major point of the section requires all connection to be capable of sustaining an interstory drift angle of .04 radians for at least two cyclic cycles. The clause provides two methods to prove connections are capable of the proposed limit. First is to find physical tests from research that closely represent the given project conditions while conforming to Appendix S. The second is to conduct physical tests for the given project with the same member sizes, materials strengths and connection configurations while still conforming to the requirements of Appendix S. This process of pre-qualifying connections can severely limit the designer to choosing few connections on which researcher is available, for designers will rarely have the budget to pre-qualify their own connections. Connections in this paper will be assumed to pass the rigors of prequalification. References to research with similar connection will be used to substantiate this assumption.

Design Approach:
The proceeding sections will discuss the design procedure for the frames of interest in this paper. Detail of the loading schemes and framing layout are provided along with the reasoning and benefits for the major design decisions as they apply to the use of semi-rigid connections in frame design.

Loading IBC2000:
The International Building Code 2000 (IBC2000) was the primary source in addition to ASCE 7-02 for the determination of all gravity, wind and seismic loadings for the buildings. For the design of gravity loads an 80 PSF live load was applied on all levels except the roof. The roof level had an applied live load of 20 PSF. In addition to live loads a 65 PSF dead load was applied to the elevated floors to account

for self weight of the structure in addition to mechanical, electrical and plumbing equipment. For the roof a 45 PSF dead load was applied to account for roofing self weight, ballast, and roof top mechanical equipment. No allowance for partition loads was provided, but was compensated for by the increased live loads in accordance with AISC Design Guide 5.

The seismic and wind load analysis was performed in accordance with IBC2000. For the building of interest a seismic design category of II was used, which implies an importance factor of 1.15 for the building. In addition the idealized location of the building, in the Los Angeles, California area, resulted in a mapped 85 mph peak wind velocity, a 150% g short period spectral acceleration, and a 100% g long period spectral acceleration. Based on the code loadings and geometry of the building it was determined through static analysis that wind load would not control the lateral design unless the building was to reach a height of over 10 stories or approximately 120 feet, much higher than the buildings used in the analysis of this paper.

To determine the applied seismic load per IBC2000 the mass, period and force reduction factor must be specified. For the seismic mass of the building, the approach suggested in IBC2000 was followed. This method accounts for the entire dead load of the structure in addition to a 10 PSF live load to account for partition walls not included in the dead load calculation. In some instances an additional 25% of the live load would be included in determining the seismic mass, however for the buildings of this paper which model a typical commercial office building, the additional seismic mass would not be appropriate. To determine the periods of the building a simple eigen value analysis was performed for each of the buildings. The periods ranged from .65 seconds for the rigidly connected building to .87 seconds for the most flexible building employing semi-rigid connections. To determine the force reduction factor IBC2000 was again followed, for a special moment resistant frame, the frames used here, a generous force reduction factor of 8 is provided. Dynamic analysis that follows will verify the appropriateness of this factor based on the ductility and deformation capacity of the frames.

Using the values from above, the lateral seismic load was determined and distributed in accordance with the methods provided in the code. The distribution of the lateral load was done proportionally to the stiffness of each of the lateral resisting frames in the plan of the building. The lateral loading was then divided vertically in the shape of an inverted triangle and applied as a point load at each story height.

Frame Types:
In additional to loadings, IBC 2000 provides story drift limits. It was quickly noted in initial frame designs that for semi-rigid connections to effectively control drift, all frames in the building must be lateral resistant frames. This approach is not common to US design practice, where typical buildings will use portal frames, or the outer most frames only to resist the lateral loading. However, the use of all frames as lateral resistant frames is not uncommon outside of the US, and in fact can provide better design, behavior and reliability in the event of a large earthquake.

One primary advantage for all frames in a building being lateral resistant frames is the redundancy in the building. For typical design practice, consisting of two outer lateral resistant frames, the possibility for collapse is increased. In the event that one frame is compromised the building will be introduced to large torsional effects, caused by the eccentricity between center of mass and center of rigidity, that can then cause the progressive failure of other members and frames. In buildings with multiple lateral resistant frames, more than two, there is a redundancy, and a decrease in the chance for torsional effects to take control of the building.

In addition to redundancy the efficiency of the system is improved by using all lateral resistant frames. In the case of semi-rigid connections, where connections are bolted and require little skill or time in the field for erection, it becomes economical to take advantage of the lateral capacity of interior beams that might otherwise only be used to resist the gravity loading on the building. It has been found through the analysis of many frames that there is a little to no increase in the sizing

of beams to resist the lateral loads, only a more rigorous connections must be provided and accounted for in analysis, which is the basics of the methodology when using semi-rigid connections.

Frame Design:
To conclude the section a brief overview of the remainder of design decision for the frames used in this thesis will be discussed, including beam spans, inter-story heights, framing approaches and loading considerations.

To make the frames the most economical, it was found that the beam sizing to resist the gravity loading needed to closely match the beam sizing required for the applied lateral loads in the frame design. To effectively do this two design approaches were applied. The first is that frame beams should be used as collector girders for all filler beams between column lines. This framing method will widen the tributary area of the loading that the beam must resist to half of the bay on either side. The second framing decision is to use longer spans between columns. For this paper, it was found that buildings with column centers at 30 feet worked well at balancing gravity and lateral loads. A 30 foot span though long, is not impractical, especially for low rise commercial buildings, where unobstructed office and retail space is preferred. In addition it was always found that beam sizing was controlled by strength and not stiffness, in all cases live and dead load deflections were not in control.

To keep with the realistic modeling of actual buildings, interstory heights were chosen as 14 feet for the first level and 12 feet for each level above that. For this analysis interstory heights are measured between the top of slabs at each floor. Interestingly, it can be noted that the interstory height has little effect on the buildings of interest. Clearly the interstory height has little effect on the seismic loading, since the seismic weight changes are relatively small with respect to the interstory heights; however, attention should be paid to possible period changes in the building. The larger first story will slightly effect the distribution of the seismic forces vertically in the frame. Since deflection limitations are linearly proportional to the height of the

building there will be no significant changes in drift verse drift limits. Wind loading on the building is heavily influenced by the interstory heights due to a greater surface area. But, as discussed earlier, wind loading does not control the design for buildings less than 10 stories in this region. Though structurally the change in cost due to interstory heights may not be great, the designer can not overlook the change in cost of interior and exterior finishes that would result.

Global design considerations for the building are based on two different structural types. The first and foremost of interest for this paper are the moment resistant frames consisting of fully restrained and partially restrained connections as the only source of lateral resistance. In this case, all frames in the east-west direction act as lateral resistant frames, for reasons as discussed above. In addition all columns in the moment resistant frames are in the strong axis of bending, meaning all beam connections are to the flanges of the columns and not the webs. In the transverse direction is found the second structural type, braced frames. The use of braced frames in the opposite direction serves two purposes. First, it simplifies the analysis, allowing for all research to focus on the moment-resisting frames and minimize the behavior and design considerations with respect to the braced frames, a topic which has been well documented by others. In addition, and with consistency in the research goals, is to model real building design, where there are often mixed methods to resist the lateral forces, such as braced frames in one direction and lateral resistant frames in the other.

For all frames and building designs serviceability requirements including drift and deflection limits were satisfied in accordance with IBC2000. All frames and buildings are also capable of resisting all applied loads both vertical and horizontal, though as discussed before not all frames member sizes conform to all the seismic design provisions set forth in order to test the true behavior of semi-rigid frames.

MODELING

Procedure:

The modeling of the buildings for this research is broken into two main components. First is the two dimensional modeling of the lateral resisting frames of the building. For this research it is assumed that each or the frames in the building are identical, having the same stiffness, and therefore will attract the same seismic loading. The gravity loading will be reduced by half for the exterior frames due to floor loading, but will be partially compensated for by the exterior façade load. The second modeling that must be performed is that of the connections. For this research a completely analytical component based model is used to determine the moment rotation curves for each of the partially restrained connections.

Moment Frames:

A total of nine different frames are analyzed in this paper that range in member fixity and code compliance. For the three bay by three bay building there were two options for the lateral resistant frames. One, to use only exterior frames for lateral resistance, in this case all the seismic load would be resisted by only the outermost frames on each side. The other option is to use all frames as lateral resistant frames that equally share the seismic load, the benefits of which were discussed earlier. Both framing options were modeled and analyzed using the static analysis features of SAP2000 to choose the best option.

Analysis began with the conventional framing approach using only exterior lateral resistant frames. Gravity loading was applied from the tributary area of one bay width, or 30 feet. Half of the seismic loading was then applied to the frames. Load cases as provided in IBC-2000 were used. It was found that the .5L+1.2D+1.0E was the most stringent case for loading. All static analysis that followed used this loading scenario. It was also determined that drift limits were being approached quickly with the fully constrained connection. When partially restrained connections where applied to the building drift limits were exceeded using static analysis. Two options resulted, one the partially restrained frames could be beefed up to limit drifts, or more lateral resistant frames could be used. For economy the later choice was chosen. It is also important to realize that this is a static analysis and the increased drift in the partially restrained connections

will not necessarily follow through to a dynamic analysis were frames have longer periods and are capable of displacing greater amounts of energy.

For the selected framing method where all frames are lateral resistant frames a few of the modeling details are provided. Again it was found that the .5L+1.2D+1.0E loading was the most critical loading under a seismic event. Each building consisted of four identical lateral resistant frames. One of the inner frames was chosen as a representative frame to be modeled in the analysis software in two dimensions. For the loading the .5L+1.2D gravity loads were applied for a 30 foot tributary area to the beams. In addition a portion of the seismic load was applied as vertical loads as required by code. The lateral loading for the frame consisted of one quarter of the entire seismic load of the structure, appropriate because each of the four frames have the same stiffness and will therefore share the seismic loading equally under the assumption of a rigid diaphragm at each level, which is provided by the concrete slab.

Connections:
The modeling of the connections is the most critical aspect of this research, for improper modeling would invalidate the results of the behavior and performance of the buildings. As discussed, two types of connections were used in the frame design. First is a base line frame using the traditional fixed end or fully restrained connections. The second is the partially restrained connection, which may be implemented using many different connection methods, a few of these are presented below.

Fixed Connections:
To create the base line building for comparison to the semi-rigid frames, fully restrained connections were used. A typical connection method was implemented which consists of full joint penetration welds on the top and bottom flanges for bending, with fillet welds on each side of the web to transfer the shear forces. For modeling these connections a traditional fixed joint was implemented with allowances for the shear panel deformation as required by code for calculation of

drift. These connections are designed to transfer the full plastic capacity of the beam to the column. In addition in high seismic areas they must be well detailed to prevent fracture of the welds, allow acceptable rotation limits of .04 radians and force the formation of the plastic hinge into the beam and away from the connection. Little attention is paid here for the detailing of these connections for an abundant resource has been provided through the SAC projects post the Northridge earthquake.

Semi-Rigid Connections:

The modeling of semi-rigid or partially restrained connections is the area of great interest for this research. The task quickly becomes difficult for any designer because there are no US design guides or specifications for the use of a partially restrained connection, especially in high seismic areas. One may turn to Europe where Eurocode 3 has partially codified the use of extended end plate connections, but stops short of including other partially restrained alternatives such as the top and seat angle connections. To model these connections a compilation of sources is used from research, foreign and domestic codes.

In all cases the final goal is to develop a tri-linear rotation curve that can be implemented as a tri-linear spring in analysis software. It has been found through much comparison of experimental and analytical research that a tri-linear stiffness approximation is ideal and closely models the true behavior of the connection (Faella 2000). This concept has been partially coded in Eurocode 3, but has no domestic equivalent. To implement the tri-linear curve five data points are required the primary, secondary and tertiary stiffness and the rotation between each change in stiffness. Designers may be relieved to find out that with great certainty three of the data points can be calculated from the other two with simple mathematical relationships, dependent upon the type of connection.

The two required data points for creation of the tri-linear rotation curve are the initial stiffness and the ultimate strength of the connection. For the connections discussed below the initial stiffness was determined using a component based approach. At its most basic level each

component of the connection, from the column flange, to the washer on the bolt is modeled as a spring, the final stiffness can then be calculated by resolving all the linear springs into one rotational spring by geometry. To determine the ultimate strength of the connection a yield line method was used that accounted for prying action. The yield line patterns were found from research and are discussed in the sections below.

Extended End Plate Connections:
Extended end plate connections are the first type of connection to be codified in Eurocode 3. The Eurocode component based approach was the method implemented in this thesis to determine the initial rotational stiffness of the connection. In order to determine the ultimate strength research from Murray was used which is well documented in dissertations and adopted in AISC design guides, all of which is based on yield line analysis of the connection. For the connections of the buildings used in this work it was found that 6 bolt extended end plate connections without stiffeners was ideal for geometry, strength and rotational capacity.

The first step to designing the connections is to choose the rotational capacity desired for the connection. In this work three capacities were used: 80%, 65% and 50% of the full plastic capacity of the beam. Knowing the desired strength of the connection the process is reversed finding the required bolt size and end plate geometry necessary to restrain the desired forces. Once the geometry of the connection is designed the component based approach can be used to determine the initial rotational stiffness of the connections. Finally with the available data points the remainder of the necessary data points can be calculated, and the full moment rotation curve for the connection is developed for one connection.

Using the initial stiffness for each of the connections a static analysis of the frame can be performed to determine if strength and drift limits are acceptable. The process like most frame design becomes iterative, where column and beam sizes need to change to force ideal behavior of the frame. Except with semi-rigid connections the rotational stiffness

and strength of the connection must be recalculated and implemented for each iteration. The problem can become even more cumbersome for designers without experience using the connections, for it is difficult to find a reasonable starting point, and no guides currently exist for doing so. For this work a complex excel spreadsheet has been written that takes the beam and column size and desired strength as a percentage and outputs the required bolt, weld and endplates sizes along with the tri-linear rotational stiffness to be implemented in the dynamic analysis. The spreadsheet also checks to make sure all geometry is in accordance with LRFD specifications.

There are several benefits to using the extended end plate connection. First is the wide range of geometries available. Since end plates are made from stock steel plate it is possible to specify thicknesses in 1/16 inch increments and milling the required heights and widths is simple. In addition all welding for the connection is done by the fabricator in the shop leaving only bolted connections in the field. This affords much better quality control and cheaper labor. One of the drawbacks to an extended end plate connection is their excessive stiffness at required strengths. The true partially restrained behavior does not begin until the connection is at 50% of the beam capacity which is too weak to be economically used in frames. However, there is still a change in the stiffness for capacities above 50% and this work looks to exploit those.

Top & Seat Angle Connections:

The top & seat angle connections followed a similar design approach as the extended end plate connections above. However, different sources had to be implemented because Eurocode has not adopted a component based rotational stiffness model for these connections and AISC has not adopted a yield line method in their design guides. To proceed with comparison of the connections a similar component based model was found written by Faella. Again each element of the connection was modeled by linear springs and then compiled into one tri-linear rotational spring. To determine the ultimate strength of the connection a yield line method was adopted that was proposed by Elnashai. Again an Excel spreadsheet was used to size the angle and bolts to resist the

required force and output the tri-linear rotational stiffness for implementation into analysis software.

Using the top & seat angle connection has several advantages. First there are no welds, all element connections are bolted, which require less skilled labor, and can be assembled much quicker. In addition, since semi-rigid connections seek to force the plastic hinges in the connection, it offers an easily replaceable mechanism for the plastic hinges to form, something that is not possible with extended end plate connections which are welded to the beam. A major drawback to the use of top & seat angles is the relative limited availability of angles in the size needed to restrain the forces. For buildings in this work it was found that the largest available angel, L8x8x1 1/8 was only capable of restraining 30% of the plastic capacity of the beam, far too little to be practical. In addition it was found that the moment rotation curve for extended end plates and top & seat angles where almost identical. Therefore for the remainder of the work, extended end plate connections will be solely used, though there may be a benefit in exploring top & seat angles if an economical method was found to obtain larger angles.

Conclusion

This paper introduced the reader to the application and design considerations when using semi-rigid connections, especially in areas of high seismicity. Continued publication and research will follow this paper and the models proposed and designed to determine the adequacy and conservatism of US design code and practice. Designers should not stray from the possibility of adopting such connections in their work. It is clear these connections offer a viable alternative that is both economical and safe for their clients. Difficulties in modeling and design are sure to be overcome with increased use, and code modification and guidance should follow to better allow for the implementation of these connections.

REFERENCES:

FEMA (Federal Emergency Management Agency). "Seismic Design Criteria for Steel Moment-Frame Structures", FEMA 355, Washington, D.C., 2000

American Institute of Steel Construction, Inc. *Manual of Steel Constructions, Load and Resistance Factor Design*, Third Edition. AISC, Chicago, IL, 2001

American Institute of Steel Construction, Inc. *Manual of Steel Constructions, Allowable Stress Design*. 9th Ed, AISC, Chicago, IL, 1989

American Society of Civil Engineers, *Minimum Design Loads for Buildings and Other Structures*, 7-02, ASCE, Reston, VA, 2003

International Code Council, *International Building Code 2000*, IBC2000, Falls Church, VA, 2000

CEN, Eurcode 3 – Part 1.1 Revised Annex J: Joint in Building Frames, European Committee of Normalization, Brussels, Belgium, 1987

American Institute of Steel Construction, Inc, *Steel Design Guide Series 4, Extended End-Plat Moment Connections*, AISC, Chicago, IL, 2003

American Institute of Steel Construction, Inc, *Steel Design Guide Series 16, Flush and Extended Multiple-Row Moment End-Plate Connections*, AISC, Chicago, IL, 2003

Salmon, C. and Johnson, J, Steel *Structures, Design and Behavior*, 4th Ed., Prentice Hall, Upper Saddle river, NJ, 1996

Faella, C., Piluso, V., and Rizzano, G., *Structural Steel Semi-Rigid Connections, Theory, Design and Software*, CRC Press LLC, 2000

Sumner, E. A. "Unified Design of Extended End-Plate Moment Connections Subject to Cyclic Loading", PhD Dissertation, Department of Civil Engineering, Virginia Polytechnic Institute and State University, Blacksburg, VA, June 17, 2003

Ohtori, Y., Christenson R.E. and Spencer, B.F., "Benchmark Control Problems for Seismically Excited Nonlinear Buildings", University of Notre Dame, Notre Dame, IN, 2000

Springfield, J., "Semi-Rigid Connections in Structural Steel Framing: A Practicing Engineer's View", *Journal of construction Steel Research 8*, 1987

Elnasahi, A.S., Elghazouli, A.Y., and Denesh-Ashtiani, F.A., "Response of Semi-Rigid Steel Frames to Cyclic and Earthquake Loads", 1999

Elnashai, A.S., Elghazouli, A.Y., "Seismic Behavior of Semi-Rigid Steel Frames", *Journal of Construction Steel Research 29*, 1994

Carter, C.J., Disque, P.E., "Flexible Moment Connections, a new look an on old favorite", *Modern Steel Construction Magazine*, September 2005

STIFFNESS REQUIREMENTS FOR METAL DECK FORMS USED FOR STABILITY BRACING OF STEEL BRIDGE GIRDERS

O. Ozgur Egilmez[1]
Todd A. Helwig[2]
Reagan Herman[3]

ABSTRACT

Permanent metal deck forms (PMDF) are frequently relied upon for bracing in the building and bridge industries. In the building industry the forms are typically modeled as a shear diaphragm that restrains the warping deformation of the girders' top flanges. The forms in the bridge industry differ from those used in the building industry primarily in the methods of connection to the girders. This paper reports results from a research investigation on the bracing behavior of PMDF used in the bridge industry. The study has focused on improving the PMDF connection details, while also improving the understanding of the stability bracing behavior of shear diaphragms systems. Recommendations from the study are currently being implemented in the design and construction of two bridges in Houston, Texas. This paper focuses on the results from a parametrical study to determine the brace stiffness requirements for PMDF used for stability bracing of steel bridge girders. Both eigenvalue and large displacement finite element analyses results are presented. In addition, results from large displacement finite element analyses are compared with laboratory buckling test results of a 50 ft twin-girder system braced by PMDF.

---

[1] Post Doctoral Research Engineer, Civil Eng. Dept., University of Houston, Houston, TX 77204-4003.

[2] Assistant Professor, Civil Eng. Dept., University of Texas at Austin, Austin, TX 78758.

[3] Assistant Professor, Civil Eng. Dept., University of Houston, Houston, TX 77204-4003.

INTRODUCTION

Corrugated metal deck forms, which are commonly utilized to support the concrete deck during construction in both the building and bridge industries, have a substantial amount of stiffness and strength in the plane of the sheeting and the forms can provide substantial lateral bracing to the beams provided that the forms are attached properly. In the building industry, metal deck forms are continuous over the tops of the beams, enabling the forms to be directly fastened to the top flange, and are generally modeled as shear diaphragms that restrain the warping deformations of the beam top flanges.

Although metal deck forms are frequently relied upon for lateral bracing in the building industry, the American Association of State Highway and Transportation Officials (AASHTO) Standard Specifications (2002) do not currently permit the forms to be considered for bracing in the bridge industry. The primary difference between the formwork used in the building and bridge industries are the connection details that are employed between the formwork and the steel girders. In the building industry the forms are typically fastened directly to the girder top flange. In the bridge industry, the formwork is typically connected to the girders using the eccentric connection shown in Figure 1, which allows the contractor to adjust the form elevation to account for constructability issues. Although the support angle helps with construction issues, the eccentric connection hurts the bracing potential since it results in a substantial reduction in the in-plane stiffness of the PMDF system. Previous laboratory buckling tests conducted at the University of Houston have shown that the bracing behavior of PMDF in the bridge industry can be substantially enhanced by providing better connection

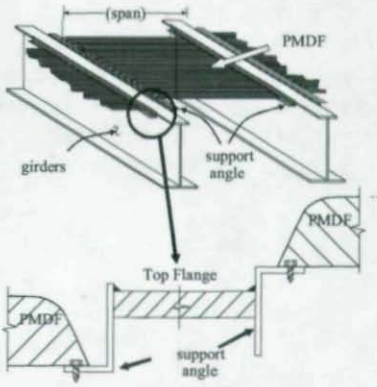

Fig. 1: PMDF Connection used in Bridge Applications

details utilizing transverse stiffening angles intermittently spaced along the girder length at select PMDF sidelap locations (Jetann et al. 2002, Egilmez et al. 2004). Figure 2 shows a plan view of a PMDF panel with stiffening angles and a photograph of the modified connection detail.

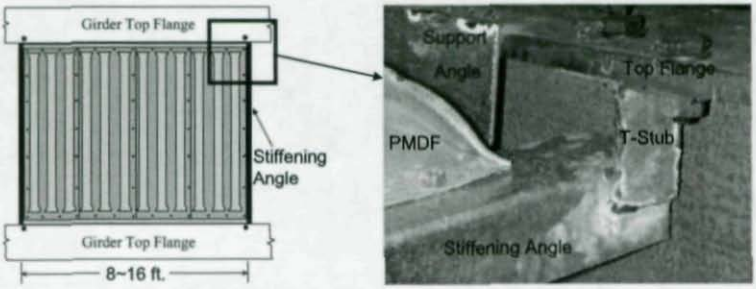

Fig. 2: PMDF Panel with Stiffening Angles

A research study is being conducted at the University of Houston to investigate the bracing behavior of PMDF systems commonly used in the bridge industry. The research consists of both experimental and computational studies. Experimental tests were performed on PMDF systems with and without modified connection details. Jetann et al. (2002) and Egilmez et al. (2003 and 2004) reported results from shear frame, lateral displacement, and buckling tests, respectively. Egilmez et al. (2005) also reported results from the computational study that focused on the stability brace forces of the intermittent fasteners used to connect the PMDF along the sidelaps of the sheets and also to the girders. This paper presents results from the computational study on the stiffness requirements for PMDF used for stability bracing of steel bridge girders.

The paper begins by presenting background information, followed by a description of the finite element model as well as a comparison of results from large displacement finite element analyses with laboratory buckling test results from a twin-girder system with a 50-ft. span braced by PMDF. Eigenvalue buckling and large displacement finite element analytical (FEA) results are then presented for various cross-sectional shapes and compared with design equations proposed in the paper.

BACKGROUND INFORMATION

From a stiffness perspective, the property of interest for PMDF bracing is the shear rigidity, Q, of the PMDF system, which has the units of kips/rad. The following expression relates the shear rigidity to the effective shear stiffness of the PMDF system:

$$Q = G' s_d, \qquad (1)$$

where: G′ = effective modulus of shear rigidity and s_d = tributary width of diaphragm bracing a single girder. The effective shear modulus, G′, can be determined experimentally by utilizing a testing frame as shown in Figure 3. Parameters shown in Figure 3 include: γ = shear strain, Δ = lateral deflection at the end of the testing frame, P = lateral load, L = length of the testing frame, f = spacing between test frame support beams, and w = PMDF specimen panel width.

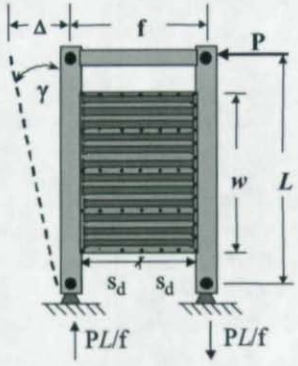

Fig. 3: Shear Test Frame with PMDF Specimen

A more practical method to *determine the effective shear* modulus is to use the equations and design tables that are provided by the Steel Deck Institute Diaphragm Design Manual (Luttrell 2004). The SDI equations and design tables are for various building PMDF systems and must be modified for applications with bridge PMDF systems. Currah (1993), as well as Egilmez (2005) found reasonable agreement between shear diaphragm test results on bridge decking and estimates from modified SDI expressions.

Although current AASHTO Standard Specifications (2002) do not permit the use of PMDF for lateral bracing of steel bridge girders, the building industry has long relied on the in-plane shear stiffness of the deck forms for beam bracing. There have been a number of previous

investigations on the bracing behavior of shear diaphragms including studies by Errera and Apparao, Nethercot and Trahair (1975), Nethercot and Lawson (1985), and Helwig and Frank (1999). Although Errera and Apparao (1976) presented an energy based solution for the buckling behavior of diaphragm braced beams, they also provided the following approximate solution that is more practical for design:

$$M_{cr} = M_g + 2Qe, \tag{2}$$

where M_g is the buckling capacity of the girder with no deck for bracing, Q is the shear rigidity of the diaphragm, and e is the distance from the center of gravity of the girder to the plane of the shear diaphragm. Nethercot and Trahair (1975) recommended a similar solution around the same time as Errera and Apparao. The approximate solution was intended for doubly-symmetric beams with diaphragm bracing and uniform moment loading. Helwig and Frank (1999) compared Equation (2) with finite element analytical (FEA) solutions on a variety of girders and showed that the simple expression provided quite accurate estimates of the bucking behavior of diaphragm braced beams. They also showed that the solution was valid for both doubly- and singly-symmetric beams provided the variable e was taken as half the girder depth.

In addition to uniform moment loading, Helwig and Frank (1999) considered a variety of loading conditions on both singly- and doubly-symmetric sections. They recommended the following general solution, which was similar to the form given in Equation (2):

$$M_{cr} = C_b^* M_g + mQd, \tag{3}$$

where C_b^* is the moment gradient factor including load height effects, m is a constant that depends on load height and web slenderness ratio, and d is the depth of the section. The rest of the parameters are as previously defined. Equation (3) is applicable to general loading conditions on both singly and doubly-symmetric sections and takes into account the effects of both moment gradient and load height. Table 1 presents the values for "m", for cases with uniformly distributed load applied at the top flange as given by Helwig and Frank (1999). For

cross-sections with slenderness ratios (h/t_w) greater than 90, web buckling due to bending or shear stresses needs to be considered. In such cases the buckling capacity for diaphragm-braced beams will be limited to the lowest value based on the limit states of web bend buckling, shear buckling, or lateral-torsional buckling.

Table 1: Design *m* Values for Equation (5), (Helwig and Frank, 1999)

Web Slenderness	Top Flange Loading w/o Midspan Torsional Brace
$h/t_w \leq 60$	0.5
$h/t_w > 90$	0.375

The ideal effective shear stiffness of a diaphragm can be calculated from Equations (1) and (3) and is given by:

$$G'_{ideal} = \frac{\left(M_u - C_b^* M_g\right)}{s_d md}, \qquad (4)$$

where M_u is the design ultimate moment, s_d is the tributary width of the deck bracing a single girder and the rest of the parameters are as defined previously. To control the deformation and fastener forces, Helwig and Yura (2005) suggested using four times the ideal effective shear stiffness in design. This stiffness requirement ($4G'_{ideal}$) for shear diaphragms is based on finite element analysis of beams with an initial twist of $\theta_o = L/(500d)$, where d is the depth of the section and L is the spacing between cross-frames.

LABORATORY TESTS AND FINITE ELEMENT MODEL

This investigation included laboratory experiments and finite element analyses (FEA). The laboratory studies played an important role in validating the FEA modeling techniques and were divided into three phases: shear panel tests, full-scale lateral displacement tests, and full-scale buckling tests on a twin girder system with a 50-ft. span braced by PMDF. Laboratory tests will be briefly presented, followed by the description of the FEA model and the parameters used in the parametrical study.

The main purpose of the first phase of testing was to determine the shear properties of metal deck forms used in the bridge industry and to

develop a simple modified connection detail that would increase the shear stiffness of PMDF system used in bridge applications. The laboratory tests were conducted in a testing frame similar to the one shown in Figure 3 in which the PMDF specimens were subjected to shear deformations so that the shear stiffness and strength of the panels could be measured. The failure of deck panels with conventional eccentric connections typically involves a severe deformation of the support angle at the corners of the panels. To control the deformations of the support angles, transverse stiffening angles were provided that spanned between adjacent girder flanges as discussed by Jetann et al. (2002) and Egilmez et al. (2004). The stiffening angles were positioned to coincide with a sidelap so that the deck forms could be directly fastened to the stiffening angles. The deck tests were conducted with conventional eccentric connection details as well as with the stiffened eccentric connections. The stiffening angles provided substantial increases in the stiffness of the PMDF systems (Jetann et al. 2002).

The second phase of testing focused on measuring the lateral stiffness of the PMDF panels subjected to deformations similar to the actual deflected top flange profile of buckled girders. PMDF panels were attached to the top flanges of a twin-girder test set-up using both the conventional eccentric detail and the stiffened eccentric connection. The twin girder system was loaded laterally at the top flanges of the girders to subject the PMDF to a variety of lateral deformation profiles so that the stiffness characteristics of the PMDF systems could be measured. The parameters that were investigated included metal deck thickness (20, 18, and 16 gage), girder type (W18x71, W18x119, and a W30x90 with a reduced top flange to make a singly-symmetric section), stiffening angle spacing (8, 16, and 24 ft), and support and stiffening angle size (L3x2 and L3x3 10 gage galvanized angle). The laboratory test results from this phase of the investigation were then compared with FEA results. The initial FEA model consisted of shear diaphragm truss panels and stiffening truss elements, which was presented by Egilmez et al. (2004), in which the stiffness of the shear diaphragm truss panels reflected the stiffness of the unstiffened PMDF panels and the stiffening truss elements accounted for the additional lateral stiffness of the system due to the direct connection between the

decks and the stiffening angles. The finite element model utilized in the results presented in this paper consists of only shear diaphragm truss panels (Figure 4) that simulate the shear stiffness of the metal decks with stiffening angles spaced at 8 or 16 ft. Comparisons of eigenvalue buckling and large displacement analyses of the two FEA models (one with shear diaphragm truss panels only, and the other with both shear diaphragm truss panels and a stiffening truss) revealed that there was not a significant difference in the behavior of the two systems. The reason for the similarity in buckling behavior of the two models is most probably due to the fact that with a moderately stiff diaphragm, the buckling behavior of the girders is often controlled by bottom flange flexibility.

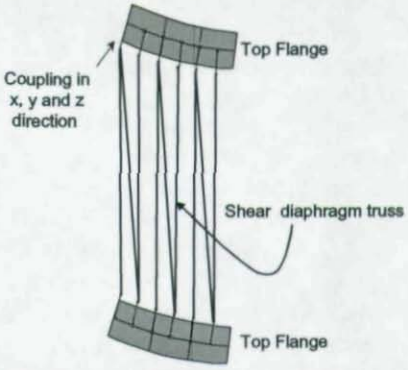

Fig. 4: Truss Elements used to Simulate the Shear Diaphragm

The third phase of laboratory experiments focused on buckling tests of twin girder systems with PMDF for bracing. Loading was applied with gravity load simulators that applied transverse point loads to the girders without restraining lateral movement (Figure 5). Concrete panels were used to increase the friction between the forms and the support angles similar to

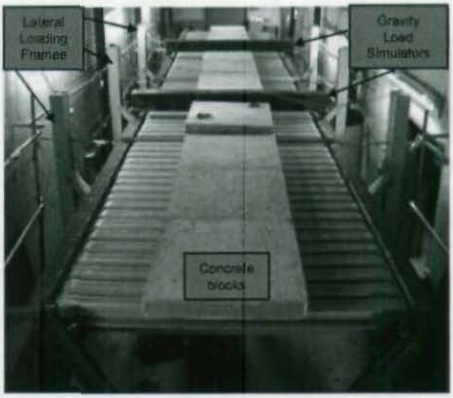

Fig. 5: Twin-Girder Lateral Displacement/Buckling Test Setup

the friction resulting under the weight of the wet concrete during deck casting operations, however, the primary loading on the twin girders were applied using the gravity load simulators. The purpose of the buckling tests was to improve the understanding of the buckling behavior of steel I-girders braced with PMDF as well as to provide results to check the accuracy of the shear diaphragm FEA model that was used for the parametric studies. Figure 6 shows a comparison of the midspan moment vs. twist curve from one of the laboratory buckling tests and a large displacement FEA solution. The results in Figure 6 are for tests of the modified W30x90 girders braced by 20 gage PMDF with stiffening angles spaced at 16 ft. Up to a moment level of about 500 k-ft the FEA results match well with the behavior of the actual system; however, since the FEA was conducted using linear elastic material properties, the finite element model can not capture the behavior of the system once the bracing system starts behaving inelastically. Since the PMDF bracing will typically be designed to remain well within the elastic range, the difference between the FEA solution and the test results in the inelastic range is not a concern in this study. The twin girder buckling tests showed that the girders braced with the stiffened deck systems could reach approximately twice the moment capacity that would have been achieved with a conventional cross-frame bracing system (conventional cross-frame bracing system producing an unbraced girder length of 25 ft., which is consistent with historical spacing limits typically imposed in the AASHTO Standard Specifications) (Egilmez et al. 2004).

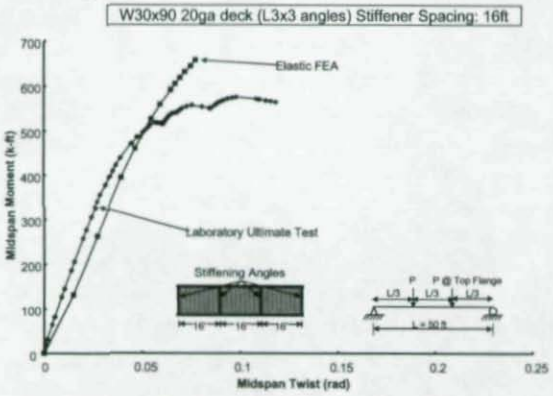

Fig. 6: Comparison of Ultimate Buckling Test with Elastic FEA Model

The three-dimensional finite element program ANSYS (2002) was used to perform parametric studies on the behavior of steel I-girders braced with PMDF. As previously explained, the metal deck forms with stiffening angles were modeled as shear diaphragms by utilizing shear truss panels as shown in Figure 4. Although the stiffening angle spacings tested in the laboratory were 8 ft, 16 ft, and 24 ft, the finite element model utilized in this study reflects the shear stiffness of PMDF systems with stiffening angles spaced at 16 ft. The results presented in this paper can also be applied to PMDF systems with stiffening angles spaced at 8 ft; however, further analyses are still underway considering stiffening angles spaced at 24 ft. Only simply supported girders with uniformly distributed load along the girder length applied at top flange were considered in the investigation. Bracing in the negative moment regions must be provided using conventional bracing such as cross-frames. Since the top flange is in tension in these regions, the top flange shear diaphragm will have a minimal effect on the buckling behavior.

The parameters that were considered include: girder span to depth ratio (15, 20, and 30), girder cross section (singly and doubly symmetric as shown in Figure 7), and shear rigidity of the deck system (Q=0 to 2200 kip/rad). Laboratory results on the shear stiffness of the shear diaphragms generally ranged from approximately G'=11 k/in.-rad for the unstiffened connection and G'=34 k/in.-rad for the 16 ft stiffened connection. For a tributary width of deck (s_d) of 4.5 ft (54 in.), this would give a range of Q of 594 to 1836 k/rad.

In the analysis, the spacing of the girders was set to 115 in., similar to the spacing of the modified W30x90 girders utilized in the laboratory tests. Hence, the deck shear rigidity, Q, was varied by changing the effective shear stiffness, G', of the deck. Only twin-girder systems were considered in the analyses. Most bridges actually have more than two girders and therefore the shear rigidity provided to each girder will tend to go up since there will be more deck form bracing provided per girder than the single PMDF panel bracing two girders as in the twin-girder system. For example, for the same PMDF system, bridges with 3, 4,

and 5 girders will have respective increases in the shear rigidity of 33%, 50%, and 60% compared to that of a twin-girder system.

The girder sections used in the study (Figure 7) include four doubly-symmetric rolled sections (W30x90, W18x119, W18x71, and W33x169), four singly-symmetric built-up sections labeled Sections #2, #6, #7, and #8, and one doubly-symmetric built-up section labeled Sections #9. All of the sections were chosen in accordance with Texas Department of Transportation Steel Beam Standard Design Drawings (TxDOT, SBSD-24/28/30). Web slenderness ratios of the sections ranged between 23.1 and 100 (Figure 7), and length to depth ratios were in the range of 15 to 30. The degree of mono-symmetry can be determined with the ratio $\rho = I_{yc}/I_y$ where I_{yc} and I_y are the respective moments of inertia of the compression flange and the entire cross-section about an axis through the web. The ratios of the mono-symmetry, ρ, for singly-symmetric sections were 0.18, 0.24, 0.41, and 0.43 for Sections #6, #2, #8, and #7, respectively. Section #6 matched the dimensions of the modified W30x90 section with reduced top flange used in the laboratory twin-girder tests. The AASHTO Standard Specifications (1992) requires the ratio of mono-symmetry to be within the following limits: $0.1 \leq I_{yc}/I_y \leq 0.9$.

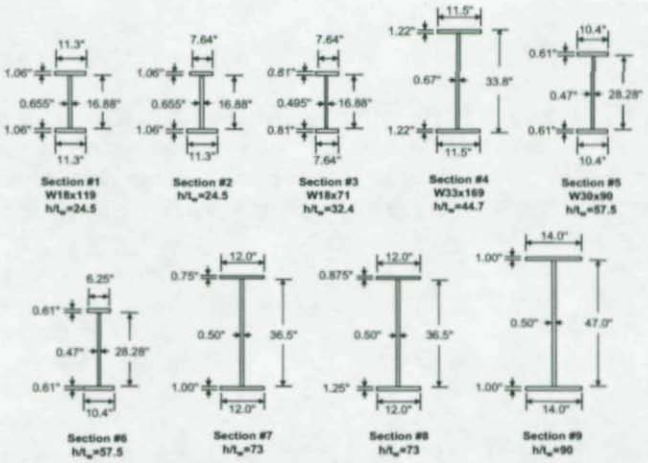

Fig. 7: Girder Cross-Sections used in Parametrical Studies

The general philosophy for the design of stability bracing systems is to achieve a design load while controlling the deformations under this load. Therfore, an adequate bracing system must possess sufficient strength and stiffness to support the design loads and control deformations. An elastic eigenvalue buckling analysis provides a linear-elastic solution that gives the critical buckling load of a system. For bracing problems, the solution establishes the ideal stiffness requirements for the bracing. Since the eigenvalue solution is relatively insensitive to imperfections, the analysis is generally performed on perfect systems. Since there is always an initial imperfection associated with the structural members of a system, a non-linear analysis that reflects the effects of geometrical imperfections is required to investigate the buckling behavior of the girders and total deformations in the system. Eigenvalue buckling analyses results will be presented first followed by large displacement analyses results. These results are then used to calculate the stiffness requirements for PMDF systems used to brace steel bridge girders.

EIGENVALUE BUCKLING FEA RESULTS

The buckling estimate of the girders will be calculated using Equation (3) given by Helwig and Frank (1999). Equation (3) is repeated here for convenience:

$$M_{cr} = C_b^* M_g + mQd \,. \qquad (5)$$

The deck contribution (*mQd*) in Equation (5) is a function of the girder depth and the deck shear rigidity as well as the constant 'm', which depends on the type of loading, the presence of intermediate braces, and web slenderness. In the graphs presented in this section the girder buckling capacity with no bracing (the $C_b^* M_g$ component of Equation (5)) has been subtracted from the FEA buckling solutions; therefore the contribution of the deck from the FEA is directly compared with the deck component, *mQd*, of Equation (5) for various L/d ratios. The curves are denoted by the section number, presented in Figure 7, web slenderness ratio, h/t_w, and the span to depth ratio. In addition to the FEA solutions, the expected *mQd* contribution required during construction is also shown in the graphs. The required moment capacity was calculated by assuming the critical construction loading would

create a stress of 25 ksi at the extreme fiber of the cross section. The stress level of 25 ksi is somewhat arbitrary; however, it represents a reasonable level of in-plane bending stresses expected during construction. The $(mQd)_{reqd}$ value shown in the graph was calculated by subtracting the girder buckling capacity ($C_b{}^*M_g$), assuming no bracing, from the construction moment corresponding to an extreme fiber stress of 25 ksi. Only the largest $(mQd)_{reqd}$ for the sections in each plot is shown for simplicity. The $(mQd)_{reqd}$ represents the ideal bracing moment required for the defined construction moment level.

Figure 8 shows the comparison of the FEA results for Sections #1, #2 and #3 and the deck components of Equation (5). Using an 'm' factor of (1/2) in the deck component resulted in conservative buckling estimates for all three girders and L/d ratios. Providing even a small amount of deck shear rigidity is sufficient to allow the system to carry the service load moment.

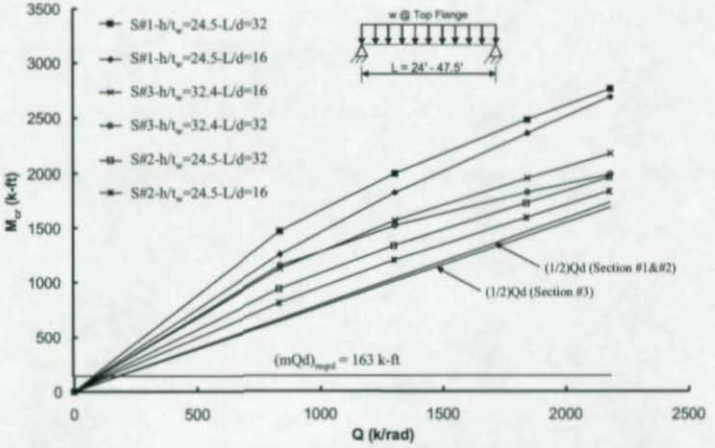

Fig. 8: Comparison of FEA Results and Eq. (7) for Sections #1, #2, #3

Figure 9 shows the comparison of results from the FEA and deck component of Equation (5) for Section #4. This section has an h/t_w ratio of 44.7 and using an 'm' factor of (1/2) still results in conservative buckling estimates for L/d ratios of 20 and 30. A deck shear rigidity of approximately 500 kip/rad is required to carry the service load moment.

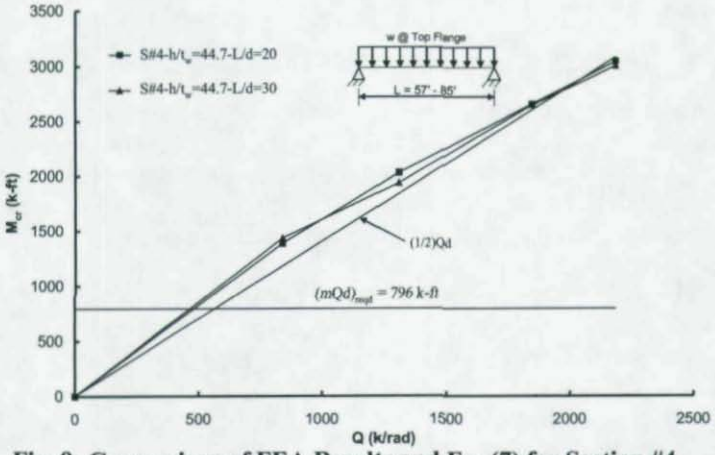

Fig. 9: Comparison of FEA Results and Eq. (7) for Section #4

Figure 10 shows the comparison of results from the FEA and deck components of Equation (5) for Sections #5 and #6. These sections have an h/t_w ratio of 57.5. Section #5, which is a rolled W30x90, has one of the most slender webs among rolled W-shapes. For these sections, a smaller 'm' factor of (3/8) instead of (1/2) was required to provide conservative buckling estimates. A deck shear rigidity of approximately 400 kip/rad is required to enable the girders to reach the service load moment corresponding to 25 ksi.

Figure 11 shows the comparison of results from FEA and deck component of Equation (5) for Sections #7 and #8. FEA analyses have been performed for L/d ratios of 20 and 30. These two sections had a web slenderness ratio of 73, and using an 'm' factor of (3/8), resulted in conservative buckling estimates. A deck shear rigidity of approximately 650 kip/rad is required to enable the girders to reach the service load moment corresponding to 25 ksi.

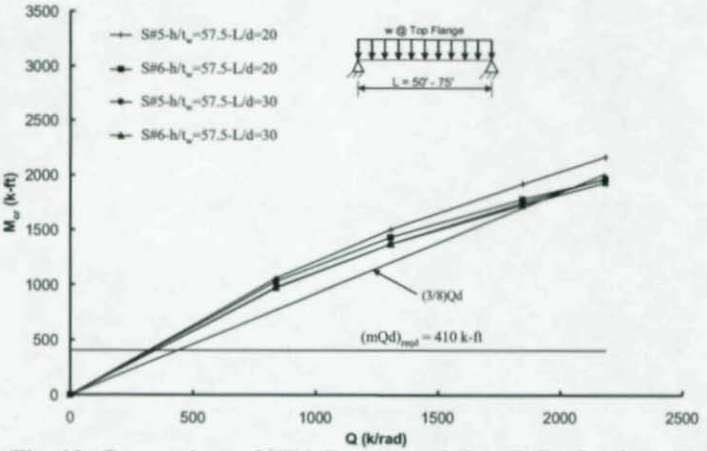

Fig. 10: Comparison of FEA Results and Eq. (7) for Sections #5 and #6

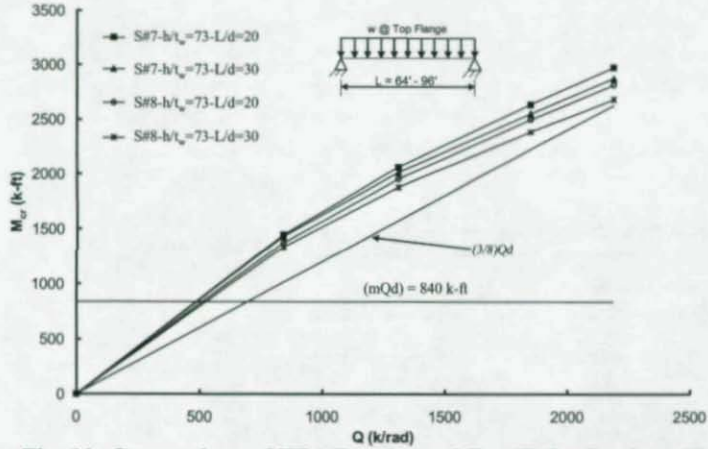

Fig. 11: Comparison of FEA Results and Eq. (7) for Sections #7 and #8

Figure 12 shows the comparison of results from FEA and deck component of Equation (5) for Section #9 with a web slenderness ratio of 90. Using an 'm' factor of (3/8) resulted in conservative buckling estimates. A deck shear rigidity of approximately 750 kip/rad is required to enable the girders to reach the service load moment corresponding to 25 ksi.

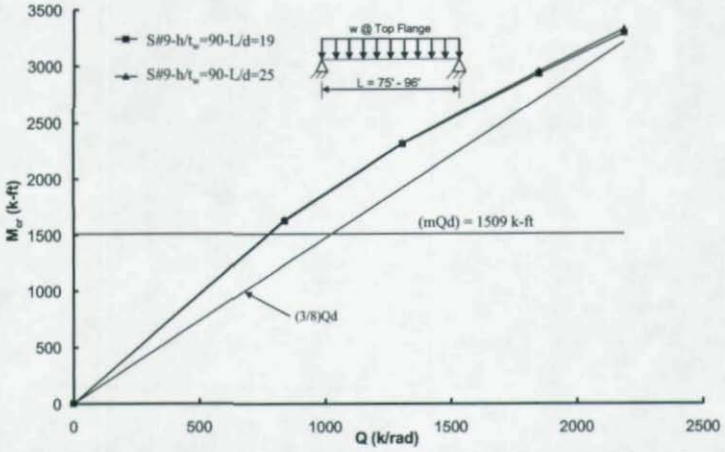

Fig. 12: Comparison of FEA Results and Eq. (7) for Section #9

It was observed from the eigenvalue analyses that the stiffened deck provided a substantial increase in the buckling capacity of the girders. For girder cross-sections with web slenderness ratio of up to 90, Equation (5) resulted in conservative estimates for the buckling capacity of the girders. Eigenvalue buckling analyses are still underway for girders with web slenderness ratios greater than 90. Table (2) presents the recommended m values for stiffened deck braced girders with stiffeners spaced no more than 16 ft.

Table 2: Design *m* Values for Equation (5)

Web Slenderness	Top Flange Loading w/o Midspan Torsional Brace
$h/t_w \leq 50$	0.5
$50 < h/t_w \leq 90$	0.375

Equation (5) can be rewritten to calculate the ideal deck shear stiffness for a given moment level, as presented by Equation (4). For steel bridge girders this moment level was taken to be the moment that would create a stress level of 25 ksi, which is a stress level that can reasonably be expected to occur during construction. The ideal deck shear rigidities ranged between 100 kip/rad, for girders with web slenderness ratios of 20-30, to 1000 kip/rad, for girders with web slenderness ratios of 90. These ideal deck shear rigidities correspond to ideal deck shear

stiffnesses of 1.83 kip/in.-rad to 18.3 kip/in.-rad for the given spacing of the tw in girders analyzed (115.25 in.). Previous laboratory lateral displacement tests on a 50 ft long twin-girder test set up revealed that the deck shear stiffnesses of bridge metal deck form systems with stiffening angles spaced at 16 ft ranged between 24 kip/in.-rad to 34 kip/in.-rad for 20 to 16 gage PMDF, respectively. These measured shear stiffnesses of PMDF systems indicate that for girders with web slenderness ratios smaller than 60 (rolled sections), 6 to 8 times the ideal stiffness requirements could easily be provided to control deformations. However, for girders with web slenderness ratios greater than 60, only up to 2 times the ideal stiffness requirement can be provided, which might yield to problems in controlling deformations.

LARGE DISPLACEMENT FEA RESULTS

As discussed in the previous section the eigenvalue buckling analysis is generally used to determine the ideal stiffness requirements for bracing. Large displacement analyses are then used to study the effects of imperfections. In the large displacement analyses, the initial twist of the cross-sections was taken as $\theta_o = L/(500d)$, where d is the depth of the section and L is the spacing between cross-frames. The rationale of this imperfection as well as the shape and distribution of the critical imperfection was discussed in Wang and Helwig (2005). The philosophy behind stability bracing is to achieve a specified load while also limiting the deformations of the system to be equal to twice the initial imperfections. In the construction stage the loads that are of interest are the construction loads and the construction stresses are generally in the range of 10 to 20 ksi. As mentioned in the previous section the construction stresses were assumed to be 25 ksi in this study. Therefore, for the sections studied, the ideal stiffness would be the stiffness calculated from Equation (5), which would enable the system to reach a buckling moment that would create a maximum stress of 25 ksi. If the ideal stiffness is used to brace the system, the deformations and brace forces become very large. Hence, generally a stiffness that is greater than the ideal stiffness is used in large displacement analyses in order to control the displacements.

The eigenvalue buckling analyses performed on Section #6 revealed that the ideal shear stiffness of the PMDF system to permit the girders to reach the service stress limit of 25 ksi was about 6 kip/in.-rad. Large displacement analyses were then performed on girders with L/d ratios of 20 and 30 by providing two and three times the ideal stiffness. Figure 13 shows the moment vs. twist behavior of Section #6 obtained from large displacement analyses. The total twist of the cross-section has been normalized by the initial twist. For girders with an L/d ratio of 30, providing neither 2 nor 3 times the ideal stiffness was sufficient to control the deformations. However, for girders with an L/d ratio of 20, providing twice the ideal stiffness did a better job in controlling the deformations as compared to a girder with an L/d ratio of 30. Since deformations during laboratory tests were often controlled by bottom flange displacements (Egilmez et. al, 2004), decreasing the length of the girders had a significant effect on controlling the deformations.

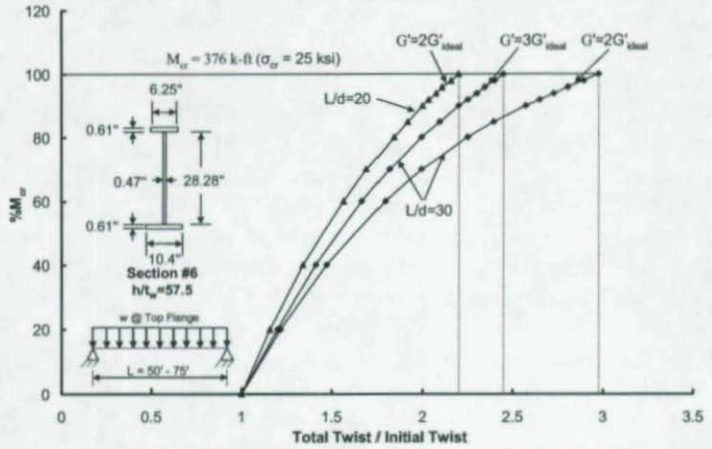

Fig. 13: Moment vs. Twist Behavior of Section #6

Figure 14 shows the moment vs. twist behavior of Section #7 obtained from large displacement analyses. The eigenvalue buckling analyses performed on Section #7 indicated that the ideal shear stiffness of the PMDF system to reach service stress limit of 25 ksi was about 12.8 kip/in.-rad. Large displacement analyses were performed on girders with L/d ratios of 20 and 30 by providing two and three times the ideal

stiffness. For girders with an L/d ratio of 30, using twice the ideal stiffness instead if three times the ideal stiffness decreased the total twist over initial twist ratio from 3.3 to 2.6. For girders with an L/d ratio of 20, three times the ideal stiffness was required to bring the total twist over initial twist ratio closer to 2.

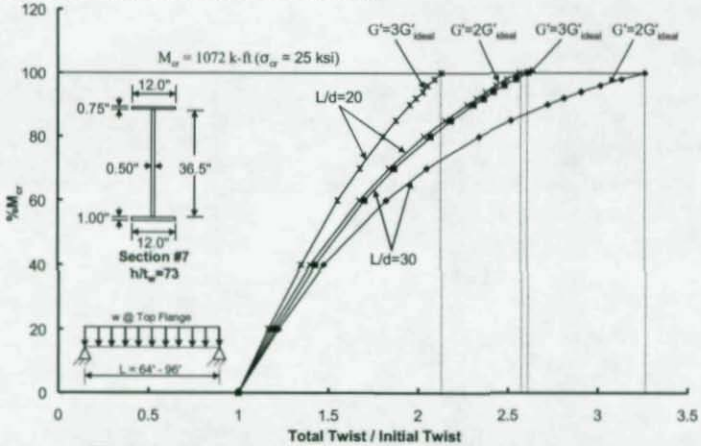

Fig. 14: Moment vs. Twist Behavior of Section #7

Comparison of the large displacement analyses results for Sections #6 and #7 revealed that although two times the ideal stiffness was sufficient to control the deformations for Section #6, three times the ideal stiffness was required to control the deformations for Section #7. This implies that as the depth and length of the girders increase, so as the stiffness requirements to control the deformations increase. Hence, there should be a limit to the unbraced length of bridge girders braced by PMDF. The large displacement analyses are currently underway to further investigate the stiffness requirements of PMDF systems.

SUMMARY

Eigenvalue and large displacement analyses results have been presented in this paper on the stiffness requirements of PMDF used for lateral bracing of steel bridge I-girders. Additional parametrical studies are currently underway focusing on a wider variety of girder cross-sections and length to depth ratios. Results from the additional computational study as well as results from laboratory tests will be

utilized to formulate design expressions for stability bracing of bridge girders with PMDF for bracing.

ACKNOWLEDGEMENTS

The authors would like to thank TxDOT for funding this study. Special thanks go to TxDOT engineers J.C. Liu, John Vogel, and Brian Alcott.

REFERENCES

AASHTO, Standard Specifications for Highway Bridges, 17th Ed. 2002

Egilmez, O., "Lateral Bracing of Steel Bridge Girders by Permanent Metal Deck Forms," Ph.D. Dissertation, UH, Houston 2005

Egilmez, O., Charles J., and Todd H., "Bracing Behavior of Permanent Metal Deck Forms", Proceedings of 2003 SSRC Annual Stability Conference, Baltimore, Maryland, April 2-5, 2003, p 133-152

Egilmez, O. O., Todd Helwig, "Buckling Behavior of Steel Bridge Girders with Permanent Metal Deck Forms", Proceedings of 2004 SSRC Annual Stability Conference, March 24-27,2004, p39-58

Egilmez, O., Todd H., and Reagan H., "Strength of Metal Deck Forms Used for Stability Bracing of Steel Bridge Girders", Proceedings of 2005 SSRC Annual Stability Conference, April 6-9, 2005, p257-276.

Errera, S., and Apparao, T., "Design of I-shaped beams with diaphragm bracing," J. of the Str. Div., ASCE, Vol. 102(4), 1976, pp. 769-781

Helwig, T. A. and Frank, K. H., "Stiffness Requirements for diaphragm bracing of beams," *Journal of Structural Engineering, ASCE*, Vol. 125, No. 11, November 1999, pp. 1249-1256

Helwig, T. A., and Yura, J. A., "Strength requirements for diaphragm bracing of beams," Draft manuscript to be submitted, 2005

Jetann, C. A., Helwig, T. A., and Lowery, R. "Lateral Bracing of Bridge Girders by PMDF", Proceedings of 2002 SSRC Annual Stability Conference, Seattle, WA, April 24-27, p. 291-310.

Lawson, R, and Nethercot, P., "Lateral Stability of I-beams Restrained by Profiled Sheeting", *Str. Eng.*, Vol. 63B, No.1, 03/1985, pp.3-13

Luttrell, L. D., SDI Diaphragm Design Manual, Third Edition, 2004.

Nethercot, D., and Trahair, N., "Design of diaphragm-braced I-beams," *Structural Division, ASCE*, Vol. 101(10), 1975, pp. 2045-2061

TxDOT, Bridge Div., Steel Beam Standard Designs, SBSD-24/28/30.

Wang, L; and Helwig, T A., "Critical Imperfections for Beam Bracing Systems",*J. of Str. Eng., ASCE*,Vol.131, No. 6, pp.933-940, 06/2005.

INELASTIC DESIGN AND RATING OF STEEL I-GIRDERS BASED ON GIRDER ROTATION CAPACITY

Jennifer Righman[1], Karl Barth[2], and Michael Barker[3]

ABSTRACT

Recent research has culminated in the development of inelastic rating and design procedures based on a "rotation compatibility" procedure. This procedure explicitly compares the moment versus rotation characteristics exhibited by a given girder to the rotation required for moment redistribution. This paper will highlight the key aspects of the rotation compatibility method leading to a series of simple equations that may be used for both design and rating of continuous-span steel girders.

Several advantages of the rotation compatibility method are also presented herein. Most significantly, the rotation compatibility method provides a rational basis for removing the previous restrictions on permissible girder geometries for use with moment redistribution provisions. In other words, sections that are more slender than previously permitted for use with inelastic procedures may be considered. This is particularly beneficial for incorporating inelastic methods into rating specifications as many existing bridges have geometries such that they have previously been regarded as outside the

[1] Jennifer Righman, University of Delaware, Department of Civil and Environmental Engineering, 358A Dupont Hall, Newark, DE 19716
[2] Karl Barth, West Virginia University, Department of Civil and Environmental Engineering, PO Box 6103, Morgantown, WV 26506
[3] Michael Barker, University of Wyoming, Department of Civil and Architectural Engineering, 1000 E. University Ave., Laramie, WY 82071

scope of applicability of inelastic procedures. Additionally, using the rotation compatibility procedures, the maximum allowable redistribution moments are computed in contrast to the current methods where any redistribution moment less than 20% of the elastic moment is considered acceptable. The favorable economic consequences of this alternative approach are demonstrated herein.

INTRODUCTION

Design procedures incorporating inelastic methods are currently incorporated in AASHTO Load and Resistance Factor Design (LRFD) Specifications (2004) as optional provisions, termed "moment redistribution" procedures. These methods assume that the ductility necessary for moment redistribution can be attained by implementing two restrictions. These restrictions limit (1) the types of girders that may be used in conjunction with moment redistribution procedures and (2) the magnitude of moment that may be redistributed. Consequently, these requirements decrease the potential economic benefits of inelastic design procedures. Furthermore, at the present time, moment redistribution procedures are included in the design specifications only; these procedures are not included in the AASHTO Load and Resistance Factor Rating (LRFR) Specifications (2003). One primary reason for this is that the majority of existing bridge girders do not satisfy the current requirements for use of moment redistribution provisions. Therefore, by extending the range of girders for which moment redistribution is applicable, there is the potential for significant economic benefits to both the design and rating processes.

This paper presents the development of the rotation compatibility approach to moment redistribution, which overcomes the limitations of the AASHTO (2004) moment redistribution provisions highlighted above. The rotation compatibility method is founded on an explicit evaluation of the rotations required for moment redistribution and comparison of these values to the ductility of individual girders. The ultimate result of these procedures is design and rating specifications that do not contain the previous restrictions on girder geometry and maximum permissible levels of redistribution. Instead, the rotation compatibility procedures developed herein: are valid for any girder

cross-section that satisfies the cross-section proportion limits specified by AASHTO (2004) for general steel I-girders, explicitly compute maximum levels of redistribution, and are in a format such that the suggested procedures may be conveniently adopted into both the AASHTO LRFD and LRFR Specifications.

This paper is organized into four main sections. The first section summarizes the relationships for available and required relationships developed in previous work by the first author and then presents the formulation of the rotation compatibility method, which is carried out through comparison of these available rotation and required rotation relationships. The second section presents rotation compatibility design specifications for steel bridges. Here the range of applicability of the specifications, an overview of the design process, and a series of equations in a format suitable for incorporation into design specifications are presented. Similarities and differences between the rotation compatibility design procedure and the AASHTO (2004) moment redistribution procedure are also discussed. Similarly, the third section of this paper presents the synthesis of the rotation compatibility procedures into a format suitable for use in rating applications such as the AASHTO LRFR Specifications (2003). The use of the rotation compatibility procedure in design is presented in the last section of this paper. This example design is also compared to a design resulting from use of the existing AASHTO (2004) specifications. These examples show that the use of the rotation compatibility procedures is both convenient and economically advantageous.

FORMULATION OF ROTATION COMPATIBILITY APPROACH

Summary of Available Rotations The available rotation of steel I-girder pier sections may be represented by one of two models (Righman 2005). For girders satisfying the lateral bracing requirement of

$$L_b \le \frac{r_t E}{F_{yc}}\left[0.1 - 0.06\left(\frac{M_1}{M_2}\right)\right], \qquad (1)$$

the moment-rotation behavior is represented by the model shown in Fig. 1(a), while the moment-rotation behavior of girders that do not satisfy Eq. 1 is represented by Fig. 1(b). It is noted that Eq. 1 represents the maximum allowable lateral bracing permitted by the AASHTO 2004 moment redistribution specifications.

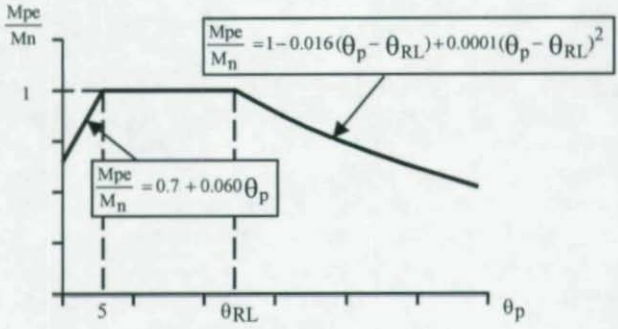

(a) For girders satisfying Eq. 1

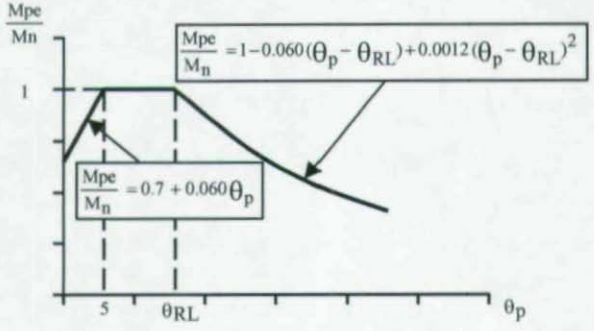

(b) For girders violating Eq. 1

Figure 1. Moment-Rotation Models

In both models, θ_{RL} (in mrads) may be expressed by the equation

$$\theta_{RL} = 128 - 143\frac{b_{fc}}{t_{fc}}\sqrt{\frac{F_{yc}}{E}} - 43.2\frac{D_{cp}}{b_{fc}} + 48.2\frac{b_{fc}}{t_{fc}}\frac{D_{cp}}{b_{fc}}\sqrt{\frac{F_{yc}}{E}} - \max\left[0, 0.5\left(\frac{L_b}{r_t} - 30\right)\right] \geq 5 . \quad (2)$$

Equation 2 gives nearly identical results to the current (AASHTO 2004) θ_{RL} equation for girders that satisfy Eq. 1; linear decreasing values of θ_{RL} then result as the lateral bracing distance is increased beyond the unbraced length given by Eq. 1.

Summary of Required Rotations Based on an analysis procedure detailed in Righman and Barth (2005) and Righman (2005), the required rotation may be expressed as a function of the percentage of moment to be redistributed and the pier location, with alternative expressions being required based on the grade of material used in the pier section (Righman 2005). Specifically, rotation requirements were formulated for homogeneous Grade 50 girders as well as hybrid girders comprised of Grade 70 flanges in negative bending and Grade 50 steel for positive bending flanges and webs; higher rotations are required for hybrid girders due to the smaller moment of inertia of these girders. Additionally, higher rotation requirements are required for piers between internal spans of the girder compared to piers adjacent to end spans due to the fact that the redistribution moments applied at adjacent piers influence the rotation requirements. The alternative expressions for rotation requirements are given below in Eqs. 3 through 5 where θ_{pR} represents the required plastic rotation, C is the rotation coefficient given by Eq. 4 or 5, M_{rd}/M_e represents the normalized redistribution moment, and n represents the number of adjacent piers where redistribution moments are applied, i.e., n is equal to 0, 1, or 2.

$$\theta_{pR} = C(M_{rd} / M_e) \quad (3)$$

- For homogeneous pier sections:

$$C = 80 + 20n \quad (4)$$

- For hybrid pier sections:

$$C = 90 + 22.5n \quad (5)$$

Comparison of Available and Required Rotations The rotation compatibility procedure is based on an explicit comparison of available and required rotations. Moment redistribution is valid for all cases where the available rotation is greater than or equal to that which is required, and conversely, moment redistribution may not be used when the available rotation is less than the required rotation. The comparison of available and required rotation is facilitated through the relationships for available and required rotations summarized in the previous two sections in conjunction with the general equation for moment redistribution,

$$M_e = M_{pe} + M_{rd}. \tag{6}$$

It may be observed that Eq. 3 expresses the rotation requirements in terms of M_{rd}/M_e and that Fig. 1 presents the available rotations in terms of M_{pe}. Thus, through algebraic manipulation of Eq. 6, available and required rotations may be directly compared.

Specifically, Eq. 6 may be used to express the required rotation in terms of M_{pe}/M_n. Because the available rotation is already expressed in this format, a similar expression for the required rotations will allow for direct comparison of the two rotations. This is accomplished by first dividing Eq. 6 by M_e.

$$\frac{M_{pe}}{M_e} + \frac{M_{rd}}{M_e} = 1 \tag{7}$$

This produces the term M_{rd}/M_e, which is also used in the rotation requirement expression given in Eq. 3. This term is then subtracted from both sides of the equation, giving

$$\frac{M_{pe}}{M_e} = 1 - \frac{M_{rd}}{M_e}. \tag{8}$$

Multiplication by M_e/M_n then results in the desired format of the equation,

$$\frac{M_{pe}}{M_n} = \left(1 - \frac{M_{rd}}{M_e}\right) \bullet \frac{M_e}{M_n}. \tag{9}$$

Furthermore, rearranging Eq. 3 allows M_{rd}/M_e to be expressed in the following format,

$$M_{rd}/M_e = \theta_{pR}/C. \tag{10}$$

Substitution of Eq. 10 into Eq. 9 then results in

$$\frac{M_{pe}}{M_n} = \left(1 - \frac{\theta_{pR}}{C}\right) \bullet \frac{M_e}{M_n}, \tag{11}$$

which expresses the required rotation in terms of M_{pe}/M_n such that the required rotations can be directly compared to the available rotations.

Such a comparison of required and available rotations is presented in Fig. 2 for an example two-span continuous homogeneous Grade 50 girder. First, Eq. 4 may be used to determine the value of C. Because n is equal to zero for a two-span girder,

$$C = 80 \tag{12}$$

for the present example. Thus, the moment versus required rotation is expressed as

$$\frac{M_{pe}}{M_n} = \left(1 - \frac{\theta_{pR}}{80}\right) \bullet \frac{M_e}{M_n}, \tag{13}$$

which obviously varies with the ratio M_e/M_n. To determine the variation in the available rotation, it is assumed that the lateral bracing

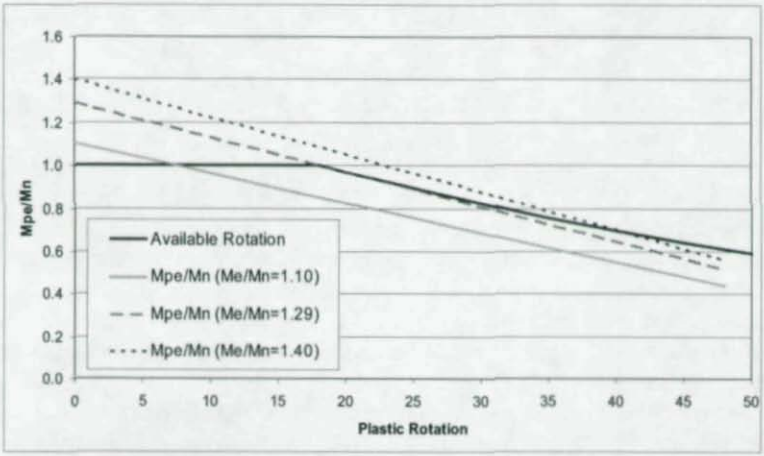

Figure 2. Comparison of Available and Required Rotations for Example Girder with L_b satisfying Eq. 1

requirements of Eq. 1 are satisfied such that the moment-rotation behavior is as depicted in Fig. 1(a). Furthermore, θ_{RL} is determined using Eq. 2 and is taken as 18 mrads, which is the value for a representative continuous span girder with two 90 ft spans.

$$\theta_{RL} = 18 \text{ mrads.} \tag{14}$$

Equation 14 is then substituted for θ_{RL} into the unloading equation in Fig. 7-1(a), giving

$$M_{pe}/M_n = 1 - 0.016(\theta_p - 18) + 0.0001(\theta_p - 18)^2, \tag{15}$$

which may also be expressed as

$$M_{pe}/M_n = 0.0001\ \theta_p^{\ 2} - 0.0196\ \theta_p + 1.3204. \tag{16}$$

Equation 13 is plotted in Fig. 2 for various M_e/M_n ratios along with the available rotation curve, which is equal to one up to θ_{RL} and is then expressed by Eq. 16 for θ_p values greater than θ_{RL}.

Figure 2 shows that for M_e/M_n ratios less than 1.29 the required rotations are less than the available rotation throughout the unloading region of the moment versus rotation response and the unloading curves do not intersect. Thus, the effective plastic moment capacity is equal to M_n for M_e/M_n ratios less than 1.29. Alternatively, for M_e/M_n ratios greater than 1.29 the required rotations are initially greater than the available rotation. Consequently, the effective plastic moment in these cases is determined by the intersections of the two unloading curves, which is shown to be $0.7M_n$ for a M_e/M_n ratio of 1.40 in Fig. 2.

It should be apparent from Fig. 2 that above a certain limit (1.29 for this example), increasing ratios of M_e/M_n reduce the effective plastic moment capacity of the girder. In terms of the physical girder, this represents a point where the girder can no longer sustain its nominal moment capacity due to excessive stresses in the girder. It should also be apparent that some maximum limit should be placed on the amount of moment that is permitted to be redistributed. For example, in the current AASHTO (2004) Specifications this limit is 20% of the elastic moment. However, it is suggested that a more appropriate limit would be to limit the maximum allowable level of redistribution in accordance with the moment level at which the moment capacity decreases below M_n. Such an approach not only establishes a rational criterion for the maximum level of moment redistribution, but will also decrease girder

distortions compared to allowing the girder to unload to moment levels below M_n. Thus, the objectives of the current 20% limit (to control girder deformations) are also better satisfied. For these reasons, the maximum allowable elastic moment is limited to the magnitude of moment at which the effective plastic moment is equal to M_n in the present work. This maximum value of elastic moment may also be thought of as the moment level where the available and required rotation curves intersect at a rotation equal to θ_{RL}.

Mathematically, the maximum allowable value of M_e/M_n may be obtained by setting θ_{pR} equal to θ_{RL} in Eq. 13. Realizing that M_{pe}/M_n will equal one at θ_{RL} and substituting this value into Eq. 13, the maximum M_e/M_n ratio is expressed as

$$M_e/M_n \leq 1/(1- \theta_{RL}/C) \quad (17)$$

ROTATION COMPATIBILITY DESIGN SPECIFICATIONS

Scope As with the AASHTO 2004 moment redistribution specifications, the moment redistribution specifications suggested herein are limited to straight girders with skews less than 10 degrees having neither staggered cross-frames nor holes in the top/tension flange over a distance of two times the web depth from either side of interior-pier sections where moments are redistributed. Also consistent with the AASHTO 2004 procedures, the current specifications restrict the length over which the girder may be analyzed for reduced negative moments due to moment redistribution to a distance equal to one unbraced length on each side of the pier. However, the rotation compatibility specifications contain no cross-section or lateral bracing limits outside of the cross-section proportion limits for general I-girders contained in AASHTO 2004 Section 6.10.2. Thus, the rotation compatibility specifications are applicable for a considerably larger class of girders. The procedures are applicable for girders having yield strengths up to 70 ksi.

Overview of Design Procedure While there are no explicit requirements on lateral bracing distance in the rotation compatibility specifications, the beneficial effects of shorter bracing spacing are

incorporated through the last term of the θ_{RL} equation (Eq. 2). For designs satisfying Eq. 1, this last term is equal to zero. Thus, for preliminary design, the designer may wish to initially assume that the last term of Eq. 2 is equal to zero when determining cross-section geometry requirements, and then subsequently select the lateral bracing distance.

The rotation coefficient, C, is then used in combination with θ_{RL} to determine the maximum permissible level of elastic moment. Specifically, by rearranging Eq. 17, we arrive at the moment requirements at the pier section using the rotation compatibility method,

$$M_e(1 - \theta_{RL}/C) \leq M_n, \quad (18)$$

Positive bending sections must also be analyzed for the effects of moment redistribution. This is performed by computing the redistribution moment. At the piers the redistribution moment is equal to the difference between the applied moments and the moment capacity,

$$M_{rd} = M_e - M_n. \quad (19)$$

The redistribution moment at other locations is then determined by linear interpolation between the redistribution moments at the ends of each span, where redistribution moments are equal to zero at abutments (as is done in the AASHTO (2004) procedures).

The following section will present the equations given above in a format suitable for incorporation into design specifications.

Rotation Compatibility Design Specification Equations Negative bending capacity at the strength limit state may be evaluated using

$$M_e(1 - \theta_{RL}/C) \leq M_n,, \quad (18)$$

where:

M_n = nominal moment capacity of the girder computed using applicable AASHTO Specifications,

$$\theta_{RL} = 128 - 143\frac{b_{fc}}{t_{fc}}\sqrt{\frac{F_{yc}}{E}} - 43.2\frac{D_{cp}}{b_{fc}} + 48.2\frac{b_{fc}}{t_{fc}}\frac{D_{cp}}{b_{fc}}\sqrt{\frac{F_{yc}}{E}} - \max\left[0, 0.5\left(\frac{L_b}{r_t} - 30\right)\right] \geq 5$$

C = $80 + 20n$ for homogeneous girders with $F_y \leq 50$ ksi,

C = $90 + 22.5n$ for hybrid girders with $F_{yf} \leq 70$ ksi, and

n = number of piers adjacent to the pier under consideration where moment redistribution occurs.

- Positive bending capacity must then be evaluated using

$$M_n \geq M_e + M_{rdL} + (x/L)(M_{rdR} - M_{rdL}), \quad (20)$$

where:

M_n = nominal moment capacity of the girder computed using applicable AASHTO Specifications,

M_{rdL} = redistribution moment at left end of the span under consideration, computed using Eq. 19,

M_{rdR} = redistribution moment at right end of the span under consideration, computed using Eq. 19,

x = location where moment is being evaluated expressed as distance from left end of span

L = span length

Comparison to AASHTO 2004 Moment Redistribution Procedures

While the underlying theory of the AASHTO (2004) moment redistribution procedures and the rotation compatibility design procedures is the same, the resulting design equations are markedly different. The AASHTO 2004 moment redistribution procedures are primarily based on the computation of two quantities, the effective plastic moment (M_{pe}) and the redistribution moment (M_{rd}). The basis of the rotation compatibility procedures is also the quantities M_{pe} and M_{rd}, however the primary quantities used in the design are θ_{RL} and C.

In the AASHTO 2004 procedures, M_{pe} for a given limit state (strength or service) is expressed by one of two equations depending on the web slenderness and transverse stiffener configuration. These equations

express M_{pe} as a function of M_n, geometric properties, and steel yield strength and are limited to a maximum value of M_n. This is based on the premise that compact beams will have sufficient rotation available to redistribute moment at M_n, but that more slender beams will have reduced rotation available at M_n and a lower level of moment must be used to achieve the needed rotation. Furthermore, the AASHTO (2004) specifications limit the maximum allowable level of moment redistribution to 20% of the elastic moment. Conversely, in the present rotation compatibility procedures, the M_{pe} value is equal to M_n in all cases and the maximum allowable level of redistribution varies based on the rotation requirements and girder ductility.

To compare the consequences of these two alternative approaches to limiting maximum levels of redistribution, a girder that has an M_{pe} value equal to M_n according to the AASHTO (2004) specifications is first considered. Substituting M_n for M_{pe} in Eq. 6 and setting the magnitude of redistribution moment equal to the maximum value permissible using the AASHTO (2004) specifications, $M_{rd} = 0.2M_e$, gives

$$M_e = M_n + 0.2M_e, \tag{21}$$

which can be solved to determine the maximum allowable value of the elastic moment in terms of M_n, giving

$$M_e \leq 1.25M_n. \tag{22}$$

In the rotation compatibility procedure, the maximum value of M_{rd} varies based on the available and required rotations of the girder under consideration and (from Eqs. 18 and 19) can be expressed as

$$M_{rd}/M_e = \theta_{RI}/C. \tag{23}$$

For illustrative purposes, a representative girder for which M_{pe} is equal to M_n according to AASHTO (2004) procedures is selected and the maximum value of normalized redistribution moment is computed using Eq. 23. Eq. 2 is used to compute a θ_{RL} value equal to 24.1 mrads for the sample girder under consideration. (The reader is referred to Righman (2005) for additional details of this girder.) Then, from Eqs. 4 and 5, it is shown that C may vary between a minimum value of 80 and a maximum value of 135. Substituting the minimum value of C

into Eq. 23 and rearranging the equation gives that the maximum allowable value of redistribution moment is equal to

$$M_{rd} = (\theta_{RL}/C)M_e = 24.1/80M_e = 0.30M_e. \quad (24)$$

Substituting Eq. 24 for M_{rd} and M_n for M_{pe} into Eq. 6 gives

$$M_e = M_n + 0.30M_e. \quad (25)$$

The maximum allowable value for the elastic moment is then equal to

$$M_e \leq 1.43M_n, \quad (26)$$

which represents a 15% increase in the allowable value of the elastic moment compared to the AASHTO (2004) specifications. Alternatively, substituting the maximum value of C into Eq. 23 gives

$$M_{rd} = (\theta_{RL}/C)M_e = 24.1/135M_e = 0.18M_e, \quad (27)$$

which results in a maximum allowable elastic moment of

$$M_e \leq 1.22M_n. \quad (28)$$

The above example illustrates that for a girder that has a M_{pe} value equal to M_n in the AASHTO (2004) procedures, the rotation compatibility procedure results in maximum allowable elastic moment values that are appreciably higher (15% in this example) or slightly lower (2% in this example) than those permitted by the AASHTO (2004) specifications depending on the continuity conditions of the girder.

The consequences of the alternative methodologies in the AASHTO (2004) and rotation compatibility procedures are also illustrated for a representative girder that has a M_{pe} value less than M_n in the AASHTO (2004) specifications. The AASHTO (2004) M_{pe} equations give a value of $0.65M_n$ for this girder. Thus, the maximum value of the elastic moment using the AASHTO (2004) moment redistribution procedures is

$$M_e = 0.65M_n/0.8 = 0.81M_n. \quad (29)$$

Alternatively, using the rotation compatibility procedures and the maximum possible value of C (which results in the minimum allowable value of M_e) gives a maximum redistribution moment of

$$M_{rd} = (\theta_{RL}/C)M_e = 5/135M_e = 0.04M_e. \quad (30)$$

Substituting this value of M_{rd} into Eq. 7.6 gives

$$M_e = M_n + 0.04M_e, \quad (31)$$

and an allowable elastic moment of

$$M_e \leq 1.04M_n, \quad (32)$$

which is 28% higher than the allowable moment permitted by the AASHTO (2004) specifications. Thus, it is concluded that limiting the value of M_{pe} to M_n in the rotation compatibility procedures has either negligible or positive effects on girder economy.

The AASHTO 2004 moment redistribution provisions also give alternative design equations for the strength and service limit states, where the differing equations are based on the premise that girders will need to undergo less rotation to achieve moment redistribution at service limit states due to the lower magnitudes of load at this limit state. Conversely, the rotation compatibility procedures suggested above can be applied for either limit state as these procedures directly evaluate the moment redistribution characteristics of the girder for a given magnitude of applied loading.

ROTATION COMPATIBILITY RATING SPECIFICATIONS

Scope The rotation compatibility specifications are uniformly applicable to both design and rating of continuous-span steel bridges. Thus the scope of the rating and design procedures (which were outlined above) are identical.

Overview of Rating Procedure The LRFR procedures utilize member capacities calculated from LRFD procedures. Thus, because the effective plastic moment capacity is equal to M_n in the rotation compatibility procedures, M_n is the girder capacity used for both inelastic and elastic rating. However, inelastic rating procedures offer the engineer the ability to account for the reduction in moment levels that occurs in the negative bending regions due to moment redistribution. This effect is incorporated into the rotation compatibility rating specifications through the use of moment redistribution load factors that decrease the applied moment in negative bending regions and increase the applied moments in positive bending regions. These load factors are represented by the variables $\gamma_{\theta-}$ and $\gamma_{\theta+}$, respectively. The rating procedure then proceeds in the same manner as would be used for an elastic design.

The load factor $\gamma_{\theta-}$ is easily computed as

$$\gamma_{\theta-} = 1 - \theta_{RL}/C. \tag{33}$$

If this optional load factor is used in the rating analysis of negative bending regions, the inelastic action that this assumes must be accounted for in the rating of the positive bending sections. This is done by using Eq. 23 to compute the redistribution moment as a ratio of the elastic moment at each end of the span under consideration,

$$M_{rd}/M_e = \theta_{RL}/C. \tag{23}$$

Linear interpolation of the θ_{RL}/C or M_{rd}/M_e ratio at each end of the span is used to determine the factor by which the elastic positive bending moments should be increased in the rating analysis, represented as $\gamma_{\theta+}$. Using the subscripts "L" and "R" to refer to the left and right ends of the span, x to represent the distance from left end of the span to the point where the rating factor is to be computed, and L to represent the span length, Eq. 34 gives the equation to compute $\gamma_{\theta+}$,

$$\gamma_{\theta+} = 1 + \left(\frac{M_{rd}}{M_e}\right)_L + \frac{x}{L}\left[\left(\frac{M_{rd}}{M_e}\right)_R - \left(\frac{M_{rd}}{M_e}\right)_L\right] \tag{34}$$

Rotation Compatibility Rating Specification Equations The rotation compatibility procedure is easily incorporated into LRFR specifications through the addition of the load factor γ_θ. Specifically, the general rating equation of LRFR is given by

$$RF = \frac{C - \gamma_{DC}(DC) - \gamma_{DW}(DW) \pm \gamma_P(P)}{\gamma_L(LL + IM)}, \tag{35}$$

Which, for rating using the rotation compatibility procedures, may be modified as

$$RF = \frac{C - \gamma_\theta\left[\gamma_{DC}(DC) + \gamma_{DW}(DW) \pm \gamma_P(P)\right]}{\gamma_\theta\gamma_L(LL + IM)}. \tag{36}$$

As discussed in the previous section, alternative formulas γ_θ are given for the negative and positive bending regions, where

$$\gamma_{\theta-} = 1 - \theta_{RL}/C \tag{33}$$

and

$$\gamma_{\theta+} = 1 + \left(\frac{M_{rd}}{M_e}\right)_L + \frac{x}{L}\left[\left(\frac{M_{rd}}{M_e}\right)_R - \left(\frac{M_{rd}}{M_e}\right)_L\right]. \quad (34)$$

EXAMPLES

This primary purpose of this section is to illustrate the use of the *rotation compatibility procedure in a design example. The resulting* girder design is also compared to a girder design resulting from use of AASHTO (2004) moment redistribution specifications.

Design Criteria This section will present the design of a two-span continuous bridge having equal 90' spans and the bridge cross-section shown in Fig. 3. The bridge is designed for all applicable limit states, i.e., strength, service, fatigue, and constructibility. It is assumed that the girders are comprised of Grade 50 steel and the concrete deck of the bridge is assumed to have a minimum compressive strength of 4 ksi and standard Grade 60 steel reinforcement. Section transitions are provided at 27' from the pier. Standard design loads, as detailed in Righman (2005), are assumed to act on the structure. Additional details relating to the design process, which are omitted here for conciseness, may also be found in Righman (2005).

Rotation Compatibility Design The girder design using the rotation compatibility procedure begins with selection of a trial lateral bracing layout, where three lateral bracing segments of 25 ft. followed by a 15 ft. lateral bracing segment at the pier are initially assumed. The girder geometry in the positive bending section is then determined. The web depth was selected based on the results of preliminary designs with varying web depths, which indicated that the most economical web depth was equal to 42 in. The web thickness was then based on the thickness necessary to satisfy shear requirements without the need for web stiffeners, which was equal to 7/16 in. at the abutments and 1/2 in. at the pier. Constructibility requirements dictate the geometry of the top flange; based on a lateral bracing distance of 25 ft., a 16 in. by ¾ in. top flange is selected. Given these web and top flange dimensions, a 16

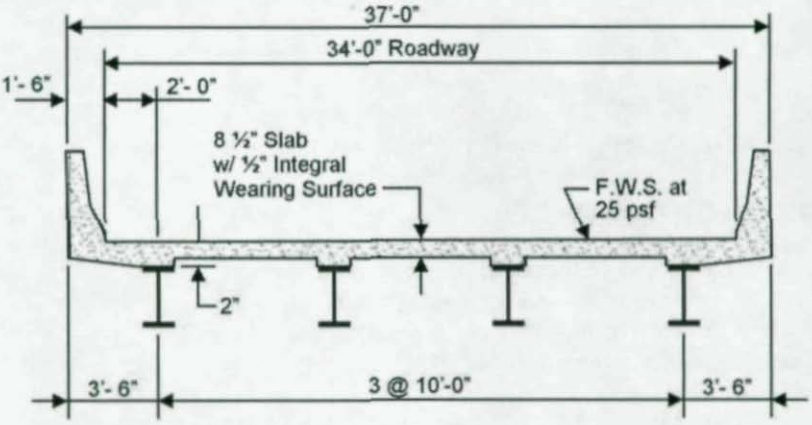

Figure 3. Design Example Bridge Cross-Section

in. by 1-¼ in. bottom flange is required in the positive bending region, which is governed by the fatigue limit state.

For the design of the negative bending section, it is initially assumed that the geometry of the negative bending cross-section is the same as the positive bending section. Evaluation of the pier section at the strength limit state, which typically controls the negative bending section design, is carried out using Eq. 18,

$$M_e(1- \theta_{RL}/C) \leq M_n, \quad (18)$$

where

M_n = 4035 ft-kips,
θ_{RL} = 27.65 mrads using Eq. 2,
C = 80, and
M_e = 5353 ft-kips.

Substituting the above quantities into Eq. 18 gives,

$$5353(1-27.65/80) = 3502 < 4035, \quad (35)$$

and thus the strength requirements at the pier are satisfied with a performance ratio of 3502/ 4035 = 0.86.

The negative bending section is then evaluated for strength 15' from the pier (moment redistribution is only permitted within one lateral bracing segment), service, fatigue, and constructibility requirements. These design checks are performed using the same processes and design equations that would be utilized in an elastic analysis and result in performance ratios equal to 0.50, 0.92, 0.66, and 0.77, respectively. Thus, the assumed geometry of the negative bending section results in an acceptable design.

It must then be verified that the positive bending section has adequate capacity to resist the elastic positive bending moments in addition to the redistribution moments at the strength limit state. Using Eq. 20 to evaluate this requirement at 36 ft from the abutment (the critical positive bending location) gives

$$M_n = 6198 \text{ ft-kips} > 4169 \text{ ft-kips} + M_{rdL} + (36/90)(M_{rdR} - M_{rdL}), \quad (36)$$

where:

M_{rdL} = 0 (at the abutment) and

M_{rdR} = $M_e - M_n = 5353 - 4035 = 1318$ ft-kips.

Substitition of these values into Eq. 36 then gives

$$M_n = 6198 > 4169 + 0 + (36/90)(1318 - 0) = 4696, \quad (37)$$

resulting in a performance ratio of 0.76 (4696/6198) at the strength limit state and indicating that the positive bending section has sufficient reserve capacity to resist redistribution moments. The performance ratios at the service *(0.70)*, fatigue *(1.00)*, and constructibility *(0.78)* limit states also indicate that the positive bending section design is adequate.

The high performance ratio (1.00) of the positive bending section and the desire to have a negative bending section that is not smaller than the positive bending section indicates that the girder geometry has been optimized for the assumed lateral bracing configuration. It is possible to then determine the optimal lateral bracing configuration using a procedure given in Righman (2005). Use of this procedure would show that the lateral bracing distance in the negative bending region cannot be appreciably altered and thus the lateral bracing configuration and cross-section geometry used above are optimal for this design.

AASHTO 2004 Design The same design criteria were also used to perform the girder design using the AASHTO (2004) moment redistribution procedures. The only difference between the two girder designs resulting from the AASHTO (2004) and rotation compatibility procedures is that a 1/4 in. greater top flange thickness is required in the negative bending region when using the AASHTO (2004) procedures. This increase in cross-section is required in the AASHTO (2004) design due to the requirement that the redistribution moment may not exceed 20% of the elastic moment.

Comparision of Rotation Compatibility and AASHTO 2004 Designs The comparison of the girder designs resulting from use of the rotation compatibility and AASHTO (2004) procedures suggests that reasonable girder designs producing economic savings result from use of the rotation compatibility procedures. Furthermore, it is noted that additional economic savings were possible using the rotation compatibility procedure, but were not incorporated due to the desire to avoid using a smaller cross-section in negative bending than in positive bending. The other primary difference between the rotation compatibility and AASHTO (2004) procedures is that longer lateral bracing distances are permitted at interior piers in the rotation compatibility procedures. While this only allowed for a small increase in the present example, this feature of the rotation compatibility procedures has significant applications in the rating of existing bridges that have bracing distances that violate Eq. 1.

Comparisons of rating examples performed using the rotation compatibility and LRFR procedures are also favorable towards the use of the rotation compatibility procedures (Righman 2005).

SUMMARY

This paper has demonstrated the development of the rotation compatibility procedure, which was formulated through direct comparison of the required and available rotations. These procedures were then further developed into design and rating specifications for use with continuous-span I-girders. An illustrative example demonstrating the use of these specifications was also presented. This

example demonstrates that use of the rotation compatibility procedures is convenient and results in rational economic savings.

REFERENCES

AASHTO. (2003). "Guide Manual for Condition Evaluation and Load and Resistance Factor Rating (LRFR) of Highway Bridges", 1st Edition, Washington, DC.

AASHTO. (2004). "LRFD Bridge Design Specifications", 3rd Edition, Washington, DC.

Righman, J. E. (2005). "Rotation Compatibility Approach to Moment Redistribution for Design and Rating of Steel I-Girders", Doctoral Dissertation, West Virginia University, Morgantown, WV.

Righman, J. E. and K. E. Barth. (2005). "Rotation Capacity Requirements for Continuous-Span Steel Bridge Girders", *Proceedings Structural Stability Research Council*, Montreal, QC.

STABILITY OF COMPOSITE CFT COLUMNS UNDER FIRE LOADING

Amit H. Varma[1], *Sangdo Hong*[2], *Nestor Iwankiw*[3]

Abstract

This paper presents the development and verification of a detailed analytical approach for investigating the fundamental behavior of CFT columns under fire loading. This approach includes three sequential analysis steps, namely, fire analysis, heat transfer analysis, and stress analysis. The heat transfer and stress analyses are conducted using the 3D finite element method, while accounting for nonlinear temperature-dependent material thermal and mechanical properties. The analytical approach and models were verified by using them to predict the overall thermal and structural behavior of CFT columns with different material, geometric, loading, and fire protection parameters, and subjected to the standard fire test by different researchers around the world. The analytical predictions compare reasonably with the experimental results with some discrepancies and exceptions. Further investigations indicated that the *stability* of CFT columns under fire loading is influenced significantly by the column end conditions and axial load levels achieved in the experiments, and the discrepancies between the analytical and experimental results may have been caused by them. The analytical approach and models are recommended for investigating the fundamental behavior of CFT columns under realistic fire loading.

---

[1] Assistant Professor, Dept. of Civil and Env. Eng., Purdue University, 550 Stadium Mall Drive, West Lafayette, IN 47906; Ph (765) 496-3419; FAX (765) 496-1105; email: ahvarma@purdue.edu

[2] Grad. Resrch. Asst., Dept. of Civil and Env. Eng., Purdue Univ., email: hong20@purdue.edu

[3] Senior Engineer, Hughes Assoc. Inc., Suite 800 South, 8700 W. Bryn Mawr Ave., Chicago, IL., 60631. Ph No. (773) 714 4857, Email: niwankiw@haifire.com

Fire Resistant Design

Building structures are occasionally subjected to extreme fire loading events. The current building design codes, e.g., IBC 2003 and NFPA 2003, emphasize prescriptive fire resistant design provisions. These provisions prescribe minimum fire resistant rating (FRR) values for the components of the building structure (columns, beams, etc.) depending on the building use, occupancy, plan dimensions and height, active and passive fire resisting mechanisms, and construction materials. The FRR values are prescribed as the time duration of standard ASTM E119 (1999) fire loading (time-temperature *T-t* curve) that the components must resist without failing structurally or thermally.

Fire resistant design is achieved by selecting components (or fire protection) with design FRR values greater than the prescribed FRR values. The design FRR value can be determined by: (a) testing prototypes according to the ASTM E119 standard, or (b) standard calculation methods outlined in design guides (AISC 2003, IBC 2003) and based on the results of ASTM E119 tests. Thus, the ASTM E119 test forms the basis of the current fire resistant design provisions.

Composite CFT Construction

Steel-concrete composite construction combines the advantages of both steel and concrete construction materials. A typical example consists of structural steel frames with composite (concrete filled steel tube CFT) columns. This type of construction effectively combines the advantages of both steel (speed of construction) and reinforced concrete (economy, damping, and fire resistance) structures. It is popular abroad (Japan, China, and Australia), and is gaining popularity in the U.S.

Significant research has been conducted on the structural behavior of composite CFT columns and structures subjected to various static, cyclic, and dynamic loading conditions. These research results are being used to develop rational design provisions for CFT columns and structures located in non-seismic (AISC 2005, ECCS 2001), or seismic regions (FEMA 2000, AISC 2002). A major *potential* advantage of composite CFT construction is enhanced fire resistance due to the presence of concrete. Hence, their fire behavior has also been studied.

Standard Fire Tests of CFT Columns

The behavior of CFT columns subjected to fire loading has been investigated by conducting tests according to the ASTM E119 standard. These tests also provided the design FRR values required by the current design approach. Researchers at the National Research Council (NRC) of Canada conducted extensive studies on the fire behavior of CFT columns. They conducted standard fire tests on *fifty-eight* CFT columns including circular and square columns filled with; (a) plain concrete, (b) reinforced concrete, or (c) steel fiber-reinforced concrete (Kodur and McKinnon 2000). The CFT columns had diameters (D) or widths (b) ranging from 140 to 410mm, length-to-width (l/b) ratios ranging from 10 to 20, and concrete strengths (f'_c) ranging from 20 to 55 MPa.

The columns were subjected to constant axial load and heating in a specially designed and constructed furnace. The axial load was applied and maintained constant at values ranging from 10% to 60% of the factored axial load capacity. The fire loading was applied by increasing the air temperature inside the furnace according to the ASTM E119 T-t curve. Experimental results from these studies are presented in Lie and Stringer (1994), Lie and Kodur (1996). The heated CFT columns failed due to crushing or column buckling. Experimental results indicated that CFT columns filled with plain concrete have a fire resistance of approximately 2 hours, and columns filled with reinforced concrete or steel fiber-reinforced concrete have a fire resistance of 3 hours. Based on their findings, these researchers also developed design equations for predicting the FRR values for CFT columns.

Chinese researchers (Han et al. 2003) have conducted standard fire tests on eleven *rectangular* and square CFT columns with *fire protection*. The columns had widths (b) ranging from 200 to 350 mm, aspect ratios ranging from 1.5 to 2.0, length to width (l/b) ratios ranging from 10 to 25, and concrete f'_c ranging from 19 to 50 MPa. The steel and concrete material properties, and the fire proofing material thermal properties were reported. The columns were subjected to constant axial load (77% of the design load capacity) and the standard fire T-t curve. The experimental results included the thermal response of the CFT cross-sections, and the structural displacement-time responses of the columns. These results were used to evaluate the effects of various parameters

(section dimensions, load eccentricity ratio, and fire protection thickness), and to develop equations for predicting the design fire resistance.

Japanese researchers (Sakumoto et al. 1994) have conducted standard fire tests on CFT columns made from *fire-resistant* FR or conventional steel tubes. FR steel has better σ–ε behavior than conventional steels at elevated temperatures. The column specimens were 300 mm square tubes with wall thickness equal to 9 mm, length equal to 3000 mm, and filled with 38 MPa strength concrete. Eighteen CFT columns were tested in a special furnace built at the Japan Building Research Corporatio. The parameters included were the steel type, the fire protection type, the axial loading magnitude, and the load eccentricity. Their experimental results indicated that: (a) using FR results in better fire resistance, (b) columns without reinforcement are sensitive to eccentric loading, (c) using even small amounts of fire protection results in good resistance.

Prior Analytical Models

NRC researchers (Lie 1994, Lie and Irwin 1995) have developed and validated analytical models for predicting the fire resistance of CFT columns. These models simulate the heat transfer from the furnace air (controlled to follow the ASTM *T-t* curve) to the column surfaces and through the composite CFT cross-section using the finite difference approximation of the complete heat balance equation. Temperature-dependent thermal properties (based on values in research literature) were used for the steel and concrete materials of the CFT cross-section. The results from the thermal analysis included the *T-t* curves for the surfaces and points in the cross-section.

The structural response of the column was determined by adapting the conventional fiber model approach. The CFT cross-section was discretized into fibers, and temperature-dependent uniaxial σ–ε curves were assumed for the materials. Additional assumptions included: (a) plane sections remain plane, (b) linear curvature variation along column length, (c) no slip, and (d) no transverse interaction between the steel and concrete. The structural response was determined by assuming the magnitude of curvature and axial strain and computing

iteratively the section stress-state and internal forces for equilibrium at each time step.

These analytical models were found to predict the experimental results with reasonable accuracy, and formed the basis of models developed by other researchers (Han et al. 2003). However, they include several assumptions that are not justified based on experimental behavior or detailed analytical studies. Additionally, the results from the analytical simulations do not provide knowledge of the fundamental behavior and the complex multiaxial stresses and strains in the column at failure.

Currently, there is a significant need for more *detailed* analytical models that can be used to investigate fundamental behavior or conduct parametric studies for *non-standard realistic* fire loading. These models are needed to develop fundamental knowledge of fire-structure interaction behavior, and to conduct parametric studies for eventually developing performance-based design provisions (Sunder et al. 2005).

Proposed Analytical Approach

This paper presents the development and verification of a detailed analytical approach for predicting the behavior of CFT columns subjected to fire loading. This approach consists of three sequential analysis steps, namely: (1) fire analysis, (2) nonlinear heat transfer analysis, and (3) nonlinear stress analysis, where the results from each analysis step are required to continue analysis in the subsequent step.

The first step (fire analysis) simulates the heat transfer from the fire source to the *surface* of the structural component. It is done using the Fire Dynamics Simulator program (FDS; McGrattan 2005), developed by the researchers at the NIST-BFRL. FDS is a computational fluid dynamics (CFD) model that numerically solves a form of the Navier-Sokes equations to simulate the heat transferred by radiation and convection to the surfaces of the structure. The analysis results include gas temperatures and velocities within the compartment, and the *T-t* curves for the surfaces of the structural component.

The surface *T-t* curves define the thermal loading for the second step (nonlinear heat transfer analysis), which simulates the heat transfer through the cross-section and along the height. This analysis is

conducted using the 3D finite element method and ABAQUS (2003), which is commercially available finite element analysis software. The analysis simulates the heat conduction by using a finite element formulation of the first variation of the basic energy balance equation together with Fourier's law. The results include the *T-t* curves for all nodes of the finite element model (mesh).

The nodal *T-t* curves define the thermal loads for the third (nonlinear stress analysis) step, which determines the structural response of the component subjected to structural and thermal loads. It is also conducted using the finite element method and ABAQUS (2003). The finite element meshes (node locations) for the heat transfer and stress analyses have to be identical to use the nodal *T-t* curves effectively. This analysis includes the effects of thermal deformations, geometric nonlinearity, and temperature-dependent material nonlinear constitutive relationships. The results from the analysis include the complete time history of deformations, 3D stresses, and strains in the component.

CFT Column Specimen Details

The analytical approach was verified by using it to predict the behavior of CFT columns tested according to the *standard* ASTM E119 fire test by different researchers around the world (identified earlier in this paper). The analytical approach was used to predict the behavior of ten CFT columns with different material, geometric, axial loading, and fire protection parameters. Table 1 lists these ten CFT column specimens with their cross-section dimensions, length, reinforcement, steel yield stress f_y, concrete strength f'_c, fire protection type, and load eccentricity.

Columns 1-3 in Table 1 were tested by NRC researchers (Lie and Irwin 1995) in Canada. These columns are conventional square CFTs with no fire protection. The standard fire tests were conducted using a specially designed and constructed column furnace, the details of which were provided by Lie (1980). The researchers reported the *measured* steel yield stress (f_y) and concrete strength f'_c for each specimen. They also reported temperature-dependent thermal (conductivity, specific heat) and mechanical properties (uniaxial σ–ε curve) for the steel and concrete materials based on values in literature and test results. All three steps of the analytical approach were used to simulate the

behavior of columns 1-3. The first (fire analysis) step was used to simulate the convection and radiation heat transfer within the furnace chamber, and determine the CFT surface *T-t* curves. The second and third steps simulated the nonlinear heat transfer and structural analyses.

Columns 4-5 were tested in Japan by Sakumoto et al. (1994). They were made from fire resistant FR steel. Column 4 is a hollow FR steel tube, and column 5 is a concrete filled FR steel tube with ceramic fire protection. The standard fire tests were conducted in a special furnace at the Japan Building Research Corporation. Sakumoto et al. did not provide details of the furnace chamber, or the thermal properties of the ceramic fireproofing material. They provided the measured steel yield stress f_y, the measured concrete strength f'_c, and the *measured* steel surface *T-t* curves for the column specimens. Therefore, the second and third steps of the analytical approach were used directly to simulate the behavior of the columns 4 and 5.

Columns 6-10 were tested in China by Han et al. (2003). Columns 6 and 7 are *rectangular* concrete filled steel tubes with aspect ratios of 1.5 and 2.0, respectively. Columns 8, 9, and 10 are conventional *square* CFTs. As shown in Table 1, Column 10 is the only specimen subjected to eccentric axial loading. All the column specimens (6-10) have spray-applied fire proofing material. The standard fire tests were conducted in a special furnace in Tianjin, China. Han et al. provided some details regarding the furnace chamber and the fire proofing material thermal properties. However, these were not as complete as those provided by Lie (1980) and Lie and Irwin (1995). Fortunately, Han et al. also provided the measured surface *T-t* curves for the column specimens. Therefore, the second and third steps of the analytical approach were used directly to simulate the behavior of the columns 6-10.

Fire Analysis Models and Results

Fire analysis was conducted for columns 1-3 using FDS (McGrattan 2005). A model of the furnace chamber was developed using FDS. Symmetry was considered and only a quarter (1/4) of the furnace and CFT column in the center was modeled in order to reduce the computational time. The planes of symmetry were specified with the mirror function in FDS. The ceiling and floor were specified thermal

boundary conditions to simulate no heat loss. The walls were used as the source of heating within the furnace. They were specified with a hot air blowing velocity of 0.5 m/s to heat the furnace chamber. The hot air was specified to follow the ASTM standard T-t curve. A low fluid velocity equal to 0.5 m/s was used in order to reduce high fluid velocity influence. No-slip condition was assumed for the CFT column surfaces. The pressure inside the furnace was kept constant at the atmospheric pressure. Figure 1 shows the plan and elevation view of the FDS model of the furnace with CFT column inside.

The results from the FDS analysis included: (a) the air temperatures 25 mm from the column surfaces, and (b) the column surface temperatures. These temperatures were measured at 50 mm intervals along the column height, and were found to be reasonably uniform with respect to column height. The air temperatures were verified by comparing with the ASTM E119 *T-t* curve. The predicted surface temperatures were verified by comparing with the experimental and analytical results reported by Lie and Irwin (1995).

Figure 2 compares the surface T-t curves predicted by the FDS models with those measured experimentally and predicted analytically by Lie and Irwin using the finite difference method (FDM). The comparisons are shown for columns 1, 2, and 3 that were 200, 250, and 300 mm squares in cross-section, respectively. Figure 2 shows that the surface *T-t* curves predicted by the FDS model compare favorably with the experimental results and the FDM predictions. The FDS model slightly overestimates, while the FDM model slightly underestimates the column surface temperatures. Figure 2 also indicates that the size of the CFT column has small influence on the surface *T-t* response. This is probably because the variations in column size (200-300 mm) were small compared to the overall furnace setting.

Heat Transfer Analysis Models and Results

The column surface *T-t* curves were specified as thermal loading for conducting the nonlinear heat transfer analyses using the finite element method and ABAQUS. The surface *T-t* curves obtained from the FDS analyses were used to specify the thermal loading for columns 1-3. The

measured surface *T-t* curves were used to specify the thermal loading for columns 4-10 for reasons explained earlier.

The 3D finite element models for conducting the heat transfer analyses were developed and analyzed using ABAQUS. The concrete infill and the steel tube were modeled using eight-node continuum and four-node shell *heat transfer elements*, respectively. The steel and concrete thermal properties, i.e., the thermal conductivity and the thermal capacity (specific heat x density) were adapted based on values reported in the literature including Lie and Irwin (1995). These temperature-dependent thermal properties for steel and concrete are provided in Table 2. The effects of *moisture evaporation* from the concrete due to heating were modeled by specifying a latent heat for the concrete elements. The specified latent heat was equal to the *measured* moisture content (6-7% by weight) multiplied by the latent heat of water (2.3×10^6 J/kg). The phase transformation corresponding to the latent heat was assumed to occur between 100 and 120°C.

The heat transfer analysis results include the thermal responses and *T-t* curves for all nodes of the CFT finite element models. These results were verified by comparing them with experimentally measured *T-t* curves reported by the researchers. For example, Figures 3(a), (b), and (c) compare the *T-t* curves predicted by the heat transfer analyses with those measured experimentally by Lie and Irwin (1995). These figures illustrate the favorable comparisons between the predicted and measured *T-t* curves at various points within the CFT sections. The slight differences are caused probably by variations in the material thermal properties and assumptions in the modeling approach.

The heat transfer analysis results also include the overall thermal responses of the CFT sections. For example, Figure 3(d) shows the temperature contours for column 1 after 160 minutes of standard fire loading. This figure illustrates the higher temperatures and significant variation through the section for CFTs without fire protection. Figure 3(e) shows the temperature contours for column 9 (with spray applied fire proofing) after 140 minutes of standard fire loading. This figure illustrates the lower temperatures and variation through the section for CFTs with fire protection.

Stress Analysis Models and Results

The 3D finite element models for conducting the nonlinear stress analyses were also developed and analyzed using ABAQUS. The finite element meshes for these models were identical to those for the corresponding heat transfer analyses. This is required when specifying the nodal *T-t* curves from the heat transfer analyses as the thermal loading for the subsequent stress analyses. The finite element models explicitly accounted for thermal deformations, geometric nonlinearity, and material inelasticity at elevated temperatures.

The concrete infill of the CFT columns was modeled using eight-node stress/displacement continuum elements. The steel tube was modeled using four-node stress/displacement shell elements. The steel tube was bonded (tied) to the concrete infill along the length of the column, except for the failure segment (length = 2 x width) located at the column midspan. The steel tube was unbonded and free to buckle locally within this region.

The *concrete damaged plasticity* model in ABAQUS was used to model the behavior of the concrete elements. This model is based on the damage-plastic model developed by Lee and Fenves (1998). It uses concepts of isotropic damaged elasticity in tension combined with non-associated multi-hardening plasticity in compression to model the complete inelastic behavior of concrete. The temperature-dependent uniaxial stress-strain (σ–ε–T) behavior of concrete is required to completely define this model. Therefore, the empirical σ–ε–T relationships for concrete presented by Lie and Irwin (1995) were used for columns 1-5, and those presented by Han et al. (2003) were used for columns 6-10. Both these σ-ε-T relationships are very similar. Figure 4(a) shows the concrete compression σ-ε-T curves for columns 1-5.

The *isotropic metal plasticity* model with the Von Mises yield surface, associated plastic flow, and isotropic strain hardening was used to model the behavior of the steel elements. The temperature-dependent uniaxial stress-strain (σ–ε–T) behavior of steel is required to completely define this mode. Therefore, the empirical σ-ε-T relationships for conventional steel presented by Lie and Irwin (1995) were used for columns 1-3 and columns 6-10, and the empirical σ-ε-T

relationships for FR steel presented by Sakumoto et al. (1994) were used for columns 4 and 5. These uniaxial σ–ε-T relationships for conventional and FR steel are shown in Figures 4(b) and (c).

Temperature-dependent thermal expansion coefficients (α) were specified for the steel and concrete materials. These values are given in Table 2. Geometric imperfections were added to the finite element model to stimulate global (column) and local buckling. The magnitude of the out-of-plane geometric imperfection along the column length was equal to the length L/1000. Fixed-end conditions were specified for columns 1-3 and 6-10. Pinned-end conditions were specified for columns 4-5. The finite element models were analyzed for combined axial loads (P) and thermal loading. The axial loads P (given in Table 1) were applied first and maintained constant while applying the thermal loading, which was specified using the nodal T-t curves obtained from the previous heat transfer analysis step.

The results from the finite element analyses included the complete deformation and 3D stress and strain histories for the CFT columns. Figure 5 shows the deformed shape of column 1 after 115 minutes of standard fire loading. This figure emphasizes the global and local buckling deformations of the CFT column 1 as it approaches failure. Figure 5(a) shows the deformed shape and the longitudinal strains (ε_{33}) in the concrete infill. Figure 5(b) shows the buckling shape and the longitudinal strain (ε_{22}) along with local buckling of the steel tube. These figures demonstrate the typical behavior and buckling failure mode for columns with fixed-end conditions. They compare favorably with the experimental observations and results.

Figures 6(a-i) present the axial displacement-time (δ-t) responses predicted by the finite element models, and compare them with those measured experimentally for columns 1-10. Converged solutions were obtained from the finite element analyses only up to the last point of the predicted δ-t curves. Figures 6(a-i) show that the predicted δ-t responses follow the *general trend* of experimental behavior, i.e., expansion in the early stages followed by shortening. Some of the analytical predictions compare favorably with the experimental results, for examples, columns 4 and 5 (Fig. 6 d and e). However, some of the

analytical predictions do not compare well with the experimental results, for examples, columns 2, 3, and 7 (Fig. 6 b, c, and g)

Parametric Sensitivity Studies

Further analytical investigations were conducted to: (a) identify the reasons for the differences between the analytical predictions and the experimental results, and (b) to evaluate the effects of various parameters on the analytically predicted δ-t responses. The parameters included in the study were (i) the column end conditions, (ii) the axial load level, (iii) the concrete strength f'_c, and (iv) the magnitude of geometric imperfection. The effects of these parameters on the δ-t responses for CFTcolumns were investigated analytically.

For example, Figures 7 and 8 show the relevant results from the analytical investigations of CFT columns 1 and 2. Figure 7(a) and (b) show that the column end conditions (simply supported, fixed, or intermediate fixity) have significant influence on the predicted δ-t responses of CFT columns. The time to failure reduced significantly as the end conditions changed from fixed, to partially restrained, to simply supported conditions.

Figure 8(a) and (b) show that the axial load level (P) also has a significant influence on the predicted δ-t responses for CFT columns. The time to failure and the initial expansion decreased significantly when the applied load was increased by 5% of the section axial load capacity P_o, which is equal to the sum of yield strength of the steel tube and 85% of the strength of the concrete infill ($P_o=A_s f_y+0.85f'_c A_c$). The time to failure and the initial expansion increased significantly when the applied load was decreased by 5% or 10% of P_o.

Variations in the concrete strength (f'_c) were found to have small influence on the predicted δ-t responses of the columns subjected to low or medium applied load level (columns 1-3). Variations in f'_c have greater effect on the columns subjected to higher load levels. Variations in geometric imperfections (from L/500 to L/1500) also had small influence on the predicted δ-t responses of CFT columns.

Therefore, the differences between the predicted and experimental δ-t responses are caused probably by: (1) slight changes in the columns end conditions or applied load levels achieved in the experiments, or (2) the differences between the assumed empirical stress-strain-temperature (σ–ε-T) relationships and the thermal expansion-temperature (α-T) for the concrete and steel and the actual behavior of the materials.

Summary and Conclusions

The paper developed and verified a detailed analytical approach for investigating the fundamental behavior of CFT columns under fire loading. This approach consists of three sequential analysis steps, namely, fire analysis, heat transfer analysis, and stress analysis. The results from each step are required to continue the analysis in the subsequent step. The analytical approach and models were verified by using them to predict the overall thermal and structural behavior of CFT columns tested under standard fire loading by various researchers around the world. The analytical predictions from the fire analysis and heat transfer analysis steps compared favorably with the corresponding experimental results. The results from the stress analysis followed the general trends of the experimental results with some discrepancies.

Further investigations were conducted to identify the causes for the discrepancies between the analytical and experimental results. The findings indicate that the column end conditions and axial load levels have a significant influence on the structural behavior and failure of the CFT columns subjected to standard fire loading. The discrepancies are caused probably by slight changes in the column end conditions or applied axial load levels achieved in the experiments, or assumptions in the modeling approach including material σ–ε-T curves.

The analytical approach and models provide knowledge of the overall thermal and structural behavior of CFT columns under standard fire loading. They can be used to further investigate the fundamental behavior of CFT columns subjected to realistic fire loading conditions.

Acknowledgements

This research was funded by NSF Grant CMS-0453913.

References

ABAQUS. (2003). *ABAQUS/Standard Version 6.3 User's Manuals: Volumes I-III*, Hibbitt, Karlsson, and Sorenson, Inc., Pawtucket, RI.

AISC (2003). *Design Guide 19- Fire Resistance of Structural Steel Framing.* AISC, Chicago, IL

AISC (2005). *Specification For Structural Steel Buildings.* AISC, Chicago, IL.

AISC (2002). *Seismic Provisions for Structural Steel Buildings.* AISC, Chicago, IL.

ASTM. (1999). "Standard Test Methods for Fire Testing of Building Construction and Materials," *E119*, American Society for Testing & Materials, W. Conshohoken, PA.

ECCS (2001). *Model Code on Fire Engineering*, ECCS Technical Committee 3, European Convention forConstructional Steelwork, First Edition.

FEMA-350 (2000). "Recommended Seismic Design Criteria for New Steel Moment-Frame Buildings."*FEMA 350/July 2000*, Building Seismic Safety Council, Washington, D.C.

Han, L. H., Yang, Y. F., and Xu, L. (2003). "An Experimental Study and Calculation on the Fire Resistance of Concrete-Filled SHS and RHS Columns," *J. of Constr. Steel Res.*, 59(4), 427-452.

IBC. (2003). *International Building Code*, Intl. Code Council, Inc., Falls Church, VA.

Kodur, V. K. R., and Mackinnon, D. H. (2000). "Design 0f Concrete-Filled Hollow Structural Steel Columns for Fire Endurance," *Eng. Journal*, 1st Qtr., 13-24.

Lee, J., and Fenves, G. L. (1998). "Plastic-Damage Model for Cyclic Loading of Concrete Structures," *J. of Eng. Mech.*, 124(8), 892-900.

Lie, T. T. (1980). "New Facility to determine Fire Resistance of Columns," Division of Building Research, National Research Council of Canada.

Lie, T. T., and Irwin, R. J. (1995). "Fire Resistance of Rectangular Steel Columns Filled with Bar-Reinforced Concrete," *J. of Struct. Eng.*, 121(5), 797-805.

Lie, T.T. (1994). "Fire Resistance of Circular Steel Columns Filled with Bar-Reinforced Concrete," *Jour. of Struct. Eng.*, Vol. 120, No. 5, pp. 1489 - 1509.

Lie, T. T., and Stringer, D. C. (1994). "Calculation of Fire Resistance of Steel Hollow Structural Steel Columns Filled with Plain Concrete," *Can. J. of Civil Eng.*, 21(3), 382-385.

Lie. T.T. and Kodur, V.K.R. (1996). "Fire Resistance of Steel Columns Filled with Bar-Reinforced Concrete," *Jour. of Struct. Eng.*, ASCE, Vol. 122, No. 1, pp. 30-36.

McGrattan, K. (2005) "Fire Dynamics Simulator (Version 4). Tech. Reference Guide." *NIST Sp. Pub.1018.*

NFPA (2003). *Building Construction and Safety Code – NFPA 5000.* NFPA.

Sakumoto, Y., Okada, T., Yoshida, M., and Takasa, S. (1994). "Fire Resistance of Concrete-Filled, Fire-Resistant Steel-Tube Columns," *J. of Matrls. In Civil Eng.*, 6(2), 169-184

Sunder, S.S., Gann, R.G. et al., (2005). "Final Report of the National Consortium Safety Team on the Collapses of the World Trade Center Towers (Draft)." *NIST NCSTAR 1 (Draft).* NIST, U.S. Dept. of Commerce, Gaithersburg, MA.

Table 1. CFT column details

Column	Cross-Section (mm x mm x mm)	Length (mm)	Reinforcement	f_y (MPa)	f'_c (MPa)	Load (kN)	Eccentricity (mm)	Fire Protection
1	200x200x6.35	3810	4 x 16 mm	350	47	500	0	-
2	250x250x6.35	3810	4 x 16 mm	350	47	1440	0	-
3	300x300x6.35	3810	4 x 25 mm	350	47	2000	0	-
4	300x300x9	3500	-	357.9		2020	0	-
5	300x300x9	3500	-	357.9	37.5	1350	0	ceramic
6	300x200x7.96	3810	-	341	49	2486	0	spray-type
7	300x150x7.96	3810	-	341	49	1906	0	spray-type
8	219x219x5.30	3810	-	246	18.7	950	0	spray-type
9	350x350x7.70	3810	-	284	18.7	2700	0	spray-type
10	350x350x7.70	3810	-	284	18.7	1670	52.5	spray-type

Table 2. Steel and concrete thermal properties at elevated temperatures

Steel				Concrete			
Temp. (C)	Thermal Conductivity *k (W/m-C)*	Thermal Capacity *(10^6 J/m^3-C)*	Thermal Expansion *α (10^{-6} C^{-1})*	Temp. (C)	Thermal Conductivity *k (W/m-C)*	Thermal Capacity *(10^6 J/m^3-C)*	Thermal Expansion *α (10^{-6} C^{-1})*
0	48.0	3.30	12.0	0	1.355	2.566	6.0
100	45.8	3.70	12.4	100	1.355	2.566	6.8
200	43.6	4.10	12.8	200	1.355	2.566	7.6
300	41.4	4.50	13.2	300	1.344	2.566	8.4
400	39.2	4.90	13.6	400	1.220	2.566	9.2
500	37.0	5.30	14.0	410	1.207	4.330	9.3
600	34.8	5.70	14.4	445	1.164	2.565	9.6
650	33.7	5.90	14.6	500	1.096	2.566	10.0
700	32.6	9.30	14.8	600	0.972	4.169	10.8
725	32.1	11.00	14.9	635	0.928	4.730	11.1
800	30.4	4.55	15.2	700	0.848	15.543	11.6
900	28.2	4.55	15.6	715	0.829	18.038	11.7
1000	28.2	4.55	16.0	785	0.742	2.565	12.3
1100	28.2	4.55	16.0	800	0.723	2.566	12.4
1200	28.2	4.55	16.0	900	0.599	2.566	13.2
				1000	0.475	2.566	14.0
				1100	0.351	2.566	14.8
				1200	0.227	2.566	15.6

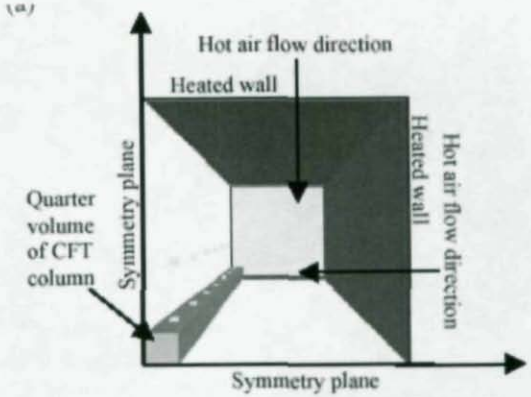

Figure 1. FDS model of NRCCfurnace with CFT column

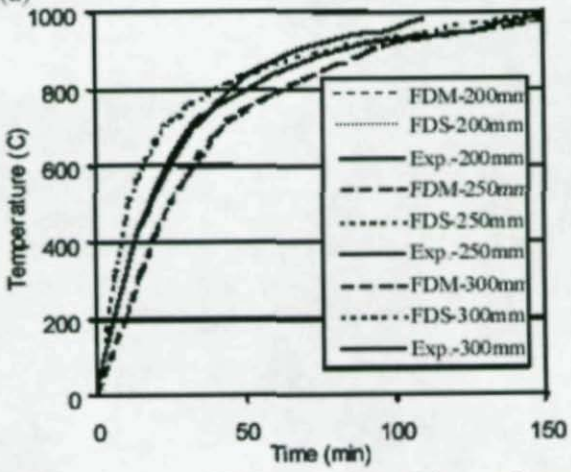

Figure 2. Comparisons of FDS predictions with experimental and FDM results

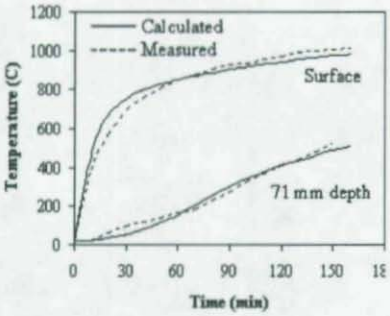

Fig. 3(a). *T-t* responses in col. 1

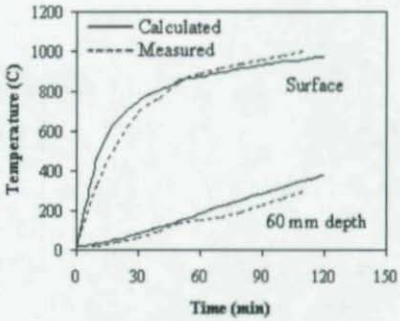

Fig. 3(b). *T-t* responses in col. 2

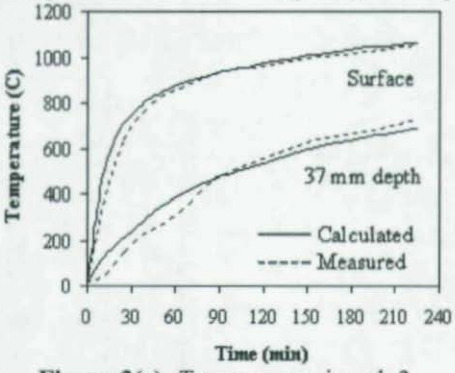

Figure 3(c). *T-t* responses in col. 3

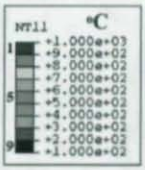

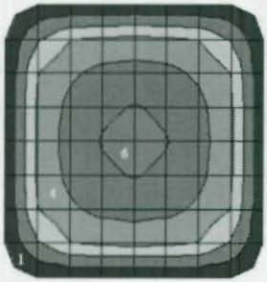

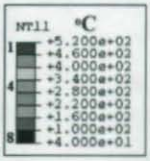

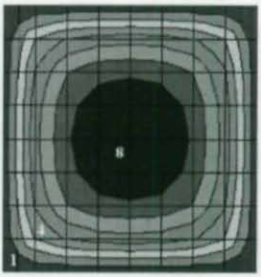

Fig. 3(d). Col. 1 temp. at t=160 min. **Fig. 3(e).** Col. 9 temp. t=140 min

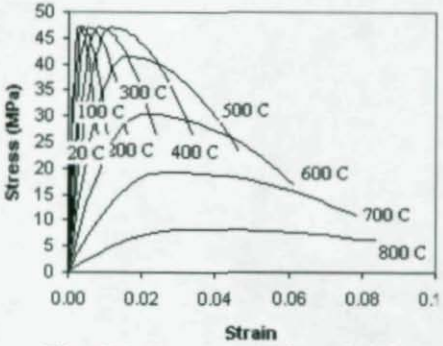

Fig. 4(a) Conc. σ-ε-T for col. 1-3

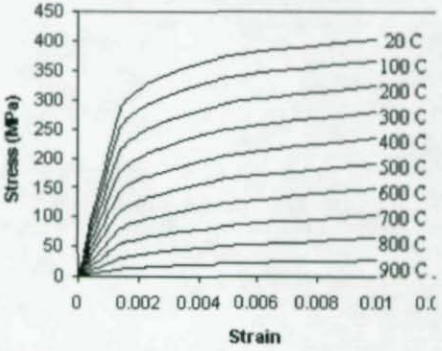

Fig. 4(b) Steel σ-ε-T for col. 1-3

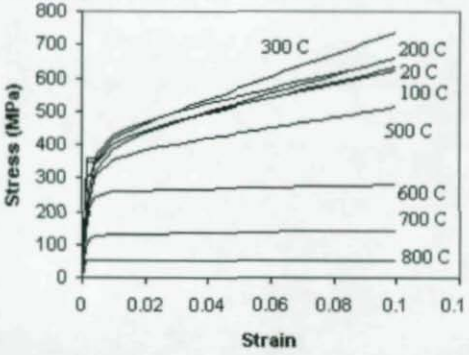

Fig. 4(c) Steel σ-ε-T for col. 1-3

(a) concrete infill

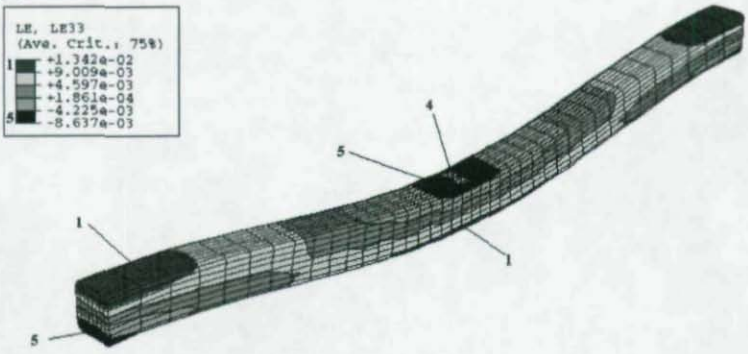

(b) steel tube

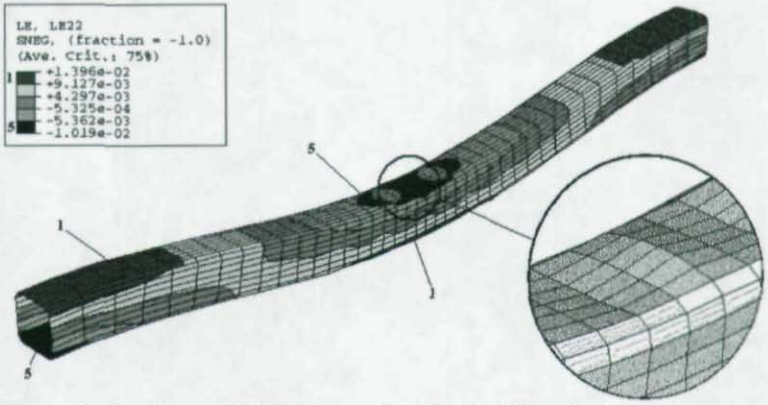

Figure 5. Buckling of CFT column 1 at time = 115 minutes: (a) deformation of concrete infill, and (b) deformation of steel tube with local buckling enlarged

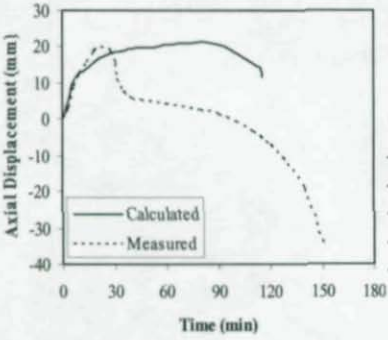

Fig. 6(a). δ-t of col. 1

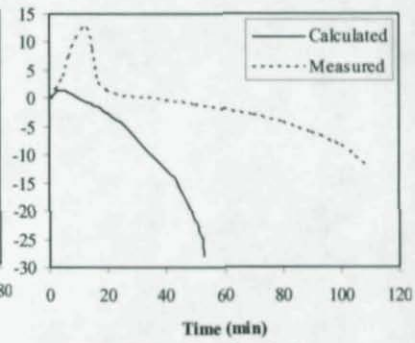

Fig. 6(b). δ-t of col. 2

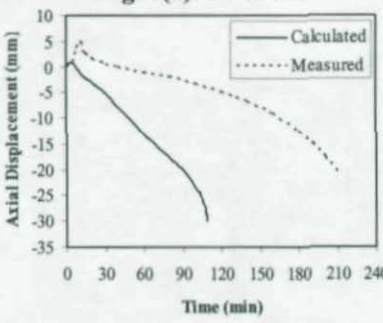

Fig. 6(c). δ-t of col. 3

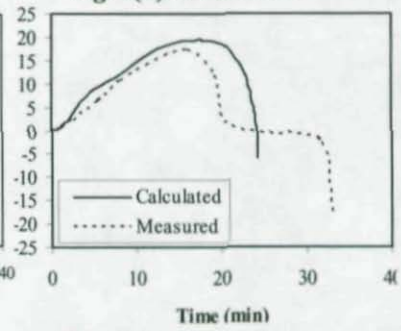

Fig. 6(d). δ-t of col. 4

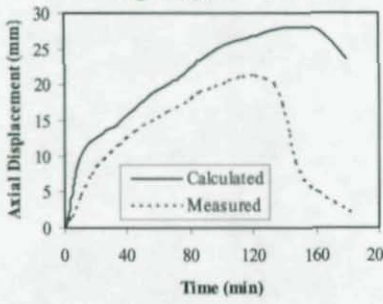

Fig. 6(e). δ-t of col. 5

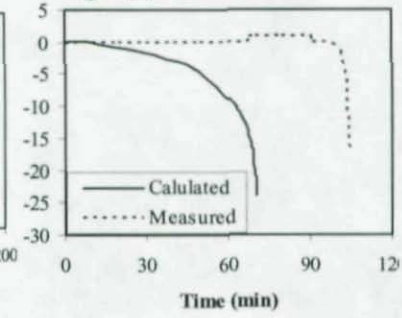

Fig. 6(f). δ-t of col. 6

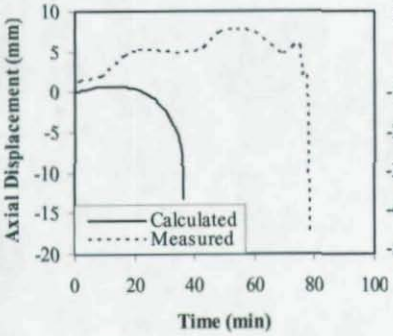

Fig. 6(g). δ-t of col. 7

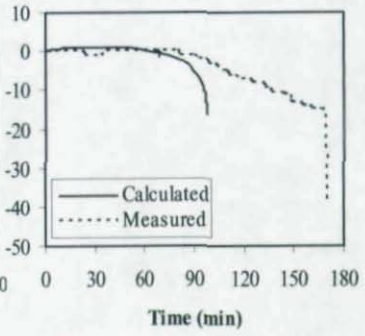

Fig. 6(h). δ-t of col. 8

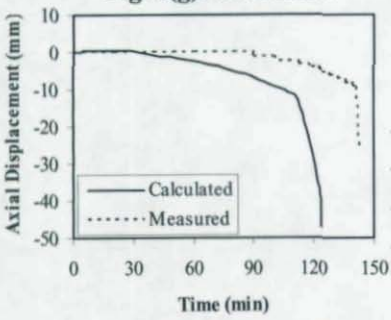

Fig 6(i). δ-t of col. 9

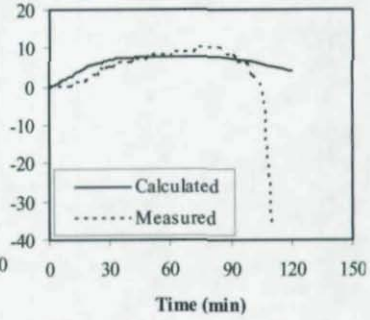

Fig. 6(j). δ-t of col. 10

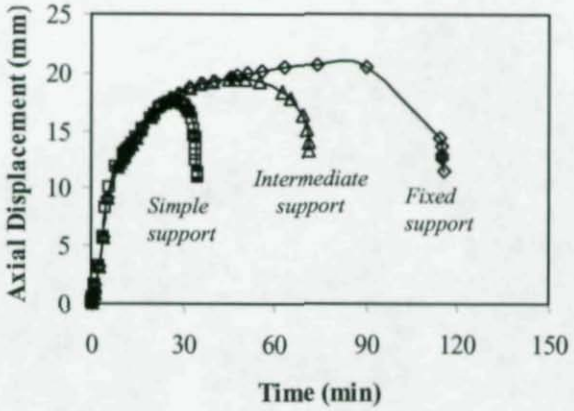

Fig. 7(a). Influence of end conditions on col. 1

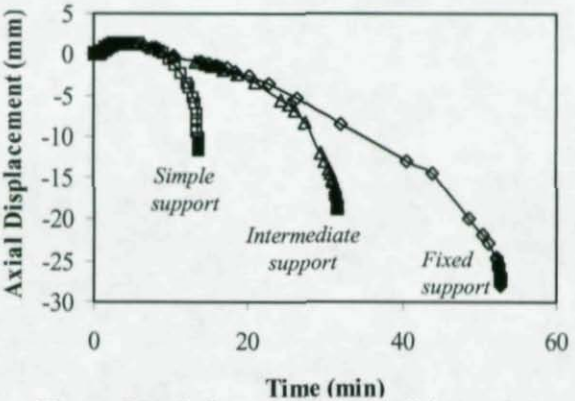

Figure 7(b). Influence of end conditions col. 2

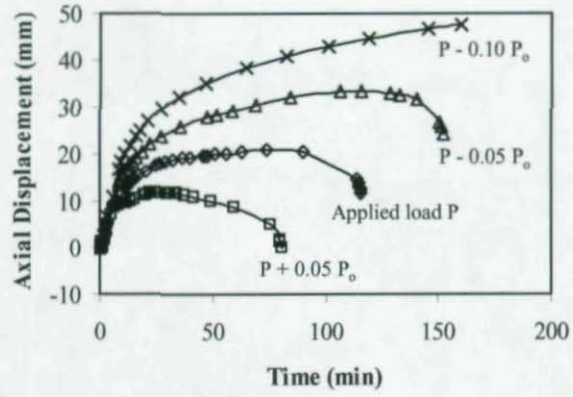

Fig. 8(a). Influence of load levels on col. 1

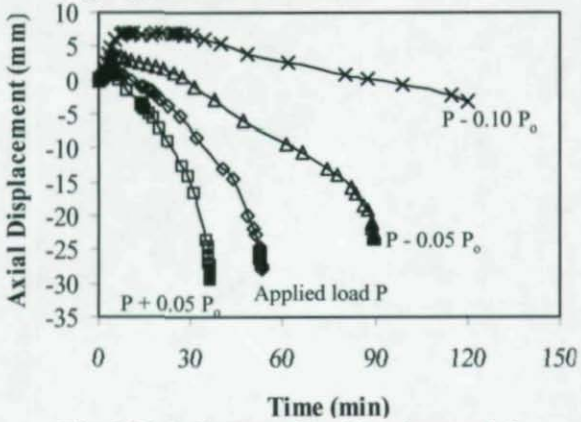

Fig. 8(b). Influence of load levels on col. 2

FURTHER STUDIES ON THE LATERAL-TORSIONAL BUCKLING OF STEEL WEB-TAPERED BEAM-COLUMNS

Gabriel A. Jiménez[1]

ABSTRACT

This paper presents solutions for the elastic and inelastic lateral-torsional buckling of steel web tapered beam-columns. The beam-columns are subjected to an axial force and to bending moments applied at both ends of the member.

Two different computational procedures are utilized; the first method is based on the finite difference method using a direct discretization of the differential equations of lateral-torsional buckling. The coefficients appearing in the finite difference equations are determined considering the reductions of the flexural and torsional stiffnesses due to yielding in the inelastic range. The effects of residual stresses are included. The resulting simultaneous equations are then set up to compute the buckling determinant which yields the critical load. The second method investigated is based on the finite element method using a commercially available software (ANSYS).

The results of the numerical solutions are presented and compared to the design equations in the current AISC-LRFD Specification [1999]. Comparisons are also made with various test results. Recommendations are made for changes and improvements in the current design criteria.

INTRODUCTION

The general behavior of a typical beam-column is illustrated in Figure 1, where the relationship between the applied end-moment M_o and the resulting end-slope θ is shown for a wide-flange member bent about its strong-axis, in which the length as well as the axial force P is assumed to remain constant as the moment M_o is increased from zero to its maximum value and past the maximum moment into the unloading zone.

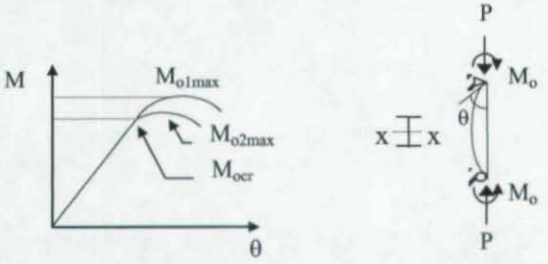

Figure 1.- M-θ curves for beam-columns

The optimum performance of the beam-column is reached if failure is due to excessive bending in the plane of the applied moment, and this behavior is represented by the upper branch of the curve in Figure 1. The corresponding maximum moment is M_{o1max}. If no lateral bracing is provided, failure will be due to lateral-torsional buckling and the resulting moment is M_{o2max} represented by the lower branch of the curve in Figure 1. The additional incremental moment represented by M_{o2max} beyond M_{ocr} is small, and, therefore, the bifurcation point is considered to reasonably determine the buckling limit to the beam-column. The work described in this paper deals with the determination of the value of M_{ocr} for web-tapered beam-columns.

DIFFERENTIAL EQUATIONS OF LATERAL-TORSIONAL BUCKLING

---

[1] Gabriel A. Jiménez, Ph.D., P.E., Principal, Walter P. Moore and

The differential equations governing the lateral-torsional buckling of tapered members subjected to centroidal axial forces P and to end moments M_o and ρM_o are given by Jimenez [1998] and are repeated here for convenience:

$$B_x(z)\frac{d^2v}{dz^2} + Pv - M_o\left[\rho + (1-\rho)\frac{z}{L}\right] = 0 \qquad (1a)$$

$$B_y\frac{d^2u}{dz^2} + Pu - \beta\left[M_o\left\{\rho + (1-\rho)\frac{z}{L}\right\} - P\,y_o(z)\right] = 0 \qquad (1b)$$

$$C_w(z)\frac{d^3\beta}{dz^3} - \left[C_T(z) - \overline{K}(z)\right]\frac{d\beta}{dz} - \left[M_o\left\{\rho + (1-\rho)\frac{z}{L}\right\} - P\,y_o(z)\right]\frac{du}{dz} + M_o\frac{u}{L}(1-\rho) = 0 \qquad (1c)$$

The beam-column prescribed by the above differential equations is shown in Figure 2. It is subjected to end bending moments M_o at $z = L$ and ρM_o at $z = 0$, where "z" is the coordinate axis along the undeformed centroidal axis and "L" is the length of the member. The coefficient "ρ" is the ratio of the end moments. The deformations of the shear center are: "*u*" in the x-direction, "*v*" in the y-direction and the cross-section twists about the shear center an angle "β".

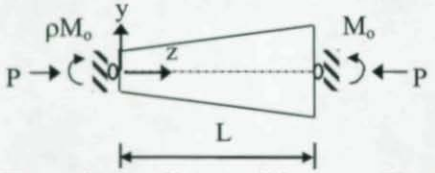

Figure 2.- Loading condition

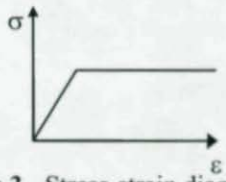

Figure 3.- Stress-strain diagram

Associates, 3131 Eastside; Houston, TX 77098

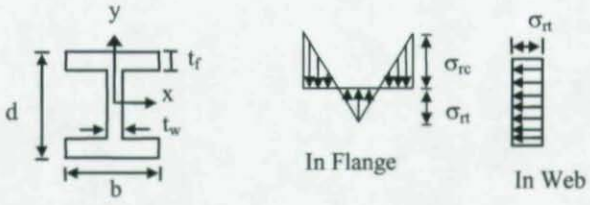

Figure 4.- Residual stress pattern

The stress-strain diagram of the material is shown in Figure 3. The residual stress pattern is symmetric and the residual stresses are distributed in the flanges and in the web as shown in Figure 4. A value of $\sigma_{rc}/\sigma_y = 0.3$ is used in this work.

The coefficients $B_x(z)$, B_y, $C_T(z)$, $C_w(z)$, $y_o(z)$ and $\overline{K}(z)$ in the differential equations are defined as follows: $B_x(z)$ is the bending stiffness about the x-axis; B_y is the bending stiffness about the y-axis; $C_T(z)$ is the St. Venant's torsional stiffness; $C_w(z)$ is the Warping stiffness; $y_o(z)$ is the distance between the centroid "C" and the shear center "S" in the plane of symmetry; $\overline{K}(z) = \int_A \sigma s^2 dA$ where: σ = is the stress on any cross-sectional element dA (positive in compression) and "s" is the distance of element dA from the shear center.

These coefficients vary with respect to the coordinate "z" to account for the non-uniform variation of the cross-section properties along the length of the column. Also, when the beam-column is in the inelastic range the coefficients will vary with the different patterns of the yielding.

FINITE DIFFERENCE SOLUTION

The lateral-torsional buckling of tapered beam-columns is determined by using equations (1b) and (1c) where the cross-section coefficients are variable with respect to "z". Therefore, a direct solution is difficult and a numerical method using a finite-difference solution is applied. The finite difference equations corresponding to the equations (1b) and (1c) at each station by first-order central differences becomes:

$$u_{i-1}\left[\mathrm{By}(i)\right]+u_i\left[\mathrm{P}h^2-2\mathrm{By}(i)\right]+u_{i+1}\left[\mathrm{By}(i)\right]+\beta_i\left[\lambda(i)h^2\right]=0 \qquad (2a)$$

$$u_{i-1}\left[-\lambda(i)h^2\right]+u_i\left[\frac{2\mathrm{M}_0(1-\rho)h^2}{n}\right]+u_{i+1}\left[\lambda(i)h^2\right]+\beta_{i-2}\left[-\mathrm{C_w}(i)\right]+$$

$$\beta_{i-1}\left[2\mathrm{C_w}(i)+\mathrm{C_T}(i)h^2\left(1-\frac{\overline{\mathrm{K}}(i)}{\mathrm{C_T}(i)}\right)\right]+\beta_{i+1}\left[-\left\{2\mathrm{C_w}(i)+\mathrm{C_T}(i)h^2\left(1-\frac{\overline{\mathrm{K}}(i)}{\mathrm{C_T}(i)}\right)\right\}\right]+$$

$$\beta_{i+2}\left[\mathrm{C_w}(i)\right]=0 \qquad (2b)$$

where: $\lambda(i)=\mathrm{Py}_0(i)-\mathrm{M}(i)$, $\quad \mathrm{M}(i)=\mathrm{M}_0\left[\rho+(1-\rho)\frac{i}{n}\right]$

The ends of the beam-column are allowed to rotate, the end sections are free to warp, and the ends of the member are not permitted to twist or to translate. These boundary conditions can be written as follows: $u_o = 0$, $u_n = 0$, $\beta_{-1} = -\beta_1$, $\beta_{n+1} = -\beta_{n-1}$, $\beta_o = 0$, $\beta_n = 0$.

This leads to a set of simultaneous algebraic equations in the lateral displacement u and the rotation β at a number of discrete points spaced at $h = L/n$, in which n is an odd number to which the beam-column is divided. This set of simultaneous equations may be written in matrix form: $[\mathrm{A}]\begin{Bmatrix} u \\ \beta \end{Bmatrix}=0$. In this equation the matrix [A] is a set of the coefficients A_{ij} representing combinations of the cross-section

properties (B_y, $C_T(z)$, $C_w(z)$, $y_o(z)$, and $\overline{K}(z)$), the load parameters (P and M_o) and the length of the member (L).

In order to compute the stiffness of a cross-section it is necessary to know how much of the section is plastic and how much of the section is elastic, and where the corresponding regions are located on the cross-section. The non-dimensionalized M/M_y, ϕ/ϕ_y, P/P_y, relationships about the strong-axis for an I-shape section have been determined by Jimenez [1998]. Figure 5 shows these relationships for the following cases of yielding:

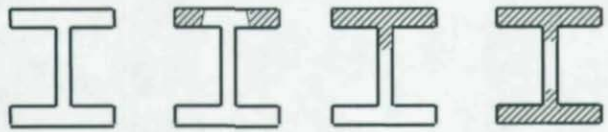

Figure 5.- Yielded patterns for wide-flange cross-section

In outline form, the steps that are used in computing the critical moment M_{ocr} for steel web-tapered beam-columns are as follows:

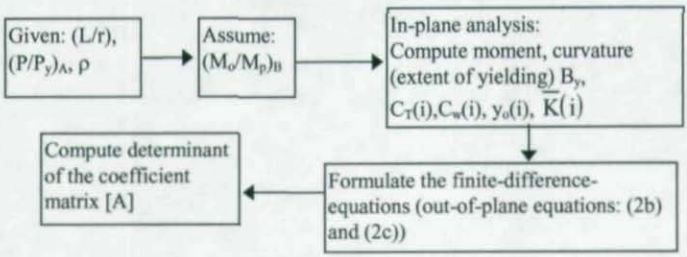

This process is repeated for different load levels until a zero value for the determinant is found.

FINITE ELEMENT STABILITY ANALYSIS USING ANSYS

To create the finite element model, several steps had to be performed including element selection, laying out the mesh and determining boundary conditions.

The finite element mesh is comprised of BEAM188 elements. BEAM188 elements are suitable for analyzing slender to moderately stubby/thick structures. This element is based on Timoshenko beam theory. Shear deformation effects are included. The BEAM188 is a quadratic beam element in 3-D. This element is well-suited for linear, large rotation, and/or large strain nonlinear applications. Furthermore, the provided stress stiffness terms enable the elements to analyze flexural, lateral, and torsional stability. The cross-section associated with the element may be linearly tapered. Elasticity and plasticity models are supported.

Figure 6 presents a typical tapered beam-column member as modeled in ANSYS.

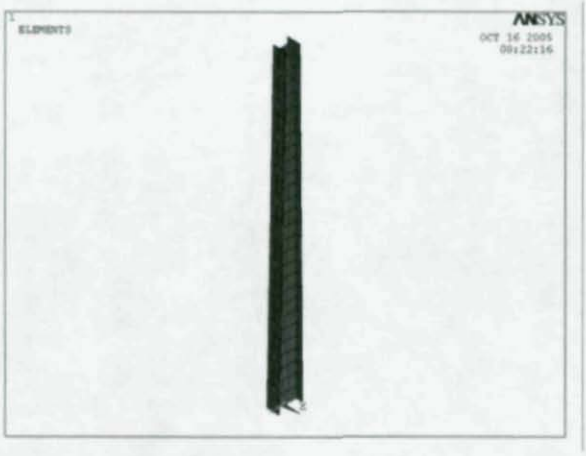

Figure 6.- Discretization of web-tapered beam-column

AISC-LRFD SPECIFICATION

The development of the current code for web-tapered members is based on the research performed by Lee et al. [1972]. The general design approach used in the AISC-LRFD Specification [1999] for the design of web-tapered members is to apply modification factors to convert the tapered members into appropriately proportioned prismatic members in order that the prismatic equations can be applied. The equations developed by Lee et al. [1972] took into account the St. Venant's torsional and warping resistance of the tapered beams. Length modification factors were added to both St. Venant's and warping terms in the prismatic beam equations so that they can be applied to tapered members. The length modification factors create an equivalent prismatic beam that is analogous to the web-tapered I-shaped beam-column of a different length. For tapered members subjected to compression and bending about the major axis, the AISC-LRFD Specification recommends the use of an interaction equation for prismatic members with the axial and bending strengths of tapered members.

Results

Figure 7 compares the Finite Difference (FD) solution with the ANSYS solution for a typical tapered beam-column subjected to the forces shown.

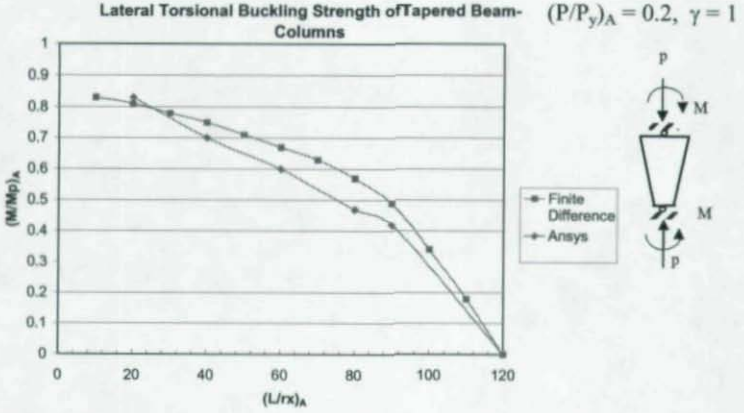

Figure 7.- Comparison Between FD and ANSYS models.

It appears that the ANSYS solution produces more conservative results for the slenderness ratios between 40 to 90. This behavior is due to the gradual yielding in the ANSYS model versus the four defined yielded patterns from Figure 5 utilized in the FD method.
Figure 8 corresponds to the overall buckled shape of the tapered beam-column as depicted by ANSYS. Yielding of both flanges at the smaller end is evident. A close-up look of the smaller end is depicted in Figure 9.

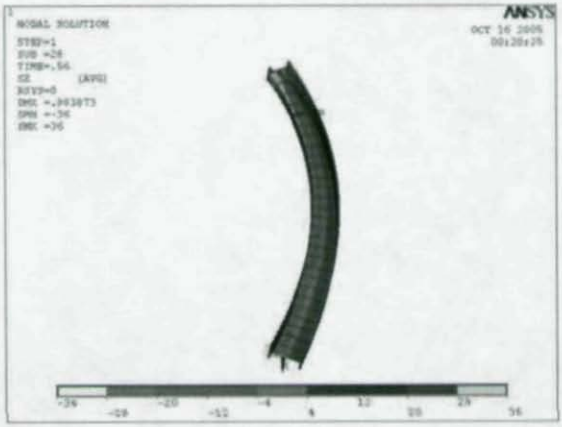

Figure 8.- Overall view of buckled tapered beam-column

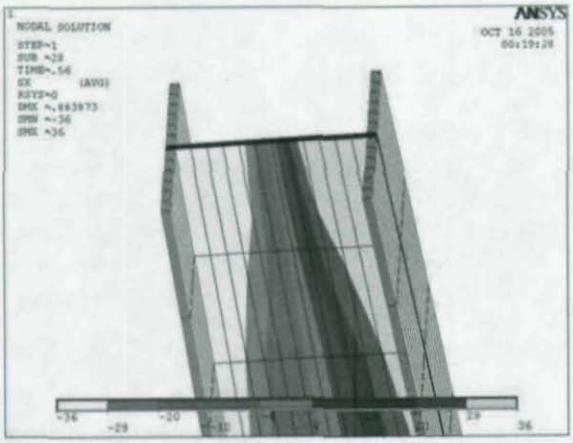

Figure 9.- Close up view of yielded flanges/web at the smaller end of a tapered beam-column

Comparison with current code. Comparisons were made between the AISC-LRFD code and this study. Figure 10 illustrates a typical case of a tapered beam-column subjected to compressive axial load and end moments.

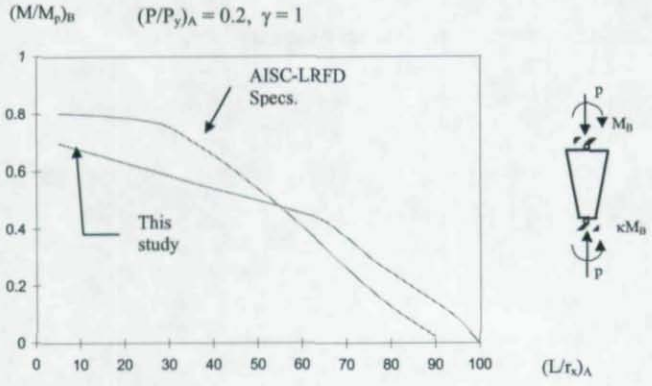

Figure 10.- Lateral-torsional buckling strength of tapered beam-column

The beam-column problem is treated in the AISC-LRFD Specs. through an interaction equation as shown in Figure 10. It can be seen that for values of M/M_p greater than about 0.4 the predictions of the interaction equation are unsafe.

Comparison with test results. The results of this study were compared with test results in order to provide an indication of the validity of the assumptions made in the theoretical derivations.

Salter et al. [1980] performed 5 tests of web-tapered I-section steel beam-columns. The ends of each member were pinned, with torsion and warping prevented. Cross-sectional dimensions are referred to Salter et al. [1980]. Comparisons are given in Table 1. It should be noted that the test results represent the maximum load the particular member sustained, whereas the theoretical results represent the start of lateral-torsional buckling. Additional comparisons are given by Jimenez [1998].
From the test comparisons, it appears that a good correlation exists between the theoretical solution and the test results. This conclusion was further determined by comparing the theoretical results from this study with other experiments.

Test No.	$(P/P_y)_s$	Test Result $(M/M_y)_L$	This study $(M/M_y)_L$
C1	0.167	0.97	0.88
C2	0.335	0.69	0.71
C3	0.337	0.67	0.70
C4	0.250	0.89	0.79
C5	0.499	0.60	0.57

"s" =smaller end, "L"= larger end.

Table 1.- Comparison of test results with this study.

RECOMMENDATIONS

The current AISC-LRFD Specs. [1999] recommendations to determine the moment capacity of tapered beams subjected to bending moments

intended to produce equal stress at both ends in the inelastic range gives unconservative results. Figure 11 depicts a beam curve proposed by *Jimenez [1998] which is a function of the slenderness ratio* $(L/r_x)_A$ at the smaller end A where r_x represents the radius of gyration about the strong-axis.

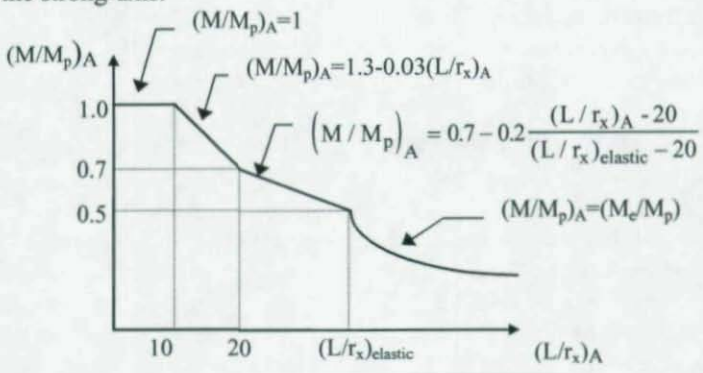

$$\left(M/M_p\right)_A = 0.7 - 0.2\frac{(L/r_x)_A - 20}{(L/r_x)_{elastic} - 20}$$

Where: $$M_e = \sqrt{\left(\frac{\pi^2 EI_y GK_{TA}}{(h_s L)^2}\right) + \left(\frac{\pi^4 EI_y EI_{wA}}{(h_w L)^4}\right)}$$

$$h_s = 1 + 0.0230\gamma\sqrt{Ld_A/A_f} \qquad h_w = 1 + 0.00385\gamma\sqrt{L/r_{TA}}$$

Figure 11.- Suggested beam curve

Once the values of h_s and h_w are substituted into equation 3, the value of $L_{elastic}$ can be determined using an iterative process.

$$\sqrt{\left(\frac{\pi^2 EI_y GK_{TA}}{(h_s L_{elastic})^2}\right) + \left(\frac{\pi^4 EI_y EI_{wA}}{(h_w L_{elastic})^4}\right)} - 0.5\sigma_y Z_{xA} = 0 \qquad (3)$$

Where: σ_y is the steel yield stress, ZxA is the plastic modulus at the smaller end, and h_s, hw, r_T, A_f are defined in the AISC-LRFD Specs. [1999].

Figure 12 shows the application of the suggested methodology with the AISC-LRFD interaction equation. It can be observed that the suggested equations produce safe results. For very short members the suggested

methodology is slightly on the non-conservative side, but in general, it may be used with confidence.

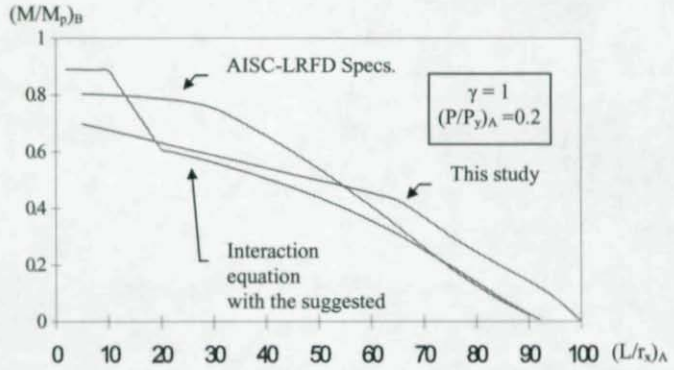

Figure 12.- Lateral-torsional buckling strength of tapered beam-columns

CONCLUSION REMARKS

This paper presents additional studies for the lateral-torsional buckling of tapered beam-columns using ANSYS and the Finite Difference method. It was shown that the ANSYS solution produces slightly more conservative results due to the progressive yielding of the flanges and web. In addition, the current AISC-LRFD Specs. [1999] continues to produce unsafe results for beam-columns with medium and low slenderness ratios. An equation developed in 1998 by the author for tapered beams was utilized with the AISC-LRFD interaction equation in order to provide an alternative for design use. When combined with the interation equation these new equations have shown a satisfactory agreement with the results of this study.

REFERENCES

AISC [1999], "Load and Resistance Factor Design Specification for Structural Steel Buildings," American Institute of Steel Construction, Chicago, IL.

Fukumoto, Y. [1963], "Inelastic Lateral-Torsional Buckling of Beam-Columns," thesis presented to Lehigh University, at Bethlehem, Pa. in partial fulfillment of the requirements for the degree of Doctor of Philosophy.

Galambos, T.V. [1959], "Inelastic Lateral-Torsional Buckling of Eccentrically Loaded Wide-Flange Columns," thesis presented to Lehigh University, at Bethlehem, Pa. in partial fulfillment of the requirements for the degree of Doctor of Philosophy.

Jimenez, Gabriel [1998], "Inelastic Stability of Tapered Structural Members," Ph.D. Dissertation. University of Minnesota. Minneapolis, MN.

Jimenez, G. and Galambos T.V. [1998], "Inelastic Lateral-Torsional Buckling of Tapered Beam-Columns," Structural Stability Research Council Proceedings, Atlanta, Georgia.

Lee,G.C., Morrell, M.L. and Ketter, R.L. [1972], "Design of tapered members," Welding Research Council Bulletin. No. 173, pp 1-32.

Salter et al. [1980], "Test on Tapered Steel Columns," The Structural Engineer, Vol. 58A, No. 6, pp. 189-193.

INELASTIC CYCLIC ANALYSIS AND STABILITY EVALUATION OF STEEL BRACES

Iraj H.P. MAMAGHANI[1]

ABSTRACT

This paper deals with the inelastic cyclic analysis and stability (strength and ductility) evaluation of steel braces subjected to axial tension and compression. The inelastic cyclic performance of cold-formed steel braces of circular hollow sections is examined through finite element analysis using the commercial computer program ABAQUS. First some of the most important parameters considered in the practical design and ductility evaluation of steel braces of tubular sections are presented. Then the details of finite element modeling and numerical analysis are described. Later the accuracy of the analytical model employed in the analysis is substantiated by comparing the analytical results with the available test data in the literature. Finally the effects of some important structural and material parameters on cyclic inelastic behavior of steel braces are discussed and evaluated.

INTRODUCTION

Steel braced frames are one of the most commonly used structural systems because of their structural efficiency in providing significant

[1]Assistant Professor, Department of Civil Engineering, University of North Dakota, Grand Forks, ND, 58202-8115, USA.
Email: irajmamaghani@mail.und.edu

lateral strength and stiffness. The steel braces contribute to seismic energy dissipation by deforming inelastically during an earthquake. The use of this type of construction indeed avoids the brittle fracture found in beam-to-column connections in moment resisting steel frames that occurred in the Northridge earthquake in 1994 and the Kobe earthquake in 1995 (ASCE 2000, IGNTSDSS 1996). However, careful design of steel braced frames is necessary to avoid possible catastrophic failure by brace rupture in the event of a severe seismic loading. The current capacity design procedure adopted in most seismic design steel specifications (AISC 1997, CAN-CSAS16.1 1989), for concentrically braced frames requires yielding in the braces as primary members, whereas the secondary members of the frame should remain elastic and hence carry forces induced by the yielding members. The transition from current perspective seismic codes to performance-based design specifications requires accurate predictions of inelastic limit states up to structural collapse.

The cyclic behavior of steel brace members is complex due to the influence of various parameters such as, material nonlinearity, structural nonlinearity, boundary condition, and loading history. The material nonlinearity includes structural steel characteristics such as, residual stresses, yield plateau, strain hardening and Bauschinger effect. The structural nonlinearity includes parameters such as, brace slenderness parameter, cross-section slenderness, width-to-thickness ratio of the cross-section's component elements (or radius-to-thickness ratio of circular hollow sections), and initial out of straightness of the brace. The complex behavior results in various physical phenomena, such as, yielding in tension, buckling in compression, postbuckling deterioration of compressive load capacity, deterioration of axial stiffness with cycling, and low cycle fatigue fractures at plastic regions.

Steel braces can be designed to resist only tensile forces, or to resist both tensile and compressive axial forces. Recent earthquakes and experiments have shown that the tension-compression braces provide better performance under cyclic loading (during an earthquake) as compared with the tension-only braces having almost no compressive

strength. Under severe earthquakes, the braces are subjected to cyclic axial forces and they are allowed to undergo compression buckling or tensile yield to dissipate the imposed energy while columns and collector beams respond elastically. Therefore, understanding the behavior of the bracing members under idealized cyclic loading is an important step in the careful design of steel braced frames.

This paper deals with the inelastic cyclic analysis of steel braces. The most important parameters considered in the practical design and ductility evaluation of steel braces of tubular sections are presented. The cyclic performance of steel braces is examined through finite element analysis using the computer program ABAQUS. The accuracy of the analytical model employed in the analysis is substantiated by comparing the analytical results with the available test data in the literature. The effects of some important structural and material parameters on inelastic cyclic behavior of steel braces are discussed and evaluated.

BRACE PARAMETERS

Energy absorption through hysteretic damping is one of the great interests in seismic design, because it can reduce the amplitude of seismic response, and thereby reduce the ductility demand on the structure. Steel braces are very effective structural members and are widely used as energy dissipaters in skeletal buildings and offshore structures under extreme loading conditions such as severe earthquake and wave motion. They also minimize story drift of high-rise buildings for possible moderate earthquakes during their lifetime.

The most important parameters considered in the practical design and ductility evaluation of steel braces of tubular sections are the section slenderness λ_s (Mamaghani et al. 1996a, 1996b, 1997; Mamaghani 2005) and the slenderness ratio parameter of the member λ_c (AISC 1997, AISC-LRFD 1999). While the former influences local buckling of the section, the latter controls the overal stability. They are given by:

$$\lambda_s = \frac{1}{\pi}\frac{b}{t}\sqrt{3(1-\nu^2)\frac{\sigma_y}{E}} \quad (for\ box\ section) \tag{1}$$

$$\lambda_s = \frac{d}{2t}\sqrt{3(1-\nu^2)}\frac{\sigma_y}{E} \quad (for\ circular\ section) \tag{2}$$

$$\lambda_c = \frac{1}{\pi}\frac{KL}{r}\sqrt{\frac{\sigma_y}{E}} \tag{3}$$

where, b = flange width of a box section; t = plate thickness of the cross-section elements; σ_y = the measured yield stress; E = Young's modulus; ν = Poisson's ratio; d = outer diameter of the circular section; K = effective length factor; L = measured length of the brace; and r = radius of gyration of the cross section. It is worth noting that the section slenderness, λ_s, represents width-thickness ratio parameter of the flange plate for box section and diameter-thickness ratio of circular hollow section for a given material.

The limiting diameter-thickness ratio specified in AISC (1997) for plastic design of circular hollow sections is $d/t = 0.045E/\sigma_y$. This d/t limit can be converted to a limiting slenderness parameter for compact element according to Equation 2. The corresponding value of λ_s, considering $\upsilon = 0.3$ for structural steels, is:

$$\lambda_s = \frac{0.045E}{2\sigma_y}\sqrt{3(1-0.3^2)}\frac{\sigma_y}{E} = 0.037 \tag{4}$$

This implies that when $\lambda_s \le 0.037$, no local buckling occurs before the cross-section attains full plastic capacity. The limiting width-

thickness ratio specified in AISC (1997) for non-compact circular hollow sections is $d/t = 0.11E/\sigma_y$ which corresponds to $\lambda_s = 0.09$. The ductility behavior of the circular hollow section braces is significantly sensitive to λ_s when it is less than 0.09. The maximum member slenderness limits specified in AISC (1997) for special concentrically braced frames (SCBF) and ordinary concentrically braced frames are $\lambda_c = 1.87$ ($KL/r \le 1000/\sqrt{\sigma_y}$) and $\lambda_c = 1.35$ ($KL/r \le 720/\sqrt{\sigma_y}$), respectively. SCBF are expected to withstand significant inelastic deformation when subjected to the force resulting from the motion of the design earthquake. SCBF have increased ductility due to lesser strength degradation when compression braces buckle.

NUMERICAL METHOD

Steel braces are vulnerable to damage caused by local and overall interaction buckling during a major earthquake. A sound understanding of the inelastic behavior of steel braces is important in developing a rational seismic design methodology and ductility evaluation of steel braced frame structures.

An accurate cyclic analysis of braced frames requires precise methods to predict the cyclic inelastic large deflection response of the braces. This has been a subject of intensive research work and a variety of analytical methods were developed to simulate the hysteretic behavior of braces over the past few decades. The main research approaches used for the cyclic analysis of braces may be classified as: (1) empirical models, (2) plastic-hinge models, and (3) elastoplastic finite element models (Mamaghani et al. 1996a). The more accurate models were based on the finite element method considering geometric and material nonlinearities. This method is generally applicable to many types of problems, and it requires only the member geometry and material properties (constitutive law) to be defined.

Finite Element Method

The finite element analysis is carried out by using the commercial computer program ABAQUS. The shell element S4R is used in modeling the brace member (ABAQUS 2005). The S4R element is a three-dimensional, double-curved, four-node shell element with six degrees of freedom per node that uses bilinear interpolation. As for the S4R element in which there is only one sample point but five layers are assumed across the thickness, the spread of plasticity is considered through both the thickness and plane of the element. This shell element which uses reduced integration, is applicable to both thin and thick shells, and can be used for finite strain applications.

In the analysis, both material and geometrical nonlinearities are considered. For large displacement analysis, the elements are formulated in the current configuration, using current nodal positions. Elements therefore distort from their original shapes as the deformation increases. The stiffness matrix of the element is obtained from the variational principle of virtual work. The modified Newton-Raphson iteration technique coupled with the displacement control method is used in the analysis (Zienkiewicz 1977). The displacement convergence criterion is adopted and the convergence tolerance is taken as 10^{-5}. The details of elastoplastic large displacement formulation and solution scheme are reported in the work by the author (Mamaghani 1996).

Analytical Modeling

A series of numerical studies on the cyclic behavior of steel braces are carried out using the numerical finite element method described in the previous section, and the results are compared with the experiments. The results for three typical examples, S7A, S7B, and S7C, (Elchalakani et al. 2003), presented hereafter are intended to verify the accuracy of the numerical method. These specimens are subjected to three loading histories in order to better understand the cyclic behavior

Table 1: Properties of the analyzed braces.

Test Number	Specimen Shape	A_g (mm^2)	L (mm)	λ_s	λ_c	δ_y (mm)	P_y (kN)
S7A	CHS 139.7x3.5	1498	2820	0.06	0.4	5.344	567.6
S7B	CHS 139.7x3.5	1498	2820	0.06	0.4	5.344	567.6
S7C	CHS 139.7x3.5	1498	2820	0.06	0.4	5.344	567.6

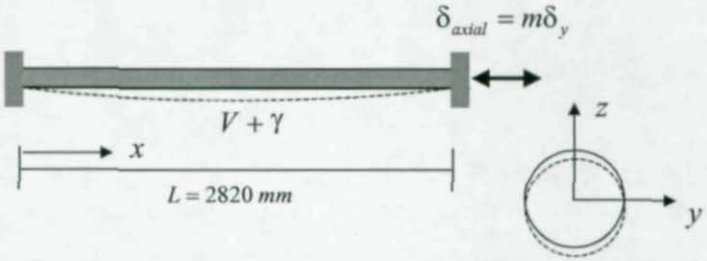

Figure 1: Analyzed circular hollow section steel brace and initial imperfection.

of cold-formed circular hollow section braces. The details of the test can be found in Elchalakani et al. (2003).

The shape and dimension of the analyzed braces are given in Table 1. For comparison, the selected brace parameters ($\lambda_c = 0.4$ and $\lambda_s = 0.06$) are kept the same. These parameters represents a non-compact member having inelastic behavior. The analyzed fix-ended tubular braces subjected to cyclic concentric axial loading are modeled as shown in the Figure 1. An initial imperfection of

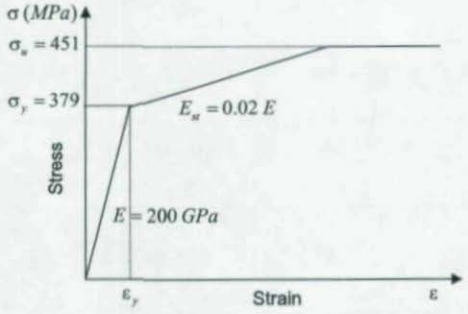

Figure 2. Tri-linear stress-strain model for steel.

$$\gamma_x = \gamma_0 \sin\left(\frac{\pi x}{L}\right) \tag{5}$$

is assumed in the analysis, where the initial deflection at midspan of the member γ_0 is taken as the measured value of L/3160 during the test.

Material Models

The analyzed cold-formed circular hollow sections are AS 1163 grade C350L0 (equivalent to ASTM A500 tubes) with the yield stress of $\sigma_y = 379$ MPa and the ultimate tensile strength of $\sigma_u = 451$ MPa. In the analysis, the material nonlinearity is accounted for by using the kinematic hardening rule. Figure 2 shows the tri-linear stress-strain material model adopted in the analysis. The Young modulus of elasticity of the steel is assumed to be E = 200 GPa. The strain hardening modulus is assumed to be 2 percent of the initial Young modulus ($E_{st} = 0.02E$).

Cyclic Loading History

In the analysis three cyclic loading histories are applied. The first loading history is a large compression-tension monocycle with a maximum normalized displacement amplitude $m = \delta_{max} / \delta_y$, where

δ_{max} is the maximum displacement in the compression-half cycle at load reversal and $\delta_y = \varepsilon_y L = P_y L / EA$ is the yield displacement corresponding to the squash load of cross section $P_y = \sigma_y A$ (A = area of the cross-section; σ_y = yield stress; L= the length of the brace). The large amplitude used in the monocycle is applied to examine the inelastic response of the brace when subjected to very large seismic demand during a possible near field excitation (Krawinkler et al. 2000). The second loading history is a uniform increase of displacement amplitude up to failure with the maximum normalized displacement amplitudes of m = 1, 2, 3, ..., where each amplitude is repeated only once. In the third loading history, uniform increase of the displacement is used similar to the second loading history except that the oscillations are repeated three times at each amplitude (m = 1, 2, 3, ..., etc.).

Finite Element Meshing and Boundary Conditions

The details of finite element meshing pattern adopted in the analysis of hollow circular sections is shown in Figure 3. The brace is subdivided into a total number of 2100 shell elements (70 elements along the brace length and 30 elements in the circumferential direction). A finer mesh pattern is used at the center and the ends of the brace, where large deformation is expected, as shown in Figure 3. In the analysis, the left end of brace is fully fixed and the right end is modeled as a guided support to apply axial displacement, as shown in Figure 3. The axial load, P, and vertical deflection at midspan, V, are obtained from analysis.

NUMERICAL RESULTS

Example 1

The first example is concerned with analysis of the brace S7A, which has nominal length of 2820 mm, member slenderness parameter of $\lambda_c = 0.4$ and section selenderness of $\lambda_s = 0.06$ (Table 1). These parameters represent a non-compact member having inelastic behavior.

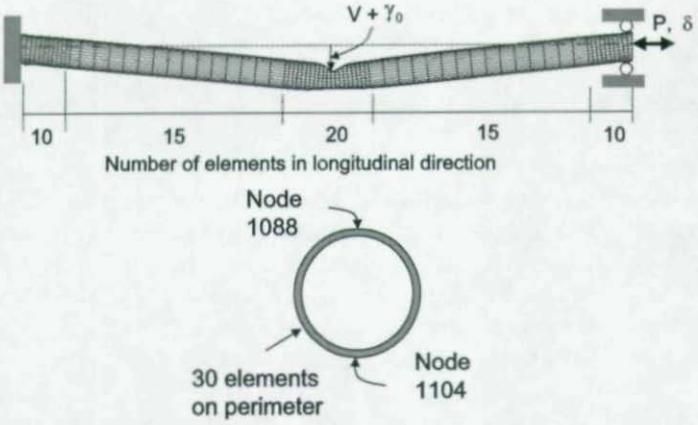

Figure 3. Meshing details and boundary conditions.

This brace is subjected to a large compression-tension monocycle with maximum normalized displacement amplitude of $m = 18.24$ (the first loading history) to examine the inelastic response of the brace under very large seismic demand. This value is larger than the upper limit for $m = 10$ likely to occur in near source excitation (Krawinkler et al 2000). In order to check the effects of mesh density and loading increment (loading time steps) on the inealstic cyclic behavior of the brace, three analyses are carried out on this brace. The first analysis, desinated as original analysis, uses the original meshing pattern shown in Figure 3 with a total number of 2100 shell elements. The second analysis, designated as mesh-inceremnt analysis, uses a finer mesh density at the central segment and at the ends of the brace by doubling the mesh number in these regions with a total number of 3300 shell elements. The third analysis, designated as step-increment analysis, utilizes the original meshing but doubling the time step by reducing the displacement incerement to half of that used in the original analysis.

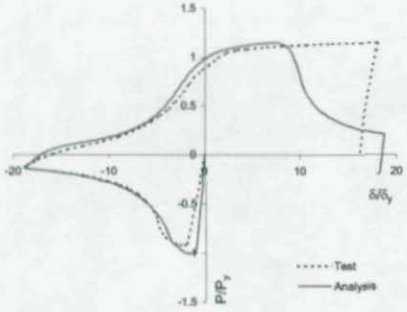

(a) Axial load versus axial displacement.

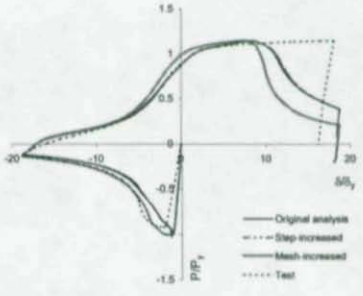

(b) Effects of mesh density and load steps.

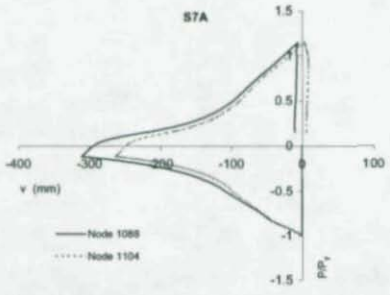

(c) Deflection at the top face (Node 1088) and bottom face (Node 1104) of the cross-section at midspan.

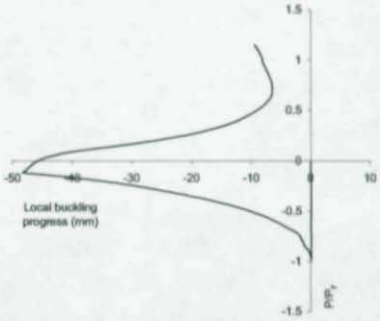

(d) Local buckling progress at midspan

Figure 4. Comparison between experimental and predicted hysteretic loop for brace S7A.

Figures 4a and 4b compare the normalized axial load P/P_y-axial deformation δ/δ_y hysteresis loop obtained from the experiment and analyses. With reference to these figures, the following observations can be made:

1. The initial stiffness and buckling load capacity are slightly lower in the experiment than those predicted by the analyses using various mesh sizes and loading inceremens. This may be due to the experimental boundary conditions (unavoidable rotation at the fix-ends) and the assumed initial imperfection in the analysis. In the analysis the cross-section out of straightness and residual stress are not accounted for. It is worth noting that the previous research by the author indicates that the initial residual stresses and initial section imperfection significantly decrease the initial stiffness and initial buckling load capacity and have almost no effect on the subsequent cyclic behavior of the member (Mamaghani et al. 1996b, Banno et al. 1998).
2. Under compressive load, the overall buckling was followed by local buckling at the center and brace ends. From Figures 4a and 4b, it can be observed that the overall shape of the predicted hystersis loop are significantly closer to the experiment.
3. Under tension load, the behavior of the brace is well predicted up to $\delta / \delta_y = 9.3$, where there is a sharp decrease in predicted tensile strength beyond this displacement. The observed discrepancy between experimental and analytical results when the specimen is stretched beyond $\delta / \delta_y = 9.3$ might be due to the formation of a plastic hinge at the member midspan under combined biaxial hoop stress and axial stress. By further stretching the member, the spread of plasticity fully covered the whole cross section at midspan and extended on both sides of this section, leading to the reduction of load carry capacity, see Figure 5.
4. The results in Figure 4(b) show that the increase in time step and use of refined mesh do not have significant effects on the overall predicted behavior except a slight improvement in the postbuckling behavior where the predicted results closely fit the test results. During the tensile loading beyond the $\delta / \delta_y = 9.3$, the predicted tensile load capacity drops

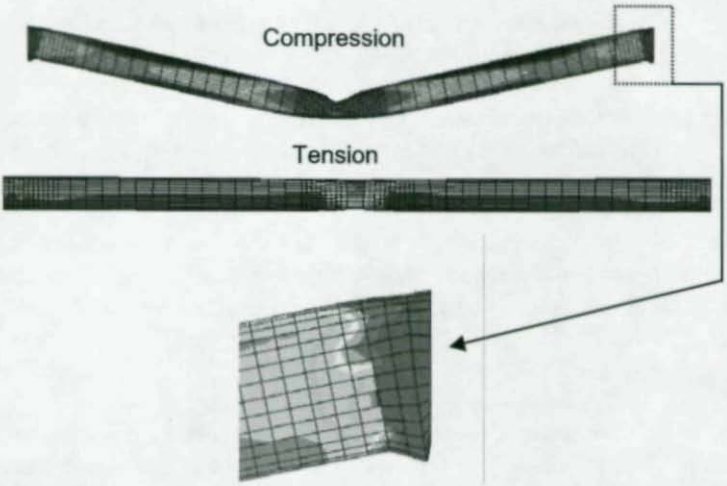

Figure 5. Deformed configuration of brace S7A at the final stage of compression and tension cyclic loading.

sligthly earlier for the analysis using refined mesh as compared with the other analyses. This is because the spread of plasticity and formation of the plastic hinge takes place faster for the refined mesh model.

Figure 4(c) shows the normalized axial load P/P_y versus vertical deflection V, at the top face (Node 1088) and bottom face (Node 1104) of the cross-section at the midspan of the member (Figure 3), obtained from the analysis. The results in this figure show that the relative vertical deflection at the top and bottom faces of the cross-section at midspan increases as the member undergoes large axial deformation. The difference between vertical displacement of the top face and bottom face at midspan indicates the progress of local buckling, which is plotted in Figure 4(d). Figure 5 shows the deformation of the specimen at the end of compression load and tension stretching. Under compression load, the overall buckling was followed by local buckling

at the center and brace ends. A smooth kink formed at midspan of the brace under compression load. A semi-elephant-foot (an outward folding mechanism) was formed at the fix-ends of the brace, as shown in Figure 5. During the tensile stretching, the brace suffered excessive stretching at the midspan because of the development of the plastic hinge caused by a very large accumulation in local deformation. This represent a tear-through-failure mode as the specimen exhibited during the test (Elchalakani et al. 2003). These observed behaviors under compression and tension loads are reflected in the normalized load-displacement hysteretic loop shown in Figure 4.

Example 2

The second example is concerned with the analysis of the brace S7B, which has nominal length of 2820 mm, member slenderness parameter of $\lambda_c = 0.4$ and section slenderness of $\lambda_s = 0.06$ (Table 1). This brace is subjected to a uniform increase of displacement amplitude up to failure with the maximum normalized displacement amplitudes of m = 1, 2, 3, ..., where each amplitude is repeated only once (the second loading history). The original meshing pattern shown in Figure 3, with a total number of 2100 shell elements, is utilized in the analysis.

Figure 6(a) compares the normalized axial load P/P_y-axial deformation δ/δ_y hysteresis loops obtained from the experiment and analysis. Figure 6(b) shows the normalized axial load P/P_y versus vertical deflection V, at the midspan of the member (Figure 3), obtained from the analysis. Comparison between hysteresis loops in Figure 6(a) shows that there is a relatively good agreement between analytical results and experiments. An observed small discrepancy between experimental and analytical hysteresis loops is that the predicted cyclic load capacities in compression direction of loading, are slightly higher than those of the experiment. The possible reasons are: (a) the tri-linear kinematic hardening rule adopted in the analysis does not accurately consider the reduction of the elastic range due to plastic

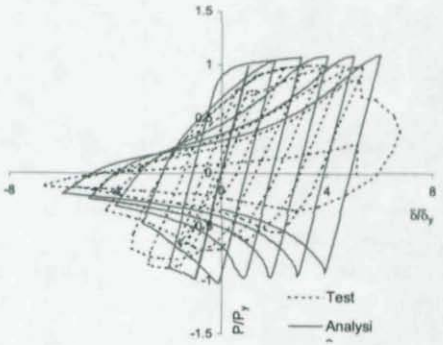

(a)

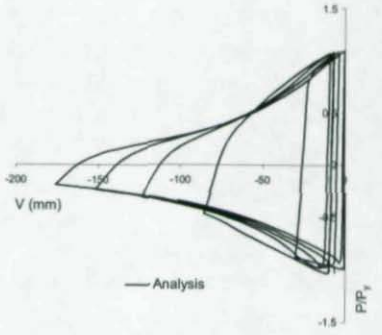

(b)

Figure 6. Comparison between experimental and predicted hysteretic loop for brace S7B.

deformation (Bauschinger effect). In this model the size of elastic range is taken to be constant which does not represent the actual behavior of structural steel (Mamaghani et al. 1995, Shen et al. 1995). More accurate results can be obtained from analysis by using a cyclic constitutive law representing the more realistic behavior of the material; (b) the brace fix-ended boundary conditions may have shown

some degree of flexibility during the tests, which is not considered in the analysis; and (c) in the analysis the cross-section's out of straighness and residual stresses, which affect the initial buckling load, are not considered.

Figure 6(b) shows that there is a residual midspan deflection at the end of tensioning in each cycle. The residual deflection of the brace at the end of previous tensioning has a large effect on the buckling capacity and subsequent cyclic behavior. Figure 6(b) shows a progress of residual midspan deflection due to cycling obtained from analysis. In spite of large progress in buckling, the buckling load does not decrease significantly due to cyclic strain hardening.

Example 3

The third example is concerned with analysis of the brace S7C, which has nominal length of 2820 mm, member slenderness parameter of $\lambda_c = 0.4$ and section selenderness of $\lambda_s = 0.06$ (Table 1). This brace is subjected to a uniform increase of displacement amplitude up to failure with the maximum normalized displacement amplitudes of m = 1, 2, 3, ..., where each amplitude is repeated three times (the third loading history). The original meshing pattern as shown in Figure 3, with a total number of 2100 shell elements, is utilized in the analysis.

Figure 7(a) compares the normalized axial load P/P_y -axial deformation δ/δ_y hysteresis loop obtained from experiment and analysis. Figure 7(b) shows the normalized axial load P/P_y versus vertical deflection V, at the midspan of the member (Figure 3), obtained from the analysis. Comparison between hysteresis loops in Figure 7(a) shows there is a relatively good agreement between analytical results and experiments. These results indicate that the numerical method and finite element modeling employed in the numerical analysis can predict with a reasonable degree of accuracy the experimentally observed cyclic behavior of axially loaded fix-ended steel braces of circular hollow sections.

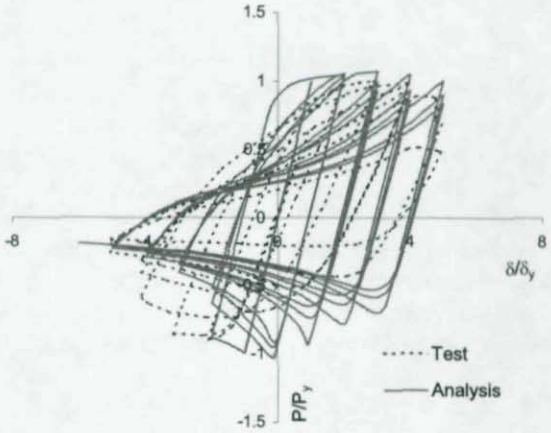

(a)

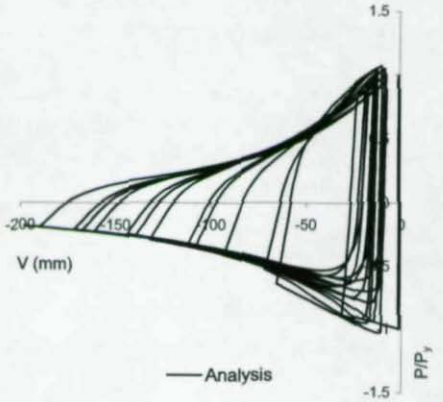

(b)

Figure 7. Comparison between experimental and predicted hysteretic loop for brace S7C.

CONCLUSIONS

This paper dealt with the inelastic cyclic analysis and stability (strength and ductility) evaluation of steel braces subjected to axial tension and compression. The most important parameters considered in the practical seismic design and ductility evaluation of steel braces of tubular sections, such as brace slenderness parameter, cross-section slenderness, material behavior, and loading history, were presented. The inelastic cyclic performance of cold-formed steel braces of circular hollow sections was examined through finite element analysis using the commercial computer program ABAQUS and employing a tri-linear kinematic strain hardening model to account for material nonlinearity. The details of finite element modeling and numerical analysis were described. The accuracy of the analytical model employed in the analysis was substantiated by comparing the analytical results with the available test data in the literature. The effects of some important structural, material, and loading history parameters on cyclic inelastic behavior of steel braces were discussed and evaluated with reference to the experimental and analytical results. It has been shown that the numerical method and finite element modeling employed in the numerical analysis can predict with a reasonable degree of accuracy the experimentally observed cyclic behavior of axially loaded fix-ended steel braces of circular hollow sections.

REFERENCES

ABAQUS / Standard User's Manual 2005. Ver. 6.5, Hibbitt, Karlsson and Sorensen, Inc.

ASCE 2000. Steel moment frames after Northridge. *J. Struct. Eng.*, 126(1) (special issue).

Banno, S., Mamaghani, Iraj H.P., Usami, T., Mizuno, E. 1998. Cyclic elastoplastic large deflection analysis of thin steel plates. *Journal of Engineering Mechanics,* ASCE, USA, Vol. 124, No. 4, 363-370.

Amrican Institute of Steel Constructions (AISC-LRFD). 1999. Load and resistance factor design specification for structural steel buildings, 3rd Edition, Chicago.

Amrican Institute of Steel Constructions (AISC) 1997. Seismic provisions for structural steel buildings, Chicago, Illinois.

Canadian Standards Associations (CAN-CSA S16.1) 1989. Steel structures for buildings, limit state design.

Elchalakani, M., Zhao, X. L., and Grzebieta, R. 2003. Test of cold-formed circular tubular braces under cyclic axial loading. J. of Struct. Eng., ASCE, 129(4), pp. 507-514.

Interim Guidelines and New Technologies for Seismic Design of Steel Structures (IGNTSDSS). 1996. In Usami, T. (eds), Committee on New Technology for Steel Structures, Japan Society of Civil Engineers (JSCE), Japan, (in Japanese).

Krawinkler, H., Akshay, G., Medina, R., and Luco, M. 2000. Development of loading histories for testing of steel-to-beam assemblies. Report prepared for SAC Steel Project, Dept. Of Civil and Environmental Engineering, Stanford University.

Mamaghani, I.H.P. 2005. Seismic performance evaluation of thin-walled steel tubular columns, *Structural Stability*, Structural Stability Research Council, Montreal, Quebec, Canada. pp. 1-10.

Mamaghani, I.H.P., Usami, T. and Mizuno, E. 1996a. Inelastic large deflection analysis of structural steel members under cyclic loading. *Engineering Structures*, UK, Elsevier Science, 18(9), 659-668.

Mamaghani, I.H.P., Usami, T., Mizuno, E. 1996b. Cyclic elastoplastic large displacement behaviour of steel compression members. *Journal of Structural Engineering,* JSCE, Japan, Vol. 42A, 135-145.

Mamaghani, I.H.P., Usami, T., Mizuno, E. 1997. Hysteretic behavior of compact steel box beam-columns. *Journal of Structural Engineering*, JSCE, Japan, Vol. 43A, 187-194.

Mamaghani, I.H.P., Shen, C., Mizuno, E., Usami, T. 1995. Cyclic behavior of structural steels. I: experiments. *Journal of Engineering Mechanics*, ASCE, USA, Vol.121, No.11,1158-1164.

Shen, C., Mamaghani, I.H.P., Mizuno, E. and Usami, T. 1995. Cyclic behavior of structural steels. II: theory. *Journal of Engineering Mechanics*, ASCE, USA, Vol.121, No.11, 1165-1172.

Mamaghani, I.H.P. 1996. Cyclic elastoplastic behavior of steel structures: theory and experiments. *Doctoral Dissertation,* Department of Civil Engineering, Nagoya University, Nagoya, Japan.

Zienkiewicz, O.C. 1977. *The finite element method.* 3rd Ed., McGraw-Hill, New York.

ON THE INFLUENCE OF STRESS GRADIENTS ON THE LOCAL-PLATE, DISTORTIONAL AND GLOBAL BUCKLING BEHAVIOR OF THIN-WALLED STEEL MEMBERS

Rui Bebiano[1], *Nuno Silvestre*[2] & *Dinar Camotim*[3]

ABSTRACT

In this paper, one first presents the main steps involved in the formulation and numerical implementation of a GBT-based finite element incorporating the geometric stiffness reduction associated with applied stresses displaying non-uniform (linear, quadratic or cubic) longitudinal distributions. Then, taking full advantage of the GBT modal features, the above finite element is employed to investigate the influence of the longitudinal stress gradients on the local-plate, distortional and global buckling behavior of thin-walled steel beams. In particular, one presents and discusses numerical results concerning the buckling behavior of simply supported lipped channel cold-formed steel beams subjected to various non-uniform bending moment diagrams. For validation purposes, one also compares some GBT-based critical stresses with values reported in the literature.

INTRODUCTION

Due to the high slenderness of their walls, the structural efficiency of thin-walled steel members (particularly the cold-formed ones) depends heavily on their susceptibility to local and/or global instability phenomena, namely

[1] Ph.D. Student, [2]Assistant Professor and [3]Associate Professor at the Department of Civil Engineering and Architecture, ICIST/IST, Technical University of Lisbon, Av. Rovisco Pais, 1049-001 Lisbon, Portugal.

local-plate, distortional or flexural-torsional buckling. Thus, the elaboration, validation and calibration of design formulae and/or procedures for such members requires the acquisition of in-depth knowledge about their buckling behavior, a task involving (i) the evaluation of critical buckling stresses and (ii) the determination of the corresponding buckling mode shapes.

If one excludes shell finite element analyses, still prohibitive for routine application in design offices, the buckling behavior of thin-walled members is currently assessed by means of either (i) the finite strip method (*e.g.*, Hancock 1998a or Schafer 2003) or (ii) approximate analytical formulae (*e.g.*, Rhodes & Lawson 1993 or Hancock 2003). Quite recently, it has been shown that the use Generalized Beam Theory (GBT) (*e.g.*, Camotim *et al.* 2004, 2005) provides a very efficient and elegant alternative to perform this task – however, the lack of proper dissemination severely hampers its use for the time being. But it should be mentioned that all the above methods share an important limitation: their application is restricted to members subjected to longitudinally uniform normal stress distributions.

In practice, the vast majority of thin-walled steel members (beams or beam-columns) are acted by normal stress distributions varying along the length – *e.g.*, the ones stemming from transverse loads. Even so, it seems fair to say that virtually all the information available concerning the influence of longitudinal stress gradients on the member stability deals with global buckling, mostly with lateral-torsional buckling of beams – aside from the classical results included in books or manuals, the recent works of Li (2004) and Chu *et al.* (2004) deserve to be mentioned. As far as the local (local-plate or distortional) buckling behavior is concerned, the amount of research work on the effect of stress gradients is still very scarce – in this context, it is worth noting the experimental study undertaken by Yu (2005), the shell finite element results reported by Yu & Schafer (2004) and Yu (2005) or the finite strip analyses carried out by Chu *et al* (2005). Up to now, GBT has never been used to solve buckling problems involving stress gradients – even if no fundamental limitation exists in the theory, an efficient numerical implementation is required to address this type of problems.

The objective of this paper is two-fold: (i) to describe the main steps involved in the formulation and numerical implementation of a GBT-based beam

finite element incorporating the geometric stiffness reduction due to applied stresses displaying non-uniform (linear, quadratic or cubic) longitudinal distributions and, taking full advantage of the GBT modal features, (ii) to employ the above finite element to study the local-plate, distortional and global buckling behavior of simply supported lipped channel cold-formed steel beams subjected to various non-uniform bending moment diagrams. These diagrams are due to unequal end moments, uniformly distributed loads or mid-span point loads. One investigates mainly the effect of the longitudinally varying stresses on the beams critical moments/loads and buckling mode shapes – the modal features of the GBT analyses are ideally suited to provide in-depth understanding about the mechanics involved in the buckling behavior of the lipped channel beams. For validation purposes, one also compares some GBT-based critical stresses with values obtained by other authors and reported in the literature.

GBT CROSS-SECTION ANALYSIS

Because the cross-section displacement field is expressed as a combination of mechanically meaningful *deformation modes*, GBT analyses (i) lead to equilibrium equations written in a rather convenient form and (ii) make it possible to perform *modal* analyses that provide a very clear insight on the member structural behavior.

Consider the arbitrary open unbranched thin-walled steel profile shown in figure 1(a) – in each plate, one defines the local coordinate system *x-s-z* depicted in figure 1(b), associated to the displacement components *u*, *v*, *w*. In the context of a GBT buckling analysis, its cross-section is discretized into (i) *n+1 natural* nodes (located at the ends of the *n* walls forming the cross-section) and (ii) *m intermediate* nodes (located within the walls).

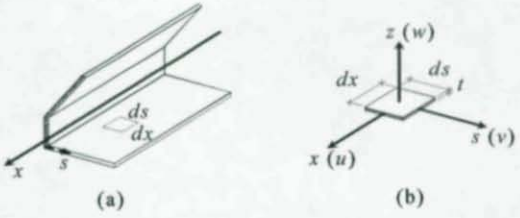

(a) (b)

Figure 1. Unbranched open profile (a) geometry and (b) local coordinate system and displacement components

In order to comply with the classical thin-walled beam theory (Vlassov 1959), the displacement components are expressed as

$$u(x,s)=u_k(s)\phi_{k,x}(x) \qquad v(x,s)=v_k(s)\phi_k(x) \qquad w(x,s)=w_k(s)\phi_k(x) \ , \quad (1)$$

where (i) $u_k(s)$, $v_k(s)$, $w_k(s)$ are deformation mode components and (ii) $\phi_k(x)$ are amplitude functions describing their longitudinal variation. Following the usual GBT procedure (*e.g.*, Silvestre & Camotim 2003), the above cross-section discretization yields $n+m+1$ deformation modes: (i) the *4* classical rigid-body modes, (ii) n-1 distortional modes and (iii) m local-plate modes – the amplitudes of these modes are the cross-section degrees of freedom.

To provide some insight on the GBT cross-section analysis procedure and outcome, figures 2(b) and 3 show (i) the discretization adopted to obtain the numerical results presented and discussed further ahead in the paper (the beam cross-section dimensions and material properties are given in figure 1(a)) and (ii) the in-plane deformed configurations of the *10* (out of *13*) most relevant deformation modes.

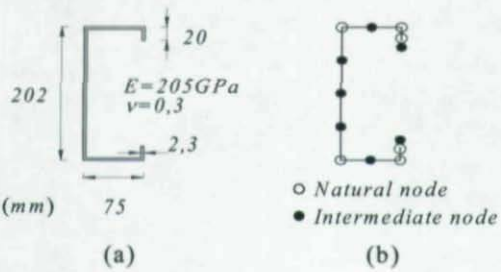

Figure 2. Cross-section (a) geometry and (b) discretization

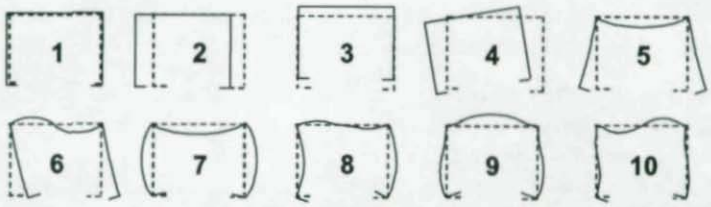

Figure 3. In-plane shapes of the *10* most relevant deformation modes

GBT MEMBER BUCKLING ANALYSIS

After performing the cross-section analysis (identification of the deformation modes), to derive the GBT system of equilibrium equations associated with the member buckling analysis becomes a rather straightforward matter – by applying the Principle of Virtual Work, one is led to

$$C_{ik}\phi_{k,xxxx} - D_{ik}\phi_{k,xx} + B_{ik}\phi_k - \lambda X_{ikj}\left(W_j\phi_{k,x}\right)_{,x} = 0 \quad , \quad (2)$$

where λ is the (single) load parameter, W_j is the generalized force related to mode j. As for the stiffness tensors C_{ik}, D_{ik}, B_{ik} and X_{ikj} are given by

$$C_{ik} = \frac{Et}{1-\nu^2}\int_S u_i u_k\, ds + \frac{Et^3}{12\left(1-\nu^2\right)}\int_S w_i w_k\, ds$$

$$B_{ik} = \frac{Et^3}{12\left(1-\nu^2\right)}\int_S w_{i,ss} w_{k,ss}\, ds$$

$$D_{ik} = D^1_{ik} - \nu\left(D^2_{ik} + D^2_{ki}\right) \quad , \quad (3)$$

$$D^1_{ik} = \frac{Gt^3}{3}\int_S w_{i,s} w_{k,s}\, ds \qquad D^2_{ik} = \frac{Et^3}{12\left(1-\nu^2\right)}\int_S w_i w_{k,ss}\, ds$$

$$X_{ikj} = t\int_S \frac{u_j}{C_{jj}}\left(v_i v_k + w_i w_k\right) ds$$

where (i) E, G and ν are Young's modulus, shear modulus and Poisson's ratio, and (ii) t and S are the cross-section thickness and mid-line width.

System (2) can only be solved analytically for simply supported members subjected to longitudinally uniform internal forces and moments. In other (more general), solutions can only be found by resorting to approximate numerical techniques – *e.g.*, the finite difference, finite element or Galerkin's method. Among these techniques, the finite element method is definitely the most versatile, in the sense that it can cover a wider range of situations. Silvestre & Camotim (2003) were the first to formulate and validate a GBT-based beam finite element – although originally developed in the context of pultruded composite members, this element has also been extensively employed to analyze the buckling behavior of cold-formed steel members (*e.g.*, Dinis *et al.* 2005). However, because the above finite element was formulated under the assumption of longitudinally uniform internal forces and moments, its use to solve buckling problems involving normal stress gradients is not efficient, in the sense that excessively fine discretizations are required to obtain accurate results. In order to overcome this limitation, Gonçalves & Camotim (2004) formulated a finite element that can handle linear bending moment diagrams and used it to study the buckling behavior of cold-formed steel cantilevers subjected to tip loads. In the next sub-section, one extends these authors' work, by formulating a GBT-based finite element that can account for the stiffness reduction due to internal forces and moments exhibiting uniform, linear, quadratic or cubic longitudinal distributions.

Finite element formulation. The main steps involved in the formulation of the abovementioned GBT-based finite element can be briefly described as follows:

(i) Rewrite system (2) in variational form, which leads to

$$\int_{L_e} (C_{ik}\phi_{k,xx}\delta\phi_{i,xx} + D^1_{ik}\phi_{k,x}\delta\phi_{i,x} + D^2_{ik}\phi_k\delta\phi_{i,xx} + D^2_{ik}\phi_{k,xx}\delta\phi_i + \\ + B_{ik}\phi_k\delta\phi_i + \lambda W_j X_{jik}\phi_{k,x}\delta\phi_{i,x})dx \quad , \quad (4)$$

where L_e is now the finite element length and one has $2<k<n+m+1$ – recall that the axial extension mode ($k=1$) never contributes to the member buckling mode shape.

(ii) Approximate the modal amplitude functions $\phi_k(x)$ by means of linear combinations of cubic Hermite polynomials, *i.e.*, one assumes

$$\phi_k(x)=Q_1\Psi_1(\xi)+Q_2\Psi_2(\xi)+Q_3\Psi_3(\xi)+Q_4\Psi_4(\xi) \quad , \quad (5)$$

where $Q_1=\phi_{k,x}(0)$, $Q_2=\phi_k(0)$, $Q_3=\phi_{k,x}(L_e)$, $Q_4=\phi_k(L_e)$, $\xi=x/L_e$ and

$$\Psi_1=L_e(\xi^3-2\xi^2+\xi) \quad \Psi_2=2\xi^3-3\xi^2+1 \quad \Psi_3=L_e(\xi^3-\xi^2) \quad \Psi_4=-2\xi^3+3\xi^2 \; . \quad (6)$$

(iii) Assume a longitudinal variation of the stress resultants W_j given by

$$W_j=W_{0j}+W_{1j}\xi+W_{2j}\xi^2+W_{3j}\xi^3 \quad , \quad (7)$$

where W_{ij} is the coefficient of the i-th order stress resultant component associated with the j-th deformation mode – see figure 4.

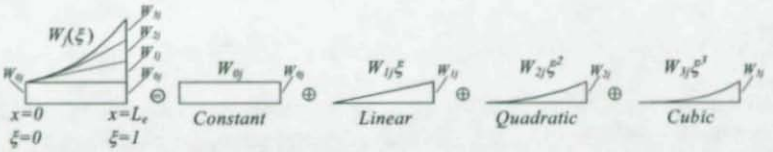

Figure 4. Stress resultant decomposition

(iv) Incorporate (5)-(7) into (4) and carry out the integrations, in order to obtain the usual finite element matrix equation

$$([K^{(e)}]+\lambda[G^{(e)}])\{d^{(e)}\}=\{0\} \quad , \quad (8)$$

where $[K^{(e)}]$, $[G^{(e)}]$ are the finite element linear and geometric stiffness matrices and $\{d^{(e)}\}$ is the corresponding nodal displacement vector – their dimension is $4(m+n)\times 4(m+n)$ and they are of the form

$$[K^{(e)}]=\begin{bmatrix} [K^{22}] & [0] & [0] & [K^{25}] & \cdots \\ & [K^{33}] & [0] & [K^{35}] & \cdots \\ & & [K^{44}] & [K^{45}] & \cdots \\ & & & [K^{55}] & \cdots \\ sym. & & & & \ddots \end{bmatrix} \tag{9}$$

$$[G^{(e)}]=\begin{bmatrix} [G^{22}] & [G^{23}] & [G^{24}] & [G^{25}] & \cdots \\ & [G^{33}] & [G^{34}] & [G^{35}] & \cdots \\ & & [G^{44}] & [G^{45}] & \cdots \\ & & & [G^{55}] & \cdots \\ sym. & & & & \ddots \end{bmatrix} \tag{10}$$

$$\{d^{(e)}\}=\{\{d^2\}^{\mathrm{T}}\ \{d^3\}^{\mathrm{T}}\ \{d^4\}^{\mathrm{T}}\ \{d^5\}^{\mathrm{T}}\ \ldots\}^{\mathrm{T}} \quad . \tag{11}$$

The superscripts in the *4×4* sub-matrices appearing in (9) and (10) identify the deformation modes involved and their components read

$$K_{pr}^{ik} = C_{ik}\int_{L_e}\Psi_{p,xx}\Psi_{r,xx}dx + D_{ik}\int_{L_e}\Psi_{p,x}\Psi_{r,x}dx + B_{ik}\int_{L_e}\Psi_{p}\Psi_{r}dx \tag{12}$$

$$G_{pr}^{ik} = -W_{lj}X_{ikj}T_{pr}^{l} = -W_{lj}X_{ikj}\int_{L_e}\xi^{l}\Psi_{p,x}\Psi_{r,x}dx \quad , \tag{13}$$

where the summation convention applies to l ($l=0,\ldots,3$), which is associated with the order of the W_{lj} term. The T_{pr}^{l} components, which incorporate the stress gradient effects, are presented in appendix.

ILLUSTRATIVE EXAMPLES: LIPPED CHANNEL BEAMS

The GBT-based finite element developed in the previous section is now employed to investigate the local and global buckling behavior of simply

supported[2] lipped channel beams (i) exhibiting the cross-section dimensions and material properties given in figure 2(a) and (ii) subjected to the three different loadings depicted in figures 5(a)-(c): (ii_1) unequal end moments related by the parameter r, (ii_2) a point transversal load applied at mid-span and (ii_3) a uniformly distributed transversal load – in addition, a number of combinations of these three loadings were also dealt with. The reference moments M adopted in each case are also indicated in figures 5(a)-(c).

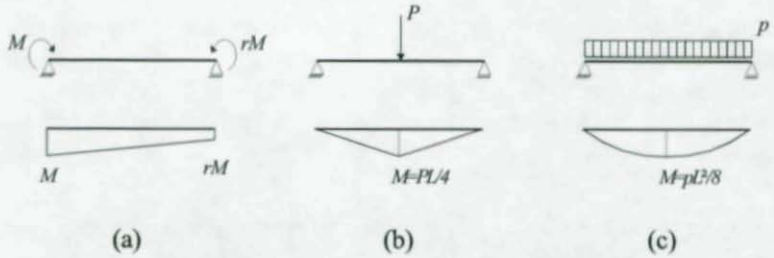

Figure 5. Beam loadings considered: (a) unequal end moments, (b) mid-span point load and (c) uniformly distributed load

Naturally, the finite element geometric stiffness matrix is evaluated on the basis of (major axis bending) (i) $W_2=W_{02}+W_{12}\xi$, in the first two cases (linear moment diagrams), and (ii) $W_2=W_{02}+W_{12}\xi+W_{22}\xi^2$, in the third one (quadratic moment diagram). All the beam analyses were based on the cross-section dicretization depicted in figure 2(b), which means that *13* deformation modes were involved – moreover, it was found that only the *10* first, shown in figure 3, have relevant participations in the beam local-plate, distortional and flexural-torsional buckling modes. Concerning the beam longitudinal discretizations, it is worth mentioning that:

(i) Obviously, the number of finite elements required to obtain accurate critical buckling moments/loads and modes decreases as one travels from local-plate to distortional and flexural-torsional buckling (even if the beam length increases) – this is due to the variation in the number of inflexion points exhibited by the buckling modes. Nevertheless, it became clear that the incorporation of the stress gradients in $[G^{(e)}]$ considerably lowers the mesh refinement needs.

---

[2] Beams with end sections that (i) are locally and globally pinned and (ii) can warp freely.

(ii) Generally speaking, it was found that *4* finite elements per half-wave are enough to obtain virtually exact local-plate, distortional and flexural-torsional buckling results. This figure is less than *50%* of the number of "uniform stress" finite elements required to achieve equally accurate results – a ratio providing a rough idea about the computational savings due to the incorporation of the stress gradients in the finite element.

Unequal end moments. Figure 6(a) provides the variation of the critical moment M_{cr} with the length L, for beams acted by unequal end moments defined by five r values (see figure 5(a)): *1.0*, *0.5*, *0*, *–0.5*, *–1.0*. Figure 6(b), on the other hand, concerns the beam under uniform bending (r=*1.0*) and makes it possible to assess the contribution of the various deformation modes to the buckling mode shapes of this beam.

The observation of figures 6(a)-(b) prompts the following remarks:

(i) Obviously, a stress gradient increase (*i.e.*, a decrease in r) leads to higher M_{cr} values. The difference between the values associated with r=*–1.0* (sharpest gradient) and r=*1.0* (no gradient) is never below *33%*.

(ii) The well defined local minima exhibited by the uniform bending curve, which are associated with local-plate and distortional buckling

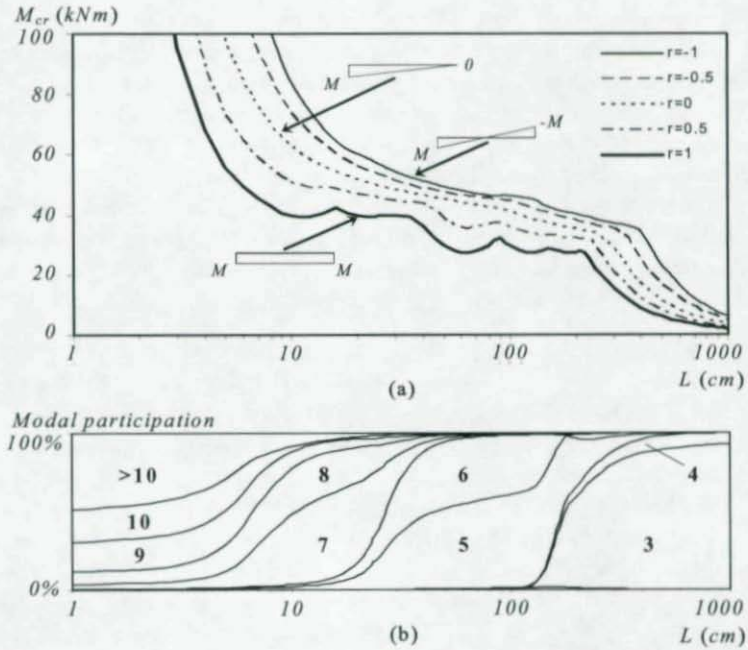

Figure 6. (a) M_{cr} –L curves associated with r=*1.0, 0.5, 0, –0.5, –1.0* and (b) modal participation diagram for uniformly bended beams (r=*1.0*)

(Hancock 1998b), become clearly attenuated as the stress gradient increases – indeed, they practically disappear for $r \leq 0$.

(iii) The modal participation diagram of the uniformly bended beams, which is qualitatively similar to the remaining four ones (not shown), provides clear evidence that (iii_1) beams with $L<25cm$ exhibit local-plate buckling (except for very short beams, predominance of modes **7** and **8**), (iii_2) beams with $25cm<L<150cm$ exhibit distortional buckling (equal contributions of modes **5** and **6**) and (iii_3) beams with $L>150cm$ exhibit flexural-torsional buckling (combinations of modes **3** and **4**[3]).

[3] The GBT normalization procedure leads to (apparently) very small participations of mode **4**.

Taking advantage of the GBT modal nature, it is possible to acquire a deep understanding on how the stress gradients influence the beam critical buckling mode shapes. Indeed, figures 7 to 15 show various aspects of these buckling mode shapes for beams having lengths $L=20cm$ (local-plate buckling), $L=120cm$ (distortional buckling) and $L=600cm$ (flexural-torsional buckling). In each case, one considers loadings associated with $r=1.0, 0.0, -1.0$ and the results presented include (i) deformed configurations of selected beam cross-sections and (ii) longitudinal displacement profiles at judiciously chosen mid-line points – the latter show also the contributions of the relevant participating deformation modes.

The buckling modes of the $L=20cm$ beams are given in figures 7 ($r=1.0$), 8 ($r=0.0$) and 9 ($r=-1.0$) – their analysis leads to the following comments:

(i) In the uniformly bended beam ($r=1.0$), the two web displacement profiles shown in figures 7(b_1)-(b_2) exhibit the expected sinusoidal patterns (two half-waves in this case) – these web displacements ($w_{1/4}$ and $w_{3/4}$) are almost exclusively due to modes **7** and **8** (there are also small participations of modes **5** and **6**). However, their contributions are in phase for $w_{1/4}$ and in counter-phase for $w_{3/4}$ – this stems from the fact that the shapes of modes **7** and **8** are symmetric and anti-symmetric w.r.t. the web mid-point (see figure 3). As a result, the web deformed configuration is much more pronounced in its (compressed) upper half – figures 7(a_1)-(a_2) show the deformed configurations of the *1/4* and *3/4*-span cross-sections (inward and outward web deflections).

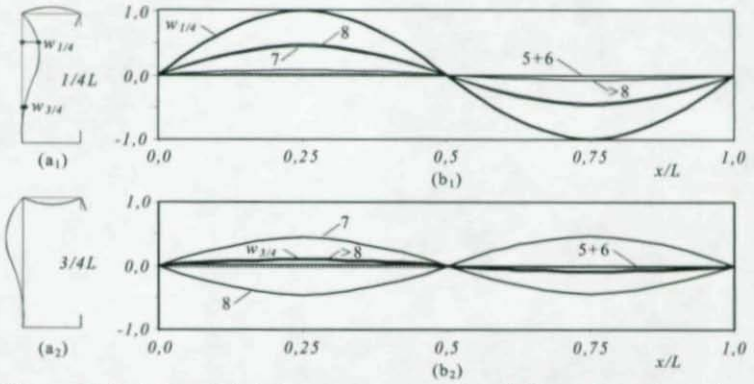

Figure 7. (a_1) *1/4* and (a_2) *3/4*-span cross-section deformed configurations; (b_1) $w_{1/4}$ and (b_2) $w_{3/4}$ longitudinal profiles (L=*20cm*, r=*1.0*, M_{cr}=*39.9 kNm*)

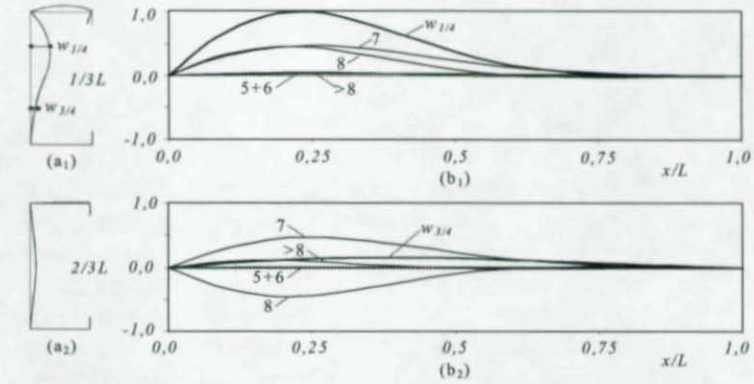

Figure 8. (a_1) *1/3* and (a_2) *2/3*-span cross-section deformed configurations; (b_1) $w_{1/4}$ and (b_2) $w_{3/4}$ longitudinal profiles (L=*20cm*, r=*0.0*, M_{cr}=*51.8 kNm*)

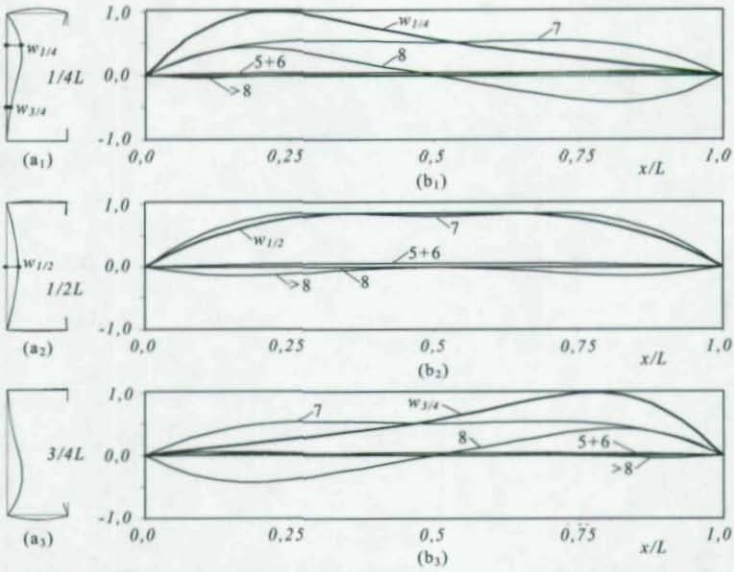

Figure 9. (a_1) *1/4*, (a_2) *1/2* and (a_3) *3/4*-span cross-section deformed shapes; (b_1) $w_{1/4}$, (b_2) $w_{1/2}$ and (b_3) $w_{3/4}$ profiles (L=*20cm*, r=*–1.0*, M_{cr}=*60.0 kNm*)

(ii) In the beam acted by a "triangular" diagram (r=*0.0*), the two web displacement profiles presented in figures 8(b_1)-(b_2) show that (ii$_1$) the largest displacements occur approximately at the *1/4*-span cross-section and that (ii$_2$) the displacements almost vanish beyond the *3/4*-span one. Concerning the cross-section deformed configurations, one notices that the location of the largest web displacement moves downwards along the beam length – *e.g.*, see the configurations of the *1/3* and *2/3*-span cross-sections in figures 8(a_1)-(a_2). Surprisingly, since the moment is always positive, $w_{1/4}$ becomes gradually less relevant than $w_{3/4}$ and virtually vanishes near the *5/6*-span cross-section – this is due to the opposing contributions of modes **7** and **8**.

(iii) In the beam acted by a "bi-triangular" diagram (r=*–1.0*), the three web displacement profiles presented in figures 9(b_1)-(b_3) show that (iii$_1$) $w_{1/4}$ and $w_{3/4}$ exhibit similar ("complementary") behaviours, with the largest values occurring at the *1/5* and *4/5*-span cross-sections, and that (iii$_2$) $w_{1/2}$ is surprisingly symmetric. The qualitative differences

between these displacement profiles stem from the anti-symmetric variation of the mode **8** amplitude and from the fact that this mode contributes very little to $w_{1/2}$ – note that the amplitude of mode **7** has a symmetric variation for $w_{1/4}$, $w_{1/2}$ and $w_{3/4}$. The web anti-symmetry of mode **8** (see figure 3) is also responsible for the differences between the deformed configurations of the *1/4*, *1/2* and *3/4*-span cross-sections, shown in figures $9(a_1)$-(a_3) – in particular, note the symmetry of the *1/2*-span cross-section deformed configuration (very similar to mode **7**).

(iv) As expected, in view of the bending moment diagrams, the three beam critical buckling modes exhibit considerable deflections in the upper flange and half-web at the first half-span. However, considerable differences exist concerning the second half-span – see the cross-section deformed configurations shown in figures $7(a_2)$, $8(a_2)$, $9(a_3)$.

(v) All the modal amplitude functions of the uniformly bended beam (symmetric diagram) are two half-wave sinusoids, *i.e.*, anti-symmetric[4]. When the diagram is "bi-triangular" (anti-symmetric) these functions are either anti-symmetric (even modes) or symmetric (odd modes) – but not sinusoidal. Finally, the amplitude functions of the beam acted by the (asymmetric) "triangular" diagram have no symmetry property.

The buckling modes of the *L=120cm* beams are given in figures 10 (*r=1.0*), 11 (*r=0.0*) and 12 (*r=–1.0*) – from their observation, one may draw the following conclusions:

(i) In the uniformly bended beam (*r=1.0*), the flange-lip node vertical displacement profile shown in figure 10(b) exhibits once more a sinusoidal pattern (again two half-waves) – this displacement (v) is due to the equally important contributions of modes **5** and **6**[5]. The deformed configuration of the *1/4*-span cross-section, presented in figure 10(a), makes it clear that only the beam (compressed) upper half experiences meaningful deformations.

(ii) In the beam acted by a "triangular" diagram (*r=0.0*), the flange-lip node vertical displacement profile presented in figure 11(b) shows that (ii_1) the largest upward displacement occurs approximately at the

[4] They would be symmetric if the number of sinusoidal half-waves was odd (instead of even).
[5] There are extremely small (negligible) participations of modes **2**, **4** and **>6** (local-plate).

1/4-span cross-section and that (ii_2) inward displacements occur in the second half-length – its maximum value is about *13%* of the outward one and occurs near the *3/4*-span cross-section. Once again, v is mostly due to the contributions of modes **5** and **6** – the participations of modes **2**, **4** and **>6** (local-plate) remain negligible. The deformed configuration of the *1/4*-span cross-section, depicted in figure 11(a), is very similar to the one appearing in figure 10(a) (uniform bending).

(iii) Figures 12(b_1)-(b_2) concern the beam subjected to a "bi-triangular" diagram ($r=-1.0$) and show the longitudinal profiles of (iii_1) the flange-lip node vertical displacement v and (iii_2) the quarter-web flexural displacement $w_{1/4}$. It is interesting to notice the high similarity between this v longitudinal profile and its $w_{1/4}$ counterpart of the $L=20cm$ beam (see figure 9(b_1)) – now, the contributions of modes **5** and **6** "replace" those of modes **7** and **8**. Moreover, due to the anti-symmetry of the mode **6** amplitude function, the deformed configuration of the *1/2*-span cross-section shown in figure 12(a_2) virtually coincides with the mode **5** shape. Finally, it is worth mentioning the *irregularity* of the $w_{1/4}$ longitudinal profile depicted in figure 12(b_2), which stems from the non-negligible participation of the **>6** (local-plate) modes in the vicinity of the beam ends, particularly in the left one (in the right end, the influence is mostly felt on the $w_{3/4}$ value, not shown) – participations of these modes are negligible in the other two load cases.

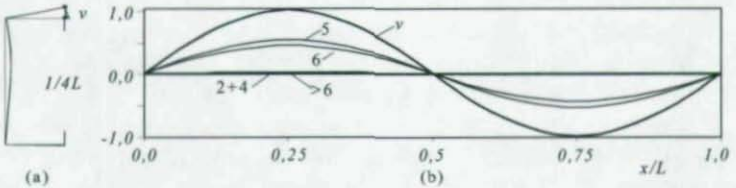

Figure 10. (a) *1/4*-span cross-section deformed configurations and (b) axial profile of displacement v ($L=120cm$, $r=1.0$, $M_{cr}=27.5\ kNm$)

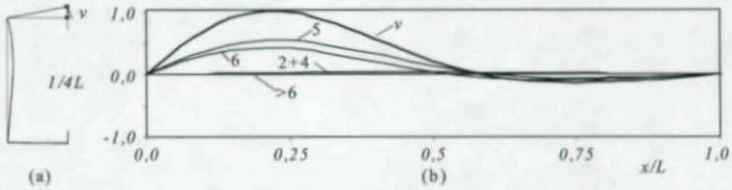

Figure 11. (a) *1/4*-span cross-section deformed configurations and (b) axial profile of displacement v ($L=120cm$, $r=0.0$, $M_{cr}=40.0\ kNm$)

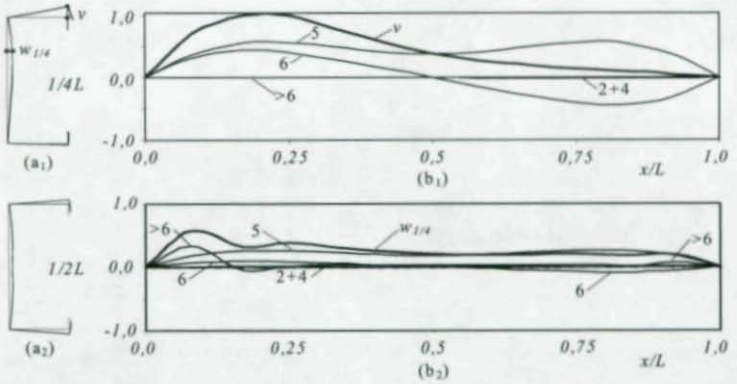

Figure 12. (a_1) *1/4* and (a_2) *1/2*-span cross-section deformed configurations; (b_1) v and (b_2) $w_{1/4}$ longitudinal profiles ($L=120cm$, $r=-1.0$, $M_{cr}=45.8\ kNm$)

Lastly, the buckling modes of the $L=600cm$ beams are given in figures 13 ($r=1.0$), 14 ($r=0.0$) and 13 ($r=-1.0$) – their joint observation shows that:

(i) As expected, only modes **3** and **4** participate in the buckling mode shapes of the three beams and the displacements are larger in the compressed half-section – see figures 13(a), 14(a) and 15(a_1)-(a_3).

(ii) In the beam under uniform bending ($r=1.0$), modes **3** and **4** contribute almost equally to the flange-lip node horizontal displacement u – see the longitudinal profile shown in figure 13(b), which exhibits a single half-wave sinusoidal pattern.

(iii) In the beam acted by a "triangular" diagram ($r=0.0$), the maximum value of the flange-lip node horizontal displacement u occurs in

the vicinity of the *2/5*-span cross-section. Naturally, the longitudinal profile of u is no longer sinusoidal.

(iv) In the beam acted by a "bi-triangular" diagram ($r=-1.0$), the flange-lip node horizontal displacement u is given by the sum of a symmetric contribution from mode **3** and an anti-symmetric one from mode **4** – this provides an explanation for the facts that (iv_1) the larger displacements "shift" from the upper to the lower part of the cross-section at mid-span and that (iv_2) the deformed configuration of the *1/2*-span cross-section involves only flexure.

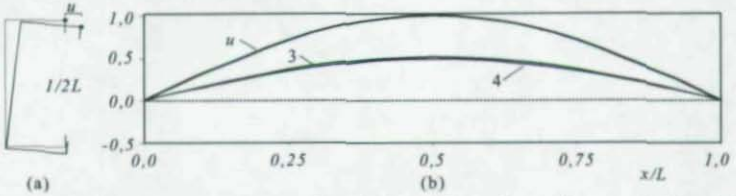

Figure 13. (a) *1/2*-span cross-section deformed configurations and (b) axial profile of displacement u ($L=600cm$, $r=1.0$, $M_{cr}=4.4\ kNm$)

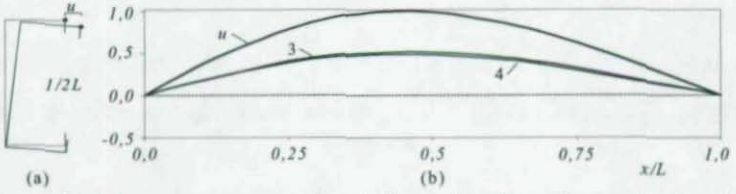

Figure 14. (a) *1/2*-span cross-section deformed configurations and (b) axial profile of displacement u ($L=600cm$, $r=0.0$, $M_{cr}=8.1\ kNm$)

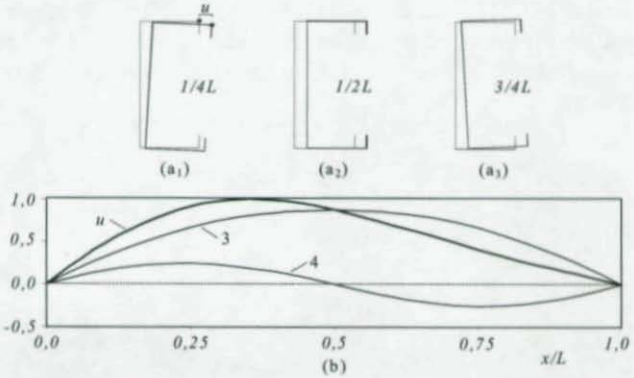

Figure 15. (a_1) *1/4*, (a_1) *1/2* and (a_3) *3/4*-span cross-section deformed configurations; (b) *u* longitudinal profile (L=*600cm*, r=*–1.0*, M_{cr}=*16.3 kNm*)

Uniformly distributed and mid-span point loads. In this sub-section, one addresses the buckling behavior of beams subjected to uniform bending (for comparison purposes), a uniformly distributed transverse load and a point transverse load applied at mid-span – bending always takes place about the major axis ($W_y \equiv W_2$). The beam cross-section dimensions and material properties as the ones already considered earlier (see figure 2(a)).

Figure 16 shows numerical results concerning the variation of the critical moment M_{cr} with the length L, for beams acted by the three loadings described in the previous paragraph. For validation purposes, this figure also includes some critical moment values recently reported by Chu *et al.* (2005) and obtained using the finite strip method. The observation of the numerical results presented in figure 16 makes it possible to conclude that:

(i) As expected and regardless of the L value, the beams subjected to the mid-span point loads always exhibit higher critical moments than the ones acted by uniformly distributed loads – note that the stress gradient is steeper in the first case. Moreover, it was also found that the M_{cr} increases with respect to the uniformly bended beams never fall below *17%* and *34%*, respectively.

(ii) The GBT-based results concerning the uniformly distributed load case exhibit an excellent agreement with the ones reported by Chu *et al.* (2005) – the maximum difference never exceeds *2.5%*.

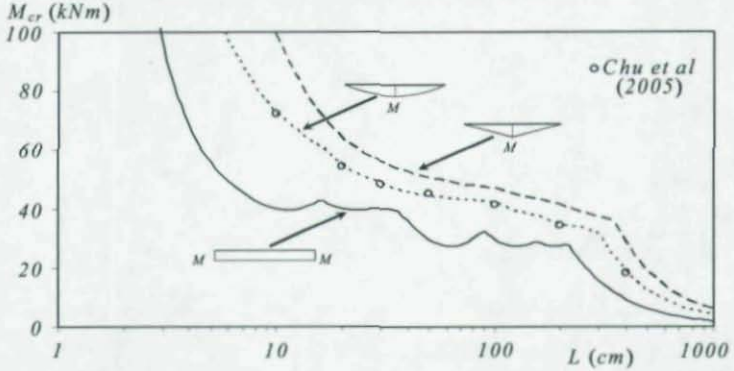

Figure 16. $M_{cr}-L$ curves concerning beams subjected to uniform bending, mid-span point loads and uniformly distributed loads

As before, figures 17 to 19 show (i) cross-section deformed configurations and (ii) displacement profiles for beams with lengths *L=20cm* (local-plate buckling), *L=120cm* (distortional buckling) and *L=600cm* (flexural-torsional buckling). Moreover, their critical buckling modes include once again highly predominant participations of (i) modes **7** and **8** (*L=20cm*), (ii) modes **5** and **6** (*L=120cm*) and modes **3** and **4** (*L=600cm*). The close observation of the results presented in the above three figures leads to the following comments:

(i) The modal amplitude functions are similar for both load cases. They exhibit (i_1) two "half-waves" for *L=20cm* and *L=120cm*, and (i_2) a single "half-wave" for *L=600cm*[6].

(ii) For the *L=20cm* and *L=600cm* beams, the displacement patterns and cross-section deformed configurations associated with the point and distributed loads are very similar – thus, figures 17(a) and 19(a) only include a single cross-section deformed configuration.

(iii) Figures 18(b_1)-(b_2) show that the distortional buckling mode shapes of the two *L=120cm* beams differ considerably, as far as the web $w_{1/4}$

[6] Note that these modal amplitude functions are not sinusoids (as in the uniform bending case).

displacements are concerned[7]. This difference is due to the participation of the local-plate modes (**>6**) in the vicinity of the mid-span cross-section – due to the much higher stress gradient, this participation is considerably larger and more localized in the point load case. As a result, the deformed configurations of the two *2/5*-span cross-sections, depicted in figures 18(a_1)-(a_2), are also somewhat different: the deformation is more pronounced in the web and upper flange of the cross-section belonging to the beam subjected to a point load.

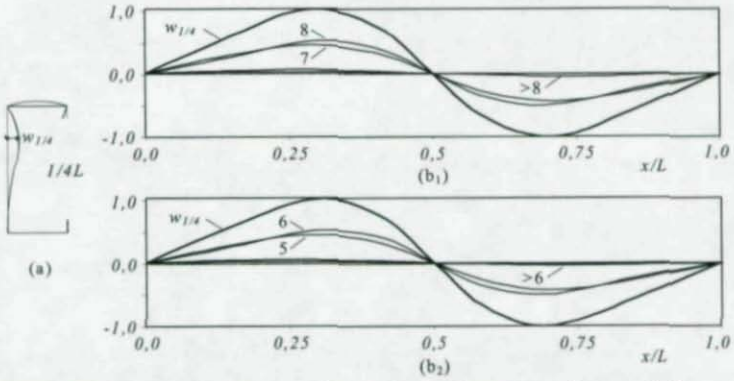

Figure 17. (a) *1/4*-span cross-section deformed configurations and (b) $w_{1/4}$ longitudinal profiles for (b_1) distributed and (b_2) point loads (L=*20cm*, M_{cr}=*54.6 kNm* and M_{cr}=*63.6 kNm*)

[7] Conversely, the vertical displacements of the compressed flange-lip corner are very similar.

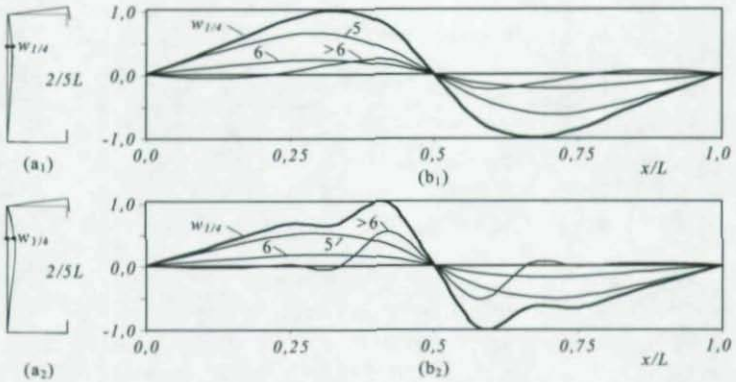

Figure 18. ($a_{1\text{-}2}$) *2/5*-span cross-section deformed configurations and (b) $w_{1/4}$ longitudinal profiles for (b_1) distributed and (b_2) point loads (L=*120cm*, M_{cr}=*39.4 kNm* and M_{cr}=*45.3 kNm*)

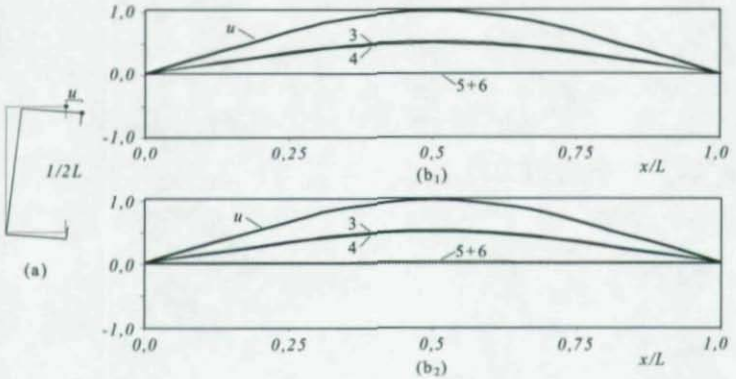

Figure 19. (a) *1/2*-span cross-section deformed configurations and (b) u longitudinal profiles for (b_1) distributed and (b_2) point loads (L=*600cm*, M_{cr}=*9.0 kNm* and M_{cr}=*13.7 kNm*)

Transverse loads and end moments. This sub-section is devoted to the analysis of the buckling behavior of beams subjected to "combined" loadings shown in figure 20: they consist of a transverse load and a left end moment ("triangular" diagram – r=*0.0*). As also indicated in figure 20, the parameter s provides the relation between the maximum bending

moments due to the transverse load and end moment (reference value M). In this study, the parameter s takes values comprised between 0.0 and -5.0.

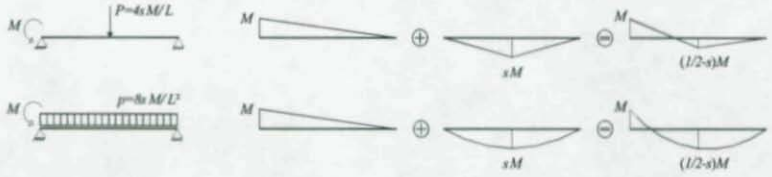

(a) (b)

Figure 20. Beam (a) "combined" loadings conditions and (b) corresponding bending moment diagrams

Figures 21(a)-(b) show the M_{cr}–L curves of beams subjected to "combined" loadings conditions defined by the $s=0.0$; -0.25; -0.5; -1.0; -2.0; -5.0 and also the s value that maximizes the critical moments ($s=-1.1$ and $s=-1.25$, respectively for the uniformly distributed and mid-span point loads). Note that the curve associated with $s=0$ was already shown in figure 6(a) – $r=0.0$. The observation of these results leads to the following remarks:

(i) In both cases, the variation of the critical moment with s, for any given beam length, exhibits the following characteristics: (i_1) up to a certain limit value of s ($s=-1.1$ or $s=-1.25$), M_{cr} increases as the absolute value of s grows; then, when that limit value is exceeded, (i_2) M_{cr} begins to decrease gradually and the critical moment even falls the value associated with $s=0$. This behaviour stems from the dependence of the bending moment diagram on the value of s – while for $s=0$ the instability is triggered by the beam left half-span (see figures 8, 11 and 14), an increase in s leads to (i_1) a negative moment reduction in the left half-span and (i_2) a positive moment growth in the right one – the maximization of the critical moments occurs for the s value that "balances" these two effects. Below (above) that limit value, the instability is triggered by the beam left (right) half-span.

(ii) As mentioned earlier, the values of s maximizing the critical moments are $s=1.1$ (uniformly distributed load) and $s=1.25$ (mid-span point

load). It is not surprising that the second value is higher – the positive bending moments due to the uniformly distributed load are more significant than those generated by the mid-span point load.

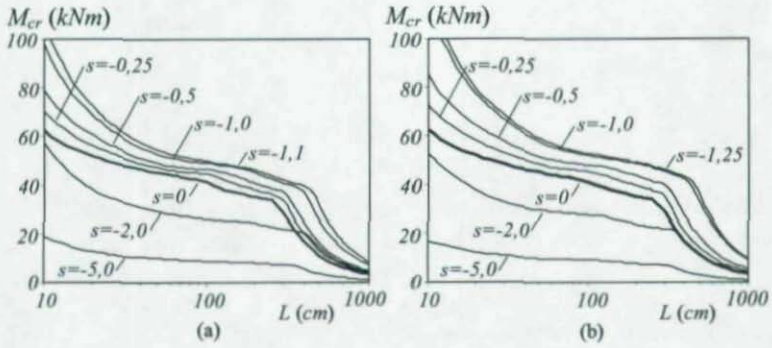

Figure 21. $M_{cr}-L$ curves concerning beams subjected to a left end moment and (a) uniformly distributed or (b) mid-span point loads

CONCLUDING REMARKS

Initially, this paper addressed the formulation and numerical implementation of a GBT-based finite element intended to analyze the buckling behaviour of thin-walled steel members in the presence of longitudinal stress gradients – it incorporates the geometric stiffness reduction associated with linear, quadratic or cubic applied stress distributions. This finite element was then employed to investigate the local-plate, distortional and flexural-torsional buckling behaviour of cold-formed steel simply supported lipped channel beams subjected to various non-uniform bending moment diagrams, due to (i) several unequal end moment combinations, (ii) uniformly distributed loads, (iii) mid-span point loads or (iv) combinations of the above. Some GBT-based results (all concerning beams under uniformly distributed loads) were compared with values yielded by finite strip analyses reported by Chu *et al.* (2005) – an excellent agreement was found in all cases.

The results of the analyses performed provided clear evidence about the influence of the longitudinal stress gradients on the buckling behaviour (critical moment value and corresponding buckling mode shape) of the

lipped channel beams – naturally, this influence was shown to be higher for steeper bending moment diagrams. It is worth pointing out that the modal features of the GBT-based finite element implementation made it possible to acquire an in-depth understanding of the mechanical aspects associated with the presence of longitudinal stress gradients.

Finally, one last word to mention that the local-plate and distortional buckling results presented and discussed in this work are fairly novel[8] – moreover, they are bound to have some impact on the development of more efficient design methodologies for cold-formed steel lipped channel beams.

APPENDIX: Determination of the Geometric Stiffness Matrix

The components of the matrices T_{pr}^{l}, which incorporate the longitudinal stress gradient effects and are involved in the determination of the geometric stiffness matrix $[G^{(e)}]$ (see (8)), are given by (the four coefficients read $A_0 = 1/30L_e$, $A_1 = L_e/60$, $A_2 = L_e^3/210$ and $A_3 = L_e^5/840$)

$$T_{pr}^{0} = -A_0 \begin{bmatrix} 4L_e^2 & 3L_e & -L_e^2 & -3L_e \\ & 36 & 3L_e & -36 \\ & & 4L_e^2 & -3L_e \\ sym & & & 36 \end{bmatrix} \quad T_{pr}^{2} = -A_2 \begin{bmatrix} 4L_e^2 & 15L_e & -3L_e^2 & -15L_e \\ & 72 & -6L_e & -72 \\ & & 18L_e^2 & 6L_e \\ sym & & & 72 \end{bmatrix}$$

$$T_{pr}^{1} = -A_1 \begin{bmatrix} 2L_e^2 & 6L_e & -L_e^2 & -6L_e \\ & 36 & 0 & -36 \\ & & 6L_e^2 & 0 \\ sym & & & 36 \end{bmatrix} \quad T_{pr}^{3} = -A_3 \begin{bmatrix} 11L_e^2 & 42L_e & -11L_e^2 & -42L_e \\ & 180 & -30L_e & 180 \\ & & 65L_e^2 & 30L_e \\ sym & & & 180 \end{bmatrix}$$

REFERENCES

Camotim D, Silvestre N, Gonçalves R, Dinis PB (2004). GBT analysis of thin-walled members: new formulations and applications, *Thin-Walled Structures: Recent Advances and Future Trends in Thin-Walled Structures Technology*, J. Loughlan (Ed.), Canopus Publishing, Bath, 137-168.

[8] The same cannot be said about the flexural-torsional buckling results.

Camotim D, Silvestre N, Dinis PB (2005). Numerical analysis of cold-formed steel members, *International Journal of Steel Structures*, **5**(1), 63-78.

Chu X T, Kettle R, Li LY (2004). Lateral-torsion buckling analysis of partial-laterally restrained thin-walled channel-section beams, *Journal of Constructional Steel Research*, **60**(8), 1159-1175.

Chu X.T, Ye ZM, Kettle R, Li LY (2005). Buckling behaviour of cold-formed channel sections under uniformly distributed loads, *Thin-Walled Structures*, **43**(4), 531-542.

Dinis PB, Camotim D, Silvestre N (2005). GBT formulation to analyse the buckling behaviour of thin-walled members with arbitrarily 'branched' open cross-sections, *Thin-Walled Structures*, accepted for publication.

Gonçalves R, Camotim D (2004). Application of generalised beam theory (GBT) to investigate the local and global stability of cold-formed steel beams, *Computational Methods in Engineering*, CM Soares *et al.* (Eds.), Lisboa, p. 191. (full paper in CD-ROM Proceedings) (Portuguese)

Hancock GJ (1998a). Finite strip buckling and nonlinear analyses and distortional buckling analysis of thin-walled structural members, *Coupled Instabilities in Metal Structures: Theoretical and Design Aspects*, J. Rondal (Ed.), CISM course nº 379, 225-289 (Part V), Springer-Verlag, Wien.

Hancock GJ (1998b). *Design of Cold-Formed Steel Structures*, Australian Institute of Steel Construction (3rd Edition).

Hancock GJ (2003). Cold-formed steel structures, *Journal of Constructional Steel Research*, **59**(4), 473-487.

Li LY (2004). Lateral-torsional buckling of cold-formed zed-purlins partial-laterally restrained by metal sheeting, *Thin-Walled Structures*, **42**(7), 995-1011.

Rhodes J, Lawson RM (1993). *Design of Structures using Cold-Formed Steel Sections*, SCI Publication, 089, The Steel Construction Institute.

Schafer B (2003). *Elastic Buckling Analysis of Thin-Walled Members using the Classical Finite Strip Method. CUFSM Version 2.6*, Johns Hopkins University. (see http://www.ce.jhu.edu/bschafer/)

Silvestre N, Camotim D (2003). GBT buckling analysis of pultruded FRP lipped channel members, *Computers & Structures*, **81**(18-19), 1889-1904.

Yu C, Schafer BW (2004). Stress gradient effect on the buckling of thin plates, *Proceedings of 17th International Specialty Conference on Cold-Formed Steel Structures*, Orlando, 47-69.

Yu C (2005). *Distortional Buckling of Cold-Formed Steel Members in Bending*, Ph.D. Thesis, Johns Hopkins University, Baltimore.

Vlassov BZ (1959). *Thin-Walled Elastic Bars*, Fizmatgiz, Moscow. (in Russian – English translation: Israel Program for Scientific Translation, Jerusalem, 1961).

GBT LINEAR AND BUCKLING ANALYSIS OF THIN-WALLED MULTI-CELL BOX GIRDERS

R. Gonçalves[1], P. B. Dinis[2] and D. Camotim[3]

ABSTRACT

One presents the derivation, validation and illustration of a Generalized Beam Theory (GBT) formulation to perform first-order and buckling analyses of thin-walled members with fully arbitrary cross-section shapes, namely cross-sections combining multiple closed cells with open branches. Following a very brief overview of the so-called "conventional GBT", the paper addresses the modifications that must be incorporated into the GBT cross-section analysis procedure in order to handle the simultaneous presence of closed single or multiple cells and any number of open branches. The proposed formulation is then employed to analyze (i) the first-order behavior of a composite bridge formed by a concrete slab and a double-cell box girder and (ii) the buckling behavior of a simply supported I-shaped steel girder with closed cells separating the web from two unequal flanges. For validation purposes, the GBT-based numerical results are compared with values yielded by shell finite element and finite strip analyses.

INTRODUCTION

Generalized Beam Theory (GBT) was originally developed by Schardt (Schardt 1983, 1989, 1994) and may be seen as an extension Vlassov's classical prismatic bar theory that incorporates genuine folded-plate concepts and, therefore, accounts for cross-section in-plane deformations. Moreover, the deformed configuration or buckling/vibration mode shape

[1] Adjunct Professor, High Technological School of Barreiro, Polytecnic Institute of Setúbal, R. Stinville 14, 2830-114 Barreiro, Portugal

[2] Assistant and [3] Associate Professor, Civil Engineering Department, ICIST/IST, TechnicaL University of Lisbon, Av. Rovisco Pais, 1049-001 Lisbon, Portugal

of a given member is expressed in terms of pre-determined cross-section *deformation modes* (with longitudinally varying amplitudes). This quite unique modal nature renders the application of GBT considerably more versatile and efficient than similar finite strip or shell finite element analyses, even if one must call the reader's attention to the very interesting work carried out recently by Schafer & Ádány (2005) and concerning the incorporation of the GBT modal features into semi-analytical finite strip analyses. Indeed, it has been shown that GBT provides a powerful, elegant and clarifying tool to solve structural problems involving prismatic thin-walled members (*e.g.*, Davies 1998 or Camotim *et al.* 2004).

However, the vast majority of the research work devoted to GBT was done in the context of thin-walled members with either open unbranched or closed single-cell cross-sections (see figures 1(a) and 1(c_1)). In fact, a GBT formulation that can handle members exhibiting arbitrary open branched cross-sections, like the ones shown in figure 1(b), only became available very recently, developed and validated by Dinis *et al.* (2005)[1]. Concerning closed multi-cell cross-sections (see figure 1(c_2)) and cross-sections combining closed cells with open branches (see figure 1(d)), it seems fair to say that the GBT formulation that was first developed (Möller 1982) somewhat deviates from the "spirit" of the one originally proposed by Schardt. Moreover, it involves an unnecessarily large number of deformation modes, a feature that makes it less efficient, particularly when applied to cross-sections combining closed cells with open branches (see figures 1(d_1)-(d_2)).

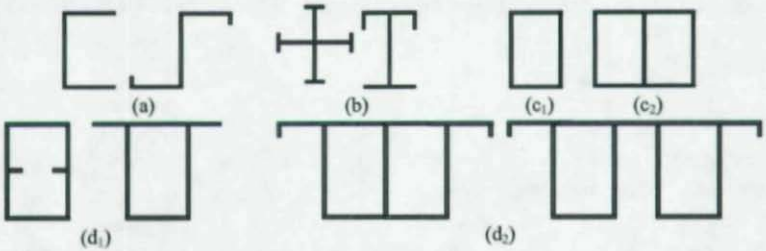

Figure 1. Cross-sections types: (a) open unbranched, (b) open branched, (c) closed single and multi-cell and (d) closed cells with open branches.

[1] However, note that specific GBT applications involving open branched members had been previously addressed by Möller (1982), Mörschardt (1990) and Dégée & Boissonnade (2004).

The aim of this paper is to derive, validate and illustrate the application of a GBT formulation to perform linear (first-order) and buckling analyses of thin-walled members with *fully arbitrary* cross-sections, *i.e.*, cross-sections combining any number of closed cells (with or without common walls) with an arbitrary amount of "open branches" (*i.e.*, walls that do not belong to any closed sub-section) – these branches may either (i) exhibit a free end or (ii) connect two adjacent closed cells (*e.g.*, the second cross-section in figure 1(d_2)). Initially, one presents a brief overview of the available GBT formulations, which make it possible to analyze (i) open unbranched members (Schardt 1989, 1994)[1] (ii) open branched members (Dinis *et al.* 2005) and (iii) closed single-cell members (Schardt 1989, Gonçalves & Camotim 2004a). Then, one addresses the modifications that must be incorporated into a GBT formulation in order to (i) retain the "spirit" of Schardt's original work and (ii) be able to handle members exhibiting simultaneously single or multiple closed cells and open branches. At this point, it is worth noting that these modifications concern exclusively issues related to the performance of the GBT cross-section analysis, namely the choice of the most appropriate warping, shear and local-plate "elementary functions". Finally, the efficiency and versatility of the proposed GBT formulation are illustrated through its application to determine the elastic (i) first-order behavior of a composite bridge subjected to eccentric vertical loads and (ii) buckling behavior of a simply supported I-shaped steel girder with closed cells separating the web from two unequal flanges and subjected to uniform bending. For validation purposes, the GBT-based results are compared with values yielded by shell finite element and semi-analytical finite strip analyses performed in the codes ADINA (Bathe 2003) and CUFSM$_{2.6}$ (Schafer 2003).

OVERVIEW OF THE CONVENTIONAL GBT ANALYSIS

The so-called "conventional GBT" is intended to analyze the behavior of elastic isotropic prismatic thin-walled members with *open unbranched* cross-sections. Its application involves the performance of two main tasks, namely (i) a cross-section analysis, which concerns the identification of the deformation modes and the evaluation of the associated modal mechanical

[1] Henceforth designated as "conventional GBT".

properties, and (ii) a member (first-order, buckling, vibration, etc.) analysis, in which the appropriate differential equilibrium equations must be solved (*e.g.*, Schardt 1989, Davies 1998 or Camotim *et al.* 2002). Next, the main concepts and procedures related to the performance of the first of these tasks – the one constituting the GBT "trademark" – are briefly reviewed.

Cross-Section Analysis. For illustrative purposes, one considers the arbitrary member shown in figure 2(a), having a cross-section formed by q walls and where (i) x, s and z are coordinates along the member length, cross-section mid-line and wall thickness, and (ii) u, v and w are the displacement components at member mid-surface (see figure 2(b)), given by

$$\begin{aligned} u(x,s) &= u_k(s)\,\phi_{k,x}(x) \\ v(x,s) &= v_k(s)\,\phi_k(x) \\ w(x,s) &= w_k(s)\,\phi_k(x) \end{aligned} \quad , \quad (1)$$

where (i) the summation convention applies to subscript k, (ii) the comma indicates differentiation, (iii) the functions $u_k(s)$, $v_k(s)$, $w_k(s)$ provide the definition of the cross-section *deformation modes* and (iv) $\phi_k(x)$ are their common amplitude functions.

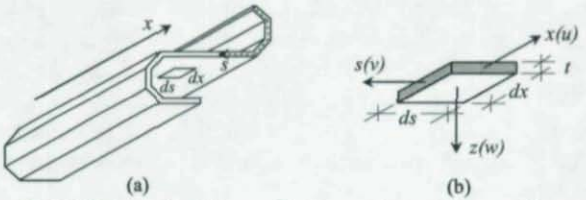

Figure 2. (a) Prismatic thin-walled member with an arbitrary open unbranched cross-section and (b) infinitesimal wall element.

The most unique feature of a GBT analysis resides in its cross-section *modal* discretization, *i.e.*, the identification of the functions $u_k(s)$, $v_k(s)$ and $w_k(s)$ appearing in (1). The selection procedure is by no means straightforward and involves two steps (*e.g.*, Schardt 1989 or Silvestre & Camotim 2002a): (i) a systematic selection of a set of *initial* shape functions and (ii) an elaborate and rational evaluation of a set of mechanically meaningful *final* shape functions – the deformation modes. Concerning the choice of the initial shape functions, it is worth noting the following aspects:

(i) A q-walled member cross-section is discretized into $q+1$ natural nodes (the wall ends) and m intermediate nodes (within the walls).

(ii) The initial shape functions $u_{0k}(s)$, $v_{0k}(s)$ and $w_{0k}(s)$ are obtained by sequentially imposing (ii$_1$) an elementary warping (u) function at each natural node and (ii$_2$) an elementary local-plate (w) function at each intermediate node.

(iii) Given the null membrane shear strain assumption ($\gamma(x,s)=u_{,s}+v_{,x}=0$), each elementary warping function is associated with a piecewise constant transverse displacement function $v_{0k}(s)$. In each cross-section wall i, the value of $v_{0k}(s)$ is obtained through

$$v_{0ki}(s) = -u_{0ki,s}(s) \quad . \quad (2)$$

(iv) The functions $w_{0k}(s)$, stemming from the imposition of the elementary warping and flexural functions are determined taking into account the (iv$_1$) compatibility between the in-plane transverse displacements $v_{0k}(s)$ and $w_{0k}(s)$ and (iv$_2$) continuity of the flexural rotations $w_{0k,s}(s)$. Thus, the determination of each $w_{0k}(s)$ requires the solution of a statically indeterminate folded-plate problem, a task traditionally performed by means of the force method.

(v) Then, the elementary warping and local-plate functions are defined by $u_{0k}(s)$, $v_{0k}(s)$ and $w_{0k}(s)$. Their common amplitudes ϕ_{0k} are the *initial degrees of freedom* of the discretized cross-section, which means that the functions $\phi_{0k}(x)$ are the member *initial unknowns*.

On the basis of $u_{0k}(s)$, $v_{0k}(s)$ and $w_{0k}(s)$, one readily obtains the initial cross-section stiffness (C_{0ik}, D_{0ik}, B_{0ik}) and geometric (X_{0jik}) matrices, given by

$$C_{0ik} = \int_S t\, u_{0i} u_{0k} ds + \frac{1}{12(1-\nu^2)} \int_S t^3 w_{0i} w_{0k} ds$$

$$B_{0ik} = \frac{1}{12(1-\nu^2)} \int_S t^3 w_{0i,ss} w_{0k,ss} ds$$

$$D_{0ik} = \frac{1}{3} \int_S t^3 w_{0i,s} w_{0k,s} ds - \frac{\nu E}{12G(1-\nu^2)} \int_S t^3 (w_{0i} w_{0k,ss} + w_{0k} w_{0i,ss}) ds$$

$$X_{0jik} = \int_S \frac{t\,u_{0j}}{C_{0jj}} (v_{0i}v_{0k} + w_{0i}w_{0k})ds \quad , \quad (3)$$

where ν is Poisson's ratio, t is the wall thickness and S is the cross-section mid-line. In order to obtain a system of differential equilibrium equations as uncoupled as possible, as well as mechanically meaningful degrees of freedom, one performs a change of base functions leading to the simultaneous diagonalization of matrices $[C_{0ik}]$ and $[B_{0ik}]$ (*e.g.*, Schardt 1989 or Silvestre & Camotim 2002a). This procedure leads to the *final* shape functions, *i.e.*, the cross-section *deformation modes* $u_k(s)$, $v_k(s)$, $w_k(s)$ – their amplitudes ϕ_k are the *final* degrees of freedom of the discretized cross-section.

Then, by employing, for example, the principle of stationary potential or the principle of virtual work, one is led to a *GBT system* of differential equilibrium equations, which differs according to the nature of the problem to be solved. For first-order and buckling analyses, one has, respectively,

$$EC_{ik}\phi_{k,xxxx} - GD_{ik}\phi_{k,xx} + EB_{ik}\phi_k - q_i = 0 \quad (4)$$

$$EC_{ik}\phi_{k,xxxx} - GD_{ik}\phi_{k,xx} + EB_{ik}\phi_k + \lambda W^{\sigma}_{j,0} X_{jik}\phi_{k,xx} = 0 \quad , \quad (5)$$

where (i) E and G are the Young's and shear moduli, (ii) q_i is the consistent applied load vector, (iii) λ is the load parameter and (iv) EC_{ik}, GD_{ik}, EB_{ik} and X_{jik} are the new stiffness and geometric matrices, which are obtained by plugging $u_k(s)$, $v_k(s)$ and $w_k(s)$ into equations $(3)_1$-$(3)_4$, and (iv) $W^{\sigma}_{j,0}$ are the pre-buckling internal force/moment profiles, deemed *uniform*.

Member Analysis. In order to obtain the solution of systems (4) or (5), *i.e.*, the modal amplitude functions $\phi_k(x)$, one adopts methods commonly used in structural analysis. In general, such amplitude functions can only be found by resorting to approximate numerical techniques, such as the finite element, Rayleigh-Ritz's or Galerkin's methods – among them, the finite element method is, by far, the one covering a wider range of situations. Silvestre & Camotim (2003a) formulated and validated the first GBT-based beam finite element, in the context of the buckling analysis of pultruded composite members – this element was later used to assess also the buckling behavior of cold-formed steel members (*e.g.*, Dinis *et al.* 2005). It is also worth noting the beam finite element developed by Gonçalves & Camotim (2004b), which

can handle linear bending moment diagrams and was employed to study the buckling behavior of cold-formed steel cantilevers acted by tip loads.

The numerical results concerning the illustrative examples presented in this work were obtained by means of two different methods:

(i) The first-order behavior of the composite bridge is determined by means of a GBT-based shear deformable finite element, which was formulated very recently by two of the authors (Gonçalves & Camotim 2004b).

(ii) The buckling behavior of the simply supported I-girders subjected to uniform bending moments is determined through the application of Galerkin's method and adopting sinusoidal shape functions – it is well known that these functions provide *exact solutions* for this problem.

MEMBERS WITH OTHER CROSS-SECTION SHAPES

One addresses now the modifications and/or extensions that need to be incorporated in the conventional GBT procedure in order to be able to handle members exhibiting other cross-section types (*i.e.*, cross-sections that are not open unbranched). First of all, it is important to mention that these modifications/extensions concern exclusively the *cross-section analysis*, namely (i) the choice and characterization of the initial shape functions, (ii) the identification of the cross-section deformation modes. As for the establishment and solution of the GBT system of differential equilibrium equations, they are absolutely identical to the conventional ones. In the next sections, one (i) *reviews* available formulations for arbitrary open branched sections (see figure 1(b)) and (ii) closed single-cell sections (see figure 1(c_1)), and (iii) *proposes* a novel formulation applicable to fully arbitrary sections, including closed multi-cell ones (see figure 1(c_2)) and sections that combine closed cells with open branches (see figure 1(d)).

Open Branched Cross-Sections. A GBT formulation to handle this type of cross-sections was very recently developed and validated by Dinis *et al.* (2005). It differs from the conventional one in the need to select the most appropriate set of "warping elementary functions", which stems from the fact that the nodal warping displacements cannot be chosen arbitrarily at the walls emerging from branching nodes due to transversal displacement compatibility requirements. This automatically implies that the number of elementary warping functions included in the cross-section analysis is *smaller*

than the number of natural nodes, making it necessary to distinguish between *dependent* and *independent* natural nodes. Moreover, an alternative way to determine the initial transverse bending shape functions was also proposed. Concerning these two aspects, the following methodologies were employed:

(i) A branched cross-section is viewed as a combination of an unbranched sub-section with an ordered sequence of branches. This makes it easy to select the dependent and independent natural nodes – the former are the first nodes of the various branches (excluding the branching node) and no "warping elementary function" is associated with them.

(ii) Each elementary warping function has (ii_1) a unit warping value at one independent natural node, (ii_2) null values at the remaining independent natural nodes and (ii_3) warping values at the dependent natural nodes (u_{rj}) that must be determined through the expression

$$u_{rj} = u_r - v_{rj}\, b_{rj} \quad , \quad (6)$$

where u_r is the warping value at the branching node r, and b_{rj} and v_{rj} are the width and transverse membrane displacement of the wall rj (branched wall uniting the branching node r and the dependent natural node j). The value of v_{rj} is obtained from the compatibility between the transverse displacements of the walls sharing node r.

(iii) The initial flexural shape functions are determined by means of the *displacement method* (instead of the force method, traditionally employed in the conventional formulation) – one takes advantage of the fact that only a single kinematical unknown is associated with each branching node, regardless of the number of branches emerging from it.

Closed Single-Cell Cross-Sections. A GBT formulation to handle this type of cross-sections was already developed by Schardt (1989). It is based on the well known fact that membrane shear strains and stresses cannot be neglected in closed cross-sections, which means that one must have cross-section deformation modes that do not comply with Vlassov's assumption (*i.e.*, such that $\gamma(x,s)=u_s+v_x\neq 0$). Schardt proposed a methodology that consists of supplementing the conventional GBT deformation modes (stemming from the imposition of the warping and local-plate elementary functions – note that, in closed single-cell cross-sections, all natural nodes are independent) with *membrane shear deformation modes*. These new

modes are obtained through the sequential imposition of constant (unit) transverse displacements ($v=1$) at each cross-section wall, while keeping $v=0$ at all remaining walls and $u=0$ in all natural nodes. This procedure is illustrated in figure 3 and the cross-section deformed configurations shown constitute the additional *initial shape functions* that take into account the membrane shear strains. As before, the corresponding *deformation modes* can be obtained by means of a suitable change of base functions, *i.e.*, diagonalizing two stiffness matrices simultaneously[1].

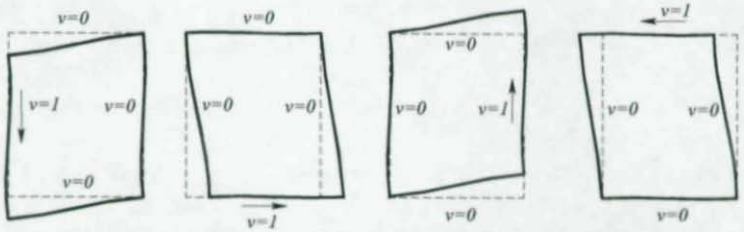

Figure 3. Initial shape functions accounting for the membrane shear strains.

The presence of non-null membrane shear strains makes it necessary to include the corresponding virtual work term, which leads to the definition a new GBT matrix (tensor) D_{ij}^{3} that must be added to the matrix D_{ij} given in (3). Then, one has

$$D_{ij}^{3} = \int_{S} G t (u_{i,s} u_{j,s} + v_i u_{j,s} + v_j u_{i,s} + v_i v_j) ds \tag{7}$$

$$D_{ij} = D_{ij}^{1} - (D_{ij}^{2} + D_{ji}^{2}) + D_{ij}^{3} \quad . \tag{8}$$

Arbitrary Cross-Sections. As far as the authors know, a GBT formulation applicable to fully arbitrary cross-sections has never been proposed[2]. Indeed, neither closed multi-cell cross-sections (*i.e.*, closed branched cross-sections) nor cross-sections exhibiting closed and open sub-sections (either branched

[1] It may be convenient not to change the base functions, *i.e.*, take the initial shape functions as the additional membrane shear deformation modes.

[2] Although the authors claimed to have done it a few months ago (Gonçalves *et al.* 2005), it was found later that certain types of cross-section fell outside the domain of application of the developed GBT formulation. Hopefully, this will not happen this time.

or not) can be handled by the available GBT formulations. Naturally, a formulation making it possible to analyze the aforementioned cross-section types must combine features of the two previous ones – indeed, this is case.

Next, one presents a fairly detailed description of the steps and procedures involved in the novel GBT formulation, which will be illustrated through its application to the cross-section depicted in figure 4(a): an I-shaped steel section with closed cells separating the web from the two unequal flanges – it comprises 13 walls (W_1–W_{13}), 2 closed-cells and has 12 natural nodes, 6 of which are branching ones (B_1–B_6). The proposed methodology involves the performance of the following sequence of operations:

(i) Choice of the dependent cross-section natural nodes, as in the case of the open branched cross-sections – there are several options and, in general, some are more convenient than others (in the sense that they render the analysis simpler). Figures 4(b_1)-(b_2) show two possible choices for the *6* dependent and *6* independent natural nodes to be considered in the analysis of the cross-section given in figure 4(a).

(ii) Determination of the cross-section "warping initial shape functions", *i.e.*, the ones stemming from imposing elementary warping functions at each independent natural node and presuming that Vlassov's assumption holds in the whole cross-section (*i.e.*, in the wall belonging to either closed or open sub-sections). This is done adopting the methodology developed for open branched cross-sections (Dinis *et al.* 2005).

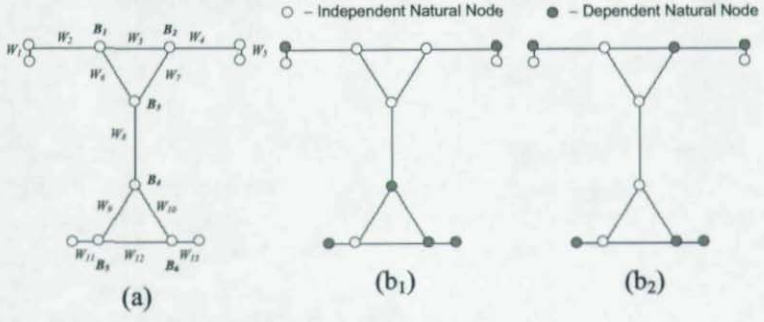

Figure 4. Illustrative example: (a) cross-section geometry and (b) choice of the dependent and independent natural nodes.

(iii) As in the conventional GBT, impose elementary local-plate functions in each intermediate node, thus obtaining the "local-plate initial shape functions", related to transverse bending of the walls: both membrane displacements (u and v) are null. In the illustrative example, one has included *13* intermediate nodes– see the cross-section discretization depicted in figure 13.

(iv) On the basis of the "warping and local-plate initial shape functions" determined in the two previous steps, identify the cross-section "conventional" *deformation modes*, associated with the simultaneous diagonalization of the stiffness matrices $[C_{0ik}]$ and $[B_{0ik}]$. In the case of the illustrative example, this procedure leads to the identification of *19* deformation modes, *11* of which are shown in figure 5: *5* "warping modes" (**2**–**6**) and *6* "local-plate modes" (**13**–**18**) – note that modes **2**–**4** are "rigid-body" ones and mode **1** (axial extension) has been omitted.

(v) Sequential imposition of unit membrane shear strains in each wall belonging to a closed cell, while keeping all the remaining walls free of membrane shear strains. In the illustrative example, this means that one must impose *6* unit membrane shear strains (3 in each closed cell) and, then, determine the corresponding initial shear shape functions. These unit membrane shear strains are enforced by a combination of u and v displacements and their calculation may be quite cumbersome.

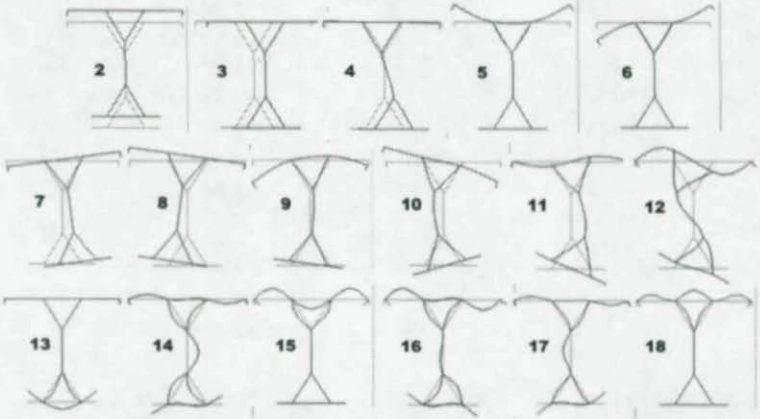

Figure 5. Illustrative example: in-plane deformed configurations of the *17* most relevant warping (**2**–**6**), shear (**7**–**12**) and local-plate (**13**–**18**) modes.

Indeed, it varies with both the particular cross-section geometry and the choice of dependent natural nodes. Next, one provides some guidelines concerning this issue and figures 4(b$_1$)-(b$_2$) are used to illustrate them:

(v.1) In closed cell walls comprised between independent natural nodes, a unit membrane shear strain can only be achieved through a transverse displacement $v=1$[1]. This is the case of walls W_3, W_6 and W_7, in figure 4(b$_1$), and walls W_6 and W_9, in figure 4(b$_2$).

(v.2) In closed cell walls linking one or two dependent natural nodes, a unit membrane shear strain may be achieved through $v=1$ and/or $u_{,s}=1$, *i.e.*, warping displacements with unit slope[2]. For instance, in figure 4(b$_1$) it is impossible to impose simultaneously $\gamma=1$ in wall W_{10} and $\gamma=0$ in walls W_9 and W_{12} without resorting to warping displacements – indeed, one must impose $v=0$ and $u_{,s}=1$ in wall W_{10} (*i.e.*, $u\neq 0$ in dependent nodes). In figure 4(b$_2$), on the other hand, this same shear strain combination is associated with the imposition of $v=1$ and $u_{,s}=0$ in wall W_{10} – nevertheless, one must have $u_{,s}\neq 0$ in wall W_{12}. Finally, note that the imposition of $\gamma=1$ in wall W_{12} and $\gamma=0$ in walls W_9 and W_{10} may be achieved with $u_{,s}=0$ in these three walls for both figure 4(b$_1$) and 4(b$_2$).

(v.3) In most situations, warping displacements at the dependent natural nodes are indispensable to ensure, at the same time, compatibility of the transverse displacements and $\gamma=0$ in all walls but one. One exception is the imposition of $\gamma=1$ in wall W_{12} in figure 4(b$_1$): one has $u=0$ at all dependent natural nodes.

(vi) On the basis of the "shear initial shape functions" determined in the previous step, to identify the cross-section *shear deformation modes*, again by simultaneously diagonalizing the stiffness matrices $[C_{0ik}]$ and $[B_{0ik}]$[3]. In the illustrative example, this procedure leads to the *6* shear deformation modes shown in figure 5 – modes (**7**–**12**).

Local Modes. In conventional GBT, one includes warping and *local-plate* deformation modes in the analysis. The latter (i) stem from the imposition of elementary flexural functions at the intermediate nodes and (ii) involve

---

[1] Note that all the walls of a closed single-cell cross-section fall into this category.

[2] Recall that the membrane shear strain is given by $\gamma(x,s) = u_{,s} + v_{,x} = u_{k,s}\,\phi_{k,s} + v_k\,\phi_{k,x}$.

[3] Since the "conventional" and shear modes are not identified jointly, the overall matrices $[C_{ik}]$ and $[B_{ik}]$ are not diagonal – only their principal sub-matrices exhibit this property.

no displacements of the natural nodes (except the free end ones). At this stage, it is important to point out that it may be also necessary to include in a GBT analysis other types of "local modes": modes stemming from the sequential imposition of elementary warping (u) and transversal (v) functions at the intermediate nodes – this was done, for instance, by Silvestre & Camotim (2003a,b) and Gonçalves & Camotim (2005)[1].

ILLUSTRATIVE EXAMPLES

In order to illustrate the application and capabilities of the proposed GBT formulation, one presents and discusses next numerical results concerning (i) the first-order behavior of a steel-concrete composite bridge and (ii) the buckling behavior of simply supported girders exhibiting the I-shaped cross-section depicted in figure 4(a) and subjected to uniform bending. For validation purposes, the GBT-based results are compared with values yielded by (i) shell finite element analyses performed in the code ADINA (Bathe 2003) – steel-concrete composite bridge – and (ii) finite strip analyses carried out in CUFSM$_{2.6}$ (Schafer 2003) – I-shaped beams.

Steel-Concrete Composite Bridge. Initially, one considers the first-order behavior of a simply supported composite bridge with a span $L=20\,m$. Its cross-section is shown in figure 6 and comprises a C50/60 concrete ($E=37\,GPa$, $\nu=0.1$) slab and a steel ($E=210\,GPa$, $\nu=0.3$) double-cell box girder. The loading consists of two eccentric vertical loads Q applied at mid-span and symmetrically located with respect to the bridge axis (see figure 6). Due to the cross-section and loading symmetry, one only needs to analyze "a quarter of the bridge". Since the cross-section discretization adopted, given in figure 7, involves only *3* independent nodes, one obtains *3* warping and *4* shear deformation modes (no local modes were included in the analysis) – their in-plane deformed configurations are shown in figure 8 (the axial extension mode is again omitted). Moreover, figure 9 illustrates the procedures involved in determining the *4* initial shear deformation modes[2]. It was found that, in order to conveniently isolate the shear deformation

[1] For instance, the "local modes" due to the imposition of elementary warping functions at the intermediate nodes play an important role in the buckling behavior of FRP composite members.

[2] In this case, the shear deformation modes coincide with the associated initial shape functions, which means that no matrix diagonalization was carried out.

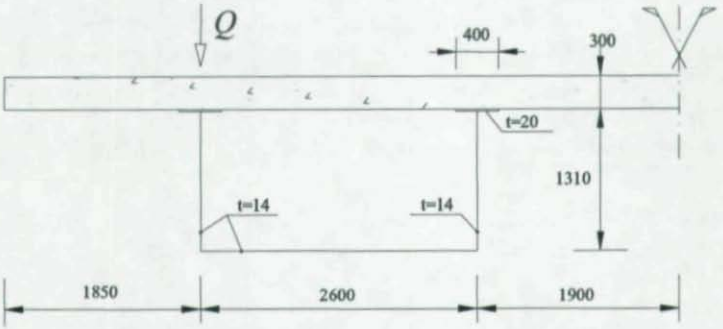

Figure 6. Composite bridge cross-section geometry, dimensions (in *mm*) and loading – due to symmetry, only "half section" is shown.

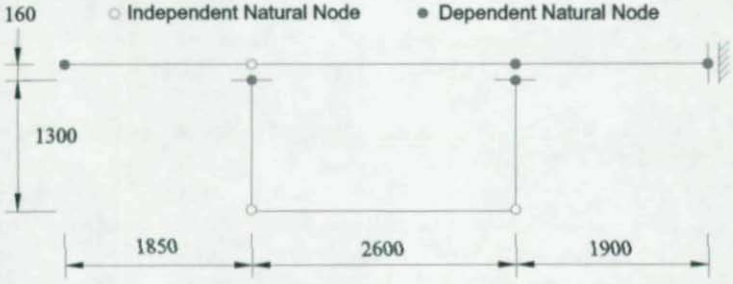

Figure 7. Composite bridge GBT cross-section discretization.

associated with the bending mode **2**, it is necessary to "recombine" the shear modes **5** and **7**, a procedure that leads to the "new" modes **5** and **7** shown in figure 10. Concerning the bridge end support conditions, it is worth noting that one assumes that all deformation modes exhibit "simply supported conditions", a fact automatically presupposing the existence of diaphragms preventing the occurrence of cross-section distortion at the supports.

The analysis of the bridge is carried out by means of a GBT-based beam finite element (BFE) recently developed by two of the authors (Gonçalves & Camotim 2004b) – the modal amplitude functions $\phi_k(x)$ are approximated by means of Hermite cubic polynomials. Concerning the formulation of

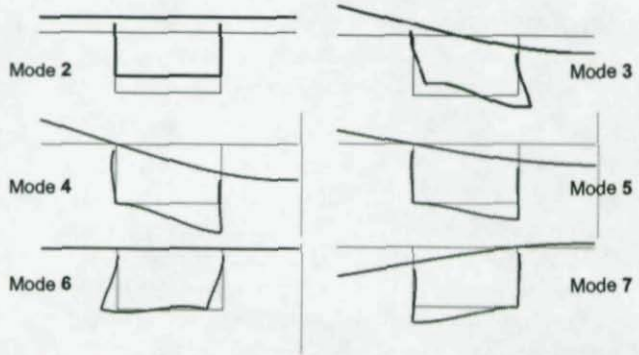

Figure 8. In-plane deformed configurations of the bridge cross-section warping (**2**–**3**) and shear (**4**–**7**) deformation modes.

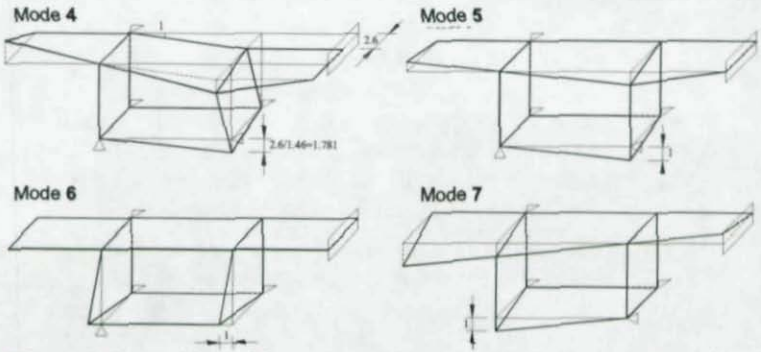

Figure 9. Imposition of the unit membrane shear strains in each of the *4* closed-cell walls – deformed configurations of the shear modes **4**–**7**.

Figure 10. "New" shear modes **5** (old **5**+**7**) and **7** (old **7**–**5**).

this BFE, it should be pointed out that it requires C^1 continuity, even if the classical formulations that account for shear deformation (*e.g.*, Timoshenko beams or Mindlin plates) only require C^0 continuity – this is due to the fact

that the displacements associated with wall bending are based on Kirchhoff's theory. Since the analysis includes *7* deformation modes (*3* warping and *4* shear), the finite element stiffness matrix has dimension *28×28*.

Figure 11 shows numerical results concerning the vertical displacement at the point of load application (mid-span cross-section), for *Q=1kN*. These results are obtained by means of (i) GBT, considering all the deformation modes (with the individual modal participations also shown), and (ii) the code ADINA, adopting a shell element discretization – moreover, they are presented as a function of the number of BFE included in the analysis. Figures 12 and 13, on the other hand, show (i) the undeformed and deformed configurations of the "quarter of bridge" and (ii) the axial normal stress distribution at the mid-span cross-section provided by the GBT and ADINA (Bathe 2003) analyses, adopting 5 BFE (shown in different colors) and a fine shell element mesh, respectively. The close observation of the above results prompts the following remarks

(i) The GBT and ADINA results virtually coincide, even when only *3* BFE are used (*e.g.*, in figure 11 the two values differ by *1.2%*). This is quite remarkable, particularly because (i_1) only *7* deformation modes were considered and (i_2) no "local modes" were included in the GBT analysis – obviously, the inclusion of local-plate and longitudinal shear (*i.e.*, shear-lag) deformation modes would improve the accuracy.

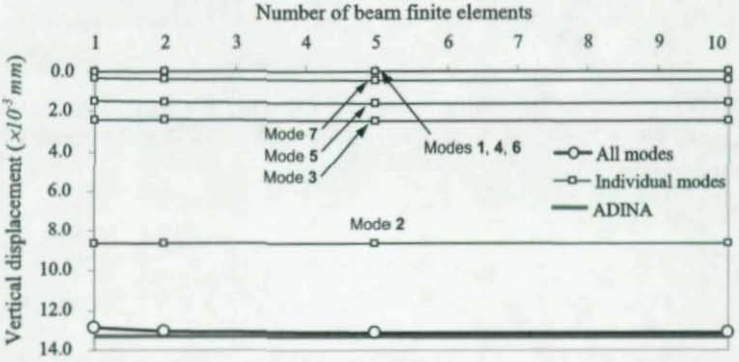

Figure 11. Variation of the vertical displacement at the point of load application with the number of BFE.

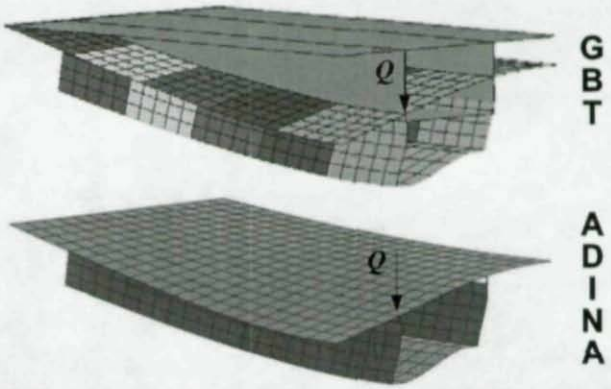

Figure 12. Deformed configurations of the "quarter of bridge" provided by the GBT and ADINA analyses (magnifying factor of 1E5).

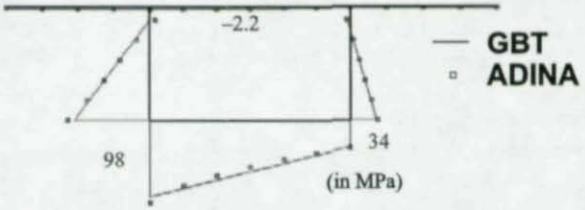

Figure 13. Mid-span cross-section normal stress distributions provided by the GBT and ADINA analyses (only the GBT values are indicated).

(ii) Although the bridge response is mainly governed by major axis bending (mode **2**), modes **3** (distortion) and **5** (vertical shear) also play a relevant role. Indeed, figure 11 shows that the contributions of these modes to the vertical displacement of the point of load application amounts to *19%* (mode **3**) and *12%* (mode **5**) – the participation of mode **7** is only *3%*. This considerable participation of the distortion mode **3** is responsible for the non-linearity of the lower flange normal stress distribution, clearly visible in figure 13.

I-Section Girders. Next, one presents numerical results concerning the buckling behavior of simply supported (the end sections are locally and

globally pinned and may warp) I-section girders with the cross-section geometry and dimensions depicted in figure 14(a) and subjected to uniform positive and negative major axis bending. Their elastic constant values read $E=210\ GPa$ and $\nu=0.3$ and figure 14(b) shows the cross-section discretization adopted, which leads to the identification of *25* deformation modes: *6* warping, *6* shear and *13* local-plate – the in-plane configurations of the *18* most relevant ones have already been depicted in figure 5. The GBT member analysis is carried out by means of Galerkin's method, using sinusoidal shape functions (they provide exact solutions). The GBT-based results are validated through the comparison with values yielded by finite strip analyses performed in the code CUFSM$_{2.6}$ (Schafer 2003).

The curves shown in Figure 15(a) provide the variation of the positive and negative moments M_b concerning single-wave buckling with the girder length L (in logarithmic scale). Figure 15(b), on the other hand, shows the modal participation diagrams that give information on how the individual deformations modes contribute to the beam buckling modes. One notices that the latter figure does not include the modal participations of girders acted by *positive* moments with lengths $12<L<135\,cm$ (length range associated with critical distortional buckling) – these participations are given separately, in figure 17, and will be addressed later in the paper. Figure 15 also includes the M_b values yielded by the finite strip analyses carried out with CUFSM$_{2.6}$. In addition, figure 16 enables the comparison

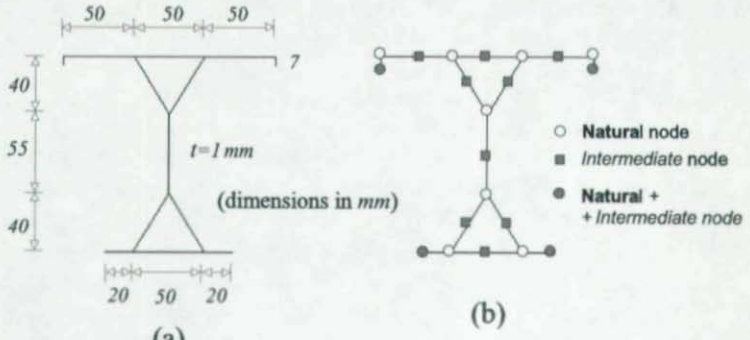

Figure 14. I-section (a) geometry/dimensions and (b) GBT discretization.

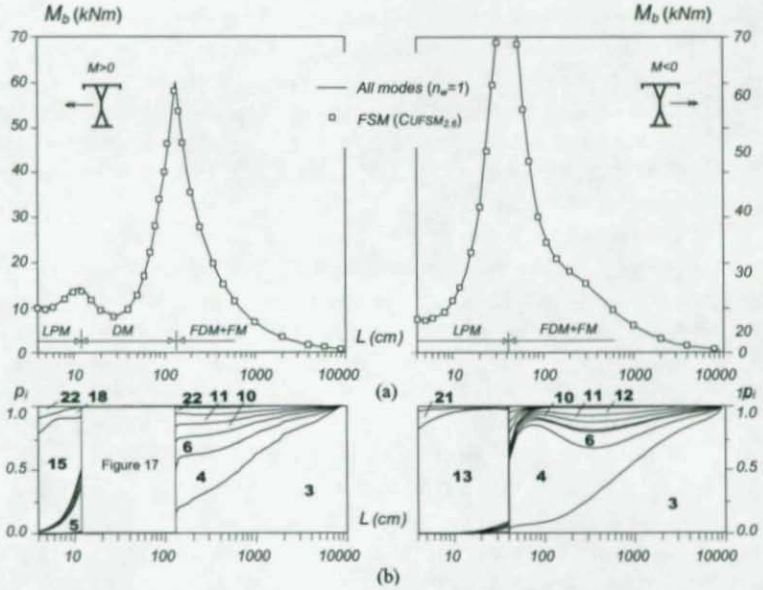

Figure 15. I-section girders: single-wave (a) M_b *vs.* L curves and (b) modal participation diagrams p_i *vs.* L – $M_b>0$ and $M_b<0$.

between the buckling mode shapes obtained through CUFSM$_{2.6}$ and GBT analyses: they concern girders with three different lengths and acted by positive and negative uniform moments ($M_b>0$ and $M_b<0$). The observation of all these buckling results leads to the following conclusions:

(i) The nearly perfect coincidence between the M_b values and buckling mode shapes provided by GBT and CUFSM$_{2.6}$ further validates the proposed formulation. The larger M_b differences never exceed *7%* and occur for $M_b>0$ and girder lengths in the transition from local-plate to distortional buckling. Previous studies showed that including additional local modes eliminates these differences (Silvestre & Camotim 2003a).

(ii) As expected, the buckling curves concerning positive and negative moments are qualitatively different. While the $M_b>0$ curve exhibits *three* distinct zones, corresponding to (ii_1) local-plate ($L<12$ *cm*), (ii_2) distortional ($12<L<135$ *cm*) and (ii_3) flexural-torsional buckling ($L>135$ *cm*), its $M_b<0$ counterpart only exhibits *two* zones, associated

with (ii_1) local-plate ($L<40cm$) and (ii_2) flexural-torsional buckling ($L>40cm$) – distortional buckling is never critical for $M_b<0$.

(iii) For $M_b>0$, the buckling curve exhibits local minima at $L\approx5\ cm$ and $L\approx30cm$. While the former corresponds to local-plate buckling that combines a dominant mode **15** with small contributions from modes **5**, **18** and **22**, the latter is associated with distortional buckling that is predominantly due to the participation of mode **5** *or* **6** (see figure 17 and related discussion), with small contributions from a few local-plate and shear modes (*e.g.*, modes **15**, **16**, **17**, **9**, **10**, **11**).

(iv) For $M_b<0$, the buckling curve exhibits only one local minimum at $L\approx5\ cm$, corresponding to local-plate buckling mode combining a clearly dominant contribution of mode **13** and a fading participation of mode **21**. Note also that, for $L\approx5\ cm$, the negative minimum M_b value is equal to $7.3\,kNm$, about 33% below its positive counterpart ($9.7kNm$) – recall that different walls trigger the local-plate buckling.

(v) The modal participation diagram of figures 15(b) (and also 17(b_1)-(b_2)) show that several portions of the M_b *vs.* L buckling curves can be accurately determined through GBT analyses that include only a handful of properly selected deformation modes. For instance, the inclusion of the *single* modes **15** ($M_b>0$), **13** ($M_b<0$) and **5** *or* **6** ($M_b>0$) would probably yield fairly accurate local-plate and distortional buckling moment estimates (with very little computational effort).

(vi) Due to the cross-section major axis asymmetry, the flexural-torsional buckling modes in the final descending branches of the two M_b vs. L curves combine mode **3** with distortion modes **4**, **6** and shear modes **10**, **11**[1] – this asymmetry also leads to smaller negative M_b values.

(vii) The buckling mode shapes shown in figure 16 concern (vii_1) local-plate (flange) buckling ($L=6cm$), (vii_2) symmetric distortional buckling ($L=60cm$ and $M_b>0$), (vii_3) "lateral buckling" with considerable shear deformation ($L=60cm$ and $M_b<0$ – note the strong contribution of mode **4** in figure 15(b_2)) and (vii_4) flexural-torsional buckling ($L=800cm$).

Finally, one addresses the modal participations of the girders with lengths $12<L<135\ cm$ and acted by *positive* bending moments. Although all these

[1] It is worth mentioning that the cross-section torsion is not associated with a single deformation mode. Indeed, pure torsion corresponds to a combination of warping and shear modes.

girders exhibit distortional buckling, an interesting phenomenon occurs: there are two different distortional buckling modes associated with nearly coincident buckling moments. One of these distortional buckling modes is symmetric (*D–S*), due to the dominant contribution of mode **5**, and the other is anti-symmetric (*D–AS*), due to the predominance of mode **6**. Because of numerical problems stemming from the virtual coincidence of the two buckling moments, it was found that the buckling mode shapes yielded by both the GBT and CUFSM$_{2.6}$ analyses "oscillate" between the *D–S* and *D–AS* configurations. This explains why it makes no sense to display the modal participation diagram for $12<L<135$ *cm*. Instead, one

	M_b (kNm)				
	GBT			CUFSM$_{2.6}$	
L(cm)	all modes	no mode **6** (D–S)	no mode **5** (D–AS)	critical mode	second mode
14*	13.16	13.61	13.16	12.69 (D-S)	13.00 (D-AS)
20	9.32	9.69	9.32	9.35 (D-AS)	9.36 (D-S)
30	8.04	8.04	8.24	8.00 (D-S)	8.29 (D-AS)
40	9.57	9.57	10.13	9.57 (D-S)	10.17 (D-AS)
60	16.93	16.94	17.70	16.90 (D-S)	17.72 (D-AS)
80*	28.06	28.11	28.06	28.02 (D-S)	28.06 (D-AS)
100	40.00	42.15	40.00	39.99 (D-AS)	41.99 (D-S)
120	52.69	55.57	52.69	52.66 (D-AS)	57.93 (D-S)
130	58.44	62.83	58.44	58.18 (D-AS)	63.80 (D-S)

(a)

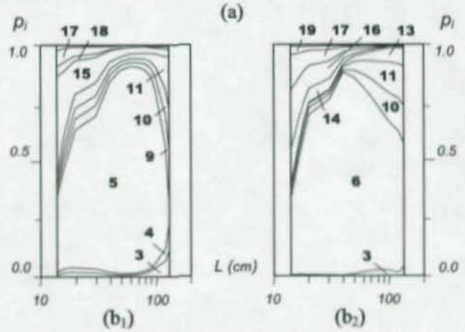

Figure 17. (a) GBT and CUFSM$_{2.6}$ $M_b>0$ values for $12<L<135$ *cm* and (b) modal participation diagrams without modes (b_1) **6** (*D–S*) and (b_2) **5** (*D–AS*).

presents in figure 17(a) M_b values yielded by (i) GBT analyses including all deformation modes, excluding mode **6** and excluding mode **5** (always the lowest buckling moment), and (ii) a CUFSM$_{2.6}$ analysis (the two lowest buckling moments)[1]. Figures 17(b_1) and 17(b_2), show the modal participations diagrams related to the last two GBT analyses (without mode **6** or mode **5**). These results confirm the closeness of the two buckling moments and provide a logical explanation for the "erratic" buckling mode shape estimation of both GBT and CUFSM$_{2.6}$.

CONCLUSION

After presenting a brief overview of the available GBT formulations, the paper addressed the derivation, validation and illustration of a GBT formulation intended to perform linear and buckling analyses of thin-walled members with *fully arbitrary* cross-sections, *i.e.*, cross-sections combining any number of closed cells with an arbitrary amount of open branches. A key issue resides in the identification of the shear modes, which stem from imposing unit membrane shear strains in each closed-cell wall.

In order to illustrate the application and potential of the proposed GBT formulation, numerical results concerning (i) the first-order behavior of a steel-concrete composite bridge and (ii) the buckling behavior of a complex I-shaped girder were presented and discussed. These results were validated through the comparison with "exact" values yielded by shell finite element (composite bridge) and finite strip (I-shaped girder) analyses.

REFERENCES

Bathe KJ (2003). ADINA System, ADINA R&D Inc.

Camotim D, Silvestre N, Gonçalves R and Dinis PB (2004). GBT analysis of thin-walled members: new formulation and applications, *Thin-Walled Structures: Recent Advances and Future Trends in Thin-Walled Structures Technology*, J Loughlan (Ed.), Canopus Publishing Ltd., Bath, 137-168.

Davies JM (1998). Generalised beam theory (GBT) for coupled instability

[1] The asterisks identify the girder lengths for which the GBT and CUFSM$_{2.6}$ M_b values correspond to different buckling mode shapes.

problems, *Coupled Instability in Metal Structures: Theoretical and Design Aspects*, J Rondal (Ed.), Springer Verlag, Vienna, 151-223.

Degée H and Boissonnade N (2004). An investigation on the use of GBT for the study of profiles with branched cross-sections, *Proceedings of Fourth International Conference on Coupled Instabilities in Metal Structures* (CIMS'04 – Roma, 27-29/9), 87-96.

Dinis PB, Camotim D and Silvestre N (2005). GBT formulation to analyse the buckling behaviour of thin-walled members with arbitrarily 'branched' open cross-sections, *Thin-Walled Structures*, accepted for publication.

Gonçalves R and Camotim D (2004a). GBT Local and Global Buckling Analysis of Aluminium and Stainless Steel Columns, *Computers & Structures*, **82**(17-19), 1473-1484.

Gonçalves R and Camotim D (2004b). Application of generalised beam theory (GBT) to investigate the local and global stability of cold-formed steel beams, *Computational Methods in Engineering*, CM Soares *et al.* (Eds.), Lisboa, 191. (full paper in CD-ROM Proceedings) (Portuguese)

Gonçalves R and Camotim D (2005). Physically non-linear analysis of thin-walled members using generalised beam theory (GBT), *Numerical Methods in Engineering* (CMNI 2005 Granada, 4-7/7), J Aparício *et al.* (Eds.), 138. (full paper in CD-ROM Proceedings) (Portuguese)

Gonçalves R, Dinis PB and Camotim D (2005). GBT Formulation to analyze the stability of thin-walled members with fully arbitrary cross-section shapes, *CD-ROM Proceedings of 2005 Joint ASME/ASCE/SES Conference on Mechanics and Materials* (McMat 2005 – Baton Rouge, 1-3/6).

Möller R (1982). *Zur Berechnung Prismatischer Strukturen mit Beliebigem nicht Formtreuem Querschnitt*, Institut für Statik, TH Darmstadt. (German)

Mörschardt S (1990). Die verallgemeinerte technische biegetheorie für faltwerke mit kragteilen, *Festschrift Richard Schardt*, TH Darmstadt, 259-275. (German)

Schafer BW and Ádány S (2005). Understanding and classifying local, distortional and global buckling in open thin-walled members, *Proceedings of SSRC 2005 Annual Stability Conference* (Montreal – 6-9/4), 27-46.

Schardt R (1989). *Verallgemeinerte Technische Biegetheorie*, Springer Verlag, Berlin. (German)

Schardt R (1983). The generalized beam theory, *Instability and Plastic Collapse of Steel Structures* (Proceedings of M.R. Horne Conference), University of of Manchester, 469-475.

Schardt R (1994). Generalised beam theory: an adequate method for coupled stability problems, *Thin-Walled Structures*, **19**(2-4), 161-180.

Schafer B (2003). *CUFSM2.6*, www.ce.jhu.edu/bschafer.

Silvestre N and Camotim D (2002a). First-order generalized beam theory for arbitrary orthotropic materials, *Thin-Walled Structures*, **40**(9), 755-789.

Silvestre N and Camotim D (2002b). Second-order generalized beam theory for arbitrary orthotropic materials, *Thin-Walled Structures*, **40**(9), 791-820.

Silvestre N and Camotim D (2003a). GBT buckling analysis of pultruded FRP lipped channel members, *Computers & Structures*, **81**(18-19), 1889-1904.

Silvestre N and Camotim D (2003b). Non-linear generalised beam theory for cold-formed steel members, *International Journal of Structural Stability and Dynamics*, **3**(4), 461-490.

MECHANICS OF WEB PANEL POSTBUCKLING BEHAVIOR IN SHEAR

Chai H. Yoo[1], Sung C. Lee[2] and Doo S. Lee[3]

ABSTRACT

This paper revisits a fundamental assumption used in most classical failure theories for postbuckled web plates under shear, namely that the compressive stresses that develop in the direction perpendicular to the tension diagonal do not increase any further once elastic buckling has taken place. This assumption naturally led to a well-known theory that tension field action in plate girders with transverse stiffeners must be anchored by flanges and stiffeners in order for the webs to develop their full postbuckling strength. However, a careful examination of the results of the nonlinear finite element analyses carried out for this study reveals that the diagonal compression continuously increase in close proximity to the edges after buckling, thereby producing in the web panel a self-equilibrating force system that does not depend on the flanges and stiffeners. These findings provide a fuller understanding of the actual mechanics of tension field action.

---

1 Professor, Dept. of Civil Eng., Auburn Univ., Auburn, Alabama

2 Professor, Dept. of Civil and Environmental System Eng., Dongguk Univ. Seoul, Korea

3 Post-Doctoral Researcher, Dept. of Civil and Environmental System Eng., Dongguk Univ., Seoul, Korea

INTRODUCTION

Wilson (1886) is credited with the first study of the postbuckling strength of plate girder web panels. Since Wagner (1931) first presented a diagonal tension theory for aircraft structures with very thin web panels, many researches have studied the tension field action for plate girders, as summarized in SSRC (1998). These researchers include Basler (1963), Takeuchi (1964), Fujii (1968, 1971), Komatsu (1971), Chern and Ostapenko (1969), Porter et al. (1975), Herzog (1974a, 1974b), Sharp and Clark (1971), and Steinhardt and Schroter (1971).

Fig. 1 shows the yield zones assumed in classical failure theories of plate girder web panels for the case where a diagonal tension develops. Basler (1963), Takeuchi (1964), Porter et al (1975), and Herzog (1974a, 1974b) all assumed that the diagonal tension field develops in a limited portion of the web panel. Note that Basler' formula gives the shear strength for the entire web panel. In contrast, Fujii (1968, 1971), Komatsu (1971), and Chern and Ostapenko (1969) assumed that the diagonal tension field develops all over the web panel, but the intensity of the diagonal tension varies across the perpendicular direction of the tension diagonal. The assumption by Steinhardt and Schroter (1971) falls on between the above two assumptions. Wagner (1931) used a uniform tension field to determine the strength of a thin panel in pure shear.

Although these classical failure theories assumed different yield zones, the following fundamental assumption was implicit in all the theories: compressive stresses that develop in the direction perpendicular to the tension diagonal do not increase any further once elastic buckling has taken place. The application of this fundamental assumption to the whole web panel leads naturally to the well-known theory that the tension field action in plate girder with transverse stiffeners needs to be anchored by flanges and stiffeners in order for the webs to develop their full postbuckling strength. It should be remembered that Wagner (1931) was the first to make this fundamental assumption and to arrive at the

theory.

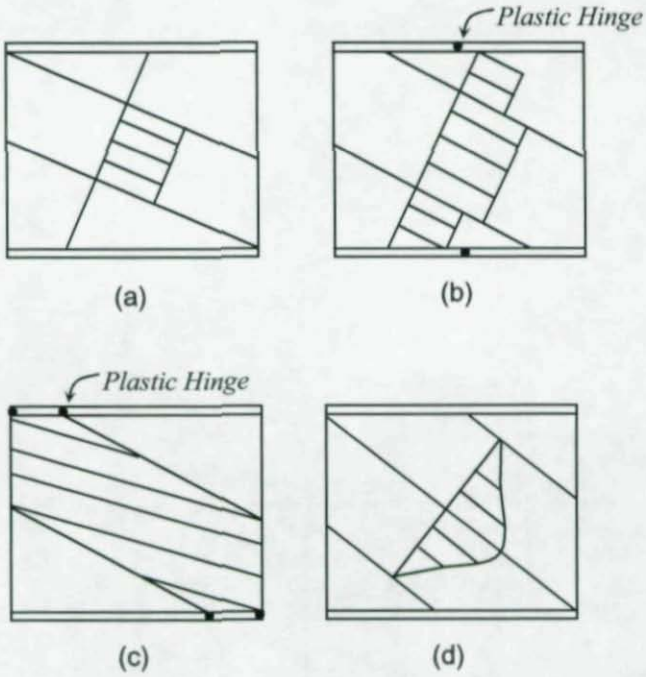

Fig. 1 Tension field theories: (a)Basler(1963); (b)Fujii(1968, 1971); (c)Porter et al.(1975); (d)Steinhardt and Schroter(1971), reprinted with permission by SSRC.

A well-known illustration (SSRC 1998) based upon this fundamental assumption is shown in Fig. 2. It is obvious from Fig. 2 that the flanges must be rigid to fully anchor the diagonal tension. Since Wagner (1931) used a uniform tension field, he assumed the flanges were rigid. Basler (1963) took a different approach assuming that the flanges used in practical designs are too flexible to support a lateral loading from the diagonal tension field so that the yield band is away from the flanges,

as shown in Fig. 1(a). Porter et al. (1975) suggested the sway failure mechanism that assumes that the web reaches failure when plastic hinges are formed at the flanges due to the diagonal tension field, as shown in Fig. 1(b).

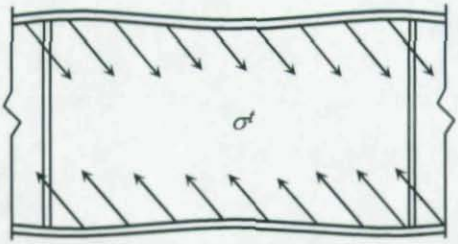

Fig. 2 Tension field action, reprinted with permission by SSRC

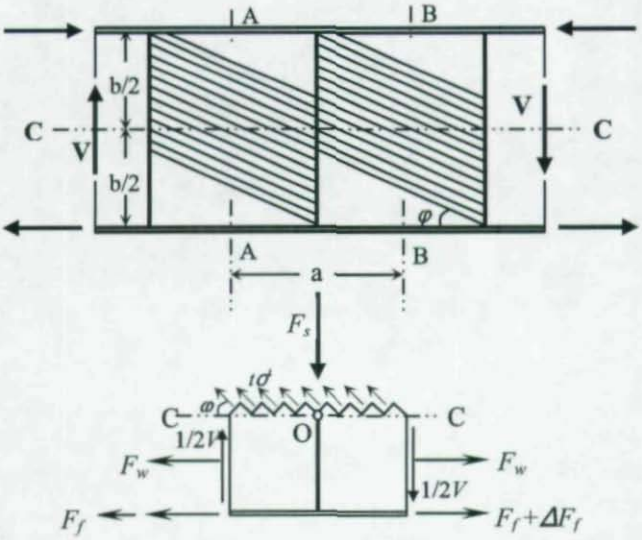

Fig. 3 Free body diagram (Basler, 1963), reprinted with permission by ASCE

Fig. 3 shows another famous free body diagram (Basler 1963). Only diagonal tensile stresses are shown in the diagonal since it was assumed that the diagonal compression would not increase any further at any part of the web after buckling. From this free body diagram it is obvious that the vertical component of the diagonal tensions must be equilibrated by an external anchor system. Basler believed that the transverse stiffener would act as this anchor.

Basler (1963) is credited with developing a method to account for the postbuckling reserve strength due to tension field action in plate girders fabricated from hot-rolled plates. Basler's theory is applicable to many civil engineering structures and was first adopted in the AISC (1963) specifications. A similar formula recognizing the contribution of tension field action was later adopted in the AASHTO (1977). The Rockey, or Cardiff, model (Porter et al. 1975) was independently developed in the U.K. and became the basis for the BS5400 (1982) provisions on shear resistance. Both the Basler model and the Rockey model predict reasonably well the postbuckling strength of plate girder web panels subjected to pure shear for panels having an aspect ratio (stiffener spacing/web depth) less than 1.5. These models yield conservative results when applied to panels with an aspect ratio equal to 3 (Lee and Yoo, 1998). This may be because the maximum value of the aspect ratio was limited to 1.5 in Article 1.7.43(D), AASHTO (1977) and there may not have been enough experimental data available at the time of calibration. Although the majority of all steel bridges in the world have been designed and built based on these two major theories of their derivatives that recognize the reserve strength afforded by tension field action in the postbuckling stage, no single theory has ever emerged that explains the seemingly elusive stress distributions present in web panels during postbuckling.

In a recent series of analytical and experimental studies, Lee and Yoo (1998, 1999) and Lee et al. (2002, 2003), showed that the flanges and transverse stiffeners do not necessarily behave as anchors. For example, both analytical and experimental studies (Lee et al. 2002, 2003) have

confirmed that the intermediate transverse stiffeners are not subjected to a compressive force in order to equilibrate the vertical component of the diagonal tensile force, as required in the Basler model (Fig. 3). In other words, there should be no net vertical force at the mid-depth of the web panels. Likewise, Lee and Yoo (1998, 1999) demonstrated that the flanges are not subjected to the lateral loading shown in Fig. 2.

Lee et al. (2002) introduced an approach that they referred to as the shear cell analogy to resolve the discrepancy between the previous understanding and their new finding that the flanges and transverse stiffeners do not behave as anchors. The shear cell analogy was also developed based upon the original fundamental assumption. However, one of the reviewers of Lee et al. (2003) raised questions regarding the validity of the shear cell analogy. On reexamining their theory in the light of this query, the authors noticed that the shear cell analogy does in fact contain a serious flaw. An important stress component was inadvertently omitted during the transformation process from a two-dimensional stress state to an assembly of one-dimensional bar element. As a result, the shear cell analogy does not satisfy the fundamental two-dimensional state of stresses represented in Mohr circle. Furthermore, there should be no limitation imposed as to the way a free-body is isolated. The reviewer pointed out that Lee et al. (2002) also failed to note this discrepancy.

There has been an ongoing controversy among researchers as they attempt to adequately explain the physical postbuckling behavior of web panels. The nonlinear shear stress and normal stress interaction that takes place from the onset of elastic shear buckling to the ultimate strength state is so complex that any attempt to address this phenomenon using classical closed form solutions appears to be a futile exercise. The fact that there have been more than a dozen theories and their derivatives suggested to explain the phenomenon is testimony to the complexity of tension field action. This may be the largest number of failure theories devoted to a single topic in structural mechanics. In fact, the reviewer of Lee et al. (2003) stated "the physical postbuckling behavior of the web is complex, and tends to defy explanation by

simple strength of material models. To the knowledge of the reviewer, no complete explanation of this behavior exists."

Ever since Wagner (1931) proposed the fundamental assumption, no one has examined it critically. Although Marsh et al. (1988) found that the diagonal compression at the tension diagonal corners of the web increased after buckling, they still concluded that the flanges would contribute to the shear capacity of the panel due to their bending strength, which would permit the development of some diagonal tension.

A series of studies led by Harding (Rahal and Harding 1990a, 1990b, 1991) and Chapman (Stanway et al. 1993, 1996, Xie and Chapman 2003) based on finite element nonlinear analyses revealed that the large compressive axial force (Fig. 3) expected in the transverse stiffener did not, in fact, exist. The stiffener axial force was found to be relatively unimportant and need not be taken into account in the development of a new design method for transverse stiffeners. Findings by Lee and Yoo (1998, 1999) and Lee et al. (2002) that the actual behavior of the flanges and transverse stiffeners disagrees with the behavior expected from the fundamental assumption support these conclusions. These recent finding strongly suggest that it is time to revisit the fundamental assumption. The objective of the present study is to examine the validity of the fundamental assumption using nonlinear finite element analysis and thus shed light on the mechanics of the postbuckling behavior of shear web panels.

NUMERICAL INVESTIGATION

Finite Element Models

Four-node quadrilateral shell elements, CQUAD4 of MSC/NASTRAN (2004), were selected for all bifurcation type eigenvalue and incremental nonlinear analyses. CQUAD4 is essentially the same as S4R of ABAQUS (2004) and QUAD4 of ADINA (2001). For the example selected for the convergence study given in Table 1, all three

programs computed essentially the same eigenvalue. The aspect ratio of the CQUAD4 element was set equal to one in order to eliminate any potential adverse shape effect of the element and a 30×30 mesh was selected for all subsequent analyses.

Table 1. Boundary conditions used for the web panel in Fig. 5

	u_x	u_y	u_z	θ_x	θ_y	θ_z
B.C.[1]	Free	Fixed	Free	Free	Fixed	Fixed
B.C.[2]	Free	Fixed	Free	Fixed	Fixed	Free
Point[1]	Fixed	Fixed	Fixed	Fixed	Fixed	Fixed
Point[2]	Free	Fixed	Free	Fixed	Fixed	Fixed

Article 6.10.9.3, AASHTO LRFD (2004) divides web panels into three zones: (1) the yield zone; (2) the transition zone; and (3) the elastic shear buckling zone, as shown in Fig. 4. When the slenderness parameter, λ, is equal to 1.40, the ratio of the shear buckling resistance to the shear yield strength ($C = V_{cr} / V_p$) becomes 0.8. The slenderness parameter, λ, is defined by Eq. (1).

$$\lambda = \frac{D}{t_w \sqrt{\frac{Ek}{F_{yw}}}} \tag{1}$$

When the slenderness parameter is greater than 1.40, the ratio of the shear buckling strength to the shear yield strength is given by Eq. (2).

$$C = \frac{1.57}{\left(\frac{D}{t_w}\right)^2}\left(\frac{Ek}{F_{yw}}\right) \tag{2}$$

From Eq. (1),

$$\frac{D}{t_w} = \lambda\sqrt{\frac{Ek}{F_{yw}}} = 1.40\sqrt{\frac{Ek}{F_{yw}}} \tag{3}$$

Substituting Eq. (3) into Eq. (2) gives C=0.80.

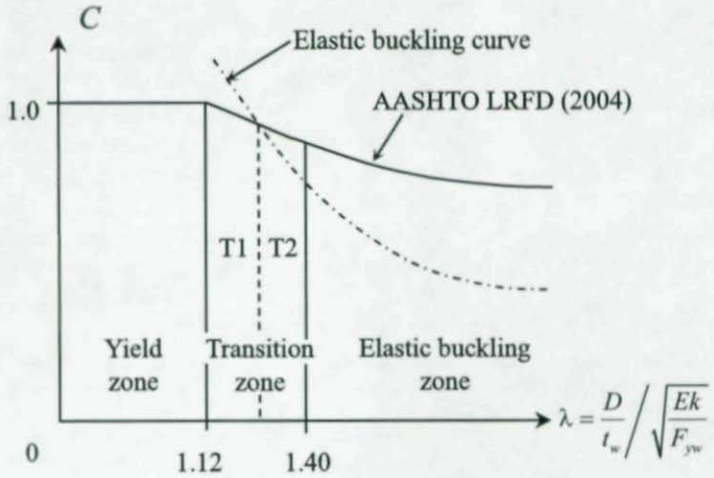

Fig. 4 Shear strength curve of shear web panels

In order to demonstrate their considerable postbuckling reserve strengths, most of the web panels used in this study were assigned high web slendernesses values. For a square panel, the elastic shear buckling coefficients, k, is computed to be 9.34 from SSRC (1998). For material properties, E=200Gpa, F_{yw}=345Mpa and a web slenderness ratio, D/t_w=150, the slenderness parameter, λ, becomes 2.04, which is in the elastic shear buckling zone. Likewise, the slenderness parameter, λ, becomes 1.02 in the yield zone for a web slenderness ratio of 75. The material was assumed to be linearly elastic and perfectly plastic with no strain hardening considered in all subsequent incremental nonlinear analyses.

Convergence Study

In order to establish an acceptable level of accuracy, a simple convergence study was carried out on a square web panel simply supported on all four edges and subjected to pure shear. Fig. 5 shows the finite element model and the loading scheme for the square web panel. In the incremental nonlinear analysis, an initial imperfection shape corresponding to the lowest eigen-model of elastic shear buckling as suggested by Bathe (1996) was introduced. Four different initial imperfection magnitudes, D/100,000, D/10,000, D/1,000, D/100, were incorporated in the model. An arbitrary small initial imperfection value of D/100,000 was included in an attempt to discern a bifurcation-type buckling load. D/100 is the maximum value allowed by the Bridge Welding Code (2002). Fig. 6 shows the effects of the initial imperfection on the ultimate shear strength. The boundary conditions on all four edges of the isolated square panel are given in Table 1. With material properties of E=200Gpa, F_{yw}=345Mpa, and μ=0.3, and panel dimensions of D=1,000mm, d_0=1,000mm, t_w=6.67mm, and k=9.34, the theoretical elastic shear buckling load was computed to be 500.49kN from Eq. (4).

$$V_{cr} = (Dt_w)\frac{k\pi^2 E}{12(1-\mu^2)\left(\frac{D}{t_w}\right)^2} \tag{4}$$

Table 2 shows the convergence trend for various levels of mesh pattern of 30×30 was chosen for all subsequent analyses as this gave a solution accuracy of within 0.1 percent of from the exact value.

Table 2 Convegence trend(D=1,000mm, D/t_w=150, d_0/D=1.0, E=200GPa, μ=0.3, F_{yw}=345MPa)

Mesh	5×5	10×**10**	20×**20**	30×**30**	40×**40**	50×50
Vcr(kN)	596.4	524.3	503.4	501.1	500.5	500.2
% diff	19.2	4.7	0.6	0.1	0.0	-0.0

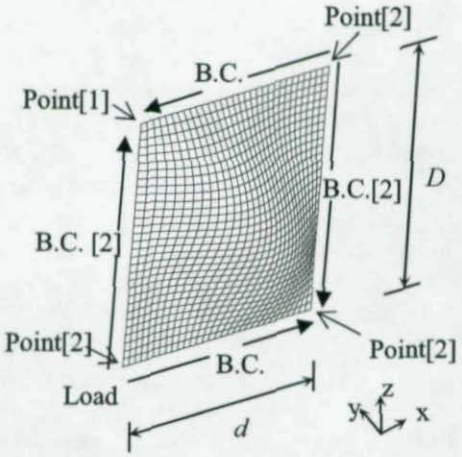

Fig. 5 Finite element model of web panel with loading scheme

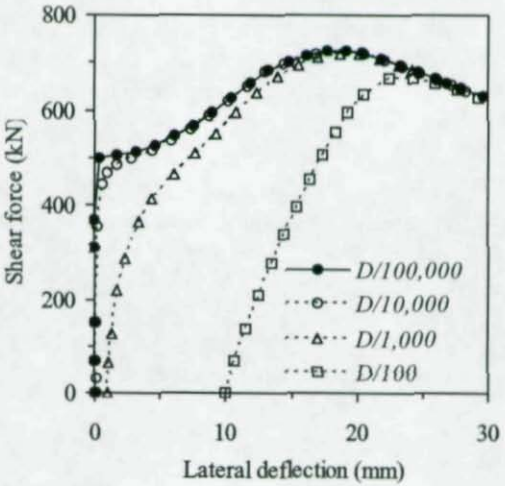

Fig. 6 Effect of initial imperfection

Effect of Flanges on Postbuckling Strength of Web Panels

The fact that the flanges do not necessarily act as an anchor was affirmed through large displacement nonlinear finite element analyses. The same panel model used in the convergence analysis was used for ultimate load analyses. In order to assess the effect of flanges, the web panel was analyzed for three different sizes of a flange with no transverse stiffeners. Instead, the web panels were simply supported along the two transverse edges. The boundary conditions at the transverse and longitudinal edges of flanges were set free for the model with top and bottom flanges. The dimensions of each flange are given in Table 3. Fig. 7 illustrates the effect of flange size on the ultimate shear strength of the panel. Table 3 summarizes the ultimate strengths, elastic buckling strengths, and postbuckling strengths of three web panels. The presence of flanges increases the elastic shear buckling strength, as expected, by stiffening the boundary condition at the flanges and web juncture more toward a clamped boundary. However, the presence of flanges does not increase the postbuckling strength proportionately, in contrast to the requirements of Rockey model (Porter et al. 1975, Rockey et al. 1981). This observation indicates that the web panel does not need any anchor system, such as flanges or transverse stiffeners, as the simply supported condition is sufficient to develop the full potential postbuckling strength. Certainly the continuity of the flanges between adjacent panels, particularly, the slab of composite I-girders, results in additional contributions to the shear resistance due to frame action similar to that in a Vierendeel truss or a beam with large web holes. Shear strengths computed from AASHTO (2004) are also tabulated in Table 3. As stated in Commentary C6.10.9.3.2, AASHTO computes the elastic shear buckling strengths are consistently smaller. The postbuckling strengths are generally found to be higher when calculated using the AASHTO formula.

Table 3 Ultimate strength comparison(E=200Gpa, Fyf=Fyw=345Mpa)

		(1)	(2)	(3)	(4)	AASHTO(2004)	
						I	II
Panel A	V_{cr}(kN)	501	554	660	671	540	540
	V_u(kN)	726	796	861	861	827	1030
	$V_{P.B}=V_u-V_{cr}$	225	242	201	201	286	489
	$V_{P.B}/V_{cr}$	0.45	0.44	0.31	0.31	0.53	0.91
Panel B	V_{cr}(kN)	62	69	82	82	-	-
	V_u(kN)	200	228	235	235	-	-
	$V_{P.B}=V_u-V_{cr}$	138	159	153	153	-	-
	$V_{P.B}/V_{cr}$	2.21	2.31	1.87	1.87	-	-
Panel C	V_{cr}(kN)	352	395	519	519	338	338
	V_u(kN)	567	670	775	775	543	726
	$V_{P.B}=V_u-V_{cr}$	215	275	256	256	205	388
	$V_{P.B}/V_{cr}$	0.61	0.69	0.49	0.49	0.61	1.15

Notes: Panel A: d_0/D=1.0, d_0=1,000 mm, t_w=6.67 mm, D/t_w=150
Panel B: d_0/D=1.0, d_0=1,000 mm, t_w=3.33 mm, D/t_w=300
Panel C: d_0/D=2.0, d_0=2,000 mm, t_w=6.67 mm, D/t_w=150
(1) Simply supported
(2) Light flange: b_f/D=0.25, t_f/t_w=1.0
(3) Moderate flange: b_f/D=0.30, t_f/t_w=3.0
(4) Heavy flange: b_f/D=0.35, t_f/t_w=5.0
D/t_w=300 is not allowed by AASHTO without longitudinal stiffeners. AASHTO computes the elastic shear buckling strength assuming the panel to be simply supported. There are only two separate equations for the postbuckling strength computation in AASHTO. Panels are assumed to be simply supported and with light flanges belong to "I" and those with moderate and heavy flanges belong to "II" above.

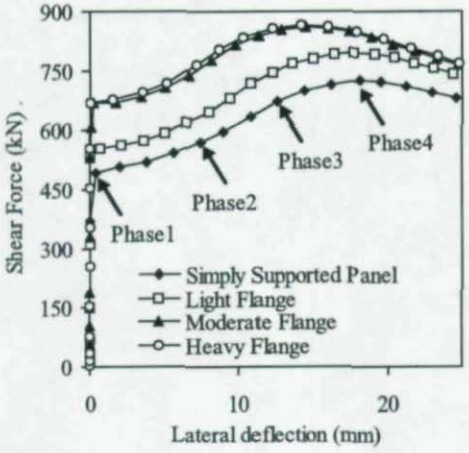

Fig. 7 Ultimate strength vs. flange size

Stress Development in Shear Panel During Postbuckling -Assumed stress development and associated behaviors of flange and transverse stiffener

Fig. 8 illustrates the typical stress development in a panel subjected to pure shear before buckling. Every element maintains the initial pure shear stress state, with equal magnitude diagonal tensile stress and diagonal compressive stress (principal stresses), until the initiation of elastic shear buckling. If the diagonal compression can not increase after buckling, as assumed in the classical failure theories (fundamental assumption), the equilibrium is obviously violated without any other stresses on the vertical and horizontal planes, as shown in Fig. 9(b). This necessitates the development of normal stresses, as shown in Fig. 10.

If the fundamental assumption is indeed valid throughout the whole panel, then the following conclusions would be clear: (1) the normal

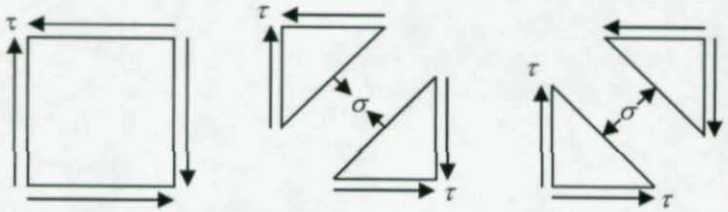

(a) (b) (c)

Fig. 8 Stress development at prebuckling stage: (a) Shear stress; (b) Diagonal tension; (c) Diagonal compression

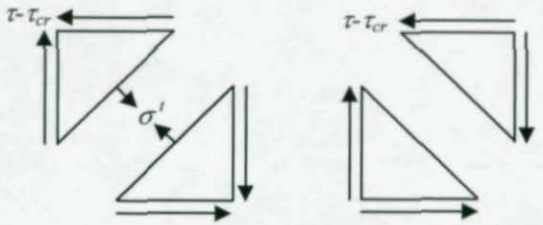

(a) (b)

Fig. 9 Incomplete stress state after buckling: (a) Diagonal tension; (b) No diagonal compression

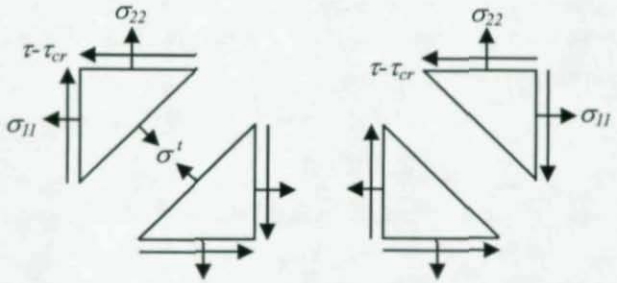

(a) (b)

Fig. 10 Complete stress development after buckling: (a) Diagonal tension; (b) No diagonal compression

stresses must be resisted by the flanges, as shown in Fig. 2; and (2) the horizontal normal stresses must be resisted by adjacent panels, since there is no adjacent panel to balance the horizontal normal stresses developed in the postbuckling stage (Fig. 10). In addition, AISC (2001) considers that postbuckling strength is not available in interior panels having an opening in an adjacent panel.

-Results of nonlinear finite element analysis

In reality, according to a series of nonlinear finite element analyses, the flanges and transverse stiffeners do not exhibit any the behavior that is typically related to this anchoring action. This discrepancy strongly implies that the fundamental assumption may not in fact be applicable at certain parts of the web panel. To test this, the stress history of a simply supported shear panel was traced from the inception of loading to failure.

Figs. 11 and 12 show the normal stress distributions along central strips taken in the vertical and horizontal directions, respectively. The four load phases in these figures correspond to those shown in Fig. 7. It can be seen from Figs. 11 and 12 that normal stresses begin to develop as soon as elastic buckling takes place. At the center of the panel, both the horizontal and vertical normal stresses are not only in tension but also equal in magnitude, which is consistent with the stress state shown in Fig. 10 resulting from the fundamental assumption. However, it is of interest to note that the vertical normal stress (σ_{22}) in the vertical strip and the horizontal normal stress (σ_{11}) in the horizontal strip reduce to zero at the edges. This clearly explains why this simply supported panel is able to develop its postbuckling strength without anchors such as flanges and adjacent panels. Also, it can be seen from Fig. 12(c) that the vertical normal stresses (σ_{22}) developed in the horizontal strip are in the self-equilibrating force system within the strip. Thus, no net vertical force exists, thereby indicating that the direct compression shown in Fig. 3 does not in fact develop in the transverse stiffener.

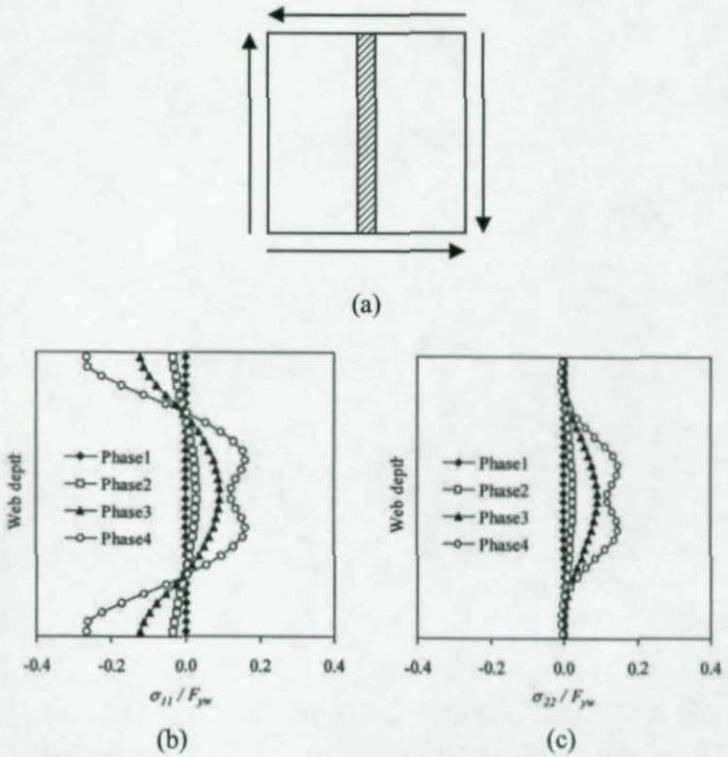

Fig. 11 Normal stress distribution in vertical strip: (a) Vertical strip; (b) Normal stress in horizontal direction; (c) Normal stress in vertical direction

The observation that the vertical normal stress at the top and bottom edges and the horizontal normal stress at the transverse edges disappear can be explained by examining the distribution of principal stresses shown in Fig. 13. After buckling, diagonal compression increases considerably, not only at the tension corners (Fig. 13(b), upper left and lower right) as found by Marsh et al. (1988), but also at every edge. The diagonal compression is even greater than the diagonal tension near the edges. Fig. 14 shows the principal stresses in the top element

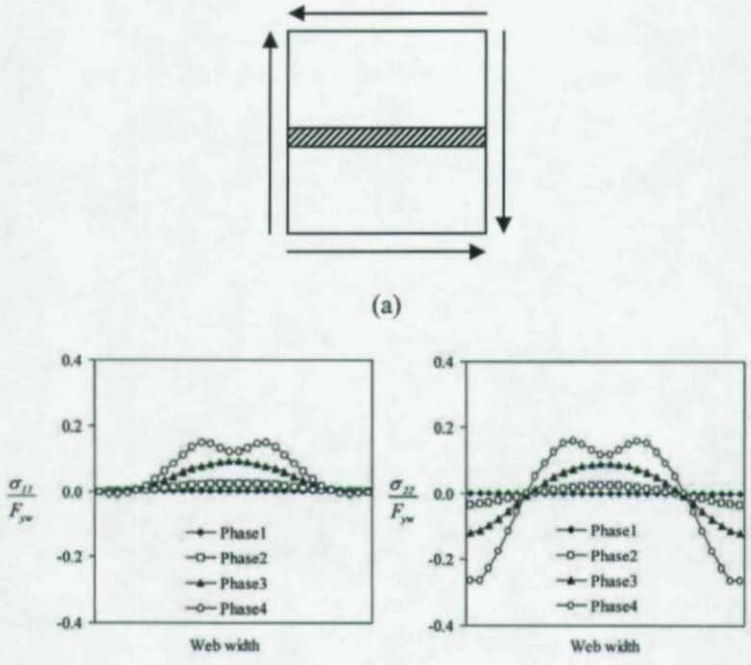

Fig. 12 *Normal stress distribution in horizontal strip: (a)Horizontal* strib; (b) Normal stress in horizontal direction ; (c) Normal stress in vertical direction

of the vertical strip at the ultimate load, where the equilibrium is maintained without the presence of vertical normal stresses due to the increment of the diagonal compression. On the other hand, in the middle of the panel, the diagonal compression remains almost the same as that at the instant of buckling (Fig. 13(b)). A closer examination of Fig. 13 reveals that there are two fundamental errors in the free body diagram shown in Fig. 3: (1) diagonal compression is missing for the planes perpendicular to the tension diagonal; and (2) diagonal tension is uniform. Fig. 15 shows a new free body diagram where the sum of vertical components of the diagonal forces is equal to zero (self-

equilibrating). Again, this free body diagram reveals that the transverse stiffener is not necessarily subjected to the direct compression shown in Fig. 3.

Recent finite element studies conducted herein and elsewhere (Rahal and Harding 1990a, 1990b, 1991, Xie and Chapman 2003) do not support the fundamental assumption employed in the classical theory. Contrary to the incorrect assumption that the compressive stresses remain more or less constant, they actually increase progressively, particularly around the edges of the web panel as evidenced in Fig. 13.

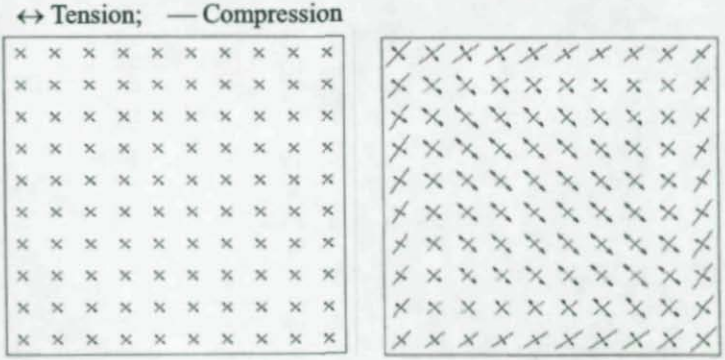

(a) Prebuckling stage (b) Ultimate stage

Fig. 13 Distribution of principal stresses under pure shear (D/t_w=150, d_0/D=1.0)

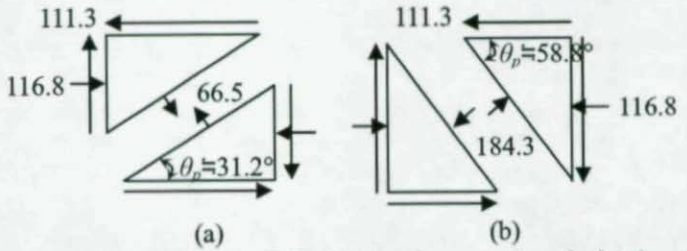

(a) (b)

Fig. 14 Principal Stresses(MPa) in top element of vertical strip at ultimate stage; (a) Diagonal tension; (b) Diagonal compression

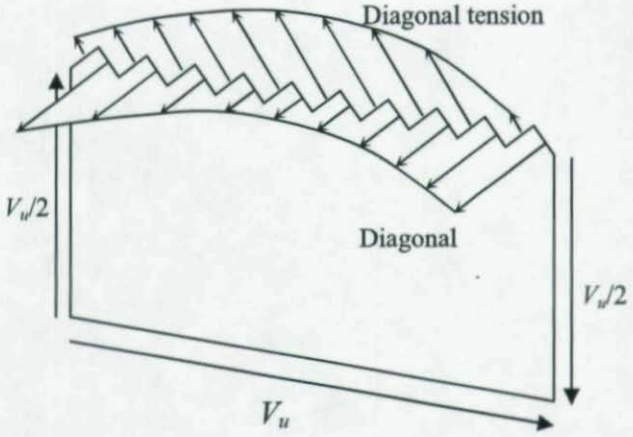

Fig. 15 Digonal stress diagram at ultimate stage

FURTHER EXPLANATION

Based on Figs. 11 through 15, it is clear that an external anchor system is not required for the development of substantial postbuckling shear strength.

Figs. 16 and 17 show a history of the out-of-plane deflections of the panel. The four load phases in these figures correspond to those shown in Fig. 7. Thin plates are much weaker against plate bending actions than against in-plane actions (stretching and contraction). The diagonal compression tends to magnify the out-of-plane deformations after buckling, as in a column with an initial crookedness. The magnified out-of-plane deformations, in turn, reduce the axial rigidity. Therefore, if the element is located near the center of the panel, the axial rigidity in the direction of the compression diagonal will be suddenly reduced almost to zero as soon as elastic buckling takes place due to the large out-of-plane deformations shown in Figs. 16 and 17. This is why diagonal compression does not increase after buckling near the center

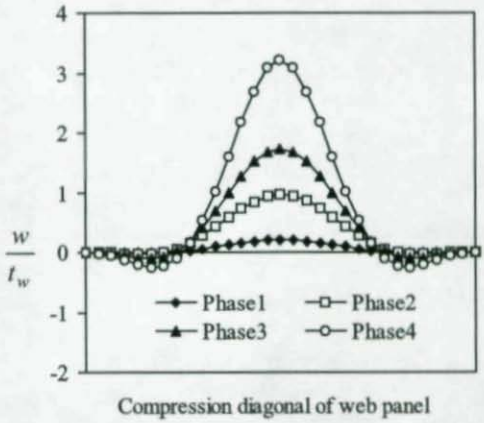

Fig. 16 Deflection of web panel along compression diagonal

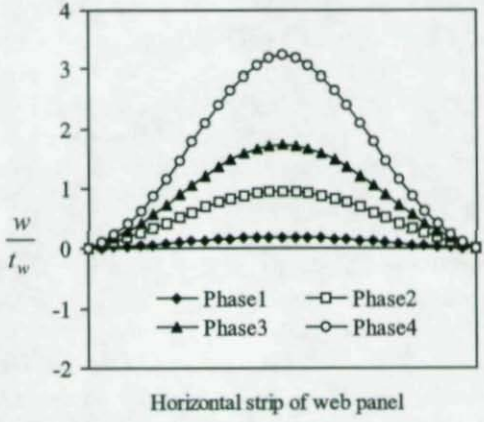

Fig. 17 Deflection of web panel along horizontal strip

of the panel, as shown in Fig. 13(b). On the other hand, the out-of-plane deflections remain relatively small near the edges. The axial rigidities in the direction of the compression diagonal near the edges are, therefore, not likely to be severely reduced after buckling. This is why diagonal compression near the edges continuously increases to failure,

as illustrated in Fig. 13(b). This behavior of the shear panel near the edges is very similar to that of a simply supported thin rectangular panel subjected to a uniform compression applied in one longitudinal direction only. Such a thin compression panel is able to exhibit considerable postbuckling strength, because out-of-plane deformations are restrained in the vicinity of the transverse edges (SSRC 1998).

It has been shown that if out-of-plane deflections are restrained along the edges with simple supports, anchors are not necessary for the development of the meaningful postbuckling strength that is expected in plate girder web panels. This implies that the simply supported boundary condition is a sufficient condition for a shear panel to develop postbuckling strength. It appears from Table 3 that the flanges used in practical plate girders are rigid enough to provide the web panels with this simple support. However, it should be noted that the bending rigidity of the transverse stiffener required in AASHTO LRFD (2004) is not sufficient to provide the simply supported boundary condition in the postbuckling stage (Lee et al. 2002). Lee et al. (2003) recommended that the bending rigidity of the transverse stiffeners should be increased six times in order for the web panels to develop near full capacity of the strength of comparable simply supported panels. Lee et al. (2003) also showed that transverse stiffeners having bending rigidities sufficiently high to facilitate the development of the postbuckling reserve strength of the panel near or at full capacity have smaller cross-sectional areas as compared with those required by AASHTO LRFD (2004) and AISC (2001). In the case of double-sided transverse stiffeners, the AASHTO area requirement will often be exceeded when sufficient rigidity is provided. The area requirement in these specifications was based on a free-body (Basler, 1963), shown in Fig. 3, which is now shown to be irrelevant. It is noted here that the studies by Stanway et al. (1996) and Rahal and Harding (1990a, 1990b, 1991) suggest that rigidities larger than 6 times the AASHTO rigidity requirement are needed in certain cases, while less than 6 times the AASHTO rigidity requirement is sufficient in other cases.

SUMMARY AND CONCLUDING REMARKS

Despite their adoption of incorrect assumptions, most of the existing theories predict the shear strength well enough for design purposes as the suggested equations were derived through extensive calibration with experimental data. It is hoped, however, that the examination of the mechanics of diagonal tension field action presented in this paper will finally shed light on the hitherto elusive behavior that runs counter to the universally accepted explanation. The consequences resulting from this examination are summarized as follow:

(1) If out-of-plane deflections are restrained along the edges of a rectangular panel by means of simple supports, an external anchor system is not necessary for the development of practically meaningful postbuckling strength (Table 3 and Fig. 7). This is possible only because the diagonal compression increase near the edges after elastic shear buckling.

(2) Diagonal compression continuously increases near the edges of panels after buckling (Fig. 13(b)), which is contrary to the fundamental assumption adopted previously. Due to this increase in the diagonal compression, the normal stress perpendicular to the edge shown in Fig. 10 (fundamental assumption) is not necessary for equilibrium. Hence, a simply supported panel is able to develop postbuckling strength with no external anchor system.

(3) In the postbuckling stage, an increase in the diagonal compression is possible near the simply supported edges because the axial rigidity in the direction of the compression diagonal is not rapidly reduced, as in the center of the web.

(4) The axial rigidity in the direction of diagonal compression does not undergo a rapid reduction near a simply supported edge, since the out-of-plane deformations are restrained by the edge (Figs. 16 and 17).

(5) Since the intermediate transverse stiffeners are not subjected to the direct axial compressive force predicted by the Basler model, the requirement for the area of the transverse stiffener developed by Basler (1963) is irrelevant.

(6) All forces developed during postbuckling are self-equilibrated

within the web panel, as shown in Figs. 11(b), 12(c), and 15. This means that even end panels can develop postbuckling strengths. As bearing stiffeners are designed to carry a large compressive force as columns, they have more than an adequate bending rigidity to function as simple supports needed for a self-equilibrated end panel to develop postbuckling. The restriction of ignoring any tension field in the end panels, therefore, needs to be revisited.

APPENDIX 1. REFERRENCES

1. *AASHTO LRFD Bridge Design Specifications*, 3rd ed. (2004). American Association of State Highway and Transportation Officials, Inc., Washington, D.C.
2. *AASHTO Standard Specifications for Highway Bridges*, 12th ed. (1977). American Association of State Highway and Transportation Officials, Inc., Washington, D.C.
3. ABAQUS (2004). Standard user's manual ver. 6.3-1. Hibbit, Karlsson & Sorensen, Inc., Pawtucket, RI.
4. ADINA (2001). *Theory and Modeling Guide*: Volume 1, Report ARD 00-7, ADINA R & D, Inc.
5. *AISC Manual of Steel Construction, Load and Resistance Factor Design*, 3rd ed. (2001). American Institute of Steel Construction, New York, N.Y.
6. *AISC Specification for the Design, Fabrication and Erection of Structural Steel for Building*, 6th ed. (1963). American Institute of Steel Construction, New York, N.Y.
7. Basler, K. (1963). "Strength of plate girders in shear." *Transactions*, ASCE, 128(II), 683-719. (Also as paper No. 2967, *J. Struct. Div.*, ASCE, October 1961, 87(7), 151-181.
8. Bathe, K. (1996). *Finite Element Procedures*. Prentice Hall, Englewood Cliffs, N.J.
9. *Bridge Welding Code* (2002). ANSI/AASHTO/AWS D1.5M/D1.5:2002, A Joint Publication of American Association of State Highway and Transportation Officials, Inc., Washington, D.C.

and American Welding Society, Miami, FL.

10. *BS 5400 (1982). Steel, concrete and composite bridges, Part 3*, Code of practice for design of steel bridges, British Standards Institution.
11. Chern, C., and Ostapenko, A. (1969). "Ultimate strength of plate girder under shear." *Friz Engrg. Lab. Rep. No. 328.7*, Lehigh Univ., PA.
12. Fujii, T. (1968). "On an improved theory for Dr. Basler's theory." *Final Report, IABSE 8th Congress,* New York.
13. Fujii, T. (1971). "A comparison between the theoretical values and the experimental results for the ultimate shear strength of plate girders." *IABSE Reports of the Working Commisions, Volume - Band 11, Colloquium, Design of Plate and Box Girders for Ultimate Strength*, London, pp. 161-171.
14. Herzog, M. (1974a). "Die Traglast unversteifter und versteifter, dunnwandiger Blechtrager unter reinem Schub und Schub mit Biegung nach Versuchen." Bauingenieur.
15. Herzog, M. (1974b). "Ultimate strength of plate girders from tests." *J. Struct. Div.*, ASCE, 100(5), 849-864.
16. Komatsu, S. (1971). "Ultimate strength of stiffened plate girders subjected to shear." *IABSE Reports of the Working Commissions, Volume - Band 11, Colloquium, Design of Plate and Box Girders for Ultimate Strength*, London, pp. 49-65.
17. Lee, S. C., and Yoo, C. H. (1998). "Strength of plate girder web panels under pure shear." *J. Struct. Engrg.*, ASCE, 124(2),184-194.
18. Lee, S. C., and Yoo, C. H. (1999). "Experimental study on ultimate shear strength of web panels." *J. Struct. Engrg.*, ASCE, 125(8), 847-853.
19. Lee, S. C., Yoo, C. H., and Yoon, D. Y. (2002). "Behavior of intermediate transverse stiffeners attached on web panel." *J. Struct. Engrg.*, ASCE, 128(3), 337-345.
20. Lee, S. C., Yoo, C. H., and Yoon, D. Y. (2003). "New design rule for intermediate transverse stiffeners attached on web panels." *J. Struct. Engrg.*, ASCE, 129(12), 1607-1614.
21. Marsh, C., Ajam, W., and Ha, H. (1988). "Finite element analysis of postbuckled shear webs." *J. Struct. Engrg.*, ASCE, 114(7), 1571-

1587.

22. *MSC/NASTRAN (2004)*. Reference Manual - version 2004.0.0. The MacNeal-Schwindler Corp., Los Angeles, CA.
23. Porter, D. M., Rockey, K. C., and Evans, H. R. (1975). "The collapse behavior of plate girders loaded in shear." *Struct. Engrg.*, 53(8), 313-325.
24. Rahal, K.N., and Harding, J.E. (1990a). "Transversely stiffened girder webs subjected to shear loading - part 1: behavior." *Proc. Instsn Civ. Engrs*, Part 2, 89(3), 47-65.
25. Rahal, K.N., and Harding, J.E. (1990b). "Transversely stiffened girder webs subjected to shear loading - part 2: stiffener design." *Proc. Instsn Civ. Engrs*, Part 2, 89(3), 67-87.
26. Rahal, K.N., and Harding, J.E. (1991). "Transversely stiffened girder webs subjected to combined in-plane loading." *Proc. Instsn Civ. Engrs*, Part 2, 91(6), 237-258.
27. Rockey, K.C., Valtinat, G., and Tang, K.H. (1981), "The design of transverse stiffeners on webs loaded in shear - an ultimate load approach." *Proc. Instsn Civ. Engrs*, Part 2, 71(12), 1069-1099.
28. Sharp, M. L., and Clark, J. W. (1971). "Thin aluminum shear webs." *J. Struct Div.*, ASCE, 97(4), 1021-1038.
29. SSRC (1998). *Guide to Stability Design Criteria for Metal Structures*, edited by Galambos, T.V., 5th ed., John Wiley & Sons, New York, NY.
30. Stanway, G.S., Chapman, J.C., and Dowling, P.J. (1993). "Behavior of a web plate in shear with intermediate stiffener." *Proc. Instsn Civ. Engrs*, Structs & Bldgs, 99(8), 327-344.
31. Stanway, G.S., Chapman, J.C., and Dowling, P.J. (1996). "A design model for intermediate stiffeners." *Proc. Instsn Civ. Engrs*, Structs & Bldgs, 116(2), 54-68.
32. Steinhardt, O., and Schroter, W. (1971). "Postcritical behavior of aluminum plate girders with transverse stiffeners." *IABSE Reports of the Working Commissions, Volume - Band 11, Colloquium, Design of Plate and Box Girders for Ultimate Strength*, London, pp. 179-184.
33. Takeuchi, T. (1964). "Investigation of the load carrying capacity of plate girders." M.S. thesis, University of Kyoto (in Japanese).

34. Wagner, H. (1931). "Flat sheet metal girder with very thin metal web." *Tech Memo. 604-606*, National Advisory Committee for Aeronautics (NACA).
35. Wilson, J. M. (1886). "On specifications for strength of iron bridges." *Trans.*, ASCE, 15(1), 401-403 and 489-490.
36. Xie, M., and Chapman, J.C. (2003). "Design of web stiffeners: axial forces." *J. Constructional Steel Research*, 59, 1035-1056.

APPENDIX 2. NOTATIONS

b_f = width of the flange;

C = shear strength ratio($C=V_{cr}/V_p$);

D = depth of the girder;

d_0 = transverse stiffener spacing;

E = modulus of elasticity;

F_s = compressive force in transverse stiffener;

F_{yf} = mill specified minimum yield stress of the flange;

F_{yw} = mill specified minimum yield stress of the web;

k = elastic shear buckling coefficient;

t_f = thickness of the flange;

t_w = thickness of the web;

V_{cr} = elastic shear buckling strength;

V_n = nominal shear strength;

V_p = shear yield strength;

$V_{P.B}$ = postbuckling strength;

V_u = ultimate shear strength($V_u=V_{cr}+V_{P.B}$);

w = out-of-plane displacement of web;

θ_p = principal plane angle;

λ = slenderness parameter;

μ = Poisson's ratio;

σ = normal stress or principal stress;

σ_{11} = horizontal normal stress;

σ_{22} = vertical normal stress;

σ^t = diagonal tensile stress;

τ = shear stress;

τ_{cr} = elastic shear buckling stress.

PLASTIC BUCKLING BEHAVIOUR OF PURE ALUMINIUM MULTI-STIFFENED SHEAR PANELS

G. De Matteis[1], A. Formisano[2], S. Panico[2], F. M. Mazzolani[2]

INTRODUCTION

In the last years the vibration control methods have been largely investigated in the field of earthquake engineering aiming at developing new techniques for checking the effects induced into the structures by the quake ground motions. In this field, many passive control systems exploiting the energy dissipation capability by means of the hysteretic behaviour of the base material have been proposed. In particular, to this purpose, the combination of low-yield metal and plate working in shear could be very effective. In fact, some decades ago many researchers and leading structural engineers in the United States, Canada and Japan recognized that the application of metal shear walls in new and existing buildings provided a very effective lateral load resisting system [1]. In addition, recent studies shown that when low-yield strength material are adopted these devices can be considered as one of the most ductile earthquake resistant systems, presenting robust cyclic behaviour with little degradation [2].

The main function of a metal plate shear wall (MPSW) system is to resist shear forces and overturning moments due to lateral loads. Such a system may be composed by steel panels connected at all four sides to a steel frame consisting of beams and columns. Typically, the beams are positioned at floor levels and the column location is determined by architectural requirements. The metal plate is connected to the bearing frames by closely spaced bolts or continuous welding. Openings required by windows and doors can generally be accommodated within

1 Dept. of Design, Rehabilitation and Control of Architectural Structures (PRICOS), University of Chieti/Pescara "G.d'Annunzio", V.le Pindaro, 42 – 65127 Pescara

2 Dept. of Structural Analysis and Design (DAPS), University of Naples "Federico II", P.le Tecchio, 80 – 80125 Naples

the steel plates by stiffening the shear panel around the openings. The main lateral load-resisting element in a MPSW system is the infill plate. Thin steel plates are expected to buckle along compressive diagonals under relatively small shear forces [3]. After buckling, the story shear forces are resisted by the plates through the development of a tension field mechanism. Low-yield strength material allows to delay the buckling phenomena in plastic field, checking that the shear yielding strength is lower than the buckling shear strength. The scarce availability on the market of the Low Yield Strength (LYS) steel suggests the employment of aluminium alloys as an appropriate material to realise a low yielding device for reducing the seismic input induced into the structure. While unstiffened aluminium shear panels provide a poor hysteretic behaviour with a strong "pinching" effect due to out-of-plane displacements produced by shear buckling, stiffened shear panels may allow a pure shear dissipative mechanism with shear plastic deformations developing before the occurrence of significant buckling phenomena.

In this paper, a numerical and experimental research recently carried out at the University of Naples "Federico II" in cooperation with the University of Chieti-Pescara "G. d'Annunzio", aiming at investigating the seismic performance of pure aluminium multi-stiffened shear panels under cyclic loading, is presented. The used material is the AW 1050A aluminium alloy, which is characterised by a very low percentage of alloying elements and by a conventional yield strength much lower than the LYS steel.

Two preliminary experimental cyclic tests on 1000x1500 mm aluminium shear panels, characterised by different stiffener configurations, are presented. The obtained cyclic response of tested specimens is interpreted by defining some significant behavioural phases and adequate numerical parameters to evaluate the supplied structural performance in terms of dissipated energy, secant stiffness and plastic strength. In addition a sophisticated FEM model, which takes into account both the relief geometrical imperfections and the partial connection between the plate and the ribs, has been developed. Finally the numerical model, whose effectiveness has been confirmed by a detailed comparison between experimental and numerical results, has been used to develop a parametrical study, which is oriented at

defining an useful design chart for the selection of optimal configurations of aluminium shear panels to be adopted as hysteretic devices for the seismic protection of steel framed structures.

THE EXPERIMENTAL ACTIVITY

The proposed shear panel is fabricated by the wrought aluminium alloy EN-AW 1050A, a commercial material, with a degree of purity of 99.50%. To improve the mechanical features, according to the purpose of this study, the basic material is subjected to a heat treatment, favouring the increase of ductility and the reduction of yielding stress. A number of specimens have been submitted to a cycle of heat treatment characterised by different phases with constant temperature, each one having a duration of four hours [4]. This process is also useful to reduce the residual stresses produced by welding during the fabrication of the panel. In Figure 1, the comparison of two typical tensile curves related to the adopted material before and after the heat treatment is shown. For the sake of comparison, in Figure 2 the mechanical features of the above aluminium alloy have been also compared with the ones of other typical metal materials, namely a low-yield strength (LYS) steel and a different low-strength heat treated aluminium alloy (EN-AW 5154A). It should be noted that the aluminium alloy EN-AW 1050A is characterised by a higher value of the $E/f_{0.2}$ ratio and therefore is more suitable for the application under consideration [5]. Another important aspect that should be observed is represented by the high hardening ratio (over 3) of the proposed material. It allows not only an added resource of resistance in the plastic field but also a dissipative capacity increasing with applied strains.

The presented experimental activity is related to two different aluminium alloy shear panels (called type B and type F) measuring 1500 by 1000 mm, having thickness of 5 mm and stiffened with longitudinal and transversal open rectangular-shaped stiffeners (see Figure 3). The ribs of panel type F and type B, which provide a b/t ratio of the single plate portion equal to 50 and 100, respectively, have a depth of 60 mm and are connected to the sheeting by means of inert gas

shielded arc welding based on consumable metal electrode (MIG system). In order to reduce the sheeting shape distortion produced by shrinkage, the welding has been carried out by small segments. In case of panel type B, the ribs have been applied on both sides of the sheeting so to have a grid pattern and balance the residual strain produced during the fabrication of the specimens. Contrarily, the panel type F has been stiffened with ribs alternatively placed on the two sides of the plate, in order to optimise the rib employment.

After the fabrication of the shear panels, a heat treatment has been carried out both to reduce the residual stresses due to welding and to improve the mechanical features of the material. Anyway, it is important to observe that, due to the welding process, after the heat treatment the specimens exhibited a distorted shape characterized by significant out-of-plane displacements. The maximum out-of-plane initial deformation of the single plate portions was measured respect to the surrounding stiffeners, which resulted without any significant initial deformation (see Figure 14a for panel type B, where the values are assumed to be positive if displacements are directed toward the observer).

The shear load on the panels was applied by means of an articulated steel frame composed by very rigid members and equipped with lateral out-of-plane braces (Figure 4a). Beam and column members were obtained by using double channel shapes (depth equal 200 mm) and connected to each other with pin joints at the four corners. The external load was applied at the top beam of the frame by means of a servo-hydraulic actuator (MTS System Corporation), characterised by a range of displacement of ±250 mm and a load capacity of 500 kN in compression and 300 kN in tension. The actuator was connected to a very rigid lateral support steel frame used as reaction structure (Figure 4b). Testing specimens were connected to the loading steel frame by steel cover plates with friction high-strength grade 8.8 steel bolts with a diameter of 14 mm and with pitch of 50 mm. In order to balance the viscosity phenomena due to low yield strength of used heat treated aluminium alloy and to avoid the slippage of connections, the bolts were tightened with a torque of 200 Nm, which is higher than the one prescribed by technical provisions (144 Nm). Tests were carried out under symmetric cyclic loading, following a complete testing procedure

with the applied deformations increasing in amplitude up to the global collapse of the specimen.

The obtained hysteretic curves for the two tested specimens, in terms of average shear stress τ and equivalent shear strain γ (obtained by deducting from the panel deformation both the bolts slip and the frame displacement), and the applied displacement histories are shown in Figures 5 and 6, respectively. In the initial phases of the loading process, the initial imperfections and local buckling of plate portions produced some slipping phenomena. Then, when the pure shear strength of the system was attained, the dissipative behaviour significantly increased. Finally, a remarkable strength degradation occurred when significant global buckling phenomena developed up to the complete collapse of the system.

INTERPRETATION OF EXPERIMENTAL RESULTS

The experimental behaviour of the tested aluminium shear panels can be divided into four main macro-behavioural phases, corresponding to different values of lateral displacement, which influence both the stiffness and the energy dissipation capacity and produce a different hysteretic response of the system.

Such macro-behaviours may be synthesised as follows [6]:

1. Buckling phenomena developing in the lower portions of the panels, due to normal stresses equilibrating the flexural moment at the plate basis, for an applied displacement amplitude equal to ± 8 mm for panel type F (Figure 7a) and ± 5 mm for panel type B (Figure 7c). As a consequence, the shape of the shear stress – shear strain curve shows a pronounced "pinching" effect (Figure 7b).
2. Local shear buckling of the single plate portions, developing for an applied displacement amplitude equal to ± 30.0 mm for panel type F (Figure 8a) and ± 23.0 mm for panel type B (Figure 8c). In this phase the phenomenon increases as long as it involves more panel portions and the activation of diagonal tension fields is evident. It is important to observe that, at this deformation history, the shear stress on the panel, being

decidedly larger than the one corresponding to the conventional elastic limit, produces significant plastic deformations. Due to the stable post-buckling behaviour, an increase of the global stiffness and dissipative capacity of the system is evident, especially for panel type F (Figure 8b).

3. Buckling phenomena of the ribs, occurring when the applied displacement is larger than ± 47.0 mm for panel type F (Figure 9a) and ± 55.0 mm for panel type B (Figure 9c). This phenomenon is characterised by a strength degradation followed by a significant increase of stiffness. A complete plastic behaviour is developed by the shear panels, since the applied shear stress is corresponding to the maximum resistance of the material ($\tau=\tau_u = f_u/\sqrt{3}$). Due to rib buckling, the shear stress – shear strain diagram shows a sort of "double bulge" effect (Figure 9b).
4. Global buckling behaviour, appearing for displacements larger than ± 53.0 mm for panel type F (Figure 10a) and than ± 80.0 mm for panel type B (Figure 10c). A global buckling of the panel, a material tearing visible in the central part of some panel portions and a very strong deformation of the applied stiffeners are observed. These phenomena led to a remarkable strength degradation. Cyclic shapes, especially for panel configuration type B, appear to be stretched owing to failure of surrounding connections (Figure 10b).

The obtained cyclic curves have been interpreted in terms of three numerical parameters, representing the maximum hardening ratio (τ_{max}/τ_{02} with $\tau_{02}=f_{02}/\sqrt{3}$), the secant shear stiffness (G_{sec}) and the equivalent viscous damping factor (ξ_{eq}), defined according to the equations reported in Figure 11.

The experimental data have been processed by drawing for each panel the τ_{max}/τ_{02} - $\Delta\gamma$, G_{sec}- $\Delta\gamma$ and ξ_{eq} - $\Delta\gamma$ diagrams (Figures 12 and 13). Moreover, for evaluating the degradation of strength, energy dissipation capacity and secant shear stiffness due to low-cycle fatigue effects, τ_{max}/τ_{02}, G_{sec} and ξ_{eq} have been also represented in the form of histograms versus the number of cycles, showing also the corresponding deformation ranges.

From the observation of the above diagrams, it can be noted that the examined F and B panels present an average equivalent viscous damping ξ_{eq} equal to 26% and 23%, respectively, while the maximum value (even larger than 30%) is obtained in the initial and in the final deformation phases. A strong reduction of this parameter is instead visible in both cases for intermediate deformation amplitude, represented by $\Delta\gamma$ ranging from 1.3% to 5.4% for panel type F and from 0.5% to 4.5% for panel type B. This situation shows that the dissipative behaviour of the tested shear panels can be exploited for small deformation amplitude (i.e. at the serviceability limit state) and for very large deformation amplitude (i.e. at the collapse condition). As a consequence, the dissipative capacity of panel types B and F appears to be reduced for intermediate deformations, assuming a minimum value of about 13% for $\Delta\gamma$ =0.03 rad .

The trend assumed by the G_{sec}-$\Delta\gamma$ curves evidences that the global stiffness of tested specimens rapidly decreases as far as the applied deformation amplitude increases. In particular, for $\Delta\gamma$ tending to zero, it is possible to evaluate the initial stiffness of the specimen, that is not coincident with the nominal shear stiffness of the specimen (about 26000 MPa). This is due to the premature plastic deformations occurring into the specimens because of the very limited material strength.

On the other hand, the remarkable reduction of the G_{sec} value in comparison to the initial one shows that the buckling susceptibility of the specimens for displacements larger than 1% is significantly larger than the one that can be predicted on the basis of the nominal value. Finally, the $\tau_{max}/\ \tau_{02}$ - $\Delta\gamma$ diagrams, representing the mechanical behaviour of the specimens, allow the determination of the maximum strength of the system for a given deformation amplitude. In both cases, the maximum value of $\tau_{max}/\ \tau_{02}$ is greater than 3, assuming a value similar to the hardening ratio exhibited by tensile tests, evidencing the actual possibility to exploit the full shear strength of the system. This phenomenon shows as buckling phenomena do not limit the shear capacity of the system.

THE FINITE ELEMENT MODEL

Aiming at developing a parametrical study to investigate the effect of the main influential parameters on the performance of the structural system under consideration, a refined FEM model has been set up by using the ABAQUS non linear numerical analysis code [7]. Such a model can be used to define optimum geometrical configurations with respect to the required deformation capacity and energy dissipation capability.

In the current study the development of a detailed FEM model has been carried out for describing the behavioural performance of panel type B [8]. The material has been modelled by considering the non-linear behaviour of the applied aluminium alloy, as it was obtained from uniaxial tensile tests. In addition, for considering the presence of the heat affected zones deriving from the use of spot-weld connections between ribs and the panel, a reduced conventional yield stress $f_{0.2}$, assumed equal to half of the original one, has been considered for the panel portions having a distance from the spot-welds equal to 25 mm. On the contrary, both the ultimate stress f_u and deformation ε_u of the HAZs have been assumed as for the non-affected material.

Beams and columns of the external frame have been modelled by using a two-nodes linear element (B31 type), while four-nodes two-dimensional elements (S4R type) have been used to model both the aluminium sheeting and the stiffeners. In the numerical model, the existing eccentricity between the members of the external reaction frame and the internal plate element due to connecting system and the effective size of the member cross-sections have been considered. The steel frame-panel connection, which is realised by means of tightened steel bolts having a pitch of 50 mm, has been introduced in the model by considering that no slip between the different parts occurs. This has been modelled by using the TIE constraint in the ABAQUS program library, which considers the same behaviour between panel sides and the corresponding frame members. The same command has been also used to model the interaction between the stiffeners and the aluminium plate, considering the presence of fixed connection points every 50 mm to simulate the spot-weld connections.

In addition, at the aim of reproducing the exact panel configuration, appropriate friction contact conditions have been introduced to consider the contact forces arising at the aluminium plate-to-stiffener interfaces. On the basis of a preliminary study, a mesh of 50x50 mm has been chosen, which represented the best compromise between time of analysis and accuracy of the obtained results.
According to the experimental lay-out, the external load is applied to the top beam of the external lateral reaction frame. The system response has been obtained by using the modified Riks algorithm, which uses the Newton-Raphson procedure and belongs to the "arc-length" analysis method. In this algorithm, used to resolve problems characterised by strong instabilities, the equilibrium condition is determined by iterative runs, which move along the same equilibrium curve. The mechanical behaviour of thin plates under shear load can be significantly influenced by initial geometrical imperfections induced by fabrication phases, shrinkage of welds and out-of-plane deflection of boundary loading frame. The imperfection shape has been selected according to a detailed survey of the initial out-of-plane deformation of the panel. In particular, the imperfection amplitudes have been assumed in the numerical model considering the maximum out-of-plane of the middle point of each portion panel revealed on the initial panel configuration (Figure 14a). Then, for each panel portion, a sinusoidal shape of the imperfection has been applied, having a zero value on the boundary stiffeners (Figure 14b).

THE CALIBRATION OF THE FEM MODEL

In the present Section a comparison between the results related to the application of the developed FEM model and the experimental ones is presented. Such a comparison is shown in terms of the previously described main parameters (dissipated energy, secant stiffness and equivalent viscous damping ratio), which have been obtained according to the relationships provided in Figure 11.
In particular, the above comparison is proposed for the last three "macro behaviours" of the panel type B [9]. In fact, it has to be considered that the proposed system is able to provide a significant

dissipative capacity for large shear deformations. In addition, since the adopted material is characterised by a very limited elastic strength and a pronounced non-linear behaviour, surely the initial stresses and the effects of welding have a significant influence on the response of the system in the early deformation stages. At this phase of the research, exact informations on the distribution of residual stresses in the panel are not still available. Therefore they have not been considered into the numerical model. For this reason the FEM model is not able to interpret the experimental results in the very initial phases of the loading process, as it is evident by examining the Figure 15a. On the other hand, it is evident that the numerical-experimental comparison gives quite satisfactory results for a large deformation demand, namely shear displacement larger than 20 mm. This comparison is quite accurate in terms of dissipated energy and also secant stiffness, while the comparison in terms of viscous damping ratio shows improving results with increasing deformations (see Figures 15 b,c,d).
A detailed comparison in terms of deformed shape and corresponding load-displacement curves has been carried out for panel type B, with reference to specific values of the applied deformation, which have been chosen according to the above significant behavioural phases. The reliability of the proposed numerical model is clearly evident in Figure 16 where, for the sake of example, the comparison between the real and numerical deformed shape and cyclic response is shown for the panel type B in the third macro-behavioural phase.

THE PARAMETRIC STUDY

The aim of setting up the above numerical model was the definition of a useful design tool for the selection of shear panels in order to ensure their suitable behaviour under both monotonic and cyclic loading conditions in relation to different shear deformation demands. In fact a dissipative shear panel is able to provide a stable cyclic behaviour if it is designed in such a way to avoid any buckling phenomenon, which can be of both local and global type, before the occurrence of plastic deformation. In the following, in order to generalise the obtained results, the numerical study is related to a generic initial deformation, considering a panel configuration similar to the above panel type F, i.e.

with stiffeners placed alternatively on the two sides of the sheeting. At this aim a generic imperfection shape, represented by an out-of-plane displacement of 3 mm of one upper corner of the panel, has been considered [9]. Starting from this configuration and varying both the width-to-thickness ratio of the plate portions and the second moment of area of the ribs several panel configurations have been selected. In particular, the stiffness of the ribs has been changed by varying the depth, while their thickness has been always assumed equal to the one of the base sheeting. The numerical analysis have been carried out by assuming width-to-thickness ratios b/t equal to 25, 37.5, 50, 75, 100 and 200, considering the distance among the ribs b constant and equal to 250 mm, while the thickness of the plate t ranging from 1.25 mm to 10 mm.

It is worth noticing that for each b/t ratio, the selection of ribs having a second moment of area equal to $I_{st,lim}$, which is the limit value of the flexural stiffness beyond which the stiffener may be considered as "rigid" according to EC9 provisions, has been also considered. This parameter is expressed as a function of the second moment of area of the total number of intermediate transversal stiffeners placed into the panel, considering that in this case $b/h_w<\sqrt{2}$, where h_w is the width of panel [9]. For each value of the b/t ratio, the stiffener limit stiffness $I_{st,lim}$, the corresponding limit values of the stiffener depth $h_{st,lim}$ and the corresponding normalized stiffness parameter $\gamma_{st,lim}$ have been computed [10].

The monotonic analysis of the several examined panel configurations have been given in terms of $F/F_{0.2}$ - γ curves, where $F_{0.2}$ is the yielding shear force and γ is the panel shear deformation. All the analyses have been carried out up to 20% of shear deformation, which can be considered a limit value for practical applications. In Figure 17a, for the sake of example, the obtained $F/F_{0.2}$ - γ curves for b/t = 25 are presented. This diagram shows that for increasing values of rib stiffness the obtained $F/F_{0.2}$ - γ curves approach a sort of envelope curve, which corresponds to the full plastic capacity of the system. As far as the stiffener depth decreases, the separation of the relevant curve from the envelope curve is representative of the effect due to global buckling phenomena involving the stiffeners. In all cases, after shear buckling,

which can be either of local or global type depending on the rib stiffness, the system is characterised by a stable post-buckling behaviour due to tension field mechanism.

In Figure 17b, the shear strength level $F/F_{0.2}$ is plotted as function of the normalised stiffness parameter γ_{st} for a shear deformation of γ=7.5%. This curve allows the definition of an optimal value of the stiffness parameter ($\gamma_{st,opt}$), which determines the attainment of the maximum shear strength value. In fact, the obtained curves show that the shear strength of the system increases with the rib stiffness up reaching a maximum value identified by the curve plateau.

The performance of the system for different shear deformation levels γ can be synthetically represented by a design chart (Figure 18), where for a fixed design value of shear strength $F/F_{0.2}$ and plastic shear strain γ, both the b/t ratio and the optimum value of the stiffness parameter $\gamma_{st,opt}$ are given. In the same chart the limit related to the attainments of buckling phenomena can be provided. In fact, the right side of the diagram (large b/t values) is related to the attainment of elastic buckling ($\tau_{cr} \leq \tau_{0.2}$). The corresponding elastic buckling curve clearly represents a limit for the use of shear panels as a dissipative device. Obviously, such buckling phenomena could be either of local or global type, depending on the panel configuration. In particular, global buckling is more relevant for reduced shear deformation levels, where the applied ribs have a lower flexural stiffness. Shear panel configurations falling on the right of the above buckling curve can be defined as "slender", meaning that they suffer buckling phenomena before being involved into plastic deformation. Similarly, the buckling curve depicted on the left side of the above charts (small b/t values) is representative of panel configurations where the buckling phenomena occur for shear stress (τ_{cr}) equal or larger than the one corresponding to the attainment of the design deformation demand (τ_γ) (plastic buckling curve). Shear panel configurations falling on the left of the above buckling curve can be defined as "compact", meaning that they do not suffer buckling phenomena up reaching the required plastic deformation. As a consequence, shear panel configurations falling between plastic buckling curve and elastic buckling curve can be defined as "semi-

compact", meaning that suffer buckling phenomena while developing plastic deformation.

CONCLUSIVE REMARKS

In this paper the experimental and numerical behaviour of pure aluminium stiffened shear panels has been investigated. Firstly, the experimental tests have shown that the adopted system is characterised by a significant energy dissipation capability. On the other hand, the occurrence of several buckling modes (both of local and global types), the peculiar material features (very low-yield strength) and the fabrication process (effect of welding) severely affect the response of the system. Aiming at generalising the experimental results, a detailed FEM model has been set up, which is able to well reproduce the main behavioural phases exhibited by tested panels. The comparison with experimental results has shown that the application of the proposed model provides a satisfactory result in terms of shear stress-shear strain curve and also of the main global features of the system, presenting also deformed shapes in good agreement with the ones evidenced by the experimental tests. On the other hand, it has been noted that the proposed model is not able to well interpret the very early stages of the loading process, because of the effect of the residual stresses, which have been not yet contemplated due to the lack of experimental data. For this reason, further improvements of the numerical model throughout this direction are desirable. Finally, a wide numerical study finalised to the evaluation of the influence of the main geometrical and mechanical parameters on the panel behaviour has been carried out. The obtained results allowed the definition of a design chart, as a tool for the selection of the optimum values of the geometrical parameters of shear panels, namely width-to-thickness ratio and flexural stiffness of the applied ribs. Such a design chart allows also the definition of the main behavioural classes of shear panels in relation to the possible buckling phenomena occurring in the plastic field as a function of the required ductility.

ACKNOWLEDGMENT

This study has been developed in the framework of the research project "Innovative steel structures for the seismic protection of new and existing buildings: design criteria and methodologies" financed by the Italian Ministry of Education, University and Research (MIUR) for the years 2003-2005. Part of this work has been carried out with the financial support of the National Research Council (CNR), grant No. CU04.00108.

REFERENCES

[1] M. Rezai, C. E. Ventura, H. Prion, "Simplified and detailed finite element models of steel plate shear walls", Proc. 13th World Conference on Earthquake Engineering, Vancouver, Canada, 2004.

[2] M. Nakashima, S. Iwai, M. Iwata, T. Takeuchi, S. Konomi, T. Akazawa, and K. Saburi, "Energy Dissipation Behaviour of Shear Panels Made of Low Yield Steel", Earthquake Engineering and Structural Dynamics, John Wiley & Sons, 23, 1994, 1299-1313.

[3] G. De Matteis, R. Landolfo and F.M. Mazzolani, "Seismic Response of MR Steel Frames with low-yield Steel Shear Panels", Engineering Structures-The Journal of Earthquake Wind and Ocean Engineering, 25, 155-168, 2003.

[4] G. De Matteis, F.M. Mazzolani and S. Panico, "Pure aluminium shear panels as passive control system for seismic protection of steel moment resisting frames", Proc. IV International Conference STESSA '03 (Behaviour of Steel Structures in Seismic Areas), Balkema, 609-614, Naples, Italy, 2003.

[5] G. De Matteis, A. Formisano, F.M. Mazzolani and S. Panico, "Design of low-yield metal shear panels for energy dissipation", Proc. COST C12 Final Conference, Innsbruck, 2005.

[6] G. De Matteis, S. Panico, A. Formisano, F.M. Mazzolani, "Experimental tests on pure aluminium shear panels under cyclic loading", Proc. EE-21C International Conference (Earthquake Engineering in the 21st Century), Skopje-Ohrid, Macedonia, 2005.

[7] Hibbitt, Karlsson & Sorensen, Inc. "ABAQUS/Standard, version 6.4-1", Patwtucket, RI, U.S.A., 2004.

[8] G. De Matteis, A. Formisano, F.M. Mazzolani, S. Panico, "Experimental tests and numerical simulation on stiffened pure aluminium shear panels", Proc. of the 10th Int. Conf. on Civil, Structural and Environmental Engineering Computing, Roma, 2005.

[9] G. De Matteis, F. Addelio, F.M. Mazzolani, "Sul dimensionamento dei pannelli di alluminio puro per la protezione sismica dei telai di acciaio", Proc. 11th National Congress "L'ingegneria sismica in Italia", Genova, 2004.

[10] G. De Matteis, A. Formisano, F.M. Mazzolani and S. Panico, "Design of dissipative aluminium shear panels: comparison between numerical analysis and experimental results", Proc. Eurosteel Conference on Steel and Composite Structures, Maastricht, The Netherlands, 2005.

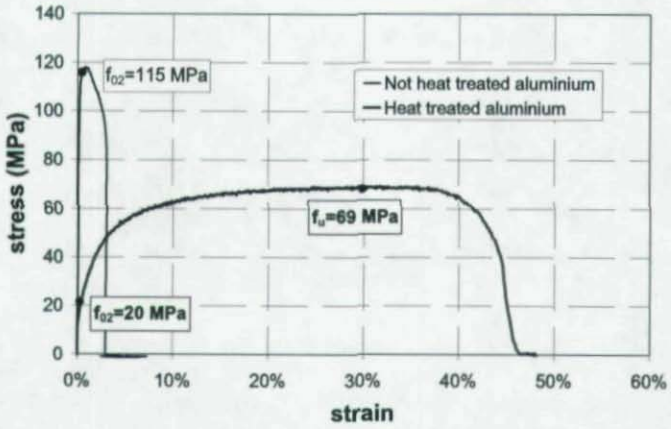

Figure 1: Comparison between AW 1050A aluminium alloy curves before and after the heat treatment.

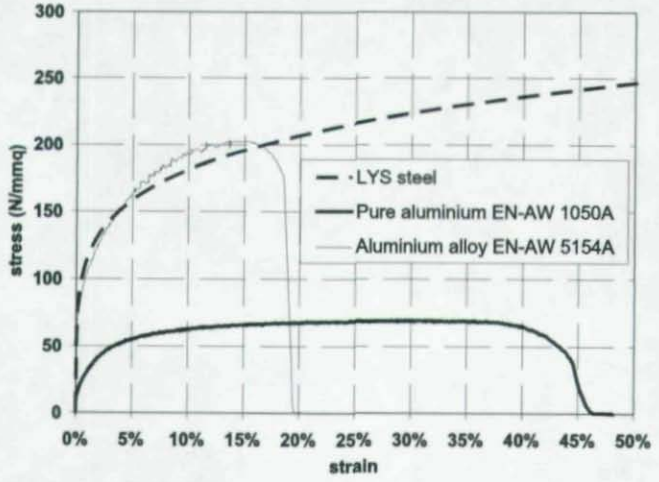

Figure 2: Comparison among different low-strength materials.

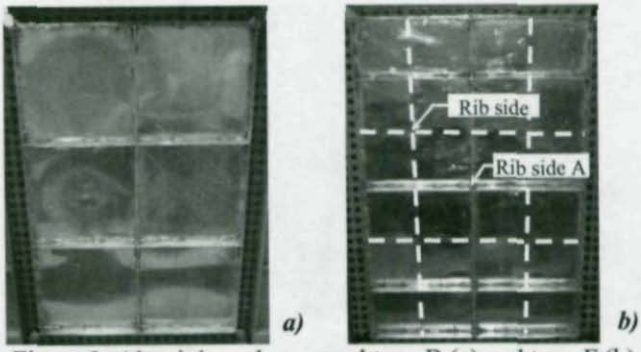

Figure 3: Aluminium shear panel type B (a) and type F (b).

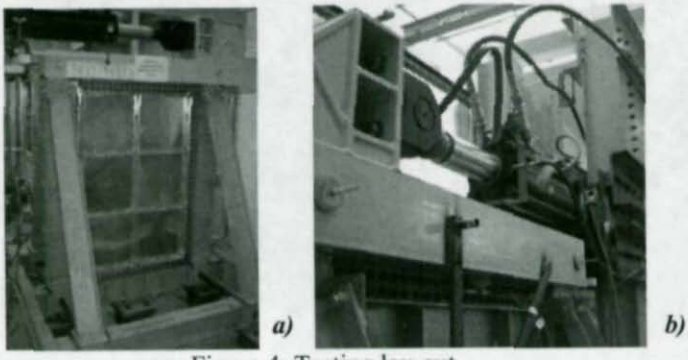

Figure 4: Testing lay-out.

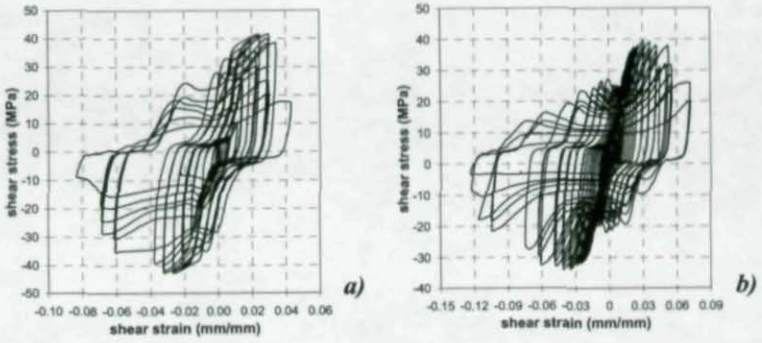

Figure 5: Cyclic response of shear panel type F (a) and type B (b).

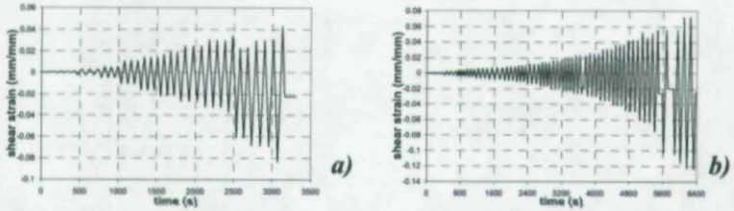

Figure 6: Deformation history for shear panel type F (a) and type B (b).

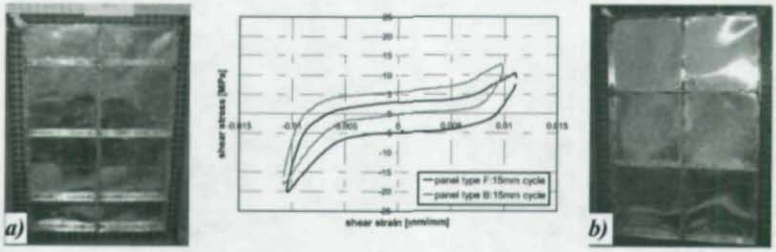

Figure 7: Pinching effect due to compression in the lower panel fields for shear panel type F (a) and type B (b).

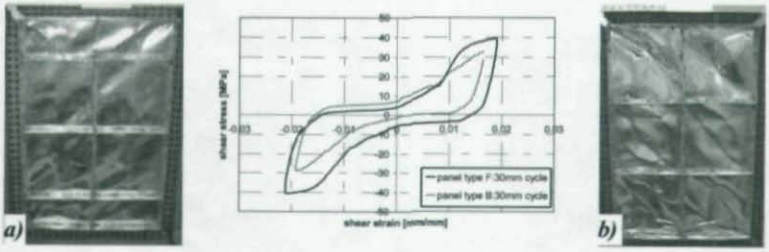

Figure 8: Development of plastic shear buckling phenomena for shear panel type F (a) and type B (b).

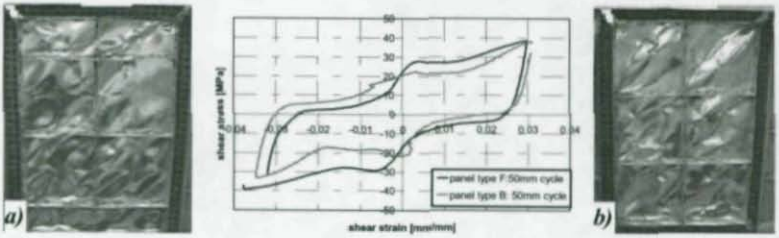

Figure 9: Buckling phenomena of the ribs for shear panel type F (a) and type B (b).

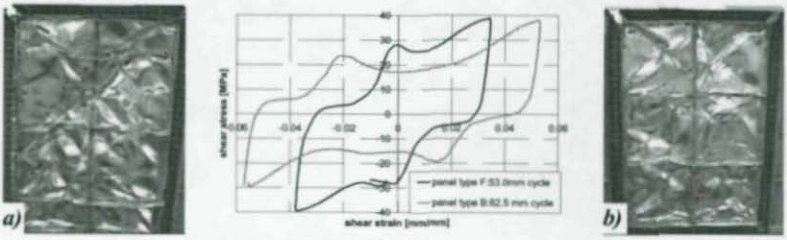

Figure 10: Tearing of sheeting material and connection failure for shear panel type F (a) and type B (b).

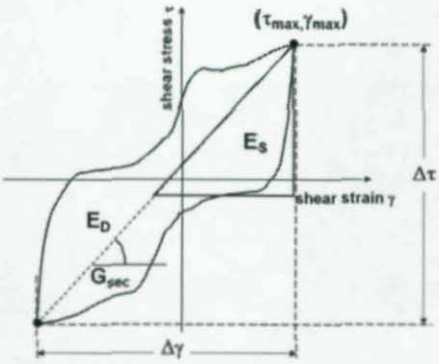

$$E_S = \frac{1}{8}\Delta\tau \cdot \Delta\gamma$$

$$\zeta_{eq} = \frac{1}{4\pi}\frac{E_D}{E_S}$$

$$G_{sec} = \frac{\Delta\tau}{\Delta\gamma}$$

Figure 11: Definition of equivalent viscous damping (ξ_{eq}) and secant shear stiffness (G_{sec}).

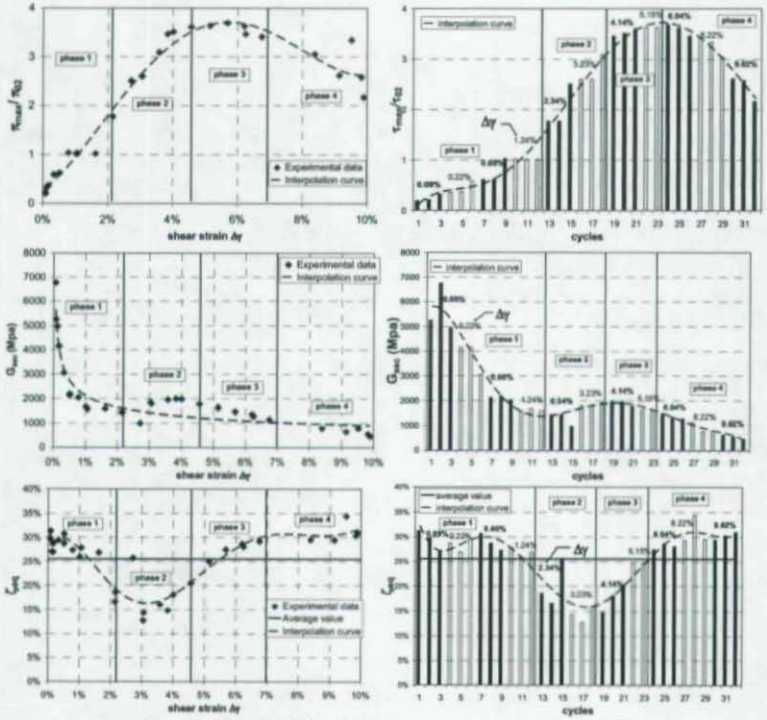

Figure 12: Cyclic performance of panel type F.

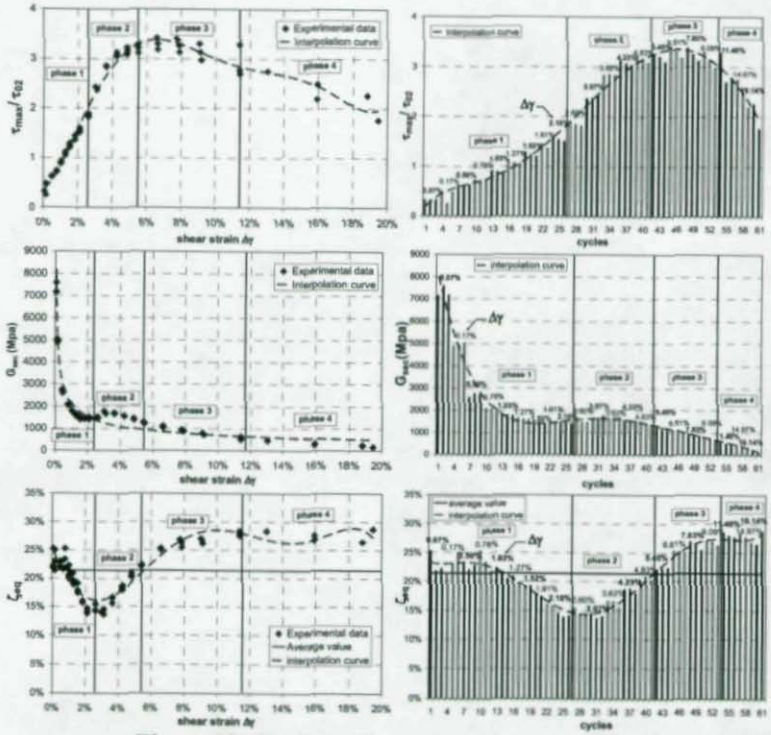

Figure 13: Cyclic performance of panel type B.

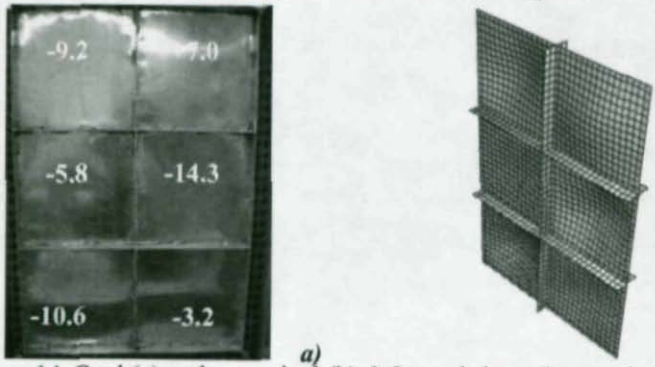

Figure 14: Real (a) and numerical (b) deformed shape for panel type B.

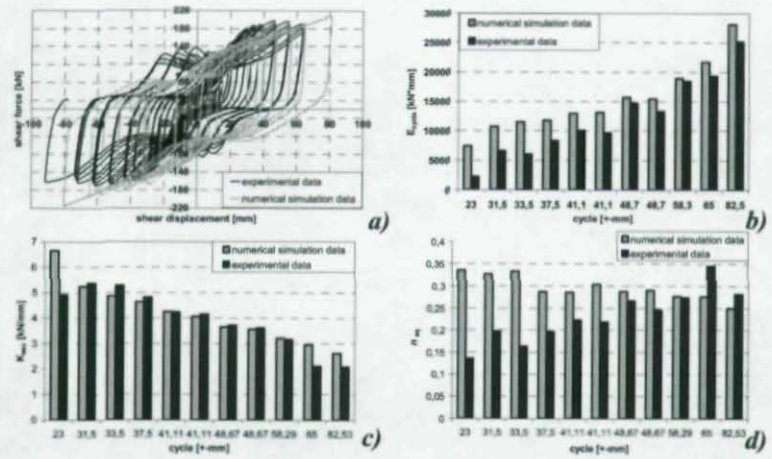

Figure 15: Comparison between experimental and numerical results for panel type B - (a) cyclic behaviour, (b) dissipated energy, (c) secant stiffness, (d) equivalent viscous damping ratio.

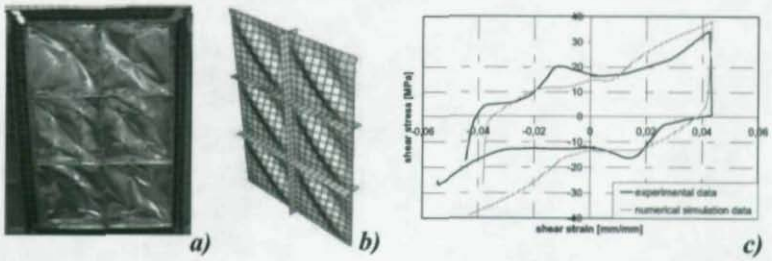

Figure 16: Comparison between experimental and numerical results at the cycle ±65.0mm for panel type B: a) experimental deformed shape; b) numerical deformed shape; c) comparison between experimental and numerical cyclic behaviour.

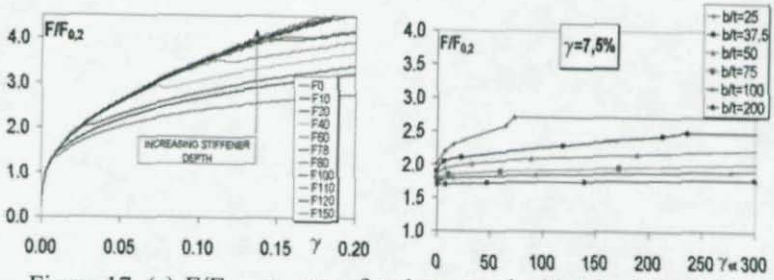

Figure 17: (a) $F/F_{0.2}$ - γ curves for shear panel with $b/t = 25$ and (b) $F/F_{0.2} - \gamma_{st}$ curves for shear deformation γ=7.5%.

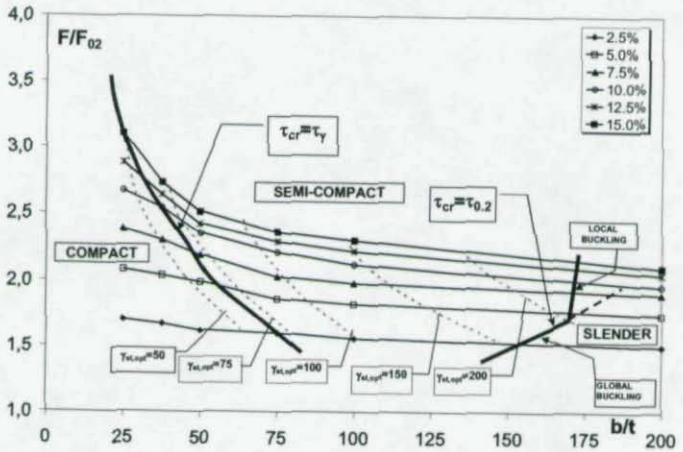

Figure 18: Design chart for pure aluminium shear panels.

Stability of Thin Plates under Longitudinal Stress Gradients

Cheng Yu[1], *Benjamin W. Schafer*[2]

ABSTRACT

When thin-walled cross-sections are subjected to moment gradients, the plates that comprise the compression flange are themselves subject to a longitudinal stress gradient. This paper analyzes the effect of longitudinal stress gradients on both elastic buckling and ultimate strength of isotropic thin plates. Two types of thin plates are investigated: (1) stiffened plates with two supported longitudinal edges, and (2) unstiffened plates with one longitudinal edge supported and the other longitudinal edge free. A semi-analytical method is derived to calculate the elastic buckling stresses of both types of thin plates subjected to longitudinal stress gradients. The semi-analytical method is verified by finite element analyses in ABAQUS. Further finite element analyses are employed to study the effect of longitudinal stress gradient on the ultimate strength of thin plates. The results indicate that the presence of longitudinal stress gradient increases both the elastic buckling stress, and ultimate strength of thin plates, with the increase being most pronounced in unstiffened plates. The influence of longitudinal stress gradient in the stability and strength of thin plates may be accounted for in design by applying a modified buckling coefficient. A closed-form formula for calculating the modified buckling coefficient is provided in this paper.

---

[1] Assistant Professor, Department of Engineering Technology, University of North Texas, Denton, TX 76207. (cyu@unt.edu)
[2] Assistant Professor, Department of Civil Engineering, Johns Hopkins University, Baltimore, MD 21218. (schafer@jhu.edu)

INTRODUCTION

The design of thin-walled cold-formed steel beams requires examinations of both the stability of the component plates (e.g., local buckling) and the stability of whole member (e.g., lateral-torsional buckling). In practice, beams are subjected to a variety of loading and boundary conditions such that non-uniform internal moment (moment gradient) develops along the length. The moment gradient, which greatly influences the member as a whole, also creates a longitudinal stress gradient on the component plates. The moment gradient effect on lateral-torsional buckling is considered in design; however, the same effect is not considered in the design of the component plates. In this paper, we investigate the influence of longitudinal stress gradients on the elastic buckling and ultimate strength of two types of thin plates: (1) stiffened elements where the plate is supported along both longitudinal edges, such as the top flange of the hat section in Fig. 1(a), and (2) unstiffened elements where the plate is supported along only one longitudinal edge, such as the compression flange of the channel section in Fig. 1(b). A semi-analytical solution based on the energy method is developed to calculate the elastic buckling stress of these thin plates and the commercial finite element (FE) package ABAQUS (ABAQUS 2001) is used to determine the ultimate strength. The results are intended to aid in the development of design provisions to include the effect of longitudinal stress gradient on cold-formed steel members.

(a) hat section (b) channel section

Figure 1 Typical thin-walled cross-sectional shapes

EFFECT OF LONGITUDINAL STRESS GRADIENTS ON THE ELASTIC BUCKLING OF THIN PLATES

Semi-Analytical Solution for Elastic Buckling

Figs. 2 and 3 respectively present the semi-analytical models for the stiffened plate and the unstiffened plate subjected to a longitudinal stress gradient. The stiffened plate is simply supported (free rotation

and free in-plane displacement) at all four edges. For the unstiffened plate, three edges are simply supported and one longitudinal edge is free. An additional rotational spring is applied to the supported longitudinal edge(s) for both types of plates to simulate the restraint provided by the web in a typical section (Fig. 1). Unequal stresses (transversely uniform) are applied at both ends to create a longitudinal stress gradient and the difference in force is equilibrated by a uniform shear stress applied along the supported longitudinal edge(s).

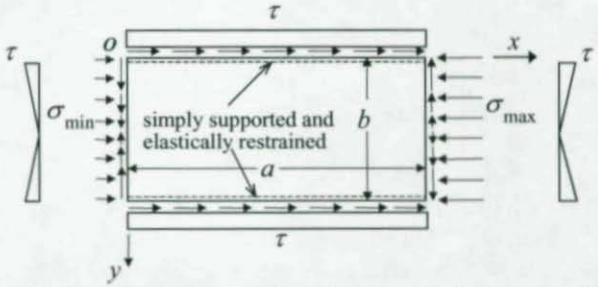

Figure 2 Stiffened plate under a longitudinal stress gradient

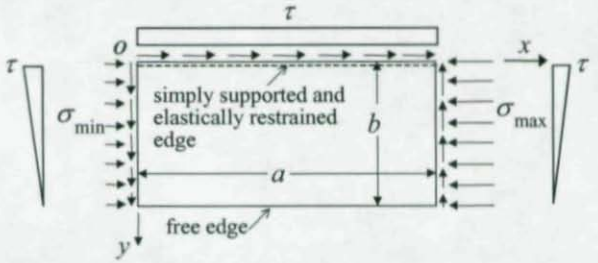

Figure 3 Unstiffened plate under a longitudinal stress gradient

The Rayleigh-Ritz method is employed to determine the elastic buckling stress of the plates. In this method, an assumed deflection function $w(x,y)$ satisfying the boundary conditions is used in the expression for the total potential energy, Π , which is the summation of the strain energy of the plate due to bending, U_1, the strain energy due to the elastic restraint, U_2, and the work done by the external forces, T. Classical solutions from thin plate theory (e.g. Timoshenko and Gere 1961) are listed in Eq.'s 1 to 4.

$$\Pi = U_1 + U_2 + T \tag{1}$$

$$U_1 = \frac{D}{2}\int_0^b\int_0^a \left\{ \left(\frac{\partial^2 w}{\partial x^2} + \frac{\partial^2 w}{\partial y^2} \right)^2 - 2(1-\mu)\left[\frac{\partial^2 w}{\partial x^2}\frac{\partial^2 w}{\partial y^2} - \left(\frac{\partial^2 w}{\partial x \partial y} \right)^2 \right] \right\} dxdy \tag{2}$$

$$U_2 = \frac{S}{2}\int_0^a \left[\left(\frac{\partial w}{\partial y} \right)_{y=0}^2 \right] dx + \frac{S}{2}\int_0^a \left[\left(\frac{\partial w}{\partial y} \right)_{y=b}^2 \right] dx \quad \text{(for stiffened plates)} \tag{3a}$$

$$U_2 = \frac{S}{2}\int_0^a \left[\left(\frac{\partial w}{\partial y} \right)_{y=0}^2 \right] dx \quad \text{(for unstiffened plates)} \tag{3b}$$

$$T = -\frac{t}{2}\int_0^b\int_0^a \left[\sigma_x \left(\frac{\partial w}{\partial x} \right)^2 + \sigma_y \left(\frac{\partial w}{\partial y} \right)^2 + 2\tau_{xy}\frac{\partial w}{\partial x}\frac{\partial w}{\partial y} \right] dxdy \tag{4}$$

where D is the plate flexural rigidity and S is the stiffness of the elastic rotational restraint. Using the principle of minimum total potential energy, the equilibrium equations of the plate can be identified:

$$\frac{\partial \Pi}{\partial w_i} = 0 \quad (i = 1,\ 2 \ldots\ N) \tag{5}$$

Eq. 5 represents a system of N simultaneous homogeneous equations with w_i and stress σ (σ_{max} is used in the present work) as unknowns. For a nontrivial solution of the w_i's, the determinant of the coefficient matrix of the system of equations must vanish. Thus, the eigenvalues of Eq. 5 provide the buckling stresses and the eigenvectors the buckling shapes. The accuracy of the Rayleigh-Ritz method depends on the appropriateness of the assumed deflection function. In comparison to FE solutions the proposed semi-analytical model is computationally more efficient, and the derivations more transparent.

Elastic Buckling of Stiffened Plates Subjected to Longitudinal Stress Gradients

Stress Distribution

The stress functions σ_x, σ_y, and τ_{xy} are required in the expression of the total potential energy (Eq. 1). It is assumed that the normal stress σ_x varies linearly in x-direction, and its magnitude is uniform in the y-

direction. It is also assumed that no normal stress develops in the transverse direction. The two assumptions along with equilibrium and plane stress conditions (Eq.'s 6 and 7, body force is ignored) lead to the stress distribution functions shown below (Eq.'s 8, 9, 10) for the stiffened plate subjected to longitudinal stress gradients.

$$\frac{\partial \sigma_x}{\partial x} + \frac{\partial \tau_{xy}}{\partial y} = 0 \tag{6}$$

$$\frac{\partial \sigma_y}{\partial y} + \frac{\partial \tau_{xy}}{\partial x} = 0 \tag{7}$$

$$\sigma_x = \sigma_{\max}\left[\frac{(1-r)x}{a} + r\right] \tag{8}$$

$$\sigma_y = 0 \tag{9}$$

$$\tau_{xy} = \sigma_{\max}\frac{(1-r)}{2}\left(\frac{b}{2} - y\right) \tag{10}$$

where r is the longitudinal stress gradient factor, $r = \sigma_{\min}/\sigma_{\max}$, and $\sigma_{\max}$ is the applied stress at the maximum loaded edge. Eq.'s 8, 9, and 10 satisfy the equilibrium conditions as well as compatibility, and therefore represent a physically possible set of stresses for the plate.

Boundary Conditions

Six boundary conditions are observed for the stiffened plates. Simple support at the transverse edges (two conditions):

$$(w)_{x=0,a} = 0 \tag{11}$$

Elastic rotational restraint along both simply supported longitudinal edges (four conditions):

$$(w)_{y=0,b} = 0 \tag{12}$$

$$D\left(\frac{\partial^2 w}{\partial y^2} + \mu\frac{\partial^2 w}{\partial x^2}\right)_{y=0,b} = S\left(\frac{\partial w}{\partial y}\right)_{y=0,b} \tag{13}$$

The form of Eq. 13 implies that the deflection function $w(x,y)$ can be formed as $\Sigma A_i(y)B_i(x)$, where A_i is a function of y alone and B_i is a function of x alone. If for every i, $A_i(y)B_i(x)$ is compatible with all the

boundary conditions, then the linear summation of each term satisfies all the boundary conditions as well.

Deflection Functions

Three trial deflection functions for the stiffened plates are considered herein. The first trial deflection function (DF_S1) reflects the early work of Libove et al. (1949). They employed a double Fourier sine series:

$$w = \sum_{i=1}^{M}\sum_{j=1}^{N} w_{ij} \sin\frac{i\pi x}{a}\sin\frac{j\pi y}{b} \tag{14}$$

The stability determinant matrix can be obtained via Eq. 5 and the size of this matrix is determined by the number ($M \times N$) of w_{ij} terms included in the deflection function. Due to the limit of computational tools at that time, the work of Libove et al. (1949) considered only up to M.= 7 and N = 5, further their model is *not* applicable to plates with elastic rotational restraints or fixed edges, only simple supports (ss-ss).

The second deflection function (DF_S2) proposed by the authors is a linear combination of polynomial and trigonometric functions as given in Eq. 15. Each term consists of the product of a fourth order polynomial (the transverse deflection) and a sine function (the longitudinal deflection). DF_S2 applies to general stiffened plates with elastic rotational restraint or fixed edges.

$$w = \sum_{i=1}^{N} w_i \left(p_i y(y-b) + q_i y^2 (y-b)^2\right)\sin\left(\frac{i\pi x}{a}\right) \tag{15}$$

The third trial deflection function (DF_S3), as given in Eq. 16, is based on the same principle as DF_S2. Unlike DF_S2, DF_S3 employs a sine function plus a second order polynomial for the transverse deflection in each term, this idea is motivated by Lundquist and Stowell (1942a).

$$w = \sum_{i=1}^{N} w_i \left(p_i y(y-b) + q_i \sin(\frac{\pi y}{b})\right)\sin\left(\frac{i\pi x}{a}\right) \tag{16}$$

The parameters in deflection functions $w(x,y)$ are determined by substituting $w(x,y)$ into the boundary conditions of Eq.'s 11 to 13, detailed results can be found in Yu (2005).

Table 1 Ratios of semi-analytical to FE results for stiffened plates

	DF_S1/FEM	DF_S2/FEM	DF_S3/FEM
Mean	106.77%	93.65%	101.67%
Standard deviation	6.35%	12.87%	1.89%

Finite element analysis using ABAQUS was employed to determine the elastic buckling stress of the stiffened plates and to evaluate the proposed deflection functions. A total of 52 stiffened plates were analyzed by ABAQUS and the average ratios of semi-analytical to FE results are given in Table 1. In general, DF_S1 and DF_S2 give fair agreements with the FE results. DF_S3 has the best result, and is therefore chosen for further study. A convergence study was performed to decide on the number of terms (N) to keep in the deflection function (and thus the size of the $N \times N$ matrix to be solved), the resultant algorithm follows: for $a/b <= 10$, $N = 20$; for $a/b > 10$ and $a/b <= 20$, $N = 40$; for $a/b > 20$ and $a/b <= 40$, $N = 60$. For complete details of the FE model and convergence studies see Yu (2005).

Effect of Longitudinal Stress Gradients on Elastic Buckling of Stiffened Plates

Figs. 4 and 5 respectively demonstrate the influence of longitudinal stress gradient on ss-ss and fix-fix stiffened plates, the results are determined by the semi-analytical model with DF_S3 (Eq. 16). It indicates that for both types of plates, the longitudinal stress gradient increases the buckling stress at the maximum loaded edge, and the increase becomes significant when the longitudinal stress gradient is high and the plate is short (small aspect ratio, β, where $\beta=a/b$). The influence vanishes when the aspect ratio (β) becomes larger, and the buckling coefficients converges to traditional values for uniform compression cases ($k = 4$ for ss-ss plates and $k = 6.97$ for fix-fix plates).

It can be concluded that the influence of longitudinal stress gradient diminishes quickly with the length for local buckling of a stiffened plate, but perhaps not as quickly as is generally assumed in design. For example, for a simply supported plate with aspect ratio 5, when a longitudinal stress gradient $r = 0$ (loaded on only one edge) is applied, the buckling coefficient k_{max} will equal 4.712 - still an 18% increase in buckling stress compared with the uniform compression case.

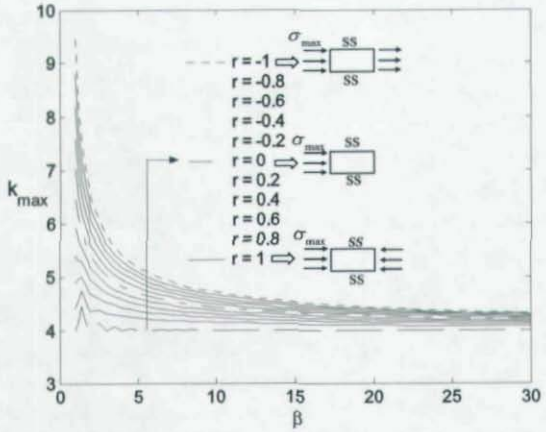

Figure 4 k_{max} vs. plate aspect ratio (β) for ss-ss stiffened plates

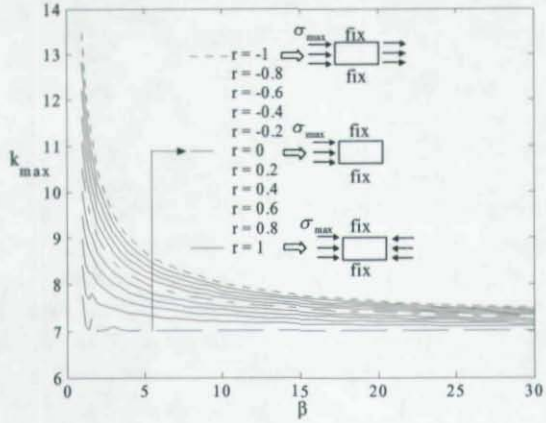

Figure 5 k_{max} vs. plate aspect ratio (β) for fix-fix stiffened plates

Elastic Buckling of Unstiffened Plates Subjected to Longitudinal Stress Gradients

Stress Distribution

Two assumptions are made for the semi-analytical model for unstiffened plates as shown in Fig. 3: (1) the distribution of shear stress τ_{xy} is linear in the y-direction and (2) uniform in the x-direction. By

assuming plane stress conditions (Eq.'s 6, 7) and ignoring the body force the stresses can be obtained in functional form as given below:

$$\sigma_x = \sigma_{\max}\left[\frac{(1-r)x}{a} + r\right] \tag{17}$$

$$\sigma_y = 0 \tag{18}$$

$$\tau_{xy} = \sigma_{\max}\frac{(1-r)}{a}(b-y) \tag{19}$$

Boundary Conditions

A total of six boundary conditions are observed for the unstiffened plates. Simply supported at the transverse, loaded edges:

$$(w)_{x=0,a} = 0 \tag{20}$$

Elastic rotational restraint along one supported longitudinal edge:

$$(w)_{y=0} = 0 \tag{21}$$

$$D\left(\frac{\partial^2 w}{\partial y^2} + \mu\frac{\partial^2 w}{\partial x^2}\right)_{y=0} = S\left(\frac{\partial w}{\partial y}\right)_{y=0} \tag{22}$$

One free longitudinal edge:

$$D\left(\frac{\partial^2 w}{\partial y^2} + \mu\frac{\partial^2 w}{\partial x^2}\right)_{y=b} = 0 \tag{23}$$

$$D\left[\frac{\partial^3 w}{\partial y^3} + (2-\mu)\frac{\partial^3 w}{\partial x^2 \partial y}\right]_{y=b} = 0 \tag{24}$$

Deflection Functions

Three trial deflection functions are considered for the semi-analytical model of unstiffened plates. The first proposed deflection function (DF_u1), Eq. 25, is motivated by the work of Lundquist and Stowell (1942b) who explored the buckling of unstiffened plates subjected to uniform compressive stresses.

$$w = \sum_{i=1}^{N} w_i \left\{\frac{y}{b} + \frac{Sb}{2a_3 D}\left[\left(\frac{y}{b}\right)^5 + a_1\left(\frac{y}{b}\right)^4 + a_2\left(\frac{y}{b}\right)^3 + a_3\left(\frac{y}{b}\right)^2\right]\right\}\sin\left(\frac{i\pi x}{a}\right) \tag{25}$$

In DF_u1, the transverse deflection curve is taken as the sum of a straight line and a cantilever-deflection curve. The values of a_1, a_2, and a_3 (a_1 = -4.963, a_2 = 9.852, and a_3 = -9.778) were determined by taking the proportion of two deflection curves that gave the lowest buckling stress for a fixed-edge flange with a Poisson's ratio μ = 0.3 under uniform compression. It should be noted that DF_u1 is *not* compatible with all the boundary conditions, Eq.'s 20 to 24. However, it was found to give reasonable results in the research done by Lundquist and Stowell (1942b) and was thus considered here.

Unlike DF_u1 which is based on a physical representation of the expected shape, the second trial deflection function (DF_u2), Eq. 26, is a more general expression of a product of a fourth order polynomial (transverse) and a sine function (longitudinal).

$$w = \sum_{i=1}^{N} w_i \left(c_{i1} y + c_{i2} y^2 + c_{i3} y^3 + c_{i4} y^4\right) \sin\left(\frac{i\pi x}{a}\right) \tag{26}$$

As an extension of DF_u2, a third deflection function (DF_u3), Eq. 27, using a fifth order polynomial in the transverse direction and a sine function for the longitudinal deflection is also considered.

$$w = \sum_{i=1}^{N} \left[w_{i1}\left(p_{i1} y + p_{i2} y^2 + p_{i3} y^3 + p_{i4} y^4\right) + w_{i2}\left(q_{i1} y^3 + q_{i2} y^4 + q_{i3} y^5\right)\right] \sin\left(\frac{i\pi x}{a}\right) \tag{27}$$

The parameters in these final two deflection functions (Eq.'s 26, 27) are determined by substituting Eq.'s 26 and 27 into the boundary conditions of Eq.'s 20 to 24, the results can be found in Yu (2005).

Table 2 Semi-analytical v. FE results for unstiffened plates

	DF_U1/FEM	DF_U2/FEM	DF_U3/FEM
Mean	102.37%	99.71%	99.58%
Standard deviation	4.27%	0.26%	0.26%

An FE model in ABAQUS was developed to examine the three proposed deflection functions. A total of 52 thin plates were analyzed and the comparison of semi-analytical vs. FE results is summarized in Table 2. In general, all three trial deflection functions give good agreements with the FE results. DF_U2 and DF_U3 yield closer results to the FE results than DF_U1, with average errors less than 1%. Since DF_U2

provides both accuracy and reasonable computational efficiency when compared to the other trial functions, it is selected for further study. The number of terms to be kept in the expansion is determined by a convergence study as follows: for $a/b <= 10$, $N = 20$; for $a/b > 10$ and $a/b <= 20$, $N = 40$; for $a/b > 20$ and $a/b <= 40$, $N = 60$. For complete details of the convergence study and FE analyses see Yu (2005).

Effect of Longitudinal Stress Gradients on Elastic Buckling of Unstiffened Plates

Two unstiffened plates under longitudinal stress gradients are investigated by the semi-analytical solution with DF_U2: one where the supported longitudinal edge has no rotational restraint (ss-free) and one where the supported edge has infinite rotational restraint (fix-free). Figs. 6 and 7 provide a graphic representation of the effect of longitudinal stress gradient on these two unstiffened plates. The stress gradient boosts the buckling stress at the maximum loaded edge greatly, for both types of plates, especially when the plate aspect ratio (β) is less than 10. For a ss-free plate even with $\beta = 30$ at $r = -1$ the buckling stress is still 19% above the uniform compression case. As β increases the buckling coefficient k_{max}, $k_{max} = \sigma_{max}(tb^2)/(\pi^2 D)$, gradually converges to the uniform compression values.

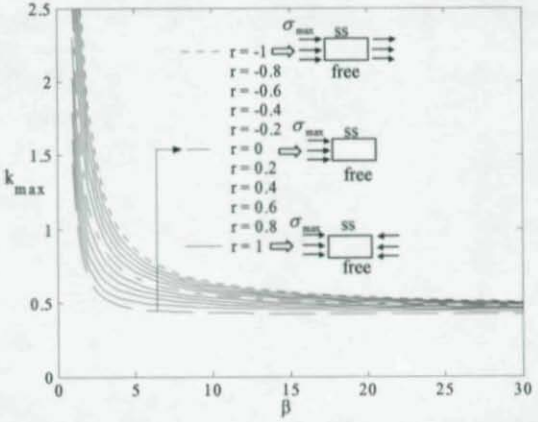

Figure 6 k_{max} vs. β for ss-free unstiffened plates

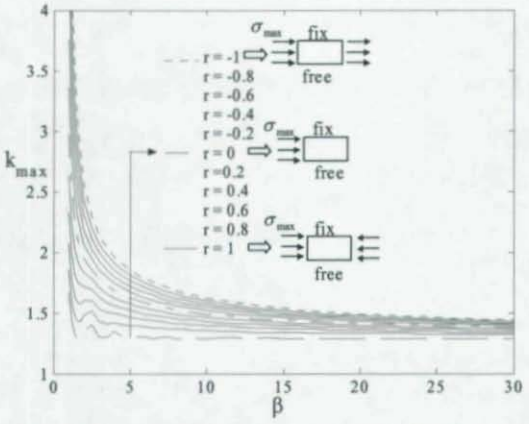

Figure 7 k_{max} vs. β for fix-free unstiffened plates

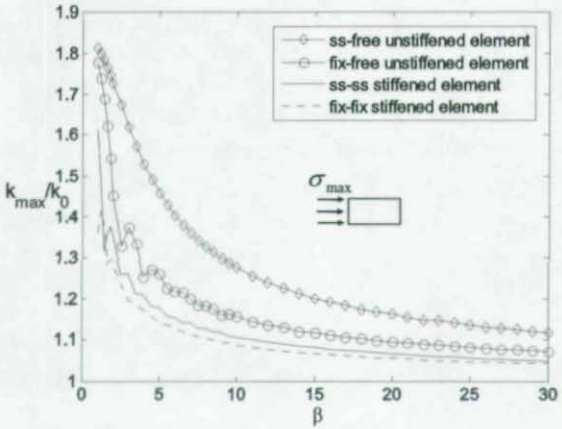

Figure 8 Comparison of thin plates under stress gradients $r = 0$

Discussion of Buckling Considering Longitudinal Stress Gradients

Under a longitudinal stress gradient, the buckling stress at the maximum loaded end is higher than that for the same plate under uniform compressive stress. Fig. 8 provides a comparison of the longitudinal stress gradient ($r = 0$) effect on elastic buckling for four typical thin plates. In the Figure the plate buckling coefficient k_{max} *is*

normalized by k_0 the solution for uniform compression ($r = 1$). For the same longitudinal stress gradient, unstiffened plates have a higher increase in the elastic buckling stress than stiffened plates. The ss-free unstiffened plate is most influenced by the longitudinal stress gradient, even for a plate with length/width (β) of 10, the buckling stress increases ~30%. The plate buckling coefficient for the stiffened plate converges rapidly to ~$1.1k_0$, and then more slowly to $1.0k_0$. For the ss-free unstiffened plate, $k_{max}>1.1k_0$ even for β as large as 30.

Local buckling of the compression flange of the hat section of Fig. 1(a) is somewhere between the ss-ss and fix-fix cases in Fig. 8. The moment gradient must be sharply varying to increase the buckling stress significantly. However, for the channel section of Fig. 1(b). As the compression flange buckles the web/flange juncture provides support somewhere between the fix-free and ss-free cases in Fig. 8. Here, the potential that moment gradient may have influence the buckling results is much greater.

Design Expression for Plate Buckling with a Longitudinal Stress Gradient

The analyses demonstrate that longitudinal stress gradients can have a significant impact on the elastic buckling stress of both stiffened and unstiffened plates. To facilitate the inclusion of this effect in design, a series of simplified expressions of the following form were produced:

$$k = k_\infty + \frac{\alpha_1 r + \alpha_2}{\alpha_3 r + \alpha_4 + \beta^{\alpha_5}} \tag{28}$$

Table 3 Coefficients for *k* under longitudinal stress gradients

	k_∞	α_1	α_2	α_3	α_4	α_5
ss-ss	4.000	-1.70	1.70	0.20	-0.20	0.75
fix-fix	6.970	-2.20	2.20	0.20	-0.20	0.65
ss-free	0.425	-0.80	1.00	0.00	-0.60	0.95
fix-free	1.277	-0.60	0.60	0.00	-0.65	0.60

Note: applicable for $1 \leq \beta \leq 30$ and $-1 \leq r \leq 1$, ss = simply supported

In Eq. 28, k_∞ is the traditional plate buckling coefficient (i.e., k for pure compression as the plate length tends to infinity), r is the stress gradient, β is the plate aspect ratio, and α_1 through α_5 are empirical coefficients dependent on the plate boundary conditions along the unloaded longitudinal edges. The α coefficients were arrived at by minimizing the sum squared error between the Rayleigh-Ritz solution and a solution of the form of Eq. 28 for $r = \{-1, -0.8, -0.6, -0.4, -0.2, 0, 0.2, 0.4, 0.6, 0.8, 1\}$ and $\beta = \{1, 4, 30\}$.

EFFECT OF LONGITUDINAL STERSS GRADIENT ON THE ULTIMATE STRENGTH OF THIN PLATES

Ultimate Strength of Thin Plates Subjected to Uniform Compression - Relationship to Winter's Equation

Current specifications adopt the effective width concept to determine the ultimate strength of cold-formed steel members. The North American Specification (NAS 2001) uses Winter's equation (Eq. 29) to calculate the effective width for both stiffened and unstiffened plates under uniform compression. Since NAS ignores the rotational restraint provided by the web for both stiffened elements (e.g. the flange of a hat section in Fig. 1a) and unstiffened elements (e.g. the top flange of a channel section in Fig. 1b), our studies on the ultimate strength will emphasize the ss-ss stiffened plates and ss-free unstiffened plates. Winter's reduction in the actual width of the plate is encompassed by:

$$\rho = (1 - 0.22/\lambda)/\lambda \leq 1 \tag{29}$$

where ρ = reduction factor for effective width; λ = plate slenderness factor, $\lambda = \sqrt{\frac{f_{\max}}{f_{cr}}} = \frac{1.052}{\sqrt{k}}\left(\frac{d}{t}\right)\sqrt{\frac{f_{\max}}{E}}$; d = plate width; t = thickness of the thin plates; E = modulus of elasticity; f_{cr} = elastic buckling stress; f_{max} = maximum compressive edge stress in the plate (often f_y), and f_y = yield stress.

Finite element models are created in ABAQUS to evaluate Winter's equation. Fig. 9 shows the FE models for both ss-ss stiffened plates and ss-free unstiffened plates. The modified Riks method was selected in

ABAQUS for the solution control. The S4R5 shell element was selected for both models, along with an element size set to 0.1 in. × 0.1 in. Geometric imperfection is considered in the FE models and the shape is assumed to be the first buckling mode of each type of plate under uniform compression, with a maximum amplitude, δ, equal to $0.34t$. This magnitude was selected based on the mean value of measured imperfections in stiffened plates from Schafer and Peköz (1998). The material stress-strain curves were selected from values observed in tensile tests taken from cold-formed steel C and Z specimens (Yu and Schafer 2003). Five different yield strength levels were used: 33.0 ksi, 44.0 ksi, 56.1 ksi, 62.2 ksi, and 73.4 ksi. Residual stresses were not included in the model.

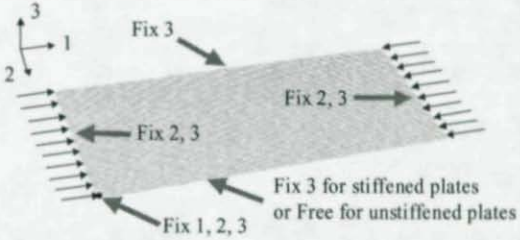

Figure 9 FE models for thin plates under uniform compression

Twenty-five stiffened and unstiffened plates under uniform compression are analyzed by the FE models. The obtained ultimate strength is compared with Winter's prediction and summarized in Table 4. Qualitatively, the strength prediction using Winter's equation has good agreement with the FE results for both types of plates. However, imperfection magnitudes, details of the material model, loading, and boundary conditions all have an impact on the FE predicted strength. Boundary conditions are particularly important, the FE models as shown in Fig. 9 leaves the longitudinal simply supported sides free to deform in plane. This is a conservative approximation of a simply supported boundary condition. Since Winter's equation was originally derived from tests on hat sections, the web in those tests provided a small amount of beneficial restraint to the flange (stiffened plate). Further, only one geometric imperfection magnitude was investigated for each plate. We conclude that the FE model is a conservative predictor of the strength for both stiffened and unstiffened plates

subjected to uniform compression, and Winter's equation captures the basic behavior.

Table 4 FE vs. Winter's results for uniform compression

	For stiffened plates $\rho_{FE,1}/\rho_{Winter,1}$	For unstiffened plates $\rho_{FE,1}/\rho_{Winter,1}$
Mean	93.7%	105.7%
Standard deviation	1.3%	7.0%

Ultimate Strength of Stiffened Plates Subjected to Longitudinal Stress Gradients

An FE model similar to that used for the uniform compression cases is employed to study the same plates subjected to a longitudinal stress gradient. In the FE model, as shown in Fig. 10, the longitudinal stress gradient is achieved by applying compression forces at only one end ($r = 0$), and applying shear forces along the two longitudinal edges, such that the shear forces equilibrate the compression load.

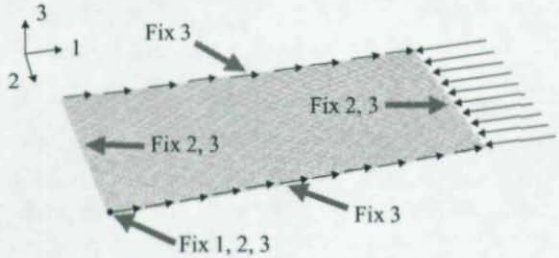

Figure 10 FE model for ss-ss plates under a stress gradient $r = 0$

A total of 25 ss-ss stiffened plates under a stress gradient ($r = 0$) were analyzed by the FE model. The results are summarized in Table 5. Fig. 11 shows a comparison of FE results vs. Winter's predictions, where the x-axis is the plate slenderness λ, and the y-axis is the reduction factor for effective width, ρ. The "o" in the plot represents the FE results with uniform compression, $k = 4.0$ is used for Winter's equation, and the results show Winter's equation provides a reasonable prediction. The "×" represents the results of the same plates under a longitudinal stress gradient. Still, $k = 4.0$ is used in Winter's equation and the results show that the strength of stiffened plates is increased by

the stress gradient. However, the increase is not large; on average only 4.6% (see "$\rho_{FE,0}/\rho_{FE,1}$" column in Table 5). Finally, the "▲" in the plot represents the same stress gradient cases, but using a plate buckling coefficients that accounts for the stress gradient, k of Eq. 28. Average results are summarized in Table 5 and indicate that only a small increase is observed due to the stress gradient. Winter's equation with the modified plate buckling coefficient (k of Eq. 28) works well for the stress gradient case, but in general, the effect of longitudinal stress gradients can be ignored for stiffened plates in design.

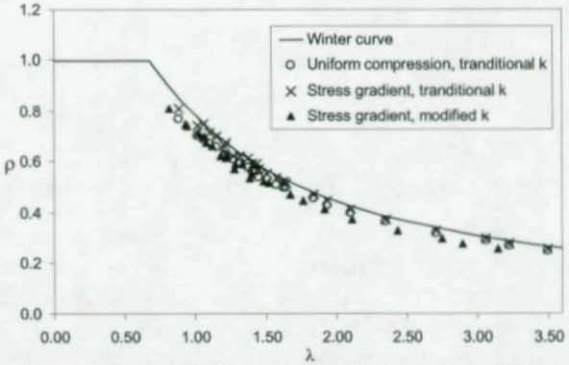

Figure 11 FE results vs. Winter's predictions for stiffened plates

Table 5 Results for stiffened plates under a stress gradient $r = 0$

	$\rho_{FE,0}/\rho_{FE,1}$	$\rho_{Winter,0}/\rho_{Winter,1}$	$\rho_{FE,0}/\rho_{Winter,0}$
Mean	104.6%	108.1%	90.5%
Standard deviation	1.7%	2.0%	2.0%

Note: $\rho_{FE,0}$: effective width ratio for $r = 0$ obtained by FE model; $\rho_{FE,1}$: effective width ratio for uniform compression ($r = 1$) obtained by FE model; $\rho_{Winter,0}$: effective width ratio for $r = 0$ predicted by Winter's equation using k of Eq. 28; $\rho_{Winter,1}$: effective width ratio for uniform compression case ($r = 1$) predicted by Winter's equation using traditional k of 4.0.

Ultimate Strength of Unstiffened Plates Subjected to Longitudinal Stress Gradients

The FE model for the unstiffened plates under longitudinal stress gradients is similar to that used for stiffened plates, shown in Fig. 10, except that the restraints and shear forces on one longitudinal edge are

removed. The unstiffened plates are subjected to a longitudinal stress gradient $r = 0$.

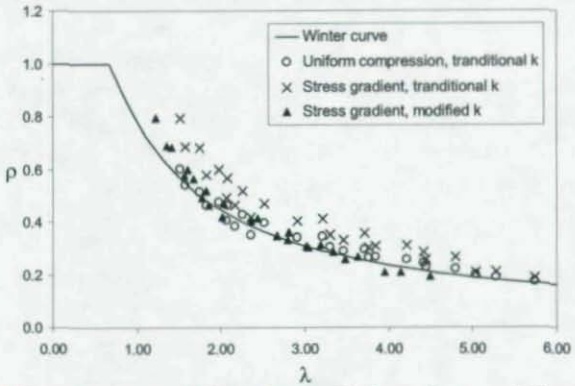

Figure 12 FE results vs. Winter's predictions for unstiffened plates

A total of 25 unstiffened plates under a longitudinal stress gradient $r = 0$ were analyzed by the FE model, the results are summarized in Table 6, while Fig. 12 provides a detailed comparison. Winter's equation has good overall agreement with the FE results for plates under uniform compression (points "o" in Fig. 12). When the longitudinal stress gradient is applied, the strength of the unstiffened plates is increased significantly (an average increase of 19.3%). Winter's equation gives highly conservative predictions for those stress gradient cases if the plate buckling coefficient is not updated accordingly. If k is modified to account for the stress gradient via Eq. 28 (Points "▲" in Fig. 12) Winter's equation provides a reliable strength prediction.

Table 6 Results for unstiffened plates under a stress gradient $r = 0$

	$\rho_{FE,0}/\rho_{FE,1}$	$\rho_{Winter,0}/\rho_{Winter,1}$	$\rho_{FE,0}/\rho_{Winter,0}$
Mean	119.3%	134.1%	103.2%
Standard deviation	6.3%	15.4%	7.7%

Note: for the subscript notations to ρ please refer to the notes for Table 5.

CONCLUSIONS

Moment gradients on thin-walled beams create longitudinal stress gradients on the component plates that make-up a cross-section. While the effect of moment gradients on lateral-torsional buckling is explicitly considered in design, the effect of longitudinal stress gradients on local buckling of the component elements is not considered in design.

Using the Rayleigh-Ritz method the influence of longitudinal stress gradients on elastic buckling of thin plates is explored. Both stiffened plates, with support on both of the longitudinal (unloaded) edges, and unstiffened plates, with support on only one of the longitudinal edges, are considered. Trial deflection functions and an assumed internal stress distribution are required to perform the solution. Verification studies using ABAQUS validate the selected approximate functions.

Elastic buckling analysis of stiffened and unstiffened plates under longitudinal stress gradients indicates that the local buckling stress is increased by the presence of the stress gradient. The increase is a function of the stress gradient itself (r), and the length or aspect ratio (β) of the plate. For long plates the influence of the longitudinal stress gradient on the local buckling stress is lessened, but for practical dimensions an effect always exists. The elastic buckling results indicate that unstiffened plates are more sensitive to longitudinal stress gradient than stiffened plates. An empirical closed-form expression for the plate buckling coefficient, account for stress gradient, is provided in Eq. 28.

Nonlinear finite element analysis is performed in ABAQUS to explore the ultimate strength of stiffened and unstiffened plates. Design predictions using Winter's equation are compared to the FE predicted ultimate strengths. The results shown that Winter's equation can reasonably predict the ultimate strength of stiffened and unstiffened plates under a longitudinal stress gradient, if the plate buckling coefficient is modified to account for the stress gradient (i.e., Eq. 28). Results of the strength increase due to longitudinal stress gradient are more pronounced and more accurate for unstiffened plates than stiffened plates. It is recommended that the effect of longitudinal stress gradient (Eq. 28) be considered in the design of unstiffened plates.

REFERENCE

ABAQUS (2001). "ABAQUS Version 6.2", ABAQUS, Inc, Pawtucket, RI.

Lundquist, E., Stowell, E. (1942a). "Critical Compressive Stress for Flat Rectangular Plates Supported along All Edges and Elastically Restrained against Rotation along the Unloaded Edges", *NACA Report No. 733*, National Advisory Committee for Aeronautics, Washington.

Lundquist E., Stowell E. (1942b). "Critical Compressive Stress for Outstanding Flanges". *NACA Report No. 734*, National Advisory Committee for Aeronautics, Washington.

Libove, C., Ferdman, S., Reusch, J. (1949). "Elastic Buckling of A Simply Supported Plate Under A Compressive Stress That Varies Linearly in the Direction of Loading", *NACA Technical Note No. 1891*, National Advisory Committee for Aeronautics, Washington.

NAS (2001). "North American Specification for the Design of Cold-Formed Steel Structural Members", American Iron and Steel Institute, Washington, DC.

Schafer, B.W., Peköz, T. (1998). "Computational Modeling of Cold-Formed Steel: Characterizing Geometric Imperfections and Residual Stresses", Elsevier, *Journal of Constructional Steel Research.* 47 (3) 193-210.

Timoshenko, S.P., Gere, J.M. (1961). "Theory of Elastic Stability", Second Edition. *McGraw-Hill Book Co.*, Columbus, OH.

Yu, C., Schafer, B.W. (2003). "Local buckling Tests on Cold-Formed Steel Beams", *Journal of Structural Engineering,* ASCE 129 (12) 1596-1606.

Yu, C. (2005). "Distortional Buckling of Cold-Formed Steel Members in Bending", *PhD Thesis*, Johns Hopkins University, Baltimore, MD.

BENCHMARK STUDIES TO COMPARE FRAME STABILITY PROVISIONS

Jose M. Martinez-Garcia[1] *and*
Ronald D. Ziemian[2]

ABSTRACT

The 2005 AISC *Specification for Structural Steel Buildings* provides engineers several opportunities to assess general requirements for the stability analysis and design of members and frames. Using eleven two- and three-dimensional structural systems, a comprehensive study was conducted that compares these opportunities. This paper will provide an overview of this research along with specific details for three of the frames investigated. As a basis for comparison, all results are calibrated against those obtained using advanced second-order inelastic analysis. General conclusions from this study are also provided.

INTRODUCTION

Structural engineers will be pleased to learn that the provisions for frame stability have been expanded in the

---

[1] Former Graduate Student at Bucknell University and currently Consulting Structural Engineer, APIA XXI S.A. Department of Structures, Santander, SPAIN
[2] Professor, Department of Civil and Environmental Engineering, Bucknell University, Lewisburg, PA 17837

upcoming 2005 American Institute of Steel Construction *Specification for Structural Steel Buildings* (AISC, 2005). Engineers should consider the following four factors in deciding which provisions to apply to their specific design:

- Main lateral resisting system employed. Braced frame, moment frame, shear wall, combined system, etc.
- Level of analysis being used as a basis for calculating second-order effects. First-order or second-order.
- Significance of second-order effects. Using an amplification factor (A.F.) such as a B_2 factor to define the ratio of second-order to first-order effects, this significance can be defined as low (A.F.<1.1), moderate (A.F.<1.5), or large (A.F.>1.5).
- Whether or not effective length (K) factors will be used to calculate the axial strength of compression members.

If the long-standing *Effective Length Method* is being employed, the Specification recognizes various methods for calculating effective lengths, which include the alignment charts, eigenvalue analysis, and story based methods. On the other hand, and new to this Specification, the engineer can now employ the *Direct Analysis Method* in which effective length factors do not need to be calculated. Instead, the unbraced length of the compression member (i.e. K=1) may be used to determine axial strength, P_n. To complete this method, two additional factors will need to be addressed

- How will the influence of material yielding or partial inelasticity be represented? Through the use of a defined stiffness reduction (τ-factor) or by the inclusion of notional loads.
- How will the influence of initial sway imperfections be represented? Through the use of equivalent notional loads or by actually distorting the geometry of the analysis model.

A summary of these two methods are provided in Table 1. Both methods require the consideration of second-order effects on the stability of the structure and its components. They both also require the use of the same interaction equation (Eq. H1-1) to confirm the strength of the member.

$$\frac{P_r}{\phi_c P_n} + \frac{8}{9} \cdot \frac{M_r}{\phi_b M_n} \leq 1.0 \quad \text{for} \quad \frac{P_u}{\phi_c P_n} \geq 0.2$$

$$\frac{P_r}{2\phi_c P_n} + \frac{M_r}{\phi_b M_n} \leq 1.0 \quad \text{for} \quad \frac{P_u}{\phi_c P_n} < 0.2$$

The difference in the two methods resides on how member inelasticity and geometric imperfections are represented. In the Effective Length Method, both of these effects are included through the column strength curve using an effective length (KL) to calculate the axial strength, P_n. In contrast, the Direct Analysis Method models both of these effects within the analysis and hence, the axial strength, Pn, can be determined by simply using the unbraced length of the member.

Table 1. Comparison of methods.

	AISC 2005 Spec.		
Effect	**Effective Length Method**	**Direct Analysis Method**	**Advanced Analysis Approach**
Member Inelasticity	Column Strength Curve	Reduce Stiffness or notional load	Inelastic Analysis
Initial Out-of-Plumbness (Erection Tolerance)	Column Strength Curve	Direct Modeling or notional load	Direct Modeling
Initial Out-of-Straightness (Fab. Tolerance)	Column Strength Curve	Column Strength Curve	Direct Modeling
Strength Check	Analysis / Interaction Eq. H1-1		Analysis
Axial Strength Term	P_n based on KL	P_n based on L (K=1.0)	N/A

Over the past several years, members of AISC's Task Committee 10-Stabilty have investigated several structural systems in developing and refining new stability provisions (AISC-SSRC, 2003) In addition, two extensive studies have been completed at the Georgia Institute of Technology (Maleck and White, 2003) and Bucknell University (Martinez-Garcia, 2003). Using benchmark studies performed in the latter study, the objective of this paper is to compare the frame stability provisions that will appear in the 2005 AISC *Specification for Structural Steel Buildings*.

MARTINEZ-GARCIA AND ZIEMIAN STUDY

In this study, eleven structural systems are investigated, ten that are modeled as two-dimensional and one as three-dimensional. All of the systems are analyzed using a rigorous second-order elastic analysis. Two Load and Resistance Factor Design (LRFD) approaches are compared, one based on the Effective Length Method and the other on the Direct Analysis Method.

For each system, twelve different design procedures are employed in investigating the Effective Length Method. These procedures are a result of using four different approaches for calculating effective lengths combined with three different ways of studying the impact of initial sway imperfections. Approaches employed for calculating effective lengths include the use of alignment charts, results from eigenvalue analyses, and two story-based methods, including

Story-Based Method 1:

$$P_e = (0.85 + 0.15R_L) \cdot \frac{P_u}{\sum_{all} P_u} \cdot \left[\frac{\sum HL}{\frac{\sum HL}{non-leaner}} \right] \leq \frac{\pi^2 EI}{L^2}, \text{ where}$$

$$R_L = \frac{\sum_{leaner} P_u}{\sum_{all} P_u}$$

Story-Based Method 2:

$$P_e = P_u \left[\frac{\Delta_{2nd} / \Delta_{1st}}{\Delta_{2nd} / \Delta_{1st} - 1} \right] \leq \frac{\pi^2 EI}{L^2}$$

Initial sway imperfections are modeled either directly in the analysis by distorting the initial frame geometry, represented by equivalent notional loads, or simply neglected.

Four approaches are used in checking the designs by the Direct Analysis Method. These approaches come from all combinations of modeling initial imperfections (either by direct modeling or notional loads) and material yielding (through the use of stiffness reductions or equivalent notional loads).

For each of the eleven frames studied, all sixteen of the above design procedures are calibrated against results from advanced second-order inelastic analyses.

ANALYSIS DETAILS

Two levels of analysis are employed throughout this study, including second-order elastic and advanced second-order inelastic.

In accordance with the Specification, all of the above design approaches are based on second-order elastic analyses. The MASTAN2 software (Ziemian and McGuire, 2002) is employed with second-order effects being accounted for by the use of an updated Lagrangian formulation and geometric stiffness matrices (McGuire et al., 2000). In the Effective Length Method, the full elastic stiffness of the section (1.0EA and 1.0EI) is used. In the Direct Analysis Method, the stiffness of the system is reduced according to provisions set forth in the Specification. When using prescribed notional loads to represent material inelasticity, the stiffness of the sections is reduced to 0.8EA and 0.8EI. As an alternative to notional loads, member inelasticity is modeled directly in the analysis by using a modified stiffness of $0.8\tau EA$ and $0.8\tau EI$, where $\tau=4(P/P_y)(1-P/P_y)$ when $P/P_y>0.5$. If initial sway imperfections are included they are either directly modeled by distorting the frame geometry according to H/500 where H is the height of the system or by equivalent notional loads prescribed by the Specification

As indicated above, advanced second-order inelastic analyses are used throughout the study to asses the adequacy of all design methods. These analyses are performed using two programs NIFA(2D) and NISFA(3D) that were both developed at the University of Sydney (Clarke, 1991, and Teh, 2002). Inelasticity is modeled through the use of a distributed plasticity model with thermal residual stresses directly incorporated. To capture effects of resistance factors, the material stiffness and strength are reduced by a factor of 0.9. Initial

imperfections are included by distorting the model geometry according to the previously mentioned H/500. Imperfections are always included in the direction that compounds the lateral effects of the applied loads.

EXAMPLES

The results of the following three examples are representative of the eleven structural systems investigated in the Martinez-Garcia and Ziemian study. In all cases, the nominal loads shown have been scaled such that an advanced second-order inelastic analysis will indicate a limit of resistance just at application of the controlling factored load combination. All lateral loads and gravity loads are applied proportionally. It should also be noted that all of the example frames can be shown to satisfy standard serviceability requirements.

IRREGULAR TWO-BAY FRAME

The dimensions and member sizes for this frame are shown in Fig. 1. The geometry is taken from a set of frames originally studied at the Virginia Polytechnic and State University by Professor T. Murray and one of his graduate students (Schimizze, 2001). The frame is moderately sensitive to second-order effects with an amplification factor A.F. = $\Delta_{2nd}/\Delta_{1st}$ = 1.3. All members are oriented with their webs in the plane of the frame and assumed to be fully restrained against out-of-plane failure behavior.

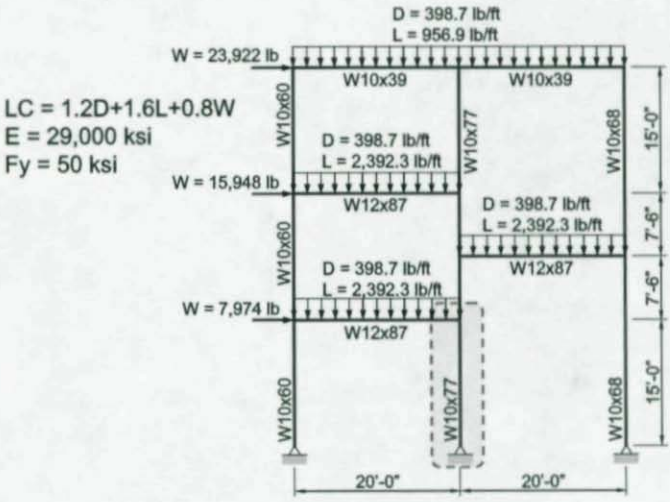

Figure 1. Irregular two-bay frame.

The advanced inelastic analysis results are shown in Fig. 2. At approximately 75% (APL=0.75) of the factored load, the upper portion of the lower story columns begin to yield. As a result of excessive yielding in this location, a significant redistribution of load occurs that eventually results in considerable yielding at the top of the left and center first-story columns. Additional lateral load is then resisted by only the right lower-story column and soon thereafter partial yielding of this column leads to a loss in the lateral stability of the frame.

It is clear from this analysis that a critical member, and in fact, the controlling member in checking the design of this frame is the first-story center column. Table 2 provides

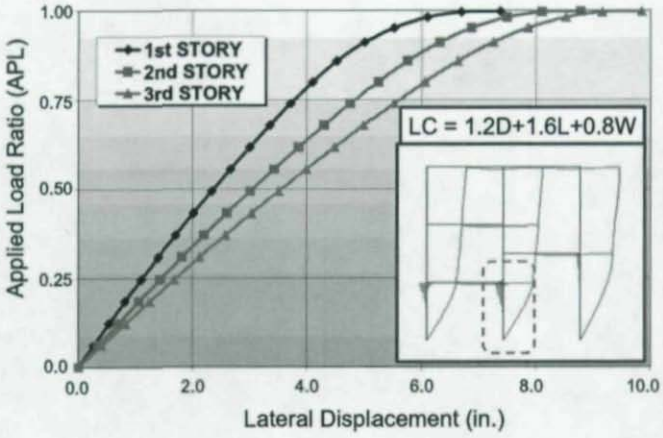

Figure 2. Results of advanced analysis.

Table 2. Design assessment of lower-story center column.

	AISC 2nd-Order Elastic Analysis/Design Methods	K	Eq. H1-1 APL = 1.0	APL @ Eq. H1-1 =1.00
Effective Length (Chapter C)	Alignment Chart	2.20	1.18	0.86
	Eigenvalue	1.84	1.13	0.90
	Story-Based 1	2.12	1.16	0.87
	Story-Based 2	1.97	1.14	0.89
Direct Analysis (Appendix 7)	NL:0.002Y_i & 0.8τEI	1.00	1.10	0.92
	Geom. Δ_o's & 0.8τEI	1.00	1.11	0.91
	NL:0.002Y_i & NL:0.001Y_i	1.00	1.10	0.92
	Geom. Δ_o's & NL:0.001Y_i	1.00	1.11	0.91

results obtained using a second-order elastic analysis to calculate the internal force distribution. Four design approaches are presented for each of the Effective Length and Direct Analysis Methods. Using these methods, the AISC interaction equation H1-1 is applied in two ways.

First, Eq. H1-1 is calculated for this column using internal forces or demands at application of the factored load combination (APL=1.0). Since all values exceed 1.0, all variations of both methods indicate that the column is inadequate. Since there is a disparity in the K-factors as a result of using different approaches to calculate effective lengths, the interaction equation values vary from 1.13 to 1.18. On the other hand, all four possibilities of the Direct Analysis Method provide consistent results which are acceptable and less conservative. This indicates that direct modeling of initial frame sway (Geom Δ_o's) and inelasticty ($0.8\tau EI$) is undistinguishable to applying equivalent notional loads (NL).

The study also investigated how much of the factored load could be applied before interaction Eq. H1-1 is exceeded. Since the frame response and corresponding analysis is nonlinear, these values cannot simply be taken as the reciprocal of the above results. As shown in the far right portion of Table 2, a second-order elastic analysis indicates that the lower-story center column becomes inadequate somewhere between 0.86 and 0.91 of the factored load depending on the design method employed. Since values less than 1.0 indicate conservative results, it is clear that

slightly more variation and conservatism exists for the Effective Length Method.

BRACED FRAME WITH LEANER EXAMPLES

Two variations of the structural system shown in Fig. 3 are presented. In the first scenario the columns are oriented with their webs in the plane of the frame and in the second, the columns are assumed rotated 90° so that they experience minor-axis bending. Member sizes and loads in square brackets ([]'s) represent attributes of the minor-axis bending design. The frame geometry was originally suggested by Professor Joseph Yura at the University of Texas, Austin.

For the major-axis design, the factored lateral load combination LC2 controls. In this case, second-order effects are low-to-moderate with an amplification factor of A.F.=1.2. An advanced second-order inelastic analysis indicates that the limit of resistance of the structure is governed by the lower portion of the center column. Using an approach similar to the previous example, Table 3 compares the four variations of the Effective Length and Direct Analysis Methods. Again, small differences in the calculated effective length factors produce a slightly varied yet conservative range of interaction equation values for this column. On the other hand, the Direct Analysis Method is shown to be in remarkable agreement with the advanced analysis results. The consistency of the four possibilities of the Direct Analysis Method is also noteworthy.

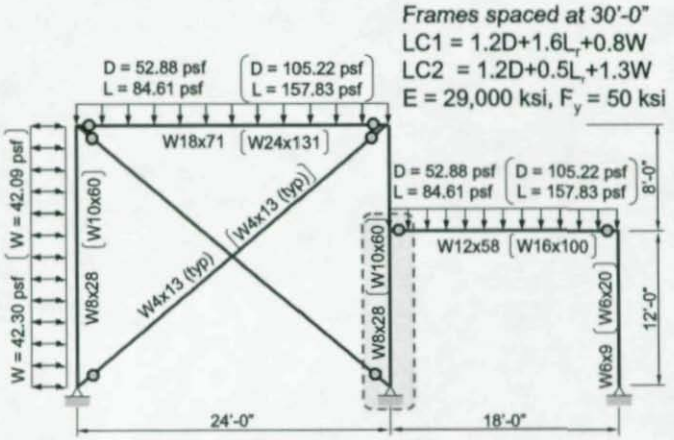

Figure 3. Braced frame with leaner.

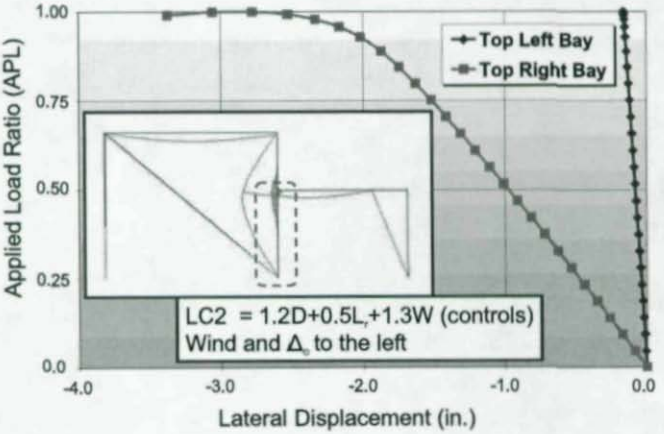

Figure 4. Results of advanced analysis (major-axis).

Table 3. Design assessment of center column (major-axis).

	AISC 2nd-Order Elastic Analysis/Design Methods	K	Eq. H1-1 APL = 1.0	APL @ Eq. H1-1 =1.00
Effective Length (Chapter C)	Alignment Chart	1.86	1.05	0.96
	Eigenvalue	1.60	1.02	0.99
	Story-Based 1	1.30	0.99	1.01
	Story-Based 2	1.56	1.01	0.99
Direct Analysis (Appendix 7)	NL:0.002Y_i & 0.8τEI	1.00	1.00	1.00
	Geom. Δ_o's & 0.8τEI	1.00	1.00	1.00
	NL:0.002Y_i & NL:0.001Y_i	1.00	1.00	1.00
	Geom. Δ_o's & NL:0.001Y_i	1.00	1.00	1.00

When all columns are rotated 90° so that they experience minor-axis bending, factored load combination LC1 controls. In this case, the second-order amplification factor is large at A.F.=1.8. Similar to the major-axis bending case, the effect of a leftward wind load combined with a natural leftward frame lean due to gravity loads results in excessive yielding in the center column.

Table 4 provides a summary of the interaction equation evaluation for this center column. There is significant variation in the effective length factors calculated by the different procedures. In fact, the authors doubt that Story-Based Method 1 should even be applied. Never the less, the Effective Length Method is shown to be accurate and slightly conservative as long as the correct effective length factor is determined. On the other hand, the Direct Analysis Method consistently appears to be slightly

Table 4. Design assessment of center column (minor-axis).

	AISC 2nd-Order Elastic Analysis/Design Methods	K	Eq. H1-1 APL = 1.0	APL @ Eq. H1-1 =1.00
Effective Length (Chapter C)	Alignment Chart	1.88	1.17	0.88
	Eigenvalue	1.60	1.05	0.98
	Story-Based 1 *	4.0*	1.26*	0.83*
	Story-Based 2	1.55	1.01	0.99
Direct Analysis (Appendix 7)	NL:0.002Y_i & 0.8τEI	1.00	0.96	1.03
	Geom. Δ_o's & 0.8τEI	1.00	0.97	1.02
	NL:0.002Y_i & NL:0.001Y_i	1.00	0.96	1.03
	Geom. Δ_o's & NL:0.001Y_i	1.00	0.97	1.02

* Upper portion of first-story center column controls

unconservative, indicating that this method suggests that the center column has a small amount of additional strength that is not predicted by a more advanced inelastic analysis.

Summary and Conclusions

This paper has presented a brief overview of two design approaches, the Effective Length Method and the Direct Analysis Method. Both approaches are appear in the 2005 AISC *Specification for Structural Steel Buildings* and viable alternatives that account for lateral stability. Three examples taken from a comprehensive comparative study of these methods is provided.

The following conclusions are made:

- In most cases the Effective Length and Direct Analysis Methods provide similar results. In other words, radically different designs are not expected when using one method instead of the other.
- The Effective Length Method tends to be slightly more conservative.
- As a consequence of employing different procedures for calculating effective length factors, a notable variation in the results obtained by the Effective Length Method can be observed. This variation tends to increase in situations when the axial force effect plays a more dominate role in the interaction equation.
- The Direct Analysis Method provides consistent results regardless of the Specification prescribed approaches for modeling inelasticity and geometric imperfections.
- The Direct Analysis Method may be slightly unconservative for beam-columns subjected to minor-axis bending.

Finally, and perhaps most importantly to the authors, the general approach and philosophy of the Direct Analysis Method provides an excellent transition for future design methods based on advanced analysis.

REFERENCES

AISC (2005), *Specification for Structural Steel Buildings*, March 9, 2005, American Institute of Steel Construction, Inc., Chicago, IL.

AISC-SSRC (2003), "Background and Illustrative Examples on Proposed Direct Analysis Method for Stability Design of Moment Frames," Technical White Paper, AISC Technical Committee 10, AISC-SSRC Ad Hoc Committee on Frame Stability, American Institute of Steel Construction, Inc., Chicago, IL.

Clarke, M.J. (1991), *NIFA*, analysis software developed at the School of Civil and Mining Engineering, University of Sydney, Australia.

Maleck, A.E., and White, D.W. (2003), "Direct Analysis Approach for the Assessment of Frame Stability: Verification Studies," Proceedings of the Annual Technical Session and Meeting, Baltimore, MD, April 2-5, 2003, Structural Stability Research Council, Bethlehem, PA, pp. 423-442.

Martinez-Garcia, J.M. (2002), "Benchmark Studies to Evaluate New Provisions for Frame Stability using Second-Order Analysis," MS Thesis, Department of Civil and Environmental Engineering, Bucknell University, Lewisburg, PA, December.

McGuire, W., Gallagher, R.H., and Ziemian, R.D. (2000), *Matrix Structural Analysis*, 2nd edition, John Wiley and Sons, Inc., New York, NY.

Schimizze, A. (2001), "Comparison of P-Delta Analyses of Plane Frames Using Commercial Structural Analysis Programs and the AISC Specifications", MS Thesis, Department of Civil and Environmental Engineering, Virginia Tech, Blacksburg, VA, May.

Ziemian, R.D. and McGuire, W. (2002), *MASTAN2*, Version 2.0, John Wiley and Sons, Inc., New York, NY.

Teh, L. (2002), *NISFA*, analysis software developed at the School of Civil and Mining Engineering, University of Sydney, Australia.

THE EFFECT OF VERTICAL GROUND ACCELERATIONS ON THE DYNAMIC STABILITY OF SIMPLE STRUCTURES

Paul W. Spears[1]

Finley A. Charney[2]

INTRODUCTION AND BACKGROUND

Based on current research, it appears that there is some disagreement as to whether vertical accelerations have a significant impact on the lateral response of a structure in a seismic event. Some research indicates that vertical accelerations are significant and other research indicates the opposite. Furthermore, most research on vertical accelerations has focused on specific buildings, thus it is not clear which types of structures would be influenced by vertical accelerations. The authors sought to determine the types of structures that might be sensitive to vertical accelerations using Single Degree of Freedom (SDOF) models with bilinear force-deformation relationships. The SDOF model parameters varied were stiffness (period of vibration), post yield stiffness ratio, yield strength, and geometric stiffness (P-Delta effects). Additional parameters allowed to vary in the study related to the ground motions were earthquake ground motion, lateral ground acceleration intensity, and vertical ground acceleration intensity. Considering both structural parameters and earthquake parameters, seven independent parameters were varied.

Of the existing literature on vertical ground accelerations, many studies have shown that vertical acceleration magnitudes can be as great or

[1] Martin/Martin Consulting Engineers, Kansas City, MO
[2] Virginia Tech, Blacksburg, VA

greater than the horizontal accelerations. Abrahamson and Litchiser (1989) showed that the ratio of vertical acceleration to horizontal acceleration (V/H) was dependent on the magnitude of the event and the distance from the site to the source. Bozorgnia et al. (1995) also noted that the V/H ratio was dependent on the site distance and earthquake magnitude. They also pointed out that the V/H acceleration response spectra ratio is dependent on the period of the structure in question. For short period structures, the ratio can be much greater than one, but for long period structures, the ratio is typically much less than one. Not only does site distance and period affect vertical accelerations, but soil conditions also affect them. Amirbekian and Bolt (1998) showed that the vertical acceleration component tends to be higher than the horizontal in alluvial basins.

There have also been many studies investigating the effects of vertical accelerations on structures. Some have concluded that vertical accelerations do not significantly affect structural response. Maison and Kasai (1997), for example, analytically tested a thirteen story steel moment frame which was damaged in the Northridge earthquake and showed that the lateral displacement of the simulated structure was very similar with and without vertical accelerations included. Furthermore, the major emphasis of their research was to examine connection failures that occurred in the building during the earthquake. They noted that increased gravity loads actually reduced damage to the connections. They reasoned that this was because the gravity loads caused a compressive preloading of the bottom flanges of the beams. They further reasoned that the lack of gravity loads in buildings under construction during the Northridge earthquake might explain why more of those buildings experienced connection damage. So, it would seem that real structures with gravity loads are less likely to be adversely affected by vertical accelerations.

Hjelmstad and Williamson (1998) examined the dynamic stability of hysteretic single-degree-of-freedom inverted pendulum systems subjected to harmonic base excitation, not actual ground motion records, and noted that vertical accelerations increased lateral displacements in some situations if the vertical forcing frequency was

twice the lateral frequency of the structure. However, they found that the vertical accelerations did not significantly increase lateral deflections of the structures they studied. Jennings and Husid (1968) and Takizawa and Jennings (1980), using a small and focused range of models and parameters, argued that vertical accelerations have a negligible effect on the lateral response of structures.

While there are many studies indicating that vertical accelerations do not significantly affect structural response, there are also many that show that vertical accelerations do affect structural response. Anderson and Bertero (1973), for example, analyzed a ten story steel moment frame subjected to horizontal and vertical ground motions from the San Fernando earthquake of 1971. From the study, they concluded that the ductility requirements at critical regions would be inaccurate if vertical accelerations were not included. In the upper stories, for example, the ductility requirements were increased by fifty percent by including vertical accelerations.

Saadeghvaziri (1988) and Saadeghvaziri and Foutch (1991) examined the effects of vertical and horizontal accelerations on bridges. They noted that vertical accelerations cause severe fluctuations in the axial loads in bridge piers and that these fluctuations result in highly erratic hysteresis loops. Moreover, the vertical accelerations tend to increase the shear demand and reduce the shear capacity in bridge piers. The increased axial loads stiffened the columns, which in turn caused the columns to attract more force. At the same time, the increased axial load reduced the shear capacity of the piers. Also, the increased axial loads reduced the ductility of the columns. Saadeghvaziri and Foutch speculated that the severe damage to bridges in some earthquakes may be primarily caused by vertical accelerations.

Hart et al. (1995) examined a six story special steel moment resisting frame subjected to both vertical and horizontal accelerations as part of the SAC Steel Project. Hart's research focused on the effects of tributary mass, both in the vertical and horizontal directions. The mass distribution caused a great deal of scatter in the axial forces in the columns. Hart noted that the effect of vertical accelerations was most

pronounced in the interior columns, which are primarily designed to withstand axial loads. In some situations, Hart found that seismic axial forces could be twice the dead load. Higazy et al. (1996) examined reinforced concrete (RC) beam-column connections under vertical accelerations. They found that should vertical accelerations cause a RC connection to go into tension, the shear capacity of the joint was reduced by eighteen to fifty percent. Also, the confinement in the joint core was rendered ineffective in the event of significant tension. Como et al. (2003) examined the likelihood that vertical accelerations would cause axial shortening in some columns and therefore increased rotations at beam ends.

A second category of vertical acceleration research has focused on how vertical accelerations contribute to lateral displacements. Iyengar and Shinozuka (1972) examined the effects of vertical accelerations on tall buildings. They modeled tall buildings as distributed mass cantilevers. They concluded that vertical accelerations considerably increased the tip deflection, base shear, and base moment for the cantilever models studied.

Lin and Shin (1980) examined the effects of vertical accelerations on single degree of freedom inverted pendulum elastic structures. They noted that the vertical accelerations had the potential to amplify lateral response. Then, Shin and Lin (1982) performed a similar study involving single-degree-of-freedom-inverted pendulums except the systems were hysteretic rather than elastic. They examined systems with both 0.1 and 0.5 post-yield stiffness ratios, and found that for hysteretic models, the vertical accelerations had more of an effect on the lateral displacement than in the elastic models. Moreover, the lower post-yield stiffness ratio model was more influenced by vertical accelerations than was the model with the higher post yield stiffness ratio. Shin and Lin also noted that the vertical accelerations had a significant impact on the amount of residual deformations in their models.

Ariaratnam and Leung (1990) analyzed a six story multiple degree of freedom building using random vibrations in both the vertical and

horizontal directions. They concluded that both gravity loads and vertical inertial loads can increase the lateral displacement when structures are subjected to earthquakes.

SDOF PARAMETER STUDY DESCRIPTION

Of all of the studies conducted, it did not appear that any of them were specifically focused on determining types of structures and situations where vertical accelerations would be particularly damaging or contribute significantly to lateral deflection. Consequently, the research program described in this paper was undertaken. The models used in this study were essentially simple single-degree-of-freedom inverted pendulum structures. They were constructed as portal frames, but acted similar to inverted pendulums. Figure 1 illustrates the form and function of the models used in this study and their relation to inverted pendulums.

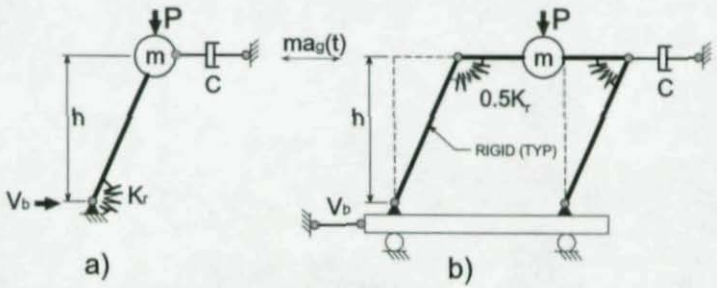

Figure 1 – a) Inverted Pendulm and b) Similar Portal Frame Structure

Seven parameters were identified and varied in an attempt to determine types of structures that might be sensitive to vertical accelerations. The first four parameters were related to the structural model and are shown in Fig. 2. The other three are related to ground motions and are described later.

The bilinear curves shown in Fig. 2 represent the force deformation relationship of the rotational springs used in this study. The horizontal axis plots rotation, and the vertical axis plots moment. The parameters

in numerical order from the above figure are rotational stiffness, yield moment, post-yield stiffness ratio, and P-Delta effects. A unit mass was used for each of the models and hence, the initial stiffness was the only variable used to determine periods of vibration. Then, the yield moment corresponded to the base shear required for design. Also, the initial stiffness was modified by the post yield ratio (r), to determine the secondary stiffness of the systems. Finally, the actual force deformation relationship followed the lower bilinear curve when P-Delta effects were considered. P-Delta effects were gauged in terms of stability ratio (Q) . The lower curve was determined by subtracting K_rQ from the upper curve.

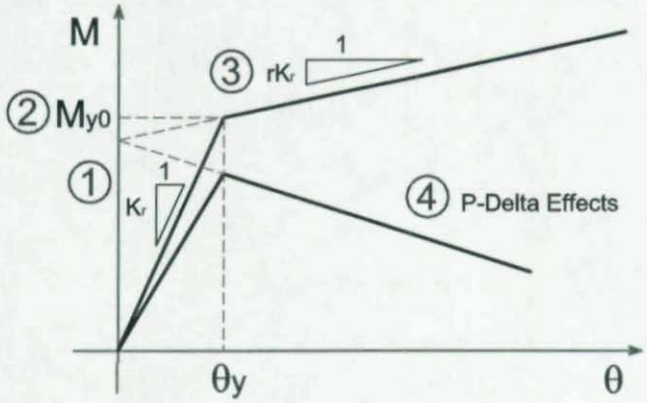

Figure 2 – OpenSees Model Parameters

The ranges of the first two parameters, stiffness and yield strength, were determined according to the Equivalent Lateral Force (ELF) method as prescribed by the 2000 NEHRP Provisions (FEMA 2000). The ELF method was used because it allowed for a relatively quick determination of structural parameters without having to perform many calculations. The third and fourth parameters were merely chosen such that the ranges would mirror realistic structures.

Earthquake parameters were also varied. Eight earthquakes were used and various lateral and vertical scale factors were also used. The

earthquakes, along with pertinent information about them, are listed in Table 1. Table 2 summarizes the structural parameters used in the study. Each of the structural parameter combinations and earthquake combinations used in the parameter study were analyzed once excluding vertical accelerations and once including vertical accelerations. Including all parameters, the total number of ground motion and model combinations used in the analyses was 8 x 7 x 7 x 6 x 5 x 6 x 2 = 141,120. As one might imagine, this generated a significant amount of data. As such, only a few representative figures are presented in this article.

Table 1 – Earthquakes Used for the Parameter Study

Earthquake	PGA (g)		Duration (sec)	Mag	Soil
	Horz	Vert			
1 Aquaba Egypt	0.097	0.109	60	7.1	-
2 Cape Mend., CA	0.590	0.163	36	7.2	D
3 Chalfant Valley, CA	0.177	0.127	40	6.2	D
4 Kern County, CA	0.156	0.107	54	7.4	D
5 Hollister, CA	0.114	0.172	40	5.4	D
6 Izmit, Turkey	0.152	0.146	30	7.4	A
7 Kobe, Japan	0.251	0.156	41	6.9	E
8 Tabas, Iran	0.328	0.183	24	7.4	B

Table 2 – Summary of Structural Parameters

Period (sec)	Yield %W	Post Yield Stiffness Ratio	Stability Ratio	Lateral Scale*	Vertical Multiplier*	Vertical Included
0.705	3	0	0.04	0.1	1.5	Yes
0.903	6	.05	0.08	0.2	2.0	No
1.093	9	0.1	0.12	0.3	2.5	
1.278	12	0.15	0.16	0.4		
1.459	16.5	0.20	0.20			
1.635	22.5	0.25				
1.808	28.5					

*Six combinations of lateral scale and vertical multiplier were used

SDOF PARAMETER STUDY RESULTS

Before describing the results of the study, it is important to define a quantity that proved to be useful in predicting potential collapse parameter combinations. As is turned out, the most important factor for determining whether a model would collapse or remain stable was the relationship between ductility demand and the post yield stiffness ratio augmented by P-Delta effects (r_p). The r_p factor is essentially the factor that the elastic stiffness K_r must be multiplied by to get the secondary stiffness of the model including P-Delta effects, that is the lower line of Fig. 2. A derivation of the r_p value may be found in Spears (2003). It is given as

$$r_p = \frac{r - Q}{1 - Q} \tag{1}$$

Figures 3 and 4 are graphs which show the changes in ductility demands that resulted from including vertical accelerations.

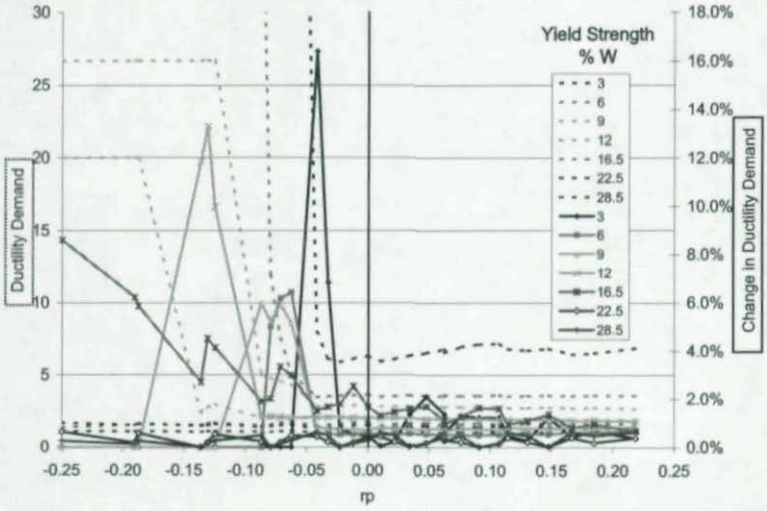

Figure 3 –, Change in Ductility Demand Due to the Inclusion of Vertical Accelerations (T= 1.459 s, EQ6, Lateral Scale = 0.2 g)

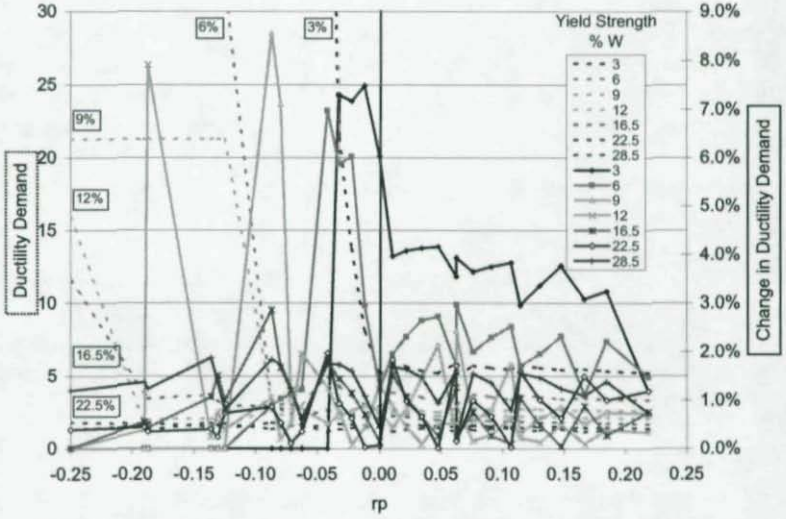

Figure 4 –Change in Ductility Demand Due to the Inclusion of Vertical Accelerations (T= 1.635 s, EQ7, Lateral Scale = 0.4 g)

In Figures 3 and 4, there are two vertical axes corresponding to two different sets of data. The vertical axis at the left of each figure is the ductility demand of the structures. The title of this axis has been boxed with a dashed line to indicate that it applies to the data that also has dashed lines. The thin dashed line data represents the maximum ductility demands excluding vertical accelerations. The legend shown within the figure lists the yield strength of the structure, as a percentage of the weight of the structure. Notice that r_p is plotted on the horizontal axis and that there is a point, if moving from the right to the left (towards more negative r_p), where the ductility demands increases rapidly, indicating collapse.

The axis on the right of the figure plots the change in ductility demand that comes from adding vertical accelerations. The title for this axis is boxed with a heavy solid line to indicate that it applies to the data represented with heavy solid lines. It is important to note that the

absolute value of the change in ductility demand has been plotted in the Figs. 3 and 4. This is because it is impossible beforehand to know whether vertical accelerations will increase or decrease lateral displacements, and if a structure shows sensitivity to vertical accelerations, then it is possible that vertical accelerations would be detrimental to particular structures subjected to particular earthquakes. As will be shown later, vertical accelerations increased the lateral displacements about half the time and about half the time it decreased them.

Notice that Figs. 3 and 4 represent an entire set of data for a model with a given period of vibration subjected to particular earthquake with a given intensity. The sets of data in each figure were then subdivided in yield forces or design base shears. Each line in Figs. 3 and 4 represents a yield moment for a corresponding yield force found in Table 2. The lower yield moments correspond to lower yield force percentages and vise versa.

Figures 3 and 4 were chosen as a representative sample of all of the parameter study data. Several observations can be made from the data created. First, given a particular structure with a given period and yield force, subjected to a particular earthquake, vertical accelerations did not significantly affect the lateral displacements until the r_p values were reduced to a particular level. For the purposes of this discussion, if the change in ductility demand was greater than about five percent, then it will be considered significant. In both the figures above, a spike in the change in ductility demand curves, if there was a spike, occurred in the negative r_p range just before collapse. Secondly, when the vertical accelerations did significantly affect the lateral displacements, it was generally not by more than about ten percent. There were a few cases where the change in ductility demands was much greater, but that was not the norm. Third, it seems that the increase in lateral displacements is only dependent on the r_p value near the point of collapse. The individual earthquakes did not have much effect on overall lateral displacement increases due to vertical accelerations. Also, the lateral scale did not influence the amount of change that vertical accelerations caused. In Fig. 3, the models were subjected to earthquake six at a

lateral PGA scale of 0.2g and the average ductility demand increases caused by vertical accelerations were around ten or twelve percent, which is relatively close to the results from the other figures which had PGAs of 0.4 g. From the data of this study, it would seem that vertical accelerations do not significantly affect the lateral displacements unless the combination of structural and earthquake parameters was inherently unstable. Even then, the change in lateral displacements due to vertical accelerations was on average around ten percent.

While the change in lateral displacements was relatively small, a small change could be enough to cause collapse in a building. The additional ductility demand may be just enough to fracture a critical steel connection or crush the concrete at a critical joint. To address this possibility, another set of figures was created that defined collapse as an increase in ductility demand greater than a specified value. Moreover, in the same figures, a structure was considered "saved" if the ductility demands decreased by a specified amount. In the figures, the number of collapses was plotted in the positive direction and the number of saves was plotted in the negative direction. This was done merely to create a visually distinguishing effect for the collapses and saves. Furthermore, three changes in ductility demand values were used to determine collapses and saves, 0.5, 1.0, and 2.0. A representative plot of the aforementioned collapse criteria is shown in Figure 5.

One thing to keep in mind about the collapse and save figures is that the total numbers of collapses and saves represent 1470 analyses. Thus, if 20 collapses occurred for a given set of models, then 1.4 percent of the models in the set would have collapsed. This is not said to minimize the potential hazards of vertical accelerations, but to provide some perspective for the data shown in the figures.

Also, each collapse or save category considers the entire set of data. As one might expect, there are fewer models in each category as the absolute value of the ductility demand range is increased. For example, when the change in ductility demand was greater than 0.5, 11 models of 1470 fell into that category. However, when the change in ductility

demand was increased to greater than 1.0, only 5 models of 1470 fell into that category.

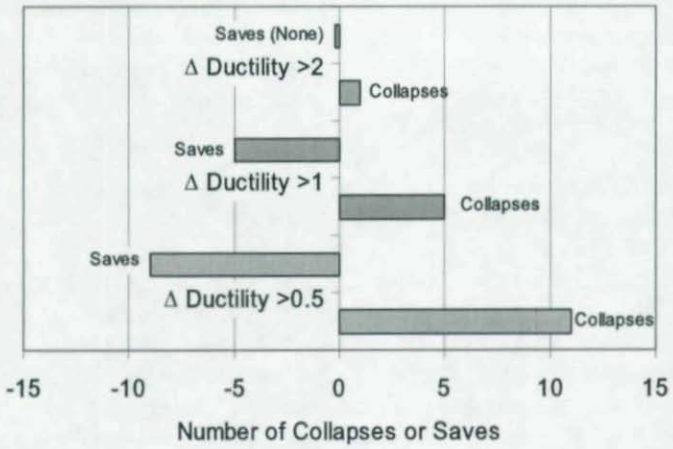

Figure 5 – Collapses and Saves Due to the Inclusion of Vertical Accelerations for the Set of Models Subjected to EQ 3 with a Lateral Scale of 0.2 g and a Vertical Multiplier of 2.5.

From Fig. 5, it is clear that vertical accelerations would both cause structures to collapse as well as save structures from collapse in the sets of data considered. However, the numbers of collapses and saves varies from earthquake to earthquake. This is why it was said earlier that it is impossible to predict beforehand the effects that vertical accelerations will have on a particular structure. There are too many factors that influence whether or not a structure's response will be altered by such accelerations. While it may not be clear before an analysis if the inclusion of vertical accelerations will cause a structure to collapse or be saved, it is clear that increasing the vertical acceleration magnitudes increases the probability that a collapse or save could occur.

An important point to make about the effect of vertical accelerations on maximum displacements is that structures should ideally be designed so that they would not come close to the point of collapse. Consequently, a well-designed structure should rarely, and possibly never, be significantly affected by vertical accelerations. This assumes, however, that the hazards and risks of a given region are known exactly and that there are no shortcomings in the current design philosophies. While the hazards and risks may be known with a fairly high degree of certainty in the Western United States (WUS) and the current design philosophies have been incrementally improved with each new earthquake, the same cannot be said about structures in the Central and Eastern United States (CEUS). There is much more uncertainty regarding the definition of a well designed CEUS structure.

Furthermore, the above statements have been based on SDOF models with bilinear stiffness. The results may be very different for MDOF models incorporating degrading strength and stiffness.

In addition to including vertical accelerations, several sets of models were analyzed for varying vertical earthquake scales. Recall from Table 2 that multipliers ranging from 1.5 to 2.5 were used to scale the vertical accelerations. In Figures 6 through 8, the effect of increasing vertical multipliers on lateral displacement is seen. All three of the figures involve earthquake three, which had an unscaled vertical PGA of 0.127 g. After multiplying the vertical PGA by 1.5, 2.0, and 2.5, the resulting values were 0.191, 0.254, and 0.318, respectively.

Notice that in all three of the figures, the maximum values increase as the vertical accelerations increase. Also notice, though, that as the vertical accelerations increase from 0.191 g to 0.318 g the change in ductility demand increases from an average of about six percent to an average of about ten percent. Thus, while the ductility demands increase by about 50 percent, the values are still relatively small whereas the vertical ground motion has increased significantly in magnitude.

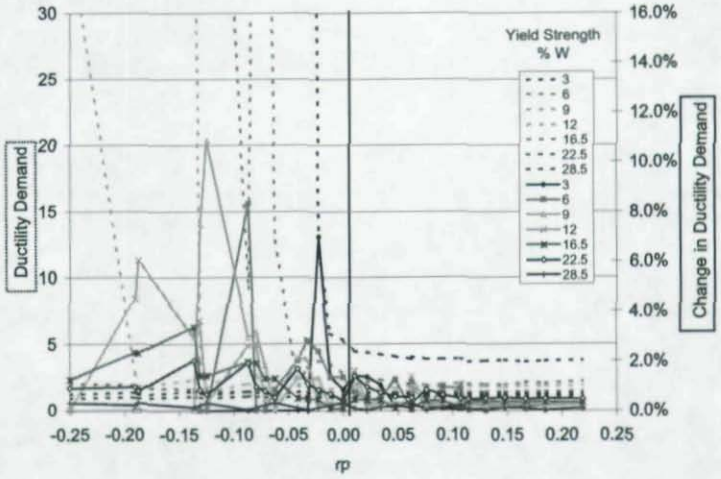

Figure 6 –Change in Ductility Demand Due to the Inclusion of Vertical Accelerations (T= 1.093s, EQ3, LS = 0.2 g, VM = 1.5)

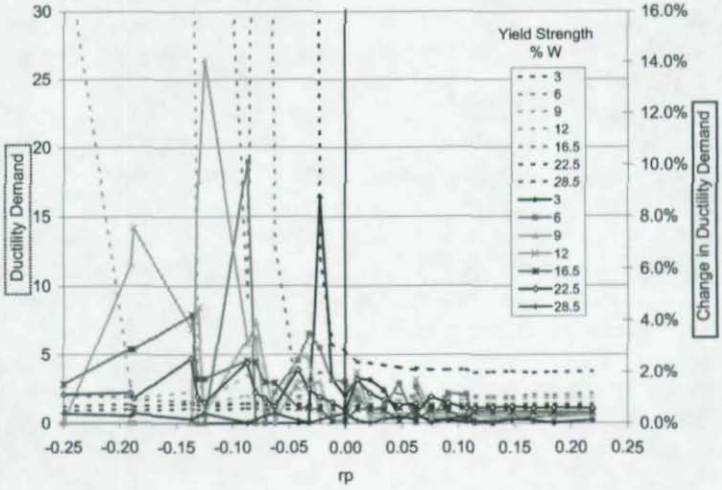

Figure 7 –Change in Ductility Demand Due to the Inclusion of Vertical Accelerations (T= 1.093s, EQ3, LS = 0.2 g, VM = 2.0)

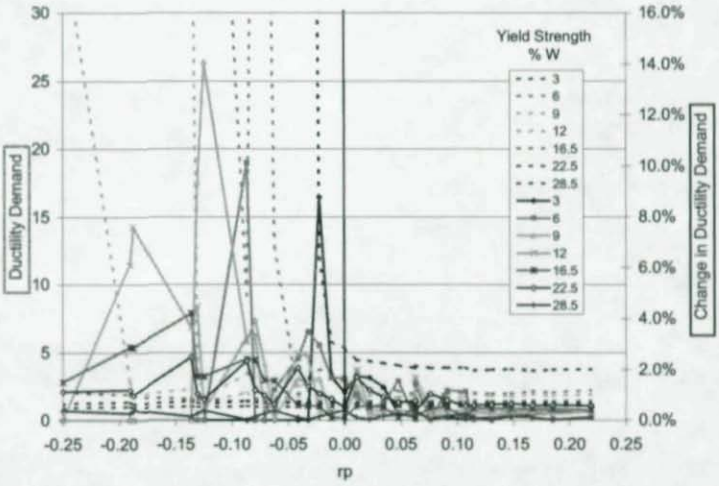

Figure 8 –Change in Ductility Demand Due to the Inclusion of Vertical Accelerations (T=1.093s, EQ3, LS = 0.2 g, VM = 2.5)

CONCLUSIONS AND NEEDS FOR FUTURE RESEARCH

Vertical accelerations typically did not significantly influence lateral displacements except for certain combinations of structural parameters and earthquake parameters. From this study, it seems that the vertical accelerations could likely increase or decrease the maximum lateral displacements by approximately 10 percent if the structure's ductility demand were close to the combination of ductility demand and r_p that would result in collapse for model with a given period and yield force subjected to a given earthquake without vertical accelerations. The 10 percent increase is, however, approximate. There were many models in the study that were never influenced by vertical accelerations and several where the vertical accelerations changed lateral displacements by up to 60 percent. It is important to note that the intensity of the

vertical accelerations influenced the amount of change in lateral displacements for those structures affected by them. As the vertical intensity increased, the change in lateral displacements generally increased.

This study may be particularly applicable to CEUS structures. As mentioned earlier, WUS structures have been incrementally improved with each new earthquake. This is not the case with CEUS structures. Also, there have been enough earthquakes in the WUS to speculate what sorts of earthquakes might occur in the future. Since no major earthquake has occurred in the CEUS for over a century, and since ground motion records are not available for these earthquakes, the characteristics of large CEUS earthquakes are not clear. Thus, it is the authors' opinion that considerable time be invested in both determining relevant ground motions for the CEUS and scrutinizing the current design codes to determine if it is possible to design a code compliant structure that would have a propensity to collapse. It would also be beneficial to scrutinize the previous design codes to determine if those structures would be inclined to collapse.

This study should also be expanded to MDOF models with degrading strength and stiffness to gain further insight into the influence of vertical accelerations on realistic structures. A variety of systems should be investigated under this study, with particular attention paid to the design basis (level of ductility as indicated by code implied R factor) supplied by the system. It is also critical that expected levels of over-strength be investigated as this parameter is expected to have a large influence on dynamic stability. Finally, it is recommended that the study explicitly include uncertainties in the analysis. This may be done both deterministically and probabilistically, with the former being used to provide physical insight into the effect of uncertainty on computed response, and the latter to quantify the effects into meaningful terms.

REFERENCES

Abrahamson, N. A., and Litehiser, J. J. (1989). Attenuation of Vertical Peak Acceleration. *Bulletin of the Seismological Society of America* 79:3, 549-567.

Amirbekian, R. V., and Bolt, B. A. (1998). Spectral Comparison of Vertical and Horizontal Seismic Strong Ground Motions in Alluvial Basins. *Earthquake Spectra*, 14:4, 573-595.

Anderson, J. C. and Bertero, V. V. (1973). Effects of Gravity Loads and Vertical Ground Acceleration on the Seismic Response of Multistory Frames. *5th World Conference on Earthquake Engineering, Rome*, Proceedings, 2914-2923.

Ariaratnam, S. T. and Leung, K. C. K. (1990). Parametric Effect of Vertical Ground Accelerations on the Earthquake Response of Elastic Structures. *Canadian Journal of Civil Engineering* 17, 209-217.

Bozorgnia, Y., Mansour N., and Campbell, K. W. (1995). Characteristics of Free-Field Vertical Ground Motion during the Northridge Earthquake. *Earthquake Spectra* 11:4, 515-525.

Como, M., De Stefano, M., and Ramasco, R. (2003). Effects of Column Axial Force – Bending Moment Interaction on Inelastic Seismic Response of Steel Frames. *Earthquake Engineering and Structural Dynamics* 32:12, 1833-1852.

Federal Emergency Management Agency (2000). *NEHRP Recommended Provisions for Seismic Regualtions for New Buildings and Other Structures.*

Hart, G. C., et al. (1995). Influence of Vertical Ground Motion on Special Moment-Resisting Frames. *SAC Technical Report 95-05*, 3:1-52.

Higazy, E. M., Elnashai, M., Amr, S., and Agbabian, M. S. (1996). Behavior of Beam-Column Connections Under Axial Column Tension. *ASCE Journal of Structural Engineering* 122:5, 501-511.

Hjelmstad, K. D., and Williamson, E. B. (1998). Dynamic Stability of Structural Systems Subjected to Base Excitation. *Engineering Structures* 20:4-6, 425-432.

Iyengar, R. N., and Shinozuka, M. (1972). Effect of Self-Weight and Vertical Acceleration on the Behavior of Tall Structures During Earthquake. *Earthquake Engineering and Structural Dynamics* 1, 69-78.

Jennings, P. C., and Husid, R. (1968). Collapse of Yielding Structures Under Earthquakes. *Journal of Engineering Mechanics* 94:5, 1045-1065.

Lin, Y. K., and Shih, T. (1980). Column Response to Horizontal-Vertical Earthquakes. *Journal of the Engineering Mechanics Division*, ASCE 106:EM6, 1099-1109.

Maison, B. F., and Kasai, K. (1997). Analysis of Northridge damaged thirteen-story WSMF building. *Earthquake Spectra* 13:3, 451-473.

Saadeghvaziri, M. A. (1988). Inelastic Response of R/C Bridges Under Horizontal and Vertical Earthquake Motions. Ph. D. Dissertation, University of Illinois at Urbana-Champaign, 1988

Saadeghvaziri, M. A., and Foutch, D. A. (1991). Dynamic Behavior of R/C Highway Bridges Under the Combined Effect of Vertical and Horizontal Earthquake Motions. *Earthquake Engineering and Structural Dynamics* 20, 535-549.

Shih, T.-Y., and Lin, Y. K. (1982). Vertical Seismic Load Effect on Hysteretic Columns. *Journal of the Engineering Mechanics Division*, ASCE 108:EM2, 242-254.

Spears, Paul (2003). Parameters Influencing Seismic Structural Collapse with Emphasis on Vertical Accelerations and the Possible Related Risks for New and Existing Structures in the Central and Eastern United States. Masters Thesis, Virginia Polytechnic Institute and State University, 2003.

Takizawa, H., and Jennings, P. C. (1980). Collapse of A Model for Ductile Reinforced Concrete Frames Under Extreme Earthquake Motions. *Earthquake Engineering and Structural Dynamics*, 8, 117-144.

FLANGE AND WEB LIMIT STATES UNDER PATCH LOADING

Gokhan Pekcan[1], *Lyle Carden*[2], *Ahmad Itani*[3]

Field observations during bridge construction revealed that some of the falsework cap and sill beams exhibited excessive flange bending under post loading. This observed vulnerability, if not detected and inhibited, may cause the instability of the post allowing it to slide laterally and lose support, thus leading to catastrophic collapse. This possibility of failure is not directly addressed in guidelines for temporary construction such as the Caltrans Falsework Manual. In addition, the AISC steel manual and other specifications do not consider patch loading from a timber post on steel beams, and past research in this area is sparse. Therefore, an experimental and analytical study was completed to investigate the interaction between timber and steel posts, and various beam sections subjected to concentric and eccentric patch loads. The limit states were identified and equations developed. It is noted that permanent web stiffeners are not typically used for temporary construction, however, where flange bending can be expected in the cap and sill beams, timber blocking placed inside the flanges at the location of the patch loading may be effective for increasing the flange capacity. Ultimately, the stability of the falsework can be maintained by preventing local failures.

---

[1] Asst Prof., University of Nevada, Reno, Dept. of Civil and Environmental Eng., MS258, Reno, NV 8955.

[2] Professional Eng., Martin & Chock, Inc., 1132 Bishop St., Suite 1550, Honolulu, HI 96813, (formerly Post-Doctoral Researcher – University of Nevada, Reno, Dept. of Civil and Environmental Eng.)

[3] Assoc. Prof., University of Nevada, Reno, Dept. of Civil and Environmental Eng., MS258, Reno, NV 89557.

INTRODUCTION

Falsework used in the construction of cast-in-place box girder bridges typically consists of: timber or concrete foundation pads; timber corbels, sand jacks and wedges; steel sill and cap beams; timber or round hollow steel posts; steel stringer beams and timber joists. Lateral stability is provided using timber elements or cable braces. Recent field observations revealed localized bending in some of the beam flanges, at the interface between the cap and sill beams and posts (Fig. 1) leading to catastrophic falsework collapses. In such applications, the flange local bending capacity due to patch loading from timber or steel post is not generally checked. Moreover, various limit states of web deformations are likely in certain conditions.

The AISC LRFD specification [1] recommends procedures for the evaluation of various limit states associated with beam flange and web deformations. Accordingly, flange local bending capacity is based on a yield line analysis from which a tensile load and uniform stress distribution is assumed [2]. However, the recommended equation may be very conservative if applied to flange bending due to compressive patch loading, as the region of flange available to resist the load would be greater for a patch load than a line load, and compression load allows large stresses around the web. Past studies [3-7] have generally assumed *rigid* patch loads which have not resulted in flange bending other than that required for the deformation of the web. A rigid patch load is defined as when the load is applied through a rigid element, thus deformations occur mostly in the loaded member and the stresses from the patch load change significantly as the loaded member deforms. This is in contrast to a *flexible* patch load, in which the patch load is able to "deform" as the loaded member deforms, resulting in a more uniform distribution of applied stresses.

Two possible limit states associated with web deformations due to patch loading are identified as; 1) local web yielding that governs for stocky webs [8], and 2) web crippling that governs for more slender webs [5]. Chen and Newlin [9] developed an expression for the localized buckling of webs for an equal and opposite concentrated load

applied to both edges of the web. As with the equation developed for flange bending, this equation is expected to be conservative for an applied patch loading, where the area of web involved in resisting the load is considerably greater than that for concentrated loads. The buckling equation developed by these researchers assumes that both flanges are restrained from lateral deformation. If there are no stiffeners along a beam, sidesway buckling of the web with lateral deformation of one of the flanges may be possible.

It is noted that the condition of a flexible patch load due to a timber post, as found in bridge falsework, has not been considered. Therefore, there is no method available for predicting accurately the resulting capacity of the beam sections. Hence, the objectives of this paper are to investigate the critical flange and web limit states, assess the effectiveness of existing equations and, where necessary develop new equations that can be used to predict the ultimate load for the various limit states, with experimental and analytical verification.

FLANGE LOCAL BENDING LIMIT STATE

From a yield line solution by Graham et al. [2], beam-column connection capacity, R_n, associated with the column flange subjected to tensile line loads from the adjoining beam flanges is given by [1],

$$R_n = 6.25 t_f^{\,2} F_{yf} \tag{1}$$

where t_f = thickness of the flange and F_{yf} = minimum specified yield stress of the flange. A similar mechanism to that used in developing (1) can be used to calculate the ultimate load for flange local bending due to a patch load,

$$R_f = \beta t_f^{\,2} F_{yf} \tag{2}$$

in which β is determined from a yield line analysis. Assuming a patch load with dimensions, b_p and d_p, as well as the yield line pattern and uniform pressure, as shown in Fig. 2,

$$\beta = \frac{b_p b_{feff}}{2 b_{peff}^{\,2}} \left(\frac{d_p}{b_{feff}} + \frac{4}{\sin 2\theta} + \frac{2}{\tan \theta} \right) \tag{3}$$

where θ = angle of the yield line, b_{feff} = effective width of the flange, and b_{peff} = effective width of the post (Fig. 2) given by,

$$b_{feff} = \frac{b_f}{2} - k_1 - \frac{t_f}{2} \quad \text{and} \quad b_{peff} = \frac{b_p}{2} - k_1 - \frac{t_f}{2} \tag{4}$$

in which k_1 = distance from the center of the web to the edge of the fillet and b_f = width of the flange.

The expression for β can be minimized with respect to θ at 55°. However, assuming θ=45° gives a result for the last two terms of (3) that is within 6% of the minimum value, allowing (3) to simplify to

$$\beta = \frac{b_p b_{feff}}{2 b_{peff}^2} \left(\frac{d_p}{b_{feff}} + 6 \right) \tag{5}$$

It is noted that if d_p tends to zero, as for a line load, b_p is equal to b_f and therefore b_{peff} is equal to b_{feff}, and b_{feff} is assumed to be 0.96 b_f/2, then β simplifies to 6.25 as in (1). For typical falsework applications, where nominal 12x12 in. (b_p and d_p) posts are used, the β values range from 10.9 to 18.1, which are all greater than 6.25 as expected due to the finite width of the post instead of the line load assumed in (1).

It is noted that a uniform stress distribution in the post may be unrealistic for many beams, particularly those with smaller flanges, as stresses are concentrated at the web of the beam. Therefore, an alternative expression for β is developed for a triangular stress distribution (Fig. 3b),

$$\beta = \frac{3 b_p^2 b_{feff}}{8 b_{peff}^3} \left(\frac{d_p}{b_{feff}} + 6 \right) \tag{6}$$

The β values for the different beam sizes assuming a triangular stress distribution, however, range from 20.1 to 41.9, indicating an ultimate load that is approximately twice that for the assumed rectangular distribution. It is expected that for the heavier sections a rectangular distribution is most appropriate as the flanges will deflect a relatively small amount allowing the stresses to be uniformly distributed in the post, while for the lighter sections the flanges will deflect a greater amount leading to triangular stress distribution. Both for heavier

sections with uniform and lighter sections with triangular stress distribution, β converges to a value of between 18 and 20.

Post Compression Strength

The strength of a timber post in compression is defined based on NDS-LRFD specifications [10]. In the beam-post bearing joint region, the nominal compressive strength, P_p, is considered over a short length of the post,

$$P_p = F_c' A_p \tag{7}$$

where A_p = nominal cross sectional area of the post and F_c' = nominal stress in the post after modification factors are applied for moisture content, temperature, size, preservative treatment, fire-retardant treatment and column stability [10]. Because the compression capacity is considered over a short length, the column stability factor in this calculation is equal to 1.0. It is noted that stability of the full length of the column should be considered as a separate limit state in the design of the post. The axial capacity of a steel post in the bearing region can be calculated as defined in the AISC specifications for a short length column [1].

Flange-Post Interaction

The force at which bending occurs in the beam flange is related to that for crushing of the post where in contact with the beam. The flange will not bend unless the post deforms to accommodate the bending and, conversely, the compression strength of the post will be reduced, if flange bending occurs. Therefore, it is helpful to consider an interaction between the flange bending and post crushing limit states. While a number of interaction equations have been proposed for different applications, for the interaction between post crushing and flange bending an elliptical relationship is assumed,

$$\left(P_u / R_f\right)^2 + \left(P_u / P_p\right)^2 \leq 1 \tag{8}$$

where P_u = applied axial load in the post.

Effective Post Bearing Area

An alternative model for calculating the ultimate load governed by the post capacity is introduced. For this model, an effective cross sectional area of the post is considered to carry the entire axial load (Fig. 4). The

effective area of the post is determined by the width of the post that is effective in carrying the load multiplied by the thickness of the post within this width (Fig. 4). The capacity of a timber post,

$$P_p = (\alpha t_f + 2k_1)t_p F_c^* \tag{9}$$

where α = constant which depends on the slope of the stress gradient assumed through the flange, which is determined based on the experimental data and finite element analysis, F_c^* = nominal compressive stress perpendicular to the grain. A similar equation for the capacity of a steel post is given by,

$$P_p = (\alpha(t_f + t_{bp}) + 2k_1)2t_p F_y \tag{10}$$

where t_{bp} = thickness of the base plate of the post, and t_p = wall thickness of the round hollow steel section. The $(2t_p)$ allows for the transfer of axial load on two sides of the round hollow steel section.

WEB LIMIT STATES

Web Yielding and Crippling

The critical web limit states in bearing joint regions are due to web yielding and crippling. The ultimate capacity of the web associated with the web yielding limit state, P_w, due to loading from a timber post can be derived as

$$P_w = (\alpha k + t_p)F_{yw}t_w \tag{11}$$

where k = distance from the outer face of the flange to the toe of the web (Fig. 5a) and t_w = thickness of the web. Based on the Caltrans Falsework Manual [12], $\alpha = 2$ for a 1:1 stress gradient. However, based on the AISC specifications, $\alpha = 5$ for an assumed 2.5:1 stress gradient through the flange and toe of the web. This value is investigated using finite element analyses. A similar equation when the load is due to a steel post bearing is given by

$$P_w = 2(\alpha(k + t_{bp}) + t_p)F_{yw}t_w \tag{12}$$

where in this case, t_p = wall thickness of the round hollow steel section (Fig. 5b). The AISC specifications [1] also specify equations for web crippling. However, the application of these equations to the typical beams used in bridge falsework with relatively thick webs, results

consistently in web crippling loads that are larger than the web yielding loads, therefore the web crippling equations are not discussed in this paper.

Lateral Web Buckling

In a typical bridge falsework, particularly sill beams are generally not braced, therefore there is a possibility that the flanges loaded with the timber or steel posts could displace due to sideways buckling of the web over a long length. The web of a beam can be treated as a column assuming that the effective length of the beam is equal to the tributary length associated with each post, approximately equal to the spacing of the posts. Based on AISC specifications [1], the capacity of the web of a beam, P_w, can be determined from

$$P_w = t_w l_{eff} F_{cr} \tag{13a}$$

where l_{eff} = effective tributary length of beam for a particular post and $F_{cr} = 0.877F_e$, in which F_e is the Euler buckling load

$$F_e = \pi^2 E / (Kh/r)^2 \tag{13b}$$

where E = elastic modulus, K = effective length factor, which will range between 1.2 and 2.1 for a member that the is free to deflect laterally at one end, h = clear height of the web less the fillet radius and r = radius of gyration for the web. This assumes that the web is slender for compression buckling such that $F_e < 0.44F_y$, which will be the case for the web of almost all beam sections. For typical beams used in bridge falsework with a relatively thick web, web buckling is unlikely to govern the design. However, for double stacked beams that are commonly used, h in (13b) will be effectively $2h$, resulting in the reduction of F_e by a factor of 4. In this case even beams with relative heavy webs will become susceptible to lateral web buckling.

EFFECT OF BLOCKING

Falsework design typically avoids the use of stiffeners as beams are reused and construction is temporary. However, in some cases timber blocking is placed between the flanges in an attempt to stiffen the beam flange. Generally, timber blocks sized between 4x4 in and 6x8 in are

used, the capacity of which can be calculated based on the axial compression capacity of a short timber member. However, experimental and analytical studies showed that the full capacity of the blocking may not be realized. Therefore, the capacity of timber blocking, P_b, may be more accurately represented by

$$P_b = \gamma F_c' A_b \tag{14}$$

where γ = blocking effectiveness factor, and A_b = combined cross sectional area of the blocking on both sides of the web.

EXPERIMENTAL INVESTIGATION

A total of 32 subassemblies of three different beam sizes (ASTM A572Gr50 HP12x53 and HP14x73 beams, and ASTM A992 W14x90), timber and steel posts were tested in various configurations to investigate the response characteristics and limit states. Typically, the flanges were restrained at the ends of the 48 in. long beam segments (Fig. 6). Monotonically increasing loads were applied to the end of the 48 in long timber or steel post through a slider which is in turn attached to a displacement controlled hydraulic actuator. Another configuration (Fig. 7a) was used to investigate the critical web limit states. In this configuration, a 12x12 in steel plate was used to apply a rigid patch load to induce web yielding, buckling and crippling without the impact of flange bending other than that required to engage the web (Fig. 7b). Finally, lateral restraints at the ends of the flanges were removed to allow potential lateral buckling of the beam segment (Fig. 7c). Corbels as well as timber blocking were used in some of the experiments. The effect of eccentric patch loading was also investigated by introducing eccentricities from 1/12th to 1/6th of the flange width. A brief discussion of experimental findings is given in what follows; a more detailed discussion can be found in [11].

Typical force-displacement curves are plotted in Figs 8 and 9. These figures show that the stiffness initially increased as any gaps due to lack of fit between the various components closes, after which the maximum stiffness is reached. The stiffness then starts to decrease as inelasticity develops in the member. The ultimate load was defined as

the load at which the stiffness dropped to 50% of the initial stiffness, where the initial stiffness was defined as that between 25% and 75% of the ultimate load (shown by dashed line). This definition of the ultimate load was consistent within 13% of the experimental observations; i.e. onset of yielding [11].

For the beams with timber posts, the capacity of the flange-post joint region was calculated using (2) and (8) (and (14) when blocking was used) with actual material strengths of post, blocking and steel obtained from component experiments. $\beta = 18$ was used in (2) to estimate the flange bending capacity. The timber blocking was assumed to be 100% effective, thus a $\gamma = 1.0$ was used in (14) and the effective blocking capacity was directly added to the flange bending capacity. The blocked or unblocked flange capacity was then combined with the timber post strength from (7) using (8). The experimental data show that there is a relatively small reduction in capacity when the post is eccentric to the centroid of the beam. Thus it is assumed that the above equations apply equally when there is an eccentricity less than the 1/6th of the width of the flange. The resulting calculated capacity of the flange-post region for the beams with timber posts is compared in Fig. 10a to the estimated ultimate force from the experimental data. The estimated forces are approximately equal to or less than the observed forces, at between 71% and 105% of that observed, for all members. The stagger in the observed capacities is mainly attributed to the variability of material properties, particularly for the timber members. The yielding observed in the beams, after considerable inelastic flange bending, was very similar to the yield pattern assumed in developing (2). Therefore, this method is deemed appropriate for predicting the capacity of the flange-post joint region with a timber post. The effective post bearing area method was used to estimate the capacity of the flange-post joint region with a steel post, based on (10). The observed failure mode in the experiments with the steel post was consistent with the effective bearing area assumed for calculating the ultimate load, with yielding and crippling of the post around where it was bearing onto the beam in line with the web. Unfortunately, the calculated ultimate load could not be directly compared to the experimental data as timber corbels were also used in experiments with

the steel posts and these affected the ultimate load of the system. Thus, finite element analyses were used for comparison with the calculated ultimate load for cases with steel posts [11].

A typical force-displacement curve for the W14x90 beam loaded concentrically with a rigid patch load and that for a beam loaded with a timber post both without lateral restraint is shown in Fig. 9. Once the entire section has yielded, the load starts to drop and is followed by lateral deformation in the web. Force-deformation response shown in Fig. 9 by solid line corresponds to a case with significant yielding of the web and then inelastic web crippling or buckling without lateral deformation of either flange (Fig. 7b). When lateral deformation of the flange occurs through lateral buckling of the web (Fig. 7c), the load dropped dramatically after reaching the maximum load (Fig. 9). Of the seven beams without lateral restraints buckling was observed in three of them at failure, while the other four resulted in post crushing and flange local bending failures. The expected capacity of the beams was calculated using (11) for the unblocked, laterally restrained beams and (13) for the unrestrained beams. For web yielding, $\alpha = 2$ was assumed in (11) and 1:1 stress gradient through the flange and fillet of the beam. For the beams resulting in lateral buckling an effective length factor of 1.7 was assumed in (13). Fig. 10b shows a comparison of the observed ultimate load from the experimental data and the calculated ultimate load. The calculated ultimate load in all cases is conservative compared to the observed ultimate load with the calculated load ranging between 65% and 98% of the observed load. For the HP12x53 and HP14x73 sections exhibiting web yielding, the calculated load was within 7% of the observed load. For the W14x90 section, the calculated ultimate load is up to 30% less than the observed load, with the larger difference attributed to the larger flange which provides a greater resistance to web yielding through flexure of the flange. It is noted that this condition is not considered in web yielding equation. Using $\alpha = 5$ as given in the AISC would result in unconservative calculated ultimate loads in each beam except for W14x90 beams. In reality, $\alpha = 4$ would be ideal, although the assumed value of 2 is conservative. The calculated ultimate loads using (13) are conservative for the concentrically loaded (both W14x90) beams but accurate for the

eccentrically loaded (HP14x73) beam that exhibited lateral buckling. The difference may be attributed to the sensitivity of (13) to the assumed effective length factor. Effective length factors of 1.48 and 1.37 respectively would result in calculated capacities identical to the observed ultimate load for the two concentrically loaded beams respectively. As the level of rotational fixity at the top of the beam is difficult to determine, assuming the more conservative value of 1.7 is appropriate.

FINITE ELEMENT ANALYSES

A series of nonlinear finite element models were developed using ABAQUS [13] and calibrated to the experimental data. These finite element models allowed a larger range of beams and configurations to be considered, without material variability affecting the results. Several beams used in these models were W12x26, W12x40, W12x53, W14x22, W14x30, W14x43, W14x61, W14x90, W14x132, HP12x53, HP14x73, HP14x89 and HP14x117. In general, the load obtained from the finite element analysis is between 76% and 121% of the experimental load, with an average of 98%. Therefore, there is good correlation between the experimental and finite element results, with the variability attributed primarily to the variability in the capacity of the different posts and blocking. Detailed description, configurations and discussions of the finite element analyses are presented in [11].

The calculated flange-timber post capacity based on the interaction equation (8) was between 80% and 105% of the capacity calculated from the finite element models. The calculated capacity based on the interaction equation was relatively accurate and generally conservative for all cases including those with timber blocking. Timber blocking was assumed 100% effective ($\gamma = 1$). With the steel posts, the ultimate capacity of the flange-post joint region is calculated using the effective bearing area method (10). As the stiffness of the post is greater than the stiffness of the blocking, the effectiveness of the blocking is reduced to 30% ($\gamma = 0.3$). While the blocking can be loaded further and the force carried by the joint continues to increase, significant flange bending

and post yielding occurs resulting in significant permanent deformations. The calculated capacity using the effective post bearing area and effective blocking capacity ((10) and (14)) and the finite element analyses is shown to be accurate and conservative, with calculated capacities between 81% and 105% of those from the finite element model. The use of a 30% effectiveness for the timber blocking gives a ratio of calculated to finite element capacity with the timber blocking relatively consistent to that without the timber blocking.

The calculated web yielding capacity was between 86 and 91% of the ultimate capacity from the finite element analysis. The larger beams, more typical of those used in falsework, were also modeled with blocking and eccentricity. The blocking was assumed to be 50% effective. The cases with blocking resulted in a calculated ultimate load of between 90 and 102% of the ultimate load from the finite element analyses. The beam capacity from the eccentrically loaded cases were almost identical to the concentric cases, confirming that with a rigid patch load an eccentricity has no significant effect. Assuming $\alpha = 5$, the ultimate load from finite element analysis, was unconservative by up to 19%. Therefore, $\alpha = 2$ is considered more appropriate. If the ultimate load was defined differently, i.e. closer to the maximum load in the beam, then the $\alpha = 5$ will become less unconservative and the load would be tolerable. However, a larger amount of permanent deformation would be observed which is undesirable in falsework construction practice.

The calculated web crippling capacity is generally greater than the ultimate load governed by the web yielding limit state for all but the smallest W12x26 and W14x22 beams. Even for these beams, use of the web yielding formula for calculating the ultimate web capacity is conservative. The comparisons indicate that, while crippling was observed in the beams, it generally occurs after yielding of the beams and can be considered a post-elastic limit state for the range of sections considered. In design, the safety factor applied to the web crippling limit state is generally greater than for web yielding, thus it may govern for the design of beams with thin webs, however not for the beams with thicker webs used in falsework.

Lateral buckling was observed in the W12x26, W12x40, W14x22, W14x30 and W14x43 beams. When two beams were stacked on top of each other, for the larger beams like those typically used in bridge falsework, lateral buckling was observed in the HP12x53, HP14x73 and W14x90 beams. The effect of post eccentricity is considered for the two beam sections most susceptible to buckling. It was found for both sections that for an eccentricity of 6 times the web thickness (36 mm), the ultimate load dropped by around 18% of the ultimate load for the concentrically loaded beams. As the drop in load was approximately linear, this corresponds to a 3% reduction in load for each multiple of web thickness of eccentricity. The analyses show that eccentricity does have an effect on the buckling capacity of the web and large eccentricities should be avoided.

DESIGN RECOMMENDATIONS

Design of Flange-Post Bearing Joint Regions

For a steel beam with a patch load from a timber post, the factored applied load in the post, P_u, should be less than a combination of flange bending capacity, including blocking, and the post compression capacity for a short length of post, such that

$$P_u < \left[\left(1/\phi R_{nf}{}^2\right) + \left(1/\phi P_{np}{}^2\right)\right]^{\frac{1}{2}} \tag{15a}$$

where ϕR_{nf} = design strength of the flange including blocking and ϕP_{np} = design strength of the post. The design strength of the flange, including blocking (when used) is given by

$$\phi R_{nf} = \phi_b 18 t_f{}^2 F_{yf} + \lambda \phi_c F_c{}' A_b \tag{15b}$$

where ϕ_b = resistance factor for flange bending, equal to 0.9 [1]; ϕ_c = resistance factor for compression in the blocking, also equal to 0.9 [10]; λ = time effect factor, equal to 1.0 for a typical falsework duration; t_f = thickness of the flange; F_{yf} = specified minimum yield stress of the beam flange; $F_c{}'$ = specified minimum compression stress of the timber blocking after applicable modification factors are applied [10] and A_b = cross sectional area of the blocking. The design strength of the post is

given by

$$\phi P_{np} = \phi_c F_c' A_p \tag{15c}$$

where ϕ_c = resistance factor for compression in the post (0.9); F_c' = specified minimum compression stress after modification factors are applied for a short length of the post [10] and A_p = cross sectional area of the post.

The design capacity of the flange-post bearing joint region with a steel post can be most accurately determined using the effective bearing area. The design of flange-post region should ensure that

$$P_u < \phi R_n \tag{16a}$$

where P_u = factored applied load and ϕR_n = design strength of the post in bearing, including the strength provided by blocking, and is given by

$$\phi R_n = \phi_{cp}(5(t_f + t_{bp}) + 2k_1)2t_p F_{yp} + \phi_{cb} 0.3F_c' A_b \tag{16b}$$

where ϕ_{cp} = resistance factor for compression in the post, which, to be consistent with that used for web yielding, should be equal to 1.0 [1]; ϕ_{cb} = resistance factor for the blocking (0.9); t_f = thickness of the beam flange, t_{bp} is equal to the thickness of the base plate for the steel post; k_1 = dimension from the center of the web of the edge of the beam fillet; F_{yp} = minimum specified yield stress in the post; t_p = thickness of the post wall and F_c' and A_b are as defined previously for the timber blocking.

Design of Beam Web in Beam-Post Connections

It was noted that the web yielding equation based on the AISC specifications [1] is adequate for calculating the capacity of a beam assuming that the beam is not susceptible to lateral buckling. Nonetheless, a modified stress gradient is proposed based on experimental and finite element analyses results. The effect of blocking can also be included to give a design capacity for the web, ϕP_n, based on LRFD specifications, given by

$$\phi P_n = \phi_y (2k + N) F_{yw} t_w + \lambda \phi_b (0.5 F_c' A_b) \tag{17}$$

where ϕ_y = 1.0 [1], λ = time effect factor, ϕ_b = 0.9

For 12 and 14 in deep beams, web crippling is unlikely to govern the

design, but for other sizes outside the range of those considered in this study, web crippling based on the AISC specifications should be considered. When no lateral bracing is used along the length of a beam associated with each post, the design strength for web buckling should be checked using the following,

$$\phi P_n = \phi_c t_w^2 l_{eff} F_{cr} \tag{18a}$$

where $\phi_c = 0.9$ (AISC 2005) and $F_{cr} = 0.877F_e$, and F_e is given by

$$F_e = \pi^2 E / (1.7h/r)^2 \tag{18b}$$

This equation assumes that $F_e < 0.44F_y$ for elastic buckling. If $F_e > 0.44F_y$ then lateral buckling of the web is unlikely to govern the response. It is also note that in order to prevent lateral buckling of the web, flange should be braced at the post locations.

SUMMARY AND CONCLUSIONS

Limit states that potentially control the design of beam-post joint regions, similar to those found in bridge falsework, were investigated both experimentally and analytically. The limit states considered are associated with: 1) beam flange bending; 2) post compression, for timber or steel posts; 3) an interaction between beam flange bending and post compression; 4) post bearing; 5) web yielding; 6) web crippling and 7) lateral web buckling. Accordingly, the critical limit states were found to be due to an interaction between flange bending and post compression, except for cases where beams were stacked on top of each other. Careful observations of the deformation and formation of yield lines suggested two alternative methods to calculate limiting loads. The first method focuses on flange bending capacity assuming both uniform and triangular stress distributions in the post. Based on the finite element analyses, this method with a constant β value of 18 is recommended for use in calculating the beam flange capacity with a timber post. The second method utilizes an effective bearing area to establish the capacity of the joint region and was more appropriate when applied patch load was due to steel post. This method assumes a similar mechanism to that for web yielding with a 2.5:1 stress gradient. The critical web limit state was due to web yielding. In

consideration of the different interactions between post and beam, 1:1 stress gradient was found to be most appropriate and conservative for a timber post, whereas 2.5:1 stress gradient characterized more accurately the joint capacity with a steel post in which yielding took place under each side of the steel post. As falsework beams are generally unbraced and unstiffened, instability of the web is possible. Lateral deformation of a beam flange through buckling of the web was observed in experimental studies and finite element analyses when no lateral bracing was provided. An equation for web buckling was also developed, which may govern in certain circumstances. An effective length factor of 1.7 is recommended for modeling a beam with a timber post that provides partial rotational restraint to the loaded flange of the beam. It was demonstrated that web crippling was unlikely to govern the design of a beam with a relatively thick web. Lateral web buckling, however, will not govern the design of single beams but may govern the design for double stacked beams.

The effect of eccentricity between the centroid of a rigid patch load and the centroid of a beam is negligible for web yielding and crippling. For beams loaded with a timber post that fail through lateral buckling of the web, an eccentricity reduces the ultimate capacity of the web by up to 3% for every unit of eccentricity multiplied by the thickness of the web. When blocking was used between the flanges of the beams, around 50% of the strength of blocking was found to be effective in increasing the web yielding and crippling capacity. Therefore, bracing should be used to prevent lateral buckling of a beam when necessary.

ACKNOWLEDGEMENTS

The authors would like to extend their gratitude to the California Department for Transportation for funding of this study under contract number 59A0445, with special thanks to John Lammers and Peter Lee for their assistance and direction.

REFERENCES

[1] American Institute of Steel Construction (AISC). Specification for Structural Steel Buildings. Chicago, IL: AISC; 2005.
[2] Graham JD, Sherbourne AN, Khabbaz RN. Welded Interior Beam-to-Column Connections. Report to American Institue of Steel Construction, Chicago, IL;1959.
[3] Roberts TM, Rockey KC. A Mechanism Solution for Predicting the Collapse Loads for Slender Plate Girders when Subjected to In-Plane Patch Loading. Proc Inst Civ Engrs 1979;67(2):155-175.
[4] Roberts TM, Markovic N. Stocky Plate Girders Subjected to Edge Loading. Proc Inst Civ Engrs 1983;75(2):539-550.
[5] Elgaaly M. Web Design Under Compressive Edge Loads. Engrg J 1983; 4th Quarter: 153-171.
[6] Roberts TM, Newark ACB. Strength of Webs Subjected to Compressive Edge Loading. J of Struct Engrg 1997;123(2):176-183.
[7] Graciano C, Edlund B. Failure Mechanism of Slender Girder Webs with a Longitudinal Stiffener under Patch Loading. J Construct Steel Res 2003;59:27-45.
[8] Galambos TV. Proposed Criteria for Load and Resistance Factor Design of Steel Building Structures. Research Report No. 45, Civil Engineering Department, Washington University, St Louis, MO; 1976.
[9] Chen WF, Newlin DE. Column Web Strength in Beam-to-Column Connections. J Struct Div 1973;99(ST9):1978-1984.
[10] American Forest and Paper Association (AFPA). Load and Resistance Factor Design – Manual for Engineered Wood Construction. AFPA: Washington, DC; 1996.
[11] Carden LP, Itani AM, Pekcan G,. Recommendations for the Design of Beams and Posts in Bridge Falsework. Center for Civil Engineering Earthquake Research Report CCEER 05-XX, University of Nevada - Reno, Reno, NV; 2005.
[12] California Department of Transportation (Caltrans). Falsework Manual (updated November 2001). Caltrans Structure Construction, Sacramento, CA; 2001.
[13] Hibbett, Karlson & Sorensen, Inc. ABAQUS – Finite Element Program. Hibbett, Karlson & Sorensen, Inc, Fremont, CA; 2003.

FIGURES

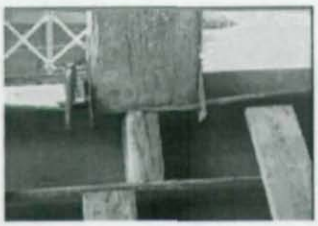

Fig. 1. Flange local bending in sill beam (courtesy of J. Lammers)

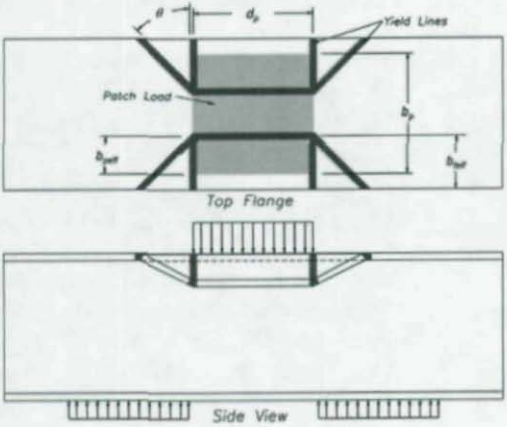

Fig. 2. Yield line pattern on beams for a patch loads

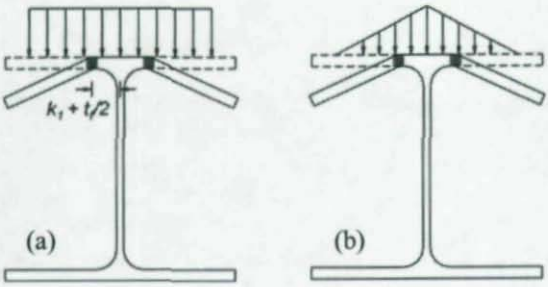

Fig. 3. Cross section of a beam for a patch load assuming (a) uniform and (b) triangular stress distribution

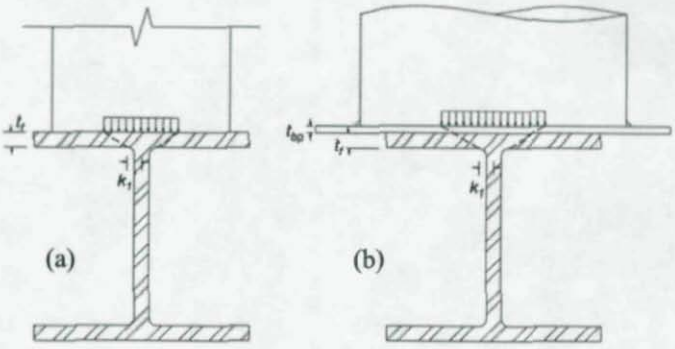

Fig. 4. Effective area of (a) timber and (b) steel posts

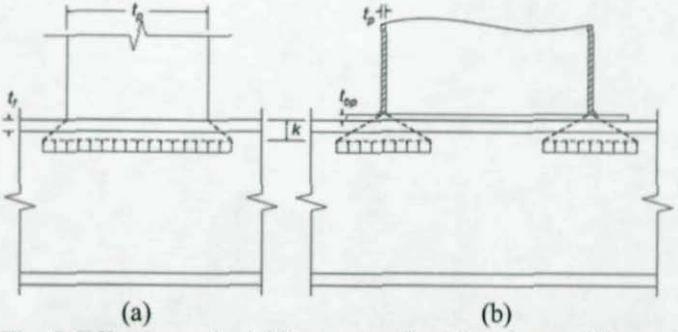

Fig. 5. Effective web yielding region for (a) timber and (b) steel posts

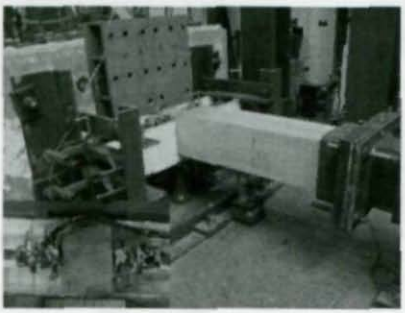

Fig. 6. Experimental setup

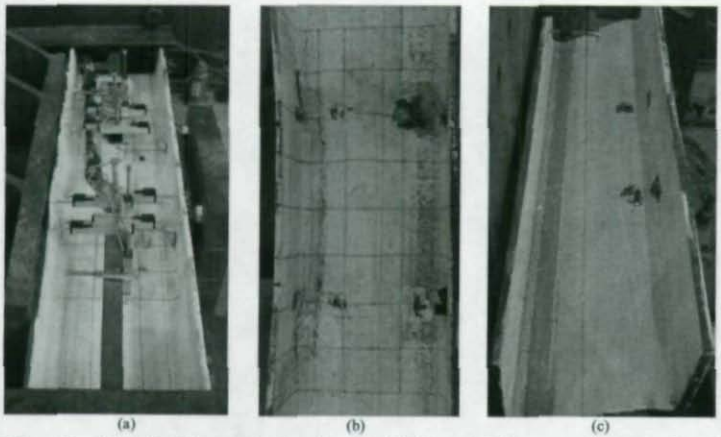

Fig. 7. (a) Rigid patch load, (b) Web yielding and post-elastic buckling, (c) Lateral buckling of the web (below)

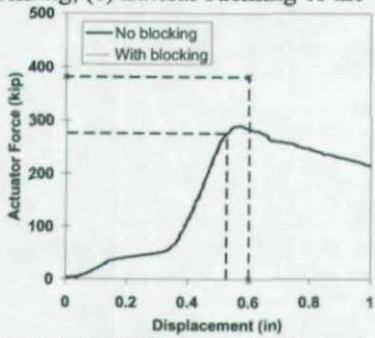

Fig. 8. HP14x73 beams (e=0)

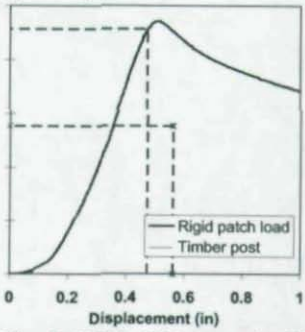

Fig. 9. W14x90 beams (e=0) - no lateral restraint

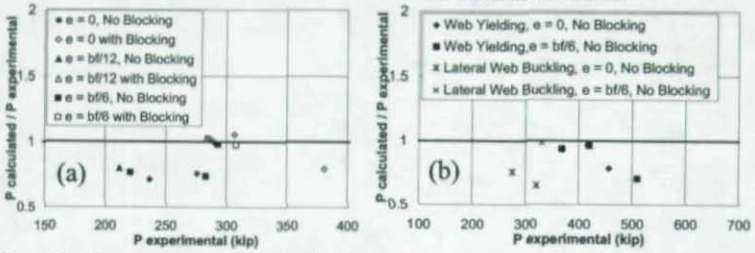

Fig. 10. Comparison of calculated ultimate force and experimental data